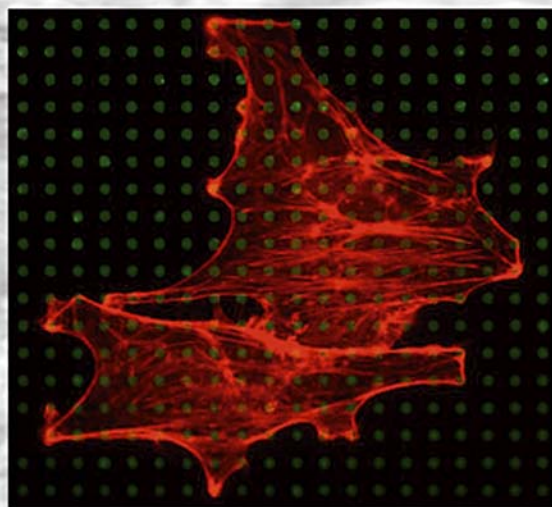




HEAT TRANSFER AND FLUID FLOW IN MINICHANNELS AND MICROCHANNELS



**S. KANDLIKAR S. GARIMELLA
D. LI S. COLIN M.R. KING**

HEAT TRANSFER AND FLUID FLOW IN MINICHANNELS AND MICROCHANNELS

Elsevier Internet Homepage

<http://www.elsevier.com>

Consult the Elsevier homepage for full catalogue information on all books, journals and electronic products and services

Elsevier Titles of Related Interest

INGHAM AND POP

Transport Phenomena in Porous Media III
2005; ISBN: 0080444903
www.elsevier.com/locate/isbn/0080449031

W. RODI AND M. MULAS

Engineering Turbulence Modelling and Experiments 6
2005; ISBN: 0080445446
www.elsevier.com/locate/isbn/0080445446

HARTNETT et al.

Advances in Heat Transfer Volume 38
2004; ISBN: 0120200384
www.elsevier.com/locate/isbn/0120200384

DONGQING LI

Electrokinetics in Microfluidics
2004; ISBN: 0120884445
www.elsevier.com/locate/isbn/0120884445

Related Journals

The following titles can all be found at: <http://www.sciencedirect.com>

Applied Thermal Engineering
Experimental Thermal and Fluid Science
Fluid Abstracts: Process Engineering
Fluid Dynamics Research
International Communications in Heat and Mass Transfer
International Journal of Heat and Fluid Flow
International Journal of Heat and Mass Transfer
International Journal of Multiphase Flow
International Journal of Refrigeration
International Journal of Thermal Sciences

To Contact the Publisher

Elsevier welcomes enquiries concerning publishing proposals: books, journal special issues, conference, proceedings, etc. All formats and media can be considered. Should you have a publishing proposal you wish to discuss, please contact, without obligation, the publishing editor responsible for Elsevier's Mechanical Engineering publishing programme:

Arno Schouwenburg
Senior Publishing Editor
Materials Science & Engineering
Elsevier Limited
The Boulevard, Langford Lane
Kidlington, Oxford
OX5 1GB, UK
Tel.: +44 1865 84 3879
Fax: +44 1865 84 3987
E-mail: a.schouwenburg@elsevier.com

General enquiries including placing orders, should be directed to Elsevier's Regional Sales Offices – please access the Elsevier internet homepage for full contact details.

HEAT TRANSFER AND FLUID FLOW IN MINICHANNELS AND MICROCHANNELS

Contributing Authors

Satish G. Kandlikar

(Editor and Contributing Author)
Mechanical Engineering Department
Rochester Institute of Technology, NY, USA

Srinivas Garimella

George W. Woodruff School of Mechanical Engineering
Georgia Institute of Technology, Atlanta, USA

Dongqing Li

Department of Mechanical and Industrial Engineering
University of Toronto, Ontario, Canada

Stéphane Colin

Department of General Mechanic
National Institute of Applied Sciences of Toulouse
Toulouse cedex, France

Michael R. King

Departments of Biomedical Engineering,
Chemical Engineering and Surgery
University of Rochester, NY, USA



ELSEVIER

AMSTERDAM BOSTON HEIDELBERG LONDON NEW YORK
OXFORD PARIS SAN DIEGO SINGAPORE SYDNEY TOKYO

ELSEVIER B.V.
Radarweg 29
P.O. Box 211, 1000 AE
Amsterdam, The Netherlands

ELSEVIER Inc.
525 B Street, Suite 1900
San Diego,
CA 92101-4495, USA

ELSEVIER Ltd
The Boulevard, Langford Lane
Kidlington, Oxford
OX5 1GB, UK

ELSEVIER Ltd
84 Theobalds Road
London
WC1X 8RR, UK

© 2006 Elsevier Ltd. All rights reserved.

This work is protected under copyright by Elsevier Ltd., and the following terms and conditions apply to its use:

Photocopying

Single photocopies of single chapters may be made for personal use as allowed by national copyright laws. Permission of the Publisher and payment of a fee is required for all other photocopying, including multiple or systematic copying, copying for advertising or promotional purposes, resale, and all forms of document delivery. Special rates are available for educational institutions that wish to make photocopies for non-profit educational classroom use.

Permissions may be sought directly from Elsevier's Rights Department in Oxford, UK: phone (+44) 1865 843830, fax (+44) 1865 853333, e-mail: permissions@elsevier.com. Requests may also be completed on-line via the Elsevier homepage (<http://www.elsevier.com/locate/permissions>).

In the USA, users may clear permissions and make payments through the Copyright Clearance Center, Inc., 222 Rosewood Drive, Danvers, MA 01923, USA; phone: (+1) (978) 7508400, fax: (+1) (978) 7504744, and in the UK through the Copyright Licensing Agency Rapid Clearance Service (CLARCS), 90 Tottenham Court Road, London W1P 0LP, UK; phone: (+44) 20 7631 5555; fax: (+44) 20 7631 5500. Other countries may have a local reprographic rights agency for payments.

Derivative Works

Tables of contents may be reproduced for internal circulation, but permission of the Publisher is required for external resale or distribution of such material. Permission of the Publisher is required for all other derivative works, including compilations and translations.

Electronic Storage or Usage

Permission of the Publisher is required to store or use electronically any material contained in this work, including any chapter or part of a chapter.

Except as outlined above, no part of this work may be reproduced, stored in a retrieval system or transmitted in any form or by any means, electronic, mechanical, photocopying, recording or otherwise, without prior written permission of the Publisher.

Address permissions requests to: Elsevier's Rights Department, at the fax and e-mail addresses noted above.

Notice

No responsibility is assumed by the Publisher for any injury and/or damage to persons or property as a matter of products liability, negligence or otherwise, or from any use or operation of any methods, products, instructions or ideas contained in the material herein. Because of rapid advances in the medical sciences, in particular, independent verification of diagnoses and drug dosages should be made.

First edition 2006

ISBN: 0-0804-4527-6

Typeset by Charon Tec Pvt. Ltd., Chennai, India
www.charontec.com

Printed in Great Britain

Working together to grow
libraries in developing countries

www.elsevier.com | www.bookaid.org | www.sabre.org

ELSEVIER

BOOK AID
International

Sabre Foundation

CONTENTS

About the Authors vi

Preface viii

Nomenclature x

Chapter 1. Introduction 1
Satish G. Kandlikar and Michael R. King

Chapter 2. Single-phase gas flow in microchannels 9
Stéphane Colin

Chapter 3. Single-phase liquid flow in minichannels and microchannels .. 87
Satish G. Kandlikar

Chapter 4. Single-phase electrokinetic flow in microchannels 137
Dongqing Li

Chapter 5. Flow boiling in minichannels and microchannels 175
Satish G. Kandlikar

Chapter 6. Condensation in minichannels and microchannels 227
Srinivas Garimella

Chapter 7. Biomedical applications of microchannel flows 409
Michael R. King

Subject Index 443

ABOUT THE AUTHORS

Satish Kandlikar

Dr. Satish Kandlikar is the Gleason Professor of Mechanical Engineering at Rochester Institute of Technology. He obtained his B.E. degree from Marathwada University and M.Tech. and Ph.D. degrees from I.I.T. Bombay. His research focuses on flow boiling and single phase heat transfer and fluid flow in microchannels, high flux cooling, and fundamentals of interfacial phenomena. He has published over 130 conference and journal papers, presented over 25 invited and keynote papers, has written contributed chapters in several handbooks, and has been editor-in-chief of a handbook on boiling and condensation. He is the recipient of the IBM Faculty award for the past three consecutive years. He received the Eisenhart Outstanding Teaching Award at RIT in 1997. He is an Associate Editor of several journals, including the *Journal of Heat Transfer*, *Heat Transfer Engineering*, *Journal of Microfluidics and Nanofluidics*, *International Journal of Heat and Technology*, and *Microscale Thermophysical Engineering*. He is a Fellow member of ASME.

Srinivas Garimella

Dr. Srinivas Garimella is an Associate Professor and Director of the Sustainable Thermal Systems Laboratory at Georgia Institute of Technology. He was previously a Research Scientist at Battelle Memorial Institute, Senior Engineer at General Motors, Associate Professor at Western Michigan University, and William and Virginia Binger Associate Professor at Iowa State University. Dr. Garimella received M.S. and Ph.D. degrees from The Ohio State University, and a Bachelors degree from the Indian Institute of Technology, Kanpur. He is Associate Editor of the ASME *Journal of Energy Resources Technology* and the *International Journal of HVAC&R Research*, and is Chair of the Advanced Energy Systems Division of ASME. He conducts research in the areas of vapor-compression and absorption heat pumps, phase-change in microchannels, heat and mass transfer in binary fluids, and supercritical heat transfer in natural refrigerants and blends. He has authored over 85 refereed journal and conference papers and several invited short courses, lectures and book chapters, and holds four patents. He received the NSF CAREER Award, the ASHRAE New Investigator Award, and the SAE Teetor Award for Engineering Educators.

Dongqing Li

Dr. Dongqing Li obtained his BA and MSc. degrees in Thermophysics Engineering in China, and his Ph.D. degree in Thermodynamics from the University of Toronto, Canada, in 1991. He was a professor at the University of Alberta and later in the University of Toronto from 1993 to 2005. Currently, Dr. Li is the H. Fort Flowers professor of Mechanical Engineering, Vanderbilt University. His research is in the areas of microfluidics and lab-on-a-chip. Dr. Li has published one book, 11 book chapters, and over 160 journal papers. He is the Editor-in-Chief of an international journal *Microfluidics and Nanofluidics*.

Stéphane Colin

Dr. Stéphane Colin is a Professor of Mechanical Engineering at the National Institute of Applied Sciences (INSA) of Toulouse, France. He obtained his Engineering degree in 1987 and received his Ph.D. degree in Fluid Mechanics from the Polytechnic National Institute of Toulouse in 1992. In 1999, he created the Microfluidics Group of the Hydrotechnic Society of France, and he currently leads this group. He is the Assistant Director of the Mechanical Engineering Laboratory of Toulouse. His research is in the area of microfluidics. Dr. Colin is editor of the book *Microfluidique*, published by Hermes Science Publications.

Michael King

Dr. Michael King is an Assistant Professor of Biomedical Engineering and Chemical Engineering at the University of Rochester. He received a B.S. degree from the University of Rochester and a Ph.D. from the University of Notre Dame, both in chemical engineering. At the University of Pennsylvania, King received an Individual National Research Service Award from the NIH. King is a Whitaker Investigator, a James D. Watson Investigator of New York State, and is a recipient of the NSF CAREER Award. He is editor of the book *Principles of Cellular Engineering: Understanding the Biomolecular Interface*, published by Academic Press. His research interests include biofluid mechanics and cell adhesion.

PREFACE

In the last few decades, new frontiers have been opened up by advances in our ability to produce microscale devices and systems. The numerous advantages that can be realized by constructing devices with microscale features have, in many cases, been exploited without a complete understanding of the way the miniaturized geometry alters the physical processes. The augmentation of transport processes due to microscale dimensions is taken advantage of in nature by all biological systems. In the engineered systems that are the focus of this book, the challenge is to understand and quantify how utilizing microscale passages alters the fluid flow patterns and the resulting, momentum, heat, and mass transfer processes to maximize device performance while minimizing cost, size, and energy requirements.

In this book, we are concerned with flow through passages with hydraulic diameters from about $1\text{ }\mu\text{m}$ to 3 mm , covering the range of microchannels and minichannels. Different phenomena are affected differently as we approach microscales depending on fluid properties and flow conditions; hence, classification schemes that identify a channel as macro, mini, or micro should be considered merely as guidelines.

The main topics covered in this book are single-phase gas flow and heat transfer; single-phase liquid flow and heat transfer; electrokinetic effects on liquid flow; flow patterns, pressure drop, and heat transfer in convective boiling; flow patterns, pressure drop, and heat transfer during convective condensation, and finally biological applications. The coverage is intended to reflect the status of our current understanding in these areas.

In each chapter, the fundamental physical phenomena related to the specific processes are introduced first. Then, the engineering analyses and quantitative methods derived from theoretical and experimental work conducted worldwide are presented. Areas requiring further research are clearly identified throughout as well as summarized within each chapter.

There are two intended audiences for this book. First, it is intended as a basic textbook for graduate students in various engineering applications. The students will find the necessary foundation for the relevant transport processes in microchannels as well as summaries of the key models, results, and correlations that represent the state-of-the-art. To facilitate the development of the ability to use the new information presented, each chapter contains several solved example problems that are carefully selected to provide practical guidance for students as well as practitioners. Second, this book is also expected to serve as a source book for component and system designers and researchers. Wherever possible, the range of applicability and uncertainty of the analyses presented is provided so that analyzing new devices and configurations can be done with known levels of confidence. The comprehensive summary of the literature included in each chapter will also help the readers identify valuable source material relevant to their specific problem for further investigation.

The authors would like to express appreciation toward the students and coworkers who have contributed significantly in their research and publication efforts in this field. The

first author would like to thank Nathan English in particular for his efforts in editing the entire manuscript and preparing the master nomenclature.

The authors are thankful to the scientific community for their efforts in exploring microscale phenomena in microchannels and minichannels. We look forward to receiving information on continued developments in this field and feedback from the readers as we strive to improve this book in the future. We also recognize that in our zest to prepare this manuscript in a rapidly developing field, we may have inadvertently made errors or omissions. We humbly seek your forgiveness and request that you forward us any corrections or suggestions.

Satish G. Kandlikar
Srinivas Garimella
Dongqing Li
Stéphane Colin
Michael King

NOMENCLATURE

A	Section area, m^2 (Chapters 2 and 6).
A, B, C, D, F	Equation coefficients and exponents (Chapters 3 and 7).
A_1	First-order slip coefficient, dimensionless (Chapter 2).
A_2	Second-order slip coefficient, dimensionless (Chapter 2).
A_3	High-order slip coefficient, dimensionless (Chapter 2).
A_c	Cross-sectional area, m^2 (Chapter 3).
A_p	Total plenum cross-sectional area, m^2 (Chapter 3).
A_T	Total heat transfer surface area (Chapter 5).
a	Speed of sound, m/s (Chapter 2); channel width, m (Chapter 3) equation constant in Eqs. (6.71), (6.83) and (6.87) (Chapter 6); coefficient in entrance length equations, dimensionless (Chapter 7).
a^*	Aspect ratio of rectangular sections, dimensionless, $a^* = h/b$ (Chapter 2).
a_1, a_2, a_3	Coefficients for the mass flow rate in a rectangular microchannel, dimensionless (Chapter 2).
$a_1 \dots a_5$	Coefficients in Eq. (6.107) (Chapter 6).
B	Parameter used in Eqs. (6.9) and (6.41) (Chapter 6).
B_B	Parameter used in Eq. (6.21) (Chapter 6).
B_n	Coefficient in cell surface oxygen concentration equation (Chapter 7).
b	Half-channel width, m (Chapter 2); channel height, m (Chapter 3); constant in Eqs. (6.71), (6.83) and (6.87) (Chapter 6).
Bo	Boiling number, dimensionless, $\text{Bo} = q''/(Gh_{LV})$ (Chapter 5).
Bo	Bond number, dimensionless, Bo $= (\rho_L - \rho_V)gD_h^2/\sigma$ (Chapter 5); $\text{Bo} = g(\rho_L - \rho_G)((d/2)^2/\sigma)$ (Chapter 6).
C, C	Constant, dimensionless (Chapter 1); coefficient in a Nusselt number correlation (Chapter 3); concentration, mol/m^3 (Chapters 4 and 7); Chisholm's parameter, dimensionless (Chapter 5); constant used in Eqs. (6.39), (6.40) and (6.157) (Chapter 6).
C	Reference concentration, mol/m^3 (Chapter 4).
C^*	Ratio of experimental and theoretical apparent friction factors, dimensionless, $C^* = f_{\text{app,ex}}/f_{\text{app,th}}$, (Chapter 3); non-dimensionalized concentration, $C^* = C(x, y)/C_{\text{in}}$ (Chapter 7).
C_0	Oxygen concentration at the lower channel wall, mol/m^3 (Chapter 7).
C_1, C_2	Empirically derived constants in Eq. (6.35) (Chapter 6); parameter, used in Eq. (6.54) (Chapter 6).
C_C	Coefficient of contraction, dimensionless (Chapter 6).
C_{in}	Non-dimensionalized gas phase oxygen concentration, $C_{\text{in}} = \tilde{C}_g/C_g$ (Chapter 7).
C_f	Friction factor, dimensionless (Chapter 2).

Co	Convection number, dimensionless, $Co = [(1 - x)/x]^{0.9} [\rho_V/\rho_L]^{0.5}$ (Chapter 5).
Co	Confinement number, dimensionless, $Co = \frac{\sqrt{\sigma/g(\rho_l - \rho_v)}}{D_h}$ (Chapter 6).
C_o	Contraction coefficient, dimensionless (Chapter 5); distribution parameter in drift flux model, dimensionless, $C_o = \langle \alpha j \rangle / (\langle \alpha \rangle \langle j \rangle)$ (Chapter 6).
C_p	Specific heat capacity at a constant pressure, J/kg K (Chapter 6).
C_S	Saturation oxygen concentration, mol/m ³ (Chapter 7).
c	Mean-square molecular speed, m/s (Chapter 2); constant in the thermal entry length equation, dimensionless (Chapter 3); constant in Eq. (6.57) (Chapter 6).
\mathbf{c}'	Molecular thermal velocity vector m/s (Chapter 2).
$\overline{c'}$	Mean thermal velocity, m/s (Chapter 2).
c_1, c_2	Coefficients used in Eq. (6.133) (Chapter 6).
c_p	Specific heat at a constant pressure, J/kg K (Chapters 2, 3 and 5).
c_v	Specific heat at a constant volume, J/kg K (Chapter 2).
Ca	Capillary number, dimensionless, $\mathbf{Ca} = \mu V/\sigma$ (Chapter 5).
CHF	Critical heat flux, W/m ² (Chapter 5).
D	Diameter, m (Chapters 1, 3, 5 and 6).
D, D^+, D^-	Diffusion coefficient, diffusivity, m ² /s (Chapters 2 and 4).
D_{cf}	Diameter constricted by channel roughness, m, $D_{cf} = D - 2\varepsilon$ (Chapter 3).
D_h, D_H	Hydraulic diameter, m (Chapters 1–5).
D_{le}	Laminar equivalent diameter, m (Chapter 3).
d	Mean molecular diameter, m (Chapter 2); diameter, m (Chapter 6).
d_B	Departure bubble diameter, m (Chapter 5).
E	Applied electrical field strength, V/m (Chapter 4); total energy per unit volume, J/m ³ (Chapter 2); diode efficiency, dimensionless, (Chapter 2); parameter used in Eq. (6.141) (Chapter 6).
E_1, E_2	Parameter used in Eq. (6.22) (Chapter 6).
E_x	Electric field strength, V/m (Chapter 4).
e	Internal specific energy, J/kg (Chapter 2); charge of a proton, $e = 1.602 \times 10^{-19}$ C (Chapter 4).
Eo, Eö	Eötvös number, dimensionless, $\mathbf{Eo} = g(\rho_L - \rho_V)L^2/\sigma$ in case of liquid gas contact (Chapters 5 and 6).
F, F	Non-dimensional constant accounting for an electrokinetic body force (Chapter 4); general periodic function of unit magnitude (Chapter 4); force, N (Chapters 5 and 6); modified Froude number, dimensionless, $F = \sqrt{\frac{\rho_g}{\rho_l - \rho_g}} \frac{U_{GS}}{\sqrt{D_g}}$ (Chapter 6); stress ratio, dimensionless, $F = \tau_w/(\rho_L g \delta)$ (Chapter 6); parameter used in Eq. (6.141) (Chapter 6); external force acting on a spherical cell, N (Chapter 7).
F	External force per unit mass vector, N/kg (Chapter 2).
F'_M	Interfacial force created by evaporation momentum, N (Chapter 5).
F'_S	Interfacial force created by surface tension, N (Chapter 5).

F_{Fl}	Fluid-surface parameter accounting for the nucleation characteristics of different fluid surface combinations, dimensionless (Chapter 5).
F_g	Function of the liquid volume fraction and the vapor Reynolds number, used in Eq. (6.128) (Chapter 6).
F_T	Dimensionless parameter of Eq. (6.112) (Chapter 6).
F_x	Electrical force per unit volume of the liquid, N/m^3 (Chapter 4).
\mathbf{f}	Volume force vector, N/m^3 (Chapter 2).
f	Fanning friction factor, dimensionless (Chapters 1, 3 and 5); single-phase friction factor, dimensionless (Chapter 6).
f_{app}	Apparent friction factor accounting for developing flows, dimensionless (Chapter 3).
f	Frequency, Hz (Chapter 2); velocity distribution function (Chapter 2).
f_{ls}	Superficial liquid phase friction factor, dimensionless (Chapter 6).
F_p	Floor distance to mean line in roughness elements, m (Chapter 3).
Fr_l	Liquid Froude number, dimensionless, $\text{Fr}_l^2 = \bar{V}_l^2/g\delta$ (Chapter 6).
Fr_m	Modified Froude number, dimensionless (Chapter 6).
Fr_{so}	Soliman modified Froude number, dimensionless (Chapter 6).
Ft	Froude rate, dimensionless $\text{Ft} = \left[\frac{G^2 x^3}{(1-x)\rho_g^2 g D} \right]^{0.5}$ (Chapter 6).
G	Mass flux, $\text{kg/m}^2\text{s}$ (Chapters 1, 5 and 6).
G_{eq}	Equivalent mass flux, $\text{kg/m}^2\text{s}$, $G_{\text{eq}} = G_l + G'_l$ (Chapter 6).
G'_l	Mass flux that produces the same interfacial shear stress as a vapor core, $\text{kg/m}^2\text{-s}$, $G'_l = G_v \sqrt{\frac{\rho_l}{\rho_v}} \sqrt{\frac{f_v}{f_l}}$ (Chapter 6).
G_t	Total mass flux, $\text{kg/m}^2\text{s}$ (Chapter 6).
g	Acceleration due to gravity, m/s^2 (Chapters 5 and 6).
Ga_l	Liquid Galileo number, dimensionless, $\text{Ga}_l = gD^3/\nu_l^2$ (Chapter 6).
H	Maximum height, m (Chapter 4); distance between parallel plates or height, m (Chapter 7); parameter used in Eq. (6.141) (Chapter 6).
h	Heat transfer coefficient, $\text{W/m}^2\text{-K}$ (Chapters 1, 3, 5 and 6); channel half-depth, m (Chapter 2); specific enthalpy, J/kg (Chapters 2 and 5); wave height, m (Chapter 7).
\bar{h}	Average heat transfer coefficient, $\text{W/m}^2\text{K}$ (Chapters 3 and 6).
h_c	Film heat transfer coefficient, $\text{W/m}^2\text{K}$ (Chapter 6).
h_{fg}	Latent heat of vaporization, J/kg (Chapter 6).
h_G	Gas-phase height in channel, m, $h_G \leq \frac{\pi}{4} \sqrt{\frac{\sigma}{\rho_g(1-\frac{\pi}{4})}}$ (Chapter 6).
h_{LV}	Latent heat of vaporization at p_L , J/kg (Chapter 5).
h_{lv}	Specific enthalpy of vaporization, J/kg (Chapter 6).
h'_{lv}	Modified specific enthalpy of vaporization, J/kg (Chapter 6).
\mathbf{I}	Unit tensor, dimensionless (Chapter 2).
I	Current, A (Chapter 3).
i	Enthalpy, J/kg (Chapter 5).
\mathbf{J}	Mass flux vector, $\text{kg/m}^2\text{s}$ (Chapter 2).
J	Electrical current, A (Chapter 4).
j	Superficial velocity, m/s (Chapters 5 and 6).

j_g^*, J_G^*	Wallis dimensionless gas velocity, $j_g^* = \frac{G_t x}{\sqrt{Dg\rho_v(\rho_l - \rho_v)}}$ (Chapter 6).
Ja	Jakob number, dimensionless, $\mathbf{Ja} = \frac{\rho_L}{\rho_V} \frac{c_{pL}}{h_{LV}} \frac{\Delta T}{h_{LV}}$ (Chapter 5).
Ja_l	Liquid Jakob number, dimensionless, $Ja_l = \frac{c_{pL}(T_{sat} - T_s)}{h_{lv}}$ (Chapter 6).
K	Non-dimensional double layer thickness, $K = D_h \kappa$ (Chapter 4); constant in Eqs. (6.56) and (6.95) (Chapter 6).
$K(x)$	Incremental pressure defect, dimensionless (Chapter 3).
$\mathbf{K}(\infty)$	Hagenbach's factor, dimensionless, $K(x)$ when $x > L_h$ (Chapter 3).
\mathbf{K}_1	Ratio of evaporation momentum to inertia forces at the liquid–vapor interface, dimensionless, $\mathbf{K}_1 = \left(\frac{q''}{G h_{LV}}\right)^2 \frac{\rho_L}{\rho_V}$ (Chapter 5).
\mathbf{K}_2	Ratio of evaporation momentum to surface tension forces at the liquid–vapor interface, dimensionless, $\mathbf{K}_2 = \left(\frac{q''}{h_{LV}}\right)^2 \frac{D}{\rho_V \sigma}$ (Chapter 5).
K_{90}	Loss coefficient at a 90° bend, dimensionless (Chapter 3).
K_c	Contraction loss coefficient due to an area change, dimensionless (Chapter 3).
K_e	Expansion loss coefficient due to an area change, dimensionless (Chapter 3).
K_m	Michaelis constant, mol/m ³ (Chapter 7).
k	Thermal conductivity, W/mK (Chapters 1–3, 5 and 6); constant, dimensionless (Chapter 7).
k_1	Coefficient in the collision rate expression, dimensionless (Chapter 2).
k_2	Coefficient in the mean free path expression, dimensionless (Chapter 2).
k_B, κ_B	Boltzmann constant, $k_B = 1.38065$ J/K (Chapters 2 and 4).
Kn	Knudsen number, $\text{Kn} = \lambda/L$, dimensionless (Chapters 1 and 2).
Kn'	Minimal representative length Knudsen number, $\text{Kn}' = \lambda/L_{\min}$ (Chapter 2).
Ku	Kutateladze number, dimensionless $\text{Ku} = C_p \Delta T / h_{fg}$ (Chapter 6).
L	Length or characteristic length in a given system, m (Chapters 1–3 and 5–7); Laplace constant, m, $L = \sqrt{\frac{\sigma}{g(\rho_l - \rho_v)}}$ (Chapter 6).
L_G, L_L	Gas and liquid slug lengths in the slug flow regime, m (Chapter 6).
$L_{\text{ent}}, L_h, L_{hd}$	Hydrodynamically developing entrance length, m, $L_{\text{ent}} = aH\text{Re}$ (Chapters 2, 3 and 7).
L_t	Thermally developing entrance length, m, $L_t = c\text{RePr}D_h$ (Chapter 3).
L_{eq}	Total pipette length, m (Chapter 7).
l	Microchannel length, m (Chapter 2).
l_{SV}	Characteristic length of a sampling volume, m (Chapter 2).
$l_{x,y,z}$	Channel half height, m (Chapter 4).
LHS	Left hand side (Chapter 7).
M	Molecular weight, kg/mol (Chapter 2).
M	Ratio of the electrical force to frictional force per unit volume, dimensionless, $M = 2n_{\infty} z e \zeta D_h^2 / \mu UL$ (Chapter 4).

M, N	Equation exponents, dimensionless (Chapter 3).
M_W	Molecular weight, g/mol (Chapter 7).
m	Molecular mass, kg (Chapter 2); liquid volume fraction, dimensionless (Chapter 6); dimensionless constant in Eq. (6.57) (Chapter 6).
\dot{m}	Mass flow rate, kg/s (Chapters 2, 3 and 5).
\dot{m}^*	Mass flow rate, $\dot{m}/\dot{m}_{\text{ns}}$, dimensionless (Chapter 2).
\dot{m}_{ns}	Mass flow rate for a no-slip flow, kg/s (Chapter 2).
Ma	Mach number, dimensionless, $\text{Ma} = u/a$ (Chapter 2).
N	Avogadro's number, $6.022137 \cdot 10^{23} \text{ mol}^{-1}$ (Chapter 2).
\dot{N}	Molecular flux, s^{-1} (Chapter 2).
N^+	Non-dimensional positive species concentration (Chapter 4).
N^-	Non-dimensional negative species concentration (Chapter 4).
N_{conf}	Confinement number, dimensionless, $N_{\text{conf}} = \frac{\sqrt{\sigma/(g(\rho_l - \rho_v))}}{D_h}$ (Chapter 6).
N_0	Cellular uptake rate, $\text{mol}/\text{m}^2 \text{ s}$ (Chapter 7).
n	Number density, m^{-3} (Chapter 2); number or number of channels, dimensionless (Chapter 3); number of channels (Chapter 5); constant in Eqs. (6.41) and (6.57) (Chapter 6); number (Chapter 7).
n_1, n_2, n_3	Constant in Eq. (6.21) (Chapter 6).
n_i	Number concentration of type- i ion (Chapter 4).
n_{io}	Bulk ionic concentration of type- i ions (Chapter 4).
n_x	Normal vector in the x direction (Chapter 4).
Nu	Nusselt number, dimensionless, $\text{Nu} = hD_h/k$, (Chapters 1–3, 5 and 6).
Nu_H	Nusselt number under a constant heat flux boundary condition, dimensionless (Chapter 3).
Nu_i	Nusselt number for high interfacial shear condensation, dimensionless (Chapter 6).
$\overline{\text{Nu}}_L$	Average Nusselt number along a plate of length L , dimensionless (Chapter 6).
Nu_0	Nusselt number for quiescent vapor condensation, dimensionless $\text{Nu}_0 = [(\text{Nu}_L^{n_1}) + (\text{Nu}_T^{n_1})]^{1/n_1}$ (Chapter 6).
Nu_T	Nusselt number for a turbulent film, dimensionless (Chapter 6).
Nu_T	Nusselt number under a constant wall temperature boundary condition, dimensionless (Chapter 3).
Nu_x	Combined Nusselt number, dimensionless, $\text{Nu}_x = [(\text{Nu}_0^{n_2}) + (\text{Nu}_i^{n_2})]^{1/n_2}$ (Chapter 6).
ONB	Onset of nucleate boiling (Chapter 5).
P	Wetted perimeter, m (Chapter 2); dimensionless pressure (Chapter 4); heated perimeter, m (Chapter 5); pressure, Pa (Chapter 6).
P_w	Wetted perimeter, m (Chapter 3).
p	Pressure, Pa (Chapters 1–3 and 5–7).
p_R	Reduced pressure, dimensionless (Chapter 6).
Pe	Peclét number, dimensionless, $\text{Pe} = UH/D$ (Chapter 7).
Pe_F	Peclét number of fluid, dimensionless (Chapter 4).

Po	Poiseuille number, dimensionless, $Po = fRe$ (Chapters 2 and 3).
Pr, Pr	Prandtl number, dimensionless, $Pr = \mu c_p / k$ (Chapters 2, 3, 5 and 6).
Q	Heat load, W (Chapter 3).
\dot{Q}	Volumetric flow rate, m^3/s (Chapters 2, 3 and 7).
\mathbf{q}	Heat flux vector, W/m^2 (Chapter 2).
q	Heat flux, W/m^2 , Chap. 2; dissipated power, W (Chapter 3); constant in Eq. (6.60) (Chapter 6).
q	Volumetric flow rate per unit width, m^2/s (Chapter 7).
q	Oxygen uptake rate on a per-cell basis, mol/s (Chapter 7).
q''	Heat flux, W/m^2 (Chapters 5 and 6).
q''_{CHF}	Critical heat flux, W/m^2 (Chapter 5).
R	Gas constant (Chapter 1); upstream to downstream flow resistance, dimensionless (Chapter 5).
R	Specific gas constant, J/kgK , $R = c_p - c_v$, (Chapter 2); radius, m (Chapter 6).
\bar{R}	Universal gas constant, $8.314511 J/molK$ (Chapter 2).
R^+	Dimensionless pipe radius (Chapter 6).
R_1, R_2	Radii of curvature of fluid–liquid interface, m.
R_p	Mean profile peak height (Chapter 3); Pipette radius, m (Chapter 7).
$R_{p,i}$	Maximum profile peak height of individual roughness elements, m (Chapter 3).
R_{pm}	Average maximum profile peak height of roughness elements, m (Chapter 3).
r	Distance between two molecular centers, m (Chapter 2); radial coordinate, radius, radius of cavity, m (Chapters 2 and 4–7); constant in Eq. (6.60) (Chapter 6).
r_b	Bubble radius, m (Chapter 5).
r_c	Cavity radius, m (Chapter 5).
r_1	Inner radius of an annular microtube, m (Chapter 2).
r_2	Outer radius of annular microtube or a circular microtube radius, m (Chapter 2).
R_a	Average surface roughness, m (Chapter 3).
Re , Re	Reynolds number, dimensionless, $Re = GD/\mu$ (Chapters 1–5 and 7).
Re^*	Laminar equivalent Reynolds number, dimensionless, $Re^* = \rho u_m D_{le}/\mu$ (Chapter 3).
Re^+	Friction Reynolds number, dimensionless (Chapter 6).
Re_{D_h}	Reynolds number based on hydraulic diameter, dimensionless (Chapter 6).
$Re_{g,si}$	Reynolds number, based on superficial gas velocity at the inlet, dimensionless (Chapter 6).
$Re_{l,si}$	Reynolds number, based on superficial liquid velocity at the inlet, dimensionless (Chapter 6).
Re_l	Liquid film Reynolds number, dimensionless, $Re_l = G(1 - x)D/\mu_l$ (Chapter 6).
Re_m	Mixture Reynolds number, dimensionless, $Re_m = GD/\mu_m$ (Chapter 6).
Re_t	Transitional Reynolds number, dimensionless (Chapter 3).
RSm	Mean spacing of profile irregularities in roughness elements, m (Chapter 3).
S	Slip ratio, dimensionless, $S = U_G/U_L$ (Chapter 6).
s	Fin width or distance between channels, m (Chapter 3); constant in Eq. (6.60) (Chapter 6).

Sc	Schmidt number, dimensionless, $Sc = \mu/(\rho D)$ (Chapter 2).
Sh	Sherwood number, dimensionless, $Sh = \alpha H/D$ (Chapter 7).
Sm	Distance between two roughness element peaks, m (Chapter 3).
St	Stanton number, dimensionless, $St = h/c_p G$ (Chapter 3).
T	Temperature, K or °C (Chapters 1–6).
T_s	Liquid surface temperature, K or °C (Chapters 3 and 5); surface temperature of tube wall, K or °C (Chapter 6).
T_{sat}	Saturation temperature, K or °C (Chapters 5 and 6).
ΔT_{Sat}	Wall superheat, K, $\Delta T_{Sat} = T_W - T_{Sat}$ (Chapter 5).
ΔT_{Sub}	Liquid subcooling, K, $\Delta T_{Sub} = T_{Sat} - T_B$ (Chapter 5).
T_δ^+	Dimensionless temperature in condensate film (Chapter 6).
t	Time, s (Chapters 2 and 7).
U	Uncertainty (Chapter 3); reference velocity, m/s (Chapter 4); potential, such as gravity (Chapter 7); average velocity, m/s (Chapter 7).
$U_{SL}, V_{L,S}$	Superficial liquid velocity, m/s (Chapter 6).
U_{Gj}, V_{Gj}	Drift velocity in drift flux model, m/s, $v_G = j_G/\alpha = C_{qj} + V_{Gj}$ (Chapter 6).
$U_{GS}, V_{G,S}$	Superficial gas velocity, m/s (Chapter 6).
u	Velocity, m/s (Chapters 2–4, 6 and 7).
\mathbf{u}	Velocity vector, m/s (Chapter 2).
\bar{u}_{ave}	Average electroosmotic velocity, m/s (Chapter 4).
\bar{u}_z	Mean axial velocity, m/s (Chapter 2).
\bar{u}_z^*	Mean axial velocity, $\bar{u}_z^* = \bar{u}_z/u_{z0}$, dimensionless (Chapter 2).
u^*	Friction velocity, m/s, $u^* = \sqrt{\tau_i/\rho_l}$ (Chapter 6).
u_m	Mean flow velocity, m/s (Chapters 3 and 5).
u_r	Relative velocity between a large gas bubble and liquid in the slug flow regime, m/s, $u_r = u_S - (j_G + j_L)$ (Chapter 6).
u_S	Velocity of large gas bubble in slug flow regime, m/s (Chapter 6).
u_{z0}	Maximum axial velocity with no-slip conditions, m/s (Chapter 2).
UA	Overall heat transfer conductance, W/K (Chapter 6).
V	Voltage, V, (Chapter 3); velocity, m/s (Chapters 5 and 6).
V	Non-dimensional velocity, $V = v/v_0$ (Chapter 4).
\bar{V}_l	Average velocity of a liquid film, m/s (Chapter 6).
V_m	Zeroth-order uptake of oxygen by the hepatocytes (Chapter 7).
v	Velocity, m/s (Chapter 4).
v	Specific volume, $v = 1/\rho$, m ³ /kg (Chapters 2 and 5); velocity, m/s (Chapters 6 and 7).
v_0	Reference velocity, m/s (Chapter 4).
v_{LV}	Difference between the specific volumes of the vapor and liquid phases, m ³ /kg, $v_{LG} = v_G - v_L$ (Chapter 5).
W	Maximum width, m (Chapters 3 and 4).
w	Velocity, m/s (Chapter 7).
We	Weber number, dimensionless, $We = LG^2/\rho\sigma$ (Chapter 5).
We	Weber number, dimensionless, $We = \rho V_S^2 D/\sigma$ (Chapter 6).
X	Cell density (Chapter 7).

X	Martinelli parameter, dimensionless, $X = \{(dp/dz)_L/(dp/dz)_G\}^{1/2}$ (Chapters 5 and 6).
X, Y, Z	Coordinate axes (Chapter 4).
X_{tt}	Martinelli parameter for turbulent flow in the gas and liquid phases, dimensionless (Chapter 6).
x	Mass quality, dimensionless (Chapters 5 and 6).
\mathbf{x}	Position vector, m (Chapter 2).
x, y, z	Coordinate axes (Chapters 2–7); length (Chapter 6).
x^*, y^*	Cross-sectional coordinates, dimensionless (Chapter 2).
x^*	Dimensionless version of x , $x^* = x/RePrD_h$ (Chapter 3).
x^+	Dimensionless version of x , $x^+ = \frac{x/D_h}{Re}$ (Chapter 3).
Y	Chisholm parameter, dimensionless, $Y = \left[\frac{(dP_F/dz)_{GO}}{(dP_F/dz)_{LO}} \right]$ (Chapter 6).
y	Dimensionless parameter in Eq. 6.22 (Chapter 6).
y_b	Bubble height, m (Chapter 5).
y_s	Distance to bubble stagnation point from heated wall, m (Chapter 5).
Z	Ohnesorge number, dimensionless, $Z = \mu/(\rho L \sigma)^{1/2}$ (Chapter 5).
z	Heated length from the channel entrance, m (Chapter 5).
z^*	Axial coordinate, dimensionless (Chapter 2).
z_i	Valence of type- i ions (Chapter 4).

Greek Symbols

α	Convection heat transfer coefficient, W/m^2K (Chapter 2); coefficient in the VSS molecular model, dimensionless (Chapter 2); aspect ratio, dimensionless (Chapter 6); void fraction, dimensionless (Chapter 6).
$\alpha_1; \alpha_2; \alpha_3$	Coefficients for the pressure distribution along a plane microchannel, dimensionless (Chapter 2).
α_c	Channel aspect ratio, dimensionless, $\alpha_c = a/b$ (Chapter 3).
α_i	Eigenvalues for the velocity distribution in a rectangular microchannel, dimensionless (Chapter 2).
α_r	Radial void fraction, dimensionless, $\alpha_r = 0.8372 + \left[1 - \left(\frac{r}{r_w} \right)^{7.316} \right]$ (Chapter 6).
β	Coefficient in the VSS molecular model, dimensionless (Chapter 2); fin spacing ratio, dimensionless, $\beta = s/a$ (Chapter 3); angle with horizontal (Chapter 5); homogeneous void fraction, dimensionless (Chapter 6); velocity ratio, dimensionless (Chapter 6); multiplier to transition line, dimensionless, $\beta(F, X) = \text{constant}$, used by Sardesai <i>et al.</i> (1981) (Chapter 6).
$\beta_1, \beta_2, \beta_3$	Coefficients for the pressure distribution along a circular microtube, dimensionless (Chapter 2).
β_A, β_B	Empirically derived transition points for the Kariyasaki <i>et al.</i> void fraction correlation (Chapter 6).
Γ	Euler or gamma function (Chapter 2).

γ	Area ratio, dimensionless (Chapter 6); dimensionless length ratio, $\gamma = L/H$ (Chapter 7); Specific heat ratio, dimensionless, $\gamma = c_p/c_v$ (Chapter 2).
ΔP	Pressure drop, Pa (Chapter 6).
$\Delta P_2/\Delta P_1$	Ratio of differential pressure between two system conditions (Chapter 6).
Δp	Pressure drop, pressure difference, Pa (Chapters 1–3, 5 and 7).
ΔT	Temperature difference, K (Chapter 6).
ΔT_{Sat}	Wall superheat, K, $\Delta T_{\text{Sub}} = T_{\text{Sat}} - T_B$ (Chapter 5).
ΔT_{Sub}	Liquid subcooling, K, $\Delta T_{\text{Sat}} = T_W - T_{\text{Sat}}$ (Chapter 5).
Δt	Elapsed time, s (Chapter 4).
Δx	Quality change, dimensionless (Chapter 6).
δ	Mean molecular spacing, m (Chapter 2); film thickness, m (Chapter 6).
δ^+	Non-dimensional film thickness (Chapter 6).
δ_t	Thermal boundary layer thickness, m (Chapter 5).
ε	Average roughness, m (Chapter 3).
ε	Dielectric constant of a solution (Chapter 4).
$\bar{\varepsilon}$	Dimensionless gap spacing (Chapter 7).
ε_h	Turbulent thermal diffusivity, m^2/s (Chapter 6).
ε_m	Momentum eddy diffusivity, m^2/s (Chapter 6).
ε_w	Electrical permittivity of the solution (Chapter 4).
ζ	Zeta potential (Chapter 4).
ζ	Dimensionless zeta potential, $\zeta = ze\zeta/k_bT$ (Chapter 4).
ζ	Second coefficient of viscosity or Lamé coefficient, kg/m s , (Chapter 2).
ζ	Temperature jump distance, m (Chapter 2).
ζ^*	Temperature jump distance, dimensionless (Chapter 2).
η	Exponent in the inverse power law model, dimensionless (Chapter 2).
η'	Exponent in the Lennard-Jones potential, dimensionless (Chapter 2).
η_f	Fin efficiency, dimensionless (Chapter 3).
Θ	Dimensionless surface charge density (Chapter 4); angle, degrees (Chapter 6).
θ	Dimensionless time (Chapter 4).
θ_r	Receding contact angle, degrees (Chapter 5).
κ	Dimensionless Michaelis constant, $\kappa = K_m/C^*$ (Chapter 7).
κ	Debye-Huckel parameter, m^{-1} , $\kappa = (2n_\infty z^2 e^2 / \varepsilon \varepsilon_0 k_b T)^{1/2}$ (Chapter 4).
κ	Constant in the inverse power law model, N m^η (Chapter 2).
κ'	Constant in the Lennard-Jones potential, dimensionless (Chapter 2).
λ	Wavelength, m (Chapter 7); mean free path, m (Chapters 1 and 2); dimensionless parameter, $\lambda = \mu_L^2 / (\rho_L \sigma D_h)$ (Chapter 6).
λ_b	Bulk conductivity (Chapter 4).
λ_n	Roots of the transcendental equation $\tan(\lambda_n) = \text{Sh}/\lambda_n$ (Chapter 7).
λ_n	Eigenvalues (Chapter 4).
μ	Dynamic viscosity, kg/ms (Chapters 1–7).
μ	Mobility (Chapter 4).
μ_n	Eigenvalues (Chapter 4).

μ_H	Homogeneous dynamic viscosity, kg/ms, $\mu_H = \beta\mu_G + (1 - \beta)\mu_L$ (Chapter 6).
μ_m	Mixture dynamic viscosity, kg/ms, $1/\mu_m = x/\mu_G + (1 - x)/\mu_L$ (Chapter 6).
ν	Collision rate, s (Chapter 2).
ξ	Coefficient of slip, m (Chapter 2).
ξ^*	Coefficient of slip, dimensionless (Chapter 2).
Π	Inlet over outlet pressures ratio, dimensionless (Chapter 2).
ρ	Density, kg/m ³ (Chapters 1–7).
ρ_e	Local net charge density per unit volume (Chapter 4).
ρ_m	Mixture density, kg/m ³ , $1/\rho_m = (1/\rho_l)(1 - x) + (1/\rho_v)x$ (Chapter 6).
ρ_{TP}	Two-phase mixture density, kg/m ³ , $\rho_{TP} = \left[\frac{x}{\rho_G} + \frac{1-x}{\rho_L} \right]^{-1}$ (Chapter 6).
σ	Viscous stress tensor, Pa (Chapter 2); Area ratio, dimensionless (Chapter 3); surface charge density (Chapter 4); surface tension, N/m (Chapter 5); fractional saturation, $s = C/C^*$ (Chapter 7); cell membrane permeability to oxygen (Chapter 7).
σ	Tangential momentum accommodation coefficient, dimensionless (Chapter 2); surface tension, N/m (Chapter 6).
σ'	Stress tensor, Pa (Chapter 2).
s_c	Contraction area ratio (header to channel, >1), dimensionless (Chapter 5).
s_e	Expansion area ratio (channel to header, <1), dimensionless (Chapter 5).
σ_T	Thermal accommodation coefficient, dimensionless (Chapter 2).
σ_t	Total collision cross-section, m ² (Chapter 2).
τ	Dimensionless time (Chapter 4); shear stress, Pa (Chapters 6 and 7); time scale, s (Chapter 7).
τ	Characteristic time for QGD and QHD equations, s (Chapter 2).
τ_i	Shear stress at vapor–liquid interface, Pa (Chapter 6).
τ_i^*	Dimensionless shear stress, Pa (Chapter 6).
τ_m	Shear stress due to momentum change, Pa (Chapter 6).
τ_W	Frictional wall shear stress, Pa (Chapters 2, 3 and 6).
$\overline{\tau_W}$	Average wall shear, Pa (Chapter 2).
ϕ	Intermolecular potential, J (Chapter 2); ratio of the characteristic diffusion time to the characteristic cellular oxygen uptake time, dimensionless (Chapter 7); velocity potential, m (Chapter 7).
ϕ_m	Angle, degrees (Chapter 6).
Φ	Dimensionless electric field strength (Chapter 4).
φ_i	Eigenvalues for the velocity distribution in a rectangular microchannel, dimensionless (Chapter 2).
ϕ_L	Two-phase friction multiplier, dimensionless, $\phi_L^2 = \Delta p_{f,TP}/\Delta p_{f,L}$, ratio of two-phase frictional pressure drop against frictional pressure drop of liquid flow (Chapters 5 and 6).
ψ	Electrical potential (Chapter 4); dimensionless parameter, $\psi = (\sigma_w/\sigma) [\mu_L/\mu_w(\rho_w/\rho_L)^2]^{1/3}$ (Chapter 6).
ψ_h	Two-phase homogeneous flow multiplier, dimensionless (Chapter 5).

ψ_j	Eigenvalues for the velocity distribution in a rectangular microchannel, dimensionless (Chapter 2).
ψ_s, ψ_S	Two-phase separated flow multiplier, dimensionless (Chapters 5 and 6).
Ψ	Dimensionless double layer potential (Chapter 4).
Ω	Dimensionless frequency (Chapter 4). Correction parameter used in Eqs. (6.52) and (6.53) (Chapter 6).
ω	Angular speed or vorticity, rad/s (Chapter 7); frequency, Hz (Chapter 4); temperature exponent of the coefficient of viscosity, dimensionless (Chapter 2).

Subscripts

0	Lowest boundary condition (Chapters 4 and 7).
1-ph	Single phase (Chapter 5).
<i>a</i>	Air, acceleration, ambient (Chapter 5); air (Chapter 6).
AB	Augmented Burnett equations (Chapter 2).
an	Annular (Chapter 6).
annu	Flow in an annular microduct (Chapter 2).
app	Apparent (Chapter 3).
av	Average (Chapter 4).
avg	Average (Chapters 5 and 7).
B	Bulk (Chapter 5); gas bubble (Chapter 6).
B	Burnett equations, (Chapter 2).
b	Bubble (Chapter 5); bulk (Chapter 3).
BGKB	Bhatnagar-Gross-Krook-Burnett equations (Chapter 2).
c, cr, crit	Critical condition (Chapters 3, 5 and 6).
c	Channel or in a single channel (Chapter 3); cavity mouth (Chapter 5); entrance contraction (Chapter 5).
cf	Calculated based on a flow diameter constricted by roughness elements (D_{cf}) (Chapter 3).
CBD	Convective boiling dominant (Chapter 5).
CHF	Critical heat flux (Chapter 5).
circ	Flow in a circular microtube (Chapter 2).
const	Constant (Chapter 4).
cp	Constant property (Chapter 3).
crit	Critical (Chapter 5).
cst	Constant (Chapter 7).
E	Euler equations (Chapter 2).
<i>e</i>	Outlet expansion, exit (Chapter 5).
eo	Electroosmotic (Chapter 4).
ep	Electrophoretic (Chapter 4).
EQ	Set of equations (Chapter 2).
eq	Equivalent (Chapter 6).
ex	Experimental (Chapter 3).
<i>F</i>	Frictional (Chapter 5).

<i>f</i>	Fluid (Chapter 3).
<i>f</i>	Fluid (Chapters 1, 3 and 4); frictional (Chapters 5 and 6); flooded (Chapter 6).
F/B	Film-bubble region (Chapter 6).
<i>f/d</i>	Film-bubble region (Chapter 6).
<i>fd</i>	Fully developed (Chapter 3).
<i>G</i>	Gas (Chapter 6).
<i>g</i>	Gas (Chapters 6 and 7).
<i>g</i>	Gravitational (Chapters 5 and 6).
GHS	Generalized hard sphere (Chapter 2).
<i>Gn</i>	Refers to Gnielinski's correlation (Chapter 3).
<i>H</i>	Homogeneous (Chapter 6).
<i>h</i>	Hydraulic (Chapter 6).
H1	Boundary condition with constant circumferential wall temperature and axial heat flux (Chapter 3).
H2	Boundary condition with constant wall heat flux, both circumferentially and axially (Chapter 3).
hetero	Heterogeneous solution (Chapter 4).
homo	Homogeneous solution (Chapter 4).
HS	Hard spheres (Chapter 2).
<i>i</i>	Species number (Chapters 4 and 7); vapor–liquid interface (Chapter 6).
in, <i>i</i>	Inlet (Chapters 2, 3, 5 and 7).
<i>L</i>	Liquid (Chapters 5 and 6).
<i>l</i>	Liquid (Chapter 6).
LG	Gas-superficial (Chapter 6).
LS	Liquid-superficial (Chapter 6).
LO	Entire flow as liquid (Chapters 5 and 6).
lv	Liquid-vapor (Chapter 6).
<i>M</i>	Momentum (Chapter 5).
<i>M</i>	Maxwell model (Chapter 2).
<i>m</i>	Mean (Chapter 3).
max	Maximum (Chapters 4 and 5).
min	Minimum (Chapter 5).
MM	Maxwell molecules (Chapter 2).
<i>n</i>	Normal direction (Chapter 2).
NBD	Nucleate boiling dominant (Chapter 5).
NS	Navier-Stokes equations (Chapter 2).
ns	No-slip (Chapter 2).
<i>o</i>	Out, outlet (Chapters 2 and 3).
ONB	Onset of nucleate boiling (Chapter 5).
plan	Flow between plane parallel plates (Chapter 2).
QGD	Quasi-gasodynamic equations (Chapter 2).
QHD	Quasi-hydrodynamic equations (Chapter 2).
<i>r</i>	Radial coordinate, radius, <i>m</i> (Chapter 4).
rect	Flow in a rectangular Microchannel (Chapter 2).

S	Surface tension (Chapter 5).
S	Stagnation (Chapter 5); superficial (Chapter 6); liquid slug (Chapter 6).
s	Surface (Chapter 3); spherical (Chapter 7).
s	Tangential direction (Chapter 2).
Sat, sat	Saturation at system or local pressure (Chapters 5 and 6).
sh	Shear (Chapter 6).
st	Surface tension (Chapter 6).
str	Stratified (Chapter 6).
Sub	Subcooled, subcooling (Chapter 5).
SV	Sampling volume (Chapter 2).
T	Two-phase mixture (Chapter 6).
t	Total (Chapter 3); turbulent (Chapter 6).
th	Theoretical (Chapter 3).
TP	Two-phase (Chapter 5).
tp	Two-phase (Chapter 5).
tr	Transition regime (Chapter 6).
u	Unflooded (Chapter 6).
UC	Unit cell (Chapter 6).
V	Vapor (Chapter 5).
v	Vapor phase (Chapter 6).
VHS	Variable hard spheres (Chapter 2).
VSS	Variable soft spheres (Chapter 2).
W, w	Wall, heated surface (Chapter 5).
w	Fluid at the wall (Chapter 2); at the wall (Chapter 3); wall (Chapter 6).
wall	Wall (Chapter 2).
x, y, z	Local value at a location or as a function of the co-ordinates (Chapters 3, 5 and 7).
x, y	Cross-sectional coordinates (Chapter 2).
z	Axial coordinate (Chapter 2).
0	Standard conditions (Chapter 2); reference value (Chapter 2).
1	First-order boundary conditions (Chapter 2).
2	Second-order boundary conditions (Chapter 2).
∞	Infinity (Chapter 4).

Superscripts

+, −	Charge designation (Chapter 4).
+	Dimensionless parameters (Chapter 6).
*	Dimensionless parameters (Chapters 2–4, 6 and 7).

Operators

∇	Nabla function (Chapter 2).
$\tilde{\nabla}$	Dimensionless gradient operator (Chapter 4).
$\langle \rangle$	Averaged quantities (Chapter 7).

Chapter 1

INTRODUCTION

Satish G. Kandlikar

Mechanical Engineering Department, Rochester Institute of Technology, Rochester, NY, USA

Michael R. King

Departments of Biomedical Engineering, Chemical Engineering and Surgery, University of Rochester, Rochester, NY, USA

1.1. Need for smaller flow passages

Fluid flow inside channels is at the heart of many natural and man-made systems. Heat and mass transfer is accomplished across the channel walls in biological systems, such as the brain, lungs, kidneys, intestines, blood vessels, etc., as well as in many man-made systems, such as heat exchangers, nuclear reactors, desalination units, air separation units, etc. In general, the transport processes occur across the channel walls, whereas the bulk flow takes place through the cross-sectional area of the channel. The channel cross-section thus serves as a conduit to transport fluid to and away from the channel walls.

A channel serves to accomplish two objectives: (i) bring a fluid into intimate contact with the channel walls and (ii) bring fresh fluid to the walls and remove fluid away from the walls as the transport process is accomplished. The rate of the transport process depends on the surface area, which varies with the diameter D for a circular tube, whereas the flow rate depends on the cross-sectional area, which varies linearly with D^2 . Thus, the tube surface area to volume ratio varies as $1/D$. Clearly, as the diameter decreases, surface area to volume ratio increases. In the human body, two of the most efficient heat and mass transfer processes occur inside the lung and the kidney, with the flow channels approaching capillary dimensions of around $4\text{ }\mu\text{m}$.

Figure 1.1 shows the ranges of channel dimensions employed in various systems. Interestingly, the biological systems with mass transport processes employ much smaller dimensions, whereas larger channels are used for fluid transportation. From an engineering standpoint, there has been a steady shift from larger diameters, on the order of 10–20 mm,

E-mail: sgkeme@rit.edu; mike_king@urmc.rochester.edu

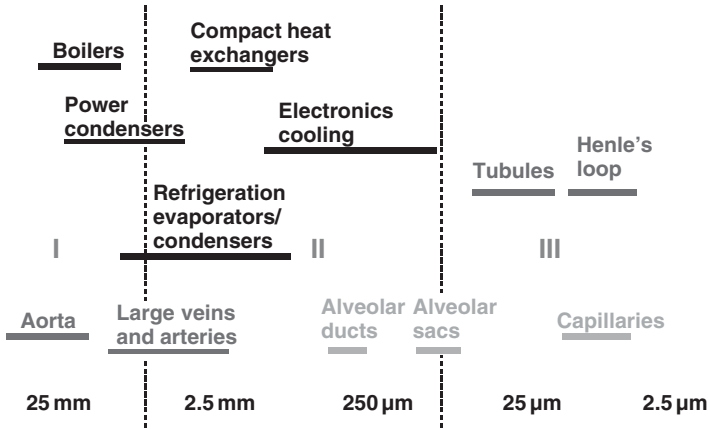


Fig. 1.1. Ranges of channel diameters employed in various applications, Kandlikar and Steinke (2003).

to smaller diameter channels. Since the dimensions of interest are in the range of a few tens or hundreds of micrometers, usage of the term “microscale” has become an accepted classifier for science and engineering associated with processes at this scale.

As the channel size becomes smaller, some of the conventional theories for (bulk) fluid, energy, and mass transport need to be revisited for validation. There are two fundamental elements responsible for departure from the “conventional” theories at microscale. For example, differences in modeling fluid flow in small diameter channels may arise as a result of:

- a change in the fundamental process, such as a deviation from the continuum assumption for gas flow, or an increased influence of some additional forces, such as electrokinetic forces, etc.;
- uncertainty regarding the applicability of empirical factors derived from experiments conducted at larger scales, such as entrance and exit loss coefficients for fluid flow in pipes, etc., or
- uncertainty in measurements at microscale, including geometrical dimensions and operating parameters.

In this book, the potential changes in fundamental processes are discussed in detail, and the needs for experimental validation of empirical constants and correlations are identified if they are not available for small diameter channels.

1.2. Flow channel classification

Channel classification based on hydraulic diameter is intended to serve as a simple guide for conveying the dimensional range under consideration. Channel size reduction has different effects on different processes. Deriving specific criteria based on the process parameters may seem to be an attractive option, but considering the number of processes and parameters that govern transitions from regular to microscale phenomena (if present), a simple dimensional classification is generally adopted in literature. The classification

Table 1.1

Channel dimensions for different types of flow for gases at one atmospheric pressure.

Gas	Channel dimensions (μm)			
	Continuum flow	Slip flow	Transition flow	Free molecular flow
Air	>67	$0.67\text{--}67$	$0.0067\text{--}0.67$	<0.0067
Helium	>194	$1.94\text{--}194$	$0.0194\text{--}1.94$	<0.0194
Hydrogen	>123	$1.23\text{--}123$	$0.0123\text{--}1.23$	<0.0123

Table 1.2

Channel classification scheme.

Conventional channels	$> 3 \text{ mm}$
Minichannels	$3 \text{ mm} \geq D > 200 \mu\text{m}$
Microchannels	$200 \mu\text{m} \geq D > 10 \mu\text{m}$
Transitional Microchannels	$10 \mu\text{m} \geq D > 1 \mu\text{m}$
Transitional Nanochannels	$1 \mu\text{m} \geq D > 0.1 \mu\text{m}$
Nanochannels	$0.1 \mu\text{m} \geq D$

 D : smallest channel dimension

proposed by Mehendale *et al.* (2000) divided the range from 1 to $100 \mu\text{m}$ as microchannels, $100 \mu\text{m}$ to 1 mm as meso-channels, 1 to 6 mm as compact passages, and greater than 6 mm as conventional passages.

Kandlikar and Grande (2003) considered the rarefaction effect of common gases at atmospheric pressure. Table 1.1 shows the ranges of channel dimensions that would fall under different flow types.

In biological systems, the flow in capillaries occurs at very low Reynolds numbers. A different modeling approach is needed in such cases. Also, the influence of electrokinetic forces begins to play an important role. Two-phase flow in channels below $10 \mu\text{m}$ remains unexplored. The earlier channel classification scheme of Kandlikar and Grande (2003) is slightly modified, and a more general scheme based on the smallest channel dimension is presented in Table 1.2.

In Table 1.2, D is the channel diameter. In the case of non-circular channels, it is recommended that the minimum channel dimension; for example, the short side of a rectangular cross-section should be used in place of the diameter D . We will use the above classification scheme for defining minichannels and microchannels. This classification scheme is essentially employed for ease in terminology; the applicability of continuum theory or slip flow conditions for gas flow needs to be checked for the actual operating conditions in any channel.

1.3. Basic heat transfer and pressure drop considerations

The effect of hydraulic diameter on heat transfer and pressure drop is illustrated in Figs. 1.2 and 1.3 for water and air flowing in a square channel under constant heat flux and fully

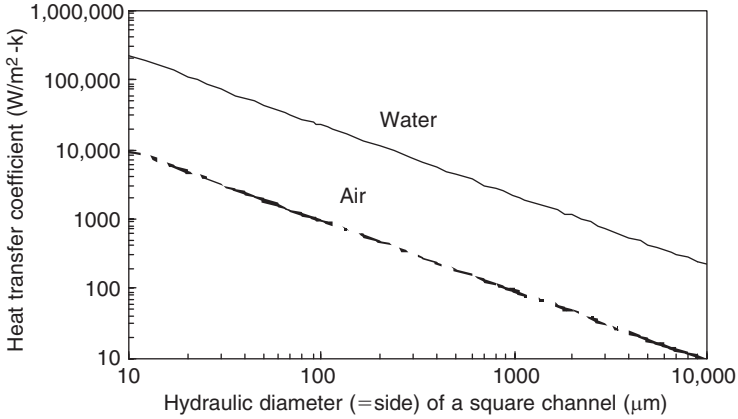


Fig. 1.2. Variation of the heat transfer coefficient with channel size for fully developed laminar flow of air and water.

developed laminar flow conditions. The heat transfer coefficient h is unaffected by the flow Reynolds number (Re) in the fully developed laminar region. It is given by:

$$h = Nu \frac{k}{D_h} \quad (1.1)$$

where k is the thermal conductivity of the fluid and D_h is the hydraulic diameter of the channel. The Nusselt number (Nu) for fully developed laminar flow in a square channel under constant heat flux conditions is 3.61. Figure 1.2 shows the variation of h for flow of water and air with channel hydraulic diameter under these conditions. The dramatic enhancement in h with a reduction in channel size is clearly demonstrated.

On the other hand, the friction factor f varies inversely with Re , since the product $f \cdot Re$ remains constant during fully developed laminar flow. The frictional pressure drop per unit length for the flow of an incompressible fluid is given by:

$$\frac{\Delta p_f}{L} = \frac{2fG^2}{\rho D} \quad (1.2)$$

where $\Delta p_f/L$ is the frictional pressure gradient, f is the Fanning friction factor, G is the mass flux, and ρ is the fluid density. For fully developed laminar flow, we can write:

$$f \cdot Re = C \quad (1.3)$$

where Re is the Reynolds number, $Re = GD_h/\mu$, and C is a constant, $C = 14.23$ for a square channel.

Figure 1.3 shows the variation of pressure gradient with the channel size for a square channel with $G = 200 \text{ kg/m}^2 \text{ s}$, and for air and water assuming incompressible flow conditions. These plots are for illustrative purposes only, as the above assumptions may not be

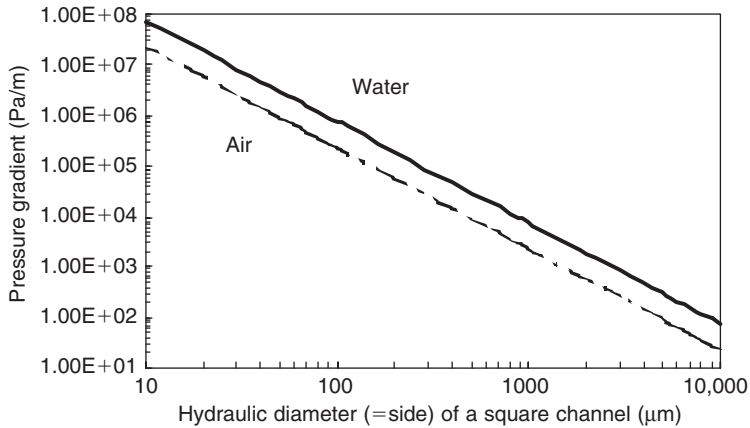


Fig. 1.3. Variation of pressure gradient with channel size for fully developed laminar flow of air and water.

valid for the flow of air, especially in smaller diameter channels. It is seen from Fig. 1.3 that the pressure gradient increases dramatically with a reduction in the channel size.

The balance between the heat transfer rate and pressure drop becomes an important issue in designing the coolant flow passages for the high-flux heat removal encountered in microprocessor chip cooling. These issues are addressed in detail in Chapter 3 under single-phase liquid cooling.

1.4. Special demands of microscale biological applications

The use of minichannels, microchannels, and microfluidics in general is becoming increasingly important to the biomedical community. However, the transport and manipulation of living cells and biological macromolecules place increasingly critical demands on maintaining system conditions within acceptable ranges. For instance, human cells require an environment of 37°C and a $\text{pH} = 7.4$ to ensure their continued viability. If these parameter values stray more than 10% then cell death will result. All protein molecules themselves have preferred pH environments, and large variations from this can cause (sometimes irreversible) denaturation and loss of biological activity due to unfolding.

High temperatures can also cause irreversible protein denaturation. However, in a polymerase chain reaction, or PCR, the rapid cycling (~ 1 min/cycle) of temperature between 94°C and 54°C for 30–40 cycles is necessary to induce repeated denaturation and annealing of DNA chains. Here, the microchannel geometry can be exploited due to the ease of changing the temperature of small liquid volumes, and in fact thermally driven natural convection can be used to achieve such temperature cycles (Krishnan *et al.*, 2002).

Additionally, the concentrations of solutes, such as dissolved gases, nutrients, and metabolic products, must be maintained within specified tolerances to ensure cell proliferation in microchannel bioreactors. Finally, local shear stresses can be critical in suspensions of biological particles. For instance, many cell types such as blood platelets

become activated to a highly adhesive state upon exposure to elevated shear stresses above 10 dynes/cm². Endothelial cells, which line the cardiovascular system, require a certain level of laminar shear stress on their luminal surface (≥ 0.5 dynes/cm²) or else they will not align themselves properly and can express surface receptor molecules which induce chronic inflammation. At much higher shear stresses such as 1500 dynes/cm², as can be produced around sharp corners for very high liquid flow rates, red blood cells are known to “lyse” or rupture. This is especially critical when designing artificial blood pumps or implantable replacement valves. All of these concerns must be separately addressed when developing new microscale flow applications for the transport and manipulation of biological materials.

1.5. Summary

Microchannels are found in many biological systems where extremely efficient heat and mass transfer processes occur, such as lungs and kidneys. The channel size classification is based on observations of many different processes, but its use is mainly in arriving at a common terminology. The heat and mass transfer rates in small diameter channels are also associated with a high pressure drop penalty for fluid flow. The fundamentals of microchannels and minichannels in various applications are presented in this book.

1.6. Practice problems

Problem 1.1 Calculate the heat and mass transfer coefficients for airflow in a human lung at various branches. Assume fully developed laminar flow conditions. Comment on the differences between this idealized case and the realistic flow conditions.

Hint: Consult a basic anatomy book for the dimensions of the airflow passages and flow rates, and a heat and mass transfer book for laminar fully developed Nusselt number and Sherwood number in a circular tube.

Problem 1.2 Calculate the Knudsen number for flow of helium flowing at a pressure of 1 millitorr (1 torr = 1 mmHg) in 0.1-, 1-, 10-, and 100-mm diameter tubes. What type of flow model is applicable for each case?

Hint: Knudsen number is given by $Kn = \lambda/D_h$, and the mean free path λ is given by $\lambda = (\mu\sqrt{\pi}/\rho\sqrt{2RT})$, where μ is the fluid viscosity, ρ is the fluid density, T is the absolute temperature, and R is the gas constant.

Problem 1.3 Calculate the pressure drop for flow of water in a 15-mm long 100- μ m circular microchannel flowing at a temperature of 300 K and with a flow Reynolds number of (a) 10, (b) 100, and (c) 1000. Also calculate the corresponding water flow rates in kg/s and ml/min.

References

- Kandlikar, S. G. and Grande, W. J., 2003, Evolution of microchannel flow passages – thermohydraulic performance and fabrication technology, *Heat Transfer Eng.*, **24**(1), 3–17, 2003.
- Kandlikar, S. G. and Steinke, M. E., 2003, Examples of microchannel mass transfer processes in biological systems, *Proceedings of 1st International Conference on Minichannels and Microchannels*, Rochester, NY, April 24–25, Paper ICMM2003-1124. ASME, pp. 933–943.
- Krishnan, M., Ugaz, V. M., and Burns, M. A., PCR in a Rayleigh–Benard convection cell, *Science*, **298**, 793.
- Mehendale, S. S., Jacobi, A. M., and Shah, R. K., Fluid flow and heat transfer at micro- and meso-scales with applications to heat exchanger design, *Appl. Mech. Rev.*, **53**, 175–193.

This page intentionally left blank

Chapter 2

SINGLE-PHASE GAS FLOW IN MICROCHANNELS

Stéphane Colin

*Department of Mechanical Engineering, National Institute of Applied Sciences of Toulouse,
31077 Toulouse, France*

Microfluidics is a rather young research field, born in the early eighties. Its older relative *fluidics* was in fashion in the sixties to seventies. Fluidics seems to have started in USSR in 1958, then developed in USA and Europe first for military purposes with civil applications appearing later. At that time, fluidics was mainly concerned with inner gas flows in devices involving millimetric or sub-millimetric sizes. These devices were designed to perform the same actions (amplification, logic operations, diode effects, etc.) as their electric counterparts. The idea was to design pneumatically, in place of electrically, supplied computers. The main applications were the concern of the spatial domain, for which electric power overload was indeed an issue due to the electric components of the time that generated excessive magnetic fields and dissipated too much thermal energy to be safe in a confined space. Most of the fluidic devices were etched in a substrate, by means of conventional machining techniques, or by insulation techniques applied on specific resins where masks protected the parts to preserve. The rapid development of microelectronics put a sudden end to pneumatic computers, but these two decades were particularly useful to enhance our knowledge about gas flows in minichannels or mini pneumatic devices.

As microfluidics concerns smaller sizes – the inner sizes of Micro-Electro-Mechanical-Systems (MEMS) – new issues have to be considered in order to accurately model gas microflows. These issues are mainly due to rarefaction effects, which typically must be taken into account when characteristic lengths are of the order of $1\text{ }\mu\text{m}$, under usual temperature and pressure conditions.

In this chapter, the role of rarefaction is explained and its consequences on the behavior of gas flows in microchannels are detailed. The main theoretical and experimental results from the literature about pressure-driven, steady or pulsed gas microflows are summarized. Heat transfer in microchannels and thermally driven gas microflows are also described. They are particularly interesting for vacuum generation, using microsystems without moving parts.

E-mail: stephane.colin@insa-toulouse.fr

2.1. Rarefaction and wall effects in microflows

In microfluidics, theoretical knowledge for gas flows is currently more advanced than that for liquid flows (Colin, 2004). Concerning the gases, the issues are actually more clearly identified: the main micro-effect that results from shrinking down the devices size is rarefaction. This allows us to exploit the strong, although not complete analogy between microflows and low pressure flows that has been extensively studied for more than 50 years and particularly for aerospace applications.

2.1.1. Gas at the molecular level

2.1.1.1. Microscopic length scales

Modeling gas microflows requires us to take into account several characteristic length scales. At the molecular level, we may consider the mean molecular diameter d , the mean molecular spacing δ and the mean free path λ (Fig. 2.1).

The mean free path is the average distance traveled by a molecule between two consecutive collisions, in a frame moving with the stream speed of the gas. If we consider a *simple gas*, that is a gas consisting of a single chemical species with molecules having the same structure, then the mean free path depends on their mean diameter d and on the number density:

$$n = \delta^{-3} \quad (2.1)$$

and the inverse $1/n$ represents the mean volume available for one molecule.

For example, a gas in standard conditions (i.e. for a temperature $T_0 = 273.15$ K and a pressure $p_0 = 1.013 \times 10^5$ Pa), has about 27 million molecules in a cube of $1 \mu\text{m}$ in width ($n_0 = 2.687 \times 10^{25}/\text{m}^3$ and $\delta_0 = 3.34$ nm) and in the case of air for which $d_0 \approx 0.42$ nm, the mean free path is $\lambda_0 \approx 49$ nm. When compared to the case of liquid water, the mean

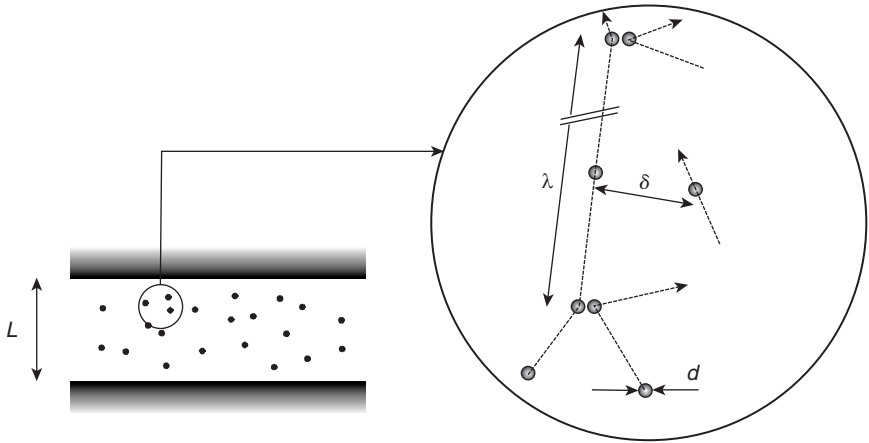


Fig. 2.1. Main characteristic length scales to take into account at the molecular level.

molecular diameter of each are nearly equal, but the mean molecular spacing is about 10 times smaller and the mean free path is 10^5 times smaller than air!

2.1.1.2. Binary intermolecular collisions in dilute simple gases

Gases that satisfy

$$\frac{d}{\delta} \ll 1 \quad (2.2)$$

are said to be *dilute gases*. In that case, most of the intermolecular interactions are binary collisions. Conversely, if Eq. (2.2) is not verified, the gas is said to be a *dense gas*. The dilute gas approximation, along with the equipartition of energy principle, leads to the classic kinetic theory and the Boltzmann transport equation.

With this approximation, the mean free path of the molecules may be expressed as the ratio of the mean thermal velocity \bar{c}' to the collision rate ν :

$$\lambda = \frac{\bar{c}'}{\nu} = \frac{\sqrt{8RT/\pi}}{\nu} \quad (2.3)$$

The thermal velocity \mathbf{c}' of a molecule is the difference between its total velocity \mathbf{c} and the local macroscopic velocity \mathbf{u} of the flow (*cf.* Section 2.1.2), and its mean value $\bar{c}' = \sqrt{8RT/\pi}$, which depends on the temperature T and on the specific gas constant R , is calculated from the Boltzmann equation. The estimation of the collision rate and consequently of the mean free path depends on the model chosen for describing the elastic binary collision between two molecules. Such a model also allows estimation of the total collision cross-section

$$\sigma_t = \pi d^2 \quad (2.4)$$

in the collision plane and the mean molecular diameter d (Fig. 2.2), as well as the dynamic viscosity μ as a function of the temperature.

A collision model generally requires the definition of the force \mathbf{F} exerted between the two considered molecules. This force is actually repulsive at short distances and weakly attractive at large distances. Different approximated models are proposed to describe this force. The more classic one is the so-called *inverse power law (IPL) model* or *point center*

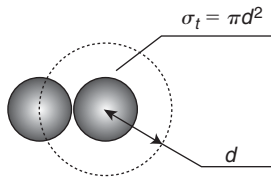


Fig. 2.2. Total collision cross-section in the collision plane.

of *repulsion model* (Bird, 1998). It only takes into account the repulsive part of the force and assumes that

$$F = |\mathbf{F}| = \frac{\kappa}{r^\eta} \quad (2.5)$$

This derives from an intermolecular potential

$$\phi = \frac{\kappa}{(\eta - 1)r^{\eta-1}} \quad (2.6)$$

where κ , as well as the exponent η have a constant value and r denotes the distance between the two molecules centers. Using the Chapman–Enskog theory, this model leads to a law of viscosity in the form

$$\mu = \mu_0 \left(\frac{T}{T_0} \right)^\omega \quad (2.7)$$

with

$$\omega = \frac{\eta + 3}{2(\eta - 1)} \quad (2.8)$$

The collision rate may be deduced as (Lengrand and Elizarova, 2004)

$$\nu = 4 \left(\frac{5}{2} - \omega \right)^{\omega - \frac{1}{2}} \Gamma \left(\frac{5}{2} - \omega \right) n \sigma_{t0} \left(\frac{T}{T_0} \right)^{\frac{1}{2} - \omega} \sqrt{\frac{RT}{\pi}} \quad (2.9)$$

where $\Gamma(j) = \int_0^\infty x^{j-1} \exp(-x) dx$ is the Euler, or gamma function and T_0 is a reference temperature for which the total collision cross-section σ_{t0} is calculated. From Eq. (2.3), we can see that the mean free path

$$\lambda = \frac{1}{\sqrt{2} \left(\frac{5}{2} - \omega \right)^{\omega - \frac{1}{2}} \Gamma \left(\frac{5}{2} - \omega \right) n \sigma_{t0}} \left(\frac{T}{T_0} \right)^{\omega - \frac{1}{2}} \quad (2.10)$$

is proportional to $T^{\omega - \frac{1}{2}}$ and inversely proportional to the number density n .

The simplest collision model is the *hard sphere* (HS) model, which assumes that the total collision cross-section σ_t is constant and for which the viscosity is proportional to the square root of the temperature. Actually, the HS model may be described from the IPL with the exponent $\eta \rightarrow \infty$ and $\omega = 1/2$.

Bird, who proposed the variable hard sphere (VHS) model for applications to the Monte Carlo method (DSMC, cf. Section 2.2.4.2), has improved the HS model. The VHS model may be considered as a HS model with a diameter d that is a function of the relative velocity between the two colliding molecules. The Chapman–Enskog method leads to a viscosity

$$\mu_{\text{VHS}} = \frac{15 m \sqrt{\pi R T}}{8 \left(\frac{5}{2} - \omega \right)^{\omega - \frac{1}{2}} \Gamma \left(\frac{9}{2} - \omega \right) \sigma_{t0}} \left(\frac{T}{T_0} \right)^{\omega - \frac{1}{2}} \quad (2.11)$$

which verifies Eq. (2.7) and where m is the molecular mass. By eliminating σ_{t0} between Eqs. (2.9) or (2.10) and (2.11) and noting that $\Gamma(j+1)=j\Gamma(j)$, the mean free path and the collision rate for a VHS model may be expressed as functions of the viscosity and the temperature:

$$\nu_{\text{VHS}} = \frac{\rho RT}{\mu} \frac{30}{(7-2\omega)(5-2\omega)} \quad (2.12)$$

and

$$\lambda_{\text{VHS}} = \frac{\mu}{\rho\sqrt{2\pi RT}} \frac{2(7-2\omega)(5-2\omega)}{15} \quad (2.13)$$

with $\rho = mn$ as the local density.

Another classic model is the Maxwell molecules (MM) model. It is a special case of the IPL model with $\eta = 5$ and $\omega = 1$. Actually, the HS and the MM models may be considered as the limits of the more realistic VHS model, since real molecules generally have a behavior which corresponds to an intermediate value $1/2 \leq \omega \leq 1$. Another expression is frequently encountered in the literature: for example, Karniadakis and Beskok (2002) or Nguyen and Wereley (2002) use the formula $\lambda_M = \sqrt{\pi/2}\mu/(\rho\sqrt{RT})$ proposed by Maxwell in 1879 (Eq. (2.57)).

Other binary collision models based on the IPL assumption are described in the literature. Koura and Matsumoto (1991; 1992) introduced the variable soft sphere (VSS) model, which differs from the VHS model by a different expression of the deflection angle taken by the molecule after a collision. The VSS model leads to a correction of the mean free path and the collision rate values:

$$\lambda_{\text{VSS}} = \beta\lambda_{\text{VHS}} \quad \nu_{\text{VSS}} = \frac{\nu_{\text{VHS}}}{\beta} \quad (2.14)$$

where $\beta = 6\alpha/[(\alpha+1)(\alpha+2)]$ and the value of α is generally between 1 and 2 (Bird, 1998). Thus, the correction introduced by the VSS model in the mean free path and in the collision rate remains limited, less than 3%. For $\alpha = 1$, the VSS model reduces to the VHS model.

Finally, some models can take into account the long-range attractive part of the force between two molecules by adding a uniform attractive potential (square-well model), or an IPL attractive component (Sutherland, Hassé and Cook or Lennard–Jones potential models) to the HS model. For example, the Lennard–Jones potential is

$$\phi = \frac{\kappa}{(\eta-1)r^{\eta-1}} - \frac{\kappa'}{(\eta'-1)r^{\eta'-1}} \quad (2.15)$$

and the widely used Lennard–Jones 12-6 model corresponds to $\eta = 13$ and $\eta' = 7$. The generalized hard sphere (GHS) model (Hassan and Hash, 1993) is a generalized model that combines the computational simplicity of the VHS model and the accuracy of complicated attractive–repulsive interaction potentials. More recently, the variable sphere (VS) molecular model proposed by Matsumoto (2002) provides consistency for diffusion and viscosity coefficients with those of any realistic intermolecular potential.

Table 2.1

Mean free path, dynamic viscosity, and collision rate for classic IPL collision models.

Model	$F = \frac{\kappa}{r^\eta}$ η	$\mu \propto T^\omega$ ω	$\nu = k_1 \frac{\rho RT}{\mu}$ k_1	$\lambda = k_2 \frac{\mu}{\rho \sqrt{RT}}$ k_2
HS	∞	$\frac{1}{2}$	$\frac{5}{4}$	$\frac{16}{5\sqrt{2\pi}} \approx 1.277$
VHS	η	$\omega = \frac{\eta + 3}{2(\eta - 1)}$	$\frac{30}{(7 - 2\omega)(5 - 2\omega)}$	$\frac{2(7 - 2\omega)(5 - 2\omega)}{15\sqrt{2\pi}}$
MM	5	1	2	$\sqrt{\frac{2}{\pi}} \approx 0.798$
VSS	η	$\omega = \frac{\eta + 3}{2(\eta - 1)}$	$\frac{5(\alpha + 1)(\alpha + 2)}{\alpha(7 - 2\omega)(5 - 2\omega)}$	$\frac{4\alpha(7 - 2\omega)(5 - 2\omega)}{5(\alpha + 1)(\alpha + 2)\sqrt{2\pi}}$

Table 2.1 resumes the relationships between the collision rate, the mean free path, the viscosity, the density and the temperature for classic IPL collision models. As the mean free path λ is an important parameter for the simulation of gas microflows (*cf.* Section 2.1.2), we should be careful when comparing some theoretical results from the literature and verify from which model λ has been calculated. Note that for the formula of Maxwell, $k_{2,M} = \sqrt{\pi}/2$ is 2% lower than the value $k_{2,HS} = 16/(5\sqrt{2\pi})$ obtained from a HS model.

Equation (2.11) is also interesting because it allows estimation of the mean molecular diameter d from viscosity data and a VHS model. Table 2.2 gives the value of d for different gases under standard conditions, obtained by Bird (1998), from a VHS or a VSS hypothesis. The ratio δ_0/d is calculated for the mean value d of d_{VHS} and d_{VSS} . For any gas, we can see that the condition (2.2) is roughly verified and the different gases can reasonably be considered as dilute gases under standard conditions. However, the dilute gas approximation will be better for He than for SO_2 .

2.1.2. Continuum assumption and thermodynamic equilibrium

When applicable, the continuum assumption is very convenient since it erases the molecular discontinuities, by averaging the microscopic quantities on a small sampling volume. All macroscopic quantities of interest in classic fluid mechanics (density ρ , velocity \mathbf{u} , pressure p , temperature T , etc.) are assumed to vary continuously from point to point within the flow.

For example, if we consider an air flow in a duct, for which the macroscopic velocity varies from 0 to 1 m/s and is parallel to the axis of the duct, the velocity of a molecule is of the order of 1 km/s and may take any direction. Similar considerations also concern the other mechanical and thermodynamic quantities.

In order to respect the continuum assumption, the microscopic fluctuations should not generate significant fluctuations of the averaged quantities. Consequently, the size of a representative sampling volume must be large enough to erase the microscopic fluctuations, but it must also be small enough to point out the macroscopic variations, such as velocity or

Table 2.2

Molecular weight, dynamic viscosity and mean molecular diameters under standard conditions ($p_0 = 1.013 \times 10^5$ Pa and $T_0 = 273.15$ K) estimated from a VHS or a VSS model (data from Bird (1998)) with corresponding values of the ratio δ_0/d .

Gas	$M \times 10^3$ (kg/mol)	$\mu_0 \times 10^7$ (N-s/m ²)	ω	d_{VHS} (pm)	α	d_{VSS} (pm)	δ_0/d
Sea level air	28.97	171.9	0.77	419	—	—	7.97
Ar	39.948	211.7	0.81	417	1.40	411	8.06
CH ₄	16.043	102.4	0.84	483	1.60	478	6.95
Cl ₂	70.905	123.3	1.01	698	—	—	4.78
CO	28.010	163.5	0.73	419	1.49	412	8.04
CO ₂	44.010	138.0	0.93	562	1.61	554	5.98
H ₂	2.0159	84.5	0.67	292	1.35	288	11.51
HCl	36.461	132.8	1.00	576	1.59	559	5.88
He	4.0026	186.5	0.66	233	1.26	230	14.42
Kr	83.80	232.8	0.80	476	1.32	470	7.06
N ₂	28.013	165.6	0.74	417	1.36	411	8.06
N ₂ O	44.013	135.1	0.94	571	—	—	5.85
Ne	20.180	297.5	0.66	277	1.31	272	12.16
NH ₃	17.031	92.3	1.10	594	—	—	5.62
NO	30.006	177.4	0.79	420	—	—	7.95
O ₂	31.999	191.9	0.77	407	1.40	401	8.26
SO ₂	64.065	116.4	1.05	716	—	—	4.66
Xe	131.29	210.7	0.85	574	1.44	565	5.86

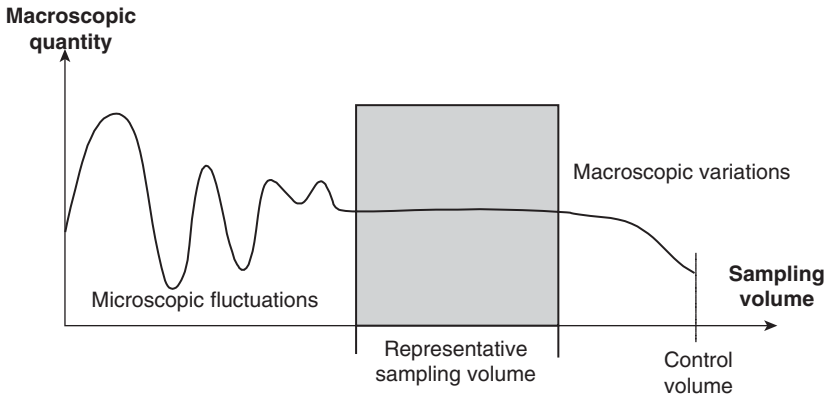


Fig. 2.3. The existence of a representative sampling volume (shaded area) is necessary for the continuum assumption to be valid.

pressure gradients of interest in the control volume (Fig. 2.3). If the shaded area on Fig. 2.3 does not exist, the sampling volume is not representative and the continuum assumption is not valid.

It may be considered that sampling a volume containing 10,000 molecules leads to 1% statistical fluctuations in the macroscopic quantities (Karniadakis and Beskok, 2002). Such a fluctuation level needs a sampling volume which characteristic length l_{SV} verifies

$l_{SV}/\delta = 10^{4/3} \approx 22$. Consequently, the control volume must have a much higher characteristic length L , that is

$$\frac{L}{\delta} \gg 10^{4/3} \quad (2.16)$$

so that the *statistical fluctuations* can be *neglected*. For example, for air at standard conditions, the value of l_{SV} corresponding to 1% statistical fluctuations is 72 nm. This is comparable to the value of the mean free path $\lambda_0 = 49$ nm.

Moreover, the continuum approach requires that the sampling volume is in *thermodynamic equilibrium*. For the thermodynamic equilibrium to be respected, the frequency of the intermolecular collisions inside the sampling volume must be high enough. This implies that the mean free path $\lambda = \bar{c}/\nu$ must be small compared with the characteristic length l_{SV} of the sampling volume, itself being small compared with the characteristic length L of the control volume. As a consequence, the thermodynamic equilibrium requires that

$$\frac{\lambda}{L} \ll 1 \quad (2.17)$$

This ratio

$$\text{Kn} = \frac{\lambda}{L} \quad (2.18)$$

is called the Knudsen number and it plays a very important role in gaseous microflows (see Section 2.1.3). If λ is obtained from an IPL collision model,

$$\lambda = k_2 \mu / \rho \sqrt{RT} \quad (2.19)$$

with k_2 given by Table 2.1, and the Knudsen number can be related to the Reynolds number

$$\text{Re} = \frac{\rho u L}{\mu} \quad (2.20)$$

and the Mach number

$$\text{Ma} = \frac{u}{a} \quad (2.21)$$

by the relationship

$$\text{Kn} = k_2 \sqrt{\gamma} \frac{\text{Ma}}{\text{Re}} \quad (2.22)$$

Here, γ is the ratio of the specific heats of the gas and a , the local speed of sound, with $a = \sqrt{\gamma RT}$ for an ideal gas (Anderson, 1990), which is verified for a dilute gas (*cf.* Section 2.2.1). Equation (2.22) shows the link between rarefaction (characterized by Kn) and compressibility (characterized by Ma) effects, the latter having to be taken into account if $\text{Ma} > 0.3$.

The limits that correspond to Eqs. (2.2), (2.16) and (2.17), with the indicative values ($\delta/d = 7$, $L/\delta = 100$ and $\lambda/L = 0.1$) proposed by Bird (Bird, 1998), are shown in Fig. 2.4. In this figure, the mean free path has been estimated with an HS model, for which Eq. (2.10) can be written using Eq. (2.4) and $\omega = 1/2$, in the form

$$\lambda_{\text{HS}} = \frac{\delta^3}{\sqrt{2}\pi d^2} \quad (2.23)$$

Thus $\lambda/L = (\delta/d)^3(d/L)(1/\sqrt{2}\pi)$ and the thermodynamic equilibrium limit $\lambda/L = 0.1$ is a straight line with a slope equal to -3 in the log-log plot of Fig. 2.4.

2.1.3. Rarefaction and Knudsen analogy

It is now clear that the similitude between low pressure and confined flows is not complete, since the Knudsen number is not the only parameter to take into account (*cf.* Fig. 2.4.).

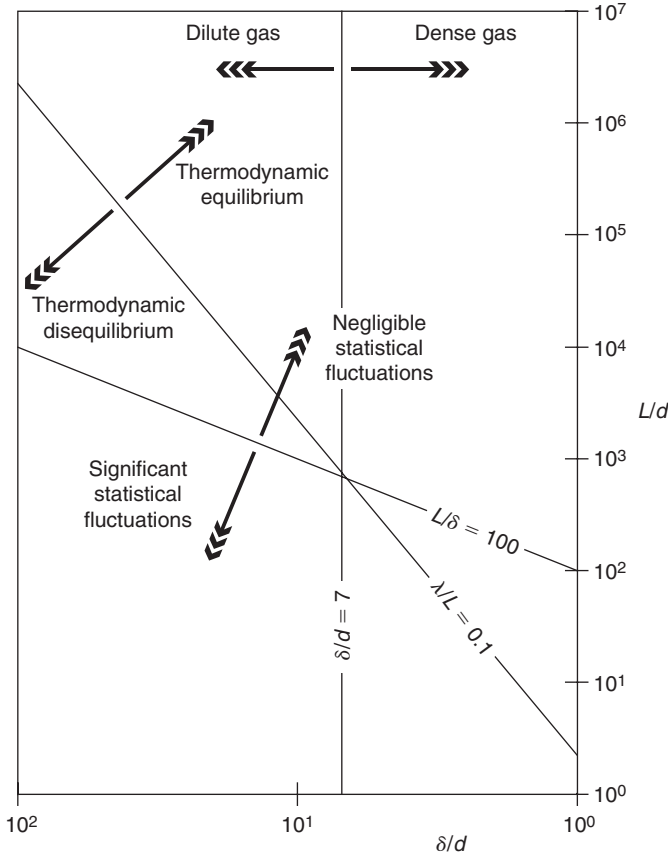


Fig. 2.4. Limits of the main approximations for the modeling of gas microflows (from Bird (1998)).

However, it is convenient to differentiate the flow regimes in function of Kn , and the following classification, although tinged with empiricism, is usually accepted:

- For $Kn < 10^{-3}$, the flow is a *continuum flow* (**C**) and it is accurately modeled by the compressible Navier–Stokes equations with classical no-slip boundary conditions.
- For $10^{-3} < Kn < 10^{-1}$, the flow is a *slip flow* (**S**) and the Navier–Stokes equations remain applicable, provided a velocity slip and a temperature jump are taken into account at the walls. These new boundary conditions point out that rarefaction effects become sensitive at the wall first.
- For $10^{-1} < Kn < 10$, the flow is a *transition flow* (**T**) and the continuum approach of the Navier–Stokes equations is no longer valid. However, the intermolecular collisions are not yet negligible and should be taken into account.
- For $Kn > 10$, the flow is a *free molecular flow* (**M**) and the occurrence of intermolecular collisions is negligible compared with the one of collisions between the gas molecules and the walls.

These different regimes will be detailed in the following sections. Their limits are only indicative and could vary from one case to another, partly because the choice of the characteristic length L is rarely unique. For flows in channels, L is generally the hydraulic diameter or the depth of the channel. In complex geometrical configurations, it is generally preferable to define L from local gradients (e.g. of the density ρ : $L = 1/|\nabla \rho/\rho|$) rather than from simple geometrical considerations (Gad-el-Hak, 1999); the Knudsen number based on this characteristic length is the so-called local rarefaction number (Lengrand and Elizarova, 2004). Figure 2.5 locates these different regimes for air in standard conditions. For comparison, the cases of helium and sulphur dioxide are also represented. For SO_2 , the dilute gas assumption is less valid than for air and He, and the binary intermolecular collision models described in Section 2.1.1.2 could be inaccurate. The shaded area roughly represents the domain of validity for classic gas flow models (**C**).

The relationship with the characteristic length L expressed in micrometers is illustrated in Fig. 2.6, which shows the typical ranges covered by fluidic microsystems described in the literature. Typically, most of the microsystems which use gases work in the slip flow regime, or in the early transition regime. In simple configurations, such flows can be analytically or semi-analytically modeled. The core of the transition regime relates to more specific flows that involve lengths under 100 nanometers, as it is the case for a Couette flow between a hard disk and a read–write head. In that regime, the only theoretical models are molecular models that require numerical simulations. Finally, under the effect of both low pressures and small dimensions, more rarefied regimes can occur, notably inside microsystems dedicated to vacuum generation.

2.1.4. Wall effects

We have seen that initial deviations from the classic continuum models appear when we shrink down the characteristic length L of the flow with respect to the boundary conditions. It is logical that the first sources of thermodynamic disequilibria appear on the boundary because at the wall there are fewer interactions between the gas molecules than in the core of the flow.

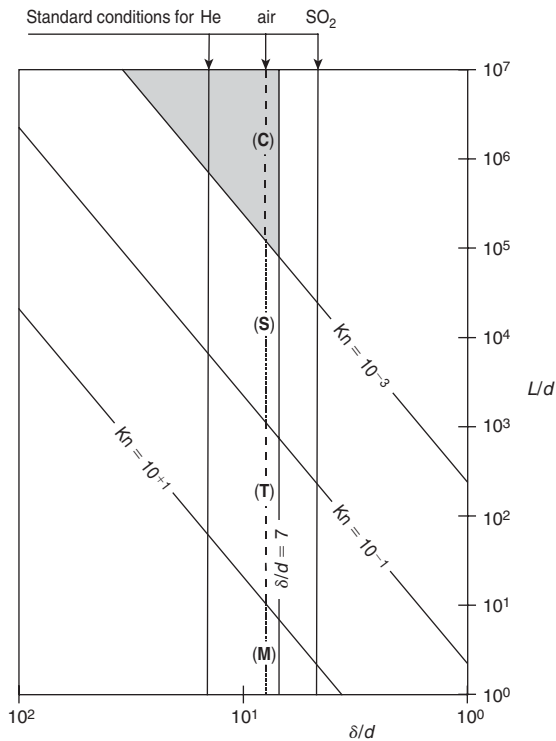


Fig. 2.5. Gas flow regimes as a function of the Knudsen number.

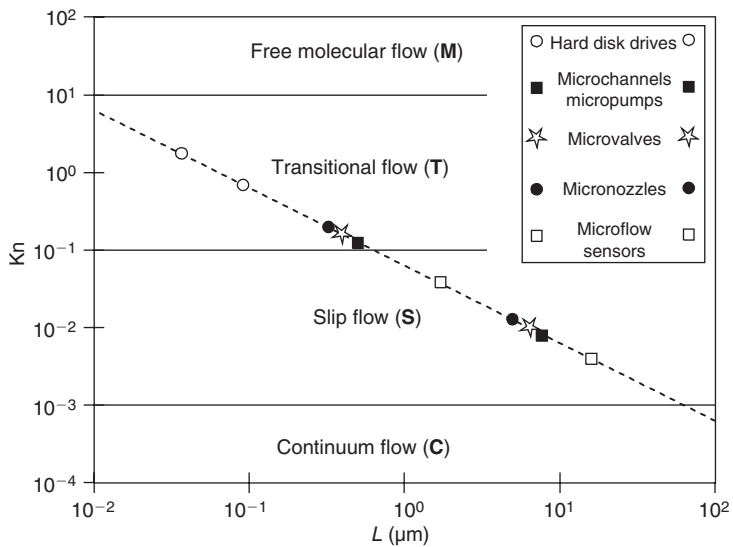


Fig. 2.6. Gas flow regimes for usual microsystems (from Karniadakis and Beskok (2002)).

Actually, the walls play a crucial role in gas microflows. First, shrinking system sizes results in an increase of surface over volume effects. It is interesting for heat transfer enhancement, but it also requires an excellent knowledge of the velocity, as well as the temperature and boundary conditions. The velocity slip and the temperature jump observed at the wall in the slip flow regime strongly depend on the nature and on the state of the wall, in relation to the nature of the gas. Thus, the roughness of the wall and the chemical affinity between the wall and the gas, although often not properly known, could highly affect the fluid flow and the heat transfer.

2.2. Gas flow regimes in microchannels

Usually, the *regime* of gas flow in a macrochannel refers to *viscous* and *compressibility* effects, respectively quantified by the Reynolds number Re and the Mach number Ma . For low Reynolds numbers (typically for $Re < 2000$), the flow is *laminar* and it becomes *turbulent* for higher values of Re . For $Ma < 1$, the flow is *subsonic* and for $Ma > 1$, it is *supersonic*. Typically, if $Ma > 0.3$, compressibility effects should be taken into account.

In microchannels on the other hand, the main effects are *rarefaction* effects, essentially quantified by the Knudsen number Kn . Consequently, the *regime* usually refers to these effects, according to the classification given in Section 2.1.3, and flows are considered as microflows for $Kn > 10^{-3}$. Actually, Eq. (2.22) shows that for a dilute gas, $Re = k_2 \sqrt{\gamma} Ma / Kn$, where $k_2 \sqrt{\gamma}$ is of the order of unity, which implies that for subsonic microflows, viscous effects are predominant and the flows are laminar.

The models used to describe gas flows in microchannels depend on the rarefaction regime. The main models are presented in Fig. 2.7, with the rough values of Kn for which

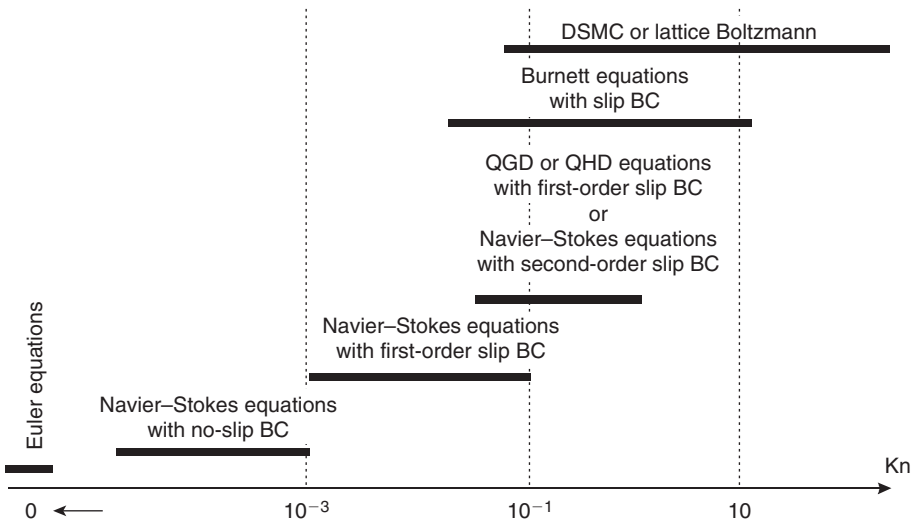


Fig. 2.7. Gas flow regimes and main models according to the Knudsen number. BC: boundary condition.

each of them is applicable, that is valid and really interesting to use. The limits are indicative and may vary according to the considered configurations.

These models are described in the following sections. Among the three main rarefied regimes (slip flow, transition flow and molecular flow), the slip flow regime is more specially detailed, since it is the most frequently encountered (*cf.* Fig. 2.6) and it allows analytic or semi-analytic developments. Moreover, the gas is considered as a dilute gas, which makes valid the ideal gas assumption.

2.2.1. Ideal gas model

The classic equation of state for an ideal gas,

$$p = \rho RT = nk_B T \quad (2.24)$$

is also called the Boyle–Mariotte’s law. Here, p is the pressure and $\rho = mn$ is the density, $k_B = R/N = (M/N)(R/M) = mR = 1.38065 \text{ J/K}$ is the Boltzmann constant, $R = 8.314511 \text{ J/mol/K}$ being the universal gas constant, $N = 6.022137 \times 10^{23} \text{ mol}^{-1}$, the Avogadro’s number and M , the molecular weight. Equation (2.24) may be obtained from a molecular analysis, assuming that the gas is a dilute gas in thermodynamic equilibrium.

If the thermodynamic equilibrium is not verified, Eq. (2.24) remains valid, providing the thermodynamic temperature T is replaced with the translational kinetic temperature T_{tr} , which measures the mean translational kinetic energy of the molecules. The specific ideal gas constant

$$R = c_p - c_v \quad (2.25)$$

is the difference between the specific heats

$$c_p = \left. \frac{\partial h}{\partial T} \right|_p \quad (2.26)$$

and

$$c_v = \left. \frac{\partial e}{\partial T} \right|_v \quad (2.27)$$

where e is the internal specific energy, $v = 1/\rho$ is the specific volume and h is the specific enthalpy. For an ideal gas, the specific heats are constant and their ratio is the index

$$\gamma = \frac{c_p}{c_v} \quad (2.28)$$

Therefore, for an ideal gas,

$$c_v = \frac{1}{\gamma - 1} R \quad c_p = \frac{\gamma}{\gamma - 1} R \quad (2.29)$$

The specific heat ratio is constant for a monatomic gas ($\gamma = 5/3$) but it is dependent of the temperature for a diatomic gas, with a value close to 7/5 near atmospheric conditions.

Finally, we can note that for an ideal gas and an IPL collision model, the Knudsen number can be written as:

$$\text{Kn} = \frac{k_2 \mu(T)}{\rho \sqrt{RT} L} = \frac{k_2 \mu(T) \sqrt{RT}}{pL} \quad (2.30)$$

with the value of k_2 given in Table 2.1.

2.2.2. Continuum flow regime

The classic continuum flow regime (which corresponds to the shaded area in Fig. 2.5) may be accurately modeled by the *compressible Navier–Stokes equations*, the ideal gas equation of state, and classic boundary conditions that express the continuity of temperature and velocity between the fluid and the wall.

2.2.2.1. Compressible Navier–Stokes equations

The compressible Navier–Stokes equations are the governing conservation laws for mass, momentum and energy. These laws are written assuming that the fluid is Newtonian, so that the stress tensor

$$\boldsymbol{\sigma}' = -p\mathbf{I} + \boldsymbol{\sigma} \quad (2.31)$$

is a linear function of the velocity gradients. Thus, the viscous stress tensor has the form $\boldsymbol{\sigma} = \mu[\nabla \otimes \mathbf{u} + (\nabla \otimes \mathbf{u})^T] + \zeta(\nabla \cdot \mathbf{u})\mathbf{I}$, where \mathbf{u} is the velocity vector, \mathbf{I} is the unit tensor, μ is the dynamic viscosity and ζ is the second coefficient of viscosity, or Lamé coefficient. With Stokes' hypothesis, $2\mu + 3\zeta = 0$, which expresses that the changes of volume do not involve viscosity, the viscous stress tensor may be written as $\boldsymbol{\sigma} = \mu[\nabla \otimes \mathbf{u} + (\nabla \otimes \mathbf{u})^T - (2/3)(\nabla \cdot \mathbf{u})\mathbf{I}]$. The validity of this assumption is discussed in Gad-el-Hak (1995).

The Navier–Stokes equations also assume that the fluid follows the Fourier law of diffusion. Thus, the heat flux vector \mathbf{q} is related to the temperature gradient by $\mathbf{q} = -k\nabla T$, where the thermal conductivity k is a function of the temperature.

With the above relations, the compressible Navier–Stokes equations may be written as:

$$\frac{\partial \rho}{\partial t} + \nabla \cdot (\rho \mathbf{u}) = 0 \quad (2.32)$$

$$\frac{\partial(\rho \mathbf{u})}{\partial t} + \nabla \cdot \left(\rho \mathbf{u} \otimes \mathbf{u} - \mu \left[\nabla \otimes \mathbf{u} + (\nabla \otimes \mathbf{u})^T - \frac{2}{3}(\nabla \cdot \mathbf{u})\mathbf{I} \right] \right) + \nabla p = \mathbf{f} \quad (2.33)$$

$$\frac{\partial E}{\partial t} + \nabla \cdot \left((E + p)\mathbf{u} - \mu \left[\nabla \otimes \mathbf{u} + (\nabla \otimes \mathbf{u})^T - \frac{2}{3}(\nabla \cdot \mathbf{u})\mathbf{I} \right] \cdot \mathbf{u} - k\nabla T \right) = \mathbf{f} \cdot \mathbf{u} \quad (2.34)$$

These conservation equations are respectively the continuity (2.32), the momentum (2.33) and the energy (2.34) equations. The total energy per unit volume

$$E = \rho \left(\frac{1}{2} \mathbf{u} \cdot \mathbf{u} + e \right) \quad (2.35)$$

is a function of the internal specific energy e that may be written for an ideal gas, using Eqs. (2.24)–(2.26) and (2.28):

$$e = \frac{p}{\rho(\gamma - 1)} \quad (2.36)$$

The external volume forces \mathbf{f} (gravitational forces, magnetic forces, etc.) are generally negligible in gas flow. It is even more the case in gas microflows, since the volume over surface ratio decreases with the characteristic length L and consequently, in microscale geometries, volume effects may be neglected when compared to surface effects.

2.2.2.2. Classic boundary conditions

The previous set of Eqs. (2.24) and (2.32)–(2.34) must be completed with appropriate boundary conditions. In the continuum flow regime, they express the continuity of the velocity,

$$\mathbf{u}|_w = \mathbf{u}_{\text{wall}} \quad (2.37)$$

and of the temperature,

$$T|_w = T_{\text{wall}} \quad (2.38)$$

at the wall, the subscripts “wall” relating to the wall itself, and “w” to the conditions in the fluid at the wall.

2.2.3. Slip flow regime

Actually, whatever the Knudsen number (even for very low values of Kn), there is in the neighborhood of the wall a domain in which the gas is out of equilibrium. This domain is called the *Knudsen layer* and has a thickness in the order of the mean free path. For very low Knudsen numbers (in the continuum flow regime), the effect of the Knudsen layer is negligible. In the slip flow regime, which is roughly in the range $10^{-3} < \text{Kn} < 10^{-1}$, the Knudsen layer must be taken into account. Actually, the flow in the Knudsen layer cannot be analyzed from continuum by use of the Navier–Stokes equations, for example. But for $\text{Kn} < 10^{-1}$, its thickness is small enough and the Knudsen layer can be neglected, providing the boundary conditions (2.37)–(2.38) are modified and express a velocity slip, as well as a temperature jump at the wall (Section 2.2.3.2).

Thus, the Navier–Stokes equations remain applicable, but it could also be convenient to replace them by another set of conservation equations, such as the quasi-hydrodynamic (QHD) equations or the quasi-gasdynamics (QGD) equations (see Section 2.2.3.1).

2.2.3.1. Continuum NS–QGD–QHD equations

In a generic form, the conservation equations may be written in the following way:

$$\frac{\partial \rho}{\partial t} + \nabla \cdot \mathbf{J}_{\text{EQ}} = 0 \quad (2.39)$$

for the continuity equation,

$$\frac{\partial(\rho \mathbf{u})}{\partial t} + \nabla \cdot (\mathbf{J}_{\text{EQ}} \otimes \mathbf{u} - \boldsymbol{\sigma}_{\text{EQ}}) + \nabla p = 0 \quad (2.40)$$

for the momentum equation and

$$\frac{\partial E}{\partial t} + \nabla \cdot \left(\frac{E + p}{\rho} \mathbf{J}_{\text{EQ}} - \boldsymbol{\sigma}_{\text{EQ}} \cdot \mathbf{u} + \mathbf{q}_{\text{EQ}} \right) = 0 \quad (2.41)$$

for the energy equation. In these equations, \mathbf{J}_{EQ} is the mass flux vector, $\boldsymbol{\sigma}_{\text{EQ}}$, the viscous stress tensor and \mathbf{q}_{EQ} , the heat flux vector. The external volume forces \mathbf{f} have been neglected.

In the case of the Navier–Stokes equations ($\text{EQ} \equiv \text{NS}$) these variables have the form:

$$\mathbf{J}_{\text{NS}} = \rho \mathbf{u} \quad (2.42)$$

$$\boldsymbol{\sigma}_{\text{NS}} = \mu [\nabla \otimes \mathbf{u} + (\nabla \otimes \mathbf{u})^T] + \zeta (\nabla \cdot \mathbf{u}) \mathbf{I} = \mu \left[\nabla \otimes \mathbf{u} + (\nabla \otimes \mathbf{u})^T - \frac{2}{3} (\nabla \cdot \mathbf{u}) \mathbf{I} \right] \quad (2.43)$$

$$\mathbf{q}_{\text{NS}} = -k \nabla T \quad (2.44)$$

These lead to the previous Eqs. (2.32)–(2.34). In the Navier–Stokes equations, the density ρ , the pressure p and the velocity \mathbf{u} correspond to space averaged instantaneous quantities.

From spatiotemporal considerations, the QGD and the QHD equations may be obtained (Lengrand and Elizarova, 2004). They are based on the same governing conservation laws (2.39)–(2.41), but these laws are closed with a different definition of \mathbf{J}_{EQ} , $\boldsymbol{\sigma}_{\text{EQ}}$ and \mathbf{q}_{EQ} . Dissipative terms are added, which involve a parameter τ . This parameter

$$\tau = \frac{\gamma \mu}{\text{Sc} \rho a^2} \quad (2.45)$$

is a time characteristic of the temporal averaging. Here, $\text{Sc} = \mu/(\rho D)$ is the Schmidt number, which represents the ratio of the diffusive mass over the diffusive momentum fluxes. In the expression of Sc , D is the diffusion coefficient, which can be expressed as a function of α and ω for a VSS molecule. Thus, for a VSS molecule,

$$\text{Sc} = \frac{5(2 + \alpha)}{3(7 - 2\omega)\alpha} \quad (2.46)$$

which reduces to 5/6 for a HS model. For an ideal gas, $a^2 = \gamma RT$ and τ may be written as:

$$\tau = \frac{1}{\text{Sc}} \frac{\mu}{p} \quad (2.47)$$

The QGD equations are appropriate for dilute gases. For these equations (EQ \equiv QGD):

$$\mathbf{J}_{\text{QGD}} = \mathbf{J}_{\text{NS}} - \tau[\nabla \cdot (\rho \mathbf{u} \otimes \mathbf{u}) + \nabla p] \quad (2.48)$$

$$\sigma_{\text{QGD}} = \sigma_{\text{NS}} + \tau[\mathbf{u} \otimes (\rho \mathbf{u} \cdot (\nabla \otimes \mathbf{u}) + \nabla p) + \mathbf{I}(\mathbf{u} \cdot \nabla p + \gamma p \nabla \cdot \mathbf{u})] \quad (2.49)$$

$$\mathbf{q}_{\text{QGD}} = \mathbf{q}_{\text{NS}} - \tau \rho \mathbf{u}[\mathbf{u} \cdot \nabla e + p \mathbf{u} \cdot \nabla(1/\rho)] \quad (2.50)$$

From Eqs. (2.18), (2.19), (2.24) and (2.47), we can deduce that for a dilute gas and an IPL collision model,

$$\tau = \frac{\text{Kn}}{\text{Sc}} \frac{1}{k_2} \frac{L}{\sqrt{RT}} \quad (2.51)$$

Therefore, $[\tau \nabla]_{(\text{Kn} \rightarrow 0)} \rightarrow 0$, which shows that the above QGD equations degenerate into the classic NS equations when rarefaction is negligible.

Another set of equations, the QHD equations, are appropriate to dense gases. In that case (EQ \equiv QHD):

$$\mathbf{J}_{\text{QHD}} = \mathbf{J}_{\text{NS}} - \tau[\rho \mathbf{u} \cdot (\nabla \otimes \mathbf{u}) + \nabla p] \quad (2.52)$$

$$\sigma_{\text{QHD}} = \sigma_{\text{NS}} + \tau \mathbf{u} \otimes (\rho \mathbf{u} \cdot (\nabla \otimes \mathbf{u}) + \nabla p) \quad (2.53)$$

$$\mathbf{q}_{\text{QHD}} = \mathbf{q}_{\text{NS}} \quad (2.54)$$

They also bring additional terms to the NS equations, which are proportional to the parameter τ .

2.2.3.2. First-order slip boundary conditions

From a series of experiments at low pressures performed in 1875, Kundt and Warburg were probably the first who pointed out that for a flow of rarefied gas, slipping occurs at the walls (Kennard, 1938). For a gas flowing in the direction s parallel to the wall, the slip velocity may be written as:

$$u_{\text{slip}} = u_s - u_{\text{wall}} = \xi \left. \frac{\partial u_s}{\partial n} \right|_{\text{w}} \quad (2.55)$$

where ξ is a length commonly called the *coefficient of slip* and n is the normal direction, exiting the wall. With appropriate assumptions, it is possible to calculate the magnitude of the coefficient of slip from the kinetic theory of gases.

Following a paper initially dealing with stresses in rarefied gases due to temperature gradients (Maxwell, 1879), Maxwell added an appendix on the advice of a referee, with the aim of expressing the conditions which must be satisfied by a gas in contact with a solid body. Maxwell treated the surface as something intermediate between a perfectly reflecting and a perfectly absorbing surface. Therefore, he assumed that for every unit

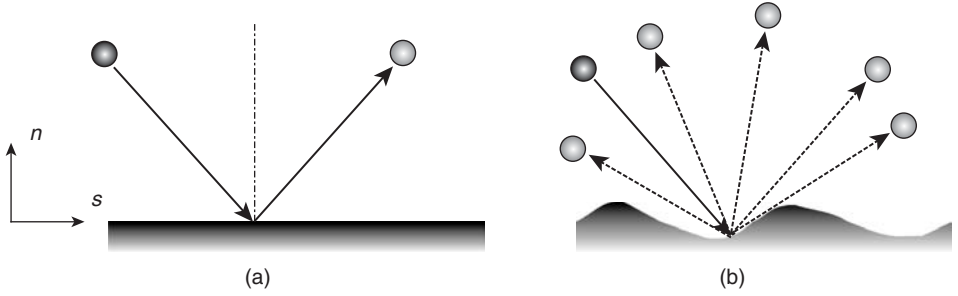


Fig. 2.8. Maxwell hypothesis. (a) Perfect (specular) reflection of a fraction $1 - \sigma$ of the molecules. (b) Absorption and diffuse reemission of a fraction σ of the molecules.

of area, a fraction σ of the molecules is absorbed by the surface (due to the roughness of the wall, or to a condensation–evaporation process (Kennard, 1938)) and is afterwards reemitted with velocities corresponding to those in still gas at the temperature of the wall. The other fraction, $1 - \sigma$, of the molecules is perfectly reflected by the wall (Fig. 2.8). The dimensionless coefficient σ is called the *tangential momentum accommodation coefficient*. When $\sigma = 0$, the tangential momentum of the incident molecules equals that of the reflected molecules and no momentum is transmitted to the wall, as if the flow was inviscid. This kind of reflection is called *specular reflection*. Conversely, when $\sigma = 1$, the gas molecules transmit all their tangential momentum to the wall and the reflection is a *diffuse reflection*.

From a momentum balance at the wall, Maxwell finally demonstrated that there is a slip at the wall, which takes the form:

$$u_{\text{slip}} = u_s - u_{\text{wall}} = \frac{2 - \sigma}{\sigma} \lambda_M \left[\frac{\partial u_s}{\partial n} - \frac{3}{2} \frac{\mu}{\rho T} \frac{\partial^2 T}{\partial s \partial n} \right]_w + \frac{3}{4} \left[\frac{\mu}{\rho T} \frac{\partial T}{\partial s} \right]_w \quad (2.56)$$

with

$$\lambda_M = \sqrt{\frac{\pi}{2}} \frac{\mu}{\sqrt{p\rho}} = \sqrt{\frac{\pi}{2}} \frac{\mu}{\rho \sqrt{RT}} \quad (2.57)$$

which is very close to the value of the mean free path λ_{HS} deduced from an HS model.

The equation of Maxwell is generally cited in the literature with the form

$$\begin{aligned} u_{\text{slip}} = u_s - u_{\text{wall}} &= \frac{2 - \sigma}{\sigma} \lambda \frac{\partial u_s}{\partial n} \Big|_w + \frac{3}{4} \frac{\mu}{\rho T} \frac{\partial T}{\partial s} \Big|_w \\ &= \frac{2 - \sigma}{\sigma} \lambda \frac{\partial u_s}{\partial n} \Big|_w + \frac{3}{4} \frac{\lambda}{k_2} \sqrt{\frac{R}{T}} \frac{\partial T}{\partial s} \Big|_w \end{aligned} \quad (2.58)$$

which omits the second term on the right-hand side of Eq. (2.56).

After non-dimensionalization with the characteristic length L , a reference velocity u_0 and a reference temperature T_0 , Eq. (2.58) is written as follows:

$$u_s^* - u_{\text{wall}}^* = \frac{2 - \sigma}{\sigma} \text{Kn} \left. \frac{\partial u_s^*}{\partial n^*} \right|_w + \frac{3}{4\gamma k_2^2} \frac{\text{Kn}^2 \text{Re}_0}{\text{Ma}_0^2} \left. \frac{\partial T^*}{\partial s^*} \right|_w \quad (2.59)$$

where $u_s^* = u_s/u_0$, $T^* = T/T_0$, $n^* = n/L$ and $s^* = s/L$. Note that this non-dimensionalization is valid only if the reference lengths are the same in the s and n directions, which is generally not the case for a flow in a microchannel. In that case, it is preferable to keep the dimensional form of Eq. (2.58). The second term on the right-hand side, which is proportional to the square of the Knudsen number $\text{Kn} = \lambda/L$, involves the Reynolds number $\text{Re}_0 = \rho u_0 L / \mu$ and the Mach number $\text{Ma}_0 = u_0 / \sqrt{\gamma R T_0}$ defined at the reference conditions. The coefficient k_2 depends on the intermolecular collision model and its value is given in Table 2.1. This second term is associated with the thermal creep, or transpiration phenomenon. It shows that a flow can be caused in the sole presence of a tangential temperature gradient, without any pressure gradient. In that case, the gas experiences a slip velocity and moves from the colder toward the warmer region. This can also result in pressure variation in a microchannel only submitted to tangential temperature gradients.

The non-dimensional form of Eq. (2.59) clearly shows that slip is negligible for very low Knudsen numbers, but should be taken into account when Kn is no longer small, typically as soon as it becomes higher than 10^{-3} .

In analogy with the slip phenomenon, Poisson suggested that there might also be a temperature jump at the wall, which could be described by an equation equivalent to

$$T - T_{\text{wall}} = \varsigma \left. \frac{\partial T}{\partial n} \right|_w \quad (2.60)$$

where ς is called the *temperature jump distance*. Smoluchowski experimentally confirmed this hypothesis (Smoluchowski, 1898) and showed that ς was proportional to the mean free path λ . As for the slip, it can be assumed that a fraction σ_T of the molecules have a long contact with the wall and that the wall adjusts their mean thermal energy. Therefore, these molecules are reemitted as if they were issuing from a gas at the temperature of the wall. The other fraction, $1 - \sigma_T$, is reflected keeping its incident thermal energy. The dimensionless coefficient σ_T is called the *energy accommodation coefficient*. From an energy balance at the wall, it can be shown that (Kennard, 1938):

$$T - T_{\text{wall}} = \frac{2 - \sigma_T}{\sigma_T} \frac{2\gamma}{\gamma + 1} \frac{k}{\mu c_v} \lambda \left. \frac{\partial T}{\partial n} \right|_w \quad (2.61)$$

After non-dimensionalization with the characteristic length L and the reference temperature T_0 , Eq. (2.61) is written as follows:

$$T^* - T_{\text{wall}}^* = \frac{2 - \sigma_T}{\sigma_T} \frac{2\gamma}{\gamma + 1} \frac{\text{Kn}}{\text{Pr}} \left. \frac{\partial T^*}{\partial n^*} \right|_w \quad (2.62)$$

where

$$\text{Pr} = \frac{\nu \rho c_p}{k} = \frac{\mu c_p}{k} \quad (2.63)$$

is the Prandtl number.

In the absence of tangential temperature gradients ($\partial T^*/\partial s^* = 0$), the boundary conditions (2.59) and (2.62) are called first-order (i.e. $\vartheta(\text{Kn})$) boundary conditions. The velocity slip (respectively the temperature jump) is then proportional to the transverse velocity (respectively temperature) gradient and to the Knudsen number Kn . These boundary conditions are classically associated with the Navier–Stokes equations, but they can also lead to interesting results when used with the QGD or QHD equations.

2.2.3.3. Higher-order slip boundary conditions

From a theoretical point of view, the slip flow regime is particularly interesting because it generally leads to analytical or semi-analytical models (*cf.* Section 2.3). For example, these analytical models allow us to calculate velocities and flow rates for isothermal and locally fully developed microflows between plane plates or in cylindrical ducts with simple sections: circular (Kennard, 1938), annular (Ebert and Sparrow, 1965), rectangular (Ebert and Sparrow, 1965; Morini and Spiga, 1998) ... These models proved to be quite precise for moderate Knudsen numbers, typically up to about 0.1 (Harley *et al.*, 1995; Liu *et al.*, 1995; Shih *et al.*, 1996; Arkilic *et al.*, 2001).

For $\text{Kn} > 0.1$, experimental studies (Sreekanth, 1969) or numerical studies (Piekos and Breuer, 1996) with the direct simulation Monte Carlo (DSMC) method show significant deviations with models based on first-order boundary conditions. Therefore, since 1947, several authors have proposed second-order boundary conditions, hoping to extend the validity of the slip flow regime to higher Knudsen numbers. Second-order boundary conditions take more or less complicated forms, which are difficult to group together in a sole equation. Actually, according to the assumptions, the second-order terms ($\vartheta(\text{Kn}^2)$) may be dependent of σ (Chapman and Cowling, 1952; Karniadakis and Beskok, 2002) and involve tangential second derivatives $\partial^2 u^*/\partial s^{*2}$ (Deissler, 1964). In the simple case of a developed flow between plane plates, the tangential second derivatives are zero and one may compare most of the second-order models that take the generic form

$$u_s^* - u_{\text{wall}}^* = A_1 \text{Kn} \frac{\partial u_s^*}{\partial n^*} + A_2 \text{Kn}^2 \frac{\partial^2 u_s^*}{\partial n^{*2}} \quad (2.64)$$

In the particular case of a fully diffuse reflection ($\sigma = 1$), the coefficients A_1 and A_2 proposed in the literature are compared in Table 2.3. We note significant differences, essentially for the second-order term. Moreover, some models based on a simple mathematical extension of Maxwell's condition predict a decrease of the slip compared to the first-order model, while other models predict an increase of the slip. This point is discussed in Section 2.3.

The implementation of the boundary conditions (2.64) with the Navier–Stokes equations is not always easy and can lead to computational difficulties. The obvious interest in using

Table 2.3

Coefficients of the main models of second-order boundary conditions proposed in the literature, for $\sigma = 1$.

Author, year (reference)	A_1	A_2
Maxwell (Maxwell, 1879)	1	0
Schamberg, 1947 (Karniadakis and Beskok, 2002)	1	$-5\pi/12$
Chapman and Cooling (Chapman and Cowling, 1952)	$\kappa_0 (\approx 1)$	$\kappa_0^2/2 (\approx 1/2)$
Deissler (Deissler, 1964)	1	$-9/8$
Cercignani, 1964 (Srekanth, 1969)	1.1466	-0.9756
Hsia et Domoto (Hsia and Domoto, 1983)	1	$-1/2$
Mitsuya (Mitsuya, 1993)	1	$-2/9$
Karniadakis et Beskok (Karniadakis and Beskok, 2002)	1	$1/2$

higher-order boundary conditions led some authors to propose new conditions, which may be more appropriate for a treatment with the Navier–Stokes equations. Thus, Beskok and Karniadakis (1999) suggested a high-order form

$$u_s^* - u_{\text{wall}}^* = \frac{2 - \sigma}{\sigma} \frac{\text{Kn}}{1 - A_3 \text{Kn}} \frac{\partial u_s^*}{\partial n^*} \quad (2.65)$$

that involves the sole first derivative of the velocity and an empirical parameter $A_3(\text{Kn})$. As for Xue and Fan (2000), they proposed

$$u_s^* - u_{\text{wall}}^* = \frac{2 - \sigma}{\sigma} \tanh(\text{Kn}) \frac{\partial u_s^*}{\partial n^*} \quad (2.66)$$

that leads to results close to that calculated by the DSCM method, up to high Knudsen numbers, of the order of 3. Other hybrid boundary conditions, such as

$$u_s^* - u_{\text{wall}}^* = \frac{2 - \sigma}{\sigma} \left[\text{Kn} \frac{\partial u_s^*}{\partial n^*} + \frac{\text{Kn}}{2} \left(\text{Re} \frac{\partial p^*}{\partial s^*} \right) \right] \quad (2.67)$$

Jie *et al.* (2000), were also proposed in order to allow a more stable numerical solution, while giving results comparable to that from Eq. (2.65) for the cases that were tested.

2.2.3.4. Accommodation coefficients

The accommodation coefficients depend on various parameters that affect surface interaction, such as the magnitude and the direction of the velocity. Fortunately, it seems that these

coefficients are reasonably constant for a given gas and surface combination (Schaaf, 1963). Many measurements of σ_T and σ have been made, most of them from indirect macroscopic measurements, while a few of them are from direct measurements using molecular beam techniques. Schaaf (1963) reported values of σ ranging from 0.60 to 1.00, most of them being between 0.85 and 1.00. Recently, good correlations for microchannel flows were found in the slip flow regime, with values of σ between 0.80 and 1.00 (Section 2.3.5.2). Schaaf also reported values of σ_T in a wide range, from 0.0109 to 0.990.

2.2.4. Transition flow and free molecular flow

Typically, for Knudsen numbers higher than unity, the continuum Navier–Stokes or QGD/QHD equations become invalid. However, in the early transition regime (for $\text{Kn} \sim 1$), a slip-flow model may still be used providing the continuum model is corrected by replacing the Navier–Stokes equations with the Burnett equations. For higher Knudsen numbers, in the full transition and in the free molecular regimes, the Boltzmann equation must be directly treated by appropriate numerical techniques such as the DSMC or the lattice Boltzmann methods (LBM).

2.2.4.1. Burnett equations

Higher-order fluid dynamic models, also called extended hydrodynamic equations (EHE), may be obtained from the conservation equations (2.39)–(2.41), deriving the form of the viscous stress tensor σ_{EQ} and of the heat flux vector \mathbf{q}_{EQ} from a molecular approach and the Boltzmann equation.

In a molecular description with the assumption of molecular chaos, a flow is entirely described if, for each time t and each position \mathbf{x} , we know the number density n , the velocity and the internal energy distribution functions (Lengrand and Elizarova, 2004). For example, if we consider a monatomic gas, the velocity distribution function $f(t, \mathbf{x}, \mathbf{u})$ represents the number of particles in the six-dimensional phase space $d\mathbf{x} d\mathbf{u}$ at time t . It verifies the Boltzmann equation

$$\frac{\partial f}{\partial t} + \mathbf{u} \cdot \frac{\partial f}{\partial \mathbf{x}} + \mathbf{F} \cdot \frac{\partial f}{\partial \mathbf{u}} = Q(f, f^*) \quad (2.68)$$

which is valid in the entire Knudsen regime, that is for $0 \leq \text{Kn} < \infty$, since it does not require a local thermodynamic equilibrium hypothesis. In Eq. (2.68), \mathbf{F} is an external body force per unit mass and $Q(f, f^*)$ represents the intermolecular collisions. From a Chapman–Enskog expansion of the Boltzmann equation with the Knudsen number as a small parameter (i.e. $f = f_0 + \text{Kn} f_1 + \text{Kn}^2 f_2 + \dots$), the form of the viscous stress tensor and of the heat flux vector may be obtained as follows:

$$\sigma_{\text{EQ}} = \sigma_{\text{EQ}}^{(0)} + \sigma_{\text{EQ}}^{(1)} + \sigma_{\text{EQ}}^{(2)} + \sigma_{\text{EQ}}^{(3)} + \dots + \sigma_{\text{EQ}}^{(i)} + \vartheta(\text{Kn}^{i+1}) \quad (2.69)$$

$$\mathbf{q}_{\text{EQ}} = \mathbf{q}_{\text{EQ}}^{(0)} + \mathbf{q}_{\text{EQ}}^{(1)} + \mathbf{q}_{\text{EQ}}^{(2)} + \mathbf{q}_{\text{EQ}}^{(3)} + \cdots + \mathbf{q}_{\text{EQ}}^{(i)} + \vartheta(\text{Kn}^{i+1}) \quad (2.70)$$

In the EHE, the mass flux vector $\mathbf{J}_{\text{EQ}} = \mathbf{J}_{\text{NS}} = \rho \mathbf{u}$ is the same as for the Navier–Stokes equations, but according to the number of terms kept in Eqs. (2.69) and (2.70), we obtain the Euler, Navier–Stokes, Burnett or super-Burnett equations.

Keeping only the first term in Eqs. (2.69) and (2.70), we obtain the zeroth-order approximation ($i = 0$) which results in the Euler (E) equations, with

$$\sigma_{\text{E}} = \sigma_{\text{EQ}}^{(0)} = 0 \quad (2.71)$$

$$\mathbf{q}_{\text{E}} = \mathbf{q}_{\text{EQ}}^{(0)} = 0 \quad (2.72)$$

The Euler equations correspond to an inviscid flow ($\mu = 0$) for which heat losses by thermal diffusion are neglected ($k = 0$). This system of equations is a hyperbolic system that can describe subsonic or supersonic flows, with the transition for $\text{Ma} = 1$ being modeled by a shock wave, which represents a discontinuity of the flow variables. The Euler equations are widely used for high speed flows in macrosystems such as nozzles and ejectors (Anderson, 1990).

With the second terms in Eqs. (2.69) and (2.70), that is for a first-order approximation, we obtain the compressible NS equations, with

$$\sigma_{\text{NS}} = \sigma_{\text{EQ}}^{(0)} + \sigma_{\text{EQ}}^{(1)} = 0 + \mu \left[\nabla \otimes \mathbf{u} + (\nabla \otimes \mathbf{u})^T - \frac{2}{3}(\nabla \cdot \mathbf{u})\mathbf{I} \right] \quad (2.73)$$

$$\mathbf{q}_{\text{NS}} = \mathbf{q}_{\text{EQ}}^{(0)} + \mathbf{q}_{\text{EQ}}^{(1)} = 0 - k \nabla T \quad (2.74)$$

These classic equations are detailed in Section 2.2.2.1. According to the associated boundary conditions, they can be valid up to Knudsen numbers in the order of 10^{-1} or 1 (*cf.* Fig. 2.7). In the case of a plane flow in the (x, y) plane, Eq. (2.73) yields

$$\begin{aligned} \sigma_{xx}^{(1)} &= \mu \left(\delta_1 \frac{\partial u_x}{\partial x} + \delta_2 \frac{\partial u_y}{\partial y} \right) \\ \sigma_{xy}^{(1)} = \sigma_{yx}^{(1)} &= \mu \left(\frac{\partial u_x}{\partial y} + \frac{\partial u_y}{\partial x} \right) \\ \sigma_{yy}^{(1)} &= \mu \left(\delta_1 \frac{\partial u_y}{\partial y} + \delta_2 \frac{\partial u_x}{\partial x} \right) \end{aligned} \quad (2.75)$$

with $\delta_1 = 4/3$ and $\delta_2 = -2/3$.

As the Knudsen number becomes higher, additional higher-order terms from Eqs. (2.69) and (2.70) are required. The Burnett (B) equations correspond to a second-order approximation, with

$$\sigma_{\mathbf{B}} = \sigma_{\mathbf{EQ}}^{(0)} + \sigma_{\mathbf{EQ}}^{(1)} + \sigma_{\mathbf{EQ}}^{(2)} \quad (2.76)$$

$$\mathbf{q}_{\mathbf{B}} = \mathbf{q}_{\mathbf{EQ}}^{(0)} + \mathbf{q}_{\mathbf{EQ}}^{(1)} + \mathbf{q}_{\mathbf{EQ}}^{(2)} \quad (2.77)$$

These new expressions for stress and heat-flux terms dramatically complicate the EHE systems. Yun *et al.* (1998) provide the expressions of these terms in the case of a plane flow:

$$\begin{aligned} \sigma_{xx}^{(2)} = \frac{\mu^2}{p} & \left[\alpha_1 \left(\frac{\partial u_x}{\partial x} \right)^2 + \alpha_2 \frac{\partial u_x}{\partial x} \frac{\partial u_y}{\partial y} + \alpha_3 \left(\frac{\partial u_y}{\partial y} \right)^2 + \alpha_4 \frac{\partial u_x}{\partial y} \frac{\partial u_y}{\partial x} + \alpha_5 \left(\frac{\partial u_x}{\partial y} \right)^2 \right. \\ & + \alpha_6 \left(\frac{\partial u_y}{\partial x} \right)^2 + \alpha_7 R \frac{\partial^2 T}{\partial x^2} + \alpha_8 R \frac{\partial^2 T}{\partial y^2} + \alpha_9 \frac{RT}{\rho} \frac{\partial^2 \rho}{\partial x^2} + \alpha_{10} \frac{RT}{\rho} \frac{\partial^2 \rho}{\partial y^2} \\ & + \alpha_{11} \frac{RT}{\rho^2} \left(\frac{\partial \rho}{\partial x} \right)^2 + \alpha_{12} \frac{R}{\rho} \frac{\partial T}{\partial x} \frac{\partial \rho}{\partial x} + \alpha_{13} \frac{R}{T} \left(\frac{\partial T}{\partial x} \right)^2 + \alpha_{14} \frac{RT}{\rho^2} \left(\frac{\partial \rho}{\partial y} \right)^2 \\ & \left. + \alpha_{15} \frac{R}{\rho} \frac{\partial T}{\partial y} \frac{\partial \rho}{\partial y} + \alpha_{16} \frac{R}{T} \left(\frac{\partial T}{\partial y} \right)^2 \right] \\ \sigma_{yy}^{(2)} = \frac{\mu^2}{p} & \left[\alpha_1 \left(\frac{\partial u_y}{\partial y} \right)^2 + \alpha_2 \frac{\partial u_x}{\partial x} \frac{\partial u_y}{\partial y} + \alpha_3 \left(\frac{\partial u_x}{\partial x} \right)^2 + \alpha_4 \frac{\partial u_x}{\partial y} \frac{\partial u_y}{\partial x} + \alpha_5 \left(\frac{\partial u_y}{\partial x} \right)^2 \right. \\ & + \alpha_6 \left(\frac{\partial u_x}{\partial y} \right)^2 + \alpha_7 R \frac{\partial^2 T}{\partial y^2} + \alpha_8 R \frac{\partial^2 T}{\partial x^2} + \alpha_9 \frac{RT}{\rho} \frac{\partial^2 \rho}{\partial y^2} + \alpha_{10} \frac{RT}{\rho} \frac{\partial^2 \rho}{\partial x^2} \\ & + \alpha_{11} \frac{RT}{\rho^2} \left(\frac{\partial \rho}{\partial y} \right)^2 + \alpha_{12} \frac{R}{\rho} \frac{\partial T}{\partial y} \frac{\partial \rho}{\partial y} + \alpha_{13} \frac{R}{T} \left(\frac{\partial T}{\partial y} \right)^2 + \alpha_{14} \frac{RT}{\rho^2} \left(\frac{\partial \rho}{\partial x} \right)^2 \\ & \left. + \alpha_{15} \frac{R}{\rho} \frac{\partial T}{\partial x} \frac{\partial \rho}{\partial x} + \alpha_{16} \frac{R}{T} \left(\frac{\partial T}{\partial x} \right)^2 \right] \\ \sigma_{xy}^{(2)} = \sigma_{yx}^{(2)} = \frac{\mu^2}{p} & \left[\beta_1 \left(\frac{\partial u_x}{\partial x} \frac{\partial u_x}{\partial y} + \frac{\partial u_y}{\partial x} \frac{\partial u_y}{\partial y} \right) + \beta_2 \left(\frac{\partial u_x}{\partial y} \frac{\partial u_y}{\partial y} + \frac{\partial u_x}{\partial x} \frac{\partial u_y}{\partial x} \right) \right. \\ & + \beta_3 R \frac{\partial^2 T}{\partial x \partial y} + \beta_4 \frac{RT}{\rho} \frac{\partial^2 \rho}{\partial x \partial y} + \beta_5 \frac{R}{T} \frac{\partial T}{\partial x} \frac{\partial T}{\partial y} + \beta_6 \frac{RT}{\rho^2} \frac{\partial \rho}{\partial x} \frac{\partial \rho}{\partial y} \\ & \left. + \beta_7 \frac{R}{\rho} \left(\frac{\partial T}{\partial x} \frac{\partial \rho}{\partial y} + \frac{\partial T}{\partial y} \frac{\partial \rho}{\partial x} \right) \right] \end{aligned} \quad (2.78)$$

$$\begin{aligned}
q_x^{(2)} &= \frac{\mu^2}{\rho} \left[\gamma_1 \frac{1}{T} \frac{\partial T}{\partial x} \frac{\partial u_x}{\partial x} + \gamma_2 \frac{1}{T} \frac{\partial T}{\partial x} \frac{\partial u_y}{\partial y} + \gamma_3 \frac{\partial^2 u_x}{\partial x^2} + \gamma_4 \frac{\partial^2 u_x}{\partial y^2} + \gamma_5 \frac{\partial^2 u_y}{\partial x \partial y} + \gamma_6 \frac{1}{T} \frac{\partial T}{\partial y} \frac{\partial u_y}{\partial x} \right. \\
&\quad \left. + \gamma_7 \frac{1}{T} \frac{\partial T}{\partial y} \frac{\partial u_x}{\partial y} + \gamma_8 \frac{1}{\rho} \frac{\partial \rho}{\partial x} \frac{\partial u_x}{\partial x} + \gamma_9 \frac{1}{\rho} \frac{\partial \rho}{\partial x} \frac{\partial u_y}{\partial y} + \gamma_{10} \frac{1}{\rho} \frac{\partial \rho}{\partial y} \frac{\partial u_x}{\partial y} + \gamma_{11} \frac{1}{\rho} \frac{\partial \rho}{\partial y} \frac{\partial u_y}{\partial x} \right] \\
q_y^{(2)} &= \frac{\mu^2}{\rho} \left[\gamma_1 \frac{1}{T} \frac{\partial T}{\partial y} \frac{\partial u_y}{\partial y} + \gamma_2 \frac{1}{T} \frac{\partial T}{\partial y} \frac{\partial u_x}{\partial x} + \gamma_3 \frac{\partial^2 u_y}{\partial y^2} + \gamma_4 \frac{\partial^2 u_y}{\partial x^2} + \gamma_5 \frac{\partial^2 u_x}{\partial x \partial y} + \gamma_6 \frac{1}{T} \frac{\partial T}{\partial x} \frac{\partial u_x}{\partial y} \right. \\
&\quad \left. + \gamma_7 \frac{1}{T} \frac{\partial T}{\partial x} \frac{\partial u_y}{\partial x} + \gamma_8 \frac{1}{\rho} \frac{\partial \rho}{\partial y} \frac{\partial u_y}{\partial y} + \gamma_9 \frac{1}{\rho} \frac{\partial \rho}{\partial y} \frac{\partial u_x}{\partial x} + \gamma_{10} \frac{1}{\rho} \frac{\partial \rho}{\partial x} \frac{\partial u_y}{\partial x} + \gamma_{11} \frac{1}{\rho} \frac{\partial \rho}{\partial x} \frac{\partial u_x}{\partial y} \right]
\end{aligned} \tag{2.79}$$

Unfortunately, these Burnett equations experience stability problems for very fine computational grids. Zhong proposed in 1991 to add linear third-order terms from the super-Burnett equations (which corresponds to $i = 3$) in order to stabilize the conventional Burnett equations and maintain second-order accuracy for the stress and heat flux terms (Agarwal *et al.*, 2001). This set of equations is called the augmented Burnett (AB) equations. Moreover, Welder *et al.* (1993) have shown that a linear stability analysis is not sufficient to explain the instability of the Burnett equations. This instability could be due to the fact that the conventional Burnett equations can violate the second law of thermodynamics at high Knudsen numbers (Comeaux *et al.*, 1995). To overcome this difficulty, Balakrishnan and Agarwal have proposed another set of equations termed the Bhatnagar–Gross–Krook–Burnett or BGK–Burnett (BGKB) equations, which are consistent with the second principle and unconditionally stable for both monatomic and polyatomic gases. The BGKB equations also use third-order terms but the second-order terms $\{\alpha_1, \dots, \alpha_{16}, \beta_1, \dots, \beta_7, \gamma_1, \dots, \gamma_{11}\}$ are different than the ones of the conventional Burnett or AB equations, as well as the first-order terms ($\delta_1 = -1.6$ and $\delta_2 = -0.4$ for $\gamma = 1.4$). The additional terms for the AB equations are

$$\begin{aligned}
\sigma_{xx}^{(a)} &= \frac{\mu^3}{p^2} RT \left[\alpha_{17} \left(\frac{\partial^3 u_x}{\partial x^3} + \frac{\partial^3 u_x}{\partial x \partial y^2} \right) + \alpha_{18} \left(\frac{\partial^3 u_y}{\partial y^3} + \frac{\partial^3 u_y}{\partial y \partial x^2} \right) \right] \\
\sigma_{yy}^{(a)} &= \frac{\mu^3}{p^2} RT \left[\alpha_{17} \left(\frac{\partial^3 u_y}{\partial y^3} + \frac{\partial^3 u_y}{\partial y \partial x^2} \right) + \alpha_{18} \left(\frac{\partial^3 u_x}{\partial x^3} + \frac{\partial^3 u_x}{\partial x \partial y^2} \right) \right]
\end{aligned} \tag{2.80}$$

$$\begin{aligned}
\sigma_{xy}^{(a)} &= \sigma_{yx}^{(a)} = \frac{\mu^3}{p^2} RT \beta_8 \left(\frac{\partial^3 u_x}{\partial y^3} + \frac{\partial^3 u_y}{\partial x^3} + \frac{\partial^3 u_x}{\partial y \partial x^2} + \frac{\partial^3 u_y}{\partial x \partial y^2} \right) \\
q_x^{(a)} &= \frac{\mu^3}{p \rho} R \left[\gamma_{12} \left(\frac{\partial^3 T}{\partial x^3} + \frac{\partial^3 T}{\partial x \partial y^2} \right) + \gamma_{13} \frac{T}{\rho} \left(\frac{\partial^3 \rho}{\partial x^3} + \frac{\partial^3 \rho}{\partial x \partial y^2} \right) \right] \\
q_y^{(a)} &= \frac{\mu^3}{p \rho} R \left[\gamma_{12} \left(\frac{\partial^3 T}{\partial y^3} + \frac{\partial^3 T}{\partial y \partial x^2} \right) + \gamma_{13} \frac{T}{\rho} \left(\frac{\partial^3 \rho}{\partial y^3} + \frac{\partial^3 \rho}{\partial y \partial x^2} \right) \right]
\end{aligned} \tag{2.81}$$

and for the BGK–Burnett equations:

$$\begin{aligned}
 \sigma_{xx}^{(B)} = & \frac{\mu^3}{p^2} RT \left[\theta_1 \frac{\partial^3 u_x}{\partial x^3} + \theta_2 \frac{\partial^3 u_x}{\partial x \partial y^2} + \theta_3 \frac{\partial^3 u_y}{\partial x^2 \partial y} + \theta_4 \frac{\partial^3 u_y}{\partial y^3} \right] \\
 & - \frac{\mu^3}{p^2} \frac{RT}{\rho} \left[\frac{\partial \rho}{\partial x} \left(\theta_1 \frac{\partial^2 u_x}{\partial x^2} + \theta_5 \frac{\partial^2 u_y}{\partial x \partial y} + \theta_6 \frac{\partial^2 u_x}{\partial y^2} \right) \right. \\
 & \quad \left. + \frac{\partial \rho}{\partial y} \left(\theta_7 \frac{\partial^2 u_y}{\partial x^2} + \theta_8 \frac{\partial^2 u_x}{\partial x \partial y} + \theta_4 \frac{\partial^2 u_y}{\partial y^2} \right) \right] \\
 & + \frac{\mu^3}{p^2} \left[\theta_9 \left(\frac{\partial u_x}{\partial x} \right)^3 + \theta_{10} \left\{ 3 \left(\frac{\partial u_x}{\partial x} \right)^2 \frac{\partial u_y}{\partial y} + \left(\frac{\partial u_y}{\partial y} \right)^3 \right\} + \theta_{11} \frac{\partial u_x}{\partial x} \left(\frac{\partial u_y}{\partial y} \right)^2 \right. \\
 & \quad \left. - \left(\theta_4 \frac{\partial u_x}{\partial x} + \theta_{12} \frac{\partial u_y}{\partial y} \right) \left\{ \left(\frac{\partial u_x}{\partial y} \right)^2 + 2 \frac{\partial u_x}{\partial y} \frac{\partial u_y}{\partial x} + \left(\frac{\partial u_y}{\partial x} \right)^2 \right\} \right] \\
 & + \frac{\mu^3}{p^2} R \left[\left(\theta_{13} \frac{\partial u_x}{\partial x} + \theta_{14} \frac{\partial u_y}{\partial y} \right) \left(\frac{\partial^2 T}{\partial x^2} + \frac{\partial^2 T}{\partial y^2} \right) \right] \\
 \sigma_{yy}^{(B)} = & \frac{\mu^3}{p^2} RT \left[\theta_1 \frac{\partial^3 u_y}{\partial y^3} + \theta_2 \frac{\partial^3 u_y}{\partial y \partial x^2} + \theta_3 \frac{\partial^3 u_x}{\partial y^2 \partial x} + \theta_4 \frac{\partial^3 u_x}{\partial x^3} \right] \\
 & - \frac{\mu^3}{p^2} \frac{RT}{\rho} \left[\frac{\partial \rho}{\partial y} \left(\theta_1 \frac{\partial^2 u_y}{\partial y^2} + \theta_5 \frac{\partial^2 u_x}{\partial x \partial y} + \theta_6 \frac{\partial^2 u_y}{\partial x^2} \right) \right. \\
 & \quad \left. + \frac{\partial \rho}{\partial x} \left(\theta_7 \frac{\partial^2 u_x}{\partial y^2} + \theta_8 \frac{\partial^2 u_y}{\partial x \partial y} + \theta_4 \frac{\partial^2 u_x}{\partial x^2} \right) \right] \tag{2.82} \\
 & + \frac{\mu^3}{p^2} \left[\theta_9 \left(\frac{\partial u_y}{\partial y} \right)^3 + \theta_{10} \left\{ 3 \left(\frac{\partial u_y}{\partial y} \right)^2 \frac{\partial u_x}{\partial x} + \left(\frac{\partial u_x}{\partial x} \right)^3 \right\} + \theta_{11} \frac{\partial u_y}{\partial y} \left(\frac{\partial u_x}{\partial x} \right)^2 \right. \\
 & \quad \left. - \left(\theta_4 \frac{\partial u_y}{\partial y} + \theta_{12} \frac{\partial u_x}{\partial x} \right) \left\{ \left(\frac{\partial u_y}{\partial x} \right)^2 + 2 \frac{\partial u_x}{\partial y} \frac{\partial u_y}{\partial x} + \left(\frac{\partial u_x}{\partial y} \right)^2 \right\} \right] \\
 & + \frac{\mu^3}{p^2} R \left[\left(\theta_{13} \frac{\partial u_y}{\partial y} + \theta_{14} \frac{\partial u_x}{\partial x} \right) \left(\frac{\partial^2 T}{\partial x^2} + \frac{\partial^2 T}{\partial y^2} \right) \right] \\
 \sigma_{xy}^{(B)} = & \frac{\mu^3}{p^2} RT \left[\theta_{15} \left(\frac{\partial^3 u_x}{\partial y \partial x^2} + \frac{\partial^3 u_y}{\partial y^2 \partial x} \right) + \frac{\partial^3 u_x}{\partial y^3} + \frac{\partial^3 u_y}{\partial x^3} \right] \\
 & - \frac{\mu^3}{p^2} \frac{RT}{\rho} \left[\frac{\partial \rho}{\partial y} \left(\theta_6 \frac{\partial^2 u_x}{\partial x^2} + \theta_{16} \frac{\partial^2 u_y}{\partial x \partial y} + \frac{\partial^2 u_x}{\partial y^2} \right) + \frac{\partial \rho}{\partial x} \left(\frac{\partial^2 u_y}{\partial x^2} + \theta_{16} \frac{\partial^2 u_x}{\partial x \partial y} + \theta_6 \frac{\partial^2 u_y}{\partial y^2} \right) \right] \\
 & - \frac{\mu^3}{p^2} \left(\frac{\partial u_x}{\partial y} + \frac{\partial u_y}{\partial x} \right) \left[\theta_4 \left\{ \left(\frac{\partial u_x}{\partial x} \right)^2 + \left(\frac{\partial u_y}{\partial y} \right)^2 \right\} + 2 \theta_{12} \frac{\partial u_x}{\partial x} \frac{\partial u_y}{\partial y} + \theta_7 \left\{ \left(\frac{\partial u_y}{\partial x} \right)^2 \right. \right. \\
 & \quad \left. \left. + 2 \frac{\partial u_x}{\partial y} \frac{\partial u_y}{\partial x} + \left(\frac{\partial u_x}{\partial y} \right)^2 \right\} \right] + \frac{\mu^3}{p^2} R \left[\theta_{17} \left(\frac{\partial u_x}{\partial y} + \frac{\partial u_y}{\partial x} \right) \left(\frac{\partial^2 T}{\partial x^2} + \frac{\partial^2 T}{\partial y^2} \right) \right]
 \end{aligned}$$

$$\begin{aligned}
q_x^{(B)} = & \frac{\mu^3}{p\rho} R \theta_{18} \left[\frac{\partial^3 T}{\partial x^3} + \frac{\partial^3 T}{\partial y^2 \partial x} - \frac{1}{\rho} \frac{\partial \rho}{\partial x} \left(\frac{\partial^2 T}{\partial x^2} + \frac{\partial^2 T}{\partial y^2} \right) \right] \\
& + \frac{\mu^3}{p\rho} \left[\frac{\partial u_x}{\partial x} \left(\theta_{19} \frac{\partial^2 u_x}{\partial x^2} + \theta_{20} \frac{\partial^2 u_y}{\partial x \partial y} + \theta_6 \frac{\partial^2 u_x}{\partial y^2} \right) \right. \\
& \quad + \frac{\partial u_y}{\partial y} \left(\theta_{21} \frac{\partial^2 u_x}{\partial x^2} + \theta_{22} \frac{\partial^2 u_y}{\partial x \partial y} + \theta_7 \frac{\partial^2 u_x}{\partial y^2} \right) \\
& \quad \left. + \left(\frac{\partial u_x}{\partial y} + \frac{\partial u_y}{\partial x} \right) \left(\theta_{23} \frac{\partial^2 u_y}{\partial x^2} + \theta_{24} \frac{\partial^2 u_x}{\partial x \partial y} + \theta_6 \frac{\partial^2 u_y}{\partial y^2} \right) \right] \\
& - \frac{\mu^3}{p\rho} \left(\frac{1}{\rho} \frac{\partial \rho}{\partial x} + \frac{1}{T} \frac{\partial T}{\partial x} \right) \left[\theta_{13} \left\{ \left(\frac{\partial u_x}{\partial x} \right)^2 + \left(\frac{\partial u_y}{\partial y} \right)^2 \right\} \right. \\
& \quad \left. + 2\theta_{14} \frac{\partial u_x}{\partial x} \frac{\partial u_y}{\partial y} + \theta_{17} \left\{ 2 \frac{\partial u_x}{\partial y} \frac{\partial u_y}{\partial x} + \left(\frac{\partial u_x}{\partial y} \right)^2 + \left(\frac{\partial u_y}{\partial x} \right)^2 \right\} \right] \\
& + \frac{\mu^3}{p\rho} \frac{R}{T} \frac{\partial T}{\partial x} \theta_{18} \left(\frac{\partial^2 T}{\partial x^2} + \frac{\partial^2 T}{\partial y^2} \right)
\end{aligned} \tag{2.83}$$

$$\begin{aligned}
q_y^{(B)} = & \frac{\mu^3}{p\rho} R \theta_{18} \left[\frac{\partial^3 T}{\partial y^3} + \frac{\partial^3 T}{\partial x^2 \partial y} - \frac{1}{\rho} \frac{\partial \rho}{\partial y} \left(\frac{\partial^2 T}{\partial x^2} + \frac{\partial^2 T}{\partial y^2} \right) \right] \\
& + \frac{\mu^3}{p\rho} \left[\frac{\partial u_y}{\partial y} \left(\theta_{19} \frac{\partial^2 u_y}{\partial y^2} + \theta_{20} \frac{\partial^2 u_x}{\partial x \partial y} + \theta_6 \frac{\partial^2 u_y}{\partial x^2} \right) \right. \\
& \quad + \frac{\partial u_x}{\partial x} \left(\theta_{21} \frac{\partial^2 u_y}{\partial y^2} + \theta_{22} \frac{\partial^2 u_x}{\partial x \partial y} + \theta_7 \frac{\partial^2 u_y}{\partial x^2} \right) \\
& \quad \left. + \left(\frac{\partial u_x}{\partial y} + \frac{\partial u_y}{\partial x} \right) \left(\theta_{23} \frac{\partial^2 u_x}{\partial y^2} + \theta_{24} \frac{\partial^2 u_y}{\partial x \partial y} + \theta_6 \frac{\partial^2 u_x}{\partial x^2} \right) \right] \\
& - \frac{\mu^3}{p\rho} \left(\frac{1}{\rho} \frac{\partial \rho}{\partial y} + \frac{1}{T} \frac{\partial T}{\partial y} \right) \left[\theta_{13} \left\{ \left(\frac{\partial u_x}{\partial x} \right)^2 + \left(\frac{\partial u_y}{\partial y} \right)^2 \right\} \right. \\
& \quad \left. + 2\theta_{14} \frac{\partial u_x}{\partial x} \frac{\partial u_y}{\partial y} + \theta_{17} \left\{ 2 \frac{\partial u_x}{\partial y} \frac{\partial u_y}{\partial x} + \left(\frac{\partial u_x}{\partial y} \right)^2 + \left(\frac{\partial u_y}{\partial x} \right)^2 \right\} \right] \\
& + \frac{\mu^3}{p\rho} \frac{R}{T} \frac{\partial T}{\partial y} \theta_{18} \left(\frac{\partial^2 T}{\partial x^2} + \frac{\partial^2 T}{\partial y^2} \right)
\end{aligned}$$

The different coefficients for the above equations are given in Table 2.4.

Table 2.4

Coefficients for AB and BGKB equations (from Yun *et al.* (1998)); the coefficients for AB equations correspond to an HS collision model, and the coefficients for BGKB equations correspond to $\gamma = 1.4$.

	α_1	α_2	α_3	α_4	α_5	α_6	α_7	α_8	α_9	α_{10}
AB	1.199	0.153	−0.600	−0.115	1.295	−0.733	0.260	−0.130	−1.352	0.676
BGKB	−2.24	−0.48	0.56	−1.2	0.0	0.0	−19.6	−5.6	−1.6	0.4
	α_{11}	α_{12}	α_{13}	α_{14}	α_{15}	α_{16}	α_{17}	α_{18}	β_1	β_2
AB	1.352	−0.898	0.600	−0.676	0.449	−0.300	0.2222	−0.1111	−0.115	1.913
BGKB	1.6	−19.6	−18.0	−0.4	−5.6	−6.9	−	−	−1.4	−1.4
	β_3	β_4	β_5	β_6	β_7	β_8	γ_1	γ_2	γ_3	γ_4
AB	0.390	−2.028	0.900	2.028	−0.676	0.1667	10.830	0.407	−2.269	1.209
BGKB	0.0	−2.0	2.0	2.0	0.0	−	−25.241	−0.2	−1.071	−2.0
	γ_5	γ_6	γ_7	γ_8	γ_9	γ_{10}	γ_{11}	γ_{12}	γ_{13}	
AB	−3.478	−0.611	11.033	−2.060	1.030	−1.545	−1.545	0.6875	−0.625	
BGKB	−2.8	−7.5	−11.0	−1.271	1.0	−3.0	−3.0	−	−	
	θ_1	θ_2	θ_3	θ_4	θ_5	θ_6	θ_7	θ_8	θ_9	θ_{10}
BGKB	2.56	1.36	0.56	−0.64	0.96	1.6	−0.4	−0.24	1.024	−0.256
	θ_{11}	θ_{12}	θ_{13}	θ_{14}	θ_{15}	θ_{16}	θ_{17}	θ_{18}	θ_{19}	θ_{20}
BGKB	1.152	0.16	2.24	−0.56	3.6	0.6	1.4	4.9	7.04	−0.16
	θ_{21}	θ_{22}	θ_{23}	θ_{24}	δ_1	δ_2				
BGKB	−1.76	4.24	3.8	3.4	−1.6	−0.4				

2.2.4.2. DSMC method

For high Knudsen numbers, the continuum approach (NS, QGD, QHD or B equations) is no longer valid, even with slip boundary conditions. A molecular approach is then required and the flow may be described from the Boltzmann equation (2.68).

However, the integral formulation of $Q(f, f^*)$, which represents the binary intermolecular collisions, is complex in the general case due to non-linearities and a great number of independent variables (Karniadakis and Beskok, 2002). Therefore, the numerical resolution of the Boltzmann equation is reserved to problems with a simple geometry or problems for which the rarefaction level allows simplifications. Thus, $Q(f, f^*)$ is zero in the free molecular regime when $\text{Kn} \rightarrow \infty$. Also, when $\text{Kn} \rightarrow 0$, a semi-analytical resolution of the Boltzmann equation can be obtained using the method of moments of Grad, for which the distribution function is represented by a series of orthogonal Hermite polynomials (Grad, 1949) or the Chapman–Enskog method (Chapman and Cowling, 1952), for which the distribution function is expanded into a perturbation series with the Knudsen number being the small parameter (*cf.* Section 2.2.4.1). In the transition regime on the other hand, the numerical resolution of the Boltzmann equation requires approximate methods based on the simplification of $Q(f, f^*)$. Sharipov and Selenev (1998) describe the different available methods – BGK equation (Bhatnagar *et al.*, 1954), linearized Boltzmann equation (Cercignani *et al.*, 1994)... – with their conditions of validity.

The Direct Simulation Monte Carlo (DSMC) method is actually better suited to the transition regime. This method was developed by Bird (1978; 1998). Initially widely used for the simulation of low-pressure rarefied flows (Muntz, 1989; Cheng and Emmanuel, 1995), it is now often used for microfluidic applications (Stefanov and Cercignani, 1994; Piekos and Breuer, 1996; Mavriplis *et al.*, 1997; Chen *et al.*, 1998; Oran *et al.*, 1998; Hudson and Bartel, 1999; Pan *et al.*, 1999; Pan *et al.*, 2000; Pan *et al.*, 2001; Wu and Tseng, 2001; Wang and Li, 2004).

As for the classical kinetic theory, the DSMC method assumes a molecular chaos and a dilute gas. The technique is equivalent to solving the Boltzmann equation for a monatomic gas with binary collisions. The DSMC technique consists in spitting off the simulations of the intermolecular collisions and of the molecular motion, with a time step smaller than the mean collision time $1/\nu$. The simulation is performed using a limited number of molecules, with each simulated molecule representing a great number W of real molecules. The control volume is divided into cells, whose size is of the order of $\lambda/3$, in order to correctly treat large gradient regions. The simulation involves four main steps (Oran *et al.*, 1998):

- (1) Moving simulated molecules and modeling molecule–surface interactions, applying conservation laws.
- (2) Indexing and tracking molecules.
- (3) Simulating collisions with a probabilistic process, generally with a VHS model.
- (4) Sampling the macroscopic flow properties at the geometric center of the cells.

The statistical error of the DSMC solution is inversely proportional to the square root of the total number of simulated molecules. The technique being explicit and time-marching, the simulation is unsteady. The solution of an unsteady problem is obtained from averaging an ensemble of many independent computations, to reduce statistical errors. For a steady problem, each independent computation is proceeded until a steady flow is established (Fig. 2.9).

2.2.4.3. *Lattice Boltzmann method*

The lattice Boltzmann method (LBM) is appropriate for complex geometries and seems particularly effective for the simulation of flows in microsystems, where both mesoscopic dynamics and microscopic statistics are important (Karniadakis and Beskok, 2002). The method, whose detailed description is proposed by Chen and Doolen (1998), solves a simplified Boltzmann equation on a discrete lattice. The use of LBM for the simulation of gas microflows is recent, but LBM is destined to be more widely used for such applications in the future. For example, Nie *et al.* (2002) demonstrated that the LBM can capture the fundamental behaviors in microchannel flows, including velocity slip, nonlinear pressure drop along the channel and mass flow rate variation with Knudsen number. The numerical results found by Lim *et al.* (2002) are also in good agreement with the data obtained analytically and experimentally for a two-dimensional isothermal pressure-driven microchannel flow.

2.3. **Pressure-driven steady slip flows in microchannels**

In this section, we consider the flow of an ideal gas through different microchannels in the slip-flow regime. The flow is steady, isothermal and the volume forces are neglected.

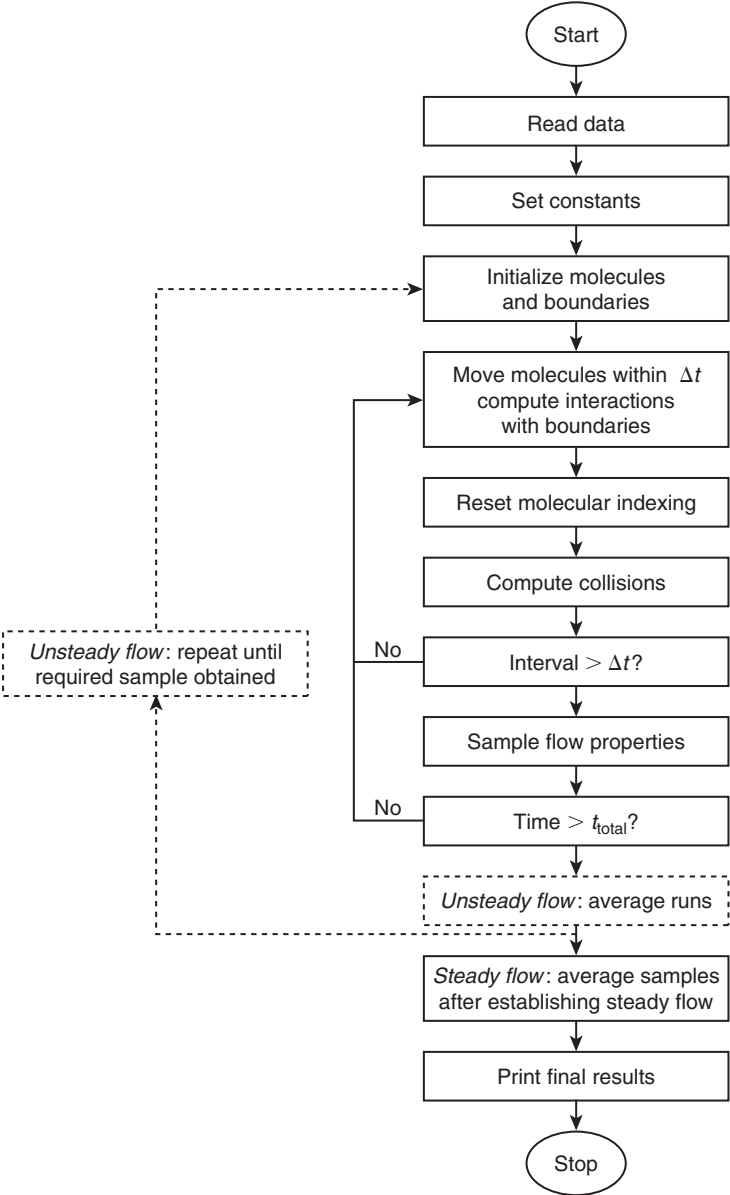


Fig. 2.9. DSMC flowchart (from Oran *et al.* (1998)).

The flow is also assumed to be locally fully developed: the velocity profile in a section is the same as the one obtained for a fully developed incompressible flow, but the density is recalculated in each cross-section and depends on the pressure and the temperature via the equation of state (2.24). This assumption is no longer valid if the Mach number is greater

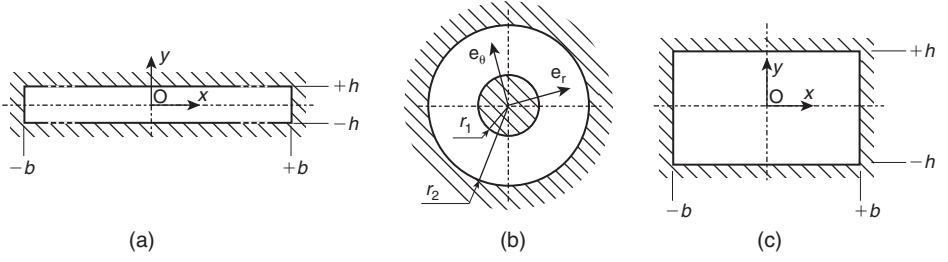


Fig. 2.10. Different microchannel sections. (a) Plane channel limited by parallel plates ($b \gg h$); (b) circular or annular duct; (c) rectangular channel.

than 0.3 (Harley *et al.*, 1995; Guo and Wu, 1998). The main sections of interest are the rectangular and the circular cross-sections. Microchannels with rectangular cross-sections are easily etched in silicon wafers, for example by reactive ion etching (RIE) or by deep reactive ion etching (DRIE). If the aspect ratio of the microchannel is small enough, the flow may be considered as a plane flow between parallel plates and the modeling is much simpler. Gas flows in circular microtubes are also frequently encountered, for example in chromatography applications. Fused silica microtubes are proposed by different suppliers with a variety of internal diameters, from one micrometer to hundreds of micrometers. Due to their low cost, they are an interesting solution as connecting lines for a number of microfluidics devices or prototypes.

The axial coordinate is z and the cross-section is in the (x, y) plane. The different sections considered in this section are represented in Fig. 2.10.

Two different Knudsen numbers are usually defined for microchannel flows.

$$\text{Kn} = \frac{\lambda}{D_H} = \frac{\lambda}{4A/P} \quad (2.84)$$

is defined from the hydraulic diameter as a reference length. The section area is noted A and the wetted perimeter is noted P .

$$\text{Kn}' = \frac{\lambda}{L_{\min}} \quad (2.85)$$

is defined from the minimal representative length of the section.

2.3.1. Plane flow between parallel plates

Here, $h/b \rightarrow 0$ and the velocity only depends on the transverse coordinate y . With the previous assumptions, the momentum equation (2.33) reduces to

$$\frac{d^2 u_z}{dy^2} = \frac{1}{\mu} \frac{dp}{dz} \quad (2.86)$$

2.3.1.1. First-order solution

The first-order boundary condition (2.58) for a fixed wall and an isothermal flow is written $u_s|_w = [(2 - \sigma)/\sigma]\lambda \partial u_s / \partial n|_w$, that is for a flow between parallel plates:

$$u_z|_{y=h} = -\frac{2 - \sigma}{\sigma} \lambda \left. \frac{\partial u_z}{\partial y} \right|_{y=h} \quad (2.87)$$

to be associated with the condition of symmetry (*cf.* Fig. 2.10)

$$\left. \frac{du_z}{dy} \right|_{y=0} = 0 \quad (2.88)$$

The general solution of Eq. (2.86) is

$$u_z = \frac{1}{\mu} \frac{dp}{dz} \left(\frac{y^2}{2} + a_1 y + a_2 \right) \quad (2.89)$$

The condition of symmetry (2.88) yields $a_1 = 0$ and the boundary condition (2.87) leads to $a_2 = -\lambda h(2 - \sigma)/\sigma - h^2/2$. Therefore, in a dimensionless form, the velocity distribution can be written as

$$u_z^* = 1 - y^{*2} + 8 \frac{2 - \sigma}{\sigma} \text{Kn} = 1 - y^{*2} + 4 \frac{2 - \sigma}{\sigma} \text{Kn}' \quad (2.90)$$

where $y^* = y/h$, $u_z^* = u_z/u_{z0}$ and $u_{z0} = u_z(y=0, \text{Kn}=0)$ represents the velocity at the center of the microchannel when rarefaction is not taken into account:

$$u_{z0} = -\frac{h^2}{2\mu} \frac{dp}{dz} \quad (2.91)$$

The Knudsen number $\text{Kn} = \lambda/L = \lambda/D_H$ in Eq. (2.90) is defined from the hydraulic diameter $D_H = 4A/P = 4h$, noting $A = 16hb$ as the area and $P = 4(b + h)$ as the wetted perimeter of the channel cross-section, with $b \gg h$ (Fig. 2.10(a)). $\text{Kn}' = \lambda/2h$ is defined from the depth of the microchannel. Equation (2.90) shows that the usual Poiseuille parabolic profile ($u_z^* = 1 - y^{*2}$) is just globally translated with a quantity $2(2 - \sigma)\lambda/(\sigma h)$, due to the slip at the wall. The integration of the velocity distribution given by Eq. (2.90) over the cross-section leads to the mean velocity

$$\overline{u_z^*} = \frac{1}{2} \int_{-1}^1 u_z^* dy^* \quad (2.92)$$

that is with Eq. (2.90):

$$\overline{u_z^*} = \frac{\overline{u_z}}{u_{z0}} = \frac{2}{3} + 8 \frac{2 - \sigma}{\sigma} \text{Kn} = \frac{2}{3} + 4 \frac{2 - \sigma}{\sigma} \text{Kn}' \quad (2.93)$$

We can now calculate the Poiseuille number Po , defined as:

$$Po = C_f Re \quad (2.94)$$

where

$$C_f = \frac{\overline{\tau_w}}{\frac{1}{2} \rho \overline{u_z}^2} \quad (2.95)$$

is the friction factor that represents a dimensionless value of the average wall shear $\overline{\tau_w}$ and

$$Re = \frac{\rho \overline{u_z} D_H}{\mu} \quad (2.96)$$

is the Reynolds number. The average wall shear is obtained from the force balance

$$\overline{\tau_w} P dz = -A dp \quad (2.97)$$

on a control volume that spans the channel and has an axial extension dz . Therefore,

$$\overline{\tau_w} = -\frac{D_H}{4} \frac{dp}{dz} \quad (2.98)$$

and

$$Po = -\frac{D_H^2}{2\mu} \frac{dp}{dz} \frac{1}{\overline{u_z}} \quad (2.99)$$

which leads with Eqs. (2.91) and (2.93) to:

$$Po_{NS1,plan} = \frac{24}{1 + 12 \frac{2-\sigma}{\sigma} Kn} = \frac{24}{1 + 6 \frac{2-\sigma}{\sigma} Kn'} \quad (2.100)$$

Equation (2.100) shows that the Poiseuille number is less than its usual value of 24 for a Poiseuille flow between parallel plates (Shah, 1975), as soon as the Knudsen number is no longer negligible. This result shows that slip at the wall logically reduces friction and consequently, for a given pressure gradient, the flow rate is increased.

Considering a long microchannel of length l with a pressure p_i at the inlet and a pressure p_o at the outlet and neglecting the entrance effects, we can deduce from Eq. (2.93) the mass flow rate $\dot{m} = \rho \overline{u_z} A = p \overline{u_z} A / RT$, which is independent of z . According to Eq. (2.30), the quantity $(Kn p)$ is constant for an isothermal flow and it can be written as a function of the outlet conditions: $Kn p = Kn_o p_o$. Therefore, the integration of Eq. (2.93) yields

$$\int_{p_i}^{p_o} \left(\frac{2}{3} p + 8 \frac{2-\sigma}{\sigma} Kn_o p_o \right) dp = -\frac{2\mu \dot{m} R T l}{h^2 A} \quad (2.101)$$

which leads to

$$\dot{m}_{\text{NS1,plan}} = \frac{2bh^3 p_0^2}{\mu RTl} \left[\frac{\Pi^2 - 1}{3} + 8 \frac{2 - \sigma}{\sigma} \text{Kn}_0 (\Pi - 1) \right] \quad (2.102)$$

where $\Pi = p_i/p_o$ is the ratio of the inlet over outlet pressures and Kn_0 is the outlet Knudsen number. The subscript NS1 refers to the Navier–Stokes equations with first-order slip flow boundary conditions. In dimensionless form that compares the actual mass flow rate \dot{m} with the mass flow rate \dot{m}_{ns} obtained from a no-slip hypothesis, Eq. (2.102) becomes:

$$\dot{m}_{\text{NS1,plan}}^* = \frac{\dot{m}_{\text{NS1,plan}}}{\dot{m}_{\text{ns,plan}}} = 1 + 24 \frac{2 - \sigma}{\sigma} \frac{\text{Kn}_0}{\Pi + 1} = 1 + 12 \frac{2 - \sigma}{\sigma} \frac{\text{Kn}_0'}{\Pi + 1} \quad (2.103)$$

The pressure distribution along the z -axis can be found by expressing the conservation of mass flow rate through the channel:

$$\begin{aligned} \dot{m}_{\text{NS1,plan}} &= \frac{2bh^3 p_0^2}{\mu RTl} \left[\frac{\Pi^2 - 1}{3} + 8 \frac{2 - \sigma}{\sigma} \text{Kn}_0 (\Pi - 1) \right] \\ &= \frac{2bh^3 p_0^2}{\mu RT(l - z)} \left[\frac{(p/p_o)^2 - 1}{3} + 8 \frac{2 - \sigma}{\sigma} \text{Kn}_0 (p/p_o - 1) \right] \end{aligned} \quad (2.104)$$

Equation (2.104) shows that the pressure $p^* = p/p_o$ is the solution of the polynomial

$$p^{*2} + \alpha_1 p^* + \alpha_2 + \alpha_3 z^* = 0 \quad (2.105)$$

where $z^* = z/l$ and

$$\alpha_1 = 24 \frac{2 - \sigma}{\sigma} \text{Kn}_0 \quad \alpha_2 = -\Pi(\Pi + \alpha_1) \quad \alpha_3 = (\Pi - 1)(\Pi + 1 + \alpha_1) \quad (2.106)$$

Equation (2.105) is plotted in Fig. 2.11, for an inlet over outlet pressure ratio $\Pi = 2$. This figure shows that rarefaction and compressibility have opposite effects on the pressure distribution. Rarefaction effects (characterized by Kn) reduce the curvature in pressure distribution due to compressibility effects (characterized by Ma).

The first-order mass-flow relation (2.102) accurately predicts the experimental data available in the literature, for moderate outlet Knudsen numbers and typically for $\text{Kn}_0 < 0.03$. For higher values of Kn_0 , some deviations appear (cf. Section 2.3.5).

2.3.1.2. Second-order solutions

Therefore, the previous model can be improved to remain accurate for higher Knudsen numbers. For this purpose, second-order – $\vartheta(\text{Kn}^2)$ – models, based on second-order boundary conditions or the QHD equations, may be used.

The use of second-order boundary conditions

$$u_z|_{y=h} = -\frac{2 - \sigma}{\sigma} \lambda \frac{\partial u_z}{\partial y} \Big|_{y=h} + A_2 \lambda^2 \frac{\partial^2 u_z}{\partial y^2} \Big|_{y=h} \quad (2.107)$$

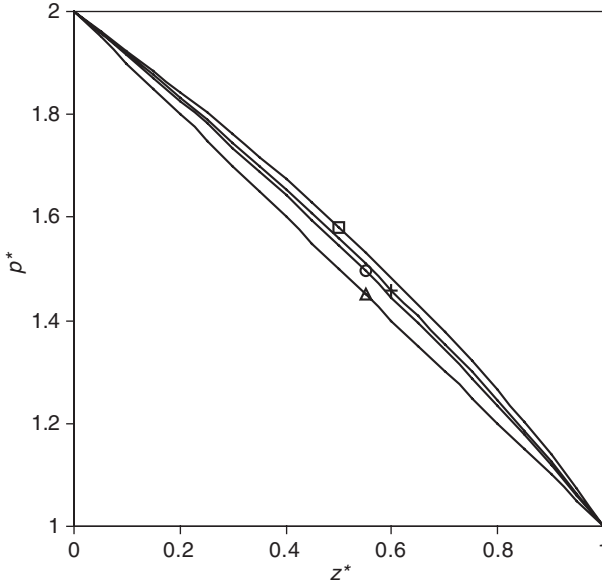


Fig. 2.11. Pressure distribution along a plane microchannel. Δ : incompressible flow; \square : $\text{Kn}_0 = 0$; $+$: $\text{Kn}_0 = 0.05$; \circ : $\text{Kn}_0 = 0.1$.

leads to a velocity distribution

$$u_z^* = 1 - y^{*2} + 8 \frac{2-\sigma}{\sigma} \text{Kn} - 32 A_2 \text{Kn}^2 = 1 - y^{*2} + 4 \frac{2-\sigma}{\sigma} \text{Kn}' - 8 A_2 \text{Kn}'^2 \quad (2.108)$$

and to a Poiseuille number

$$\text{Po}_{\text{NS2,plan}} = \frac{24}{1 + 12 \frac{2-\sigma}{\sigma} \text{Kn} - 48 A_2 \text{Kn}^2} = \frac{24}{1 + 6 \frac{2-\sigma}{\sigma} \text{Kn}' - 12 A_2 \text{Kn}'^2} \quad (2.109)$$

It is easy to verify that the mass flow rate is consequently corrected as:

$$\begin{aligned} \dot{m}_{\text{NS2,plan}}^* &= \frac{\dot{m}_{\text{NS2,plan}}}{\dot{m}_{\text{ns,plan}}} = 1 + 24 \frac{2-\sigma}{\sigma} \frac{\text{Kn}_0}{\Pi + 1} - 96 A_2 \text{Kn}_0^2 \frac{\ln \Pi}{\Pi^2 - 1} \\ &= 1 + 12 \frac{2-\sigma}{\sigma} \frac{\text{Kn}'_0}{\Pi + 1} - 24 A_2 \text{Kn}'_0{}^2 \frac{\ln \Pi}{\Pi^2 - 1} \end{aligned} \quad (2.110)$$

It is interesting to note that a close result can also be found keeping the first-order boundary conditions, but using the QHD equations in place of the NS equations (Elizarova and Sheretov, 2003). The solution of the momentum equation (2.40), with the expression

(2.53) of the viscous stress tensor and the boundary condition (2.87) yields

$$\begin{aligned}\dot{m}_{\text{QHD1,plan}}^* &= \frac{\dot{m}_{\text{QHD1,plan}}}{\dot{m}_{\text{ns,plan}}} = 1 + 24 \frac{2-\sigma}{\sigma} \frac{\text{Kn}_0}{\Pi+1} + \frac{96}{k_2^2 \text{Sc}} \text{Kn}_0^2 \frac{\ln \Pi}{\Pi^2-1} \\ &= 1 + 12 \frac{2-\sigma}{\sigma} \frac{\text{Kn}'_0}{\Pi+1} + \frac{24}{k_2^2 \text{Sc}} \text{Kn}'_0{}^2 \frac{\ln \Pi}{\Pi^2-1}\end{aligned}\quad (2.111)$$

Equations (2.110) and (2.111) only differ with their last term. For example, if we consider the second-order boundary conditions of Deissler, $A_2 = -9/8$ and $-96A_2 = 108$. This value must be compared with $96/(k_2^2 \text{Sc})$. For an HS model, $k_2 = 16/5\sqrt{2\pi}$ and $\text{Sc} = 5/6$. Therefore, $96/k_2^2 \text{Sc} = 70, 7$. The deviation on the second-order term between the two models is then around 42%. But, if we consider the more accurate VSS model, with $\omega = 0.74$ for nitrogen under standard conditions (*cf.* Table 2.2), $k_2 = 1.064$, $\text{Sc} = 0.746$ and $96/k_2^2 \text{Sc} = 114$, which corresponds to a deviation of about 5% between the second-order terms of NS2 and QDH1 models. Of course, this deviation is a function of the gas, the temperature, the choice of the second-order boundary condition and of the IPL model.

2.3.2. Gas flow in circular microtubes

With the general assumptions of this section, the momentum equation (2.33) in polar coordinates reduces to

$$\frac{1}{r} \frac{d}{dr} \left(r \frac{du_z}{dr} \right) = \frac{1}{\mu} \frac{dp}{dz} \quad (2.112)$$

2.3.2.1. First-order solution

The first-order boundary condition (2.58) for a non-moving wall and an isothermal flow is now:

$$u_z|_{r=r_2} = -\frac{2-\sigma}{\sigma} \lambda \left. \frac{\partial u_z}{\partial r} \right|_{r=r_2} \quad (2.113)$$

The general solution of Eq. (2.112) is

$$u_z = \frac{1}{\mu} \frac{dp}{dz} \left(\frac{r^2}{4} + c_1 \ln r + c_2 \right) \quad (2.114)$$

where $c_1 = 0$ since the velocity has a finite value in $r = 0$. Using the boundary condition (2.113), we find

$$c_2 = -\frac{2-\sigma}{\sigma} \lambda \frac{r_2}{2} - \frac{r_2^2}{4} \quad (2.115)$$

which leads to the dimensionless velocity profile

$$u_z^* = 1 - r^{*2} + 4 \frac{2 - \sigma}{\sigma} \text{Kn} \quad (2.116)$$

where the Knudsen number $\text{Kn} = \lambda/D_H = \lambda/(2r_2) = \text{Kn}' = \lambda/L_{\min}$ is defined from a characteristic length $L = 2r_2$. Here, $r^* = r/r_2$ and $u_z^* = u_z/u_{z0}$ where

$$u_{z0} = \frac{r_2^2}{4\mu} \left(-\frac{dp}{dz} \right) \quad (2.117)$$

is the velocity at the center of the microchannel when rarefaction is not taken into account. Equation (2.116) shows that the usual Hagen–Poiseuille velocity profile ($u_z^* = 1 - r^{*2}$) is just globally translated with a quantity $2(2 - \sigma)\lambda/(\sigma r_2)$ due to the slip at the wall. The integration of the velocity distribution given by Eq. (2.116) over the cross-section leads to the mean velocity

$$\overline{u_z^*} = \frac{1}{\pi} \int_0^1 u_z^* 2\pi r^* dr^* \quad (2.118)$$

that is with Eq. (2.116):

$$\overline{u_z^*} = \frac{1}{2} + 4 \frac{2 - \sigma}{\sigma} \text{Kn} \quad (2.119)$$

The Poiseuille number Po is still defined by Eq. (2.99), which leads with Eqs. (2.117) and (2.119) to:

$$\text{Po}_{\text{NS1,circ}} = \frac{16}{1 + 8 \frac{2 - \sigma}{\sigma} \text{Kn}} \quad (2.120)$$

If Kn is not negligible, the Poiseuille number is less than its usual value of 16 for a circular cross-section (Shah, 1975). Following the same method as for a plane flow, the integration of Eq. (2.118) with $\dot{m} = \rho \overline{u_z} A/RT$ yields

$$\dot{m}_{\text{NS1,circ}} = \frac{\pi r_2^4 p_o^2}{4\mu RT l} \left[\frac{\Pi^2 - 1}{4} + 4 \frac{2 - \sigma}{\sigma} \text{Kn}_o (\Pi - 1) \right] \quad (2.121)$$

for a long microtube, neglecting entrance effects and

$$\dot{m}_{\text{NS1,circ}}^* = \frac{\dot{m}_{\text{NS1,circ}}}{\dot{m}_{\text{ns,circ}}} = 1 + 16 \frac{2 - \sigma}{\sigma} \frac{\text{Kn}_o}{\Pi + 1} \quad (2.122)$$

The pressure distribution $p^* = p/p_0$ along the microtube is the solution of the polynomial

$$p^{*2} + \beta_1 p^* + \beta_2 + \beta_3 z^* = 0 \quad (2.123)$$

where $z^* = z/l$ and

$$\beta_1 = 16 \frac{2-\sigma}{\sigma} \text{Kn}_0 \quad \beta_3 = (\Pi - 1)(\Pi + 1 + \beta_1) \quad \beta_2 = -1 - \beta_1 - \beta_3 \quad (2.124)$$

which qualitatively leads to the same conclusions as for a plane flow.

2.3.2.2. Second-order solution

The first-order solution can easily be extended to second-order boundary conditions, following the same reasoning as in Section 2.3.1.2. We find

$$\overline{u_z^*} = \frac{1}{2} + 4 \frac{2-\sigma}{\sigma} \text{Kn} - 8 A_2 \text{Kn}^2 \quad (2.125)$$

$$\text{Po}_{\text{NS2,circ}} = \frac{16}{1 + 8 \frac{2-\sigma}{\sigma} \text{Kn} - 16 A_2 \text{Kn}^2} \quad (2.126)$$

and

$$\dot{m}_{\text{NS2,circ}}^* = \frac{\dot{m}_{\text{NS2,circ}}}{\dot{m}_{\text{ns,circ}}} = 1 + 16 \frac{2-\sigma}{\sigma} \frac{\text{Kn}_0}{\Pi + 1} - 32 A_2 \text{Kn}_0^2 \frac{\ln \Pi}{\Pi^2 - 1} \quad (2.127)$$

The problem can also be solved from the QHD equations with first-order boundary conditions. Lengrand *et al.* (2004) showed that

$$\dot{m}_{\text{QHD1,circ}}^* = \frac{\dot{m}_{\text{QHD1,circ}}}{\dot{m}_{\text{ns,circ}}} = 1 + 16 \frac{2-\sigma}{\sigma} \frac{\text{Kn}_0}{\Pi + 1} + \frac{32}{k_2^2 \text{Sc}} \text{Kn}_0^2 \frac{\ln \Pi}{\Pi^2 - 1} \quad (2.128)$$

The deviation between the QHD1 and the NS2 models with respect to the second-order terms are exactly the same as in the case of a plane flow (Section 2.3.1.2).

2.3.3. Gas flow in annular ducts

The solution for the slip-flow of a gas in a circular microduct is easily extensible to the case of an annular duct (Ebert and Sparrow, 1965). The inner radius r_1 and the outer radius r_2 are not necessarily small, but the distance $r_2 - r_1 = D_H/2$ must be small enough so that the flow between the two cylinders is rarefied. The first-order boundary conditions are

$$u_z = \frac{2-\sigma}{\sigma} \lambda \left. \frac{\partial u_z}{\partial r} \right|_{r=r_1} \quad u_z = -\frac{2-\sigma}{\sigma} \lambda \left. \frac{\partial u_z}{\partial r} \right|_{r=r_2} \quad (2.129)$$

The integration of Eq. (2.112) leads to the velocity distribution

$$u_z^* = 1 - r^{*2} + 4(1 - r_1^*) \frac{2 - \sigma}{\sigma} \text{Kn} + \frac{r_1^*(1 - r_1^{*2}) \left(1 + 4 \frac{2 - \sigma}{\sigma} \text{Kn}\right) \left[2(1 - r_1^*) \frac{2 - \sigma}{\sigma} \text{Kn} - \ln r_1^*\right]}{r_1^* \ln r_1^* - 2(1 - r_1^{*2}) \frac{2 - \sigma}{\sigma} \text{Kn}} \quad (2.130)$$

with $\text{Kn} = \text{Kn}'/2 = \lambda/(2(r_2 - r_1))$ and to its mean value

$$\overline{u_z^*} = \frac{1}{2} \left[1 + r_1^{*2} + 8(1 - r_1^* + r_1^{*2}) \frac{2 - \sigma}{\sigma} \text{Kn} + \frac{r_1^*(1 - r_1^{*2})(1 + 4 \frac{2 - \sigma}{\sigma} \text{Kn})^2}{r_1^* \ln r_1^* - 2(1 - r_1^{*2}) \frac{2 - \sigma}{\sigma} \text{Kn}} \right] \quad (2.131)$$

Thus, the Poiseuille number takes the form

$$\text{Po}_{\text{NS1, annu}} = \frac{16(1 - r_1^*)^2}{1 + r_1^{*2} + 8(1 - r_1^* + r_1^{*2}) \frac{2 - \sigma}{\sigma} \text{Kn} + \frac{r_1^*(1 - r_1^{*2})(1 + 4 \frac{2 - \sigma}{\sigma} \text{Kn})^2}{r_1^* \ln r_1^* - 2(1 - r_1^{*2}) \frac{2 - \sigma}{\sigma} \text{Kn}}} \quad (2.132)$$

which generalizes the expression (2.120) obtained for a circular microtube.

2.3.4. Gas Flow in rectangular microchannels

With the rectangular cross-section defined in Fig. 2.10(c) and the general assumptions of Section 2.3, the momentum equation takes the form

$$\frac{d^2 u_z}{dx^2} + \frac{d^2 u_z}{dy^2} = \frac{1}{\mu} \frac{dp}{dz} \quad (2.133)$$

In a dimensionless form, the momentum equation can be written

$$a^{*2} \frac{d^2 u_z^*}{dx^{*2}} + \frac{d^2 u_z^*}{dy^{*2}} = -1 \quad (2.134)$$

with

$$x^* = \frac{x}{b} \quad y^* = \frac{y}{h} \quad u_z^* = \frac{u_z}{-\frac{h^2}{\mu} \frac{dp}{dz}} \quad (2.135)$$

and $a^* = h/b$ is the aspect ratio of the section with $0 < a^* \leq 1$, if we assume $h \leq b$.

2.3.4.1. First-order solution

The first-order boundary conditions are

$$u_z^* \Big|_{y^*=1} = -\frac{2-\sigma}{\sigma} 2\text{Kn}' \frac{\partial u_z^*}{\partial y^*} \Big|_{y^*=1} \quad (2.136)$$

$$u_z^* \Big|_{x^*=1} = -\frac{2-\sigma}{\sigma} 2a^* \text{Kn}' \frac{\partial u_z^*}{\partial x^*} \Big|_{x^*=1} \quad (2.137)$$

with $\text{Kn}' = \lambda/(2h)$ and the conditions of symmetry

$$\frac{du_z^*}{dy^*} \Big|_{y^*=0} = 0 \quad (2.138)$$

$$\frac{du_z^*}{dx^*} \Big|_{x^*=0} = 0 \quad (2.139)$$

Ebert and Sparrow (1965) proposed a solution for the velocity distribution, compatible with the condition of symmetry (2.138):

$$u_z^* = -\sum_{i=1}^{\infty} \Psi_i(x^*) \cos(\alpha_i y^*) \quad (2.140)$$

The eigenvalues α_i must verify

$$\alpha_i \tan \alpha_i = \frac{\sigma}{2-\sigma} \frac{1}{2\text{Kn}'} \quad (2.141)$$

in order to be compatible with the boundary condition (2.136) without leading to a trivial velocity solution. The x^* -dependent Ψ_i functions are found by expanding the right-hand side of Eq. (2.134), that is unity, in terms of the orthogonal functions $\cos(\alpha_i y^*)$:

$$-1 = -\sum_{i=1}^{\infty} \Omega_i \cos(\alpha_i y^*) = -\sum_{i=1}^{\infty} \frac{2 \sin \alpha_i}{\alpha_i + \sin \alpha_i \cos \alpha_i} \cos(\alpha_i y^*) \quad (2.142)$$

Therefore, to verify the momentum equation (2.134), the functions Ψ_i must obey

$$\frac{d^2 \Psi_i}{dx^{*2}} - \left(\frac{\alpha_i}{a^*}\right)^2 \Psi_i - \frac{\Omega_i}{a^{*2}} = 0 \quad (2.143)$$

The solution of Eq. (2.143), with the conditions (2.137)–(2.139) and using Eq. (2.141), is

$$\Psi_i = -\frac{\Omega_i}{\alpha_i^2} \left(1 - \frac{\cosh\left(\frac{\alpha_i x^*}{a^*}\right)}{\cosh\left(\frac{\alpha_i}{a^*}\right) + 2\text{Kn}' \frac{2-\sigma}{\sigma} \alpha_i \sinh\left(\frac{\alpha_i}{a^*}\right)} \right) \quad (2.144)$$

Consequently, the velocity distribution is given by Eq. (2.140). This solution is given as a function of a Knudsen number $\text{Kn}' = \lambda/(2h)$ based on the channel depth, but it can also be expressed as a function of the previous Knudsen number $\text{Kn} = \lambda/D_H$ based on the hydraulic diameter by using the relation

$$2\text{Kn} = \text{Kn}'(1 + a^*) \quad (2.145)$$

In the special case of a square section, for which $a^* = 1$, both Knudsen numbers Kn and Kn' are identical.

2.3.4.2. Second-order solution

The above solution from Ebert et Sparrow was improved by Aubert and Colin (2001), in order to be more accurate for higher Knudsen numbers. This model is based on the second-order boundary conditions proposed by Deissler (1964):

$$u_z|_{y=h} = -\frac{2-\sigma}{\sigma}\lambda \left. \frac{\partial u_z}{\partial y} \right|_{y=h} - \frac{9}{16}\lambda^2 \left(2 \left. \frac{\partial^2 u_z}{\partial y^2} \right|_{y=h} + \left. \frac{\partial^2 u_z}{\partial x^2} \right|_{y=h} + \left. \frac{\partial^2 u_z}{\partial z^2} \right|_{y=h} \right) \quad (2.146)$$

and

$$u_z|_{x=b} = -\frac{2-\sigma}{\sigma}\lambda \left. \frac{\partial u_z}{\partial x} \right|_{x=b} - \frac{9}{16}\lambda^2 \left(2 \left. \frac{\partial^2 u_z}{\partial x^2} \right|_{x=b} + \left. \frac{\partial^2 u_z}{\partial y^2} \right|_{x=b} + \left. \frac{\partial^2 u_z}{\partial z^2} \right|_{x=b} \right) \quad (2.147)$$

This choice of Deissler boundary conditions, rather than other second-order formulations such as the ones proposed in Section 2.2.3.3, is due to the physical approach proposed by Deissler. The above equations are obtained from a three dimensional local momentum balance at the wall and the shear stress satisfies the definition of a Newtonian fluid used in the Navier–Stokes equations.

In Eqs. (2.146) and (2.147), the term $\partial^2 u_z / \partial z^2$ vanishes according to the continuity equation, which reduces to $\partial u_z / \partial z = 0$ for a locally fully developed flow. Finally, using the momentum equation (2.134), these equations may be written in a non-dimensional form as follows:

$$u_z^*|_{y^*=1} = -\frac{2-\sigma}{\sigma}2\text{Kn}' \left. \frac{\partial u_z^*}{\partial y^*} \right|_{y^*=1} - \frac{9}{4}\text{Kn}'^2 \left(\left. \frac{\partial^2 u_z^*}{\partial y^{*2}} \right|_{y^*=1} - 1 \right) \quad (2.148)$$

and

$$u_z^*|_{x^*=1} = -\frac{2-\sigma}{\sigma}2a^*\text{Kn}' \left. \frac{\partial u_z^*}{\partial x^*} \right|_{x^*=1} - \frac{9}{4}\text{Kn}'^2 \left(a^{*2} \left. \frac{\partial^2 u_z^*}{\partial x^{*2}} \right|_{x^*=1} - 1 \right) \quad (2.149)$$

The velocity distribution (2.140) proposed by Ebert and Sparrow, in the form of a single Fourier series, does not converge with second-order boundary conditions. Actually, the eigenvalues α_i obtained from the boundary condition (2.148) are such that the functions $\cos(\alpha_i y^*)$ are no longer orthogonal on the interval $[-1, 1]$. Therefore, a new form

$$u_z^*(x^*, y^*) = \sum_{i,j=1}^{\infty} A_{ij} N_{ij} \cos\left(\varphi_i \frac{x^*}{a^*}\right) \cos(\psi_j y^*) + \frac{9}{4} \text{Kn}'^2 \quad (2.150)$$

is required, based on a double Fourier series. The functions $\omega_{ij}(x^*, y^*) = \cos(\varphi_i x^*/a^*) \cos(\psi_j y^*)$ are orthogonal over the domain $[-1, 1] \times [-1, 1]$. They are solutions to the eigenvalues problem stemming from Eqs. (2.134), (2.148) and (2.149). The terms N_{ij} are such that the functions $N_{ij} \cos(\varphi_i x^*/a^*) \cos(\psi_j y^*)$ are normed over the domain $[-1, 1] \times [-1, 1]$.

The conditions (2.148) and (2.149) require ψ_j and φ_i to be solutions of Aubert (1999):

$$1 - 2 \text{Kn}' \frac{(2 - \sigma)}{\sigma} \psi_j \tan \psi_j - \frac{9}{4} \text{Kn}'^2 \psi_j^2 = 0 \quad (2.151)$$

and

$$1 - 2 \text{Kn}' \frac{(2 - \sigma)}{\sigma} \varphi_i \tan \frac{\varphi_i}{a^*} - \frac{9}{4} \text{Kn}'^2 \varphi_i^2 = 0 \quad (2.152)$$

In order to determine the terms A_{ij} , the solution (2.150) is injected into the momentum equation (2.134). Furthermore, the right-hand side of Eq. (2.134) is expanded in a double Fourier series. Finally, it is found that

$$\begin{aligned} A_{ij} N_{ij} = & \frac{1}{\varphi_i^2 + \psi_j^2} \left\{ \frac{4 \sin(\varphi_i/a^*) \sin \psi_j}{\varphi_i \psi_j} + \frac{9}{2} \frac{\sigma}{2 - \sigma} \text{Kn}' \left(\frac{\sin(\varphi_i/a^*) \cos \psi_j}{\varphi_i} + \frac{\cos(\varphi_i/a^*) \sin \psi_j}{\psi_j} \right) \right\} \\ & \times \left\{ \left(\frac{1}{a^*} + \frac{\cos(\varphi_i/a^*) \sin(\varphi_i/a^*)}{\varphi_i} \right) \left(1 + \frac{\sin \psi_j \cos \psi_j}{\psi_j} \right) \right. \\ & + \frac{9}{4} \frac{\sigma}{2 - \sigma} \text{Kn}' \left(\cos^2 \psi_j \left[\frac{1}{a^*} + \frac{\cos(\varphi_i/a^*) \sin(\varphi_i/a^*)}{\varphi_i} \right] \right. \\ & \left. \left. + \cos^2(\varphi_i/a^*) \left[1 + \frac{\sin \psi_j \cos \psi_j}{\psi_j} \right] \right) \right\}^{-1} \end{aligned} \quad (2.153)$$

Whatever the aspect ratio a^* , the convergence of the series (2.150) was verified. In every case, the asymptotic value of the sum is reached with a good precision from a number of roots ψ_j (Kn' , Kn'^2) and φ_i (a^* , Kn' , Kn'^2) from Eqs. (2.151) and (2.152) lower than 50. In Figure 2.12, the normalized velocity distribution u_z^* is plotted on the axis $x^* = 0$. The solutions proposed by Morini and Spiga (1998) and by Ebert and Sparrow (1965) and the second-order solution of Eq. (2.150) are compared for $\sigma = 1$, $\text{Kn}' = 0.1$ and for a square section ($a^* = 1$). The slight deviation observed between the velocity distributions found by Morini and Spiga and by Ebert and Sparrow results from their two different ways of solving the same first-order problem. It is pointed out that the flow rate is underestimated (about

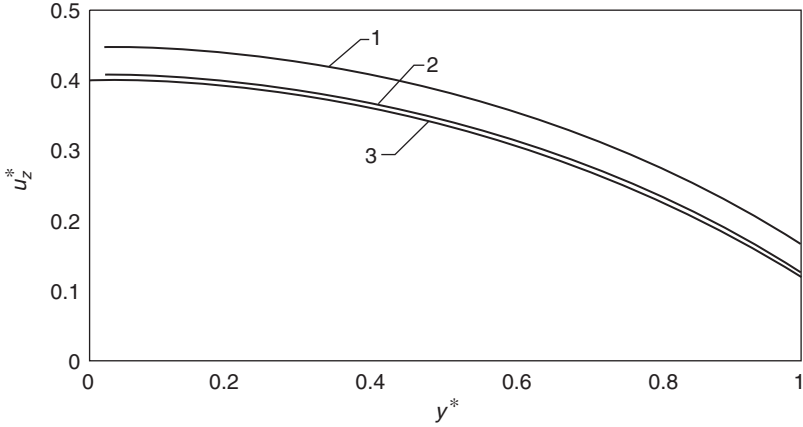


Fig. 2.12. Normalized velocity distribution in a square cross-section with diffuse reflection at the wall for $\text{Kn}' = 0.1$. 1: second-order model; 2: first-order model (Ebert and Sparrow, 1965); 3: first-order model (Morini and Spiga, 1998).

10% in the case of Fig. 2.12) when the second-order terms are not taken into account. Moreover, it is verified that the velocity distribution obtained with a second-order model cannot be deduced from a simple translation of the first-order velocity distribution.

The mass flow rate through the cross-section (Σ) is $\dot{m} = \iint_{(\Sigma)} \rho u_z dx dy$, that is with Eqs. (2.135) and (2.150):

$$\dot{m}_{\text{NS2,rect}} = -\frac{\rho h^2}{\mu} \frac{dp}{dz} \frac{4h^2}{a^*} \left[\sum_{i,j=1}^{\infty} A_{ij} N_{ij} \frac{a^* \sin(\varphi_i/a^*) \sin \psi_j}{\varphi_i \psi_j} + \frac{9}{4} \text{Kn}'^2 \right] \quad (2.154)$$

In order to obtain \dot{m} as a function of the inlet pressure p_i and the outlet pressure p_o of a long rectangular microchannel of length l , Eq. (2.154) must be integrated along the microchannel. For an isothermal flow and known geometric dimensions, the Knudsen number only depends on the pressure $p(z)$. Therefore, the solutions φ_i and ψ_j of Eqs. (2.151) and (2.152) depend on the position along the z -axis. The bracketed term of Eq. (2.154) can be precisely fitted by a polynomial function $a_1 + a_2 \text{Kn}' + a_3 \text{Kn}'^2$, where a_1 , a_2 and a_3 are coefficients depending on the aspect ratio a^* of the cross-section and on the momentum accommodation coefficient σ for a_2 and a_3 . Thus,

$$\dot{m}_{\text{NS2,rect}} = -\frac{4ph^4}{a^* RT \mu} \frac{dp}{dz} [a_1 + a_2 \text{Kn}' + a_3 \text{Kn}'^2] \quad (2.155)$$

Some numerical values of the coefficients a_1 , a_2 and a_3 , obtained with a least squares fitting method from values calculated using Eq. (2.154) for $\text{Kn}' \in [0; 1]$, are given in

Table 2.5

Values of coefficients a_1 , a_2 and a_3 for different values of σ and a^* , for Deissler second-order boundary conditions.

a^*	σ	0.5	0.6	0.7	0.8	0.9	1
0		$a_2 = 6.0000$	$a_2 = 4.6667$	$a_2 = 3.7143$	$a_2 = 3.0000$	$a_2 = 2.4444$	$a_2 = 2.0000$
$a_1 = 0.33333$		$a_3 = 4.5000$	$a_3 = 4.5000$	$a_3 = 4.5000$	$a_3 = 4.5000$	$a_3 = 4.5000$	$a_3 = 4.5000$
0.01		$a_2 = 5.9694$	$a_2 = 4.6459$	$a_2 = 3.7007$	$a_2 = 2.9917$	$a_2 = 2.4405$	$a_2 = 1.9993$
$a_1 = 0.33123$		$a_3 = 4.4528$	$a_3 = 4.4542$	$a_3 = 4.4548$	$a_3 = 4.4550$	$a_3 = 4.4549$	$a_3 = 4.4549$
0.025		$a_2 = 5.9228$	$a_2 = 4.6141$	$a_2 = 3.6797$	$a_2 = 2.9788$	$a_2 = 2.4337$	$a_2 = 1.9977$
$a_1 = 0.32808$		$a_3 = 4.3840$	$a_3 = 4.3875$	$a_3 = 4.3887$	$a_3 = 4.3895$	$a_3 = 4.3896$	$a_3 = 4.3892$
0.05		$a_2 = 5.8420$	$a_2 = 4.5591$	$a_2 = 3.6423$	$a_2 = 2.9547$	$a_2 = 2.4201$	$a_2 = 1.9925$
$a_1 = 0.32283$		$a_3 = 4.2761$	$a_3 = 4.2813$	$a_3 = 4.2843$	$a_3 = 4.2858$	$a_3 = 4.2858$	$a_3 = 4.2853$
0.1		$a_2 = 5.6774$	$a_2 = 4.4431$	$a_2 = 3.5613$	$a_2 = 2.9000$	$a_2 = 2.3860$	$a_2 = 1.9751$
$a_1 = 0.31233$		$a_3 = 4.0697$	$a_3 = 4.0832$	$a_3 = 4.0906$	$a_3 = 4.0943$	$a_3 = 4.0952$	$a_3 = 4.0944$
0.25		$a_2 = 5.1332$	$a_2 = 4.0464$	$a_2 = 3.2675$	$a_2 = 2.6823$	$a_2 = 2.2267$	$a_2 = 1.8626$
$a_1 = 0.28081$		$a_3 = 3.6073$	$a_3 = 3.6287$	$a_3 = 3.6449$	$a_3 = 3.6560$	$a_3 = 3.6626$	$a_3 = 3.6647$
0.5		$a_2 = 4.2443$	$a_2 = 3.3519$	$a_2 = 2.7120$	$a_2 = 2.2289$	$a_2 = 1.8487$	$a_2 = 1.5395$
$a_1 = 0.22868$		$a_3 = 3.3489$	$a_3 = 3.3588$	$a_3 = 3.3708$	$a_3 = 3.3856$	$a_3 = 3.4048$	$a_3 = 3.4292$
1		$a_2 = 3.1207$	$a_2 = 2.4552$	$a_2 = 1.9782$	$a_2 = 1.6187$	$a_2 = 1.3364$	$a_2 = 1.1077$
$a_1 = 0.14058$		$a_3 = 3.3104$	$a_3 = 3.3176$	$a_3 = 3.3287$	$a_3 = 3.3438$	$a_3 = 3.3644$	$a_3 = 3.3908$

Table 2.5. Note that the numerical values of the coefficient a_1 correspond closely to the analytical expression

$$a_1 = 2 \sum_{i=1}^{\infty} \frac{\sin^2 \alpha_{i,ns}}{\alpha_{i,ns}^4 (\alpha_{i,ns} + \cos \alpha_{i,ns} \sin \alpha_{i,ns})} \left(\alpha_{i,ns} - a^* \tanh \frac{\alpha_{i,ns}}{a^*} \right) \quad (2.156)$$

which can be deduced from the no-slip problem. In Eq. (2.156), $\alpha_{i,ns} = (2i - 1)\pi/2$.

Since for an isothermal flow, the quantity $\text{Kn}'p$ is constant, the integration of Eq. (2.155) along the microchannel yields

$$\dot{m}_{\text{NS2,rect}} = \frac{4h^4 p_o^2}{a^* \mu R T l} \left[\frac{a_1}{2} (\Pi^2 - 1) + a_2 \text{Kn}'_o (\Pi - 1) + a_3 \text{Kn}_o'^2 \ln \Pi \right] \quad (2.157)$$

and consequently

$$\dot{m}_{\text{NS2,rect}}^* = \frac{\dot{m}_{\text{NS2,rect}}}{\dot{m}_{\text{ns,rect}}} = \left[1 + 2 \frac{a_2}{a_1} \text{Kn}'_o \frac{1}{\Pi + 1} + 2 \frac{a_3}{a_1} \text{Kn}_o'^2 \frac{\ln \Pi}{\Pi^2 - 1} \right] \quad (2.158)$$

The mass flow rate is strongly dependent on the aspect ratio (*cf.* Fig. 2.13). If a^* is less than 0.01, the simpler plane flow model of Section 2.3.1 is accurate enough, but for higher values of a^* , it is no longer the case and the model presented in this section should be used.

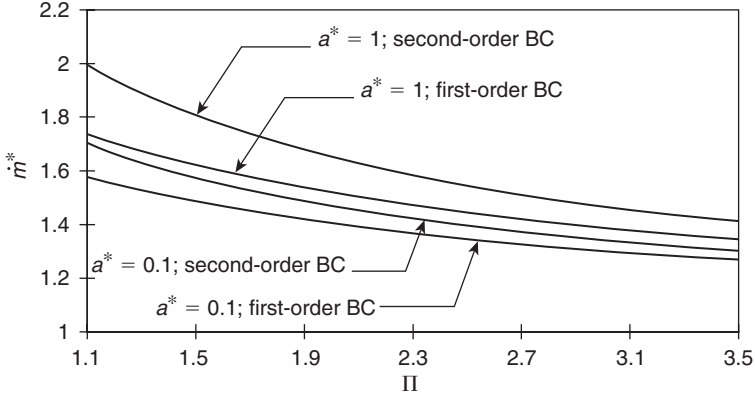


Fig. 2.13. Influence of the aspect ratio and of the slip-flow model on the normalized mass flow rate in a rectangular microchannel, for $\text{Kn}'_0 = 0.1$ and $\sigma = 1$. BC: boundary condition.

As an example, let us consider a pressure-driven flow in a long rectangular microchannel with an inlet over outlet pressure ratio $\Pi = 2$, an outlet Knudsen number $\text{Kn}'_0 = 0.1$ and an accommodation coefficient $\sigma = 1$. The flow rate deduced from Eq. (2.110)

$$\dot{m}_{\text{NS2,plan}} = [(2bh^3p_0^2)/(\mu RTl)][(\Pi^2 - 1)/3 + 4((2 - \sigma)/\sigma)\text{Kn}'_0(\Pi - 1) + 9\text{Kn}_0'^2 \ln \Pi]$$

which was calculated from a plane model with Deissler boundary conditions, overestimates the flow rate $\dot{m}_{\text{NS2,rect}}$ given by Eq. (2.157) and calculated from a rectangular model. The overestimation $[(\dot{m}_{\text{plan}} - \dot{m}_{\text{rect}})/\dot{m}_{\text{rect}}]_{\text{NS2}}$ is about 0.5% for an aspect ratio $a^* = 0.01$, it rises to 5.3% for an aspect ratio $a^* = 0.1$ and reaches 112% for a square cross-section with $a^* = 1$!

The pressure distribution $p(z)$ can also be deduced from the mass conservation. It is the solution of the equation

$$\frac{\frac{a_1}{2}[(p/p_0)^2 - 1] + a_2\text{Kn}'_0[(p/p_0) - 1] + a_3\text{Kn}_0'^2 \ln(p/p_0)}{\left[\frac{a_1}{2}(\Pi^2 - 1) + a_2\text{Kn}'_0(\Pi - 1) + a_3\text{Kn}_0'^2 \ln \Pi\right]} = (1 - z^*) \quad (2.159)$$

which can be numerically solved. An example of the non-dimensional pressure distribution $p^* = p/p_{\text{ns}}$ as a function of $z^* = z/l$ is given in Fig. 2.14, for an outlet Knudsen number $\text{Kn}'_0 = 0.1$, an accommodation coefficient $\sigma = 1$ and for $a^* = 1$ (square duct) or $a^* = 0.1$. The maximum influence of the slip at the wall corresponds to $z^* = 0.77$. A no-slip model overestimates the pressure by a few percents, as is the case for a plane microchannel (Fig. 2.11). Moreover, the greater the aspect ratio, the larger the pressure overestimation is.

2.3.5. Experimental data

A discussion of the accuracy of the different models described in the previous section requires fine experimental data, notably to know which second-order boundary conditions are more appropriate.

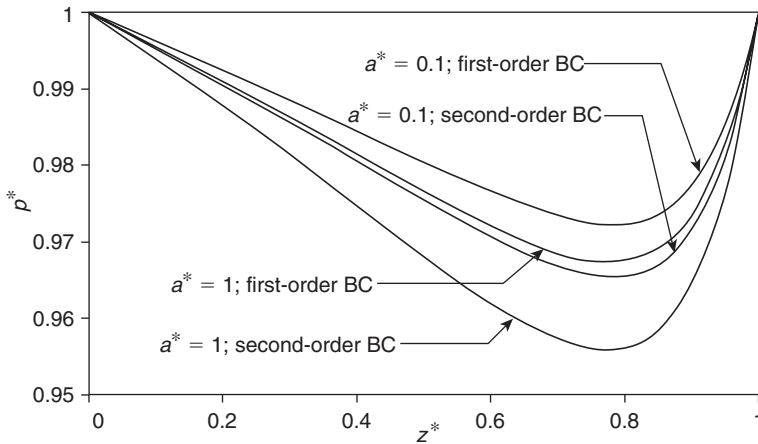


Fig. 2.14. Influence of the aspect ratio and of the slip-flow model on the normalized pressure distribution along a rectangular microchannel, for $\text{Kn}'_0 = 0.1$ and $\sigma = 1$. BC: boundary condition.

2.3.5.1. Experimental setups for flow rate measurements

Few experimental setups are described in the literature. The first techniques used to provide experimental data of gas flow rates in a microchannel were proposed by Arkilic *et al.* (1994) or by Pong *et al.* (1994). They both used accumulation techniques: the gas flowing through the microchannel accumulates in a reservoir, resulting in either a change in pressure (constant-volume technique) or a change in volume (constant-pressure technique). Actually, this method is limited because the tiny mass flows are very difficult to measure accurately using a single tank. In particular very small changes in temperature can overwhelm the mass flow measurement due to thermal expansion of the gas. To overcome this difficulty, a differential technique was used afterwards (Arkilic *et al.*, 1998). The system is schematically represented in Fig. 2.15. Gas flows through the test microchannel and into the accumulation tank A. The mass flow through the system can be inferred from a measurement of the differential pressure between the accumulation tank A and a reference tank B. This arrangement is very insensitive to temperature fluctuations and allows accurate measurements of mass flow rates, with a sensitivity announced to be as low as 7×10^{-5} kg/s.

Another experimental setup was designed by Lalonde (2001) for the measurement of gaseous microflow rates under controlled temperature and pressure conditions, in the range 10^{-7} to 10^{-13} m³/s. Its principle is based on the tracking of a drop meniscus in a calibrated pipette connected in series with the microchannel. Its main advantage, compared to other similar setups presented in the literature (Shih *et al.*, 1996; Zohar *et al.*, 2002; Maurer *et al.*, 2003), is the simultaneous measurement of the flow rate both upstream and downstream of the microchannel (Fig. 2.16). The inlet and the outlet pressures can both be independently tuned. The volume flow rate is measured by means of opto-electronical sensors that detect the passage of the two menisci of a liquid drop injected into the calibrated pipettes connected upstream and downstream of the microchannel.

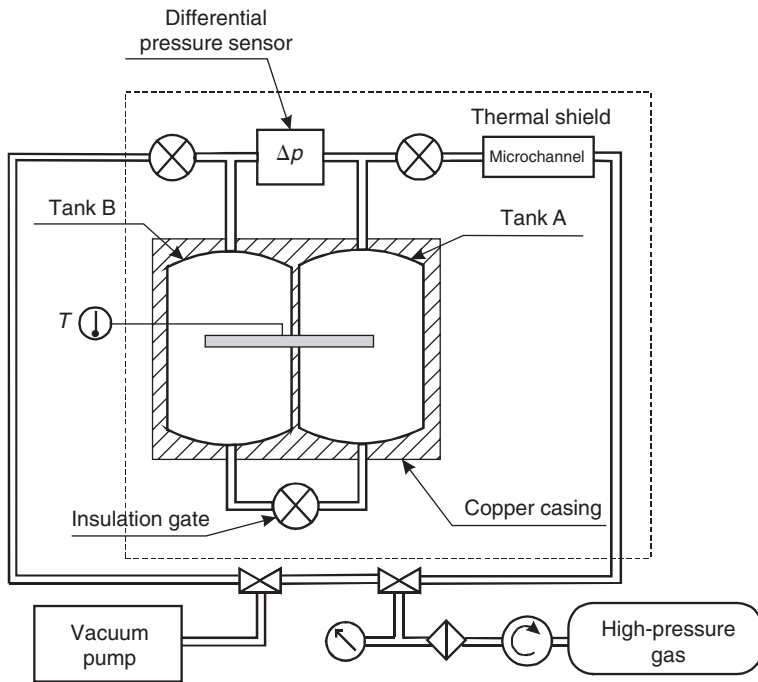


Fig. 2.15. Schematic of an accumulation mass flow measurement system. Adapted from Arkilic *et al.* (1998).

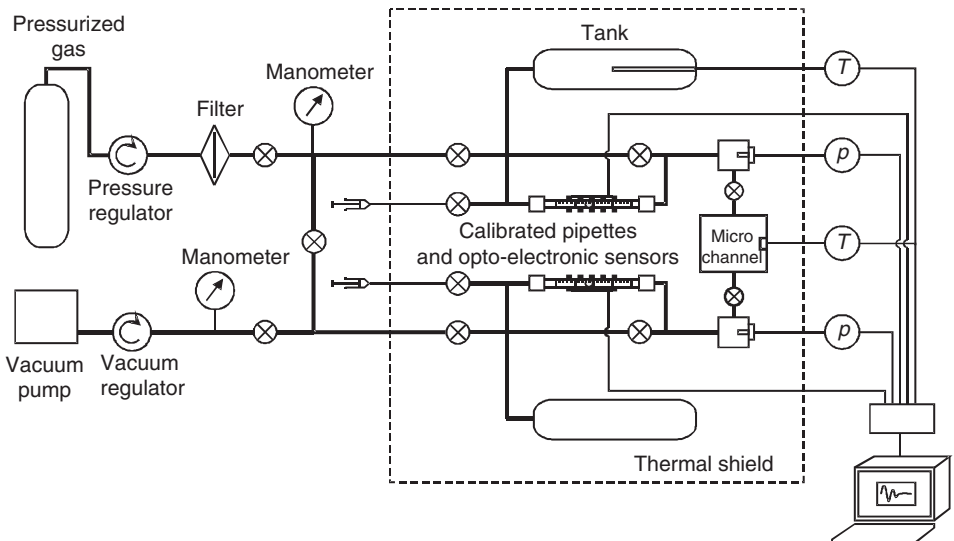


Fig. 2.16. Schematic of a pointer tracking system for the measurement of gas microflow rates (Lalonde, 2001).

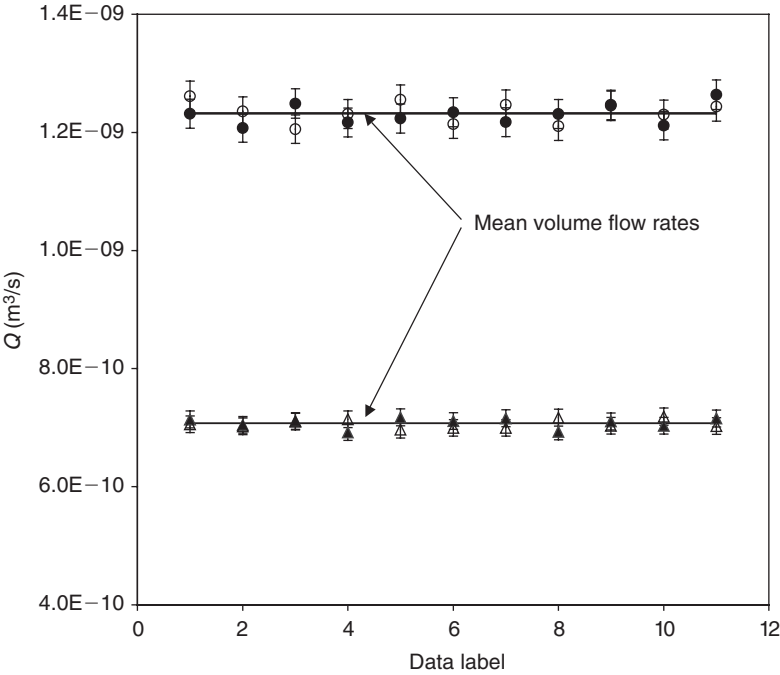


Fig. 2.17. Typical example of volumetric flow rate (Q) measurement with the setup of Lalonde (2001).

A series of individual measurements of the volumetric flow rate can therefore be obtained, which allows the determination of the mean volumetric flow rates upstream and downstream of the microchannel and consequently, the mass flow rate through the microchannel. The comparison of the individual data given by each pipette, as well as the comparison of the two mean mass flow rates deduced from the two mean volumetric flow rates, must be consistent with the experimental uncertainties to allow the validation of the acquisition. A typical example is shown in Fig. 2.17. The upper data (circles) correspond to the downstream pipette and the lower ones (triangles) to the upstream pipette, through which the volumetric flow rate is lower, since the pressure is higher. The white symbols are relative to the first, the dark symbols to the second, of the two menisci of the drop in the pipette. In total, 44 individual data values are obtained for each test. Experimental uncertainties are reported by vertical bars.

Other similar setups are described by Zohar *et al.* (2002) or by Maurer *et al.* (2003). They both provide a single but accurate measurement downstream of the microchannel. In the first case (Zohar *et al.*, 2002), the outlet pressure is always the atmospheric pressure, whereas in the second case (Maurer *et al.*, 2003), the outlet can be tuned as well as the upstream pressure.

2.3.5.2. Flow rate data

Comparing the different models available to describe the slip flow regime in microchannels, we note significant differences, essentially for the second-order term. For example, in a

plane flow between parallel plates, the mass flow rate predicted by Eq. (2.110) depends on the choice of the second-order boundary condition. According to the value of the coefficient A_2 (see Table 2.3), the calculated mass flow rate may vary significantly. Moreover, some models generally based on a simple mathematical extension of Maxwell's condition (2.58) and for which $A_2 > 0$ predict a decrease of the slip compared to the first-order model. While other models, for which $A_2 < 0$, predict an increase of the slip. It is also interesting to test the accuracy of a QHD model, which does not involve second-order boundary conditions, but is second-order Knudsen number dependent (*cf.* Eq. (2.111)).

The increase of the slip due to second-order terms was first confirmed by Lalonde (2001), who measured the flow rate of helium and nitrogen in rectangular microchannels and showed that for outlet Knudsen numbers $\text{Kn}'_{0,M}$ higher than 0.05, a first-order model underestimates the slip. For the comparison of the experimental flow rate data with the predictions from the different models presented above, the sources of error or uncertainty must be considered. They can globally be divided into three classes:

- (1) The uncertainties inherent to the fluid properties (density, viscosity, dissolved air, etc.) and to their dependence toward the experimental parameters (temperature, pressure). One can also note that some properties such as the momentum accommodation coefficient, σ , depend both on the fluid and the wall.
- (2) The uncertainties relative to the microchannel geometrical characteristics (dimensions of the section, roughness, etc.) and to their dispersion.
- (3) The uncertainties due to the flow rate measurement (metrology, leakage, operating conditions, etc.).

Most of these uncertainties can be limited within an acceptable precision. This is generally not the case for the measurement of the cross-section dimensions. When these dimensions are of the order of $1\text{ }\mu\text{m}$, the measures obtained by different means (profilometer, optical microscope, SEM) that require preliminary calibration can differ notably: up to about 5% for the width and about 10% for the depth (Anduze, 2000). Therefore, the data are hardly exploitable, since the hydraulic diameter plays a part to the power of 4 in the calculation of the flow rate. Also, an inaccuracy of only 10 nm when measuring a depth of $1\text{ }\mu\text{m}$ leads to an error of 4% in the estimation of the flow rate. The second parameter that can pose a problem is the accommodation coefficient σ , the value of which is not usually well known.

In order to avoid interpretation errors due to these two main sources of uncertainty, the idea is to compare among themselves data measured on a same microchannel, in a Knudsen number range that covers at least two of the following regimes:

- (1) In the *little rarefied* regime, differences between the flow rates predicted by the no-slip (ns), the NS1 and the NS2 models are negligible, of the order of the experimental uncertainties. The value of σ consequently does not play any significant role.
- (2) In the *lightly rarefied* regime, the difference between NS1 and NS2 models remains negligible, but the difference with the ns model is now significant. The influence of the accommodation coefficient σ may also become significant for the higher values of Kn'_0 .
- (3) In the *moderately rarefied* regime, the ns, NS1 and NS2 models predict significantly different flow rates, and σ is now a very sensitive parameter.

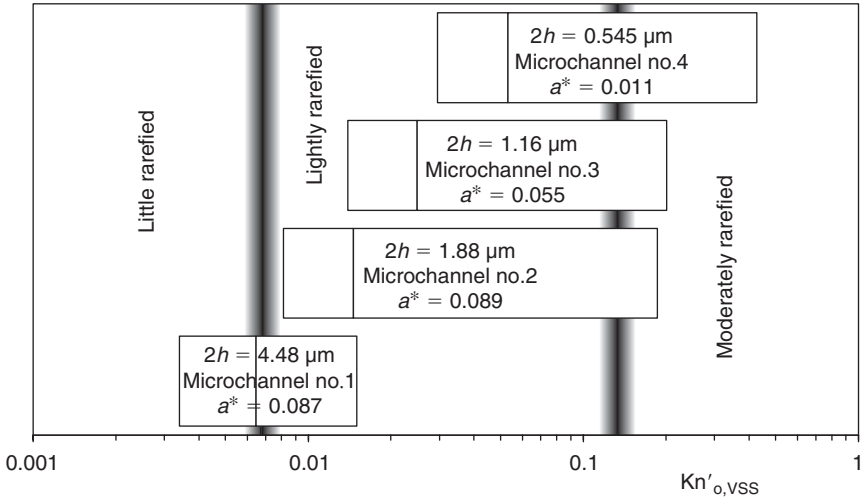


Fig. 2.18. Knudsen number ranges covered by a series of rectangular microchannels tested by Lalonde (2001), the right part of the rectangles corresponds to the outlet Knudsen number values.

Figure 2.18 represents these regimes with a series of microchannels experimentally studied by Lalonde (Colin *et al.*, 2004).

The microchannel no.1, with a measured depth $2h = 4.48 \mu\text{m}$, allows a check of the transition from ns to NS1 models. First, the flow rate is measured for low values of the outlet Knudsen number Kn'_o , that is for high values of P_o . For $\text{Kn}'_{o,VSS} = 0.007$, the differences between the flow rates predicted from the NS1 and NS2 models are negligible, whatever the value of the accommodation coefficient σ and the deviation with the ns model remains of the order of the experimental uncertainties. The depth $2h$ kept for the simulation is adjusted to $4.48 \mu\text{m}$ – exactly the measured value in that case – for a good correlation between the experimental data and the NS1 or NS2 model. Then, rarefaction is increased, by decreasing the outlet pressure; the difference between ns and NS1 or NS2 models becomes significant and the experimental data are in very good agreement with the slip flow models. The influence of σ is still negligible as is the deviation between NS1 and NS2 models.

The microchannels nos.3 and 4 allow a check of the transition from NS1 to NS2 models. As an illustration, Fig. 2.19 shows some flow rate data relative to the microchannel no.3, whose measured depth is $2h = 1.15 \mu\text{m}$. The depth for the simulation is adjusted to $1.16 \mu\text{m}$, that is $0.01 \mu\text{m}$ more than the measured value, from data at low values of Kn'_o , for which both NS1 and NS2 models accurately predict the experimental flow rates. An increase of the rarefaction leads to a deviation between these two models. The agreement between the experimental data and the NS2 model is good, whatever the gas – nitrogen (Fig. 2.19(b)) or helium (Fig. 2.19(c)) – with $\sigma = 0.93$. The rarefaction is increased even more and the difference between NS1 and NS2 models becomes very significant (Fig. 2.19(d)). The experiment shows the validity of the second-order slip flow model with Knudsen numbers higher than 0.2. This observation is confirmed with the microchannel no.4, up to Knudsen numbers around 0.25.

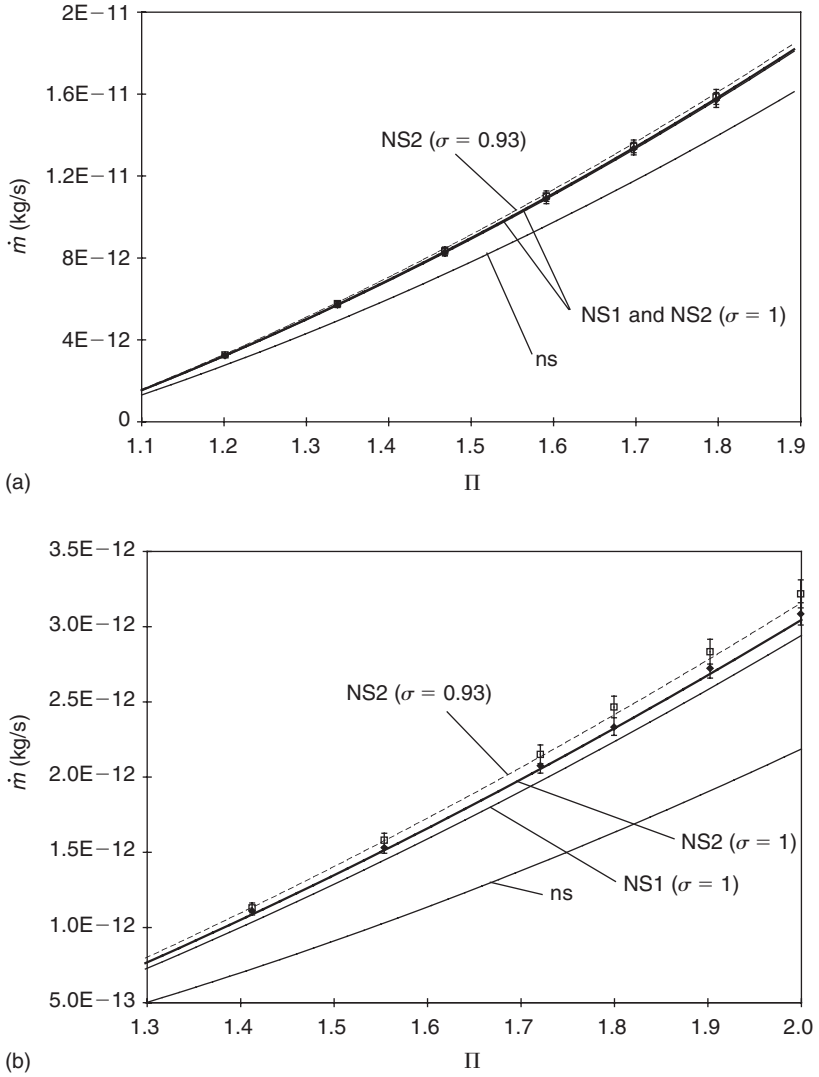


Fig. 2.19. Theoretical and experimental flow rates for a rectangular microchannel. $2h = 1.16 \mu\text{m}$, $2b = 21 \mu\text{m}$, $l = 5000 \mu\text{m}$, $T = 294.2 \text{ K}$. (a) Gas: N_2 , $p_0 = 1.9 \times 10^5 \text{ Pa}$, $\text{Kn}'_{0,\text{VSS}} = 2.5 \times 10^{-2}$; (b) gas: N_2 , $p_0 = 0.65 \times 10^5 \text{ Pa}$, $\text{Kn}'_{0,\text{VSS}} = 7.3 \times 10^{-2}$.

For nitrogen and helium flows, an attempt to summarize the results obtained with the microchannels nos.2, 3 and 4 is shown in Fig. 2.20. The dimensionless flow rate $1/\dot{m}^*$, little sensitive to the aspect ratio a^* , is plotted in function of $\text{Kn}'_{0,\text{M}}$, for an inlet over outlet pressure ratio $\Pi = 1.8$. Up to $\text{Kn}'_{0,\text{M}} = 0.05$, the first-order (NS1) and the second-order (NS2) slip flow models predict the same flow rate. For higher values of Kn'_0 , the deviation is significant and the experimental data are in very good agreement with the NS2 model,

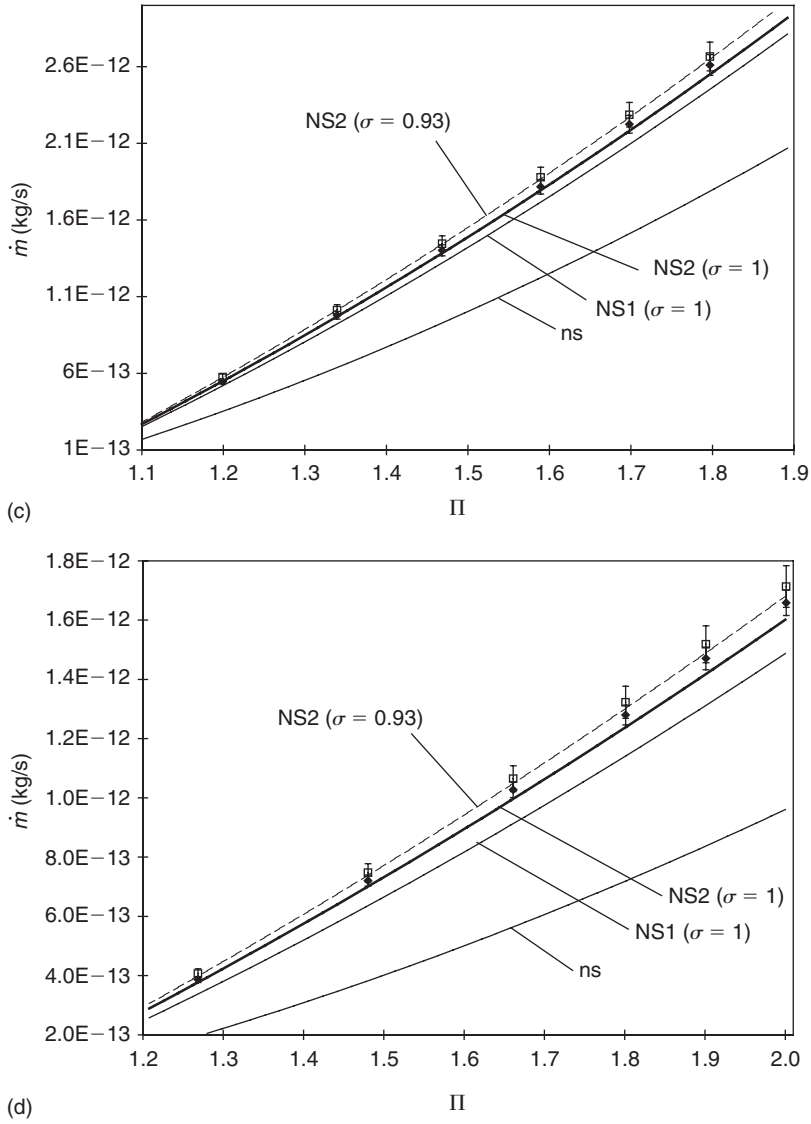


Fig. 2.19. (Continued) (c) gas: He, $p_0 = 1.9 \times 10^5$ Pa, $Kn'_{0,VSS} = 7.9 \times 10^{-2}$; (d) gas: He, $p_0 = 0.75 \times 10^5$ Pa, $Kn'_{0,VSS} = 2.0 \times 10^{-1}$.

up to $Kn'_{0,M} = 0.25$. Beyond that, the agreement is not so fine although the experimental data are closer to NS2 than to NS1 predictions.

The experiments of Maurer *et al.* (2003) follow the same trend. The latest precise experimental data provided in the literature (Table 2.6) concern different gases and are relative to microchannels with cross-sections of comparable lengths l and depths $2h$, but

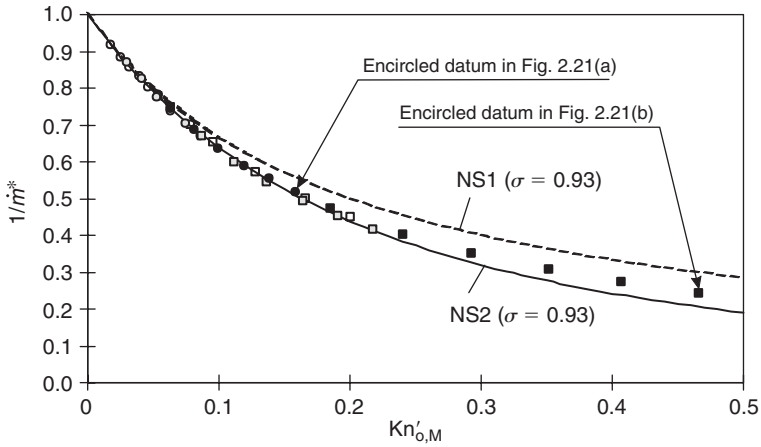


Fig. 2.20. Inverse reduced flow rate ($1/\dot{m}^*$) in rectangular microchannels: comparison of experimental data with NS1 and NS2 slip flow models; $\Pi = 1.8$; $T = 294.2$ K; microchannels no.2 (white), no.3 (grey), no.4 (black); gas: N_2 (circle) and He (square).

Table 2.6

Recent experimental data of gas flows in rectangular microchannels.

Reference	Microchannels dimensions			Experimental conditions		Theoretical comparison	
	$l(\mu\text{m})$	$2h(\mu\text{m})$	α^* (%)	Gas	Kn'_0	σ	Model
Shih <i>et al.</i> (1996)	4000	1.2	3.0	He	0.16	1.16	Plane, NS1
				N_2	0.055	0.99	
Arkilic <i>et al.</i> (2001)	7490	1.33	2.5	Ar	0.05–0.41	0.80	Plane, NS1
				N_2	0.05–0.34	0.80	
				CO_2	0.03–0.44	0.80	
Lalonde (2001); Colin <i>et al.</i> (2004)	5000	0.54–4.48	1.1–8.7	N_2	0.004–0.16	0.93; 1.00	Rectangular, NS2, $k_2 = k_{2,M}$,
				He	0.029–0.47	0.93; 1.00	$A_2 = -9/8$; plane, QHD1, $k_2 = k_{2,VSS}$
Zohar <i>et al.</i> (2002)	4000	0.53; 0.97	1.3; 2.4	He	0.21; 0.38	1.00	Plane, NS1,
				Ar	0.11; 0.20	1.00	$k_2 = k_{2,M}$
				N_2	0.065; 0.12	1.00	
Maurer <i>et al.</i> (2003)	10,000	1.14	0.6	N_2	0.054–1.1	0.87	Plane, NS2,
				He	0.17–1.46	0.91	$A_2 = -0.23_{(N_2)}$, $A_2 = -0.26_{(He)}$

manufactured with different processes. Arkilic *et al.* (2001) used two silicon wafers facing each other, Colin *et al.* (2004) studied microchannels etched by DRIE in silicon and covered with a glass sealed by anodic bonding, whereas Maurer *et al.* (2003) used microchannels etched in glass and covered with silicon. The lower and upper walls of the microchannels

fabricated by Zohar *et al.* (2002) were obtained by deposition of low-stress silicon nitride layers on a silicon wafer.

A smart comparison of the data provided by these authors is also tricky, since the aspect ratios a^* of the sections are different from one study to another. The two latter studies (Maurer *et al.*, 2003; Colin *et al.*, 2004) confirm that an adequate slip flow model based on second-order boundary conditions can be precise for high Knudsen numbers that usually apply to the transition regime.

The experimental data from Lalonde have also been compared (Colin *et al.*, 2003) to the mass flow predicted by a QHD model with first-order boundary conditions (QHD1). For the microchannel no.4, with a low aspect ratio $a^* = 0.011$, the plane assumption is acceptable and Eq. (2.111) is valid. Figure 2.21 shows that the QHD1 model could be accurate for Knudsen numbers higher than the NS2 model, but with a different accommodation coefficient, $\sigma = 1$, both for nitrogen and helium. Actually, the analysis of this result should be qualified. For this comparison, the mean free path was calculated using the formula given by Maxwell ($k_{2,M} = \sqrt{\pi}/2$) for the NS2 as well as for the QHD1 simulations, but the Schmidt value (0.74 for nitrogen and 0.77 for helium) used for the QHD1 simulation is very close to the one obtained from a VSS model, that is given by Eq. (2.46). Another comparison of the QHD1 model with the data of Lalonde is proposed in Elizarova and Sheretov (2003), using $k_{2,VSS}$ calculated from the VSS model (*cf.* Table 2.1). In this case, the better fit is found for $\sigma = 1$ for helium and $\sigma = 0.93$ for nitrogen.

To conclude, it is clear that the NS2 or QHD1 models improve the accuracy of the NS1 model, but further studies that include smart experimental data are necessary to dissociate the roles of the accommodation coefficient, the collision model and the slip flow model.

2.3.5.3. Pressure data

Pressure measurements along a microchannel have been successfully performed by different groups (Liu *et al.*, 1995; Lee *et al.*, 2002; Zohar *et al.*, 2002; Jang and Wereley, 2004), using integrated pressure microsensors connected to the microchannels via capillary connections (Fig. 2.22). These experiments confirm the theoretical pressure distribution shown in Fig. 2.11.

2.3.5.4. Flow visualization

Although micro-particle image velocimetry (micro-PIV) has been widely used to visualize liquid microflows for several years (Wereley *et al.*, 1998), this technique has not been successfully applied to gaseous microflows as yet due to seeding and inertia issues (Wereley *et al.*, 2002; Sinton, 2004). The molecular tagging velocimetry (MTV) could be an alternative and interesting technique for gas microflows visualization. This method was used to obtain the velocity profile of water in microtubes 705 μm in diameter, with a spatial resolution lower than 4% (Webb and Maynes, 1999). Recently, the technique was adapted to the analysis of gaseous subsonic or supersonic microjets generated by a 1 mm diameter nozzle. The gas was nitrogen, seeded with acetone and the spatial resolution was around 10 μm , with a maximal uncertainty of 5% for a Knudsen number between 0.002 and 0.035, that is in the slip flow regime.

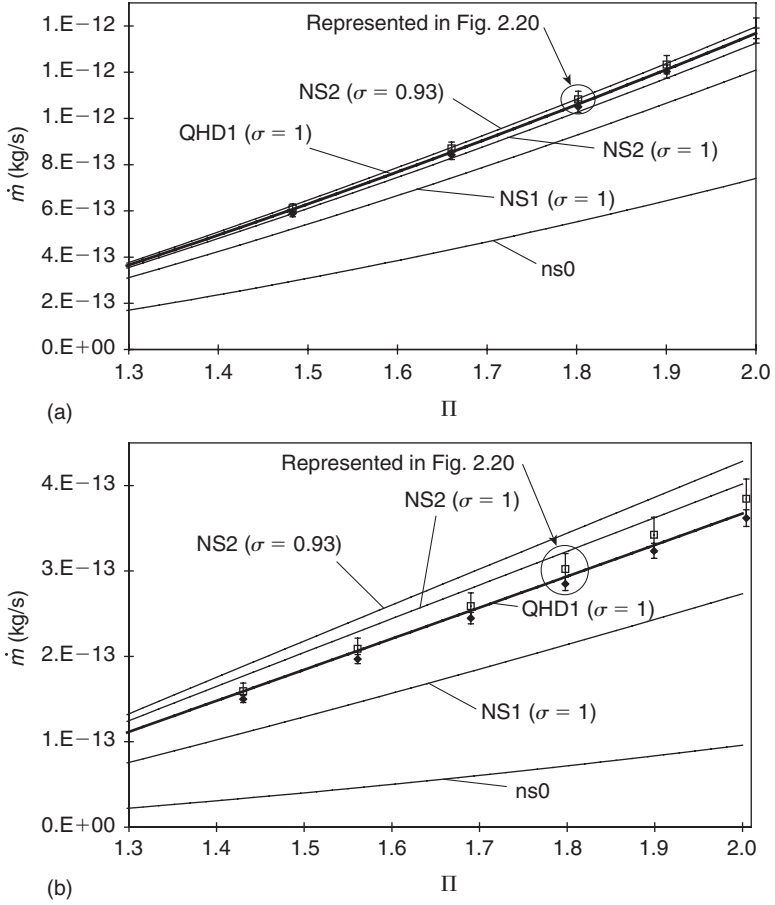


Fig. 2.21. Experimental data from Lalonde (outlet flow rate \square and inlet flow rate \blacklozenge), compared to NS2 and QHD1 models. Microchannel no.4. $P_o = 75$ kPa, $T = 294.2$ K. (a) Gas: N_2 ; $Sc = 0.74$; the encircled data correspond to $Kn'_{o,M} = 0.15$. (b): Gas: He; $Sc = 0.77$; the encircled data correspond to $Kn'_{o,M} = 0.47$.

2.3.6. Entrance effects

In the previous sections, the microchannels have been considered as long microchannels and the entrance effects have been neglected. If the microchannel is short, such that the hydrodynamic development length L_{hd} is no longer negligible compared to the microchannel length, entrance effects have to be taken into account by a numerical approach. Rarefaction increases L_{hd} in the slip flow regime, due to slip at the walls. Barber and Emerson (2002) used a two-dimensional finite-volume Navier–Stokes solver to simulate the flow of a gas entering a plane microchannel in the slip-flow regime, with first-order boundary conditions. Their simulated data, for $Kn \in [0; 0.1]$ and $Re \in [0; 400]$ were fitted

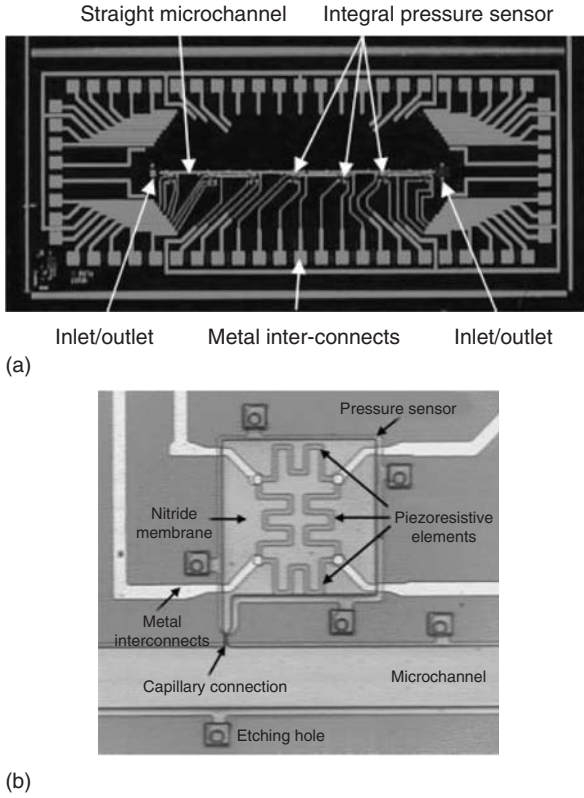


Fig. 2.22. Microchannel with integrated pressure sensors (Zohar *et al.*, 2002). (a) Microchannel with inlet and outlet; (b) close-up of the pressure sensor and its capillary connection with the microchannel.

by a least-squares technique and led to the following expression for the hydrodynamic development length:

$$\frac{L_{hd}}{D_H} = \frac{0.332}{0.0271 Re + 1} + 0.011 Re \frac{1 + 14.78 Kn}{1 + 9.78 Kn} \quad (2.160)$$

which generalizes the expression $L_{hd}/D_H = 0.315/(0.0175 Re + 1) + 0.011 Re$ found by Chen (1973) for a no-slip flow with a slight modification of the non-rarefied part of the equation. In Eq. (2.160), the Knudsen number $Kn = \lambda/D_H$ and the Reynolds number $Re = \rho \bar{u}_z D_H / \mu$ are based on the hydraulic diameter $D_H = 4h$ of the microchannel, $2h$ in depth. The hydrodynamic development length is arbitrarily defined as the longitudinal distance required for the centerline velocity to reach 99% of its fully developed value. Equation (2.160) shows that for $Kn = 0.1$ and $Re = 400$, slip at the wall increases the entrance length of about 25%.

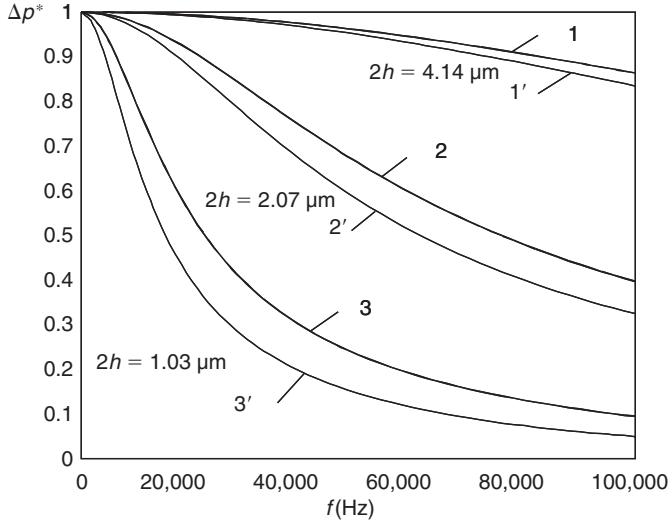


Fig. 2.23. Influence of microchannel depth $2h$ on the gain Δp^* for a square microchannel closed at its outlet. $l = 100 \mu\text{m}$, $\bar{T} = 293 \text{ K}$, $\bar{p} = 0.11 \text{ MPa}$. 1, 2, 3: slip flow; 1', 2', 3': no-slip flow.

2.4. Pulsed gas flows in microchannels

Rarefaction affects steady microflows and modifies the behavior of unsteady microflows. The case of pulsed flows is of particular interest because such flows are encountered in many applications. For example, micropump actuators often generate sinusoidal pressure fluctuations inside a chamber in order to induce a flow in microchannels through microvalves or microdiodes.

Detailed models for pulsed gaseous flows in the slip flow regime can be found in Caen *et al.* (1996) for circular microtubes or in Colin *et al.* (1998a) for rectangular microchannels. They are based on the Navier–Stokes equations with first-order slip and temperature jump conditions at the walls. If we consider a microchannel of length l , whose inlet is submitted to a sinusoidal pressure fluctuation with a small amplitude, the gain Δp^* of the microchannel, that is the ratio of the outlet Δp_o over inlet Δp_i fluctuating pressures amplitudes, can be calculated. For example, in the simple case of a microchannel closed at its outlet, this gain takes the form

$$\Delta p^* = \left| \frac{\Delta p_o}{\Delta p_i} \right| = \left| \frac{1}{\cosh(\beta l)} \right| \quad (2.161)$$

where $\beta(f, \text{Kn}) \approx \sqrt{f} \Psi(\text{Kn})$ depends on the square root of the frequency f and on the Knudsen number. It can be shown that the band pass of the microchannel is underestimated when slip at the walls is not taken into account (Fig. 2.23).

Obtaining experimental data to discuss these theoretical results is very hard, due to the very small size of the pressure sensors required for these experiments. However,

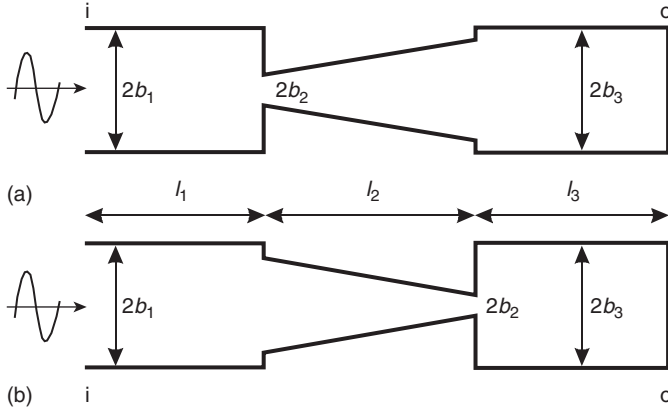


Fig. 2.24. Two layouts of a microdiode placed in a microchannel.

experimental data were obtained for microtubes down to $50\text{ }\mu\text{m}$ in diameter, using a commercially available pressure microsensor placed in a minichannel connected in series to one or several parallel microtubes (Colin *et al.*, 1998b). The behavior of the micro- and minichannels association was simulated and compared to these data. The agreement was good, both for the gain and the phase of the association.

The model for pulsed flows in constant-section microchannels can be easily extended to microchannels with slowly varying cross-sections (Aubert *et al.*, 1998). It allows an understanding of the behavior of microdiffusers subjected to sinusoidal pressure fluctuations and to test the diode effect of a microdiffuser/nozzle placed in a microchannel that is subjected to sinusoidal pressure fluctuations. In Fig. 2.24, two layouts (a) and (b) are considered.

In layout (a), the tested element is a microdiffuser, with an increasing section from inlet to outlet. In layout (b), the same element is used as a nozzle with a decreasing section from inlet to outlet. To obtain an exploitable comparison between the two layouts, the widths ($2b_1, 2b_2, 2b_3$) and the lengths (l_1, l_2, l_3) are the same in layouts (a) and (b). The angle 2α is also the same for the diffuser or the nozzle.

An analysis of the frequency behavior for each layout shows significant differences, which is characteristic of a dynamic diode effect. Therefore, in order to characterize the dissymmetry of the transmission of the pressure fluctuations, an efficiency E of the diode is introduced. This efficiency

$$E = \frac{\Delta p_{(a)}^*}{\Delta p_{(b)}^*} = \frac{|\Delta p_o / \Delta p_i|_{(a)}}{|\Delta p_o / \Delta p_i|_{(b)}} \quad (2.162)$$

defined as the ratio of the fluctuating pressure gain in layout (a) over the fluctuating pressure gain in layout (b), can be studied as a function of the frequency f . Some results are shown in Fig. 2.25, for different values of the depth $2h$ with $l_1 = l_2 = l_3 = 3\text{ mm}$, $2b_1 = 2b_3 = 467\text{ }\mu\text{m}$, $2b_2 = 100\text{ }\mu\text{m}$ and $\alpha = 3.5^\circ$.

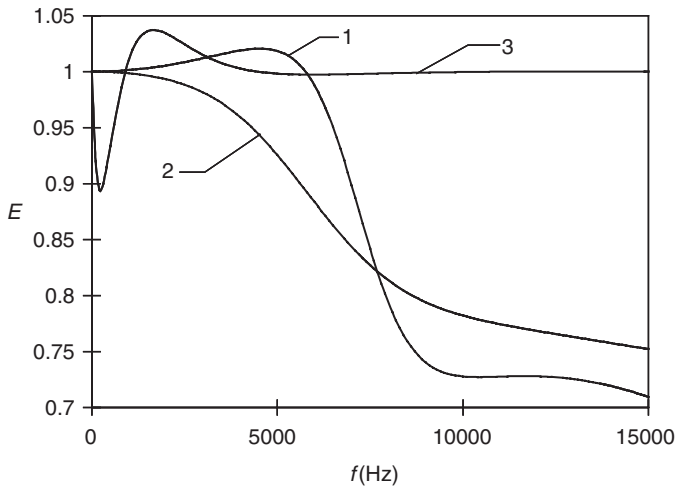


Fig. 2.25. Diode efficiency for different values of the depth. 1: $2h = 100 \mu\text{m}$; 2: $2h = 62 \mu\text{m}$, 3: $2h = 6 \mu\text{m}$.

Figure 2.25 points out that with a microdiffuser ($2h = 6 \mu\text{m}$), E appears to be less than unity *below* a critical frequency. This denotes a reversed diode effect compared to the case of a diffuser with sub-millimetric dimensions ($2h = 100 \mu\text{m}$), for which E is less than unity *beyond* a critical frequency. Note also that the influence of slip (taken into account in Fig. 2.25) is not negligible when $2h = 6 \mu\text{m}$. However, slip has little influence on the values of characteristic frequencies (i.e. the frequencies for which E is an extremum or equal to unity).

Pulsed gaseous flows are also of great interest in short microchannels, or micro-orifices, for example in synthetic microjets. The synthetic microjet is a low power, highly compact microfluidic device that has potential for application in boundary layer control (Lee *et al.*, 2003). The oscillation of an actuated membrane at the bottom of a cavity generates a pulsed flow through a micro-slit or orifice (Fig. 2.26). It results in a zero net-mass flux, but in a non-zero mean momentum flux. A series of such microjets can be used to control separation or transition in the boundary layer of the flow on a wing in order to reduce drag, to increase lift or to limit noise generated by the air flow.

2.5. Thermally driven gas microflows and vacuum generation

Generating vacuum by means of microsystems concerns various applications such as the taking of biological or chemical samples, or the control of the vacuum level in the neighborhood of some specific microsystems during working.

The properties of rarefied flows (due to both low pressure and small dimensions) allow unusual pumping techniques. For high Knudsen numbers, the flow may be generated without any moving mechanical component by only using thermal actuation, which is not possible with classical macropumps.

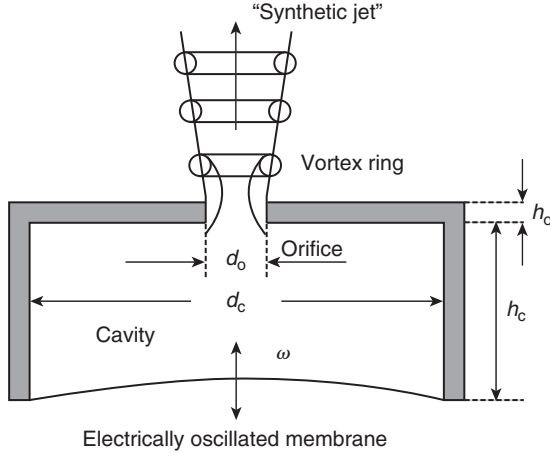


Fig. 2.26. Schematic of a micro-synthetic jet actuator (Mallinson *et al.*, 2003).

2.5.1. Transpiration pumping

Currently, the most studied technique is based on thermal transpiration. The basic principle requires two chambers filled with gas and linked with an orifice whose hydraulic diameter is small compared with the mean free path of the molecules. Chamber 1 is heated, for example with an element, so that $T_1 > T_2$. By analyzing the probability that some molecules move from one chamber across the orifice, it can be shown that if the pressure is uniform ($p_1 = p_2 = p$), a molecular flux

$$\dot{N}_{2 \rightarrow 1} = \frac{Ap}{\sqrt{2\pi mk_B}} \frac{\sqrt{T_1} - \sqrt{T_2}}{\sqrt{T_1 T_2}} \quad (2.163)$$

from chamber 2 toward chamber 1 – from cold to hot temperatures – appears (Muntz and Vargo, 2002; Lengrand and Elizarova, 2004). If the net molecular flux is constant, the pressures necessarily verify that

$$\frac{p_1}{p_2} = \sqrt{\frac{T_1}{T_2}} \quad (2.164)$$

In Eqs. (2.163) and (2.164), m is the mass of a molecule and A is the area of the orifice. If $p_2 < p_1 < p_2 \sqrt{T_1/T_2}$, there is a net flow from 2 toward 1, which results in a decrease of p_2 and/or an increase of p_1 . This indicates that a basic microscale pump is working.

Thus, a Knudsen compressor (Fig. 2.27) can be designed by connecting a series of chambers with very small orifices that have a cold region (temperature T_2) on one side and a hot region (temperature T_1) on the other side by means of an adequate local heater placed just downstream of the orifices. This multistage layout leads to important cumulated pressure drops, while keeping a satisfactory flow rate. In practice, the orifices must be

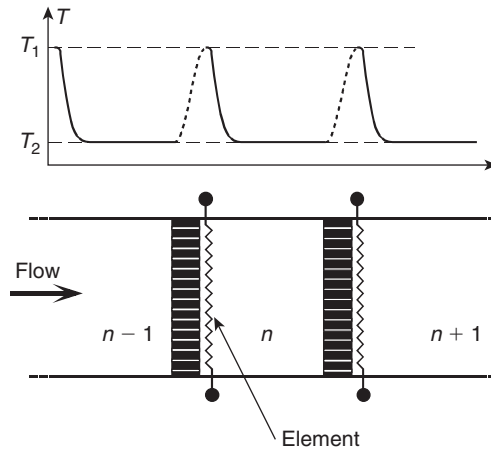


Fig. 2.27. Multistage Knudsen compressor.

replaced by microchannels and this complicates the modeling (Vargo and Muntz, 1997). Moreover, it is generally difficult to maintain simultaneously a free molecular regime in the microchannels and a continuum regime in the chambers, which are the required conditions for the optimal efficiency corresponding to Eqs. (2.163) and (2.164). More elaborate models, based on the linearization of the Boltzmann equation (Loyalka and Hamoodi, 1990), are able to take into account the transition regime ($0.05 < \text{Kn} < 10$) both in the microchannels and in the chambers (Vargo and Muntz, 1999). Several design studies are proposed in the literature that show the theoretical feasibility of microscale thermal transpiration pumps.

The first mesoscale prototypes, heated with an element at the wall (Vargo and Muntz, 1997; Vargo and Muntz, 1999; Vargo *et al.*, 1999), were tested. An alternative solution suggesting heating within the gas was also proposed (Young, 1999), but experimental data are not available for this layout.

Actually, there is yet much to do for the theoretical optimization and almost everything is to be done for the design of thermal transpiration micropumps using micro manufacturing techniques. The performances of these micropumps remain limited for technological reasons. A high vacuum level may become incompatible with the typical internal sizes of microsystems (Muntz and Vargo, 2002) because the regime in the chambers must be close to a continuum regime, which requires sizes too big for the lower pressures.

2.5.2. Accommodation pumping

Accommodation pumping is another pumping technique. It exploits the property of gas molecules whose reflection on specular walls depends on their temperature. If the wall is warmer than the gas, the mean reflection angle is greater than the incident angle. Conversely, if the wall is colder than the molecules, they have a more tangential reflection. Consequently, in a microchannel with perfectly specular walls connecting two chambers at

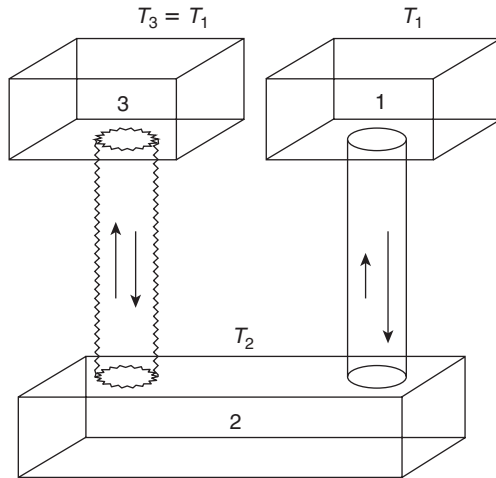


Fig. 2.28. One stage of an accommodation micropump.

different temperatures, a flow takes place from the hot toward the cold chambers (Hobson, 1970). If the walls of the microchannel give a diffuse reflection, this effect disappears. This property was confirmed with numerical simulations by the DSMC method (Hudson and Bartel, 1999). By linking two warm chambers (1 and 3) to a cold chamber (2) on one side with a smooth microchannel (1–2) and on the other side with a rough microchannel (3–2), a difference of pressure ($p_1 < p_3$) appears between the two chambers at the same temperature (Fig. 2.28).

Connecting in series several stages of that type, the pressure drops relative to each stage can be cumulated and allow the setup to reach high vacuum levels. The advantage of the accommodation pump is that it is operational without theoretical limitations concerning low pressures and contrary to the thermal transpiration pumping, the accommodation pumping does not require chambers with high dimensions. To compensate, the accommodation pump requires more stages to reach the same final pressure ratio. A pressure ratio $\Pi = 100$ requires 125 stages, whereas only 10 stages are enough for a transpiration pump with comparable temperatures. Lastly, no operational prototype was described in the literature so far, although the concept seems attractive. The highest-performance design was proposed by Hobson (1971; 1972); it requires a cold temperature $T_2 = 77$ K for an atmospheric temperature $T_1 = T_3 = 290$ K.

2.6. Heat transfer in microchannels

In the slip flow regime, heat transfer can be treated as well as mass transfer, providing the energy equation (2.41) and the temperature boundary conditions (2.61) are solved with the momentum equation and the slip-flow boundary conditions. Such heat transfer problems have an analytical solution only in the simplest cases. For example, if the compressibility of the flow can be neglected, the energy and the momentum equations are no longer

coupled and if the flow is developed, longitudinal temperature gradients are constant and longitudinal velocity gradients are zero (see example in Section 2.6.1.1). In the general case, analytical or semi-analytical solutions are not possible and numerical simulations are required.

Depending on the accommodation coefficients, heat transfer can be found to increase, decrease or remain unchanged, compared to non-slip-flow conditions.

2.6.1. Heat transfer in a plane microchannel

2.6.1.1. Heat transfer for a fully developed incompressible flow

Let us consider the case of a plane microchannel (Fig. 2.10(a)), with a lower adiabatic wall ($q_w|_{y=-h} = 0$) and an upper wall with constant heat flux ($q_w|_{y=h} = q_h$). The flow is assumed to be hydrodynamically and thermally developed and incompressible. Fluid properties are assumed uniform. Noting $y^* = y/h$, the momentum equation reduces to

$$\frac{d^2 u_z}{dy^{*2}} = \frac{h^2}{\mu} \frac{dp}{dz} \quad (2.165)$$

and the energy equation to

$$\frac{k}{h^2} \frac{\partial^2 T}{\partial y^{*2}} = \rho u_z c_p \frac{\partial T}{\partial z} \quad (2.166)$$

neglecting viscous dissipation. We introduce

$$\theta^* = \frac{T - T_{\text{wall}}}{q_h h / k} = \frac{4}{\text{Nu}} \frac{T - T_{\text{wall}}}{\bar{T} - T_{\text{wall}}} \quad (2.167)$$

with $q_h = \alpha(\bar{T} - T_{\text{wall}})$ and $\text{Nu} = \alpha D_H / k = 4 \alpha h / k$, noting α as the convection heat transfer coefficient. The flow being thermally developed, $\partial \theta^* / \partial z = 0$, $\partial \text{Nu} / \partial z = 0$ and $\partial q_h / \partial z = 0$, which implies $\partial T / \partial z = \partial \bar{T} / \partial z = \partial T_{\text{wall}} / \partial z$. Consequently, the energy equation can be written as

$$\frac{q_h}{h} \frac{d^2 \theta^*}{dy^{*2}} = \rho u_z c_p \frac{d \bar{T}}{dz} \quad (2.168)$$

Moreover, the conservation of energy on a control volume of length dz and height $2h$ yields $2h \rho c_p \bar{u}_z d \bar{T} = -q_h dz$ and Eq. (2.168) reduces to

$$\frac{d^2 \theta^*}{dy^{*2}} = -\frac{u_z}{2 \bar{u}_z} \quad (2.169)$$

Neglecting thermal creep, the first-order boundary conditions are

$$\left. \frac{du_z}{dy^*} \right|_{y^*=0} = 0 \quad u_z|_{y^*=1} = -\xi^* \left. \frac{du_z}{dy^*} \right|_{y^*=1} \quad (2.170)$$

$$\left. \frac{d\theta^*}{dy^*} \right|_{y^*=-1} = 0 \quad \theta^*|_{y^*=1} = -\zeta^* \left. \frac{d\theta^*}{dy^*} \right|_{y^*=1} \quad (2.171)$$

with a dimensionless coefficient of slip $\xi^* = \xi/h = (\lambda/h)(2 - \sigma)/\sigma = 4 \text{Kn}(2 - \sigma)/\sigma$ and a dimensionless temperature jump distance $\zeta^* = \zeta/h = (\lambda/h)[(2 - \sigma_T)/\sigma_T][2\gamma/(\gamma + 1)]/\text{Pr} = 8[(2 - \sigma_T)/\sigma_T][\gamma/(\gamma + 1)][\text{Kn}/\text{Pr}]$, where Pr is the Prandtl number. The resolution of this set of equations gives the velocity distribution

$$u_z = -\frac{h^2}{2\mu} \frac{dp}{dz} (1 - y^{*2} + 2\xi^*) \quad (2.172)$$

and, with

$$\begin{aligned} \bar{u}_z &= \frac{1}{2} \int_{-1}^1 u_z dy^* \\ \frac{u_z}{\bar{u}_z} &= \frac{3(-y^{*2} + 1 + 2\xi^*)}{2(1 + 3\xi^*)} \end{aligned} \quad (2.173)$$

The integration of Eq. (2.169) with the boundary conditions (2.171) yields

$$\begin{aligned} \theta^* = \zeta^* + \frac{1}{1 + 3\xi^*} &\left[\frac{1}{16} y^{*4} - \frac{3}{8} y^{*2} (1 + 2\xi^*) - \frac{1}{2} y^* (1 + 3\xi^*) \right. \\ &\left. + \left(\frac{13}{16} + \frac{9}{4} \xi^* \right) \right] \end{aligned} \quad (2.174)$$

T and $\bar{T} = (1/2) \int_{-1}^1 (u_z/\bar{u}_z) T dy^*$ are calculated and the Nusselt number is deduced as

$$\text{Nu}^{-1} = \frac{\zeta^*}{4} + \frac{26 + 147\xi^* + 210\xi^{*2}}{140(1 + 3\xi^*)^2} \quad (2.175)$$

Equation (2.175) shows that heat transfer depends both on the dimensionless coefficient of slip ξ^* and on the dimensionless temperature jump distance ζ^* , that is it depends on the two accommodation coefficients σ and σ_T as well as on the Knudsen number Kn . For classical values of the accommodation coefficients, the effect of the temperature jump is greater than the effect of velocity slip and the heat transfer decreases when rarefaction increases. The Nusselt number reduces to the classic value $70/13$ (Rohsenow, 1998) when $\text{Kn} = 0$.

Zhu *et al.* (2000) extended this solution to the problem of asymmetrically heated walls ($0 \neq q_0 \neq q_h$) by combining the solutions of two sub-problems similar to the above problem.

Inman (Karniadakis and Beskok, 2002) first studied the solution for a constant symmetric heat flux at the two walls.

The problem with constant wall temperature was treated by Hadjiconstantinou and Simek (2002), who extended the study to the transition regime, using DSMC. They showed that the slip flow prediction (with first-order boundary conditions) is in good agreement with the DSMC results for $\text{Kn} \leq 0.2$ and remains a good approximation beyond its expected range of applicability.

2.6.1.2. Heat transfer for a developing compressible flow

This problem was studied by Kavehpour *et al.* (1997), using the same first-order slip flow and temperature jump boundary conditions as in Section 2.6.1.1. The flow was developing both hydrodynamically and thermally and two cases were considered: uniform wall temperature or uniform wall heat flux. Viscous dissipation was neglected, but compressibility was taken into account. The numerical methodology was based on the control volume finite difference scheme. It was found that the Nusselt number was substantially reduced for slip flow compared with continuum flow.

2.6.2. Heat transfer in a circular microtube

Heat transfer in circular microtubes was simulated by Ameel *et al.* (1997), who considered a hydrodynamically fully developed incompressible flow, thermally developing with constant heat flux at the wall. Viscous dissipation and thermal creep were neglected and first-order velocity slip and temperature jump conditions were used, with accommodation coefficients taken equal to unity.

They found the thermally fully developed solution

$$\text{Nu}^{-1} = \frac{24\chi^2 - 16\chi + 3}{48(2\chi - 1)^2} \left(1 + \frac{24\gamma(\chi - 1)(2\chi - 1)^2}{(24\chi^2 - 16\chi + 3)(\gamma + 1)\text{Pr}} \right) \quad (2.176)$$

with $\chi = 1 + 4\text{Kn}$. Equation (2.176) reduces to the no-slip value $\text{Nu} = 48/11$ when $\text{Kn} = 0$. A semi-analytical solution is also given in Ameel *et al.* (1997) for the entrance region. For a Knudsen number $\text{Kn} = 0.04$, it is found that the Nusselt number for the fully developed flow is reduced 14% over that obtained with a no-slip boundary condition, with $\gamma = 1.4$ and $\text{Pr} = 0.7$.

Larrodé *et al.* (2000) treated the case of constant temperature at the wall.

2.6.3. Heat transfer in a rectangular microchannel

Yu and Ameel (2001) studied the heat transfer problem for a thermally developing flow in a rectangular microchannel. The flow was assumed to be incompressible and hydrodynamically fully developed, and a constant temperature was imposed at the walls. The velocity distribution was developed in series as discussed in Section 2.3.4.1 and the energy equation was solved by a modified generalized integral transform method. A competition between ξ and ζ was pointed out, with a transition value β_c of $\beta = \xi/\zeta$ that depends on the aspect ratio a^* (Table 2.7).

Table 2.7
Transition values of $\beta = \xi/\varsigma$ as a function of the aspect ratio, (from Yu and Ameen (2001)).

a^{*-1}	1	2	3	4	5	6	8	10	∞
β_c	0.67	0.50	0.38	0.32	0.29	0.28	0.27	0.25	0.20

For $\beta < \beta_c$, heat transfer is enhanced in comparison with the no-slip flow and if $\beta > \beta_c$, heat transfer is reduced. Moreover, for $\beta < \beta_c$, heat transfer increases with increasing ξ^* and it decreases if $\beta > \beta_c$. According to the values available in the literature, it should be noted that β may vary in a wide range from unity to 100 or more, for actual wall surface conditions. However, the value $\beta = 1.67$, which corresponds to a diffuse reflection ($\sigma = 1$) and a total thermal accommodation ($\sigma_T = 1$) for air ($\gamma = 1.4$; $Pr = 0.7$) is a representative value for many engineering applications. In this typical case, rarefaction effects result in a decrease of heat transfer, which can be as much as 40%.

2.7. Future research needs

Theoretical knowledge is currently well advanced for gas flows in microchannels. However, there is yet a need for accurate experimental data, both for steady or unsteady gas microflows, with or without heat transfer. For example, in order to definitely validate the choice of the best boundary conditions in the slip flow regime, we need to isolate the influence of the accommodation coefficients, as it remains an open issue. Relationships between their values, the nature of the substrate and the micro-fabrication processes involved are currently not available. Theoretical investigations relative to unsteady or thermally driven microflows would also need to be supported by smart experiments.

2.8. Solved examples

Example 2.1

A microchannel with constant rectangular cross-section is submitted to a pressure-driven flow of argon. The inlet and the outlet pressures are $p_i = 0.2$ MPa and $p_o = 25$ kPa respectively. The geometry is given in Fig. 2.10(c), with a width $2b = 20$ μ m, a depth $2h = 1$ μ m and a length $l = 5$ mm.

Assume a uniform temperature $T = 350$ K.

- (i) Calculate the Knudsen numbers Kn and Kn' at the inlet and at the outlet of the microchannel, assuming that the intermolecular collisions are accurately described by a variable soft spheres model.
- (ii) Compare with the values obtained from a hard spheres model.
- (iii) Assuming a diffuse reflection at the wall, calculate the mass flow rate through the microchannel.

- (iv) Calculate the mass flow rate increase (in %) due to slip at the wall.
 (v) What would be the underestimation (in %) of the mass flow rate given by a no-slip model, in the same conditions but with an inlet pressure $p_i = 0.1$ MPa?

Solution:

(i) Inlet and outlet Knudsen numbers with a VSS model (Answer: $\text{Kn}'_i = 3.48 \times 10^{-2}$; $\text{Kn}_i = 1.83 \times 10^{-2}$; $\text{Kn}'_o = 2.78 \times 10^{-1}$; $\text{Kn}_o = 1.46 \times 10^{-1}$)

From Table 2.2, the temperature exponent of the coefficient of viscosity for argon (Ar) is $\omega = 0.81$, the exponent for the VSS model is $\alpha = 1.40$ and the dynamic viscosity under standard conditions is $\mu_0 = 211.7 \times 10^{-7}$ Pa s.

From Eq. (2.7), the viscosity at $T = 350$ K is:

$$\mu(T) = \mu_0(T/T_0)^\omega = 2.117 \times 10^{-5}(350/273.15)^{0.81} = 2.588 \times 10^{-5} \text{ Pa s.}$$

The molecular weight of argon is given in Table 2.2: $M = 39.948 \times 10^{-3}$ kg/mol and its gas constant is $R = \bar{R}/M = 8.314511/39.948 \times 10^{-3} = 2.08 \times 10^2$ J/kg/K.

The mean free path is given by Table 2.1: $\lambda = k_2 \mu(T) \sqrt{RT}/p$,
 with

$$k_{2,\text{VSS}} = \frac{4\alpha(7-2\omega)(5-2\omega)}{5(\alpha+1)(\alpha+2)\sqrt{2\pi}} = 0.996.$$

At the inlet,

$$\lambda_{i,\text{VSS}} = k_2 \mu(T) \sqrt{RT}/p_i = 0.996 \times 2.588 \times 10^{-5} \times \sqrt{2.08 \times 10^2 \times 350/2 \times 10^5} \\ = 34.8 \text{ nm}$$

and at the outlet,

$$\lambda_{o,\text{VSS}} = k_2 \mu(T) \sqrt{RT}/p_o = 0.996 \times 2.588 \times 10^{-5} \times \sqrt{2.08 \times 10^2 \times 350/2.5 \times 10^4} \\ = 278 \text{ nm.}$$

The Knudsen number based on the hydraulic diameter

$$D_H = 4bh/(b+h) = 4 \times 10 \times 10^{-6} \times 0.5 \times 10^{-6}/((10+0.5) \times 10^{-6}) = 1.905 \text{ } \mu\text{m}$$

is $\text{Kn} = \lambda/D_H$, that is

$$\text{Kn}_i = \lambda_i/D_H = 3.48 \times 10^{-8}/1.905 \times 10^{-6} = 1.83 \times 10^{-2} \text{ at the inlet and} \\ \text{Kn}_o = \lambda_o/D_H = 2.78 \times 10^{-7}/1.905 \times 10^{-6} = 1.46 \times 10^{-1} \text{ at the outlet.}$$

The Knudsen number based on the microchannel depth is $\text{Kn}' = \lambda/(2h)$, that is

$$\text{Kn}'_i = \lambda_i/(2h) = 3.48 \times 10^{-8}/1 \times 10^{-6} = 3.48 \times 10^{-2} \text{ at the inlet and}$$

$$\text{Kn}'_0 = \lambda_o/(2h) = 2.78 \times 10^{-7}/1 \times 10^{-6} = 2.78 \times 10^{-1} \text{ at the outlet.}$$

(ii) Inlet and outlet Knudsen numbers with a HS model (Answer: $\text{Kn}'_{i,\text{HS}} = 4.13 \times 10^{-2}$; $\text{Kn}_{i,\text{HS}} = 2.17 \times 10^{-2}$; $\text{Kn}'_{o,\text{HS}} = 3.30 \times 10^{-1}$; $\text{Kn}_{o,\text{HS}} = 1.73 \times 10^{-1}$)
 With a HS model, $\omega = 0.5$ and the viscosity

$$\begin{aligned} \mu(T) &= \mu_0(T/T_0)^{0.5} = 2.117 \times 10^{-5} (350/273.15)^{0.5} \\ &= 2.396 \times 10^{-5} \text{ Pa s is underestimated of 7.4\%.} \end{aligned}$$

The coefficient $k_{2,\text{HS}} = 16/(5\sqrt{2\pi}) = 1.277$ (cf. Table 2.1).

Consequently,

$$\begin{aligned} \lambda_{i,\text{HS}} &= k_{2,\text{HS}} \mu(T) \sqrt{RT}/p_i = 1.277 \times 2.588 \times 10^{-5} \times \sqrt{2.08 \times 10^2 \times 350/2} \times 10^5 \\ &= 41.3 \text{ nm} \end{aligned}$$

and

$$\begin{aligned} \lambda_{o,\text{HS}} &= k_{2,\text{HS}} \mu(T) \sqrt{RT}/p_o = 1.277 \times 2.588 \times 10^{-5} \times \sqrt{2.08 \times 10^2 \times 350/2.5} \times 10^4 \\ &= 330 \text{ nm} \end{aligned}$$

which leads to:

$$\text{Kn}_{i,\text{HS}} = \lambda_{i,\text{HS}}/D_H = 41.3 \text{ nm}/1.905 \times 10^{-6} = 2.17 \times 10^{-2}$$

$$\text{Kn}_{o,\text{HS}} = \lambda_{o,\text{HS}}/D_H = 330 \text{ nm}/1.905 \times 10^{-6} = 1.73 \times 10^{-1}$$

$$\text{Kn}'_{i,\text{HS}} = \lambda_{i,\text{HS}}/(2h) = 41.3 \text{ nm}/1 \times 10^{-6} = 4.13 \times 10^{-2}$$

$$\text{Kn}'_{o,\text{HS}} = \lambda_{o,\text{HS}}/(2h) = 330 \text{ nm}/1 \times 10^{-6} = 3.30 \times 10^{-1}$$

The overestimation of the Knudsen number calculated from an HS model, compared with the more accurate solution obtained with a VSS model, is 28.2%, which corresponds to the ratio $(k_{2,\text{HS}} - k_{2,\text{VSS}})/k_{2,\text{VSS}} = 0.282$.

(iii) Mass flow rate (Answer: $\dot{m} = 4.89 \times 10^{-12} \text{ kg/s}$)

The rectangular cross-section has a non-negligible aspect ratio $a^* = h/b = 1/20 = 0.05 > 0.01$. Therefore, a rectangular model should be used. Due to the range covered by the Knudsen numbers, a second-order model (NS2) is required (cf. Fig. 2.7).

The mass flow rate is obtained from Eq. (2.157):

$$\dot{m}_{\text{NS2,rect}} = \frac{4h^4 p_o^2}{a^* \mu RTl} \left[\frac{a_1}{2} (\Pi^2 - 1) + a_2 \text{Kn}'_o (\Pi - 1) + a_3 \text{Kn}_o'^2 \ln \Pi \right]$$

with $a_1 = 0.32283$, $a_2 = 1.9925$ and $a_3 = 4.2853$ given by Table 2.5 for a diffuse reflection ($\sigma = 1$). $\Pi = p_i/p_o = 200/25 = 8$ and

$$\begin{aligned}\dot{m}_{\text{NS2, rect}} &= 4(10^{-6})^4(2.5 \times 10^{-4})^2/(0.05 \times 2.588 \times 10^{-5} \times 2.08 \times 10^2 \times 350 \\ &\quad \times 5 \times 10^{-3}) \times [0.32283(8^2 - 1)/2 + 1.9925 \times 2.78 \times 10^{-1}(8 - 1) \\ &\quad + 4.2853 \times (2.78 \times 10^{-1})^2 \ln 8] = 4.89 \times 10^{-12} \text{ kg/s}\end{aligned}$$

(iv) Mass flow rate increase (Answer: 44.9%)

From Eq. (2.158),

$$\begin{aligned}\dot{m}_{\text{NS2, rect}}^* &= \frac{\dot{m}_{\text{NS2, rect}}}{\dot{m}_{\text{ns, rect}}} = \left[1 + 2 \frac{a_2}{a_1} \text{Kn}'_o \frac{1}{\Pi + 1} + 2 \frac{a_3}{a_1} \text{Kn}'_o^2 \frac{\ln \Pi}{\Pi^2 - 1} \right] \\ &= 1 + 2 \frac{1.9925}{0.32283} 2.78 \times 10^{-1} \frac{1}{8 + 1} + 2 \frac{4.2853}{0.32283} (2.78 \times 10^{-1})^2 \frac{\ln 8}{8^2 - 1} = 1.449\end{aligned}$$

which means that slip at the wall increases the flow rate of 44.9%.

(v) Underestimation of the mass flow rate (Answer: 46.7%)

If the inlet pressure is decreased to $p_i = 0.1$ MPa, the pressure ratio is $\Pi = 4$ and

$$\dot{m}_{\text{NS2, rect}}^* = 1 + 2 \frac{1.9925}{0.32283} 2.78 \times 10^{-1} \frac{1}{4 + 1} + 2 \frac{4.2853}{0.32283} (2.78 \times 10^{-1})^2 \frac{\ln 4}{4^2 - 1} = 1.877.$$

Therefore, although the outlet Knudsen number is unchanged, the inlet pressure number is increased and rarefaction effects are enhanced. Slip at the wall now increases the flow rate of 87.7%. In others words, the underestimation of the mass flow rate with a no-slip model is 46.7%, since $(\dot{m}_{\text{NS2}} - \dot{m}_{\text{ns}})/\dot{m}_{\text{NS2}} = 1 - 1/\dot{m}_{\text{NS2}}^* = 1 - 1/1.877 = 0.467$.

Example 2.2

In a hard disk drive, the flow of gas between the hard disk and the read-write head can locally be comparable to a fully developed micro-Couette flow between parallel plane plates. The shield of the hard disk drive is sealed and the gas inside is pure nitrogen. The distance between the two plates is $2h = 0.2 \mu\text{m}$, the read-write head is at $r = 3$ cm from the center of the disk, whose speed of rotation is $\dot{\omega} = 7200$ rpm. One of the plates ($y = -h$) is fixed and the other ($y = h$) moves with a constant velocity U in the z -direction.

Assume a uniform temperature $T = 300$ K, a uniform pressure $p = 90$ kPa and an accommodation coefficient $\sigma = 0.9$.

- (i) Write the velocity distribution as a function of the Knudsen number.
- (ii) Calculate the mass flow rate per unit width and compare it to the case of a no-slip Couette flow.
- (iii) Calculate the friction factor and compare its value to the one obtained with a no-slip assumption.

*Solution***(i) Velocity distribution (Answer: $u_z = \frac{U}{2} \left(\frac{y^*}{4 \text{Kn}(2-\sigma)/\sigma + 1} + 1 \right)$)**

The momentum equation reduces to $d^2 u_z / dy^2 = 0$, and the boundary conditions are $u_z|_{y=-h} = ((2 - \sigma)/\sigma)\lambda du_z/dy|_{y=-h}$ and $u_z|_{y=+h} = U - ((2 - \sigma)/\sigma)\lambda du_z/dy|_{y=+h}$. Thus, the velocity profile is linear: $u_z = a_1 y + a_2$. The boundary conditions yields $-a_1 h + a_2 = ((2 - \sigma)/\sigma)\lambda a_1$ and $a_1 h + a_2 = U - ((2 - \sigma)/\sigma)\lambda a_1$, which leads to $2a_1 = U/(h + \lambda(2 - \sigma)/\sigma)$ and $2a_2 = U$. Then $u_z = U/2(y/(\lambda(2 - \sigma)/\sigma + h) + 1)$.

With $y^* = y/h$ and $\text{Kn} = y/D_H = y/(4h)$, the velocity distribution is written as $u_z = U/2(y^*/(4 \text{Kn}(2 - \sigma)/\sigma + 1) + 1)$. The centerline velocity is independent of the slip at the walls and the velocity transverse gradient is reduced as rarefaction is increased.

(ii) Mass flow rate (Answer: $\dot{m}' = (pM/RT)(\dot{\omega} r 2\pi/60)2h = 4.57 \times 10^{-6} \text{ kg/s/m}$)

The mass flow rate is $\dot{m} = \rho \bar{u}_z A = (p/RT) \bar{u}_z A$ with $\bar{u}_z = 1/2 \int_{-1}^1 u_z dy^* = U/2$. Therefore, the mass flow rate per unit width is:

$$\begin{aligned} \dot{m}' &= \frac{p}{RT} \frac{U}{2} 4h = \frac{pM}{RT} \frac{\dot{\omega} r 2\pi}{60} 2h \\ &= \frac{9 \times 10^4 \times 28.013 \times 10^{-3} \times 7200 \times 3 \times 10^{-2} \times 2\pi \times 2 \times 10^{-7}}{8.3145 \times 300 \times 60} = 4.57 \times 10^{-6} \text{ kg/m} \end{aligned}$$

The mass flow rate is the same as the one for a Couette flow without slip at the wall.

(iii) Friction factor (Answer: $C_f^* = C_f/C_{f,ns} = 0.57$)

From Eq. (2.95), $C_f = 2 \bar{\tau}_w / (\rho \bar{u}_z^2)$ and $\bar{\tau}_w = \tau_w = \mu du_z/dy$ is uniform since the velocity profile is linear. With $\frac{du_z}{dy} = \frac{U}{2h} \frac{1}{1 + 4 \text{Kn}(2 - \sigma)/\sigma}$, we obtain:

$$C_f = \frac{4 \mu RT}{h p U (1 + 4 \text{Kn}(2 - \sigma)/\sigma)}$$

From Table 2.2, the temperature exponent of the coefficient of viscosity for nitrogen (N_2) is $\omega = 0.74$, the exponent for the VSS model is $\alpha = 1.36$ and the dynamic viscosity under standard conditions is $\mu_0 = 1.656 \times 10^{-5} \text{ Pa s}$.

From Eq. (2.7), the viscosity at $T = 300 \text{ K}$ is:

$$\mu(T) = \mu_0(T/T_0)^\omega = 1.656 \times 10^{-5} (300/273.15)^{0.74} = 1.775 \times 10^{-5} \text{ Pa s}.$$

The molecular weight of nitrogen is given in Table 2.2: $M = 28.013 \times 10^{-3} \text{ kg/mol}$ and its gas constant is $R = R/M = 8.314511/28.013 \times 10^{-3} = 2.97 \times 10^2 \text{ J/kg/K}$.

The mean free path is given by Table 2.1: $\lambda = k_2 \mu(T) \sqrt{RT}/p$, with $k_2 = [4\alpha(7 - 2\omega)(5 - 2\omega)]/[5(\alpha + 1)(\alpha + 2)\sqrt{2\pi}] = 1.06$. Therefore, $\lambda = k_2 \mu(T) \sqrt{RT}/p = 1.06 \times 1.775 \times 10^{-5} \times \sqrt{2.97 \times 10^2 \times 300/9 \times 10^4} = 62.6 \text{ nm}$ and the Knudsen number based on the hydraulic diameter is:

$$\text{Kn} = \lambda/(4h) = 6.26 \times 10^{-8}/(4 \times 10^{-7}) = 1.56 \times 10^{-1}.$$

The influence of rarefaction on the friction is then given by:

$$\begin{aligned} C_f^* &= C_f C_{f,ns} = C_f / C_{f(Kn=0)} = \frac{1}{1 + 4Kn(2 - \sigma)/\sigma} \\ &= \frac{1}{1 + 4 \times 0.156(2 - 0.9)/0.9} = 0.57 \end{aligned}$$

The friction factor is reduced of 43%, due to slip at the walls.

2.9. Problems

Problem 2.1

A flow of helium is generated in a circular microtube by axial pressure and temperature gradients. The microtube has a length $l = 5$ mm and a uniform cross-section with a diameter $2r_2 = 10$ μm . In a section where the flow may be considered as locally fully developed, the gradients are $dp/dz = -5$ Pa/ μm and $dT/dz = 0.5$ K/ μm , for a pressure $p = 100$ kPa and a temperature $T = 400$ K.

Assume a tangential momentum accommodation coefficient $\sigma = 0.9$.

- (i) Write the velocity distribution as a function of the Knudsen number, in a dimensionless form: $u_z^*(r^*, Kn)$.
- (ii) Calculate the part of the velocity increase due to slip at the wall.
- (iii) Calculate the part of the velocity increase due to thermal creep.

Problem 2.2

A flow of air in a rectangular microchannel is generated by a pressure gradient. The inlet pressure is $p_i = 3.5$ bar and the outlet pressure is $p_o = 150$ mbar. The temperature $T = 350$ K is uniform and the tangential momentum accommodation coefficient is $\sigma = 0.8$. The microchannel length is $l = 10$ mm and its uniform section has a depth $2h = 1.2$ μm and a width $2b = 4.8$ μm .

- (i) Calculate the mass flow rate with a plane flow assumption and a no-slip model.
- (ii) Calculate the mass flow rate with a plane flow assumption and a Navier–Stokes model with first-order slip boundary conditions.
- (iii) Calculate the mass flow rate with a plane flow assumption and a Navier–Stokes model with Deissler second-order slip boundary conditions.
- (iv) Calculate the mass flow rate with a plane flow assumption and a quasi-hydrodynamic model with first-order slip boundary conditions.
- (v) Calculate the mass flow rate with a no-slip model in a rectangular section.
- (vi) Calculate the mass flow rate with a Navier–Stokes model in a rectangular section with Deissler second-order slip boundary conditions.
- (vii) Calculate the deviations of the above different models, compared to the most accurate among them.

Problem 2.3

Consider a microchannel with a uniform cross-section whose width is very large compared with its depth $2h = 5 \mu\text{m}$. A pressure-driven flow of helium is generated, the lower wall ($y = -h$) is adiabatic and the upper wall ($y = h$) has a constant heat flux $q_h = -200 \text{ W/cm}^2$. Consider a section far from the inlet, such that the flow in this section is thermally and hydrodynamically developed. The flow conditions in this section are such that the Knudsen number based on the hydraulic diameter is $\text{Kn} = 2 \times 10^{-2}$ and the accommodation coefficients are $\sigma = 0.9$ and $\sigma_T = 0.6$. The wall temperature $T_{\text{wall}} = 400 \text{ K}$ is measured with a micro-sensor.

- (i) Calculate the mean temperature \bar{T} of the gas in the section.
- (ii) Calculate the temperature T_0 at the center of the section ($y = 0$).
- (iii) Compare with the case of a similar non rarefied flow.

Problem 2.4

Consider a microchannel, with a length $l = 5 \text{ mm}$ and whose uniform rectangular cross-section has a low aspect ratio: its width is $2b = 200 \mu\text{m}$ and its depth is $2h = 1.5 \mu\text{m}$. A flow of nitrogen is generated with a pressure gradient. The inlet pressure is $p_i = 3 \times 10^5 \text{ Pa}$ and the outlet pressure is $p_o = 1 \times 10^5 \text{ Pa}$. The temperature $T = 300 \text{ K}$ is uniform and the tangential momentum accommodation coefficient is $\sigma = 0.95$.

- (i) Calculate the mean velocity in a cross-section of the microchannel, as a function of the local pressure gradient and Knudsen number.
- (ii) Calculate the mass flow rate.
- (iii) Calculate the pressure value at the middle of the microchannel (at $z = l/2$) and compare it to the no-slip value.
- (iv) Calculate the maximal velocity reached in the microchannel outside the entrance region.
- (v) Calculate the maximal Mach number and justify the locally fully developed assumption.

Problem 2.5

A multistage Knudsen compressor is designed to locally tune the pressure level of air inside a microsystem. The geometry of this Knudsen compressor is given in Fig. 2.27. Ten chambers are connected via 9 series of 100 short microchannels. These microchannels have rectangular cross-sections with a depth $2h = 0.5 \mu\text{m}$ and a width $2b = 20 \mu\text{m}$. Each chamber is assumed large enough for the flow inside to be considered as a continuum flow. The temperature in these chambers is $T_2 = 300 \text{ K}$ and each element is able to rise the temperature at the outlet of the microchannels to the value $T_1 = 600 \text{ K}$. Chamber 10 is connected to a region, whose pressure $p_{10} = 10 \text{ mbar}$ is maintained constant by means of a primary pump. The initial temperature $T_{t=0} = T_2 = 300 \text{ K}$ is uniform before the elements heating. The initial pressure in each chamber is also uniform and is equal to the pressure

in chamber 10: $p_{t=0} = p_{10} = 10$ mbar. For $t > 0$, heating of the elements can be regulated in order to tune the pressure in chamber 1 in the range 1 to 10 mbar.

- (i) Calculate the possible range covered by the Knudsen number in the microchannels during the pumping process and check that the free molecular regime assumption in the microchannel is valid.
- (ii) Calculate the maximal value of the mass flow rate between two adjacent chambers at the beginning of the pumping progress.
- (iii) Give the different reasons why the real initial mass flow rate is lower than the value calculated in (ii).
- (iv) Calculate the minimal pressure value that can be reached in chamber 1 at the end of the pumping process.

Problem 2.6

Consider a pressure-driven flow of different gases (He, O₂ or SO₂), through a microtube with rough walls, such that the accommodation coefficient can reasonably be assumed equal to unity. The microtube length is $l = 3$ mm and its inner diameter is $2r_2 = 1.2$ μm . The inlet pressure is $p_i = 2$ bar and the outlet pressure is $p_o = 1$ bar.

Assume that the intermolecular collisions are accurately described by a VSS model.

- (i) Calculate the mass flow rate through this microtube for the three different gases using a QHD1 model.
- (ii) Calculate the mass flow rate through this microtube for the different gases using a NS2 model with Deissler boundary conditions.
- (iii) Calculate the mass flow rate through this microtube for the different gases using a NS2 model with Chapman and Cooling boundary conditions.
- (iv) Calculate the mass flow rate through this microtube for the different gases using a NS2 model with Mitsuya boundary conditions.
- (v) Compare and comment on these different results.
- (vi) Propose an experimental protocol in order to check the more appropriate among the above models.

References

- Agarwal, R. K., Yun, K.-Y., and Balakrishnan, R., Beyond Navier–Stokes: Burnett equations for flows in the continuum–transition regime, *Phys. Fluids*, **13**(10), 3061–3085, 2001.
- Ameel, T. A., Wang, X., Barron, R. F., and Warrington, R. O. J., Laminar forced convection in a circular tube with constant heat flux and slip flow, *Microscale Therm. Eng.*, **1**(4), 303–320, 1997.
- Anderson, J. D., *Modern Compressible Flow*, 2 edn., New York: Mac Graw-Hill International Editions, 1990.
- Anduze, M., Etude expérimentale et numérique de microécoulements liquides dans les microsystèmes fluidiques, PhD Thesis, Toulouse: Institut National des Sciences Appliquées de Toulouse, 2000.

- Arkilic, E. B., Breuer, K. S., and Schmidt, M. A., Gaseous flow in microchannels, in *Application of Microfabrication to Fluid Mechanics*, Vol. FED-197. New York: ASME, pp. 57–66, 1994.
- Arkilic, E. B., Schmidt, M. A., and Breuer, K. S., Sub-nanomol per second flow measurement near atmospheric pressure, *Exp. Fluid*, **25**(1), 37–41, 1998.
- Arkilic, E. B., Breuer, K. S., and Schmidt, M. A., Mass flow and tangential momentum accommodation in silicon micromachined channels, *J. Fluid Mech.*, **437**, 29–43, 2001.
- Aubert, C., Ecoulements compressibles de gaz dans les microcanaux: effets de raréfaction, effets instationnaires, PhD Thesis, Toulouse: Université Paul Sabatier, 1999.
- Aubert, C. and Colin, S., High-order boundary conditions for gaseous flows in rectangular microchannels, *Microscale Therm. Eng.*, **5**(1), 41–54, 2001.
- Aubert, C., Colin, S., and Caen, R., Unsteady gaseous flows in tapered microchannels, in *First International Conference on Modeling and Simulation of Microsystems, Semiconductors, Sensors and Actuators (MSM'98)*, Vol. 1. Santa Clara Marriot: Computational Publications, pp. 486–491, 1998.
- Barber, R. W. and Emerson, D. R., The influence of Knudsen number on the hydrodynamic development length within parallel plate micro-channels, in *Advances in Fluid Mechanics IV*, M. Rahman, R. Verhoeven, and C. A. Brebbia, Eds., Southampton: WIT Press, pp. 207–216, 2002.
- Beskok, A. and Karniadakis, G. E., A model for flows in channels, pipes, and ducts at micro and nano scales, *Microscale Therm. Eng.*, **3**(1), 43–77, 1999.
- Bhatnagar, P., Gross, E., and Krook, K., A model for collision processes in gasses, *Phys. Rev.*, **94**, 511–524, 1954.
- Bird, G., Monte Carlo simulation of gas flows, *Annu. Rev. Fluid Mech.*, **10**, 11–31, 1978.
- Bird, G. A., *Molecular Gas Dynamics and the Direct Simulation of Gas Flows*. Oxford: Clarendon Press, 1998.
- Caen, R., Mas, I., and Colin, S., Ecoulements non permanents dans les microcanaux: réponse fréquentielle des microtubes pneumatiques, *C. R. Acad. Sci., Sér. II b*, **323**(12), 805–812, 1996.
- Cercignani, C., Illner, R., and Pulvirenti, M., *The Mathematical Theory of Dilute Gases*, Vol. 106. New York: Springer-Verlag, 1994.
- Chapman, S. and Cowling, T. G., *The Mathematical Theory of Non-uniform Gases*. Cambridge: University Press, 1952.
- Chen, C. S., Lee, S. M., and Sheu, J. D., Numerical analysis of gas flow in microchannels, *Numer. Heat Transf., A*, **33**, 749–762, 1998.
- Chen, R.-Y., Flow in the entrance region at low Reynolds numbers, *J. Fluid. Eng.*, **95**, 153–158, 1973.
- Chen, S. and Doolen, G., Lattice Boltzmann method for fluid flows, *Annu. Rev. Fluid Mech.*, **30**, 329–364, 1998.
- Cheng, H. and Emmanuel, G., Perspectives on hypersonic nonequilibrium flow, *AIAA Journal*, **33**, 385–400 1995.
- Colin, S., *Microfluidique*. Paris: Lavoisier – Hermès Science Publications, 2004.
- Colin, S., Aubert, C., and Caen, R., Unsteady gaseous flows in rectangular microchannels: frequency response of one or two pneumatic lines connected in series, *Eur. J. Mech. B, Fluid*, **17**(1), 79–104, 1998a.
- Colin, S., Anduze, M., and Caen, R., A pneumatic frequency generator for experimental analysis of unsteady microflows, in *Micro-Electro-Mechanical Systems (MEMS) – 1998*, Vol. DSC-66, F. K. F. Liwei Lin, Narayan. R. Aluru, Xiang Zhang, Eds., New York: ASME, pp. 231–239, 1998b.
- Colin, S., Elizarova, T. G., Sheretov, Y. V., Lengrand, J.-C., and Camon, H., Micro-écoulements gazeux: validation expérimentale de modèles QHD et de Navier–Stokes avec conditions aux

- limites de glissement, in *16ème Congrès Français de Mécanique, Proceedings on CDROM*, Nice, 2003.
- Colin, S., Lalonde, P., and Caen, R., Validation of a second-order slip flow model in rectangular microchannels, *Heat Transfer Eng.*, **25**(3), 23–30, 2004.
- Comeaux, K. A., Chapman, D. R., and MacCormack, R. W., An analysis of the Burnett equations based in the second law of thermodynamics, *AIAA Paper*, no. 95-0415, 1995.
- Deissler, R. G., An analysis of second-order slip flow and temperature-jump boundary conditions for rarefied gases, *Int. J. Heat Mass Transfer*, **7**, 681–694, 1964.
- Ebert, W. A. and Sparrow, E. M., Slip flow in rectangular and annular ducts, *J. Basic Eng.*, **87**, 1018–1024, 1965.
- Elizarova, T. G. and Sheretov, Y. V., Analyse du problème de l'écoulement gazeux dans les microcanaux par les équations quasi hydrodynamiques, *La Houille Blanche*, **5**, 66–72, 2003.
- Gad-el-Hak, M., Stokes' hypothesis for a newtonian, isotropic fluid, *J. Fluids Eng.*, **117**, 3–5, 1995.
- Gad-el-Hak, M., The fluid mechanics of microdevices – The Freeman Scholar Lecture, *J. Fluids Eng.*, Vol. 121, pp. 5–33, 1999.
- Grad, H., On the kinetic theory of rarefied gases, *Comm. Pure Appl. Math.*, **2**, 331–407, 1949.
- Guo, Z. Y. and Wu, X. B., Further study on compressibility effects on the gas flow and heat transfer in a microtube, *Microscale Therm. Eng.*, **2**(2), 111–120, 1998.
- Hadjiconstantinou, N. G. and Simek, O., Constant-wall-temperature Nusselt number in micro and nano-channels, *J. Heat Transf.*, **124**, 356–364, 2002.
- Harley, J. C., Huang, Y., Bau, H. H., and Zemel, J. N., Gas flow in micro-channels, *J. Fluid Mech.*, **284**, 257–274, 1995.
- Hassan, H. A. and Hash, D. B., A generalized hard-sphere model for Monte Carlo simulation, *Phys. Fluids A*, **5**(3), 738–744, 1993.
- Hobson, J. P., Accommodation pumping – A new principle for low pressure, *J. Vac. Sci. Technol.*, **7**(2), 301–357, 1970.
- Hobson, J. P., Analysis of accommodation pumps, *J. Vac. Sci. Technol.*, **8**(1), 290–293, 1971.
- Hobson, J. P., Physical factors influencing accommodation pumps, *J. Vac. Sci. Technol.*, **9**(1), 252–256, 1972.
- Hsia, Y.-T. and Domoto, G. A., An experimental investigation of molecular rarefaction effects in gas lubricated bearings at ultra-low clearances, *J. Lubr. Technol.*, **105**, 120–130, 1983.
- Hudson, M. L. and Bartel, T. J., DSMC simulation of thermal transpiration and accommodation pumps, in *Rarefied Gas Dynamics*, Vol. 1, R. Brun, R. Campargue, R. Gatignol, and J.-C. Lengrand, Eds., Cépaduès Editions, Toulouse, France pp. 719–726, 1999.
- Jang, J. and Wereley, S. T., Pressure distributions of gaseous slip flow in straight and uniform rectangular microchannels, *Microfluidic. Nanofluidic.*, **1**(1), 41–51, 2004.
- Jie, D., Diao, X., Cheong, K. B., and Yong, L. K., Navier–Stokes simulations of gas flow in micro devices, *J. Micromech. Microeng.*, **10**(3), 372–379, 2000.
- Karniadakis, G. E. and Beskok, A., *Microflows: Fundamentals and Simulation*. New York: Springer-Verlag, 2002.
- Kavehpour, H. P., Faghri, M., and Asako, Y., Effects of compressibility and rarefaction on gaseous flows in microchannels, *Numer. Heat Transf., A*, **32**, 677–696, 1997.
- Kennard, E. H., *Kinetic Theory of Gases*, 1st ed., New York: McGraw-Hill Book Company, 1938.
- Koura, K. and Matsumoto, H., Variable soft sphere molecular model for inverse-power-law or Lennard–Jones potential, *Phys. Fluid. A*, **3**(10), 2459–2465, 1991.
- Koura, K. and Matsumoto, H., Variable soft sphere molecular model for air species, *Phys. Fluid. A*, **4**(5), 1083–1085, 1992.
- Lalonde, P., Etude expérimentale d'écoulements gazeux dans les microsystèmes à fluides, PhD Thesis, Toulouse: Institut National des Sciences Appliquées de Toulouse, 2001.

- Larrodé, F. E., Housiadas, C., and Drossinos, Y., Slip-flow heat transfer in circular tubes, *Int. J. Heat Mass Transfer*, **43**(15), 2669–2680, 2000.
- Lee, W. Y., Wong, M., and Zohar, Y., Microchannels in series connected via a contraction/expansion section, *J. Fluid Mech.*, **459**, 187–206, 2002.
- Lee, C., Hong, G., Ha, Q. P., and Mallinson, S. G., A piezoelectrically actuated micro synthetic jet for active flow control, *Sens. Actuators, A Phys.*, **108**(1–3), 168–174, 2003.
- Lengrand, J.-C. and Elizarova, T. G., Chapter 2: Microécoulements gazeux, in *Microfluidique*, S. Colin, ed., Hermès Science Publications, Paris, France 2004.
- Lengrand, J.-C., Elizarova, T. G., and Shirokov, I. A., Calcul de l'écoulement visqueux compressible d'un gaz dans un microcanal, in *Actes sur CDROM du 2ème Congrès Français de Microfluidique (μ Flu'04)*. Toulouse: SHF, 2004.
- Lim, C. Y., Shu, C., Niu, X. D., and Chew, Y. T., Application of lattice Boltzmann method to simulate microchannel flows, *Phys. Fluid.*, **14**(7), 2299–2308, 2002.
- Liu, J., Tai, Y.-C., and Ho, C.-M., MEMS for pressure distribution studies of gaseous flows in microchannels, in *8th Annual International Workshop on Micro-Electro-Mechanical Systems (MEMS'95), An Investigation of Micro Structures, Sensors, Actuators, Machines, and Systems*. Amsterdam: IEEE, pp. 209–215, 1995.
- Loyalka, S. K. and Hamoodi, S. A., Poiseuille flow of a rarefied gas in a cylindrical tube: solution of linearized Boltzmann equation, *Phys. Fluid. A*, **2**(11), 2061–2065, 1990.
- Mallinson, S. G., Kwok, C. Y., and Reizes, J. A., Numerical simulation of micro-fabricated zero mass-flux jet actuators, *Sens. Actuators, A Phys.*, **105**(3), 229–236, 2003.
- Matsumoto, H., Variable sphere molecular model for inverse power law and Lennard–Jones potentials in Monte Carlo simulations, *Phys. Fluid.*, **14**(12), 4256–4265, 2002.
- Maurer, J., Tabeling, P., Joseph, P., and Willaime, H., Second-order slip laws in microchannels for helium and nitrogen, *Phys. Fluid.*, **15**(9), 2613–2621, 2003.
- Mavriplis, C., Ahn, J. C., and Goulard, R., Heat transfer and flowfields in short microchannels using direct simulation Monte Carlo, *J. Thermophys. Heat Transf.*, **11**(4), 489–496, 1997.
- Maxwell, J. C., On stresses in rarefied gases arising from inequalities of temperature, *Philos. Trans. Royal Soc.*, **170**, 231–256, 1879.
- Mitsuya, Y., Modified Reynolds equation for ultra-thin film gas lubrication using 1,5-order slip-flow model and considering surface accommodation coefficient, *J. Tribol.*, **115**, 289–294, 1993.
- Morini, G. L. and Spiga, M., Slip flow in rectangular microtubes, *Microscale Therm. Eng.*, **2**(4), 273–282, 1998.
- Muntz, E. P., Rarefied gas dynamics, *Annu. Rev. Fluid Mech.*, **21**, 387–417, 1989.
- Muntz, E. P. and Vargo, S. E., Microscale vacuum pumps, in *The MEMS Handbook*, M. Gad-el-Hak, ed., New York: CRC Press, pp. 29.1–29.28, 2002.
- Nguyen, N.-T. and Wereley, S. T., *Fundamentals and Applications of Microfluidics*, Boston: Artech House, 2002.
- Nie, X., Doolen, G. D., and Chen, S., Lattice Boltzmann simulations of fluid flows in MEMS, *J. Stat. Phys.*, **107**(1–2), 279–289, 2002.
- Oran, E. S., Oh, C. K., and Cybyk, B. Z., Direct Simulation Monte Carlo: recent advances and applications, *Annu. Rev. Fluid Mech.*, **30**, 403–441, 1998.
- Pan, L. S., Liu, G. R., and Lam, K. Y., Determination of slip coefficient for rarefied gas flows using direct simulation Monte Carlo, *J. Micromech. Microeng.*, **9**(1), 89–96, 1999.
- Pan, L. S., Liu, G. R., Khoo, B. C., and Song, B., A modified direct simulation Monte Carlo method for low-speed microflows, *J. Micromech. Microeng.*, **10**(1), 21–27, 2000.
- Pan, L. S., Ng, T. Y., Xu, D., and Lam, K. Y., Molecular block model direct simulation Monte Carlo method for low velocity microgas flows, *J. Micromech. Microeng.*, **11**(3), 181–188, 2001.

- Piekos, E. S. and Breuer, K. S., Numerical modeling of micromechanical devices using the direct simulation Monte Carlo method, *J. Fluid. Eng.*, **118**, 464–469, 1996.
- Pong, K.-C., Ho, C.-M., Liu, J., and Tai, Y.-C., Non-linear pressure distribution in uniform microchannels, in *Application of Microfabrication to fluid Mechanics*, Vol. FED-197, ASME Winter Annual Meeting, Chicago, P. R. Bandyopadhyay, K. S. Breuer, and C. J. Blechinger, eds. New York: ASME, pp. 51–56, 1994.
- Rohsenow, W. M., Hartnett, J. P., and Cho, Y. I., *Handbook of Heat Transfer*, 3rd edn., McGraw-Hill, 1998.
- Schaaf, S. A., Mechanics of rarefied gases, in *Encyclopedia of Physics*, Vol. Fluid Dynamics II, VII/2, Berlin, pp. 591–624, 1963.
- Shah, R. K., Laminar flow friction and forced convection heat transfer in ducts of arbitrary geometry, *Int. J. Heat Mass Transfer*, **18**, 849–862, 1975.
- Sharipov, F. and Seleznev, V., Data on internal rarefied gas flows, *J. Phys. Chem. Ref. Data*, **27**(3), 657–706, 1998.
- Shih, J. C., Ho, C.-M., Liu, J., and Tai, Y.-C., Monatomic and polyatomic gas flow through uniform microchannels, Vol. DSC-59. New York: ASME, pp. 197–203, 1996.
- Sinton, D., Microscale flow visualization, *Microfluidic. Nanofluidic.*, **1**(1), 2–21, 2004.
- Smoluchowski, M., Ueber wärmeleitung in verdünnten gasen, *Annalen der Physik und Chemie*, **64**, 101–130, 1898.
- Sreekanth, A. K., Slip flow through long circular tubes, in *6th International Symposium on Rarefied Gas Dynamics*, L. Trilling and H. Y. Wachman, eds., New York: Academic Press, pp. 667–680, 1969.
- Stefanov, S. and Cercignani, C., Monte Carlo simulation of a channel flow of a rarefied gas, *Eur. J. Mech., B/Fluids*, **13**(1), 93–114, 1994.
- Vargo, S. E. and Muntz, E. P., An evaluation of a multiple-stage micromechanical Knudsen compressor and vacuum pump, in *Proceedings of the 20th International Symposium on Rarefied Gas Dynamics*, C. Shen, ed. Beijing: Peking University Press, pp. 995–1000, 1997.
- Vargo, S. E. and Muntz, E. P., Comparison of experiment and prediction for transitional flow in a single-stage micromechanical Knudsen compressor, in *Rarefied Gas Dynamics*, Vol. 1, R. Brun, R. Campargue, R. Gatignol, and J.-C. Lengrand, eds., Cépaduès Editions, Toulouse, France pp. 711–718, 1999.
- Vargo, S. E., Muntz, E. P., Shiflett, G. R., and Tang, W. C., Knudsen compressor as a micro- and macroscale vacuum pump without moving parts or fluids, *J. Vac. Sci. Technol. A*, **17**(4), 2308–2313, 1999.
- Wang, M. and Li, Z., Simulations for gas flows in microgeometries using the direct simulation Monte Carlo method, *Int. J. Heat Fluid Flow*, **25**(6), 975–985, 2004.
- Webb, A. R. and Maynes, D., Velocity profile measurements in microtubes, in *30th AIAA Fluid Dynamics Conference*. Norfolk, VA, USA: AIAA, no. 99-3803/1-10, 1999.
- Welder, W. T., Chapman, D. R., and McCormack, R. W., Evaluation of various forms of the Burnett equations, *AIAA Paper*, no. 93-3094, 1993.
- Wereley, S. T., Meinhart, C. D., Santiago, J. G., and Adrian, R. J., Velocimetry for MEMS applications, in *ASME Annual Meeting*, Vol. DSC 66. Anaheim, pp. 453–459, 1998.
- Wereley, S. T., Gui, L., and Meinhart, C. D., Advanced algorithms for microscale particle image velocimetry, *AIAA J*, **40**(6), 1047–1055, 2002.
- Wu, J.-S. and Tseng, K.-C., Analysis of micro-scale gas flows with pressure boundaries using direct simulation Monte Carlo method, *Comput. Fluid.*, **30**(6), 711–735, 2001.
- Xue, H. and Fan, Q., A new analytic solution of the Navier–Stokes equations for microchannel flow, *Microscale Therm. Eng.*, **4**(2), 125–143, 2000.

- Young, R. M., Analysis of a micromachine based vacuum pump on a chip actuated by the thermal transpiration effect, *J. Vac. Sci. Technol. B*, **17(2)**, 280–287, 1999.
- Yu, S. and Ameel, T. A., Slip-flow heat transfer in rectangular microchannels, *Int. J. Heat Mass Transfer*, **44(22)**, 4225–4234, 2001.
- Yun, K. Y., Agarwal, R. K., and Balakrishnan, R., Augmented Burnett and Bhatnagar–Gross–Krook–Burnett equations for hypersonic flow, *J. Therm. Heat Transf.*, **12(3)**, 328–335, 1998.
- Zhu, X., Xin, M. D., and Liao, Q., An analysis for heat transfer between two unsymmetrically heated parallel plates with micro spacing in slip flow regime, in *Proceedings of the International Conference on Heat Transfer and Transport Phenomena in Microscale*, G. P. Celata, ed. Banff, Canada, pp. 114–120, 2000.
- Zohar, Y., Lee, S. Y. K., Lee, Y. L., Jiang, L., and Tong, P., Subsonic gas flow in a straight and uniform microchannel, *J. Fluid Mech.*, **472**, 125–151, 2002.

Chapter 3

SINGLE-PHASE LIQUID FLOW IN MINICHANNELS AND MICROCHANNELS

Satish G. Kandlikar

Mechanical Engineering Department, Rochester Institute of Technology, Rochester, NY, USA

3.1. Introduction

3.1.1. Fundamental issues in liquid flow at microscale

Microchannels are used in a variety of devices incorporating single-phase liquid flow. The early applications involved micromachined devices such as micropumps, microvalves, and microsensors. This was followed by a thrust in the biological and life sciences with a need for analyzing biological materials, such as proteins, DNA, cells, embryos, and chemical reagents. The field of micromixers further received attention with developments in microreactors, where two chemical species are mixed prior to introducing them into a reaction chamber. The high flux heat dissipation from high-speed microprocessors provided the impetus for studies on heat transfer in microchannels.

The developments in the microelectromechanical devices naturally require heat removal systems that are equally small. Cooling of mirrors employed in high-power laser systems involves cooling systems that cover very small footprints. Advances in biomedical and genetic engineering require controlled fluid transport and its precise thermal control in passages of several micrometer dimensions. A proper understanding of fluid flow and heat transfer in these microscale systems is therefore essential for their design and operation.

In dealing with liquid flows in minichannels and microchannels in the absence of any wall surface effects, such as the electrokinetic or electroosmotic forces that are covered in Chapter 4, the flow is not expected to experience any fundamental changes from the continuum approximation employed in macrofluidic applications. Gad-el-Hak (1999) argued that liquids such as water should be treated as continuous media with the results obtained

E-mail: sgkeme@rit.edu

from classical theory being applicable in channels larger than $1\text{ }\mu\text{m}$. However, there remain a number of unresolved issues that require further study. The main areas of current research are summarized below:

- (a) Experimental validation of the laminar and turbulent flow transport equations – the laminar flow friction factor and heat transfer equations derived from theoretical considerations are expected to hold in microchannel applications in the absence of any changes in the transport processes or any new physical phenomenon. Although explicit equations and experiments for mass transfer are not covered, the conclusions reached for the momentum and heat transfer are expected to be applicable to mass transport processes as well.
- (b) Verification of the laminar-to-turbulent flow transition at microscale – experimental evidence in this regard needs to be critically evaluated.
- (c) The effect of large relative roughness values on the flow – large values of relative roughness are more commonly encountered in microchannels. Their effect on the laminar-to-turbulent transition, friction factors, and heat transfer needs to be investigated.
- (d) Verification of empirical constants derived from macroscale experiments – a number of constants (such as for the losses due to flow area changes, bends, etc.), whose values are derived from macroscale fluid flow experiments need to be verified for microscale applications.

This chapter will be devoted to answering the above questions on the basis of the evidence available in literature.

3.1.2. Need for smaller flow passages

The flow passage dimensions in convective heat transfer applications have been shifting towards smaller dimensions for the following three main reasons:

- (a) Heat transfer enhancement.
- (b) Increased heat flux dissipation in microelectronic devices.
- (c) Emergence of microscale devices that require cooling.

Employing smaller channel dimensions results in higher heat transfer performance, although it is accompanied by a higher pressure drop per unit length. The higher volumetric heat transfer densities require advanced manufacturing techniques and lead to more complex manifold designs. An optimum balance for each application leads to different channel dimensions. For example, in the refrigeration industry, the use of microfin tubes of 6–8 mm diameter have replaced the plain tubes of larger diameters. In automotive applications, the passage dimensions for radiators and evaporators have approached a 1 mm threshold as a balance between the pumping power, heat transfer, and cleanliness constraints imposed by the overall system.

Microelectronic devices, which include a variety of applications such as PCs, servers, laser diodes, and RF devices, are constantly pushing the heat flux density requirements to higher levels. What seemed to be an impossibly high limit of 200 W/cm^2 of heat dissipation in 1993 now seems to be a feasible target. The new challenge for the coming decade is on the

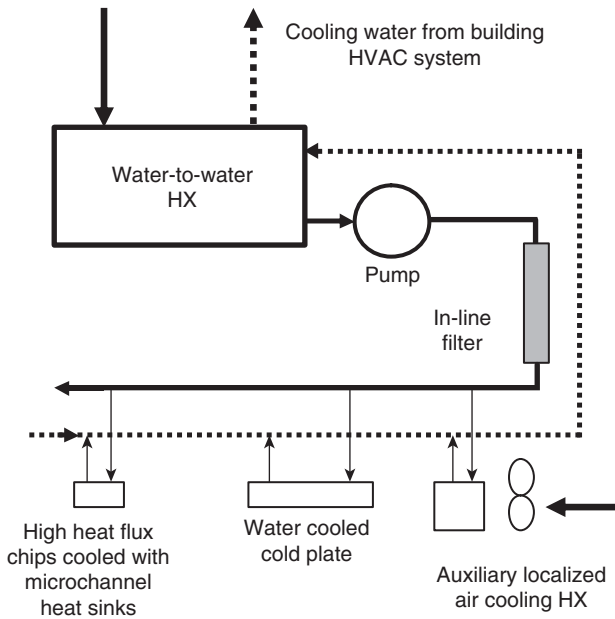


Fig. 3.1. Schematic of a cluster of servers with high heat flux chips cooled with microchannel heat sinks, cold plates, and localized air cooling integrated with a secondary chilled water loop from the building HVAC system, Kandlikar (2005).

order of $600\text{--}1000\text{ W/cm}^2$. The available temperature differences are becoming smaller, in some cases as low as only a few $^{\circ}\text{C}$ with external copper heat sinks. These high levels of heat dissipation require a dramatic reduction in the channel dimensions, matched with suitable coolant loop systems to facilitate the fluid movement away from the heat source.

A cooling system for a microscale device might require cooling channels of a few tens of micrometers as compared to more conventional sized channels with $1\text{--}3\text{ mm}$ flow passage dimensions. In addition, several such units may be clustered together and a secondary cooling loop may be employed to remove the heat with a conventional cooling system. Figure 3.1 shows a schematic of a microchannel cooling system configuration for cooling a server application. The combination of the microchannel heat exchangers, mounted directly on the chip or in the heat sink that is bonded to the chip, water cooled cold plates with minichannel or microchannel flow passages, and auxiliary localized cooling systems will be able to address the complex cooling needs of the high end servers. The cooling system is integrated with the building HVAC system as described by Kandlikar (2005).

A schematic of direct liquid cooling of a multichip module or a heat sink is shown in Fig. 3.2. The liquid flows through the cold plates that are attached to a substrate cap. In advanced designs, direct cooling of chips is accomplished by circulating water, a water-antifreeze mixture, oil, or a dielectric fluid, such as FC-72, FC-77 or FC-87 through microchannels that are fabricated on the chip surface. Copper heat sinks with integrated microchannels and minichannels are expected to dominate heat sink applications.

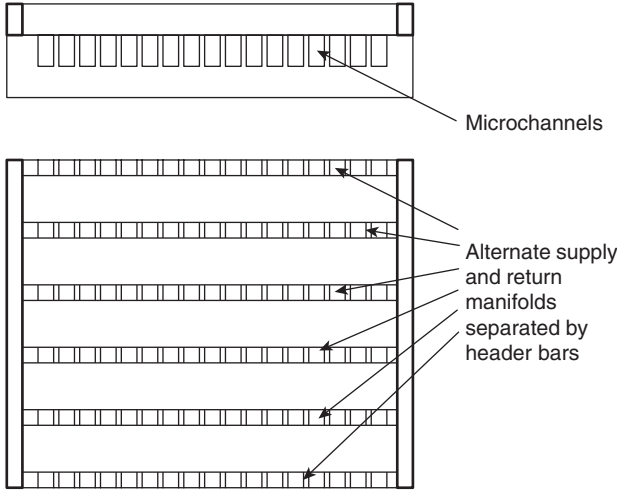


Fig. 3.2. Schematic of a microchannel cooling arrangement on a chip or a heat sink with alternate supply and return manifolds created by header bars, design originally proposed by Tuckerman (1984).

3.2. Pressure drop in single-phase liquid flow

3.2.1. Basic pressure drop relations

One-dimensional flow of an incompressible fluid in a smooth circular pipe forms the basis for the pressure drop analysis in internal flows. The following equations are readily derived based on the continuum assumption for Newtonian liquid flows in minichannels and microchannels.

Considering the equilibrium of a fluid element of length dx in a pipe of diameter D , the force due to pressure difference dp is balanced by the frictional force due to shear stress τ_w at the wall.

$$\left(\frac{\pi}{4}D^2\right)dp = (\pi D dx)\tau_w \quad (3.1)$$

The pressure gradient and the wall shear stress are thus related by the following equation:

$$\frac{dp}{dx} = \frac{4\tau_w}{D} \quad (3.2)$$

For Newtonian fluids, the wall shear stress τ_w is expressed in terms of the velocity gradient at the wall:

$$\tau_w = \mu \left. \frac{du}{dy} \right|_w \quad (3.3)$$

where μ is the dynamic viscosity. The Fanning friction factor f is used in heat transfer literature because of its ability to represent the momentum transfer process of fluid flow

in a manner consistent with the heat and mass transfer process representations:

$$f = \frac{\tau_w}{(1/2)\rho u_m^2} \quad (3.4)$$

where u_m is the mean flow velocity in the channel.

The frictional pressure drop Δp over a length L is obtained from Eqs. (3.2) and (3.4) respectively:

$$\Delta p = \frac{2f\rho u_m^2 L}{D} \quad (3.5)$$

The Fanning friction factor f in Eq. (3.5) depends on the flow conditions, the channel wall geometry and surface conditions:

- (a) laminar or turbulent flow,
- (b) flow-channel geometry,
- (c) fully developed or developing flow,
- (d) smooth or rough walls.

For non-circular flow channels, the D in Eq. (3.5) is replaced by the hydraulic diameter D_h represented by the following equation.

$$D_h = \frac{4A_c}{P_w} \quad (3.6)$$

where A_c is the flow-channel cross-sectional area and P_w is the wetted perimeter. For a rectangular channel of sides a and b , D_h is given by

$$D_h = \frac{4ab}{2(a+b)} = \frac{2ab}{(a+b)} \quad (3.7)$$

3.2.2. Fully developed laminar flow

The velocity gradient at the channel wall can be readily calculated from the well-known *Hagen–Poiseuille* parabolic velocity profile for the fully developed laminar flow in a circular pipe. Using this velocity profile, τ_w and f are obtained from Eqs. (3.3) and (3.4). The result for friction factor f is presented in the following form:

$$f = \frac{Po}{Re} \quad (3.8)$$

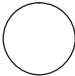
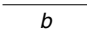
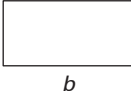


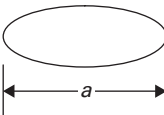
where Po is the Poiseuille number, ($Po = fRe$), which depends on the flow-channel geometry. Table 3.1 gives the fRe product and the constant Nusselt number in the fully developed laminar flow region for different duct shapes as derived from Kakac *et al.* (1987).

It can be seen that for a circular pipe,

$$Po = fRe = 16 \quad (3.9)$$

Shah and London (1978) provide the following equation for a rectangular channel with short side a and long side b , and a channel aspect ratio defined as $\alpha_c = a/b$.

Table 3.1
Fanning friction factor and Nusselt number for fully developed laminar flow in ducts, derived from Kakac *et al.* (1987).

Duct shape		Nu _H	Nu _T	Po = <i>f</i> Re	
	Circular	4.36	3.66	16	
	Flat channel	8.24	7.54	24	
	Rectangular, aspect ratio, <i>b/a</i> =	1	3.61	2.98	14.23
		2	4.13	3.39	15.55
		3	4.79	3.96	17.09
		4	5.33	4.44	18.23
		6	6.05	5.14	19.70
		8	6.49	5.60	20.58
	∞	8.24	7.54	24.00	
	Hexagon	4.00	3.34	15.05	
	Isosceles Triangle, Apex angle <i>θ</i> =	10°	2.45	1.61	12.47
		30°	2.91	2.26	13.07
		60°	3.11	2.47	13.33
		90°	2.98	2.34	13.15
		120°	2.68	2.00	12.74
	Ellipse, Major/Minor axis <i>a/b</i> =	1	4.36	3.66	16.00
		2	4.56	3.74	16.82
		4	4.88	3.79	18.24
		8	5.09	3.72	19.15
		16	5.18	3.65	19.54

Nu = hD_h/k ; Re = $\rho u_m D_h/\mu$; Nu_H – Nu under a constant heat flux boundary condition, constant axial heat flux, and uniform circumferential temperature; Nu_T – Nu under a constant wall temperature boundary condition; *f* – friction factor.

Po = f Re = 24(1 – 1.3553 α_c + 1.9467 α_c^2 – 1.7012 α_c^3
+ 0.9564 α_c^4 – 0.2537 α_c^5)

(3.10)

3.2.3. Developing laminar flow

As flow enters a duct, the velocity profile begins to develop along its length, ultimately reaching the fully developed Hagen–Poiseuille velocity profile. Almost all the analyses available in literature consider a uniform velocity condition at the inlet. The

length of the hydrodynamic developing region L_h is given by the following well-accepted equation:

$$\frac{L_h}{D_h} = 0.05 \text{ Re} \quad (3.11)$$

Since the pressure gradients found in small diameter channels are quite high, the flow lengths are generally kept low. In many applications, the length of channel in the developing region therefore forms a major portion of the flow length through a microchannel. To account for the developing region, the pressure drop equations are presented in terms of an apparent friction factor.

Apparent friction factor f_{app} accounts for the pressure drop due to friction and the developing region effects. It represents an average value of the friction factor over the flow length between the entrance section and the location under consideration. Thus the pressure drop in a channel of hydraulic diameter D_h over a length x from the entrance is expressed as:

$$\Delta p = \frac{2f_{\text{app}}\rho u_m^2 x}{D_h} \quad (3.12)$$

The difference between the apparent friction factor over a length x and the fully developed friction factor f is expressed in terms of an incremental pressure defect $K(x)$:

$$K(x) = (f_{\text{app}} - f) \frac{4x}{D_h} \quad (3.13)$$

For $x > L_h$ the incremental pressure defect attains a constant value $K(\infty)$, known as *Hagenbach's factor*.

Combining Eqs. (3.12) and (3.13), the pressure drop can be expressed in terms of the incremental pressure drop:

$$\Delta p = \frac{2(f_{\text{app}}\text{Re})\mu u_m x}{D_h^2} = \frac{2(f\text{Re})\mu u_m x}{D_h^2} + K(x) \frac{\rho u_m^2}{2} \quad (3.14)$$

For a circular tube, Hornbeck (1964) obtained the axial velocity distribution and pressure drop in a non-dimensional form. He estimated the fully developed region to begin at $x^+ = 0.0565$, with a value of $K(\infty) = 1.28$ for a circular duct. Chen (1972) proposed the following equation for $K(\infty)$ for the circular geometry:

$$K(\infty) = 1.20 + \frac{38}{\text{Re}} \quad (3.15)$$

The non-dimensionalized length x^+ given by:

$$x^+ = \frac{x/D_h}{\text{Re}} \quad (3.16)$$

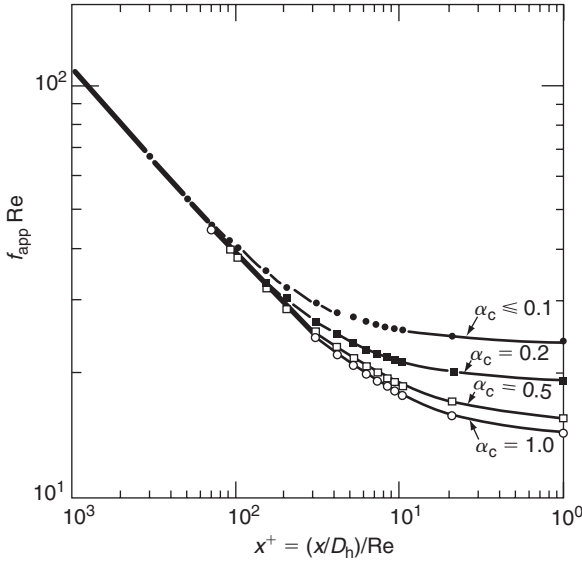


Fig. 3.3. Apparent friction factors for rectangular ducts in the developing region for different aspect ratios ($\alpha = 1/\alpha_c$), Phillips (1987).

Shah and London (1978) showed that the frictional pressure drop in the developing region of a circular duct obtained by Hornbeck (1964) can be accurately described by the following equation:

$$\frac{\Delta p}{(1/2)\rho u_m^2} = 13.74(x^+)^{1/2} + \frac{1.25 + 64x^+ - 13.74(x^+)^{1/2}}{1 + 0.00021(x^+)^{-2}} \quad (3.17)$$

Rectangular geometries are of particular interest in microfluidics applications. Shah and London (1978) and Kakac *et al.* (1987) present comprehensive summaries of the available literature. Phillips (1987) reviewed the available information, including that by Curr *et al.* (1972) and compiled the results for the apparent friction factor in a rectangular duct as shown in Fig. 3.3. It can be seen that fully developed flow is attained at different x^+ values, with low aspect ratio ducts reaching it earlier. The constant in Eq. (3.11) is around 1 ($x^+ = 10^0$) for rectangular ducts as seen from Fig. 3.3. Table 3.2 derived from Phillips (1987) gives the values of the apparent friction factor in a tabular form.

For other channel aspect ratios, a linear interpolation is suggested. Alternatively, use the curve-fit equations provided in Appendix A.

The results for the fully developed friction factors and Hagenbach's factors in trapezoidal channels are reported by Kakac *et al.* (1987). By considering the rectangular channels as a subset of the trapezoidal geometry, Steinke and Kandlikar (2005a) obtained the following curve-fit equation for the Hagenbach's factor for rectangular channels:

$$K(\infty) = 0.6796 + 1.2197\alpha_c + 3.3089\alpha_c^2 - 9.5921\alpha_c^3 + 8.9089\alpha_c^4 - 2.9959\alpha_c^5 \quad (3.18)$$

Table 3.2

Laminar flow friction factor in the entrance region of rectangular ducts.

$x^+ = (x/D_h)/\text{Re}$	$f_{\text{app}}\text{Re}$			
	$\alpha_c = 1.0$	$\alpha_c = 0.5$	$\alpha_c = 0.2$	$\alpha_c \leq 0.1$ $\alpha_c \geq 10$
0	142.0	142.0	142.0	287.0
0.001	111.0	111.0	111.0	112.0
0.003	66.0	66.0	66.1	67.5
0.005	51.8	51.8	52.5	53.0
0.007	44.6	44.6	45.3	46.2
0.009	39.9	40.0	40.6	42.1
0.01	38.0	38.2	38.9	40.4
0.015	32.1	32.5	33.3	35.6
0.02	28.6	29.1	30.2	32.4
0.03	24.6	25.3	26.7	29.7
0.04	22.4	23.2	24.9	28.2
0.05	21.0	21.8	23.7	27.4
0.06	20.0	20.8	22.9	26.8
0.07	19.3	20.1	22.4	26.4
0.08	18.7	19.6	22.0	26.1
0.09	18.2	19.1	21.7	25.8
0.10	17.8	18.8	21.4	25.6
0.20	15.8	17.0	20.1	24.7
> 1.0	14.2	15.5	19.1	24.0

For intermediate values use the curve-fit equations provided in Appendix A at the end of the chapter.

The analysis presented in this section assumes a uniform velocity profile at the entrance of the channel. In many microfluidic applications, the channels have the manifold surfaces flush with the two opposing channel surfaces. The effect of such an arrangement was investigated numerically by Gamrat *et al.* (2004). They showed that the resulting apparent friction factors in the entrance region could be up to 50% lower than the theoretical predictions.

3.2.4. Fully developed and developing turbulent flow

A number of correlations with comparable accuracies are available in literature for fully developed turbulent flow in smooth channels. The following equation by Blasius is used extensively:

$$f = 0.0791 \text{Re}^{-0.25} \quad (3.19)$$

A more accurate equation was presented by Phillips (1987) to cover both the developing and fully developed flow regions. He presented the fanning friction factor for a circular tube in terms of the following equation:

$$f_{\text{app}} = A\text{Re}^B \quad (3.20)$$

where

$$A = 0.09290 + \frac{1.01612}{x/D_h} \quad (3.21)$$

$$B = -0.26800 - \frac{0.32930}{x/D_h} \quad (3.22)$$

For rectangular channel geometries, Re is replaced with the laminar-equivalent Reynolds number (Jones, 1976) given by:

$$Re^* = \frac{\rho u_m D_{le}}{\mu} = \frac{\rho u_m [(2/3) + (11/24)(1/\alpha_c)(2 - 1/\alpha_c)] D_h}{\mu} \quad (3.23)$$

where D_{le} is the laminar-equivalent diameter given by the term in the square parenthesis in Eq. (3.23).

3.3. Total pressure drop in a microchannel heat exchanger

3.3.1. Friction factor

An earnest interest in microchannel flows began with the pioneering work on direct chip cooling with water by Tuckerman and Pease (1981). Recently, a number of investigators

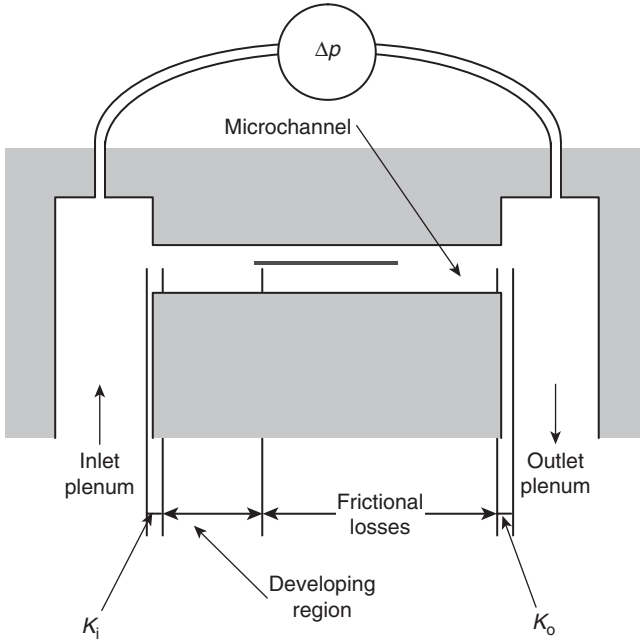


Fig. 3.4. Schematic representation of the experiments employed by researchers for pressure drop measurements in microchannels, Steinke and Kandlikar (2005a).

including Li *et al.* (2000), Celata *et al.* (2002) and Steinke and Kandlikar (2005a) critically evaluated the available literature and presented explanations for the large deviations from the classical theory reported by some of the researchers.

A schematic representation of the pressure drop experiments conducted by the researchers is shown in Fig. 3.4. Since measuring the local pressure along the flow is difficult in microchannels, researchers have generally measured the pressure drop across the inlet and outlet manifolds. The resulting pressure drop measurement represents the combined effect of the losses in the bends, entrance and exit losses, developing region effects, and the core frictional losses. Thus, the measured pressure drop is the sum of these components (Phillips, 1987):

$$\Delta p = \frac{\rho u_m^2}{2} \left[(A_c/A_p)^2 (2K_{90}) + (K_c + K_e) + \frac{4f_{app}L}{D_h} \right] \quad (3.24)$$

where A_c and A_p are the total channel area and the total plenum cross-sectional area, K_{90} is the loss coefficient at the 90 degree bends, K_c and K_e represent the contraction and expansion loss coefficients due to area changes, and f_{app} includes the combined effects of frictional losses and the additional losses in the developing flow region. Phillips (1987) studied these losses and recommends K_{90} to be approximately 1.2. The contraction and exit losses can be read from Fig. 3.5 derived from Kays and London (1984) and Phillips (1990).

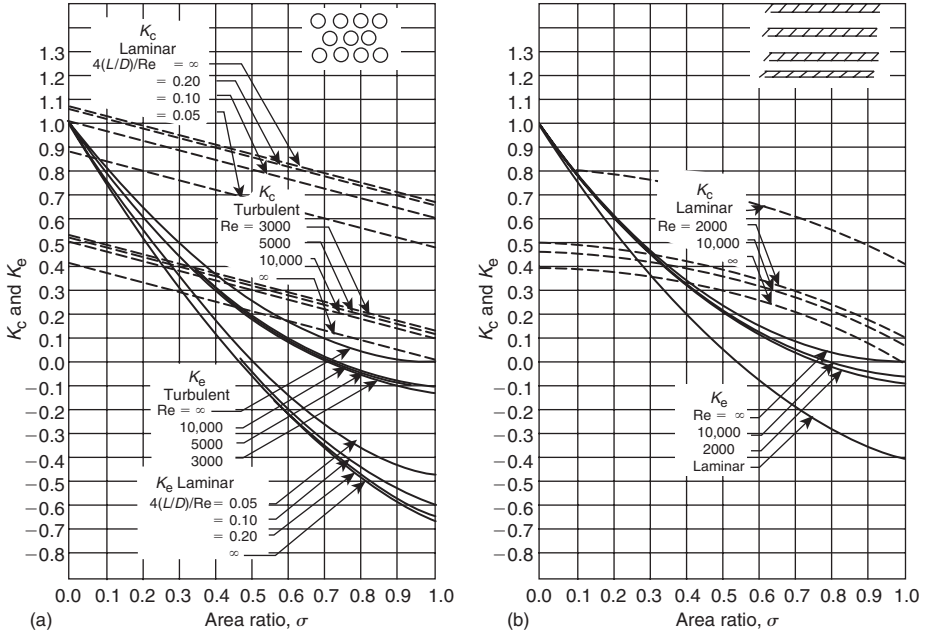


Fig. 3.5. Contraction and expansion loss coefficients for flow between inlet and outlet manifolds and the microchannels, Kays and London (1984).

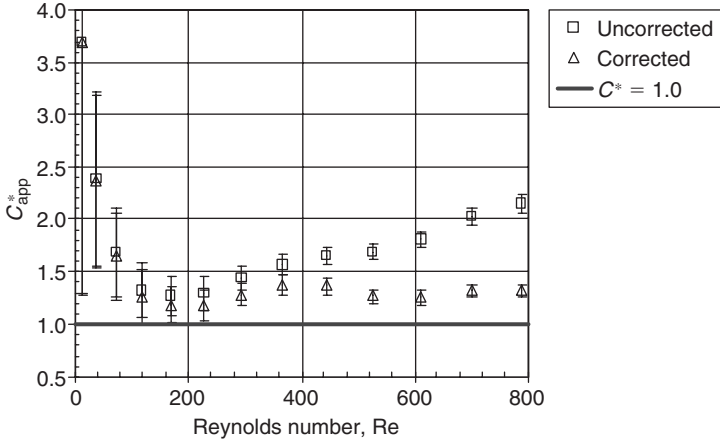


Fig. 3.6. Variation of $C^*_{app} = f_{app,ex}/f_{app,th}$ for a 200 μm square microchannel array after correcting for entrance and exit losses.

Figure 3.5(a) is applicable to the low aspect ratio channels, $\alpha_c < 0.1$ and Fig. 3.5(b) is for $0.1 \leq \alpha_c \leq 1.0$.

Equation (3.24) can also be written in terms of the fully developed friction factor f and the pressure drop defect $K(x)$:

$$\Delta p = \frac{\rho u_m^2}{2} \left[(A_c/A_p)^2 (2K_{90}) + (K_c + K_e) + \frac{4fL}{D_h} + K(x) \right] \quad (3.25)$$

For $L > L_h$, $K(x)$ is replaced by the Hagenbach's factor $K(\infty)$ as discussed earlier in Section 3.2.3. Steinke and Kandlikar (2005a) conducted experiments on square silicon microchannels with 200 μm sides and 10 mm in length, and analyzed the data in detail. A parameter C^* is introduced to represent the ratio of the experimental and theoretical apparent friction factors. Figure 3.6 shows the data before and after applying the corrections in $C^* = f_{app,ex}/f_{app,th}$, where the subscripts ex and th refer to experimental and theoretical values respectively. The uncorrected data converges to within 30% of the theoretical predictions after all corrections are applied. It is suspected that the high errors are due to slight variations in the channel cross-sectional area over its length, different entrance conditions, and errors associated with interpolations during data reduction.

Figure 3.7 shows the excellent agreement between the laminar flow theory and experimental results obtained by Judy *et al.* (2002) in 15–150 μm round and square microchannels made of fused silica and stainless steel with distilled water, methanol and isopropanol. Similar agreement is seen in Fig. 3.8 by Bucci *et al.* (2004) in 172, 290 and 520 μm diameter stainless steel circular tubes with water in the fully developed laminar flow region.

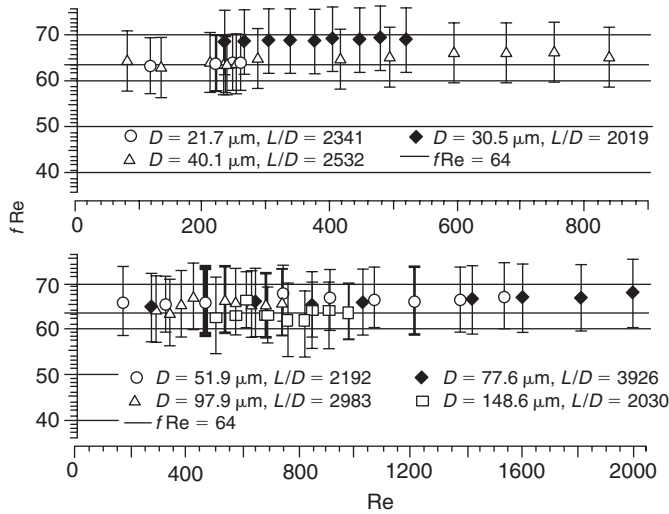


Fig. 3.7. Comparison between theory and experimental data of Judy *et al.* (2002) in 50–150 μm circular and square microchannels in the fully developed laminar region. (Note: f in this figure represents the Darcy friction factor, which is four times the Fanning friction factor used elsewhere in this text.)

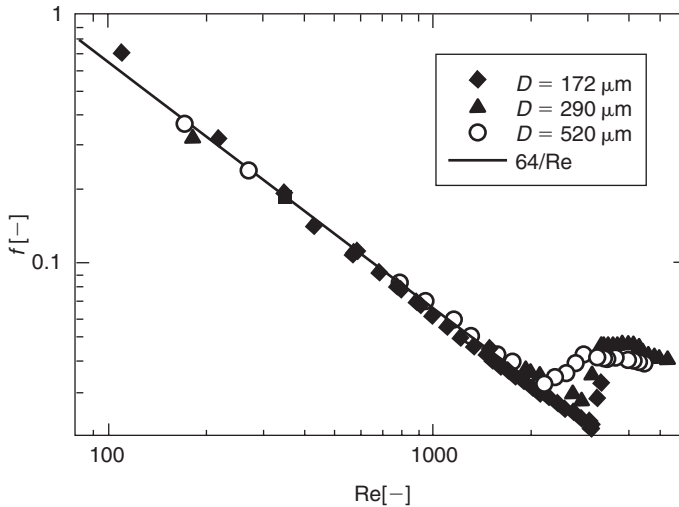


Fig. 3.8. Comparison between theory and experimental data of Bucci *et al.* (2004) in 171–520 μm diameter circular tubes in the fully developed laminar region. (Note: f in this figure represents the Darcy friction factor, which is four times the Fanning friction factor used elsewhere in this text.)

Niklas and Favre-Marinet (2003) analyzed the flow of water in a network of triangular microchannels with $D_h = 110 \mu\text{m}$. The contributions due to various losses were carefully analyzed in both their numerical as well as experimental work. They concluded that the classical theory is applicable to modeling the flow through the entire system.

Another point that needs to be emphasized is the large errors that are associated with microscale experiments as pointed out by Judy *et al.* (2002). A detailed analysis was conducted by Steinke and Kandlikar (2005a) for rectangular microchannels using actual measured parameters. Their final expression for uncertainty in estimating the product fRe for rectangular channels is given by:

$$\frac{U_{fRe}}{fRe} = \left[2 \left(\frac{U_\rho}{\rho} \right)^2 + \left(\frac{U_\mu}{\mu} \right)^2 + \left(\frac{U_{\Delta p}}{\Delta p} \right)^2 + \left(\frac{U_L}{L} \right)^2 + 3 \left(\frac{U_Q}{Q} \right)^2 + 5 \left(\frac{U_a}{a} \right)^2 + 5 \left(\frac{U_b}{b} \right)^2 + 2 \left(\frac{U_a}{a+b} \right)^2 + 2 \left(\frac{U_b}{a+b} \right)^2 \right]^{1/2} \quad (3.26)$$

The details of the derivation are given by Steinke (2005). Note that the uncertainties in the height a and width b measurements have a major influence on the overall uncertainty, followed by the uncertainties in the density and volumetric flow rate measurements. The low flow Reynolds number data in Fig. 3.6 exhibits extremely large uncertainties due to the errors associated with the flow rate measurement. The large discrepancy reported in literature by some of the earlier investigators is the result of the uncertainties in channel dimensions and flow rate measurements, entrance and exit losses, and the developing region effects.

Figure 3.9 shows a picture of a microchannel cross-section obtained with a scanning electron microscope by Steinke and Kandlikar (2005a). Note that the actual channel profile

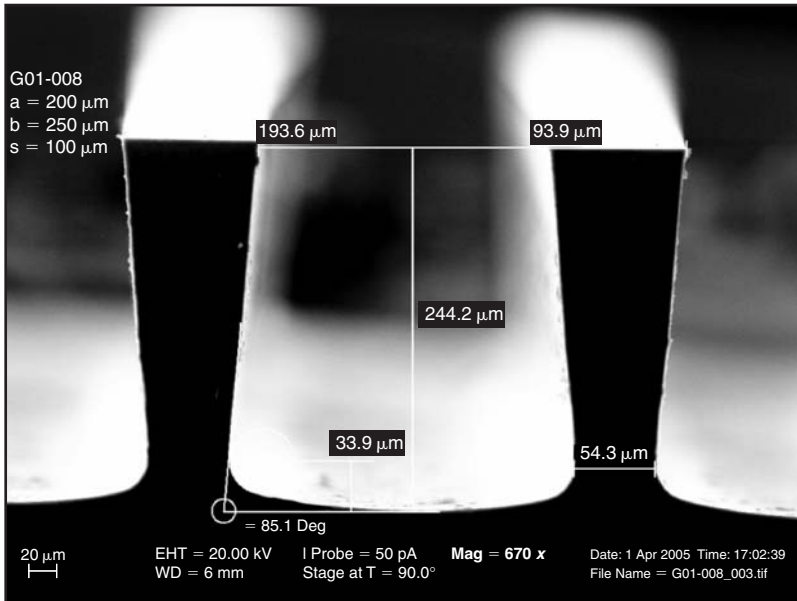


Fig. 3.9. Cross-sectional view of a rectangular microchannels etched in silicon showing distortion in channel geometry from ideal rectangular profile, Steinke and Kandlikar (2005a).

deviates significantly from the intended rectangular profile. The side walls are undercut by about 20 μm and the corners are rounded. This illustrates the need to accurately measure the flow area and the for estimating the pressure drop characteristics of microchannels.

Similar conclusions were reached by other investigators, for example, Li *et al.* (2000), Celata (2002), Judy *et al.* (2002), Baviere *et al.* (2004), and Tu and Hrnjak (2003). The increasing deviations from the theoretical values at higher Reynolds numbers in many data sets reported in literature is believed to be due to the increased length of the developing region. Baviere and Ayela (2004) measured the local pressures along the flow in a microchannel of height 7.5 μm . The range of Reynolds numbers considered was between 0.1 and 15. Their results were found to agree with the classical theory. They also identified the errors associated with the channel height measurement as being the largest source of uncertainty.

Baviere *et al.* (2004) conducted experiments with bronze, altuglas, and silicon coated microchannels with channel heights between 7.1 and 300 μm and channel widths between 1 and 25 mm. Their results were also in excellent agreement with the classical theory.

Other effects that may influence the flow in microchannels are (i) high viscous dissipation causing a change in the fluid viscosity at the wall, and (ii) electrokinetic effects, which are covered in Chapter 4. The effect of viscous dissipation is reviewed by Shen *et al.* (2004). Xu *et al.* (2000) modeled this effect and found that the velocity profile was modified due to the viscous dissipation. The resulting friction factors were predicted to be lower due to a reduction in the viscosity at higher liquid temperatures. The viscous effect was studied experimentally by Judy *et al.* (2002). Their pressure drop data correlated well with the theory when they used the average of the inlet and outlet fluid temperatures from their stainless steel microtubes, which were 15–100 μm in diameter. Koo and Kleinstreuer (2004) concluded that viscous dissipation effects increase rapidly with a decrease in the channel dimensions and hence should be considered along with the imposed heat sources at the channel walls.

Figure 3.10 shows a plot of the friction factor versus Reynolds number using the experimental data points reported in literature as compiled by Steinke and Kandlikar (2005a). The lines represent the theoretical values for different channel aspect ratios. These data points were screened to eliminate the data that were obtained with large uncertainties and those which did not account for the entrance and exit losses. It is seen that the general trends are followed, though the errors are still quite large mainly due to the uncertainties associated with channel size measurement.

3.3.2. Laminar-to-turbulent transition

The laminar-to-turbulent flow transition is another topic that was analyzed by a number of investigators. The laminar-to-turbulent transition in abrupt entrance rectangular ducts was found to occur at a transition Reynolds number of $\text{Re}_t = 2200$ for $\alpha_c = 1$ and at $\text{Re}_t = 2500$ (Hartnett *et al.*, 1962) for parallel plates with $\alpha_c = 0$. For other aspect ratios, a linear interpolation between these two values is recommended.

Some of the initial studies indicated an early transition to turbulent flow in microchannels. However, a number of recent studies showed that the laminar-to-turbulent transition

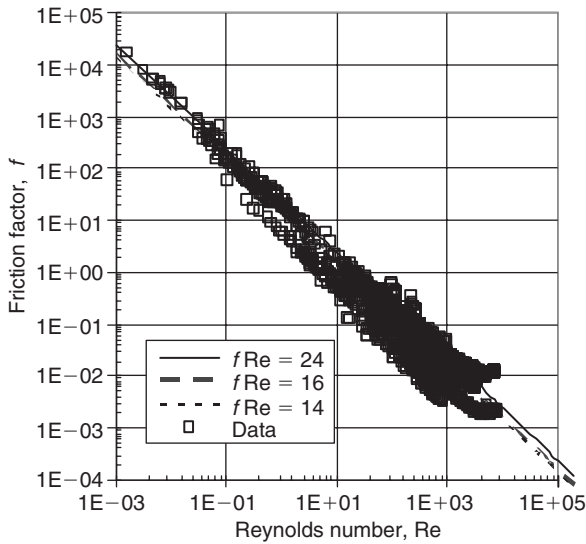


Fig. 3.10. Comparison of friction factors reported in literature with the theoretical values for different microchannel geometries. Entrance and exit losses and the developing region at the entrance were not accounted for in a number of data sets reviewed by Steinke and Kandlikar (2005a).

remains unchanged. Figure 3.8 by Bucci *et al.* (2004) shows that the transition occurred around $Re_t = 2000$ for circular microtubes 171–520 μm in diameter. The results of Baviere *et al.* (2004) also indicate that the laminar-to-turbulent transition in smooth microchannels is not influenced by the channel dimensions and occurs around 2300. Similar results were reported by a number of investigators, including Bucci *et al.* (2004), Schmitt and Kandlikar (2005), Kandlikar *et al.* (2005) for minichannels with $D_h < 1\text{ mm}$; and Li *et al.* (2000) for $80\text{ }\mu\text{m} \leq D_h \leq 166.3\text{ }\mu\text{m}$.

The transition from the laminar-to-turbulent region is influenced by the channel surface roughness. Further details of this effect are discussed in the next section on roughness.

3.4. Roughness effects

3.4.1. Roughness representation

Darcy (1857) investigated the effects of surface roughness on the turbulent flow of water in rough pipes made of cast iron, lead, wrought iron, and asphalt-covered cast iron. The pipes were 12 to 500 mm in diameter and 100 m long. Fanning (1886) proposed a correlation for the pressure drop as a function of roughness. Mises (1914) is credited with introducing the term relative roughness, which was originally defined as the ratio of absolute roughness to the pipe radius (we now use pipe diameter to normalize roughness parameters, such as average roughness R_a). Nikuradse (1933) presented a comprehensive review of the literature covering uniform roughness and roughness structures such as corrugations, and

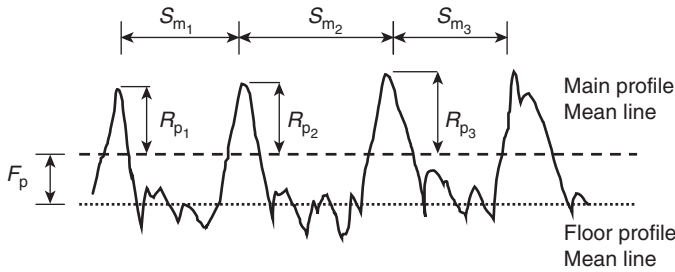


Fig. 3.11. Maximum profile peak height (R_p), Mean spacing of profile irregularities (RS_m), and Floor distance to mean line (F_p).

some of the available correlations relating friction factor to relative roughness. He also conducted a systematic study on friction factor by applying uniform diameter sand grain particles with Japanese lacquer to the inner pipe surface and measuring the pressure drop. He identified three regions which form the basis of the current Moody diagram that is used for friction factor estimation.

The term relative roughness is used for the ratio ε/D_h where ε is the average roughness. Nikuradse used the diameter of the uniform sand grain particles to represent the roughness ε . The range of relative roughness in Nikuradse's experiments on circular pipes was $0.001 \leq \varepsilon/D \leq 0.033$. Furthermore, Nikuradse identified three ranges to describe his laws of resistances. In Range I, for low Reynolds numbers corresponding to laminar flow, the friction factor was independent of surface roughness and was given by the now established classical equation $f = 16/Re$ for circular pipes. In Range II, he described the roughness effects on the friction factor in turbulent flow by $f = 0.079/Re^{1/4}$, and finally in Range III, the friction factor is independent of the Reynolds number but depends on the relative roughness, $f = 0.25/[1.74 + 2 \log(2\varepsilon/D)]^2$. Note that the original equations by Nikuradse have been modified to express them in terms of the Fanning friction factor (which is one fourth of Darcy friction factor, $f = 0.25 f_{\text{Darcy}}$).

Moody (1944) used the available data on the friction factor and developed the well-known Moody diagram covering the relative roughness range of $0 \leq \varepsilon/D \leq 0.05$. Following the earlier investigators, he used the tube root diameter of a circular pipe, similar to Nikuradse's work, in expressing the relative roughness ε/D .

A number of different parameters were studied for their suitability in representing the roughness effects. Kandlikar *et al.* (2005) investigated parameters based on various roughness characterization schemes and proposed a set of three parameters: Mean Profile Peak Height (R_p), Mean Spacing of Profile Irregularities (RS_m), and the Floor Distance to Mean Line (F_p), as shown in Fig. 3.11. Two of these parameters (R_p and RS_m) are defined in the ASME B46.1-2002 and the other (F_p) is proposed by Kandlikar *et al.* (2005).

- *Average maximum profile peak height* (R_{pm}): The distance between the average of the individual highest points of the profile ($R_{p,i}$) and the mean line within the evaluation length. The mean line represents the conventional average roughness value (R_a).

- *Mean spacing of profile irregularities (RS_m)*: Consists of the mean value of the spacing between profile irregularities within the evaluation length. The irregularities of interest are the peaks, so this is equivalent to the *Pitch*.

$$RS_m = \frac{1}{n} \sum_{i=1}^n S_{m_i} \quad (3.27)$$

- *Floor distance to mean line (F_p)*: Consists of the distance between the main profile mean line (determined by R_a) and the floor profile mean line. The floor profile is the portion of the main profile that lies below the main profile mean line.

The three parameters described above allow the characterization of the peak height, peak spacing and the distance from the floor to the mean line. These parameters will define the characteristics of the surface roughness that influence the location and shape of the fluid flow streamlines (as described by Webb *et al.*, 1971 and Kandlikar *et al.*, 2005) and, consequently, the size of the recirculation flow zones between roughness elements. From the above parameters, the equivalent roughness ε can be estimated by the following relationship:

$$\varepsilon = R_{pm} + F_p \quad (3.28)$$

For the sand grain roughness employed by Nikuradse, the new definition of roughness ε yields the same value, and hence no correction is needed for any of the friction factor correlations and charts. The use of mean spacing between profile irregularities is expected to represent the structured roughness surfaces. Such surfaces may be designed in the future to obtain specific pressure drop and heat transfer performance characteristics.

3.4.2. Roughness effect on friction factor

For microchannels, the relative roughness values are expected to be higher than the limit of 0.05 used in the Moody diagram. Kandlikar *et al.* (2005) considered the effect of cross-sectional area reduction due to protruding roughness elements and recommended using the constricted flow area in calculating the friction factor. Using a constricted diameter $D_{cf} = D - 2\varepsilon$, a modified Moody diagram was presented as shown in Fig. 3.12. In the turbulent region, it was found that such a representation yielded a constant value of friction factor above $\varepsilon/D_{cf} > 0.03$.

In the turbulent fully rough region, $0.03 \leq \varepsilon/D_{cf} \leq 0.05$, the friction factor based on the constricted flow diameter is given by:

$$f_{\text{Darcy,cf}} = 0.042 \quad (3.29a)$$

In terms of the Fanning friction factor, we get:

$$f_{cf} = f_{\text{Darcy,cf}}/4 = 0.042/4 = 0.0105 \quad (3.29b)$$

Since experimental data is not available beyond $\varepsilon/D_{cf} > 0.05$, using Eq. (3.29) for higher relative roughness values than 0.05 is not recommended. Note that the friction factor and

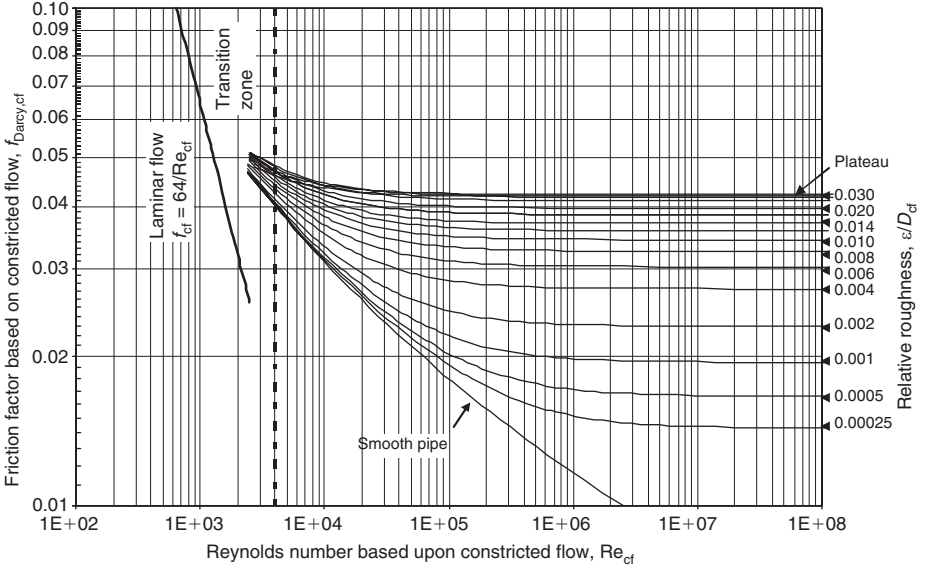


Fig. 3.12. Darcy friction factor plot based on a constricted flow diameter, Kandlikar *et al.* (2005).

the geometrical and flow parameters are based on the constricted flow diameter as given by the following equations:

$$D_{cf} = D - 2\varepsilon \quad (3.30)$$

$$\Delta p = \frac{2f_{cf}\rho u_{m,cf}^2 L}{D_{h,cf}} \quad (3.31)$$

$$u_{m,cf} = \dot{m}/A_{cf} \quad (3.32)$$

$$Re_{cf} = \frac{\rho u_{m,cf} D_{h,cf}}{\mu} \quad (3.33)$$

In the fully developed laminar flow region, the constricted friction factor is given by the following equation, Kandlikar *et al.* (2005):

Laminar region, $0 \leq \varepsilon/D_{h,cf} \leq 0.15$;

$$f_{cf} = \frac{Po}{Re_{cf}} \quad (3.34)$$

where the Poiseuille number Po is given by either Eq. (3.9) or (3.10) depending on the channel geometry. In the turbulent region, use the modified Miller equation as recommended by Kandlikar *et al.* (2005).

Fully developed turbulent region, $0 \leq \varepsilon/D_{h,cf} < 0.03$;

$$f_{cf} = \frac{0.25 \left[\log_{10} \left(\frac{\varepsilon/D_{h,cf}}{3.7} + \frac{5.74}{\text{Re}_{cf}^{0.9}} \right) \right]^{-2}}{4} \quad (3.35)$$

Fully developed turbulent region, $0.03 \leq \varepsilon/D_{h,cf} \leq 0.05$

$$f_{cf} = 0.0105 \quad (3.36)$$

No recommendation can be made for the turbulent region with $\varepsilon/D_{h,cf} > 0.05$ because of the lack of detailed experimental data in literature for this region. Further experimental work in this area is strongly recommended.

For rectangular channels with all sides having a roughness ε , the mean flow velocity is calculated using the constricted flow area and the constricted channel dimensions of $a_{cf} = a - 2\varepsilon$ and $b_{cf} = b - 2\varepsilon$. The hydraulic diameter is calculated using the constricted channel dimensions.

Schmitt and Kandlikar (2005) conducted experiments to study the effect of a large relative roughness of $\varepsilon/D_{h,cf}$ up to 0.15 in smooth and artificially roughened rectangular minichannels. They introduced sawtooth roughness elements in a 10.3 mm wide and 100 mm long test channel. Cross-sectional views of the smooth channels and channels with sawtooth roughness elements are shown in Fig. 3.13. The channel gap b_{cf} was varied to produce values of $\varepsilon/D_{h,cf}$ from 0.03 to 0.15. Differential pressure taps for measuring

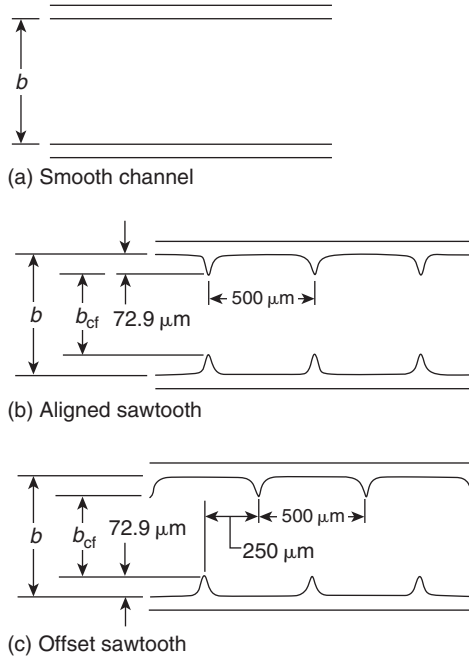


Fig. 3.13. Roughness elements used by Schmitt and Kandlikar (2005) and Kandlikar *et al.* (2005).

the local pressure drops were located at several locations along the flow length in the fully developed region.

The smooth channel results reported by Kandlikar *et al.* (2005) closely follow the classical laminar flow theory for friction factor. The experimental data from the two sawtooth structures are represented in Fig. 3.14 for flow of water with $b = 500 \mu\text{m}$, resulting in a D_h of $953 \mu\text{m}$. This plot uses the height b in calculating D_h and Re . The dashed line represents the $fRe = \text{Constant}$ line corresponding to the channel aspect ratio $\alpha_c = a/b$. It is seen that the agreement in the low Reynolds number region corresponding to laminar flow is considerably off.

Figure 3.15 shows the same data used in Fig. 3.14, but plotted with the constricted flow areas and using the constricted flow parameters given by Eqs. (3.30)–(3.33). The

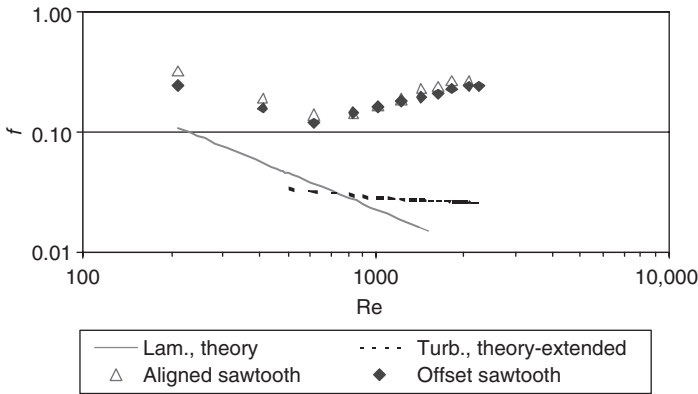


Fig. 3.14. Fully developed friction factor versus Reynolds number, both based on hydraulic diameter for water flow. $D_h = 953 \mu\text{m}$, $b = 500 \mu\text{m}$, $b_{cf} = 354 \mu\text{m}$, $w = 10.03 \text{ mm}$, $\varepsilon/D_h = 0.0735$, Kandlikar *et al.* (2005).

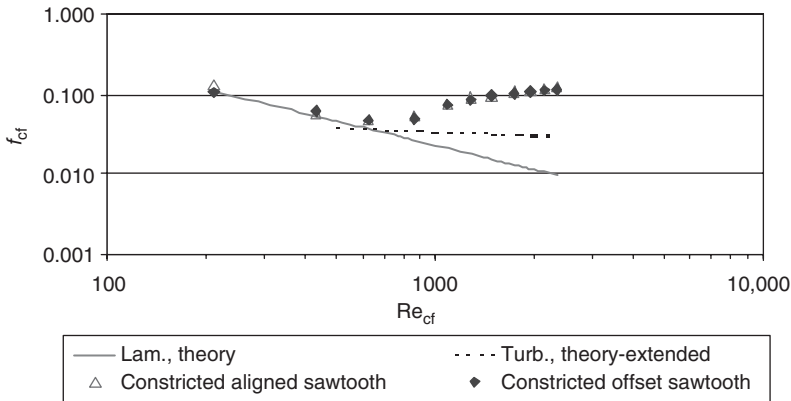


Fig. 3.15. Fully developed friction factor versus Reynolds number, both based on constricted flow hydraulic diameter; water flow. $D_{h,cf} = 684 \mu\text{m}$, $b = 500 \mu\text{m}$, $b_{cf} = 354 \mu\text{m}$, $w = 10.03 \text{ mm}$, $\varepsilon/D_{h,cf} = 0.1108$, Kandlikar *et al.* (2005).

results shown in Fig. 3.15 in the laminar region show good agreement with the accepted laminar flow theory ($f_{cf} Re_{cf} = Constant$). Similar results were obtained for different gap sizes (yielding different relative roughness values) for both the offset sawtooth and aligned sawtooth geometries.

3.4.3. Roughness effect on the laminar-to-turbulent flow transition

The transition from laminar-to-turbulent flow has been reported to occur in microchannels at Reynolds numbers considerably below 2300. In many experiments, the transition has been mistakenly identified to occur early based on experimental data uncorrected for the developing length (Steinke and Kandlikar, 2005a). Kandlikar *et al.* (2003) conducted experiments with stainless steel tubes and noted that early transition occurred for a 0.62 mm ID stainless steel tube with a surface roughness ε/D_h of 0.355%. Schmitt and Kandlikar (2005) conducted careful experiments with plain and sawtooth roughened channels with air and water. Their results for smooth rectangular channels showed a transition Reynolds number between 2000 and 2300, but for increasing relative roughness values there was a decreasing transition Reynolds numbers as seen in Figs. 3.14 and 3.15. Figure 3.16 shows the transition Reynolds number as a function of the relative roughness (based on the constricted hydraulic diameter). The following equations are used to describe the roughness effects based on their experimental data.

Laminar-to-turbulent transition criteria:

$$\text{For } 0 < \varepsilon/D_{h,cf} \leq 0.08: \quad Re_{t,cf} = 2300 - 18,750(\varepsilon/D_{h,cf}) \quad (3.37)$$

$$\text{For } 0.08 < \varepsilon/D_{h,cf} \leq 0.15: \quad Re_{t,cf} = 800 - 3270(\varepsilon/D_{h,cf} - 0.08) \quad (3.38)$$

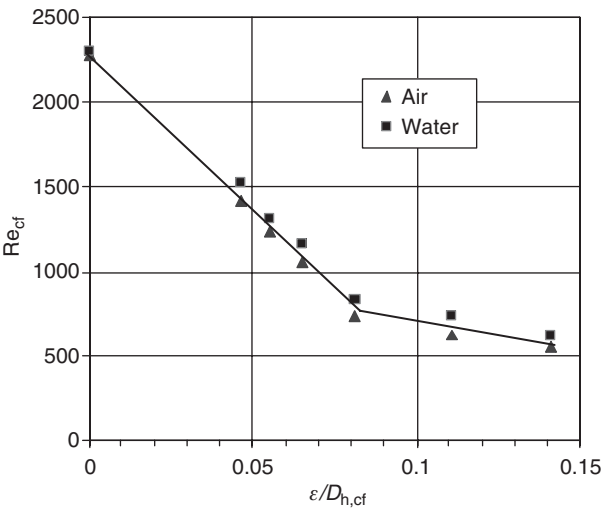


Fig. 3.16. Transition Reynolds number variation with relative roughness based on constricted flow diameter, Equations (3.37) and (3.38) plotted along with data from Schmitt and Kandlikar (2005).

Friction factor in the transition region for rough tubes with $\varepsilon/D_{h,cf} \leq 0.05$ at a given Re_{cf} can be obtained by a linear interpolation of (i) the laminar friction factor obtained from Eq. (3.34) at the transition Reynolds number, and (ii) the turbulent friction factor at $Re_{cf} = 2300$ given by Eq. (3.35) or (3.36) depending on the value of $\varepsilon/D_{h,cf}$. For $\varepsilon/D_{h,cf} > 0.05$ in the transition region, additional experimental data is needed before any recommendations can be made.

3.4.4. Developing flow in rough tubes

Developing flow in rough tubes has not been explored in literature. As a preliminary estimate, the methods described in Section 3.2.3 for smooth tubes are recommended by introducing the constricted flow diameter in calculating the flow velocity, Reynolds number and friction factor. Further research in this area is needed.

3.5. Heat transfer in microchannels

3.5.1. Fully developed laminar flow

The Nusselt number in fully developed laminar flow is expected to be constant as predicted by the classical theory. However, there are a number of investigations reported in literature that show a trend increasing with Reynolds number in this range. This results from the experimental uncertainties as discussed in Section 3.5.3.

The Nusselt number in the fully developed laminar flow is constant and depends on the channel geometry and the wall heat transfer boundary condition. Table 3.1 presents the Nusselt numbers for commonly used geometries under constant heat flux and constant wall temperature boundary conditions.

For a rectangular channel, the Nusselt number depends on the channel aspect ratio $\alpha_c = a/b$, and the wall boundary conditions. Three boundary conditions are identified in literature and the Nusselt number for each one is given below.

Constant wall temperature, T-boundary condition:

$$Nu_T = 7.541(1 - 2.610\alpha_c + 4.970\alpha_c^2 - 5.119\alpha_c^3 + 2.702\alpha_c^4 - 0.548\alpha_c^5) \quad (3.39)$$

Constant circumferential wall temperature, uniform axial heat flux, H1 boundary condition:

$$Nu_{H1} = 8.235(1 - 2.0421\alpha_c + 3.0853\alpha_c^2 - 2.4765\alpha_c^3 + 1.0578\alpha_c^4 - 0.1861\alpha_c^5) \quad (3.40)$$

Constant wall heat flux, both circumferentially and axially:

$$Nu_{H2} = 8.235(1 - 10.6044\alpha_c + 61.1755\alpha_c^2 - 155.1803\alpha_c^3 + 176.9203\alpha_c^4 - 72.9236\alpha_c^5) \quad (3.41)$$

Table 3.3
Fully developed laminar flow Nusselt numbers.

$\alpha_c = a/b$	$Nu_{fd,3}$	$Nu_{fd,4}$
0	8.235	8.235
0.10	6.939	6.700
0.20	6.072	5.704
0.30	5.393	4.969
0.40	4.885	4.457
0.50	4.505	4.111
0.70	3.991	3.740
1.00	3.556	3.599
1.43	3.195	3.740
2.00	3.146	4.111
2.50	3.169	4.457
3.33	3.306	4.969
5.00	3.636	5.704
10.00	4.252	6.700
> 10.00	5.385	8.235

a – unheated side in three-side heated case.
For intermediate values, use the curve-fit equations provided in Appendix A at the end of the chapter.

In reality, all practical situations fall somewhere in the middle of these three boundary conditions. This becomes an especially important issue in the case of microchannels because of the difficulty in identifying a correct boundary condition with discretely spaced heat sources, and two-dimensional effects in the base and the fins.

The heating in microchannel geometries generally comes from three sides, as a cover of glass or some other material is bonded on top of the microchannels to form the flow passages. The fully developed Nusselt numbers for both three- and four-side heated ducts have been compiled from various sources, including Wibulswas (1966), and Phillips (1987) and are given in Table 3.3. Note that the side with dimension a is not heated, and the channel aspect ratio is defined as $\alpha_c = a/b$.

3.5.2. Thermally developing flow

The thermal entry length is expressed by the following form for flow in ducts:

$$\frac{L_t}{D_h} = c \text{ Re Pr} \tag{3.42}$$

For circular channels, the leading constant c in Eq. (3.42) is found to be 0.05, while for rectangular channels, the plots presented by Phillips (1987) suggest $c = 0.1$.

The local heat transfer in the developing region of a circular tube is given by the following equations (Shah and London, 1978):

$$Nu_x = 4.363 + 8.68(10^3 x^*)^{-0.506} e^{-41x^*} \tag{3.43}$$

Table 3.4

Thermal entry region Nusselt numbers.

x^*	$\alpha_c \leq 0.1^*$	$Nu_{x,4}$					$\alpha_c \geq 10^{**}$
		$\alpha_c = 0.25$	$\alpha_c = 0.333$	$\alpha_c = 0.5$	$\alpha_c = 1.0$		
0.0001	31.4	26.7	27.0	23.7	25.2	31.6	
0.0025	11.9	10.4	9.9	9.2	8.9	11.2	
0.005	10	8.44	8.02	7.46	7.1	9.0	
0.00556	9.8	8.18	7.76	7.23	6.86	8.8	
0.00625	9.5	7.92	7.5	6.96	6.6	8.5	
0.00714	9.3	7.63	7.22	6.68	6.32	8.2	
0.00833	9.1	7.32	6.92	6.37	6.02	7.9	
0.01	8.8	7	6.57	6.05	5.69	7.49	
0.0125	8.6	6.63	6.21	5.7	5.33	7.2	
0.0167	8.5	6.26	5.82	5.28	4.91	6.7	
0.025	8.4	5.87	5.39	4.84	4.45	6.2	
0.033	8.3	5.77	5.17	4.61	4.18	5.9	
0.05	8.25	5.62	5.00	4.38	3.91	5.55	
0.1	8.24	5.45	4.85	4.22	3.71	5.4	
1	8.23	5.35	4.77	4.11	3.6	5.38	

$x^* = x/(\text{Re Pr } D_h)$; * – parallel plates, both sides heated; ** – parallel plates, one side heated.
For intermediate values, use the curve-fit equations provided in Appendix A.

$$x^* = \frac{x/D_h}{\text{Re Pr}} \quad (3.44)$$

For rectangular channels with the four-side heating configuration, Nusselt numbers in the thermally developing region presented in Table 3.4 are derived from Phillips' (1987) work. For the three-side heating configuration the following scheme is suggested by Phillips (1990).

Three-side heating, $\alpha_c \leq 0.1$ and $\alpha_c \geq 10$, use four-side heating table without any modification.

Three-side heating, $0.1 < \alpha_c < 10$:

$$Nu_{x,3}(x^*, \alpha_c) = Nu_{x,4}(x^*, \alpha_c) \frac{Nu_{fd,3}(x^* = x_{fd}^*, \alpha_c)}{Nu_{fd,4}(x^* = x_{fd}^*, \alpha_c)} \quad (3.45)$$

The subscripts $x, 3$ and $x, 4$ refer to the location at a distance x in the heated length for the three-sided and four-sided heating cases respectively. The Nusselt numbers in the fully developed region for both heating configurations are obtained from Table 3.3, and in the developing region Nusselt numbers for the four-sided heating are obtained from Table 3.4.

The use of fully developed hydrodynamic conditions in heat transfer analysis is reasonable for water. Garimella and Singhal (2004) noted that assuming fully developed hydrodynamic conditions and thermally developing conditions resulted in a satisfactory agreement with their data for microchannels.

3.5.3. Agreement between theory and available experimental data on laminar flow heat transfer

Laminar flow heat transfer in microchannels has been studied by a number of researchers. Agreement with the classical laminar flow theory is expected to hold, but the reported data show significant scatter due to difficulties encountered in making accurate local heat flux and temperature measurements. Steinke and Kandlikar (2005b) reviewed the available data and presented a comprehensive table showing the range of parameters employed. The laminar flow heat transfer in the fully developed region is expected to be constant, but the data taken from literature show a generally linear increase in Nusselt number with flow Reynolds number as seen in Fig. 3.17.

The main reasons for this discrepancy have been attributed to the following factors:

- (i) *Entrance region effects*: The researchers have used the fully developed theoretical values for Nusselt numbers in their comparison with the experimental data. Due to the relatively short lengths employed in microchannels, the influence of the entrance region cannot be neglected. The entrance region effects become more significant at higher Reynolds numbers, in part explaining the increasing Nusselt number trend with Reynolds number as seen in Fig. 3.17.
- (ii) *Uncertainties in experimental measurements*: The uncertainties in heat transfer measurements have been analyzed by a number of investigators, including Judy *et al.* (2002) and Steinke and Kandlikar (2005b). The following equation for the uncertainty in the Nusselt number calculation from the uncertainties in the experimental measurements is presented by Steinke and Kandlikar for a rectangular channel of base

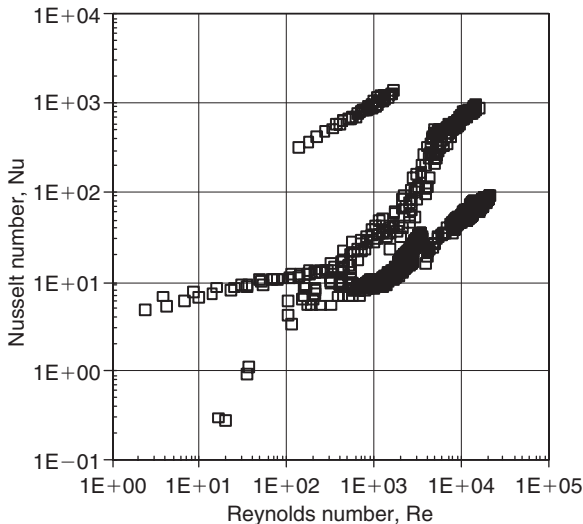


Fig. 3.17. Selected experimental data for single-phase liquid flow in microchannels and minichannels, $D_h = 50 \mu\text{m}$ to $600 \mu\text{m}$.

width a and height b :

$$U_{Nu} = Nu \cdot \left[\left(\frac{U_{k_f}}{k_f} \right)^2 + \left(\frac{U_I}{I} \right)^2 + \left(\frac{U_V}{V} \right)^2 + 4 \left(\frac{U_{T_s}}{T_s} \right)^2 + 2 \left(\frac{U_{T_i}}{T_i} \right)^2 + 2 \left(\frac{U_{T_o}}{T_o} \right)^2 + 3 \left(\frac{U_L}{L} \right)^2 + 4 \left(\frac{U_a}{a} \right)^2 + 5 \left(\frac{U_b}{b} \right)^2 + 2 \left(\frac{U_{\eta_f}}{\eta_f} \right)^2 \right]^{1/2} \quad (3.46)$$

where I – current, V – voltage, T_s – surface temperature, T_i – fluid inlet temperature, T_o – fluid outlet temperature, L – flow length, a and b – cross-section dimensions, and η_f – fin efficiency. The uncertainties in the measurement of the surface temperature and flow channel dimensions play a critical role in the overall uncertainty. The importance of accurate geometrical measurements was emphasized in the friction factor estimation as well. Accurate surface temperature measurement poses a significant challenge due to the small dimensions of the test section. Use of silicon chips with integrated circuits to measure the temperatures is recommended.

Another factor that makes the temperature measurements critical in the overall uncertainty is the small temperature difference between the surface and the fluid at the outlet. Since the heat transfer coefficients are very high in microchannels, and the flow is relatively low (low Reynolds number), the outlet temperature in many experiments approaches the surface temperature. Proper experiments need to be designed to account for this effect.

- (iii) *Ambiguity in the determination of the thermal boundary condition*: Several experiments reported in literature were conducted with microchannels or minichannels fabricated on copper or silicon substrates. The actual boundary conditions for these test sections are difficult to ascertain as they fall in between the constant temperature and constant heat flux boundary conditions. Furthermore, in many cases the heating is three-sided with the side walls acting as fins. The fin efficiency effects also alter the heat flux and temperature distributions. A clear comparison is only possible after the conjugate heat transfer effects are incorporated into a detailed numerical simulation of the test section.

3.5.4. Roughness effects on laminar flow heat transfer

Kandlikar *et al.* (2003) studied the heat transfer and pressure drop of laminar flow in smooth and rough stainless steel tubes of 1.067 and 0.62 mm ID. The surface roughness of the inner tube wall was changed by treating it with two different acid mixtures. The surface roughness actually went down after the acid treatment as the protruding peaks in the surface profile were smoothed out. The effect of changes in the relative roughness on pressure drop was minimal, but the heat transfer in the entry region showed a distinct dependence on roughness. Figure 3.18 shows the local Nusselt number at a location 52 mm from the start of the heated length. The flow was hydrodynamically fully developed prior to entering the heated section.

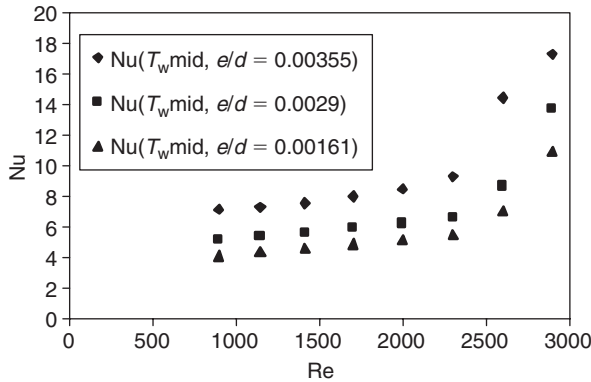


Fig. 3.18. The effect of roughness in the entrance region ($x = 52$ mm) of a 0.62 mm inner diameter tube with a fully developed velocity profile and a developing temperature profile, Kandlikar *et al.* (2003).

It is seen from Fig. 3.18 that the Nusselt number increases even for a modest increase in the relative roughness from 0.161% to 0.355%. Also note that the location where the heat transfer measurements were taken was preceded by a tube length longer than the hydraulic entry length, which was 380 mm at $Re = 2300$. A number of researchers did not correctly identify the developing region and have mistakenly reported the increasing trend in the Nu versus Re plot as being in the fully developed region.

It is not possible to present any equations for heat transfer enhancement with roughness because of the lack of systematic data covering the entire region. Further research in this area is strongly recommended. With structured roughness surfaces, the enhancement results from the combined effects of area enhancement and that due to the flow modification caused by the roughness elements.

3.5.5. Heat transfer in the transition and turbulent flow regions

A detailed discussion was presented earlier on the critical Reynolds number for the laminar-to-turbulent transition. For smooth channels, the well-established criterion of $Re_c = 2300$ is expected to hold. The effect of roughness is described by Eqs. (3.32) and (3.33). Since the transition region is encountered in many minichannel and microchannel heat exchangers, there is a need for generating accurate experimental data for both smooth and rough tubes in this region.

Phillips (1990) suggests using the following equations in the developing turbulent region. For larger values of x , the influence of the term $[1 + (D_h/x)^{2/3}]$ reduces asymptotically to 1:

$$\text{For } 0.5 < Pr < 1.5: \quad Nu = 0.0214[1.0 + (D_h/x)^{2/3}][Re^{0.8} - 100]Pr^{0.4} \quad (3.47)$$

$$\text{For } 1.5 < Pr < 500: \quad Nu = 0.012[1.0 + (D_h/x)^{2/3}][Re^{0.87} - 280]Pr^{0.4} \quad (3.48)$$

Further validation of these equations in microchannels is warranted. Adams *et al.* (1997) conducted experimental work in the turbulent region with flow of water in 0.76 and

0.109 mm diameter circular channels. Based on their data, they proposed the following equation that also matches the data by Yu *et al.* (1995) within $\pm 18.6\%$:

$$\text{Nu} = \text{Nu}_{\text{Gn}}(1 + F) \quad (3.49)$$

where

$$\text{Nu}_{\text{Gn}} = \frac{(f/8)(\text{Re} - 1000)\text{Pr}}{1 + 12.7(f/8)^{1/2}(\text{Pr}^{2/3} - 1)} \quad (3.50)$$

$$f = (1.82 \log(\text{Re}) - 1.64)^{-2} \quad (3.51)$$

$$F = C\text{Re}(1 - (D/D_0)^2) \quad (3.52)$$

Nu_{Gn} represents the Nusselt number predicted by Gnielinski (1976) correlation. The least-squares fit to all the data sets studied by Adams *et al.* (1997) resulted in $C = 7.6 \times 10^{-5}$ and $D_0 = 1.164$ mm.

Heat transfer coefficients in microchannels are very high due to their small hydraulic diameters. The high pressure gradients have led researchers to employ low flow rates. However, with the reduced flow rate, the ability of the fluid stream to carry the heat away for a given temperature rise becomes limited. In order to improve the overall cooling performance, the following two options are available.

- (a) Reduce the flow length of the channels.
- (b) Increase the liquid flow rate.

As a result, employing multiple streams with short paths in a microchannel heat exchanger is recommended, similar to a split flow arrangement providing two streams as will be discussed in Section 3.7. The reduced flow length will then enable the designer to employ higher flow rates under a given pressure drop limit. This scheme offers several advantages over a single-pass arrangement where the fluid traverses the entire length of the heat exchanger:

- (i) *The reduced flow length reduces the pressure drop:* The short flow length effectively reduces the overall pressure drop.
- (ii) *Larger developing region:* The multiple inlets result in a larger channel area being under developing conditions where the heat transfer is higher.
- (iii) *Higher flow velocities:* Some of the pressure drop reduction could be used to increase the flow velocity of individual streams. The possibility of employing turbulent flow should also be explored as the heat transfer coefficient is higher in this region.

3.5.6. Variable property effects

The property ratio method is usually recommended in accounting for the property variations due to temperature changes in the heat exchanger flow passages. The following equations are recommended for liquids:

$$f/f_{\text{cp}} = [\mu_w/\mu_b]^M \quad (3.53)$$

$$\text{Nu}/\text{Nu}_{\text{cp}} = [\mu_w/\mu_b]^N \quad (3.54)$$

where the subscript cp refers to the constant property solution obtained from appropriate equations or correlations. For laminar flow, $M = 0.58$ and $N = -0.14$, and for turbulent flow, $M = 0.25$ and $N = -0.11$ (Kays and London, 1984).

3.6. Microchannel and minichannel geometry optimization

The first practical implementation of microchannels in silicon devices was demonstrated by Tuckerman and Pease (1981). They were able to dissipate 7.9 MW/m^2 with a maximum substrate temperature rise of 71°C and a pressure drop of 186 kPa . The allowable temperature differences and the pressure drops for cooling today's microprocessor chips have become significantly smaller, and many investigators have been working towards optimization of the channel geometrical configuration.

The application of microchannels to electronics cooling imposes severe design constraints on the system design. For a given heat dissipation rate, the flow rate, pressure drop, fluid temperature rise, and fluid inlet to surface temperature difference requirements necessitate optimization of the channel geometry. A number of investigators studied the geometrical optimization of microchannel heat exchangers. For example, Phillips (1987), Harpole and Eninger (1991), Knight *et al.* (1992), Ryu *et al.* (2002), Bergles *et al.* (2003), and Kandlikar and Upadhye (2005). The results found by Kandlikar and Upadhye are presented below.

Kandlikar and Upadhye (2005) considered a microchannel system as shown in Fig. 3.19. For a chip of width $W = 10 \text{ mm}$ and length $L = 10 \text{ mm}$, they presented an analysis scheme for heat transfer and pressure drop by incorporating the entrance region effects. The number of channels was used as a parameter in developing the optimization scheme. The maximum chip temperature was set at 360 K while the fluid inlet temperature was set equal to 300 K . The channel depth was assumed to be $200 \mu\text{m}$.

Figures 3.20 and 3.21 show the parametric plots resulting from the optimization program. The fin spacing ratio, defined as $\beta = s/a$, is plotted as a function of the number of channels on a 10 mm wide chip with pressure drop, water flow rate and fin thickness as parameters. A lower limiting value of approximately $40 \mu\text{m}$ was considered achievable for

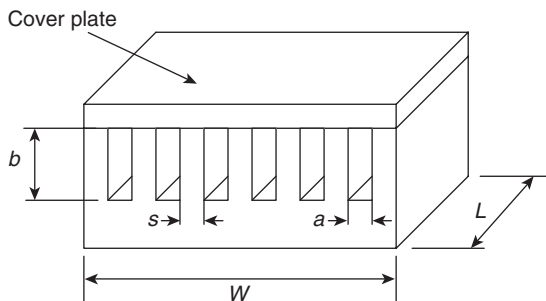


Fig. 3.19. Microchannel geometry used in microprocessor heat sink channel size optimization, Kandlikar and Upadhye (2005).

fin thickness using silicon microfabrication techniques. For a given pressure drop limit, the optimal number of channels and other channel geometrical parameters can be determined from this plot. Such plots could be generated for other system configurations as well.

The effect of introducing offset strip-fins in the microchannel flow passages and a split flow arrangement, as shown in Figs. 3.22 and 3.23 respectively, was also analyzed by

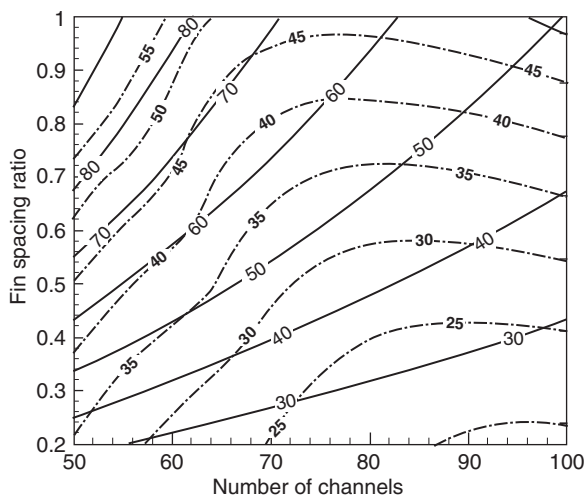


Fig. 3.20. Contour plot of fin spacing ratio β versus the number of channels with pressure drop across them in kPa (dash-dot lines) and fin thickness in μm (solid lines) as parameters for water flow in plain rectangular microchannels in a single-pass arrangement at a heat flux of 3 MW/m^2 , Kandlikar and Upadhye (2005).

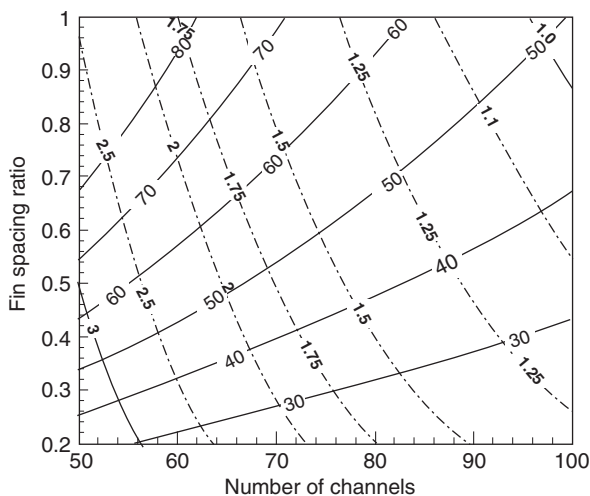


Fig. 3.21. Contour plot of fin spacing ratio β versus the number of channels with water flow rate in 10^{-3} kg/s (dash-dot lines) and fin thickness in μm (solid lines) as parameters for water flow in plain rectangular microchannels in a single-pass arrangement at a heat flux of 3 MW/m^2 , Kandlikar and Upadhye (2005).

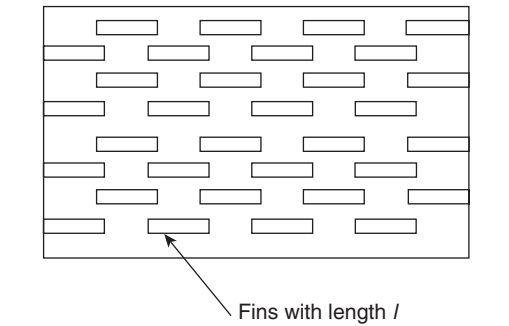


Fig. 3.22. Offset strip-fins shown in the top view, with individual fin length l along the flow length, Kandlikar and Upadhye (2005).

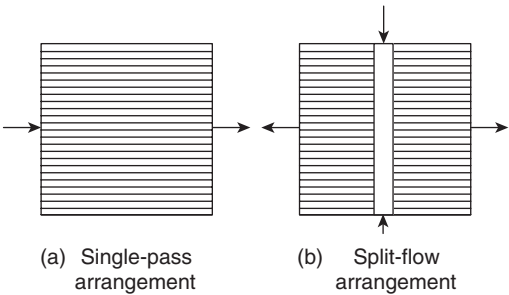


Fig. 3.23. Schematics of single-pass and split-flow arrangements for fluid flow through microchannels, Kandlikar and Upadhye (2005).

Kandlikar and Upadhye (2005). The resulting pressure drop versus the dissipated heat flux is shown in Fig. 3.24. It can be seen that the pressure drop is reduced considerably in the split flow arrangement.

3.7. Enhanced microchannels

The use of enhanced microchannels was proposed by Kishimoto and Sasaki (1987). The need for higher heat transfer coefficients than those attainable with plain microchannels was identified by Kandlikar and Grande (2004), and some specific enhancement geometries were suggested by Steinke and Kandlikar (2004). Kandlikar and Upadhye (2005) analyzed the enhanced offset strip-fin geometry and the results were presented in the previous section.

Colgan *et al.* (2005) presented detailed experimental results comparing various offset fin geometries. A three-dimensional rendition is shown in Fig. 3.25. There are several inlet and outlet manifolds, with short flow lengths through the enhanced structures.

The apparent friction factors and Nusselt numbers for plain and several enhanced configurations are shown in Figs. 3.26 and 3.27. A plot of f_{app} versus Stanton number is shown in Fig. 3.28. The relationship deviates somewhat from a linear behavior because the manifold effects are included in the data.

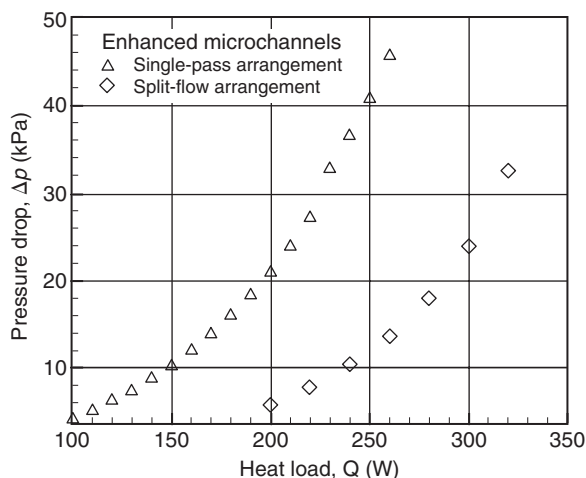


Fig. 3.24. Comparison of pressure drops for the enhanced microchannels with offset strip-fins ($l = 0.5$ mm) in single-pass and split-flow arrangements on a $10 \text{ mm} \times 10 \text{ mm}$ chip, Kandlikar and Upadhye (2005).

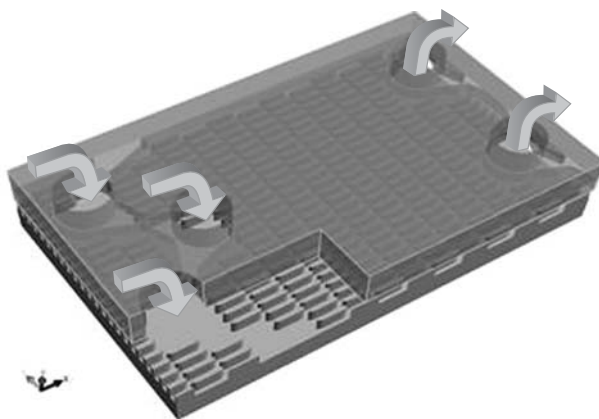


Fig. 3.25. Three-dimensional rendition of the IBM enhanced silicon chip with short multiple fluid streams. (Colgan *et al.*, 2005).

Microfabrication technology opens up a whole new set of possibilities for incorporating enhancement structures derived from past experience in compact heat exchanger development. Different manufacturing constraints enter into play for microchannels on a copper substrate as compared to the silicon microfabrication technology. Novel developments are expected to arise as we continue forward in integrating the microfabrication technology using creative ways to achieve high-performance heat transfer devices. Steinke and Kandlikar (2004) present a good overview of single-phase enhancement techniques and illustrate various enhancement configurations that may be considered especially with silicon microfabrication technology.

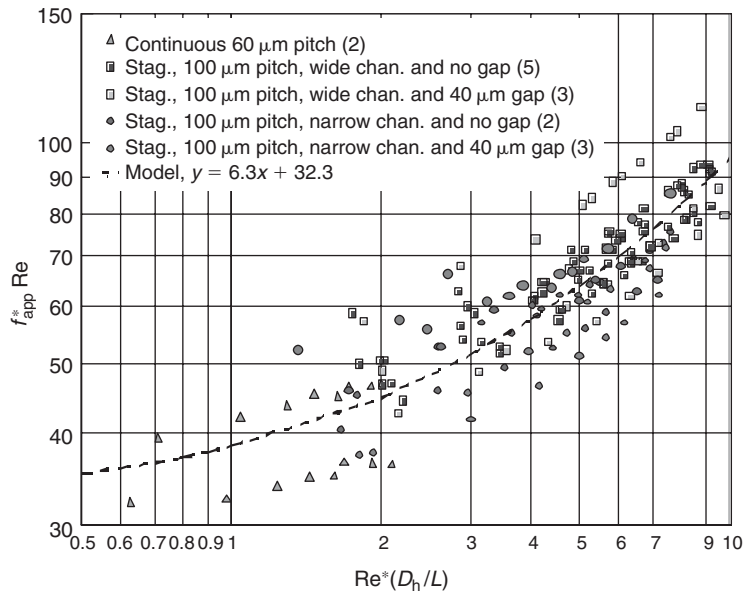


Fig. 3.26. Apparent friction factor comparison of a plain and five enhanced microchannel configurations, Colgan *et al.* (2005).

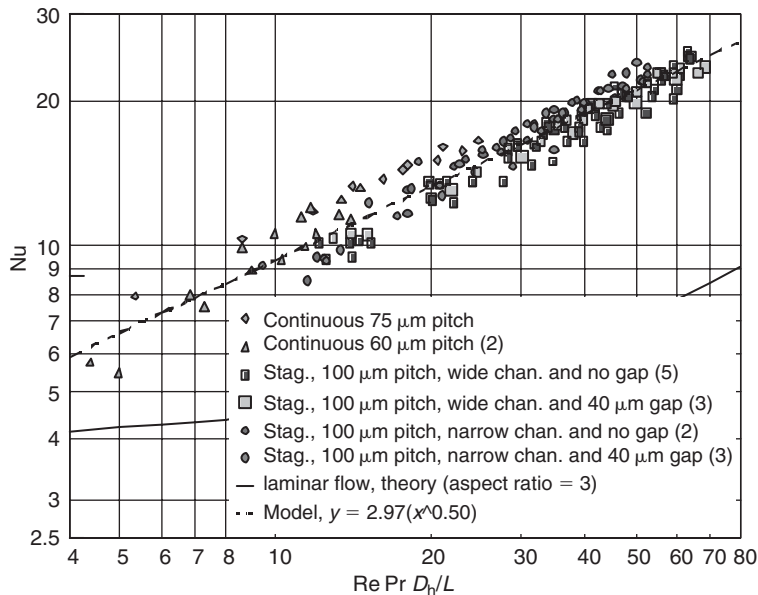


Fig. 3.27. Nusselt number comparison of a plain and five enhanced microchannel configurations, Colgan *et al.* (2005).

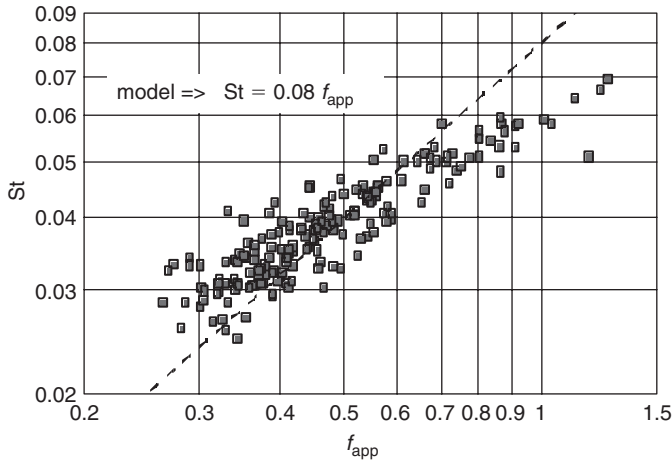


Fig. 3.28. Stanton number and friction coefficient relationship for microchannels with different fin geometries, Colgan *et al.* (2005).

3.8. Solved examples

Example 3.1

Microchannels are directly etched into silicon in order to dissipate 100 Watts from a computer chip over an active surface area of $10 \text{ mm} \times 10 \text{ mm}$. The geometry may be assumed similar to Fig. 3.19. Each of the parallel microchannels has a width $a = 50 \text{ }\mu\text{m}$, depth $b = 350 \text{ }\mu\text{m}$, and a spacing $s = 40 \text{ }\mu\text{m}$. The silicon thermal conductivity may be assumed to be $k = 180 \text{ W/m-K}$.

Assume a uniform heat load over the chip base surface and a maximum water inlet temperature of 35°C . Assume one-dimensional steady state conduction in the chip substrate.

- (i) Calculate the number of flow channels available for cooling.
- (ii) Assuming the temperature rise of the water to be limited to 10°C , calculate the required mass flow rate of the water.
- (iii) Calculate the flow Reynolds number using the mean water temperature for fluid properties.
- (iv) Check whether the fully developed flow assumption is valid.
- (v) Calculate the average heat transfer coefficient in the channels.
- (vi) Calculate fin efficiency.
- (vii) Assuming the heat transfer coefficient to be uniform over the microchannel surface, calculate the surface temperature at the base of the fin at the fluid inlet and fluid outlet sections.
- (viii) Calculate the pressure drop in the core of the microchannel.
- (ix) If two large reservoirs are used as the inlet and outlet manifolds, calculate the total pressure drop between the inlet and the outlet manifolds.

Solution

Properties: Water at 40°C (Incropera and DeWitt (2002))

$\rho = 991.8 \text{ kg/m}^3$; $\mu = 655 \times 10^{-6} \text{ N-s/m}^2$; $c_p = 4179 \text{ J/kg-K}$; $k = 0.632 \text{ W/m-K}$; $\text{Pr} = 4.33$

(i) Number of flow channels (Answer: 111 channels)*Assumptions*

(1) The first and the last channels are half the channel width from the chip edge.

The remaining width left for channels is: $10 \text{ mm} - 50 \mu\text{m} = 0.00995 \text{ m}$.

The pitch is: $50 \mu\text{m} + 40 \mu\text{m} = 90 \mu\text{m} = 90 \times 10^{-6} \text{ m}$.

Assumption 1 requires that the pitch repeat up to the last channel, but not include the last channel.

Therefore, the number of channels is found by: $(0.00995 \text{ m} - 50 \times 10^{-6} \text{ m}) / (90 \times 10^{-6} \text{ m}) = 110$ channels.

But recall that the above calculation was for a repeating pitch up to but not including the last channel so the number of channels available for cooling is $n = 111$.

(ii) Required flow rate of water (Answer: 0.00239 kg/s or 143.6 ml/min, total)

The inlet water temperature is given as 35°C, and the stated assumption is that the water temperature rise is limited to 10°C. The mass flow rate can be calculated using the properties of water at the average temperature of 40°C by using the equation $q = \dot{m}c_p\Delta T$ where q is the power dissipated from the chip, c_p is the specific heat of water at constant pressure and ΔT is the temperature change of the water. The total mass flow rate is

$$\dot{m}_t = \frac{q}{c_p\Delta T} = 100 \text{ W} / (4179 \text{ J/kg-K})(10 \text{ K}) = 0.00239 \text{ kg/s} = 143.6 \text{ ml/min},$$

and the mass flow rate in one channel is given by

$$\dot{m}_c = \frac{q}{nc_p\Delta T} = 21.6 \times 10^{-6} \text{ kg/s} = 1.3 \text{ ml/min}$$

(iii) Flow Reynolds number (Answer: Re = 164.7)

The flow Reynolds number using the mean water temperature (40°C) for fluid properties can be found using the hydraulic diameter D_h given by Eq. (3.7)

$$\begin{aligned} D_h &= \frac{2ab}{(a+b)} = 2(50 \times 10^{-6} \text{ m})(350 \times 10^{-6} \text{ m}) / (50 \times 10^{-6} \text{ m} + 350 \times 10^{-6} \text{ m}) \\ &= 87.5 \times 10^{-6} \text{ m} \end{aligned}$$

in the Reynolds number equation given by

$$\begin{aligned} \text{Re} &= \frac{\rho u_m D_h}{\mu} = \frac{\rho u_m A_c D_h}{A_c \mu} = \frac{\dot{m}_c D_h}{A_c \mu} \\ &= \frac{(21.6 \times 10^{-6} \text{ kg/s})(87.5 \times 10^{-6} \text{ m})}{(17.5 \times 10^{-9} \text{ m}^2)(655 \times 10^{-6} \text{ N-s/m}^2)} = 164.7 \end{aligned}$$

This low Reynolds number clearly indicates laminar flow regime.

(iv) Fully developed assumption (Answer: fully developed assumption is valid – hydrodynamic entrance length = 0.72 mm and thermal entrance length = 6.25 mm)

The fully developed flow assumption is valid if the thermal and hydrodynamic entrance lengths are less than the channel length. For laminar flow, the hydrodynamic entrance length is given by Eq. (3.11) as

$$L_h = 0.05 \text{ Re } D_h = 0.05(164.7)(87.5 \times 10^{-6} \text{ m}) = 720 \times 10^{-6} \text{ m} \\ = 0.72 \text{ mm},$$

and the thermal entrance length is given by Eq. (3.42) as

$$L_t = 0.1 \text{ Re } \text{Pr } D_h = 0.1(164.7)(4.33)(87.5 \times 10^{-6} \text{ m}) = 6.24 \times 10^{-3} \text{ m} \\ = 6.24 \text{ mm}$$

Since the thermal and hydrodynamic entrance lengths are less than the channel length, the fully developed flow assumption is valid.

(v) Average heat transfer coefficient (Answer: $47.4 \times 10^3 \text{ W/m}^2\text{-K}$)

Assumptions

- (1) Constant heat flux boundary condition.
- (2) Three-sided heating condition.

The Nusselt number using the thermal conductivity of water at the average temperature (40°C) is given by $\text{Nu} = \bar{h} D_h / k$. A value for the fully developed Nusselt number can be obtained from Table 3.3 using the aspect ratio of the channel $\alpha_c = a/b = 1/7$. By linear interpolation, the Nusselt number is $\text{Nu}_{\text{fd},3} = 6.567$.

The average heat transfer coefficient is

$$\bar{h} = \frac{k \text{Nu}}{D_h} = (0.632 \text{ W/m-K})(6.567)/87.5 \times 10^{-6} \text{ m} = 47.4 \times 10^3 \text{ W/m}^2\text{-K}$$

(vi) Fin efficiency (Answer: 67%)

Assumptions

- (1) Adiabatic tip condition.

For an adiabatic tip, the fin efficiency equation is given by $\eta_f = \tanh(mb)/mb$ where b is the fin height

$$(350 \times 10^{-6} \text{ m}) \text{ and } m \text{ is defined as } m = (\bar{h}P/kA_c)^{1/2}$$

In the above equation, k is thermal conductivity of the fin material (given as $k = 180 \text{ W/m-K}$), A_c is the cross-sectional area of the fin $L \times s = (0.01 \text{ m})(40 \times 10^{-6} \text{ m})$, and P is the perimeter of the fin which can be defined as $2L$ since the width of the fin is much smaller than its length. The term mb can be written as

$$mb = \left(\frac{\bar{h}2L}{ksL} \right)^{1/2} b = \left(\frac{2\bar{h}}{ks} \right)^{1/2} b \\ = \left(\frac{2(47.4 \times 10^3 \text{ W/m}^2\text{-K})}{(180 \text{ W/m-K})(40 \times 10^{-6} \text{ m})} \right)^{1/2} (350 \times 10^{-6} \text{ m}) = 1.270$$

Therefore, the fin efficiency can be calculated as $\eta_f = \tanh(1.270)/1.270 = 0.672 = 67\%$.

(vii) Inlet and outlet surface temperatures at the base of the fin (Answer: $T_{s,i} = 36.3^\circ\text{C}$ and $T_{s,o} = 48.6^\circ\text{C}$)

Assumptions

(1) The heat flux is constant over the chip surface.

The surface heat flux considering the fin efficiency is given by

$$\begin{aligned} q'' &= q/(2b\eta_f + a)nL \\ &= \frac{100 \text{ W}}{[2(350 \times 10^{-6} \text{ m})(0.672) + 50 \times 10^{-6} \text{ m}](111)(0.01 \text{ m})} \\ &= 173 \times 10^3 \text{ W/m}^2 \end{aligned}$$

The relationship between heat flux, heat transfer and temperature difference is given by $q'' = h(T_s - T_f)$ where the subscripts s and f refer to the surface and fluid, respectively. The *local* heat transfer coefficients at the inlet and outlet of the microchannels are needed in order to compute the surface temperatures. Since the flow is developing at the entrance of the microchannel, Tables 3.3 and 3.4 are used with the channel aspect ratio and x^* for the inlet, where x^* is defined by Eq. (3.44). The entrance of the channel is assumed to begin at $x = 0.1 \text{ mm}$ from the edge of the chip so x^* is

$$x_{in}^* = \frac{0.1 \times 10^{-3} \text{ m}}{(87.5 \times 10^{-6} \text{ m})(164.7)(4.33)} = 1.603 \times 10^{-3}$$

Using linear interpolation in Table 3.3, the fully developed Nusselt numbers for three-sided and four-sided heating are found to be 6.567 and 6.273, respectively. The thermal entry region Nusselt number for four-sided heating is found using Table 3.4 to be 18.42 for the inlet. Equation (3.45) is used to obtain the local Nusselt number at the entrance as

$$\text{Nu}_{x,3}(x^*, \alpha_c) = 18.42 \frac{6.567}{6.273} = 19.28$$

Alternatively, equations given in Appendix A may be used for interpolating values from Tables 3.2 to 3.4.

Using the thermal conductivity of water at the given inlet temperature (35°C), the local heat transfer coefficient at the inlet is found to be

$$h = \frac{k\text{Nu}}{D_h} = (0.625 \text{ W/m-K})(19.28)/87.5 \times 10^{-6} \text{ m} = 137.7 \times 10^3 \text{ W/m}^2\text{-K}$$

Since the flow is fully developed at the outlet, the three-sided Nusselt number from Table 3.3 is used with the thermal conductivity of water at the outlet temperature (45°C). The local heat transfer coefficient at the exit is found to be

$$h = \frac{k\text{Nu}}{D_h} = (0.638 \text{ W/m-K})(6.567)/87.5 \times 10^{-6} \text{ m} = 47.9 \times 10^3 \text{ W/m}^2\text{-K}$$

Using the value of the heat flux obtained above, the local heat transfer coefficients, and the given inlet and outlet water temperatures, the surface temperatures at the base of the fin at the fluid inlet and outlet are

$$T_s = \frac{q''}{h} + T_f \Rightarrow T_{s,i} = 36.3^\circ\text{C} \quad \text{and} \quad T_{s,o} = 48.6^\circ\text{C}$$

(viii) Pressure drop in microchannel core (Answer: 43.6 kPa)

Assumptions

- (1) The core of the microchannel includes pressure drop due to only frictional losses in the fully developed region and the loss due to the developing region.

Since the flow is fully developed at the exit, the pressure drop is defined by

$$\Delta p = \frac{2(f \text{Re})\mu u_m L}{D_h^2} + K(\infty) \frac{\rho u_m^2}{2}$$

where $K(\infty)$ is the Hagenbach factor, which is defined by Eq. (3.18) as

$$\begin{aligned} K(\infty) &= 0.6796 + 1.2197\alpha_c + 3.3089\alpha_c^2 - 9.5921\alpha_c^3 + 8.9089\alpha_c^4 - 2.9959\alpha_c^5 \\ &= 0.8969 \end{aligned}$$

The $f \text{Re}$ term is given by Eq. (3.10) as

$$\begin{aligned} f \text{Re} &= 24(1 - 1.3553\alpha_c + 1.9467\alpha_c^2 - 1.7012\alpha_c^3 + 0.9564\alpha_c^4 - 0.2537\alpha_c^5) \\ &= 20.2 \end{aligned}$$

The pressure drop in the core of the microchannel is given by Eq. (3.14) as

$$\begin{aligned} \Delta p &= \frac{2(20.2)(655 \times 10^{-6} \text{ N}\cdot\text{s}/\text{m}^2)(1.24 \text{ m/s})(0.01 \text{ m})}{(87.5 \times 10^{-6} \text{ m})^2} \\ &\quad + (0.8969) \frac{(991.8 \text{ kg}/\text{m}^3)(1.24 \text{ m/s})^2}{2} = 43.6 \text{ kPa} \end{aligned}$$

(ix) Total pressure drop (Answer: 45.0 kPa)

Assumptions

- (1) Reservoirs are large so the Area of the reservoir \gg the Area of microchannel.

The total pressure drop between the inlet and outlet manifolds would include the pressure drop calculated above (43.6 kPa) plus the minor losses at the entrance and exit.

The minor loss is defined by $\Delta p = K(\rho u_m^2/2)$ where K is a loss coefficient related to area changes at the entrance or exit. Taking the area ratio as zero, based on Assumption 1, for a laminar flow regime, the contraction and expansion loss coefficients K_c and K_e can be obtained from Fig. 3.5(b) as $K_c = 0.8$ and $K_e = 1.0$.

The total pressure drop is obtained by

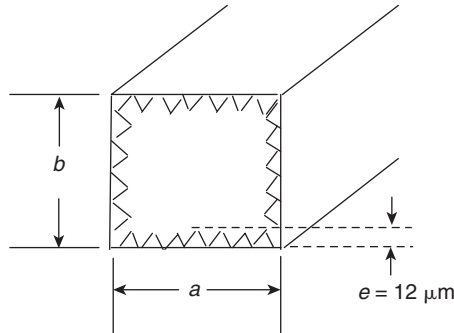
$$\Delta p = \frac{2(f \text{Re})\mu u_m L}{D_h^2} + K(\infty)\frac{\rho u_m^2}{2} + K_c\frac{\rho u_m^2}{2} + K_e\frac{\rho u_m^2}{2} = 45.0 \text{ kPa}$$

The contraction and expansion coefficients were taken as the largest values on the chart in Fig. 3.5(b) in order to design for the maximum expected pressure drop.

Example 3.2

A microchannel is etched in silicon. The microchannel surface is intentionally etched to provide an average roughness of $12 \mu\text{m}$. The microchannel dimensions measured from the root of the roughness elements are: width – $200 \mu\text{m}$, height – $200 \mu\text{m}$, length – 10 mm . Water flows through the microchannels at a temperature of 300 K . Calculate the core frictional pressure drop when, (i) $\dot{m} = 90 \times 10^{-6} \text{ kg/s}$, and (ii) $\dot{m} = 180 \times 10^{-6} \text{ kg/s}$.

Schematic



Solution

Properties: From Incropera and DeWitt (2002), saturated water at 300 K : $\mu_f = 0.855 \times 10^{-3} \text{ N}\cdot\text{s}/\text{m}^2$, $\rho = 997 \text{ kg}/\text{m}^3$, $c_{p,f} = 4179 \text{ J}/\text{kg}\cdot\text{K}$, $k_f = 0.613 \text{ W}/\text{m}\cdot\text{K}$.

(i) Core frictional pressure drop when $\dot{m} = 90 \times 10^{-6} \text{ kg/s}$ (Answer: 29,365 Pa)

Calculate the hydraulic diameter using the constricted width (a_{cf}) and constricted height (b_{cf}) in Eq. (3.6)

$$D_{h,cf} = \frac{4A_c}{P_w} = a_{cf} = b_{cf} = 0.000176 \text{ m}$$

Calculate the Reynolds number of the fluid in a microchannel using Eq. (3.33)

$$Re_{cf} = \frac{\rho u_{m,cf} D_{h,cf}}{\mu} = \frac{(997.01 \text{ kg}/\text{m}^3)(2.91 \text{ m/s})(176 \times 10^{-6} \text{ m})}{(0.855 \times 10^{-3} \text{ N}\cdot\text{s}/\text{m}^2)} = 598$$

For fully developed laminar flow, the hydrodynamic entry length may be obtained using Eq. (3.11)

$$L_{h,cf} = 0.05 \text{Re}_{cf} D_{h,cf} = 0.05(598)(0.176 \text{ mm}) = 5.26 \text{ mm}$$

Since $L > L_{h,cf}$, the fully developed flow assumption is valid.

The $f\text{Re}$ term can be obtained using Eq. (3.10)

$$\begin{aligned} f\text{Re} &= 24(1 - 1.3553\alpha_c + 1.9467\alpha_c^2 - 1.7012\alpha_c^3 + 0.9564\alpha_c^4 - 0.2537\alpha_c^5) \\ &= 14.23 \end{aligned}$$

The core frictional pressure drop can be calculated using Eq. (3.14)

$$\Delta p = \frac{2(f\text{Re})\mu_{m,cf}L}{D_{h,cf}^2} + K(\infty)\frac{\rho u_{m,cf}^2}{2}$$

where $K(\infty)$ is given by Eq. (3.18)

$$\begin{aligned} K(\infty) &= (0.6796 + 1.2197\alpha_c + 3.3089\alpha_c^2 - 9.5921\alpha_c^3 + 8.9089\alpha_c^4 - 2.9959\alpha_c^5) \\ &= 1.53 \end{aligned}$$

Hence

$$\begin{aligned} \Delta p &= \frac{2(14.23)(0.855 \times 10^{-3} \text{ Ns/m}^2)(2.91 \text{ m/s})(0.01 \text{ m})}{(176 \times 10^{-6} \text{ m})^2} \\ &\quad + (1.53)\frac{(997.01 \text{ kg/m}^3)(2.91 \text{ m/s})^2}{2} = 29,365 \text{ Pa} \end{aligned}$$

(ii) Core frictional pressure drop when $\dot{m} = 180 \times 10^{-6} \text{ kg/s}$ (Answer: 68,694 Pa)

Calculate the Reynolds number of the fluid in a microchannel using Eq. (3.33)

$$\text{Re}_{cf} = \frac{\rho u_{m,cf} D_{h,cf}}{\mu} = \frac{(997.01 \text{ kg/m}^3)(5.83 \text{ m/s})(176 \times 10^{-6} \text{ m})}{(0.855 \times 10^{-3} \text{ Ns/m}^2)} = 1200$$

For fully developed laminar flow, the hydrodynamic entry length may be obtained using Eq. (3.11)

$$L_{h,cf} = 0.05 \text{Re}_{cf} D_{h,cf} = 0.05(1200)(0.176 \text{ mm}) = 10.5 \text{ mm}$$

Since $L < L_{h,cf}$, the fully developed flow assumption is not valid.

Calculate the core frictional pressure drop with the developing laminar flow assumption. The apparent friction factor can be obtained from Table 3.2 using x^+ calculated from Eq. 3.16

$$x^+ = \frac{x/D_h}{\text{Re}_{cf}} = \frac{0.01 \text{ m}}{(176 \times 10^{-6} \text{ m})(1200)} = 0.0475$$

From Table 3.2 $f_{\text{app}} \text{Re} = 21.35$ so the core frictional pressure drop can be calculated using the following equation

$$\begin{aligned} \Delta p &= \frac{2(f_{\text{app}} \text{Re}) \mu_{\text{m,cf}} L}{D_{\text{h,cf}}^2} \\ &= \frac{2(21.35)(0.855 \times 10^{-3} \text{ Ns/m}^2)(5.83 \text{ m/s})(0.01 \text{ m})}{(176 \times 10^{-6} \text{ m})^2} = 68,694 \text{ Pa} \end{aligned}$$

Comments

- (1) The total frictional pressure drop has to consider the minor losses because the actual Δp is higher than the core frictional pressure drop.

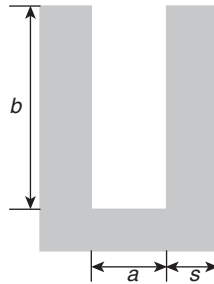
Example 3.3

Consider a copper minichannel heat sink with an area of $30 \text{ mm} \times 30 \text{ mm}$, and relevant dimensions in Fig. 3.14 with $a = 1 \text{ mm}$, $b = 3 \text{ mm}$, and $s = 1.5 \text{ mm}$. The heat dissipation is 100 W and the water inlet temperature is 30°C . The maximum surface temperature in the heat sink is limited to 80°C . Calculate the water flow rate under these conditions. Also calculate the frictional pressure drop in the core. Assume a constant heat transfer coefficient corresponding to fully developed conditions and take the thermal conductivity of copper to be 400 W/m-K .

Assumptions

Laminar flow, constant heat flux equally distributed over the surface area, one-dimensional steady state conduction, and three-sided heated condition with an adiabatic tip for fin efficiency

$a = 1 \text{ mm} = 10^{-3} \text{ m}$, $b = 3 \text{ mm} = 3 \times 10^{-3} \text{ m}$, $s = 1.5 \text{ mm} = 1.5 \times 10^{-3} \text{ m}$, $w = L = 30 \times 10^{-3} \text{ m}$, $T_{\text{f,i}} = 30^\circ\text{C}$, $T_{\text{s,o}} = 80^\circ\text{C}$, $q = 100 \text{ W}$, $k_{\text{Cu}} = 400 \text{ W/m-K}$, $A_{\text{c}} = a \times b = 3 \times 10^{-6} \text{ m}^2$, $\alpha_{\text{c}} = a/b = 1/3$



Solution

Equation 3.7 gives the hydraulic diameter,

$$D_{\text{h}} = \frac{2ab}{(a+b)} = \frac{2(10^{-3})(3 \times 10^{-3})}{(10^{-3} + 3 \times 10^{-3})} = 1.5 \times 10^{-3} \text{ m}$$

The Nusselt number can be obtained using Table 3.3 for a three-sided heated channel. Through interpolation this gives,

$$\text{Nu} = \text{Nu}_{\text{fd},3} = 5.224$$

For calculating water properties, let's assume the water exit temperature is equal to the maximum surface temperature of the heat sink. Then, the average water temperature is,

$$T_{\text{avg}} = (30^\circ\text{C} + 80^\circ\text{C})/2 = 55^\circ\text{C}$$

Properties of water at 55°C (from Incropera and DeWitt, 2002):

$$\rho = 985 \text{ kg/m}^3, \quad c_p = 4.183 \text{ kJ/kg-K}, \quad \mu = 505 \times 10^{-6} \text{ kg/m-s},$$

$$k = 648 \times 10^{-3} \text{ W/m-K}$$

The average heat transfer coefficient is calculated using the Nusselt number which is rearranged to give,

$$\bar{h} = \frac{k\text{Nu}}{D_h} = \frac{(0.648)(5.224)}{(1.5 \times 10^{-3})} = 2.26 \times 10^3 \text{ W/m}^2\text{-K}$$

By relating the conductive and convective heat transfer for a constant heat flux, the average temperature difference between the surface and the fluid is given as

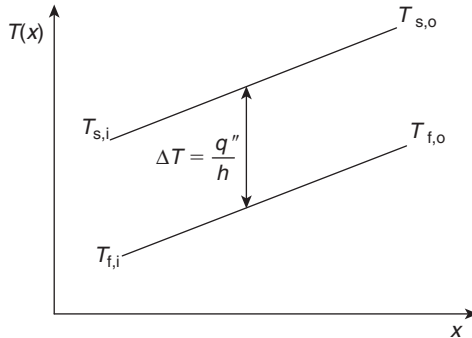
$$\Delta T = \frac{q}{h(2b\eta_f + a)nL}$$

$$\text{The number of channels is, } n = \frac{\text{overall width}}{\text{channel} + \text{fin}} = \frac{w}{a + s} = \frac{0.030}{0.001 + 0.0015} = 12$$

$$\text{The fin efficiency is, } \eta_f = \frac{\tanh(mb)}{mb}$$

$$mb = \sqrt{\frac{2\bar{h}}{k_{\text{Cu}}s}} \quad b = \sqrt{\frac{2(2.26 \times 10^3)}{(400)(1.5 \times 10^{-3})}} \times (3 \times 10^{-3}) = 0.260$$

$$\eta_f = \frac{\tanh(0.260)}{(0.260)} = 0.978$$



$$\Delta T = \frac{100}{(2.26 \times 10^3)[2(3 \times 10^{-3})(0.978) + 10^{-3}](12)(30 \times 10^{-3})} = 17.9^\circ\text{C}$$

The fluid outlet temperature is, $T_{f,o} = T_{s,o} - \Delta T = 80^\circ\text{C} - 17.9^\circ\text{C} = 62.1^\circ\text{C}$

The average water temperature is, $T_{\text{avg}} = (30^\circ\text{C} + 62.1^\circ\text{C})/2 = 46.1^\circ\text{C}$

T_{avg} is off by 9 degrees. It is necessary to iterate again with the updated average temperature of 46°C

Properties of water at 46°C (from Incropera and De Witt, 2002):

$\rho = 990 \text{ kg/m}^3$, $c_p = 4.180 \text{ kJ/kg-K}$, $\mu = 588 \times 10^{-6} \text{ kg/m-s}$, $k = 639 \times 10^{-3} \text{ W/m-K}$

Following identical steps the new values are,

$$\bar{h} = 2.23 \times 10^3 \text{ W/m}^2\text{-K}, \quad mb = 0.258, \quad \eta_f = 0.978, \quad \Delta T = 18.2^\circ\text{C}, \quad T_{f,o} = 61.8^\circ\text{C}$$

$$T_{\text{avg}} = (30 + 61.8)/2 = 45.9^\circ\text{C}$$

The calculated average temperature is approximately the same as the assumed value. No more iterations are necessary.

$$T_{s,i} = T_{f,i} + \Delta T = 30^\circ\text{C} + 18.2^\circ\text{C} = 48.2^\circ\text{C}$$

$$q = \dot{m}c_p\Delta T_{\text{fluid}}$$

$$\dot{m}_t = \frac{q}{c_p\Delta T_{\text{fluid}}} = \frac{(100)}{(4180)(61.8 - 30)} = 752 \times 10^{-6} \text{ kg/s}$$

$$Q_c = \frac{\dot{m}_t(1/n)}{\rho} = \frac{(752 \times 10^{-6})(1/12)}{(990)} = 63.3 \times 10^{-9} \text{ m}^3/\text{s} \quad \text{or} \quad 3.80 \text{ ml/min}$$

$$u_m = \frac{Q_c}{A_c} = \frac{(63.3 \times 10^{-9})}{(3 \times 10^{-6})} = 0.0211 \text{ m/s}$$

$$\text{Re} = \frac{D_h u_m \rho}{\mu} = \frac{(1.5 \times 10^{-3})(0.0211)(990)}{(588 \times 10^{-6})} = 53.3$$

Flow is laminar so original assumption is correct.

$$\text{Equation 3.14 gives the pressure drop, } \Delta p = \frac{2(f\text{Re})\mu u_m L}{D_h^2} + K(\infty) \frac{\rho u_m^2}{2}$$

$f\text{Re}$ can be determined with Eq. 3.10,

$$f\text{Re} = 24(1 - 1.3553\alpha_c + 1.9467\alpha_c^2 - 1.7012\alpha_c^3 + 0.9564\alpha_c^4 - 0.2537\alpha_c^5) = 17.1$$

Hagenbach's factor comes from Eq. (3.22),

$$\begin{aligned} K(\infty) &= 0.6796 - 1.2197\alpha_c + 3.3089\alpha_c^2 - 9.5921\alpha_c^3 + 8.9089\alpha_c^4 - 2.9959\alpha_c^5 \\ &= 1.20 \end{aligned}$$

The pressure drop in the core is therefore,

$$\Delta p = \frac{2(17.1)(588 \times 10^{-6})(0.0211)(30 \times 10^{-3})}{(1.5 \times 10^{-3})^2} + (1.20) \frac{(990)(0.0211)^2}{2} = 5.92 \text{ Pa}$$

We need to calculate the hydrodynamic and thermal entrance lengths to justify fully developed conditions.

Using Eq. (3.11) we have, $L_h = 0.05 D_h \text{ Re} = 0.05(1.5 \times 10^{-3})(53.3) = 0.00400 \text{ m} = 4.00 \text{ mm}$

Similarly Eq. (3.42) gives, $L_t = 0.05 D_h \text{ Re Pr} = 0.05(1.5 \times 10^{-3})(53.3)(3.85) = 0.0154 \text{ m} = 15.4 \text{ mm}$

This validates the fully developed assumption as given in the problem statement.

Comments

If the heat dissipation is increased to 200 W the flow rate will be 18.4 ml/min. This increases the pressure drop to 38.8 Pa. This illustrates the performance hit for increased heat dissipation and the need to develop microchannel cooling under turbulent conditions where the heat transfer coefficient will be larger. For turbulent flow more heat can be dissipated with minimal performance loss in pressure drop.

3.9. Practice problems

Problem 3.1 Solve Example 1 with the substrate as copper, with a thermal conductivity of 380 W/m-K.

Problem 3.2 For Example 3.1, plot the outlet surface temperature and pressure drop as a function of the channel depth b over a range of 200 to 600 μm .

Problem 3.3 For Example 3.1, plot the outlet surface temperature and pressure drop as a function of the channel width a over a range of 50 to 200 μm .

Problem 3.4 Solve Example 3.1 with a split flow arrangement. Neglect the area reduction caused by the central manifold.

Problem 3.5 Solve Example 3.1 with copper substrate and a split flow arrangement. Assume the channel width to be 100 μm and a depth of 800 μm . Neglect the area reduction caused by the central manifold.

Problem 3.6 For Example 3.3 with copper, plot the outlet surface temperature and the pressure drop as a function of the channel depth over a range of 200 to 2000 μm .

Problem 3.7 In Example 3.3, redesign the heat sink if the design heat load increases to 500 W. You may have to rework the channel geometry and flow arrangements.

Problem 3.8 Design a microchannel heat exchanger to dissipate 800 Watts from a copper heat sink of 20 mm \times 20 mm heated surface area. The inlet water temperature is 40°C, and

the maximum surface temperature in the heat sink is desired to be below 60°C. Check your channel dimensions from manufacturing standpoint (provide the manufacturing technique you will be implementing). Do not neglect the temperature drop occurring in the copper between the base of the channels and the bottom surface of the heat sink receiving heat. Show the details of the manifold design.

Problem 3.9 A copper minichannel heat sink with an area of 30 mm × 30 mm, and relevant dimensions in Fig. 3.14 are $a = 1$ mm, $b = 3$ mm, and $s = 1.5$ mm. Calculate the maximum heat dissipation possible with an inlet water temperature of 30°C and the maximum surface temperature in the heat sink is limited to 80°C. Calculate the water flow rate under these conditions. Also calculate the frictional pressure drop in the core under these conditions.

Problem 3.10 Design a minichannel heat exchanger to dissipate 5 kW of heat from a copper plate with a footprint of 10 cm × 12 cm. The plate surface temperature should not exceed 60°C and the inlet design temperature for water is 35°C. Calculate the water flow rate, outlet water temperature, and core frictional pressure drop. Compare the performance of (a) straight once-through flow passages and (b) split flow passages.

Problem 3.11 Design the heat exchanger for Problem 3.10 in aluminum, and compare its performance with a copper heat sink.

Appendix A

Table A.1
Curve-fit equations for Tables 3.2, 3.3, and 3.4

Equations	Constants					
	<i>a</i>	<i>b</i>	<i>c</i>	<i>d</i>	<i>e</i>	<i>f</i>
1	141.97	−7.0603	2603	1431.7	14364	−220.77
2	142.05	−5.4166	1481	1067.8	13177	−108.52
3	142.1	−7.3374	376.69	800.92	14010	−33.894
4	286.65	25.701	337.81	1091.5	26415	8.4098
5	8.2321	2.0263	1.2771	0.29805	2.2389	0.0065322
6	8.2313	1.9349	−2.295	0.92381	7.928	0.0033937
7	36.736	2254	17559	66172	555480	1212.6
8	30.354	1875.4	13842	154970	783440	−8015.1
9	31.297	2131.3	14867	144550	622440	−13297
10	28.315	3049	27038	472520	1783300	−35714
11	6.7702	−3.1702	0.4187	2.1555	2.76×10^{-6}	NA
12	9.1319	−3.7531	0.48222	2.5622	5.16×10^{-6}	NA

Equation form:

Equations 1–4: $y = \frac{a + cx^{0.5} + ex}{1 + bx^{0.5} + dx + fx^{1.5}}$; Equations 5–10: $y = \frac{a + cx + ex^2}{1 + bx + dx^2 + fx^3}$
Equations 11–12: $y = a + bx + c(\ln x)^2 + d \ln x + ex^{-1.5}$

Equation variables

Laminar flow friction factor in entrance region of rectangular ducts, Table 3.2:

y -variable – friction factor

x -variable – Equation 1: $\alpha_c = 1.0$

Equation 2: $\alpha_c = 0.5$

Equation 3: $\alpha_c = 0.2$

Equation 4: $0.1 = \alpha_c = 10$

Fully developed Nusselt number for three-side heating, Table 3.3:

y -variable – Nusselt number for three-sided heating

x -variable – Equation 5: α_c

Fully developed Nusselt number for four-side heating, Table 3.3:

y -variable – Nusselt number for four-sided heating

x -variable – Equation 6: α_c

Thermal entry region Nusselt numbers for four-sided heating, Table 3.4:

y -variable – Nusselt number for four-sided heating in the entry region

x -variable – Equation 7: $\alpha_c = 0.1$

Equation 8: $\alpha_c = 0.25$

Equation 9: $\alpha_c = 0.333$

Equation 10: $\alpha_c = 0.5$

Equation 11: $\alpha_c = 1.0$

Equation 12: $\alpha_c = 10$

References

- Adams, T. M., Abdel-Khalik, S. I., Jeter, M., and Qureshi, Z. H., An experimental investigation of single-phase forced convection in microchannels, *Int. J. Heat. Mass Trans.*, **41**(6–7), 851–857, 1997.
- ASME Standard B46.1-2002, Surface Texture (Surface Roughness, Waviness, and Lay), *The American Society of Mechanical Engineers, An American National Standard*, (ASME B46.1-2002), 1–98.
- Baviere, R. and Ayela, F., First local measurement in microchannels with integrated micromachined strain gauges, *Paper No. ICMM2004-2406, Second International Conference on Microchannels and Minichannels*, Rochester, NY USA, June 17–19, 221–228, 2004.
- Baviere, R., Ayela, F., Le Person, S., and Favre-Marinet, M., 2004, An experimental study of water flow in smooth and rough rectangular microchannels, *Paper No. ICMM2004-2338, Second International Conference on Microchannels and Minichannels*, Rochester, NY USA, June 17–19, 221–228, 2004.
- Bergles, A. E., Lienhard, J. H., V, Kendall, G. E., and Griffith, P., Boiling and condensation in small diameter channels, *Heat Transfer Eng.*, **24**, 18–40, 2003.
- Bucci, A., Celata, G. P., Cumo, M., Serra, E., and Zummo, G., Water single-phase fluid flow and heat transfer in capillary tubes, *Paper No. ICMM2004-2406, Second International Conference on Microchannels and Minichannels*, Rochester, NY USA, June 17–19, 221–228,

2004. *International Conference on Microchannels and Minichannels. Paper # 1037*, ASME, 319–326.
- Celata, G. P., Cumo, M., Guglielmi, M., and Zummo, G., Experimental investigation of hydraulic and single phase heat transfer in 0.130 mm capillary tube, *Microscale Thermophys. Eng.*, **6**, 85–97, 2002.
- Chen, R. Y., Flow in the entrance region at low Reynolds numbers, *J. Fluid. Eng.*, **95**, 153–158, 1972.
- Colgan, E. G., Furman, B., Gaynes, M., Graham, W., LaBianca, N., Magerlein, J. H., Polastre, R. J., Rothwell, M. B., Bezama, R. J., Choudhary, R., Martson, K., Toy, H., Wakil, J., Zitz, J., and Schmidt, R., A practical implementation of silicon microchannel coolers for high power chips, *Invited Paper presented at IEEE-Semi-Therm 21*, San Jose, March 15–17, 2005.
- Curr, R. M., Sharma, D., and Tatchell, D. G., Numerical predictions of some three-dimensional boundary layers in ducts, *Comput. Method. Appl. Mech. Eng.*, **1**, 143–158, 1972.
- Darcy, H., *Recherches experimentales relatives au mouvement de L'Eau dans les Tuyaux*, Paris, France: Mallet-Bachelier, 1857.
- Fanning, J. T., A practical treatise on hydraulic and water supply engineering, New York: Van Nostrand, 1886 (revised edition of 1877).
- Gad-el-Hak, M., The fluid mechanics of microdevices, *J. Fluid. Eng.*, **121**, 7–33, 1999.
- Gamrat, G., Favre-Marinet, M., and Asendrych, D., Numerical modeling of heat transfer in rectangular microchannels, *Paper No. ICM2004-2336*, ASME, *Second International Conference on Microchannels and Minichannels*, June 16–18, Rochester, NY, 205–212, 2004.
- Garimella, S. V., and Singhal, V., Single-phase flow and heat transport and pumping considerations in microchannel heat sinks, *Heat Trans. Eng.*, **25(1)**, 15–25, 2004.
- Gnielinski, V., New equations for heat and mass transfer in turbulent pipe and channel flow, *Int. Chem. Eng.*, **16**, 359–368, 1976.
- Harpole, G. and Eninger, J. E., Micro-channel heat exchanger optimization, *Proceedings – IEEE Semiconductor Thermal and Temperature Measurement Symposium*, 59–63, Feb, 1991.
- Hartnett, J. P., Koh, J. C. Y., and McComas, S. T., A comparison of predicted and measured friction factors for turbulent flow through rectangular ducts, *J. Heat Trans.*, **84**, 82–88, 1962.
- Hornbeck, R. W., Laminar flow in the entrance region of a pipe, *Appl. Sci. Res.*, **13**, 224–232, 1964.
- Jones Jr., O. C., An improvement in the calculation of turbulent friction in rectangular ducts, *J. Fluid. Eng.*, **98**, 173–181, 1976.
- Judy, J., Maynes, D., and Webb, B. W., Characterization of frictional pressure drop for liquid flows through microchannels, *Int. J. Heat Mass Trans.*, **45**, 3477–3489, 2002.
- Kakac, S., Shah, R. K., and Aung, W., *Handbook of Single-Phase Convective Heat Transfer*, New York: John Wiley and Sons, Inc., 1987.
- Kandlikar, S. G. High heat flux removal with microchannels – A roadmap of challenges and opportunities, *Heat Trans. Eng.*, **26(8)**, 2005.
- Kandlikar, S. G. and Grande, W. J., Evaluation of single-phase flow in microchannels for high flux chip cooling – thermohydraulic performance enhancement and fabrication technology, *Heat Trans. Eng.*, **25(8)**, 5–16, 2004.
- Kandlikar, S. G., Joshi, S., and Tian, S., Effect of surface roughness on heat transfer and fluid flow characteristics at low Reynolds numbers in small diameter tubes, *Heat Trans. Eng.*, **24(3)**, 4–16, 2003.
- Kandlikar, S. G. and Upadhye, H. R., Extending the heat flux limit with enhanced microchannels in direct single-phase cooling of computer chips, *Invited Paper presented at IEEE-Semi-Therm 21*, San Jose, March 15–17, 2005.
- Kandlikar, S. G., Schmitt, D., Carrano, A. L., and Taylor, J. B., Characterization of surface roughness effects on pressure drop in single-phase flow in minichannels, *Phys. Fluid.*, **17**, 2005 (accepted).

- Kays, W. M. and London, A. L., *Compact Heat Exchangers*, New York, NY: McGraw-Hill, 1984.
- Kishimoto, T. and Sasaki, S., Cooling characteristics of diamond-shaped interrupted cooling fins for high power LSI devices, *Electron. Letter.*, **23**(9), 456–457, 1987.
- Knight, R. W., Hall, D. J., Goodling, J. S., and Jaeger, R. C., Heat sink optimization with application to microchannels, *IEEE Transactions on Components, Hybrids, and Manufacturing Technology*, **15**(5), 832–842, 1992.
- Koo, J. and Kleinstreuer, C., Analyses of liquid flow in micro-conduits, *Paper No. ICMM2004-2334*, ASME, *Second International Conference on Microchannels and Minichannels*, Rochester, NY, June 17–19, 191–198, 2004.
- Li, Z. X., Du, D. X., and Guo, Z. Y., Experimental study on flow characteristics of liquid in circular microtubes, *Proceeding of the International Conference on Heat Transfer and Transport Phenomena in Microscale*, Banff, Canada, October 15–20, 162–167, 2000.
- Mises, R. v., *Elemente der Technischen Hydrodynamik*, Leipzig, B. G. Teubner, 1914.
- Moody, L. F., Friction factors for pipe flow, *ASME Transactions*, **66**, 671–683, 1944.
- Niklas, M. and Favre-Marinet, M., Pressure losses in a network of triangular minichannels, *ASME, Paper No. ICMM2003-1039*, *First International Conference on Microchannels and Minichannels*, April 24–25, 335–350, 2003.
- Nikuradse, J., *Stromungsgesetze in Rauen Rohren*, VDI-Forschungsheft 361, Belige zu Forschung auf dem Gebiete des Ingenieurwesens Aussage B Band 4, July/August 1933. English Translation *Laws of flow in rough pipes*, *NACA Tech. Mem.* 1292, 1937.
- Phillips, R. J., Forced convection, liquid cooled, microchannel heat sinks, MS Thesis, Department of Mechanical Engineering, Massachusetts Institute of Technology, Cambridge, MA, 1987.
- Phillips, R. J., Microchannel heat sinks, *Advances in Thermal Modeling of Electronic Components and Systems*, New York, NY: Hemisphere Publishing Corporation, 1990, Chapter 3.
- Ryu, J. H., Choi, D. H., and Kim, S. J., Numerical optimization of the thermal performance of a microchannel heat sink, *Int. J. Heat Mass Trans.*, **45**, 2823–2827, 2002.
- Schmitt, D. J. and Kandlikar, S. G., Effects of repeating microstructures on pressure drop in rectangular minichannels, *Paper No. ICMM2005-75111*, ASME, *Third International Conference on Microchannels and Minichannels*, Toronto, Canada, June 13–15, 2005.
- Shah, R. K. and London, A. L., *Laminar Flow Forced Convection in Ducts*, *Supplement 1 to Advances in Heat Transfer*, New York: Academic Press, 1978.
- Shen, P., Aliabadi, S. K., and Abedi, J., A review of single-phase liquid flow and heat transfer in microchannels, *Paper ICMM2004-2337*, ASME, *Second International Conference on Microchannels and Minichannels*, June 17–19, 213–220, 2004.
- Steinke, M. E., Characterization of single-phase fluid flow and heat transfer in plain and enhanced silicon microchannels, PhD Thesis, Rochester, NY: Microsystems Engineering, Rochester Institute of Technology, 2005.
- Steinke, M. E. and Kandlikar, S. G., Single-phase enhancement techniques in microchannel flows, *Paper No. ICMM2004-2328*, ASME, *Second International Conference on Microchannels and Minichannels*, Rochester, NY, June 17–19, 2004.
- Steinke, M. E. and Kandlikar, S. G., Single-phase liquid friction factors in microchannels, *Paper No. ICMM2005-75112*, ASME, *Third International Conference on Microchannels and Minichannels*, Toronto, Canada, June 13–15, 2005a.
- Steinke, M. E. and Kandlikar, S. G., Review of single-phase liquid heat transfer in microchannels, *Paper No. ICMM2005-75114*, ASME, *Third International Conference on Microchannels and Minichannels*, Toronto, Canada, June 13–15, 2005b.
- Steinke, M. E. and Kandlikar, S. G., Development of an experimental facility for investigating single-phase liquid flow in microchannels, *Paper No. ICMM2005-75070*, ASME, *Third International Conference on Microchannels and Minichannels*, Toronto, Canada, June 13–15, 2005c.

- Tu, X. and Hrnjak, P., Experimental investigation of single-phase flow and pressure drop through rectangular microchannels, *ASME, ICMM2003-1028, First International Conference on Microchannels and Minichannels*, April 24–25, 257–267, 2003.
- Tuckerman, D. B. and Pease, R. F. W., High performance heat sink for VLSI, *IEEE Electron Dev. Lett.*, EDL-2, (5), 126–129, 1981.
- Tuckerman, D.B., Heat transfer microstructures for integrated circuits, *PhD Thesis*, Stanford, CA, Stanford University, 1984.
- Webb, R. L., Eckert, E. R. G., and Goldstein, R. J., Heat transfer and friction in tubes with repeated-rib roughness, *Int. J. Heat and Mass Trans.*, **14**, 601–617, 1971.
- Wibulswas, P., Laminar flow heat transfer in non-circular ducts, *PhD Thesis*, London, UK, London University, 1966.
- Xu, B., Ooi, K. T., Wong, N. T., and Choi, W. K., Experimental investigation of flow friction for liquid flow in microchannels, *Int. Com. Heat Mass Trans.*, **27(8)**, 1165–1176, 2000.
- Yu, D., Warrington, R., Barron, R., and Ameel, T., An experimental investigation of fluid flow and heat transfer in microtubes, *Proceedings of the ASME/JSME Thermal Engineering Conference*, **1**, ASME, 523–530, 1995.

Chapter 4

SINGLE PHASE ELECTROKINETIC FLOW IN MICROCHANNELS

Dongqing Li

Department of Mechanical Engineering, Vanderbilt University, Nashville, TN, USA

4.1. Introduction

It is important to understand electrokinetic-driven liquid flow in microchannels when designing and controlling lab-on-a-chip devices. Lab-on-a-chip devices are miniaturized bio-medical or chemistry laboratories on a small glass or plastic chip. Generally, a lab-on-a-chip device has a network of microchannels, electrodes, sensors and electrical circuits. Electrodes are placed at strategic locations on the chip. Applying electrical fields along microchannels controls the liquid flow and other operations in the chip. These labs on a chip can duplicate the specialized functions as their room-sized counterparts, such as clinical diagnostics, DNA scanning and electrophoretic separation. The advantages of these labs on a chip include dramatically reduced sample size, much shorter reaction and analysis time, high throughput, automation and portability.

The key microfluidic functions required in various lab-on-a-chip devices include pumping, mixing, thermal cycling, dispensing and separating. Most of these processes are electrokinetic processes. Basic understanding, modeling and controlling of these key microfluidic functions/processes are essential to systematic design and operational control of the lab-on-a-chip systems. Because all solid-liquid (aqueous solutions) interfaces carry electrostatic charge, there is an electrical double layer (EDL) field in the region close to the solid-liquid interface on the liquid side. Such an EDL field is responsible for at least two basic electrokinetic phenomena: electroosmosis and electrophoresis. Briefly, electroosmosis is the liquid motion in a microchannel caused by the interaction between the EDL at the liquid-channel wall interface with an electrical field applied tangentially to the wall. Electrophoresis is the motion of a charged particle relative to the surrounding liquid under an applied electrical field. Essentially all on-chip microfluidic processes are realized by using these two phenomena. This chapter will review basics of the EDL field,

E-mail: dli@mie.utoronto.ca

and discuss some key on-chip microfluidic processes. A more comprehensive review of the electrokinetic-based microfluidic processes for lab-on-a-chip applications can be found elsewhere (Li, 2004).

4.2. EDL field

It is well-known that most solid surfaces obtain a surface electric charge when they are brought into contact with a polar medium (e.g. aqueous solutions). This may be due to ionization, ion adsorption or ion dissolution. If the liquid contains a certain amount of ions (for instance, an electrolyte solution or a liquid with impurities), the electrostatic charges on the solid surface will attract the counterions in the liquid. The rearrangement of the charges on the solid surface and the balancing charges in the liquid is called the EDL (Hunter, 1981; Lyklema, 1995). Immediately next to the solid surface, there is a layer of ions that are strongly attracted to the solid surface and are immobile. This layer is called the compact layer, normally about several Angstroms thick. Because of the electrostatic attraction, the counterions concentration near the solid surface is higher than that in the bulk liquid far away from the solid surface. The coions concentration near the surface, however, is lower than that in the bulk liquid far away from the solid surface, due to the electrical repulsion. So there is a net charge in the region close to the surface. From the compact layer to the uniform bulk liquid, the net charge density gradually reduces to zero. Ions in this region are affected less by the electrostatic interaction and are mobile. This region is called the diffuse layer of the EDL. The thickness of the diffuse layer is dependent on the bulk ionic concentration and electrical properties of the liquid, usually ranging from several nanometers for high ionic concentration solutions up to several microns for pure water and pure organic liquids. The boundary between the compact layer and the diffuse layer is usually referred to as the shear plane. The electrical potential at the solid–liquid surface is difficult to measure directly. The electrical potential at the shear plane is called the zeta potential ζ and can be measured experimentally (Hunter, 1981; Lyklema, 1995). In practice, the zeta potential is used as an approximation to the potential at the solid–liquid interface.

The ion and electrical potential distributions in the EDL can be determined by solving the Poisson–Boltzmann equation (Hunter, 1981; Lyklema, 1995). According to the theory of electrostatics, the relationship between the electrical potential ψ and the local net charge density per unit volume ρ_e at any point in the solution is described by the Poisson equation:

$$\nabla^2 \psi = -\frac{\rho_e}{\varepsilon} \quad (4.1)$$

where ε is the dielectric constant of the solution. Assuming the equilibrium Boltzmann distribution equation is applicable, which implies uniform dielectric constant, the number concentration of the type- i ion is of the form

$$n_i = n_{i0} \exp\left(-\frac{z_i e \psi}{k_b T}\right) \quad (4.2)$$

where n_{i0} and z_i are the bulk ionic concentration and the valence of type- i ions, respectively, e is the charge of a proton, k_b is the Boltzmann constant, and T is the absolute temperature.

For a symmetric electrolyte ($z_- = z_+ = z$) solution, the net volume charge density ρ_e is proportional to the concentration difference between symmetric cations and anions, via.:

$$\rho_e = ze(n_+ - n_-) = -2zen_0 \sinh\left(\frac{ze\psi}{k_b T}\right) \quad (4.3)$$

Substituting Eq. (4.3) into the Poisson equation leads to the well-known Poisson–Boltzmann equation:

$$\nabla^2 \psi = \frac{2zen_0}{\varepsilon} \sinh\left(\frac{ze\psi}{k_b T}\right) \quad (4.4)$$

Solving the Poisson–Boltzmann equation with proper boundary conditions will determine the local EDL potential field ψ and hence, via Eq. (4.3), the local net charge density distribution.

4.3. Electroosmotic flow in microchannels

Consider a microchannel filled with an aqueous solution. There is an EDL field near the interface of the channel wall and the liquid. If an electric field is applied along the length of the channel, an electrical body force is exerted on the ions in the diffuse layer. In the diffuse layer of the EDL field, the net charge density, ρ_e is not zero. The net transport of ions is the excess counterions. If the solid surface is negatively charged, the counterions are the positive ions. These excess counterions will move under the influence of the applied electrical field, pulling the liquid with them and resulting in electroosmotic flow. The liquid movement is carried through to the rest of the liquid in the channel by viscous forces. This electrokinetic process is called electroosmosis and was first introduced by Reuss in 1809 (Reuss, 1809).

In most lab-on-a-chip applications, electroosmotic flow is preferred over the pressure-driven flow. One of the reasons is the plug-like velocity profile of electroosmotic flow. This means that fluid samples can be transported without dispersion caused by flow shear. Generally, pumping a liquid through a small microchannel requires applying very large pressure difference depending on the flow rate. This is often impossible because of the limitations of the size and the mechanical strength of the microfluidic devices. Electroosmotic flow can generate the required flow rate even in very small microchannels without any applied pressure difference across the channel. Additionally, using electroosmotic flow to transport liquids in complicated microchannel networks does not require any external mechanical pump or moving parts, it can be easily realized by controlling the electrical fields via electrodes. Although high voltages are often required in electroosmotic flow, the required electrical power is very small due to the very low current involved, and it is generally safe. However, the heat produced in electroosmotic flow often presents problems to many applications where solutions of high electrolyte concentrations and long operation time are required.

Most channels in modern microfluidic devices and micro-electro-mechanical systems (MEMS) are made by micromachining technologies. The cross-section of these channels

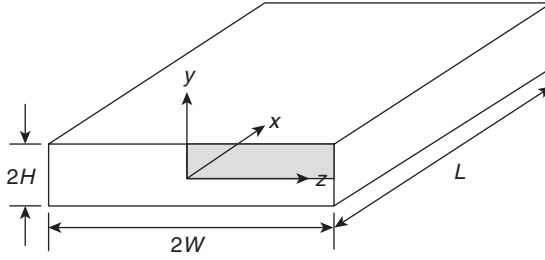


Fig. 4.1. Geometry of microchannel. The shaded region indicates the computational domain.

is close to a rectangular shape. In such a situation, the EDL field is two-dimensional and will affect the two-dimensional flow field in the rectangular microchannel. In order to control electroosmotic pumping as a means of transporting liquids in microstructures, we must understand the characteristics of electroosmotic flow in rectangular microchannels. In the following, we will review the modeling and the numerical simulation results of electroosmotic flow in rectangular microchannels (Arulanandam and Li, 2000a). The EDL field, the flow field and the volumetric flow rate will be studied as functions of the zeta potential, the liquid properties, the channel geometry and the applied electrical field.

Consider a rectangular microchannel of width $2W$, height $2H$ and length L , as illustrated in Fig. 4.1. Because of the symmetry in the potential and velocity fields, the solution domain can be reduced to a quarter section of the channel (as shown by the shaded area in Fig. 4.1).

The 2D EDL field can be described by the Poisson–Boltzmann equation:

$$\frac{\partial^2 \psi}{\partial y^2} + \frac{\partial^2 \psi}{\partial z^2} = \frac{2n_{\infty}ze}{\varepsilon\varepsilon_0} \sinh\left(-\frac{ze\psi}{k_bT}\right)$$

Along the planes of symmetry, the following symmetry boundary conditions apply:

$$\text{at } y = 0 \quad \frac{\partial \psi}{\partial y} = 0 \quad \text{at } z = 0 \quad \frac{\partial \psi}{\partial z} = 0$$

Along the surfaces of the solution domain, the potential is the zeta potential:

$$\text{at } y = H \quad \psi = \zeta \quad \text{at } z = W \quad \psi = \zeta$$

The Poisson–Boltzmann equation and the boundary conditions can be transformed into non-dimensional equations by introducing the following dimensionless variables:

$$y^* = \frac{y}{D_h} \quad z^* = \frac{z}{D_h} \quad \psi^* = \frac{ze\psi}{k_bT} \quad D_h = \frac{4A_{\text{cross-sectional}}}{P_{\text{wetted}}} = \left(\frac{4HW}{H+W} \right)$$

The non-dimensional form of the Poisson–Boltzmann equation is given by:

$$\frac{\partial^2 \psi^*}{\partial y^{*2}} + \frac{\partial^2 \psi^*}{\partial z^{*2}} = (\kappa D_h)^2 \sinh \psi^* \quad (4.5)$$

where κ , the Debye–Huckel parameter, is defined as follows:

$$\kappa = \left(\frac{2n_\infty z^2 e^2}{\varepsilon \varepsilon_0 k_b T} \right)^{1/2} \quad (4.6)$$

and $1/\kappa$ is the characteristic thickness of the EDL. The non-dimensional parameter κD_h is a measure of the relative channel diameter, compared to the EDL thickness. κD_h is often referred to as the electrokinetic diameter. The corresponding non-dimensional boundary conditions as follows:

$$\begin{aligned} \text{at } y^* = 0 \quad \frac{\partial \psi^*}{\partial y^*} &= 0 & \text{at } z^* = 0 \quad \frac{\partial \psi^*}{\partial z^*} &= 0 \\ \text{at } y^* = \frac{H}{D_h} \quad \psi^* &= \zeta^* = \frac{ze\zeta}{k_b T} & \text{at } z^* = \frac{W}{D_h} \quad \psi^* &= \zeta^* = \frac{ze\zeta}{k_b T} \end{aligned}$$

If we consider that the flow is steady, two-dimensional, and fully developed, and there is no pressure gradient in the microchannel, the general equation of motion is given by a balance between the viscous or shear stresses in the fluid and the externally imposed electrical field force:

$$\mu \left(\frac{\partial^2 u}{\partial y^2} + \frac{\partial^2 u}{\partial z^2} \right) = F_x$$

where F_x is the electrical force per unit volume of the liquid, which is related to the electric field strength E_x and the local net charge density as follows:

$$F_x = \rho_e E_x$$

Therefore, the equation for the electroosmotic flow can be written as:

$$\mu \left(\frac{\partial^2 u}{\partial y^2} + \frac{\partial^2 u}{\partial z^2} \right) = \left(\frac{2n_\infty ze}{\varepsilon \varepsilon_0} \sinh \psi \right) E_x \quad (4.7)$$

The following boundary conditions apply along the planes of symmetry:

$$\text{at } y = 0 \quad \frac{\partial u}{\partial y} = 0 \quad \text{at } z = 0 \quad \frac{\partial u}{\partial z} = 0$$

Along the surface of shear (the surface of the solution domain), the velocity boundary conditions are given by:

$$\text{at } y = H \quad u = 0 \quad \text{at } z = W \quad u = 0$$

The equation of motion can be non-dimensionalized using the following additional transformations:

$$u^* = \frac{u}{U} \quad E_x^* = \frac{E_x L}{\zeta}$$

where U is a reference velocity and L is the distance between the two electrodes. The non-dimensionalized equation of motion becomes:

$$\frac{\partial^2 u^*}{\partial y^{*2}} + \frac{\partial^2 u^*}{\partial z^{*2}} = ME_x^* \sinh \psi^* \quad (4.8)$$

M is a new dimensionless group, which is a ratio of the electrical force to the frictional force per unit volume, given by:

$$M = \frac{2n_\infty z e \zeta D_h^2}{\mu U L}$$

The corresponding non-dimensional boundary conditions are given by:

$$\begin{aligned} \text{at } y^* = 0 \quad \frac{\partial u^*}{\partial y^*} = 0 \quad \text{at } z^* = 0 \quad \frac{\partial u^*}{\partial z^*} = 0 \\ \text{at } y^* = \frac{H}{D_h} \quad u^* = 0 \quad \text{at } z^* = \frac{W}{D_h} \quad u^* = 0 \end{aligned}$$

Numerically solving Eqs. (4.5) and (4.8) with the boundary conditions will allow us to determine the EDL field and the electroosmotic flow field in such a rectangular microchannel. As an example, Let's consider a KCl aqueous solution. At a concentration of 1×10^{-6} M, $\varepsilon = 80$ and $\mu = 0.90 \times 10^{-3}$ kg/ms. An arbitrary reference velocity of $U = 1$ mm/s was used to non-dimensionalize the velocity. According to experimental results (Mala *et al.*, 1997), zeta potential values changes from 100 to 200 mV, corresponding to three concentrations of the KCl solution, 1×10^{-6} , 1×10^{-5} and 1×10^{-4} M. The hydraulic diameter of the channel varied from 12 to 250 μ m, while the aspect ratio (H/W) varied from 1:4 to 1:1. Finally, the applied voltage difference ranged from 10 V to 10 kV.

The EDL potential distribution in the diffuse double layer region is shown in Fig. 4.2. The non-dimensional EDL potential profile across a quarter section of the rectangular channel exhibits characteristic behavior. The potential field drops off sharply very close to the wall. The region where the net charge density is not zero is limited to a small region close to the channel surface. Figure 4.3 shows the non-dimensional electroosmotic velocity field for an applied potential difference of 1 kV/cm. The velocity field exhibits a profile similar to plug flow, however, in electroosmotic flow, the velocity increases rapidly from zero at the wall (shear plane) to a maximum velocity near the wall, and then gradually drops off to a slightly lower constant velocity that is maintained through most of the channel. This unique profile can be attributed to the fact that the externally imposed electrical field is driving the flow. In the mobile part of the EDL region very close to the wall, the larger electrical field force exerts a greater driving force on the fluid because of the presence of the net charge in the EDL region.

Variation of D_h affects the following non-dimensional parameters: the electrokinetic diameter, and the strength of the viscous forces in the ratio of electrical to viscous forces.

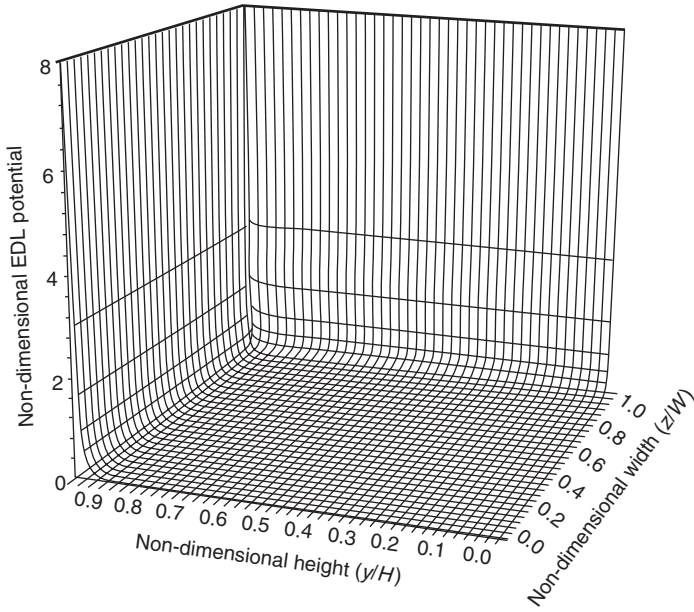


Fig. 4.2. Non-dimensional EDL potential profile in a quarter section of a rectangular microchannel with $\kappa D_h = 79$, $\zeta^* = 8$ and $H:W = 2:3$.

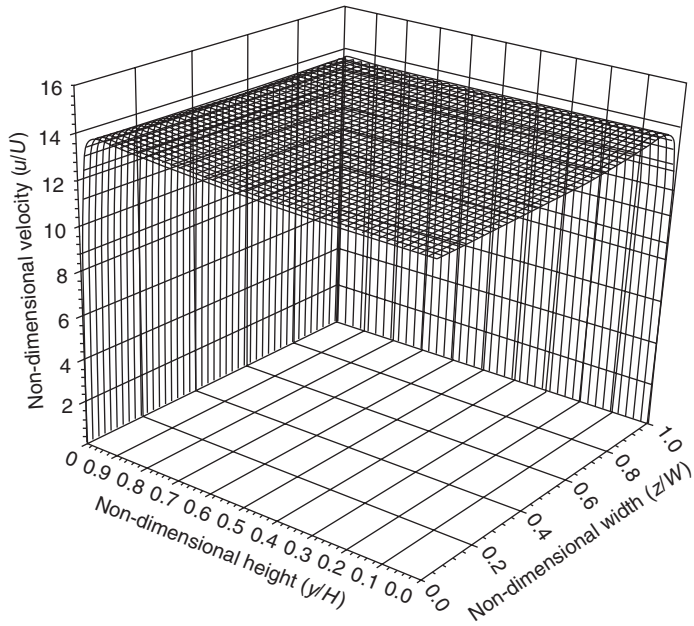


Fig. 4.3. Non-dimensional velocity field in a quarter section of a rectangular microchannel with $\kappa D_h = 79$, $\zeta^* = 8$, $H/W = 2/3$, $E_x^* = 5000$ and $M = 2.22$.

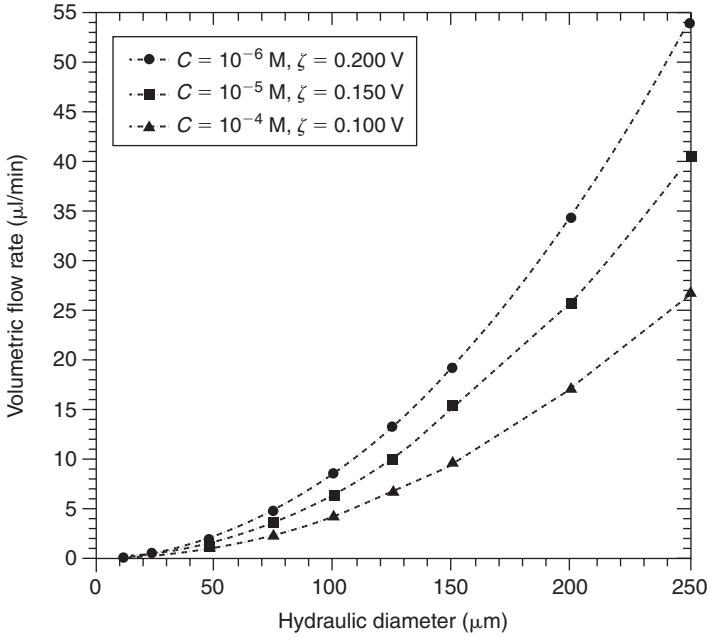


Fig. 4.4. Variation of volumetric flow rate with hydraulic diameter for three different combinations of concentration and zeta potential, with $H/W = 2/3$, and $E_x = 1 \text{ kV/cm}$.

The volumetric flow rate increased with approximately D_h^2 as seen in Fig. 4.4. This is expected, since the cross-sectional area of the channel also increases proportionately to D_h^2 . When larger pumping flow rates are desired, larger diameter channels would seem to be a better choice. However, there is no corresponding increase in the average velocity with increased hydraulic diameter. This is because the nature of electroosmotic flow – the flow is generated by the motion of the net charge in the EDL region driven by an applied electrical field. When the double layer thickness ($1/\kappa$) is small, an analytical solution of the electroosmotic velocity can be derived from an one-dimensional channel system such as a cylindrical capillary with a circular cross-section, given by

$$v_{av} = -\frac{E_z \epsilon_r \epsilon_0 \zeta}{\mu} \quad (4.9)$$

Equation (4.9) indicates that the electroosmotic flow velocity is linearly proportional to the applied electrical field strength and linearly proportional to the zeta potential. The negative sign indicates the flow direction and has to do with the sign of the ζ potential. If ζ potential is negative (i.e. a negatively charged wall surface), the excess counterions in the diffuse layer are positive, therefore the electroosmotic flow in the microchannel is towards the negative electrode.

With a rectangular microchannel not only the hydraulic diameter but also the channel shape will influence the velocity profile. This is because of the impact of the channel

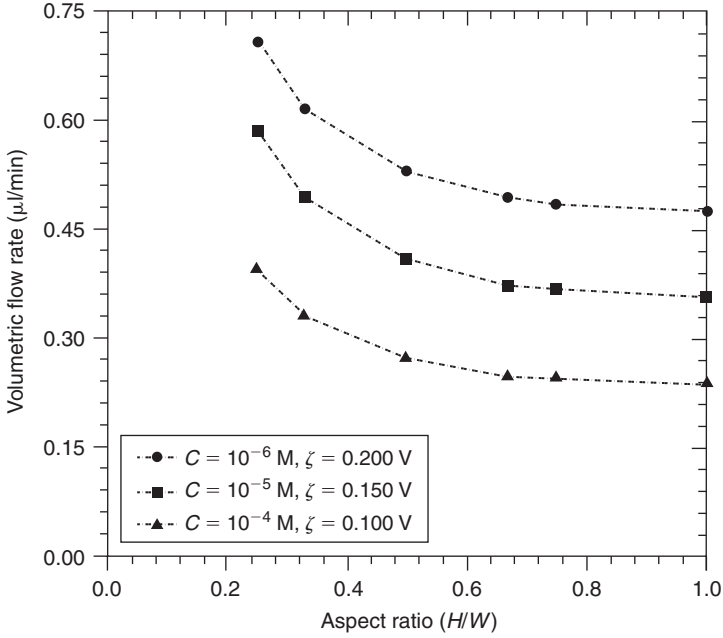


Fig. 4.5. Variation of volumetric flow rate with aspect ratio for three different combinations of concentration and zeta potential, with $D_h = 24 \mu\text{m}$ and $E_x = 1 \text{ kV/cm}$. In this case, $z/W = 1.0$ represents the channel wall, and $z/W = 0$ represents the center of the channel.

geometry on the EDL. Figure 4.5 shows the relationship between the aspect ratio (H/W) and the volumetric flow rate for a fixed hydraulic diameter. As the ratio of $H:W$ approaches 1:1 (for a square channel), the flow rate decreases. This is because of the larger role that corner effects have on the development of the EDL and the velocity profile in square channels.

From Eq. (4.6), it is clear that increasing the bulk ion concentration in the liquid results in an increase in κ or a decrease in the EDL thickness $1/\kappa$. Correspondingly, the EDL potential field falls off to zero more rapidly with distance, that is, the region influenced by the EDL is smaller. The ionic concentration effect on the velocity or the flow rate can be understood as follows. Since ionic concentration influences the zeta potential, as the ionic concentration is increased, the zeta potential decreases in value. As the zeta potential decreases, so does the electroosmotic flow velocity (Eq. (4.9)) and the volumetric flow rate.

4.4. Experimental techniques for studying electroosmotic flow

In most electroosmotic flows in microchannels, the flow rates are very small (e.g. $0.1 \mu\text{L/min}$) and the size of the microchannels is very small (e.g. $10\text{--}100 \mu\text{m}$), it is extremely difficult to measure directly the flow rate or velocity of the electroosmotic flow in microchannels. To study liquid flow in microchannels, various microflow visualization methods have evolved. Micro particle image velocimetry (microPIV) is a method that was

adapted from well-developed PIV techniques for flows in macro-sized systems (Talyor and Yeung, 1993; Herr *et al.*, 2000; Wereley and Meinhart, 2001; Singh *et al.*, 2001; Selva-ganapathy *et al.*, 2002). In the microPIV technique, the fluid motion is inferred from the motion of sub-micron tracer particles. To eliminate the effect of Brownian motion, temporal or spatial averaging must be employed. Particle affinities for other particles, channel walls, and free surfaces must also be considered. In electrokinetic flows, the electrophoretic motion of the tracer particles (relative to the bulk flow) is an additional consideration that must be taken. These are the disadvantages of the microPIV technique.

Dye-based microflow visualization methods have also evolved from their macro-sized counterparts. However, traditional mechanical dye injection techniques are difficult to apply to the microchannel flow systems. Specialized caged fluorescent dyes have been employed to facilitate the dye injection using selective light exposure (i.e. the photo-injection of the dye). The photo-injection is accomplished by exposing an initially non-fluorescent solution seeded with caged fluorescent dye to a beam or a sheet of ultraviolet (UV) light. As a result of the UV exposure, caging groups are broken and fluorescent dye is released. Since the caged fluorescent dye method was first employed for flow tagging velocimetry in macro-sized flows in 1995 (Lempert *et al.*, 1995), this technique has since been used to study a variety of liquid flow phenomena in microstructures (Dahm *et al.*, 1992; Paul *et al.*, 1998; Herr *et al.*, 2000; Johnson *et al.*, 2001; Molho *et al.*, 2001; Sinton *et al.*, 2002; 2003a; Sinton and Li, 2003a, b). The disadvantages of this technique are that it requires expensive specialized caged dye, and extensive infrastructure to facilitate the photo-injection.

Recently, Sinton and Li (Sinton and Li, 2003a) developed a microchannel flow visualization system and complimentary analysis technique by using caged fluorescent dyes. Both pressure-driven and electrokinetically driven velocity profiles determined by this technique compare well with analytical results and those of previous experimental studies. Particularly, this method achieved a high degree of near-wall resolution. Generally, in the experiment, a caged fluorescent dye is dissolved in an aqueous solution in a capillary or microchannel. It should be noted that the caged dye cannot emit fluorescent light at this stage. The UV laser light is focused into a sheet crossing the capillary (perpendicular to the flow direction). The caged fluorescent dye molecules exposed to the UV light are uncaged and thus are able to shine. The resulting fluorescent dye is continuously excited by an argon laser and the emission light is transmitted through a laser-powered epi-illumination microscope. Full frame images of the dye transport are recorded by a progressive scan CCD camera and saved automatically on the computer. In the numerical analysis, the images are processed and cross-stream velocity profiles are calculated based on tracking the dye concentration maxima through a sequence of several consecutive images. Several sequential images are used to improve the signal to noise ratio. Points of concentration maxima make convenient velocimetry markers as they are resistant to diffusion. In many ways, the presence of clearly definable, zero-concentration-gradient markers is a luxury afforded by the photo-injection process. The details of this technique can be found elsewhere (Sinton and Li, 2003a, b).

In an experimental study (Sinton and Li, 2003a), the CMNB-caged fluorescein with the sodium carbonate buffer and 102 μm i.d. glass capillaries were used. Images of the uncaged dye transport in four different electroosmotic flows are displayed in vertical sequence in

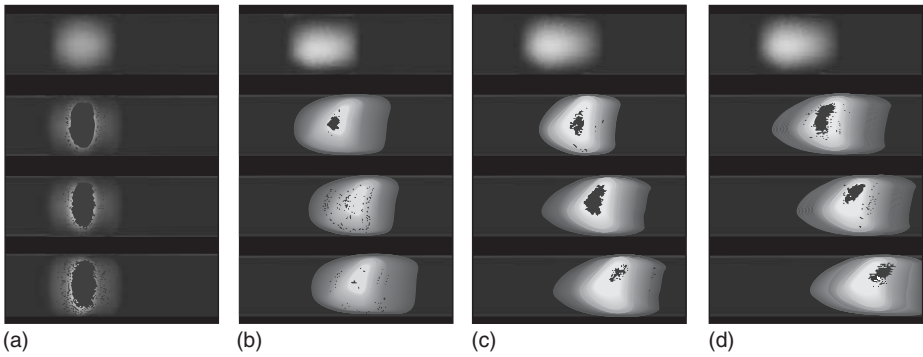


Fig. 4.6. Images of the uncaged dye in electroosmotic flows through a $102\text{ }\mu\text{m}$ i.d. capillary at 133 ms intervals with applied electric field strength: (a) $0\text{ V}/0.14\text{ m}$; (b) $1000\text{ V}/0.14\text{ m}$; (c) $1500\text{ V}/0.14\text{ m}$; and (d) $2000\text{ V}/0.14\text{ m}$.

Fig. 4.6. The dye diffused symmetrically as shown in Fig. 4.6(a). Image sequences given in Fig. 4.6(b–d) were taken with voltages of 1000 V, 1500 V, and 2000 V, respectively (over the 14 cm length of capillary). The field was applied with the positive electrode at left and the negative electrode at right. The resulting plug-like motion of the dye is characteristic of electroosmotic flow in the presence of a negatively charged surface at high ionic concentration. The cup-shape of the dye profile was observed in cases Fig. 4.6(b–d) within the first 50 ms following the UV light exposure. This period corresponded to the uncaging time scale in which the most significant rise in uncaged dye concentration occurs. Although the exact reason for the formation of this shape is unknown, it is likely that it was an artifact of the uncaging process in the presence of the electric field. Fortunately, however, the method is relatively insensitive to the shape of the dye concentration profile. Once formed, it is the transport of the maximum concentration profile that provides the velocity data. This also makes the method relatively insensitive to beam geometry and power intensity distribution.

Figure 4.7 shows velocity data for the four flows corresponding to the image sequences in Fig. 4.6. Each velocity profile was calculated using an 8-image sequence and the numerical analysis technique described in reference (Sinton and Li, 2003a). The velocity profile resulting from no applied field, Fig. 4.6(a), corresponds closely to stagnation as expected. This run also serves to illustrate that, despite significant transport of dye due to diffusion, the analysis method is able to recover the underlying stagnant flow velocity. Although the other velocity profiles resemble that of classical electroosmotic flow (Wereley and Meinhardt, 2001), a slight parabolic velocity deficit of approximately 4% was detected in all three flows. This was caused by a small back-pressure induced by the electroosmotic fluid motion (e.g. caused by the not-perfectly leveled capillary along the length direction).

In addition to these PIV and dye-based techniques, the electroosmotic flow velocity can be estimated indirectly by monitoring the electrical current change while one solution is replaced by another similar solution during electroosmosis (Arulanandam and Li, 2000b; Ren *et al.*, 2002; Sinton *et al.*, 2002). In this method, a capillary tube is filled with an electrolyte solution, then brought into contact with another solution of the same electrolyte

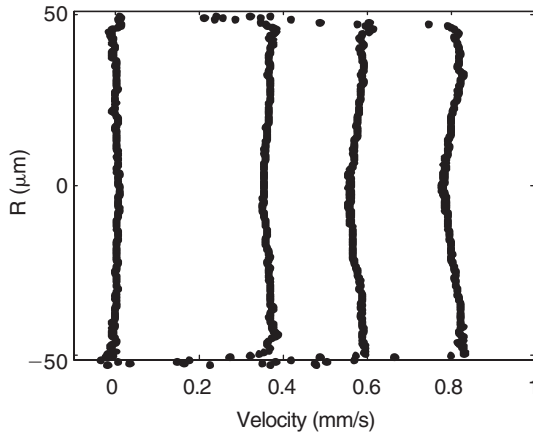


Fig. 4.7. Plots of velocity data from four electroosmotic flow experiments through a $102\text{ }\mu\text{m}$ i.d. capillary with applied electric field strengths of $0\text{ V}/0.14\text{ m}$; $1000\text{ V}/0.14\text{ m}$; $1500\text{ V}/0.14\text{ m}$ and $2000\text{ V}/0.14\text{ m}$ (from left to right).

but with a slightly different ionic concentration. Once the two solutions are in contact, an electrical field is applied along the capillary in such a way that the second solution is pumped into the capillary and the 1st solution flows out of the capillary from the other end. As more and more of the second solution is pumped into the capillary and the first solution flows out of the capillary, the overall liquid conductivity in the capillary is changed, hence the electrical current through the capillary is changed. When the second solution completely replaces the first solution, the current will reach a constant value. Knowing the time required for this current change and the length of the capillary tube, the average electroosmotic flow velocity can be calculated by:

$$u_{\text{av,exp}} = \frac{L}{\Delta t} \quad (4.10)$$

where L is the length of the capillary and Δt is the time required for the higher (or lower) concentration electrolyte solution to completely displace the lower (or higher) concentration electrolyte solution in the capillary tube.

Figure 4.8 shows an example of the measured current–time relationship in a 10-cm-long glass capillary of $100\text{ }\mu\text{m}$ in diameter with a KCl solution under an applied electrical field of 350 V/cm . An example of measured electroosmotic velocity as a function of the applied electrical field is given in Fig. 4.9. As seen in this figure, a linear relationship between the applied voltage and the average velocity is evident. In addition, it is clear that the average velocity is independent of the diameter of the capillary tubes.

However, in these experiments it is often difficult to determine the exact time required for one solution completely replacing another solution. This is because the gradual changing of the current with time and the small current fluctuations exist at both the beginning

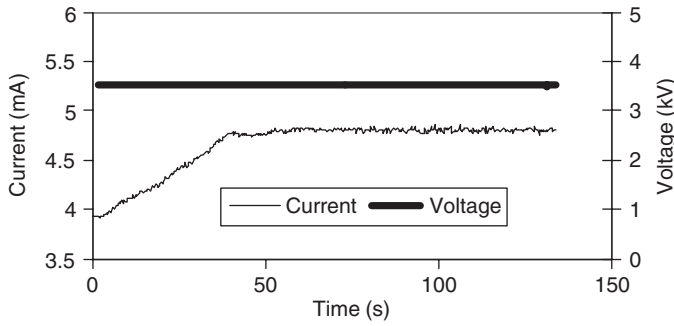


Fig. 4.8. A typical result of current versus time. For the specific case of capillary diameter $D = 100 \mu\text{m}$, $E_x = 3500 \text{ V}/10 \text{ cm}$. KCl concentration in Reservoir 1 is $C_{95\%} = 0.95 \times 10^{-4} \text{ M}$. KCl concentration in Reservoir 2 is $C_{100\%} = 1 \times 10^{-4} \text{ M}$.

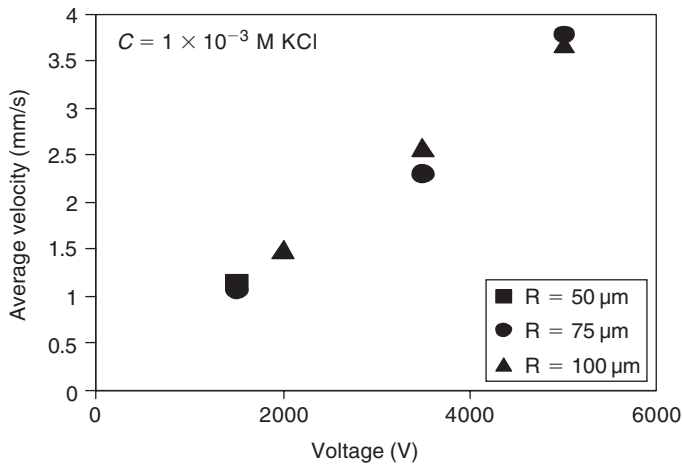


Fig. 4.9. Average velocity versus the applied voltage and the capillary diameter for a 10-cm-long polyamide coated silica capillary tube.

and the end of the replacing process. These make it very difficult to determine the exact beginning and ending time of the current change from the experimental results. Consequently, significant errors could be introduced in the average velocity determined in this way. It has been observed that, despite the curved beginning and ending sections, the measured current–time relationship is linear in most part of the process, as long as the concentration difference is small. Therefore, a new method was developed to determine the average electroosmotic velocity by using the slope of the current–time relationship (Ren *et al.*, 2002). When a high concentration electrolyte solution gradually replaces another solution of the same electrolyte with a slightly lower concentration in a microchannel under an applied electric field, the current increases until the high concentration solution completely replaces the low concentration solution, at which time the current reaches a

constant value. If the concentration difference is small, a linear relationship between the current and the time is observed. This may be understood in the following way. In such a process, because the concentration difference between these two solutions is small, for example, 5%, the zeta potential, which determines the net charge density and hence the liquid flow, can be considered as constant along the capillary. Consequently, the average velocity can be considered as a constant during the replacing process. As one solution flows into the capillary and the other flows out of the capillary at essentially the same speed, and the two solutions have different electrical conductivities, the overall electrical resistance of the liquid in the capillary will change linearly, and hence the slope of current–time relationship is constant during this process.

The slope of the linear current–time relationship can be described as:

$$\text{slope} = \frac{\Delta I}{\Delta t} = \frac{\Delta(EA\lambda_b)}{\Delta t} \cdot \frac{L_{\text{total}}}{L_{\text{total}}} = \bar{u}_{\text{ave}} \frac{EA(\lambda_{b2} - \lambda_{b1})}{L_{\text{total}}} \quad (4.11)$$

where L_{total} is the total length of the capillary and \bar{u}_{ave} is the average electroosmotic velocity, E is the applied electrical field strength, A is the cross-section area of the capillary, $(\lambda_{b2} - \lambda_{b1})$ is the bulk conductivity difference between the high-concentration solution and the low-concentration solution. Using this equation, the average electroosmotic flow velocity can be evaluated from the slope of the measured current–time relationship. Figure 4.10 shows an example of the measured average electroosmotic velocity by the slope method.

In the straightforward current–time method, the total time required for one solution completely replacing another solution has to be found, which often involves some inaccuracy of choosing the beginning and the ending points of the replacing process. In this slope method, instead of identifying the total period of time, only a middle section of the current–time data is required to determine the slope of the current–time relationship. This

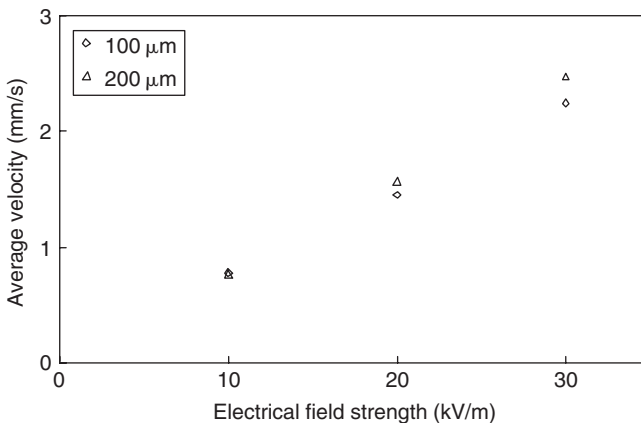


Fig. 4.10. The average velocity versus the applied voltage and the capillary diameter for 1×10^{-4} M KCl solution in a 10-cm-long capillary tube.

method is easier and more accurate than finding the exact beginning and the ending points of the replacing process.

4.5. Electroosmotic flow in heterogeneous microchannels

Many microchannels do not have uniform surface properties. The surface heterogeneity may be caused by the impurities of the materials, by adhesion of solutes (e.g. surfactants, proteins and cells) of the solution, and by desired chemical surface modification. In the majority of lab-on-a-chip systems, electrokinetic means (i.e. electroosmotic flow, electrophoresis) are the preferred method of species transport. Although the surface heterogeneity has been long recognized as a problem leading to irregular flow patterns and non-uniform species transport, only recently have researchers begun to investigate the potential benefits the presence of surface heterogeneity (non-uniform surface ζ -potential or charge density) may have to offer. Early studies examining these effects were conducted by Anderson (1985), Ajdari (1995; 1996; 2001) and Ghosal (2002). In Ajdari's works it was predicted that the presence of surface heterogeneity could result in regions of bulk flow circulation, referred to as "tumbling" regions. This behavior was later observed in slit microchannels experimentally by Stroock *et al.* (Stroock *et al.*, 2000), who found excellent agreement with their flow model. In another study Herr *et al.* (2000) used a caged dye velocimetry technique to study electroosmotic flow in a capillary in the presence of heterogeneous surface properties and observed significant deviations from the classical plug type velocity profile, an effect which was predicted by Keely *et al.* (1994). In another clever application Johnson *et al.* (2001) used a UV excimer laser to introduce surface heterogeneity to the side wall of a polymeric microchannel and demonstrated how this could reduce sample band broadening around turns. Recently the use of surface heterogeneity to increase the mixing efficiency of a T-shaped micromixer was proposed (Erickson and Li, 2002b). Here we wish to review a general theoretical analysis of 3D electroosmotic flow structures in a slit microchannel with periodic, patchwise heterogeneous surface patterns (Erickson and Li, 2003a).

Let's consider the electroosmotically driven flow through a slit microchannel (i.e. a channel formed between two parallel plates) exhibiting a periodically repeating heterogeneous surface patterns shown in Fig. 4.11. Since the pattern is repeating, the computational domain is reduced to that over a single periodic cell, demonstrated by the dashed lines in Fig. 4.11. To further minimize the size of the solution domain it has been assumed that the heterogeneous surface pattern is symmetric about the channel mid-plane, resulting in the computational domain shown in Fig. 4.12. As a result of these two simplifications, the inflow and outflow boundaries, surfaces 2 and 4 (as labeled in Fig. 4.12 and referred by the symbol Γ), represent periodic boundaries on the computational domain, while surface 3 at the channel mid-plane represents a symmetry boundary. From Fig. 4.11 it can be seen that in all cases the surface pattern is symmetric about Γ_5 and Γ_6 and thus these surfaces also represent symmetry boundaries. For a general discussion of periodic boundary conditions, however, the reader is referred to a paper by Patankar *et al.* (1977).

In order to model the flow through this periodic unit, it requires a description of the ionic species distribution, the double layer potential, the flow field and the applied potential. The

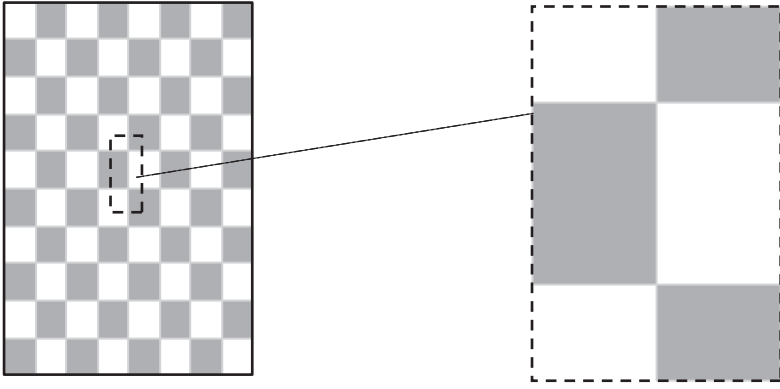


Fig. 4.11. Periodic patchwise surface heterogeneity patterns. Dark regions represent heterogeneous patches, light regions are the homogeneous surface. The percent heterogeneous coverage is 50%.

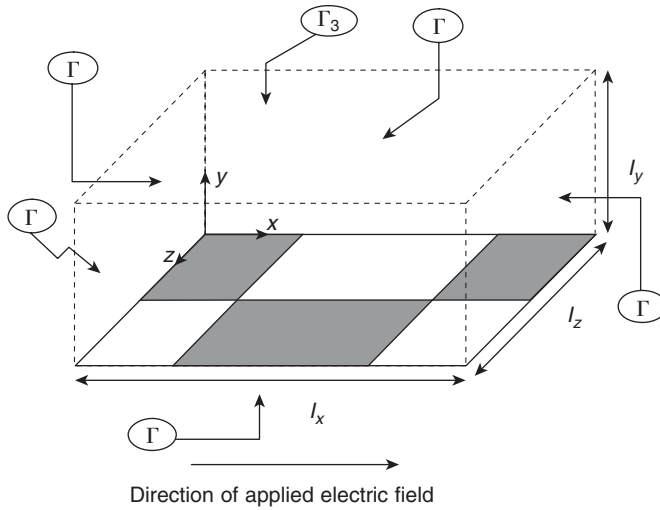


Fig. 4.12. Domain for the periodical computational cell showing location of computational boundaries.

divergence of the ion species flux (for simplicity here we consider a monovalent, symmetric electrolyte as our model species), often referred to as the Nernst–Planck conservation equations, is used to describe the positive and negative ion densities (given below in non-dimensional form),

$$\tilde{\nabla} \cdot \left(-\tilde{\nabla} N^+ - N^+ \tilde{\nabla} \Phi + Pe^+ N^+ \mathbf{V} \right) = 0 \quad (4.12a)$$

$$\tilde{\nabla} \cdot \left(-\tilde{\nabla} N^- + N^- \tilde{\nabla} \Phi + Pe^- N^- \mathbf{V} \right) = 0 \quad (4.12b)$$

where N^+ and N^- are the non-dimensional positive and negative species concentrations ($N^+ = n^+/n_\infty$, $N^- = n^-/n_\infty$ where n_∞ is the bulk ionic concentration), Φ is the

non-dimensional electric field strength ($\Phi = e\phi/k_bT$ where e is the elemental charge, k_b is the Boltzmann constant and T is the temperature in Kelvin), \mathbf{V} is the non-dimensional velocity ($\mathbf{V} = \mathbf{v}/v_0$ where v_0 is a reference velocity) and the \sim sign signifies that the gradient operator has been non-dimensionalised with respect to the channel half height (l_y in Fig. 4.12). The Peclet number for the two species are given by $Pe^+ = v_0 l_y / D^+$ and $Pe^- = v_0 l_y / D^-$ where D^+ and D^- are the diffusion coefficients for the positively charged and negatively charged species respectively.

Along the heterogeneous surface (Γ_1 in Fig. 4.12) and symmetry boundaries of the computational domain (Γ_3 , Γ_5 and Γ_6), zero flux boundary conditions are applied to both Eqs. (4.12a) and (b) (see reference (Erickson and Li, 2002a, b) for explicit equations). As mentioned earlier, along faces Γ_2 and Γ_4 , periodic conditions are applied which take the form shown below:

$$N_2^+ = N_4^+, \quad \text{on } \Gamma_2, \Gamma_4, \quad N_2^- = N_4^-, \quad \text{on } \Gamma_2, \Gamma_4$$

The velocity field is described by the Navier–Stokes equations for momentum, modified to account for the electrokinetic body force, and the continuity equation as shown below:

$$\text{Re}(\mathbf{V} \cdot \tilde{\nabla} \mathbf{V}) = -\tilde{\nabla} P + \tilde{\nabla}^2 \mathbf{V} - F(N^+ - N^-)\tilde{\nabla} \Phi \quad (4.13a)$$

$$\tilde{\nabla} \cdot \mathbf{V} = 0 \quad (4.13b)$$

where F is a non-dimensional constant ($F = n_\infty l_y k_b T / \mu v_0$) which accounts for the electrokinetic body force, Re is the Reynolds Number ($\text{Re} = \rho v_0 l_y / \mu$, where ρ is the fluid density and μ is the viscosity) and P is the non-dimensional pressure. Along the heterogeneous surface, Γ_1 , a no-slip boundary condition is applied. At the upper symmetry surface, Γ_3 , we enforce a zero penetration condition for the y -component of velocity and zero gradient conditions for the x and z terms, respectively. Similarly a zero penetration condition for the z -component of velocity is applied along Γ_5 and Γ_6 while zero gradient conditions are enforced for the x and y components. As with the Nernst–Planck equations, periodic boundary conditions are applied along Γ_2 and Γ_4 .

For the potential field, we choose to separate, without loss of generality, the total non-dimensional electric field strength, Φ , into two components

$$\Phi(X, Y, Z) = \Psi(X, Y, Z) + E(X) \quad (4.14)$$

where the first component, $\Psi(X, Y, Z)$, describes the EDL field and the second component $E(X)$ represents the applied electric field. In this case the gradient of $E(X)$ is of similar order of magnitude to the gradient of $\Psi(X, Y, Z)$ and thus cannot be decoupled to simplify the solution to the Poisson equation. As a result for this case the Poisson equation has the form shown below:

$$\tilde{\nabla}^2 \Psi + d^2 E / dX^2 + K^2(N^+ - N^-) = 0 \quad (4.15a)$$

where K is the non-dimensional double layer thickness ($K^2 = \kappa^2 l_y^2 / 2$ where $\kappa = (2n_\infty e^2 / \epsilon_w k_b T)^{1/2}$ is the Debye–Huckel parameter). Two boundary conditions commonly

applied along the solid surface for the above equation are either an enforced potential gradient proportional to the surface charge density, or a fixed potential condition equivalent to the surface ζ -potential. In this case we choose the former resulting in the following boundary condition applied along the heterogeneous surface

$$\partial\psi/\partial Y = -\Theta(X, Z) \quad \text{on } \Gamma_1 \quad (4.15b)$$

where Θ is the non-dimensional surface charge density ($\Theta = \sigma l_y e / \varepsilon_w k_b T$, where σ is the surface charge density). Along the upper and side boundaries of the computational domain, Γ_3 , Γ_5 and Γ_6 , symmetry conditions are applied while periodic conditions are again applied at the inlet and outlet, Γ_2 and Γ_4 .

In order to determine the applied electric field, $E(X)$, we enforce a constant current condition at each cross-section along the x -axis as below:

$$J_{\text{const}} = \int_0^{Z_{\text{max}}} \int_0^{Y_{\text{max}}} [J^+(X, Y, Z) - J^-(X, Y, Z)] n_x dY dZ \quad (4.16a)$$

where n_x in the above is a normal vector in the x -direction and J^+ and J^- are the non-dimensional positive and negative current densities. Assuming monovalent ions for both positive and negative species (as was discussed earlier) and using the ionic species flux terms from Eqs. (4.12a) and (b), condition 4.16(a) reduces to the following:

$$\begin{aligned} J_{\text{const}} = & \int_0^{Z_{\text{max}}} \int_0^{Y_{\text{max}}} \left(- \left[\frac{\partial N^+}{\partial X} - \frac{Pe^+}{Pe^-} \frac{\partial N^-}{\partial X} \right] - \left[N^+ + \frac{Pe^+}{Pe^-} N^- \right] \frac{\partial(\Psi + E)}{\partial X} \right) dY dZ \\ & + \int_0^{Z_{\text{max}}} \int_0^{Y_{\text{max}}} [Pe^+ (N^+ - N^-) V_x] dY dZ \end{aligned} \quad (4.16b)$$

which is a balance between the conduction (term 2) and convection (term 3) currents with an additional term to account for any induced current due to concentration gradients. Solving Eq. (4.16b) for the applied potential gradient yields:

$$\begin{aligned} \frac{dE}{dX} = & \frac{\int_0^{Z_{\text{max}}} \int_0^{Y_{\text{max}}} \left(- \left[\frac{\partial N^+}{\partial X} - \frac{Pe^+}{Pe^-} \frac{\partial N^-}{\partial X} \right] - \left[N^+ + \frac{Pe^+}{Pe^-} N^- \right] \frac{\partial\Psi}{\partial X} \right) dY dZ}{\int_0^{Z_{\text{max}}} \int_0^{Y_{\text{max}}} \left(N^+ + \frac{Pe^+}{Pe^-} N^- \right) dY dZ} \\ & + \frac{\int_0^{Z_{\text{max}}} \int_0^{Y_{\text{max}}} [Pe^+ (N^+ - N^-) V_x] dY dZ - J_{\text{const}}}{\int_0^{Z_{\text{max}}} \int_0^{Y_{\text{max}}} \left(N^+ + \frac{Pe^+}{Pe^-} N^- \right) dY dZ} \end{aligned} \quad (4.16c)$$

As an example, let us consider a $l_x = 50 \mu\text{m}$, $l_y = l_z = 25 \mu\text{m}$ computational domain, as shown in Fig. 4.12, containing a 10^{-5} M KCl solution and with an applied driving voltage of 500 V/cm and a $\sigma_{\text{homo}} = -4 \times 10^{-4} \text{ C/m}^2$. The numerical simulations of the above described model revealed three distinct flow patterns, depending on the degree of surface heterogeneity, as shown in Fig. 4.13. The grey scales in these figures represent the magnitude of the velocity perpendicular to the direction of the applied electric field ($v^2 = v_y^2 + v_z^2$) scaled by the maximum velocity in a homogeneous channel, which in this example is 1.7 mm/s .

At low degrees of surface heterogeneity ($\sigma_{\text{hetero}} = -2 \times 10^{-4} \text{ C/m}^2$) the streamline pattern shown in Fig. 4.13(a) was obtained. As can be seen a net counter-clockwise flow perpendicular to the applied electric field is present at the first transition plane (i.e. at the initial discontinuity in the heterogeneous surface pattern) and a clockwise flow at the second transition plane. This flow circulation is a pressure-induced effect. It results from the transition from the higher local fluid velocity (particularly in the double layer) region over the homogeneous surface on the right-hand side at the entrance to the left-hand side after the first transition plane (and *vice versa* at the second transition plane). To satisfy continuity then there must be a net flow from right to left at this point, which in this case takes the form of the circulation discussed above. The relatively straight streamlines parallel with the applied electric field indicate that at this level the heterogeneity is too weak to significantly disrupt the main flow.

While a similar circulation pattern at the transition planes was observed as the degree of surface heterogeneity was increased into the intermediate range ($-2 \times 10^{-4} \text{ C/m}^2 = \sigma_{\text{hetero}} = +2 \times 10^{-4} \text{ C/m}^2$), it is apparent from the darker contours shown in Fig. 4.13(b) that the strength of the flow perpendicular to the applied electric field is significantly stronger reaching nearly 50% of the velocity in the homogeneous channel. Unlike in the previous case it is now apparent that the streamlines parallel with the applied electric field are significantly distorted due to the much slower or even oppositely directed velocity over the heterogeneous patch.

At even higher degrees of heterogeneity ($+2 \times 10^{-4} \text{ C/m}^2 = \sigma_{\text{hetero}} = +4 \times 10^{-4} \text{ C/m}^2$) a third flow structure is observed in which a dominant circulatory flow pattern exists along all three coordinate axes, as shown in Fig. 4.13(c). This results in a negligible, or even non-existent, bulk flow in the direction of the applied electric field (which is to be expected since the average surface charge density for these cases is very near zero). As indicated by the grey scales, the velocity perpendicular to the flow axis has again increased in magnitude, reaching a maximum at the edge of the double layer near the symmetry planes at the location where a step change in the surface charge density has been imposed.

It is also shown (Erickson and Li, 2003a) that the induced 3D flow patterns are limited to a layer near the surface with a thickness equivalent to the length scale of the heterogeneous patch. Additionally, the effect becomes smaller in magnitude and more localized as the average size of the heterogeneous region decreases. Moreover, it was demonstrated that while convective effects are small, the electrophoretic influence of the applied electric field could distort the net charge density field near the surface, resulting in a significant deviation from the traditional Poisson–Boltzmann double layer distribution. That is the reason why the Nernst–Planck conservation equations, instead of the Boltzmann distribution equation, were used in this study.

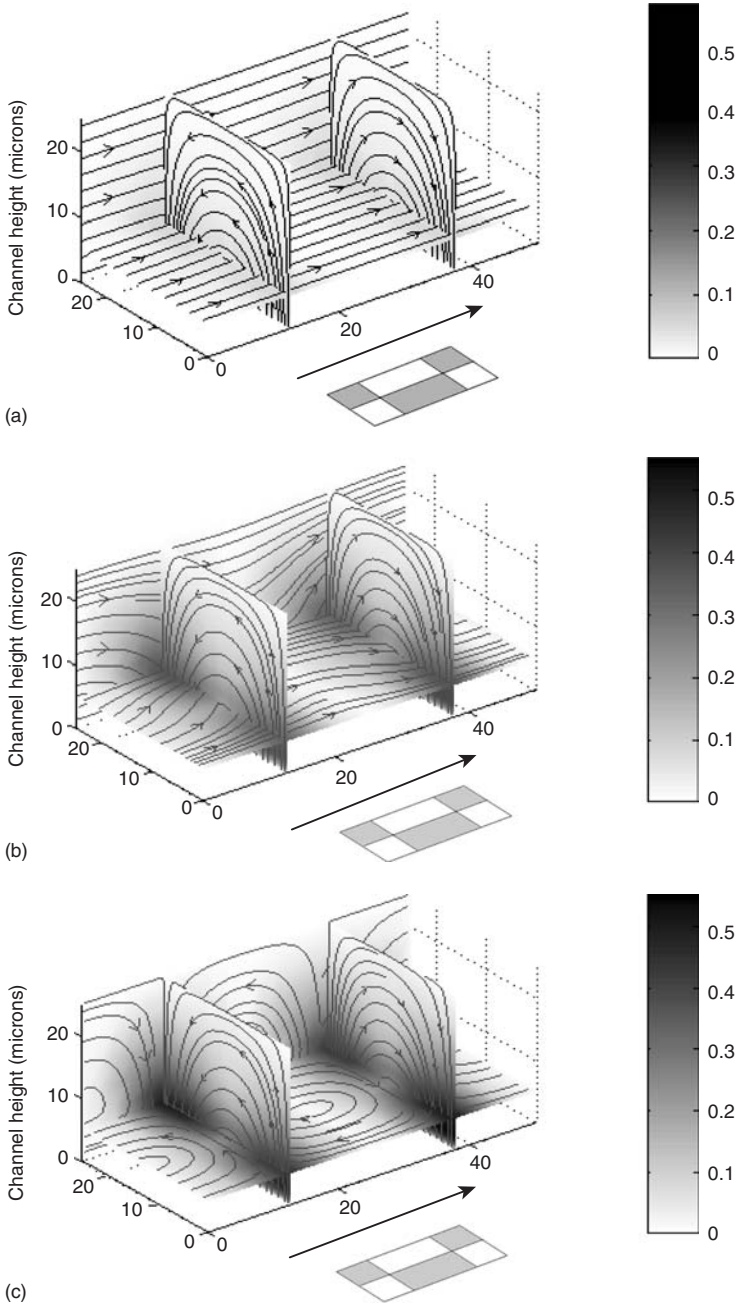


Fig. 4.13. Electroosmotic flow streamlines over a patchwise heterogeneous surface pattern with $\sigma_{\text{homo}} = -4 \times 10^{-4} \text{ C/m}^2$ and (a) $\sigma_{\text{hetero}} = -2 \times 10^{-4} \text{ C/m}^2$ (b) $\sigma_{\text{hetero}} = +2 \times 10^{-4} \text{ C/m}^2$ (c) $\sigma_{\text{hetero}} = +4 \times 10^{-4} \text{ C/m}^2$. The grey scale represents magnitude of velocity perpendicular to the applied potential field, scaled by the maximum velocity in a homogeneous channel. Arrow represents direction of applied electric field.

4.6. AC electroosmotic flow

Electroosmotic flow induced by unsteady applied electric fields or electroosmotic flow under an alternating electrical (AC) field has its unique features and applications. Oddy *et al.* (2001) proposed and experimentally demonstrated a series of schemes for enhanced species mixing in microfluidic devices using AC electric fields. In addition Oddy *et al.* (2001) also presented an analytical flow field model, based on a surface slip condition approach, for an axially applied (i.e. along the flow axis) AC electric field in an infinitely wide microchannel. Comprehensive models for such a slit channel have also been presented by Dutta and Beskok (2001), who developed an analytical model for an applied sinusoidal electric field, and Söderman and Jönsson (1996), who examined the transient flow field caused by a series of different pulse designs. As an alternative to traditional DC electroosmosis, a series of novel techniques have been developed to generate bulk flow using AC fields. For example Green *et al.* (2000) experimentally observed peak flow velocities on the order of hundreds of micrometers per second near a set of parallel electrodes subject to two AC fields, 180° out-of-phase with each other. The effect was subsequently modeled using a linear double layer analysis by González *et al.* (2000). Using a similar principal, both Brown *et al.* (2002) and Studer *et al.* (2002) presented microfluidic devices that incorporated arrays of non-uniformly sized embedded electrodes which, when subject to an AC field, were able to generate a bulk fluid motion. Also using embedded electrodes, Selvaganapathy *et al.* (2002) demonstrated what they termed fr-EOF or bubble-free electroosmotic flow in which a creative periodic waveform was used to yield a net bulk flow while electrolytic bubble formation was theoretically eliminated.

Recently, Erickson and Li presented a combined theoretical and numerical approach to investigate the time periodic electroosmotic flow in a rectangular microchannel (Erickson and Li, 2003b). This work considers the time-periodic electroosmotic flow in a straight, rectangular microchannel. Assuming a fully developed flow field and considering the geometric symmetry, the analytical domain can be reduced to the upper left-hand quadrant of the channel cross-section as shown in Fig. 4.14. For pure electroosmotic flows (i.e. absent

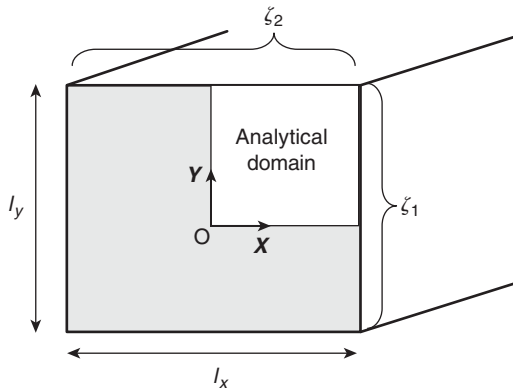


Fig. 4.14. Illustration of the analytical domain in AC electroosmotic flow in a rectangular microchannel.

of any pressure gradients) of incompressible liquids, the Navier–Stokes equations may take the following form:

$$\rho_f \frac{\partial v}{\partial t} = \mu \nabla^2 v + \rho_e E(\omega t) \quad (4.17)$$

where v is the flow velocity, t is time, ρ_f is the fluid density, ρ_e is the net charge density, μ is the fluid viscosity and $E(\omega t)$ is a general time-periodic function with a frequency $\omega = 2\pi f$ and describes the applied electric field strength. To solve this flow equation, we must know the local net charge density ρ_e . This requires solving the EDL field. Introducing the non-dimensional double layer potential, $\Psi = ze\psi/k_b T$, and non-dimensional double layer thickness $K = D_h \kappa$ (where D_h is the hydraulic diameter of the channel, $D_h = 4l_x l_y / 2(l_x + l_y)$, and κ is the Deybe–Hückel parameter). We obtain the non-linear Poisson–Boltzmann distribution equation:

$$\tilde{\nabla}^2 \Psi - K^2 \sinh \Psi = 0 \quad (4.18)$$

where the \sim signifies that the spatial variables in the gradient operator have been non-dimensionalized with respect to D_h (i.e. $X = x/D_h$, $Y = y/D_h$). Eq. (4.18) is subject to the symmetry conditions along the channel center axes, that is,

$$\partial \Psi / \partial X = 0 \text{ at } X = 0 \quad \partial \Psi / \partial Y = 0 \text{ at } Y = 0,$$

and the appropriate conditions at the channel walls,

$$\Psi = Z_1 \text{ at } X = L_x/2 \quad \Psi = Z_2 \text{ at } Y = L_y/2$$

where $Z_{1,2} = ze\zeta_{1,2}/k_b T$, $L_x = l_x/D_h$ and $L_y = l_y/D_h$.

Generally, for multi-dimensional space and complex geometry Eq. (4.18) must be solved numerically. However, under the condition that the double layer potential, $\Psi = ze\psi/k_b T$, is small, Eq. (4.18) can be linearized (the so-called the Deybe–Hückel approximation), yielding,

$$\tilde{\nabla}^2 \Psi - K^2 \Psi = 0 \quad (4.19)$$

The Deybe–Hückel approximation is considered valid only when $|ze\zeta| < k_b T$, which in principal is limited to cases where $|\zeta| \leq 25$ mV at room temperature. For the rectangular geometry shown in Fig. 4.14 an analytical solution to Eq. (4.19), subject to the aforementioned boundary conditions, can be obtained using a separation of variables technique:

$$\begin{aligned} \Psi(X, Y) = & \sum_{n=1}^{\infty} \frac{4(-1)^{n+1}}{\pi(2n-1)} \left[Z_1 \cos(\lambda_n X) \frac{\cosh([\lambda_n^2 + K^2]^{1/2} Y)}{\cosh([\lambda_n^2 + K^2]^{1/2} L_Y)} \right] \\ & + \sum_{n=1}^{\infty} \frac{4(-1)^{n+1}}{\pi(2n-1)} \left[Z_2 \cos(\mu_n Y) \frac{\cosh([\mu_n^2 + K^2]^{1/2} X)}{\cosh([\mu_n^2 + K^2]^{1/2} L_X)} \right] \end{aligned} \quad (4.20)$$

where λ_n and μ_n are the eigenvalues given by $\lambda_n = \pi(2n-1)/2L_X$ and $\mu_n = \pi(2n-1)/2L_Y$, respectively. Introducing the non-dimensional time, $\theta = \mu t / \rho_f D_h^2$, and the non-dimensional frequency, $\Omega = \rho_f D_h^2 \omega / \mu$, scaling the flow velocity by the electroosmotic slip velocity, $V = vze\mu / \varepsilon E_z k_b T$, where E_z is a constant equivalent to the strength of the applied electric field, and combining Eq. (4.17) with the Poisson equation:

$$\varepsilon \nabla^2 \psi = \rho_e$$

and Eq. (4.18) yield the non-dimensional flow equation,

$$\frac{\partial V}{\partial \theta} = \tilde{\nabla}^2 V - K^2 \sinh \Psi F(\Omega \theta) \quad (4.21)$$

where F is a general periodic function of unit magnitude such that $E(\Omega \theta) = E_z F(\Omega \theta)$. Along the channel axes Eq. (4.21) is subject to a symmetry boundary conditions,

$$\partial V / \partial X = 0 \text{ at } X = 0 \quad \partial V / \partial Y = 0 \text{ at } Y = 0$$

while no-slip conditions are applied along the solid channel walls,

$$V = 0 \text{ at } X = L_X/2 \text{ and } Y = L_Y/2$$

In order to obtain an analytical solution to Eq. (4.21), the Deybe–Hückel approximation is implemented and $F(\Omega \theta)$ is chosen to be a sinusoid function, resulting in the following form of the equation:

$$\frac{\partial V}{\partial \theta} = \tilde{\nabla}^2 V - K^2 \Psi(X, Y) \sin \Omega \theta \quad (4.22)$$

Using a Green's Function approach, an analytical solution to Eq. (4.22), subject to the homogeneous boundary conditions discussed above, can be obtained

$$\begin{aligned} V(X, Y, \theta) = & \frac{-16K^2}{L_X L_Y} \sum_{l=1}^{\infty} \sum_{m=1}^{\infty} \sum_{n=1}^{\infty} \frac{(-1)^{n+1}}{\pi(2n-1)} \cos(\lambda_l X) \cos(\mu_m Y) \\ & \times \left[\frac{(\lambda_l^2 + \mu_m^2) \sin(\Omega \theta) - \Omega \cos(\Omega \theta) + \Omega \exp(-[\lambda_l^2 + \mu_m^2] \theta)}{(\lambda_l^2 + \mu_m^2)^2 + \Omega^2} \right] [f_{1mn} + f_{2ln}] \end{aligned} \quad (4.23)$$

where f_{1mn}/f_{2ln} are given by:

$$\begin{aligned} f_{1mn} &= \begin{cases} 0 & n \neq m \\ \frac{Z_1 \mu_m (-1)^{m+1}}{\lambda_n^2 + \mu_m^2 + K^2} \left(\frac{L_X}{2} \right) & n = m \end{cases} \\ f_{2ln} &= \begin{cases} 0 & n \neq l \\ \frac{Z_2 \lambda_l (-1)^{l+1}}{\mu_n^2 + \lambda_l^2 + K^2} \left(\frac{L_Y}{2} \right) & n = l \end{cases} \end{aligned}$$

Equation (4.23) represents the full solution to the transient flow problem. The equation can be somewhat simplified in cases where the quasi-steady state time periodic solution (i.e. after the influence of the initial conditions has dissipated) is of interest. As these initial effects are represented by the exponential term in Eq. (4.23), the quasi-steady state time periodic solution has the form shown below:

$$V(X, Y, \theta) = \frac{-16K^2}{L_X L_Y} \sum_{l=1}^{\infty} \sum_{m=1}^{\infty} \sum_{n=1}^{\infty} \frac{(-1)^{n+1}}{\pi(2n-1)} \cos(\lambda_l X) \cos(\mu_m Y) \\ \times \left[\frac{(\lambda_l^2 + \mu_m^2) \sin(\Omega \theta) - \Omega \cos(\Omega \theta)}{(\lambda_l^2 + \mu_m^2)^2 + \Omega^2} \right] [f_{1mn} + f_{2ln}] \quad (4.24)$$

In the above analytical description of the uniaxial electroosmotic flow in a rectangular microchannel, the governing parameter is Ω which represents the ratio of the diffusion time scale ($t_{\text{diff}} = \rho_f D_h^2 / \mu$) to the period of the applied electric field ($t_E = 1/\omega$). Figure 4.15 compares the time-periodic velocity profiles (as computed from Eq. (4.24)) in the upper left-hand quadrant of a square channel for two cases: (a) $\Omega = 31$ and (b) $\Omega = 625$. These two Ω values correspond to frequencies of 500 Hz and 10 kHz in a 100 μm square channel or equivalently a 100 μm and a 450 μm square channel at 500 Hz. To illustrate the essential features of the velocity profile a relatively large double layer thickness has been used, $\kappa = 3 \times 10^6 \text{ m}^{-1}$ (corresponding to a bulk ionic concentration $n_{\infty} = 10^{-6} \text{ M}$), and a uniform surface potential of $\zeta = -25 \text{ mV}$ was selected (within the bounds imposed by the Deybe–Hückel linearization).

From Fig. 4.15, it is apparent that the application of the electrical body force results in a rapid acceleration of the fluid within the double layer. In the case where the diffusion time scale is much greater than the oscillation period (high Ω , Fig. 4.15(b)) there is insufficient time for fluid momentum to diffuse far into the bulk flow and thus while the fluid within the double layer oscillates rapidly the bulk fluid remains almost stationary. At $\Omega = 31$ there is more time for momentum diffusion from the double layer, however the bulk fluid still lags behind the flow in the double layer (this out-of-phase behavior will be discussed shortly). Extrapolating from these results, when $\Omega < 1$, such that momentum diffusion is faster than the period of oscillation, the plug type velocity profile characteristic of steady state electroosmotic flow would be expected at all times.

Another interesting feature of the velocity profiles shown in Fig. 4.15 is the local velocity maximum observed near the corner (most clearly visible in the $\Omega = 625$ case at $t = \pi/2\omega$ and $t = \pi/\omega$). The intersection of the two walls results in a region of double layer overlap and thus an increased net charge density over that region in the double layer. This peak in the net charge density corresponds to a larger electrical body force and hence a local maximum electroosmotic flow velocity, it also increases the ratio of the electrical body force to the viscous retardation allowing it to respond more rapidly to changes in the applied electric field.

The finite time required for momentum diffusion will inevitably result in some degree of phase shift between the applied electric field and the flow response in the channel. From Fig. 4.15, however, it is apparent that within the limit of $\Omega > 1$, this phase shift is significantly different in the double layer region than in the bulk flow. It is apparent that the response of the fluid within the double layer to the AC field is essentially immediate,

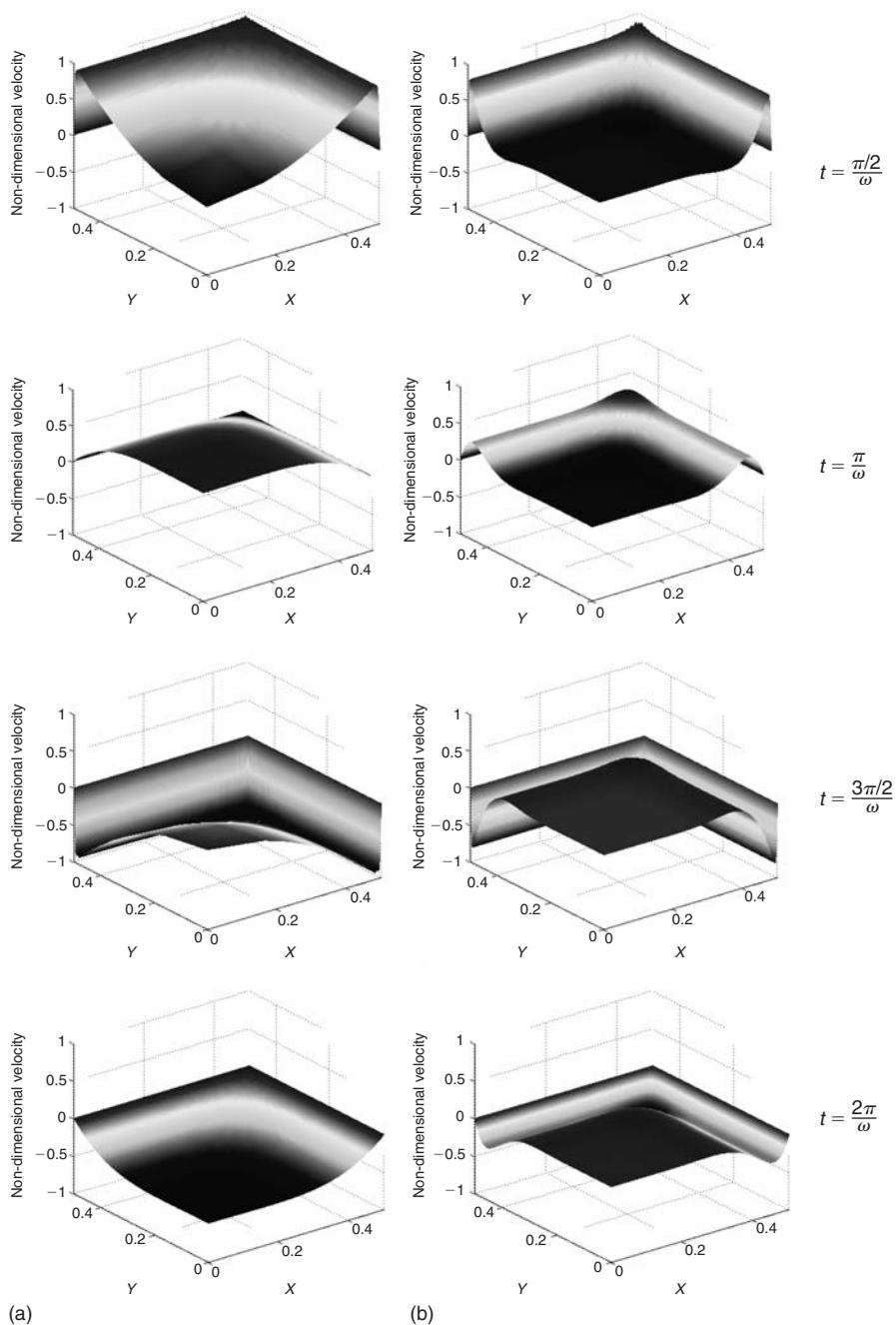


Fig. 4.15. Steady-state time periodic electroosmotic velocity profiles in a square microchannel at (a) $\Omega = 30$ and (b) $\Omega = 625$ (equivalent to an applied electric field frequency of (a) 500 Hz and (b) 10 kHz in a 100 μm square channel).

however, the bulk liquid lags behind the applied field by a phase shift depending on the Ω value. Additionally while the velocity in the double layer reaches its steady state oscillation almost immediately, the bulk flow requires a period before the transient effects are dissipated. In Eq. (4.24) the out-of-phase cosine term ($\Omega \cos(\Omega\theta)$) is proportionally scaled by Ω , thus as expected when Ω is increased, the phase shift for both the double layer and bulk flow velocities is increased as is the number of cycles required to reach the steady state. It is interesting to note the net positive velocity at the channel midpoint within the transient period before decaying into the steady state behavior. This is a result of the initial positive impulse given to the system when the electric field is first applied and is reflected by the exponential term in Eq. (4.23). The transient oscillations were observed to decay at an exponential rate, as expected from this transient term in Eq. (4.23). Similar to the out-of-phase cosine term, this exponential term is also proportionally scaled by the non-dimensional frequency, suggesting that the effect of the initial impulse becomes more significant with increasing Ω .

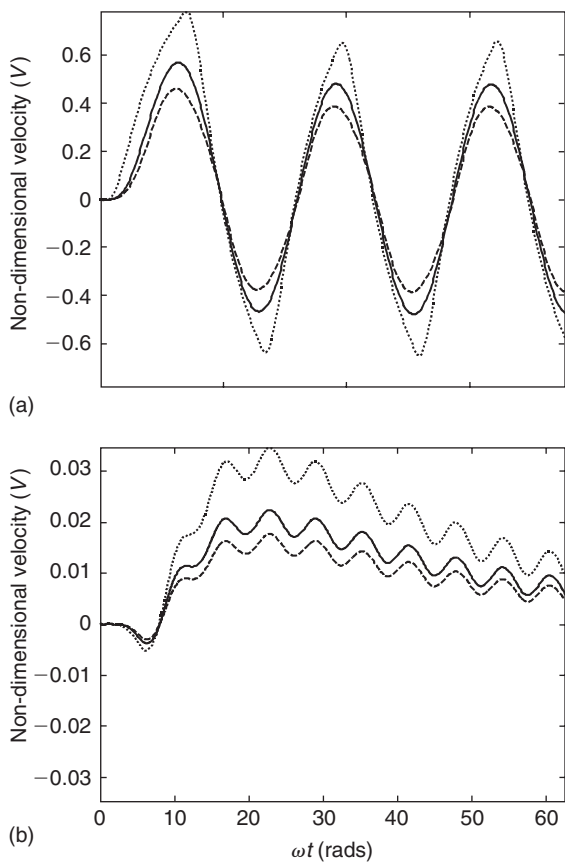


Fig. 4.16. Transient stage velocity at channel midpoint for impulsively started flows using different waveforms at (a) $\Omega = 30$ and (b) $\Omega = 625$. Solid line represents sin wave, long dashed line represents triangular wave and dotted line represents square wave.

The results presented above are limited to sinusoidal waveforms. To examine how the flow field will respond to different forms of periodic excitation, such as a square (step) or triangular waveforms, numerical solutions to Eqs. (4.17) and (4.18) are required. Figure 4.15 shows that the particular waveform also has a significant effect on the transient response of the bulk fluid (here the channel mid point is chosen as a representative point). As can be seen in Fig. 4.16(a) for the $\Omega = 31$ case, a square wave excitation tends to produce higher velocities whereas the triangular wave exhibits slightly smaller bulk velocities when compared with the sinusoidal waveform. As Ω is increased, the initial positive impulsive velocity is observed for both additional waveforms as shown in Fig. 4.16(b). As expected the fluid excited by the square waveform exhibits higher instantaneous velocities, which lead to an increase in the number of cycles required to reach the time periodic quasi-steady state oscillation.

4.7. Electrokinetic mixing

Let us consider a simple T-shaped microfluidic mixing system (Erickson and Li, 2002b). Without loss of the generality, we will consider that two electrolyte solutions of the same flow rate enter a T-junction separately from two horizontal microchannels, and then start mixing while flowing along the vertical microchannel, as illustrated in Fig. 4.17. The flow is generated by the applied electrical field via electrodes at the upstream and the downstream positions. This simple arrangement has been used for numerous applications including the dilution of a sample in a buffer (Harrison *et al.*, 1993), the development of complex species gradients (Jeon *et al.*, 2000; Dertinger *et al.*, 2001), and measurement of the diffusion coefficient (Kamholz *et al.*, 2001). Generally most microfluidic mixing systems are limited to the low Reynolds number regime and thus species mixing is strongly diffusion dominated, as opposed to convection or turbulence dominated at higher Reynolds numbers. Consequently mixing tends to be slow and occur over relatively long distances and time. As an example the concentration gradient generator presented by Dertinger *et al.* (2001) required a mixing channel length on the order of 9.25 mm for a $45 \mu\text{m} \times 45 \mu\text{m}$ cross-sectional channel or approximately 200 times the channel width to achieve nearly complete mixing. Enhanced microfluidic mixing over a short flow distance is highly desirable for lab-on-a-chip applications. One possibility of doing so is to utilize the local circulation flow caused by the surface heterogeneous patches.

To model such an electroosmotic flow and mixing process, we need the following equations. The flow field is described by the Navier–Stokes Equations and the continuity Equation (given below in non-dimensional form):

$$\text{Re} \left[\frac{\partial V}{\partial \tau} + (V \cdot \tilde{\nabla})V \right] = -\tilde{\nabla}P + \tilde{\nabla}^2 V \quad (4.25)$$

$$\tilde{\nabla} V = 0 \quad (4.26)$$

where V is the non-dimensional velocity ($V = v/v_{\text{eo}}$, where v_{eo} is calculated using Eq. (4.27) given below), P is the non-dimensional pressure, τ is the non-dimensional time and Re is

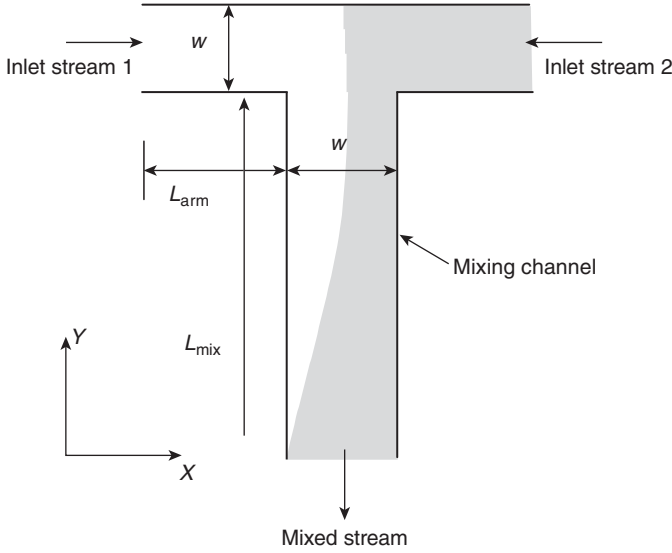


Fig. 4.17. T-Shaped micromixer formed by the intersection of two microchannels, showing a schematic of the mixing or dilution process.

the Reynolds number given by $Re = \rho v_{eo} L / \eta$ where L is a length scale taken as the channel width (w from Fig. 4.17) in this case. The \sim symbol over the ∇ operator indicates the gradient with respect to the non-dimensional coordinates ($X = x/w$, $Y = y/w$ and $Z = z/w$).

It should be noted that in order to simplify the numerical solution to the problem, we have treated the electroosmotic flow in the thin EDL as a slip flow velocity boundary condition, given by:

$$v_{eo} = \mu_{eo} \nabla \phi = \left(\frac{\varepsilon_w \zeta}{\mu} \right) \nabla \phi \quad (4.27)$$

where $\mu_{eo} = (\varepsilon_w \zeta / \mu)$ is the electroosmotic mobility, ε_w is the electrical permittivity of the solution, μ is the viscosity, ζ is the zeta potential of the channel wall, and ϕ is the applied electric field strength.

In general the high voltage requirements limit most practical electroosmotically driven flows in microchannels to small Reynolds numbers, therefore to simplify Eq. (4.25) we ignore transient and convective terms and limit ourselves to cases where $Re < 0.1$.

We consider the mixing of equal portions of two buffer solutions, one of which contains a species of interest at a concentration, c_o . Species transport by electrokinetic means is accomplished by three mechanisms: convection, diffusion and electrophoresis, and can be described by:

$$Pe \left[\frac{\partial C}{\partial \tau} + \tilde{\nabla} \cdot (C(V + V_{ep})) \right] = \tilde{\nabla}^2 C \quad (4.28)$$

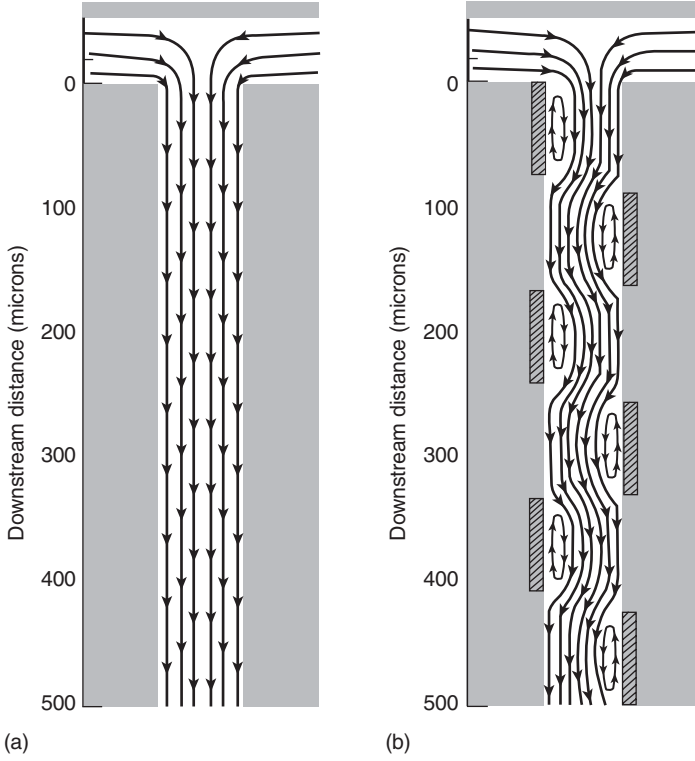


Fig. 4.18. Electroosmotic streamlines at the mid-plane of a 50 μm T-shaped micromixer for the (a) homogeneous case with $\zeta = -42$ mV, (b) heterogeneous case with six offset patches on the left- and right-channel walls. All heterogeneous patches are represented by the crosshatched regions and have a $\zeta = +42$ mV. The applied voltage is $\phi_{\text{app}} = 500$ V/cm.

where C is the non-dimensional species concentration ($C = c/c_0$, where c_0 is original concentration of the interested species in the buffer solution.), Pe is the Péclet number ($Pe = v_{eo}w/D$, where D is the diffusion coefficient), and V_{ep} is the non-dimensional electrophoretic velocity equal to v_{ep}/v_{eo} where v_{ep} is given by:

$$v_{ep} = \mu_{ep} \nabla \phi \quad (4.29)$$

and $\mu_{ep} = (\epsilon_w \zeta_p / \eta)$ is the electrophoretic mobility (ϵ_w is the electrical permittivity of the solution, μ is the viscosity, ζ_p is the zeta potential of the to-be-mixed charged molecules or particles) (Hunter, 1981). As we are interested in the steady state solution, the transient term in Eq. (4.28) can be ignored.

The above described model was solved numerically to investigate the formation of electroosmotically induced flow circulation regions near surface heterogeneities in a T-shaped micromixer and to determine the influence of these regions on the mixing effectiveness. In Fig. 4.18 we compare the mid-plane flow field near the T-intersection of a homogeneous mixing channel with that of a mixing channel having a series of 6 asymmetrically

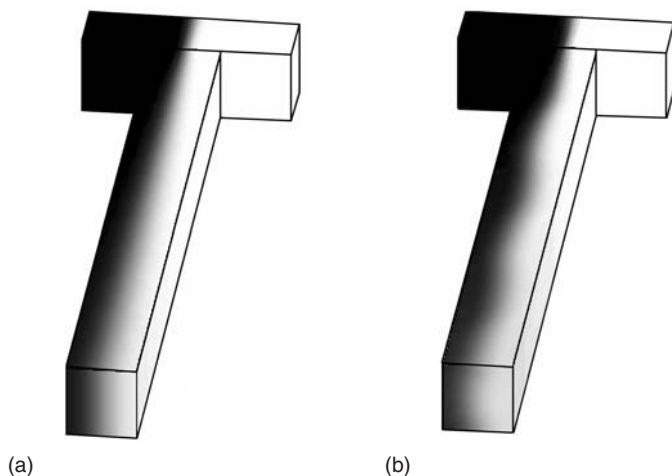


Fig. 4.19. 3D species concentration field for a $50\ \mu\text{m} \times 50\ \mu\text{m}$ T-shaped micromixer resulting from the flow fields shown in Fig. 4.23. (a) homogeneous case and (b) heterogeneous case with offset patches. Species diffusivity is $3 \times 10^{-10}\ \text{m}^2/\text{s}$ and zero electrophoretic mobility are assumed.

distributed heterogeneous patches on the left- and right-channel walls. For clarity the heterogeneous regions are marked as the crosshatched regions in this figure. The homogeneous channel surface has a ζ potential of $-42\ \text{mV}$. A ζ -potential of $\zeta = +42\ \text{mV}$ was assumed for the heterogeneous patches. Apparently, the channel with heterogeneous patches generates local flow circulations near the patches. These flow circulation zones are expected to enhance the mixing of the two streams.

Figure 4.19 compares the 3D concentration fields of the homogeneous and heterogeneous mixing channel shown in Fig. 4.18. In these figures a neutral mixing species (i.e. $\mu_{\text{ep}} = 0$, thereby ignoring any electrophoretic transport) with a diffusion coefficient $D = 3 \times 10^{-10}\ \text{m}^2/\text{s}$ is considered. While mixing in the homogeneous case is purely diffusive in nature, the presence of the asymmetric circulation regions, Fig. 4.19(b), enables enhanced mixing by convection.

Recently a passive electrokinetic micromixer based on the use of surface charge heterogeneity was developed (Biddiss *et al.*, 2004). The micromixer is a T-shaped microchannel structure ($200\ \mu\text{m}$ in width and approximately $8\ \mu\text{m}$ in depth) made from Polydimethylsiloxane (PDMS) and is sealed with a glass slide. Microchannels were fabricated using a rapid prototyping/soft-lithography technique. The glass surface was covered by a PDMS mask with the desired heterogeneous pattern, then treated with a Polybrene solution. After removing the mask, the glass surface will have selective regions of positive surface charge while leaving the majority of the glass slide with its native negative charge (Biddiss *et al.*, 2004). Finally the PDMS plate (with the microchannel structure) will be bonded to the glass slide to form the sealed, T-shaped microchannel with heterogeneous patches on the mixing channel surface.

A micromixer consisting of 6 offset staggered patches (in the mixing channel) spanning $1.8\ \text{mm}$ downstream and offset $10\ \mu\text{m}$ from the channel centerline with a width of $90\ \mu\text{m}$

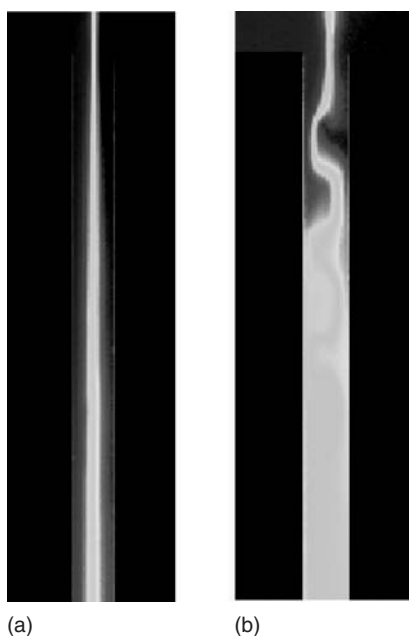


Fig. 4.20. Images of steady-state species concentration fields under an applied potential of 280 V/cm for (a) the homogeneous microchannel and (b) the heterogeneous microchannel with six offset staggered patches.

and a length of 300 μm , was analyzed experimentally. Mixing experiments were conducted at applied voltage potentials ranging between 70 and 555 V/cm and the corresponding Reynolds numbers range from 0.08 to 0.7 and Péclet numbers from 190 to 1500. The liquid is a 25 mM sodium carbonate/bicarbonate buffer. To visualize the mixing effects, 100 μM fluorescein was introduced through one inlet channel. As an example, Fig. 4.20 shows the experimental images of the steady state flow for the homogenous and heterogeneous cases at 280 V/cm. The enhanced mixing effect is obvious.

This experimental study shows that the passive electrokinetic micromixer with an optimized arrangement of surface charge heterogeneities can increase flow narrowing and circulation, thereby increasing the diffusive flux and introducing an advective component of mixing. Mixing efficiencies were improved by 22–68% for voltages ranging from 70 to 555 V/cm. For producing a 95% mixture, this technology can reduce the required mixing channel length of up to 88% for flows with Péclet numbers between 190 and 1500, and Reynolds numbers between 0.08 and 0.7. In terms of required channel lengths, at 280 V/cm, a homogeneous microchannel would require a channel mixing length of 22 mm for reaching a 95% mixture. By implementing the developed micromixer, an 88% reduction in required channel length to 2.6 mm was experimentally demonstrated. Practical applications of reductions in required channel lengths include improvements in portability and shorter retention times, both of which are valuable advancements applicable to many microfluidic devices.

4.8. Electrokinetic sample dispensing

An important component of many bio- or chemical lab-chips is the microfluidic dispenser, which employs electroosmotic flow to dispense minute quantities (e.g. 300 pico-liters) of samples for chemical and biomedical analysis. The precise control of the dispensed sample in microfluidic dispensers is key to the performance of these lab-on-a-chip devices.

Let us consider a microfluidic dispenser formed by two crossing microchannels as shown in Fig. 4.21 (Ren and Li, 2002). The depth and the width of all the channels are chosen to be $20\text{ }\mu\text{m}$ and $50\text{ }\mu\text{m}$, respectively. There are four reservoirs connected to the four ends of the microchannels. Electrodes are inserted into these reservoirs to set up the electrical field across the channels. Initially, a sample solution (a buffer solution with sample species) is filled in Reservoir 1, the other reservoirs and the microchannels are filled with the pure buffer solution. When the chosen electrical potentials are applied to the four reservoirs, the sample solution in Reservoir 1 will be driven to flow toward Reservoir 3 passing through the intersection of the cross channels. This is the so-called loading process. After the loading process reaches a steady state, the sample solution loaded in the intersection will be “cut” or dispensed into the dispensing channel by the dispensing solution flowing from Reservoir 2 to 4. This can be realized by adjusting the electrical potentials applied to these four reservoirs. This is the so called the dispensing process. The volume and the concentration of the dispensed sample are the key parameters of this dispensing process, and they depend on the applied electrical field, the flow field and the concentration field during the loading and the dispensing processes.

To model such a dispensing process, we must model the applied electrical field, the flow field and the concentration field. To simplify the analysis, we consider this as a 2D problem,

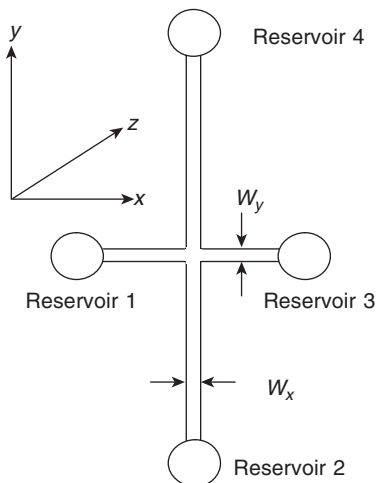


Fig. 4.21. The schematic diagram of a crossing microchannel dispenser. W_x and W_y indicate the width of the microchannels.

that is, ignoring the variation in the z -direction. The 2D applied electrical potential in the liquid can be described by:

$$\frac{\partial^2 \phi^*}{\partial x^{*2}} + \frac{\partial^2 \phi^*}{\partial y^{*2}} = 0$$

Here the non-dimensional parameters are defined by:

$$\phi^* = \frac{\phi}{\Phi}, \quad x^* = \frac{x}{h}, \quad y^* = \frac{y}{h}$$

where Φ is a reference electrical potential and h is the channel width chosen as $50 \mu\text{m}$. Boundary conditions are required to solve this equation. We impose the insulation condition to all the walls of microchannels, and the specific non-dimensional potential values to all the reservoirs. Once the electrical field in the dispenser is known, the local electric field strength can be calculated by

$$\vec{E} = -\vec{\nabla}\Phi$$

The electroosmotic flow field reaches steady state in milli-seconds, much shorter than the characteristic time scales of the sample loading and sample dispensing. Therefore, the electroosmotic flow here is approximated as steady state. Furthermore, we consider a thin EDL, and use the slip flow boundary condition to represent the electroosmotic flow. The liquid flow field can thus be described by the following non-dimensional momentum equation and the continuity equation:

$$\begin{aligned} u_{\text{eo}}^* \frac{\partial u_{\text{eo}}^*}{\partial x^*} + v_{\text{eo}}^* \frac{\partial u_{\text{eo}}^*}{\partial y^*} &= -\frac{\partial P^*}{\partial x^*} + \frac{\partial^2 u_{\text{eo}}^*}{\partial x^{*2}} + \frac{\partial^2 u_{\text{eo}}^*}{\partial y^{*2}} \\ u_{\text{eo}}^* \frac{\partial v_{\text{eo}}^*}{\partial x^*} + v_{\text{eo}}^* \frac{\partial v_{\text{eo}}^*}{\partial y^*} &= -\frac{\partial P^*}{\partial y^*} + \frac{\partial^2 v_{\text{eo}}^*}{\partial x^{*2}} + \frac{\partial^2 v_{\text{eo}}^*}{\partial y^{*2}} \\ \frac{\partial u_{\text{eo}}^*}{\partial x^*} + \frac{\partial v_{\text{eo}}^*}{\partial y^*} &= 0 \end{aligned}$$

where u_{eo} , v_{eo} are the electroosmotic velocity component in x - and y -direction, respectively, and non-dimensionalized as follows:

$$P^* = \frac{P - Pa}{\rho(v/h)^2}, \quad u_{\text{eo}}^* = \frac{u_{\text{eo}}h}{v}, \quad v_{\text{eo}}^* = \frac{v_{\text{eo}}h}{v}$$

The slip velocity conditions are applied to the walls of the microchannels, the fully developed velocity profile is applied to all the interfaces between the microchannels and the reservoirs, and the pressures in the four reservoirs are assumed to be the atmospheric pressure.

The distribution of the sample concentration can be described by the conservation law of mass, taking the following form:

$$\frac{\partial C_i^*}{\partial \tau} + (u_{\text{eo}}^* + u_{\text{ep}}^*) \frac{\partial C_i^*}{\partial x^*} + (v_{\text{eo}}^* + v_{\text{ep}}^*) \frac{\partial C_i^*}{\partial y^*} = \frac{D_i}{v} \left(\frac{\partial^2 C_i^*}{\partial x^{*2}} + \frac{\partial^2 C_i^*}{\partial y^{*2}} \right)$$

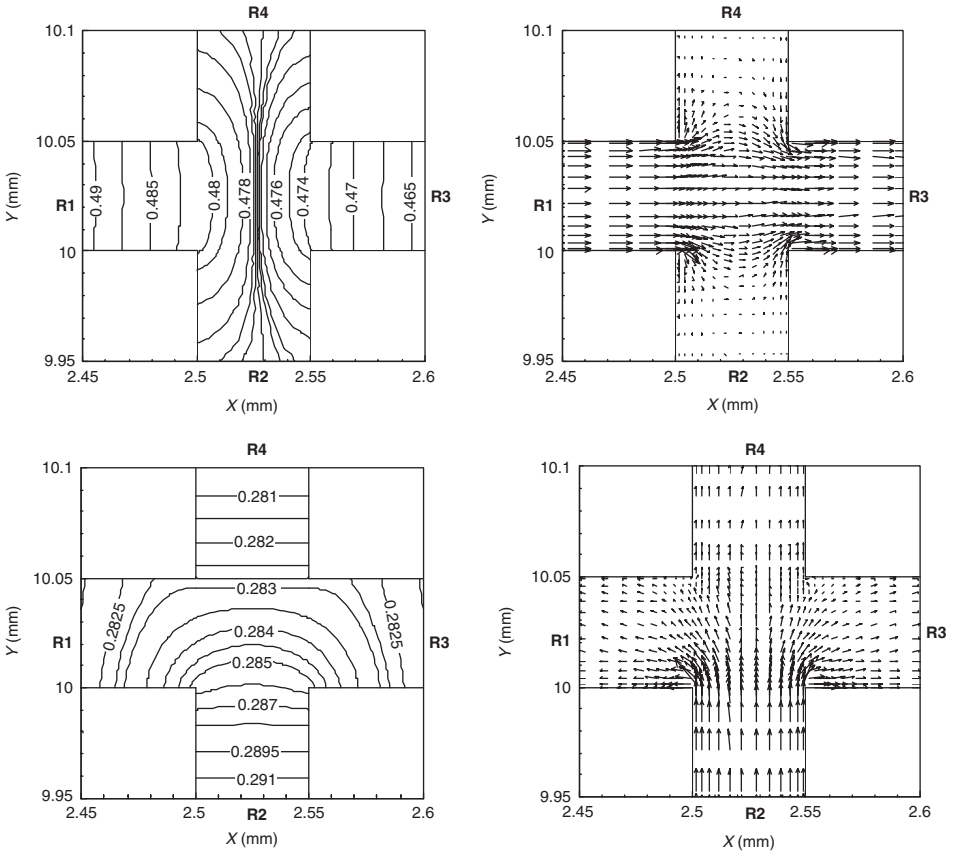


Fig. 4.22. Examples of the applied electrical field (left) and the flow field (right) at the intersection of the microchannels in a loading process (top) and in a dispensing process (bottom).

where C_i is the concentration of the i th species, u_{e0} and v_{e0} are the components of the electroosmotic velocity of the i th species, D_i is the diffusion coefficient of the i th species, and u_{epi} and v_{epi} are the components of the electrophoretic velocity of the i th species given by $u_{epi} = E\mu_{epi}$, where μ_{epi} is the electrophoretic mobility. The non-dimensional parameters in the above equation are defined by $C^* = C/\bar{C}$, and $\tau = t/(h^2/\nu)$, where \bar{C} is a reference concentration.

Figure 4.22 shows the typical electrical field and flow field (computer simulated) for the loading and dispensing process, respectively. In this figure, the non-dimensional applied electrical potentials are: $\phi^*(1) = 1.0$, $\phi^*(2) = 1.0$, $\phi^*(3) = 0.0$, $\phi^*(4) = 1.0$ for the loading process, and $\phi^*(1) = 0.2$, $\phi^*(2) = 2.0$, $\phi^*(3) = 0.2$, $\phi^*(4) = 0.0$ for the dispensing process, where $\phi^*(i)$ represents the non-dimensional applied electrical potential to i th reservoir. For this specific case, the electrical field and the flow field for the loading process are symmetric to the middle line of the horizontal channel, and the electrical field and the flow field for the dispensing process are symmetric to the middle line of the vertical channel.

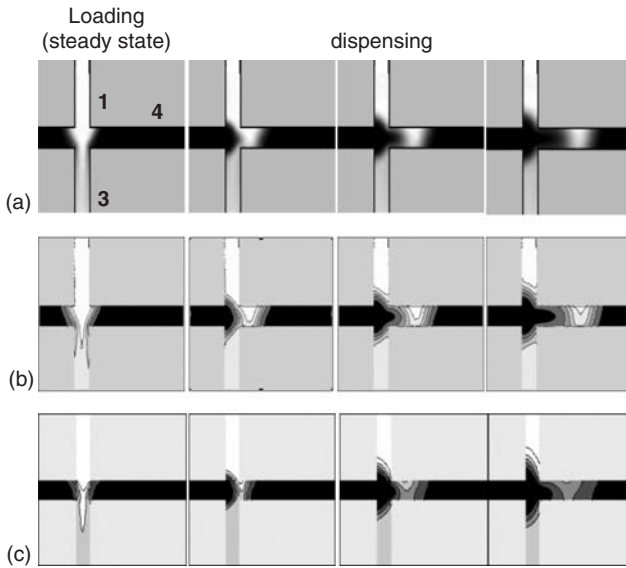


Fig. 4.23. The loading and dispensing of a focused fluorescein sample: (a) Processed images; (b) iso-concentration profiles at $0.1C_0$, $0.3C_0$, $0.5C_0$, $0.7C_0$, and $0.9C_0$, calculated from the images and (c) corresponding iso-concentration profiles calculated through numerical simulation.

The electrokinetic dispensing processes of fluorescent dye samples were investigated experimentally (Sinton *et al.*, 2003b, c, d). The measurements were conducted by using a fluorescent dye-based microfluidic visualization system. Fig. 4.23 shows a sample dispensing process and the comparison of the dispensed sample concentration profile with the numerically simulated results. Both the theoretical studies and the experimental studies have demonstrated that the loading and dispensing of sub-nanolitre samples using a microfluidic crossing microchannel chip can be controlled electrokinetically. The ability to inject and transport large axial extent, concentration-dense samples was demonstrated. Both experimental and numerical results indicate the shape, cross-stream uniformity, and axial extent of the samples were very sensitive to changes in the electric fields applied in the loading channel. In the dispensing process, larger samples were shown to disperse less than focused samples, maintaining more solution with the original sample concentration.

4.9. Practice problems

1. Model and simulate 1D steady state electroosmotic flow in a circular capillary under an applied DC field. Plot and discuss the EDL field and flow field, effects of zeta potential, bulk ionic concentration, applied voltage and diameter.
2. Model and simulate a 1D steady state electroosmotic flow in a microchannel under an applied DC field and a small externally applied pressure difference along the channel. Plot and discuss the flow field in terms of the value and the direction of the applied pressure gradient, zeta potential and the applied electrical field.

3. Model and simulate 1D electroosmotic flow in a circular capillary under an applied AC field. Plot and discuss the flow field, effects of the zeta potential, the bulk ionic concentration, the AC voltage and frequency, and diameter of the capillary.
4. Model and simulate a steady state electroosmotic flow in a microchannel with a 90 degree turn under an applied DC field. Plot and discuss the flow field in terms of the zeta potential, the channel size and the applied electrical field.
5. Model and simulate electroosmotic flow in a converging–diverging circular microcapillary with a constant zeta potential, Plot the flow field (streamlines and velocity) and the induced pressure field, and discuss the effects of the applied field strength, dimensions of the converging–diverging microchannel, and the zeta potentials.
6. Model and simulate electroosmotic mixing of two aqueous solutions in a homogeneous T-shaped microchannel. Plot the flow field (streamlines and velocity) and the concentration field in the mixing channel, and discuss the effects of the applied field strengths at the two inlets, the zeta potential and dimensions of the microchannel on the mixing length (i.e. the length required to have 99% of mixing).

References

- Ajdari, A., Electroosmosis on inhomogeneously charged surfaces, *Phys. Rev. Lett.*, **75**, 755–758, 1995.
- Ajdari, A., Generation of transverse fluid currents and forces by an electric field: electro-osmosis on charge-modulated and undulated surfaces, *Phys. Rev. E.*, **53**, 4996–5005, 1996.
- Ajdari, A., Transverse electrokinetic and microfluidic effects in micropatterned channels: lubrication analysis for slab geometries, *Phys. Rev. E.*, **65**, 016301, 2001.
- Anderson, J. L., Effect of nonuniform zeta potential on particle movement in electric fields, *J. Colloid Interface Sci.*, **105**, 45–54, 1985.
- Arulanandam, S. and Li, D., Liquid transport in rectangular microchannels by electroosmotic pumping, *Colloid Surface A*, **161**, 89–102, 2000a.
- Arulanandam, S. and Li, D., Evaluation of zeta potential and surface conductance by measuring electro-osmotic current, *J. Colloid Interface Sci.*, **225**, 421–428, 2000b.
- Biddiss, E., Erickson, D., and Li, D., Heterogeneous surface charge enhanced micro-mixing for electrokinetic flows, *Anal. Chem.*, **76**, 3208–3213, 2004.
- Brown, A. B. D., Smith, C. G., and Rennie, A. R., Pumping of water with an AC electric field applied to asymmetric pairs of microelectrodes, *Phys. Rev. E.*, **63**, 016305 1–8, 2002.
- Dahm, W. J. A., Su, L. K., and Southerland, K. B., A scalar imaging velocimetry technique for fully resolved four-dimensional vector velocity field measurement in turbulent flows, *Phys. fluid A*, **4**, 2191–2206, 1992.
- Dertinger, S. K. W., Chiu, D. T., Jeon, N. L., and Whitesides, G. M., Generation of gradients having complex shapes using microfluidic networks, *Anal. Chem.*, **73**, 1240–1246, 2001.
- Dutta, P. and Beskok, A., Analytical solution of time periodic electroosmotic flows: analogies to stokes second problem, *Anal. Chem.*, **73**, 5097–5102, 2001.
- Erickson, D. and Li, D., Influence of surface heterogeneity on electrokinetically driven microfluidic mixing, *Langmuir*, **18**, 8949–8959, 2002a.
- Erickson, D. and Li, D., Microchannel flow with patch-wise and periodic surface heterogeneity, *Langmuir*, **18**, 1883–1892, 2002b.
- Erickson, D. and Li, D., Three dimensional structure of electroosmotic flows over periodically heterogeneous surface patterns, *J. Phys. Chem. B.*, **107**, 12212–12220, 2003a.

- Erickson, D. and Li, D., Analysis of AC electroosmotic flows in a rectangular microchannel, *Langmuir*, **19**, 5421–5430, 2003b.
- Ghosal, S., Lubrication theory for electro-osmotic flow in a microfluidic channel of slowly varying cross-section and wall charge, *J. Fluid. Mech.*, **459**, 103–128, 2002.
- González, A., Ramos, A., Green, N. G., Castellanos, A., and Morgan, H., Fluid flow induced by non-uniform AC electric fields in electrolytes on microelectrodes II: A linear double layer analysis, *Phys. Rev. E.*, **61**, 4019–4028, 2000.
- Green, N. G., Ramos, A., González, A., Morgan, H., and Castellanos, A., Fluid flow induced by non-uniform AC electric fields in electrolytes on microelectrodes I: experimental measurements, *Phys. Rev. E.*, **61**, 4011–4018, 2000.
- Harrison, J. D., Fluri, K., Seiler, K., Fan, Z., Effenhauser, C., and Manz, A., Micromachining a miniaturized capillary electrophoresis-based chemical analysis system on a chip, *Science*, **261**, 895–897, 1993.
- Herr, A. E., Molho, J. I., Santiago, J. G., Mungal, M. G., Kenny, T. W., and Garguilo, M. G., Electroosmotic capillary flow with nonuniform zeta potential, *Anal. Chem.*, **72**, 1053–1057, 2000.
- Hunter, R. J., *Zeta potential in colloid science: principle and applications*, Academic Press, London: 1981.
- Jeon, N. L., Dertinger, S. K. W., Chiu, D. T., Choi, I. S., Stroock, A. D., and Whitesides, G. M., Generation of solution and surface gradients using microfluidic systems, *Langmuir*, **16**, 8311–8316, 2000.
- Johnson, T. J., Ross, D., Gaitan, M., and Locascio, L. E., Laser modification of preformed polymer microchannels: application to reduce band broadening around turns subject to electrokinetic flow, *Anal. Chem.*, **73**, 3656–3661, 2001.
- Kamholz, A. E., Schilling, E. A., and Yager, P., Optical measurement of transverse molecular diffusion in a microchannel, *Biophys. J.*, **80**, 1967–1972, 2001.
- Keely, C. A., van de Goor, T. A. A., and McManigill, D., Modeling flow profiles and dispersion in capillary electrophoresis with nonuniform zeta potential, *Anal. Chem.*, **66**, 4236–4242, 1994.
- Lempert, W. R., Magee, K., Ronney, P., Gee, K. R., and Haugland, R. P., Low tagging velocimetry in incompressible flow using photo-activated noninvasive tracking of molecular motion (PHANTOMM), *Exp. Fluids*, **18**, 249–257, 1995.
- Li, D., *Electrokinetics in microfluidics*, Academic Press, London: 2004.
- Lyklema, J., Fundamentals of interface and colloid science, Vol. II, Solid–Liquid Interfaces, Academic Press, London: 1995.
- Mala, G. M., Li, D., Werner, C., Jacobasch, H. J., and Ning, Y. B., Flow characteristics of water through a microchannel between two parallel plates with electrokinetic effects, *Int. J. Heat Fluid Flow*, **18**, 489–496, 1997.
- Meinhart, C. D., Wereley, S. T., and Santiago, J. D., PIV measurements of a microchannel flow, *Exp. Fluid.*, **27**, 414–419, 1999.
- Molho, J. L., Herr, A. E., Mosier, B. P., Santiago, J. G., Kenny, T. W., Breenen, R. A., Gordon, G. B., and Mohammadi, B., Optimization of turn geometries for microchip electrophoresis, *Anal. Chem.*, **73**, 1350–1360, 2001.
- Oddy, M. H., Santiago, J. G., and Mikkelsen, J. C., Electrokinetic instability micromixing, *Anal. Chem.*, **73**, 5822–5832, 2001.
- Patankar, S., Liu, C., and Sparrow, E., Fully developed flow and heat transfer in ducts having streamwise-periodic variation of cross-sectional area, *J. Heat Trans.*, **99**, 180–186, 1977.
- Paul, P. H., Garguilo, M. G., and Rakestraw, D. J., Imaging of pressure- and electrokinetically driven flows through open capillaries, *Anal. Chem.*, **70**, 2459–2467, 1998.

- Ren, L. and Li, D., Theoretical studies of microfluidic dispensing processes, *J. Colloid Interface Sci.*, **254**, 384–395, 2002.
- Ren, L., Escobedo, C., and Li, D., Electro-osmotic flow in micro-capillary with one solution displacing another solution, *J. Colloid Interface Sci.*, **250**, 238–242, 2002.
- Reuss, E. F., *Memoires de la societe imperiale des naturalistes de moskou.*, **2**, 327, 1809.
- Santiago, J. G., Wereley, S. T., Meinhart, C. D., Beebe, D. J., and Adrian, R. J., A particle image velocimetry system for microfluidics, *Exp. Fluid.*, **25**, 316–319, 1998.
- Selvaganapathy, P., Ki, Y. -S. L., Renaud, P., and Mastrangelo, C. H., Bubble-free electrokinetic pumping, *J. Microelectromech. Sys.*, **11**, 448–453, 2002.
- Singh, A. K., Cummings, E. B., and Throckmorton, D. J., Fluorescent liposome flow markers for microscale particle-image velocimetry, *Anal. Chem.*, **73**, 1057–1061, 2001.
- Sinton, D., Escobedo, C., Ren, L., and Li, D., Direct and indirect electroosmotic flow velocity measurements in microchannels, *J. Colloid Interface Sci.*, **254**, 184–189, 2002.
- Sinton, D., Erickson, D., and Li, D., Micro-bubble lensing induced photobleaching (μ -BLIP) with application to microflow visualization, *Exp. Fluid.*, **35**, 178–187, 2003.
- Sinton, D. and Li, D., Caged-dye based microfluidic velocimetry with near-wall resolution, *Int. J. Therm. Sci.*, **42**, 847–855, 2003a.
- Sinton, D. and Li, D., Electroosmotic velocity profiles in microchannels, *Colloid. Surfaces A.*, **222**, 273–283, 2003b.
- Sinton, D., Ren, L., and Li, D., Visualization and numerical simulation of microfluidic on-chip injection, *J. Colloid Interface Sci.*, **260**, 431–439, 2003.
- Sinton, D., Ren, L., and Li, D., A dynamic loading method for controlling on-chip microfluidic chip sample injection, *J. Colloid Interface Sci.*, **266**, 448–456, 2003c.
- Sinton, D., Ren, L., Xuan, X., and Li, D., Effects of liquid conductivity differences on multi-component sample injection, pumping and stacking in microfluidic chips, *Lab-on-a-Chip*, **3**, 173–179, 2003d.
- Söderman, O. and Jönsson, B., Electro-osmosis: velocity profiles in different geometries with both temporal and spatial resolution, *J. Chem. Phys.*, **105**, 10300–10311, 1996.
- Stroock, A. D., Weck, M., Chiu, D. T., Huck, W. T. S., Kenis, P. J. A., Ismagilov, R. F., and Whitesides, G. M., Patterning electro-osmotic flow with patterned surface charge, *Phys. Rev. Lett.*, **84**, 3314–3317, 2000.
- Studer, V., Pépin, A., Chen, Y., and Ajdari, A., Fabrication of microfluidic devices for AC electrokinetic fluid pumping, *Microelectronic Eng.*, **61–62**, 915–920, 2002.
- Taylor, J. A. and Yeung, E. S., Imaging of hydrodynamic and electrokinetic flow profiles in capillaries, *Anal. Chem.*, **65**, 2928–2932, 1993.
- Wereley, S. T. and Meinhart, C. D., Second-order accurate particle image velocimetry, *Exp. Fluids*, **31**, 258–268, 2001.

FLOW BOILING IN MINICHANNELS AND MICROCHANNELS

Satish G. Kandlikar

Mechanical Engineering Department, Rochester Institute of Technology, Rochester, NY, USA

5.1. Introduction

Flow boiling in minichannels is of great interest in compact evaporator applications. Automotive air-conditioning evaporators use small passages with plate-fin heat exchangers. Extruded channels with passage diameters smaller than 1 mm are already being applied in compact condenser applications. Developments in evaporators to this end are needed to overcome the practical barriers associated with flow boiling in narrow channels. Another application where flow boiling research is actively being pursued is in the heat removal from high heat flux devices, such as computer chips, laser diodes and other electronics devices and components.

Flow boiling is attractive over single-phase liquid cooling from two main considerations:

- (i) High heat transfer coefficient during flow boiling.
- (ii) Higher heat removal capability for a given mass flow rate of the coolant.

Although the heat transfer coefficients are quite high in single phase flow with small diameter channels, flow boiling yields much higher values. For example, the single-phase heat transfer coefficient under laminar flow of water in a 200 μm square channel is around 10,000 $\text{W/m}^2\text{°C}$ (Fig. 1.2), whereas the flow boiling heat transfer coefficients can exceed 100,000 $\text{W/m}^2\text{°C}$ (Steinke and Kandlikar, 2004). In other words, larger channel diameters can be implemented with flow boiling at comparable or even higher heat transfer coefficients than single-phase systems. This feature becomes especially important in view of the filtration requirements to keep the channels clean.

Another major advantage of flow boiling systems is the ability of the fluid to carry larger amounts of thermal energy through the latent heat of vaporization. With water, the latent heat is significantly higher (2257 kJ/kg) than its specific heat of 4.2 kJ/kg°C

E-mail: sgkeme@rit.edu

at 100°C. This feature is especially important for refrigerant systems. Although the latent heat of many potential refrigerants is around 150–300 kJ/kg at temperatures around 30–50°C, it still compares favorably with the single-phase cooling ability of water. However, the biggest advantage is that a suitable refrigerant can be chosen to provide desirable evaporation temperatures, typically below 50°C, without employing a deep vacuum as would be needed for flow boiling with water. Further research in identifying/developing specific refrigerants is needed. The specific desirable properties of a refrigerant for flow boiling application are identified by Kandlikar (2005) and are discussed in Section 5.9.

5.2. Nucleation in minichannels and microchannels

There are two ways in which flow boiling in small diameter channels is expected to be implemented. They are:

- (i) two-phase entry after a throttle valve,
- (ii) subcooled liquid entry into the channels.

The first mode is applicable to the evaporators used in refrigeration cycles. The throttle valve prior to the evaporator can be designed to provide subcooled liquid entry, but more commonly, a two-phase entry with quality between 0 and 0.1 is employed. Although this represents a more practical system, the difficulties encountered with proper liquid distribution in two-phase inlet headers have been a major obstacle to achieving stable operation. Even liquid distribution in the header provides a more uniform liquid flow through each channel in a parallel channel arrangement.

Subcooled liquid entry is an attractive option, since the higher heat transfer coefficients associated with subcooled flow boiling can be utilized. Such systems are essentially extensions of single-phase systems and rely largely on the temperature rise of the coolant in carrying the heat away.

In either of the systems, bubble nucleation is an important consideration. Even with a two-phase entry, it is expected that a slug flow pattern will prevail, and nucleation in liquid slugs will be important. With subcooled liquid entry, early nucleation is desirable for preventing the rapid bubble growth that has been observed by many investigators. An exhaustive review of this topic is provided by Kandlikar (2002a, b). A number of researchers have studied the flow boiling phenomena (e.g. Lazarek and Black, 1982; Cornwell and Kew, 1992; Kandlikar *et al.*, 1995; Kuznetsov and Vitovsky, 1995; Cuta *et al.*, 1996; Kew and Cornwell, 1996; Kandlikar and Spiesman, 1997; Kandlikar *et al.*, 1997; Kasza *et al.*, 1997; Lin *et al.*, 1998; 1999; Jiang *et al.*, 1999; Kamidis and Ravigururajan, 1999; Lakshminarasimhan *et al.*, 2000; Kandlikar *et al.*, 2001; Hetsroni *et al.*, 2002).

The inception of nucleation plays an important role in flow boiling stability, as will be discussed in a later section. The nucleation criteria in narrow channels have been studied by a number of investigators, and it is generally believed that there are no significant differences from the conventional theories for large diameter tubes proposed by Bergles and Rohsenow (1962; 1964), Sato and Matsumura (1964), and Davis and Anderson (1966). These theories are extensions of the pool boiling nucleation models proposed by Hsu and Graham (1961), and Hsu (1962). Kenning and Cooper (1965), and Kandlikar *et al.* (1997)

where σ : surface tension, and r_b : bubble radius. Whether the bubble is able to nucleate and the cavity is able to act as a nucleation site depends on the local temperature field around the bubble. The local temperature in the liquid is evaluated by assuming a linear temperature gradient in a liquid sublayer of thickness $y = \delta_t$ from the temperature at the wall to the temperature in the bulk liquid. Equating the heat transfer rates obtained from the equivalent conduction and convection equations, the thickness δ_t is given by:

$$\delta_t = k_L/h \quad (5.3)$$

where k_L is the thermal conductivity of the liquid and h is the single-phase heat transfer coefficient in the liquid prior to nucleation. The heat transfer coefficient can be obtained from equations given in Chapter 3.

At a given location z , the temperature in the liquid at $y = y_b$ is obtained from the linear temperature profile as shown in Fig. 5.1:

$$T_{L,y_b} = T_W - (y_b/\delta_t)(T_W - T_B) \quad (5.4)$$

where T_{L,y_b} : liquid temperature at $y = y_b$, and T_W : wall temperature. Neglecting the effect of interface curvature on the change in saturation temperature, and introducing the Clausius–Clapeyron equation, $dp/dT = h_{LV}/[T_{Sat}(\nu_V - \nu_L)]$, into Eq. (5.2b) to relate the pressure difference to the corresponding difference in saturation temperatures, the excess temperature needed to sustain a vapor bubble is given by:

$$(p_V - p_L) = \frac{[T_{L,Sat}(p_V) - T_{Sat}]h_{LV}}{T_{Sat}(\nu_V - \nu_L)} \quad (5.5)$$

where $T_{L,Sat}(p_V)$: saturation temperature in K corresponding to the pressure p_V , T_{Sat} : saturation temperature in K corresponding to the system pressure p_L , h_{LV} : latent heat of vaporization at p_L , and ν_V and ν_L : vapor and liquid specific volumes. Combining Eqs. (5.2a) and (5.5), and assuming $\nu_V \gg \nu_L$, we get:

$$T_{L,Sat}(p_V) = T_{Sat} + \frac{2\sigma}{r_b} \frac{T_{Sat}}{\rho_V h_{LV}} \quad (5.6)$$

As a condition for nucleation, the liquid temperature T_{L,y_b} in Eq. (5.4) should be greater than $T_{L,Sat}(p_V)$, which represents the minimum temperature required at any point on the liquid–vapor interface to sustain the vapor bubble as given by Eq. (5.6). Combining Eqs. (5.4) and (5.6) yields the condition for nucleating cavities of specific radii:

$$(y_b/\delta_t)(T_W - T_B) - (T_W - T_{Sat}) + \frac{2\sigma}{r_b} \frac{T_{Sat}}{\rho_V h_{LV}} = 0 \quad (5.7)$$

The liquid subcooling and wall superheat are defined as follows:

$$\Delta T_{Sub} = T_{Sat} - T_B \quad (5.8)$$

$$\Delta T_{Sat} = T_W - T_{Sat} \quad (5.9)$$

The bubble radius r_b and height y_b are related to the cavity mouth radius r_c through the receding contact angle θ_r as follows:

$$r_b = r_c / \sin \theta_r \quad (5.10)$$

$$y_b = r_b(1 + \cos \theta_r) = r_c(1 + \cos \theta_r) / \sin \theta_r \quad (5.11)$$

Substituting Eqs. (5.10) and (5.11) into Eq. (5.7), and solving the resulting quadratic equation for r_c , Davis and Anderson (1966) obtained the range of nucleation cavities given by:

$$\begin{aligned} \{r_{c,\min}, r_{c,\max}\} &= \frac{\delta_t \sin \theta_r}{2(1 + \cos \theta_r)} \left(\frac{\Delta T_{\text{Sat}}}{\Delta T_{\text{Sat}} + \Delta T_{\text{Sub}}} \right) \\ &\times \left(1 \mp \sqrt{1 - \frac{8\sigma T_{\text{Sat}}(\Delta T_{\text{Sat}} + \Delta T_{\text{Sub}})(1 + \cos \theta_r)}{\rho_V h_{LV} \delta_t \Delta T_{\text{Sat}}^2}} \right) \end{aligned} \quad (5.12)$$

The minimum and maximum cavity radii $r_{c,\min}$ and $r_{c,\max}$ are obtained from the negative and positive signs of the radical in Eq. (5.12), respectively.

Different investigators have used different models to relate the bubble radius to the cavity radius and to the location where the liquid temperature T_L is determined. Hsu (1962) assumed $y_b = 1.6r_b$, which effectively translates into a receding contact angle of $\theta_r = 53.1^\circ$. Substituting this value into Eq. (5.12), the range of cavities nucleating from Hsu's criterion is given by:

$$\begin{aligned} \{r_{c,\min}, r_{c,\max}\} &= \frac{\delta_t}{4} \left(\frac{\Delta T_{\text{Sat}}}{\Delta T_{\text{Sat}} + \Delta T_{\text{Sub}}} \right) \\ &\times \left(1 \mp \sqrt{1 - \frac{12.8\sigma T_{\text{Sat}}(\Delta T_{\text{Sat}} + \Delta T_{\text{Sub}})}{\rho_V h_{LV} \delta_t \Delta T_{\text{Sat}}^2}} \right) \end{aligned} \quad (5.13)$$

Bergles and Rohsenow (1964), and Sato and Matsumura (1964) considered a hemispherical bubble at the nucleation inception with $y_b = r_b = r_c$. The resulting range of nucleating cavities is given by:

$$\begin{aligned} \{r_{c,\min}, r_{c,\max}\} &= \frac{\delta_t}{2} \left(\frac{\Delta T_{\text{Sat}}}{\Delta T_{\text{Sat}} + \Delta T_{\text{Sub}}} \right) \\ &\times \left(1 \mp \sqrt{1 - \frac{8\sigma T_{\text{Sat}}(\Delta T_{\text{Sat}} + \Delta T_{\text{Sub}})}{\rho_V h_{LV} \delta_t \Delta T_{\text{Sat}}^2}} \right) \end{aligned} \quad (5.14)$$

Kandlikar *et al.* (1997) analyzed the flow around a bubble and found that a stagnation point occurred at a certain distance y_S from the bubble base as shown in Fig. 5.1(b). For receding contact angles in the range of 20 – 60° , the location of the stagnation point was given by:

$$y_S = 1.1r_b = 1.1(r_c / \sin \theta_r) \quad (5.15)$$

Since a streamline farther away from the wall at this location would sweep over the bubble as seen in Fig. 5.1(b), the temperature at $y = y_S$ was taken as the liquid temperature at $y = y_b$. The resulting range of nucleation cavities is then given by:

$$\{r_{c,\min}, r_{c,\max}\} = \frac{\delta_t \sin \theta_r}{2.2} \left(\frac{\Delta T_{\text{Sat}}}{\Delta T_{\text{Sat}} + \Delta T_{\text{Sub}}} \right) \times \left(1 \mp \sqrt{1 - \frac{8.8\sigma T_{\text{Sat}}(\Delta T_{\text{Sat}} + \Delta T_{\text{Sub}})}{\rho_V h_{\text{LV}} \delta_t \Delta T_{\text{Sat}}^2}} \right) \quad (5.16)$$

Note that there was a typographical error in the original publication by Kandlikar *et al.* (1997). The correct value for the constant is 8.8 as given in Eq. (5.16), though the actual graphs in the original publication were plotted using the correct value of 8.8 by Kandlikar *et al.* (1997).

The onset of nucleate boiling (ONB) is of particular interest in flow boiling. The radius $r_{c,\text{crit}}$ of the first cavity that will nucleate (if present) is obtained by setting the radical term in Eq. (5.16) to zero:

$$r_{c,\text{crit}} = \frac{\delta_t \sin \theta_r}{2.2} \left(\frac{\Delta T_{\text{Sat}}}{\Delta T_{\text{Sat}} + \Delta T_{\text{Sub}}} \right) \quad (5.17)$$

For a given heat flux, the wall superheat at the ONB, $\Delta T_{\text{Sat,ONB}}$ is given by:

$$\Delta T_{\text{Sat,ONB}} = \sqrt{8.8\sigma T_{\text{Sat}} q'' / (\rho_V h_{\text{LV}} k_L)} \quad (5.18)$$

If the local wall superheat at a given section is lower than that given by Eq. (5.18), nucleation will not occur. The local subcooling at the ONB can be determined from the following equation:

$$\Delta T_{\text{Sub,ONB}} = \frac{q''}{h} - \Delta T_{\text{Sat,ONB}} \quad (5.19)$$

In a channel with subcooled liquid entering, the local subcooling at the section where nucleation occurs is given by Eq. (5.19). If the subcooling is negative, it means that the local liquid is superheated and will cause extremely high bubble growth rates. Later it will be shown that such high rates result in reverse flow that leads to severe pressure drop fluctuations.

Figure 5.2 shows the comparison of different nucleation models with the experimental data by Kandlikar *et al.* (1997). A high-power microscope and a high-speed camera were used to visualize the nucleation activity and measure the underlying cavity dimensions. Cavities were largely rectangular in shape and the larger side of the opening was used in determining the cavity radius. The cavities nucleate at a certain minimum wall superheat and continue to nucleate for higher wall superheats. A majority of the data points shown in Fig. 5.2 correspond to higher values of wall superheat than the minimum required for nucleation. It is seen that all data points fall very close to or above the criterion given by Eq. (5.14).

As seen from Fig. 5.2, the criterion by Davis and Anderson predicts higher wall superheats for larger cavities, whereas Bergles and Rohsenow's criterion allows the larger cavities

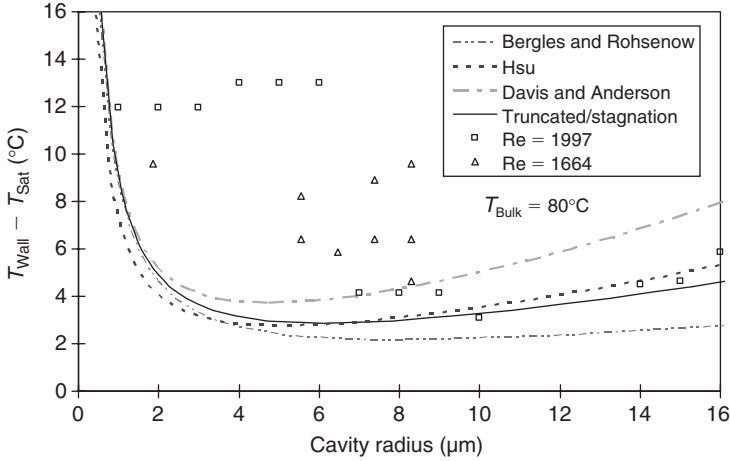


Fig. 5.2. Comparison of different nucleation criteria against the experimental data taken with water at 1 atm pressure in a 3×40 mm channel, $\theta_r = 40^\circ$, truncated/stagnation model by Kandlikar *et al.* (1997).

to nucleate at lower wall superheats, and Hsu's predictions are also quite close to the data. The criterion by Kandlikar *et al.* (1997) includes the contact angle effect.

The above analysis assumes the availability of cavities of all sizes on the heater surface. If the cavities of radius $r_{c,crit}$ are not available, then higher superheats may be required to initiate nucleation on the existing cavities. The nucleation criteria plotted in Fig. 5.2 indicate the superheat needed to activate cavities of specific radii. Alternatively, Eq. (5.7) along with Eqs. (5.3) and (5.10) may be employed to determine the local conditions required to initiate nucleation at a given cavity. The resulting equation for the wall superheat required to nucleate a given size cavity of radius r_c is given by:

$$\Delta T_{Sat}|_{ONB \text{ at } r_c} = \frac{1.1 r_c q''}{k_L \sin \theta_r} + \frac{2\sigma \sin \theta_r}{r_c} \frac{T_{Sat}}{\rho \sqrt{h_{LV}}} \quad (5.20)$$

The cavity size used in Eq. (5.20) may be smaller or larger than $r_{c,crit}$ given by Eq. (5.20). Among the available cavities, the cavity with the smallest superheat requirement will nucleate first. Equation (5.19) can be employed to find the local bulk temperature at the nucleation location for a given heat flux. Again, if the local subcooling is negative, it means that the bulk liquid at this condition is superheated and will lead to severe instabilities as will be discussed later.

The applicability of the above nucleation criteria to minichannels and microchannels is an open area. These equations were applied to design nucleation cavities in microchannels by Kandlikar *et al.* (2005) as will be discussed later in Section 5.6.

5.3. Non-dimensional numbers during flow boiling in microchannels

Table 5.1 shows an overview of the non-dimensional numbers relevant to two-phase flow and flow boiling as presented by Kandlikar (2004). The groups are classified as empirical and theoretical based.

Table 5.1

Non-dimensional numbers in flow boiling.

Non-dimensional number	Significance	Relevance to microchannels
Groups based on empirical considerations		
<p>Martinelli parameter, X</p> $X^2 = \left(\frac{dp}{dz} \right)_F \bigg _L \bigg/ \left(\frac{dp}{dz} \right)_F \bigg _V$	Ratio of frictional pressure drops with liquid and gas flow, successfully employed in two-phase pressure drop models	It is expected to be a useful parameter in microchannels as well
<p>Convection number, Co</p> $Co = [(1 - x)/x]^{0.8} [\rho_V/\rho_L]^{0.5}$	Co is a modified Martinelli parameter, used in correlating flow boiling heat transfer data	Its direct usage beyond flow boiling correlations may be limited
<p>Boiling number, Bo</p> $Bo = \frac{q''}{G h_{LV}}$	Heat flux is non-dimensionalized with mass flux and latent heat, not based on fundamental considerations	Since it combines two important flow parameters, q'' and G , it is used in empirical treatment of flow boiling
Groups based on Fundamental Considerations		
$K_1 = \left(\frac{q''}{G h_{LV}} \right)^2 \frac{\rho_L}{\rho_V}$	K₁ represents the ratio of evaporation momentum to inertia forces at the liquid–vapor interface	Kandlikar (2004) derived this number that is applicable to flow boiling systems where surface tension forces are important
$K_2 = \left(\frac{q''}{h_{LV}} \right)^2 \frac{D}{\rho_V \sigma}$	K₂ represents the ratio of evaporation momentum to surface tension forces at the liquid–vapor interface	Kandlikar (2004) derived this number that is applicable in modeling interface motion, such as in critical heat flux
<p>Bond number, Bo</p> $Bo = \frac{g(\rho_L - \rho_V) D^2}{\sigma}$	Bo represents the ratio of buoyancy force to surface tension force. Used in droplet and spray applications	Since the effect of the gravitational force is expected to be small, Bo is not expected to play an important role in microchannels
<p>Eötvös number, Eo</p> $Eo = \frac{g(\rho_L - \rho_V) L^2}{\sigma}$	Eo is similar to Bond number, except that the characteristic dimension L could be D_h or any other suitable parameter	Similar to Bo , Eo is not expected to be important in microchannels except at very low-flow velocities and vapor fractions
<p>Capillary number, Ca</p> $Ca = \frac{\mu V}{\sigma}$	Ca represents the ratio of viscous to surface tension forces, and is useful in bubble removal analysis	Ca is expected to play a critical role as both surface tension and viscous forces are important in microchannel flows
<p>Ohnesorge number, Z</p> $Z = \frac{\mu}{(\rho L \sigma)^{1/2}}$	Z represents the ratio of viscous to the square root of inertia and surface tension forces, and is used in atomization studies	The combination of the three forces masks the individual forces, it may not be suitable in microchannel research

(Continued)

Table 5.1
(Continued)

Non-dimensional number	Significance	Relevance to microchannels
Weber number, We $\text{We} = \frac{LG^2}{\rho\sigma}$	We represents the ratio of the inertia to the surface tension forces. For flow in channels, D_h is used in place of L	We is useful in studying the relative effects of surface tension and inertia forces on flow patterns in microchannels
Jakob number, Ja $\text{Ja} = \frac{\rho_L c_{p,L} \Delta T}{\rho_V h_{LV}}$	Ja represents the ratio of the sensible heat required for reaching a saturation temperature to the latent heat	Ja may be used in studying liquid superheat prior to nucleation in microchannels and effect of subcooling

Adapted from Kandlikar (2004).

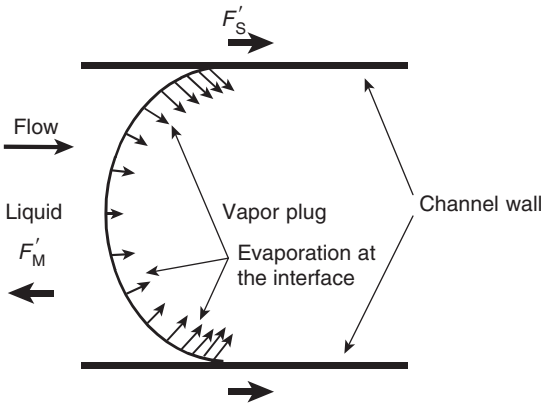


Fig. 5.3. Schematic representation of evaporation momentum and surface tension forces on an evaporating interface in a microchannel or a minichannel (Kandlikar, 2004).

With the exception of the empirically derived Boiling number, the non-dimensional numbers used in flow boiling applications have not incorporated the effect of heat flux. This effect was recognized by Kandlikar (2004) as causing rapid interface movement during the highly efficient evaporation process occurring in microchannels. Figure 5.3 shows an evaporating interface occupying the entire channel. The change of phase from liquid to vapor is associated with a large momentum change due to the higher specific volume of the vapor phase. The resulting force is used in deriving two non-dimensional groups K_1 and K_2 as shown in Table 5.1. The evaporation momentum force, the inertia force and the surface tension forces are primarily responsible for the two-phase flow characteristics and the interface shape and its motion during flow boiling in microchannels and minichannels. K_1 represents a modified boiling number with the incorporation of the liquid to vapor density ratio, while K_2 relates the evaporation momentum and surface tension forces. Future research work in this area is needed to utilize these numbers in modeling of the flow patterns and critical heat flux (CHF) phenomenon.

The Bond number compares the surface tension forces and the gravitational forces. Under flow boiling conditions in narrow channels, the influence of gravity is expected to be quite low. The Weber number and Capillary numbers account for the surface tension, inertia, and viscous forces. These numbers are expected to be useful parameters in representing some of the complex features of the flow boiling phenomena.

5.4. Flow patterns, instabilities and heat transfer mechanisms during flow boiling in minichannels and microchannels

A number of investigators have studied the flow patterns, and pressure drop and heat transfer characteristics of flow boiling in minichannels and microchannels. Kandlikar (2002a) presented a comprehensive summary in a tabular form. An abridged version of the table is reproduced in Table 5.2. The ranges of parameters investigated along with some key results are included in this table. Some of the researchers focused on obtaining the heat transfer coefficient data. Table 5.3, derived from Steinke and Kandlikar (2004), gives the details of the experimental conditions of some of the studies reported in the literature. It may be noted that there are very few local data available that report local heat transfer coefficients.

The influence of surface tension forces becomes more dominant in small diameter channels, and this is reflected in the flow patterns observed in these channels. A comprehensive summary of adiabatic flow pattern studies is presented by Hewitt (2000). Kandlikar (2002a, b) presented an extensive summary of flow patterns and associated heat transfer during flow boiling in microchannels and minichannels. Although a number of investigators have conducted extensive studies on adiabatic two-phase flows with air–water mixtures, there are relatively fewer studies available on evaporating flows. Cornwell and Kew (1992) conducted experiments with R-113 flowing in 1.2 mm \times 0.9 mm rectangular channels. They mainly observed three flow patterns as shown in Fig. 5.4 (isolated bubbles, confined bubbles and high quality annular flow). They noted the heat transfer to be strongly influenced by the heat flux, indicating the dominance of nucleate boiling in the isolated bubble region. The convective effects became important during other flow patterns. These flow patterns are observed in minichannels at relatively low heat flux conditions.

Mertz *et al.* (1996) conducted experiments in single and multiple channels with water and R-141b boiling in rectangular channels 1, 2, and 3 mm wide. They observed the presence of nucleate boiling, confined bubble flow and annular flow. The bubble generation process was not a continuous process, and large pressure fluctuations were observed. Kasza *et al.* (1997) observed the presence of nucleate boiling on the channel wall similar to the pool boiling case. They also observed nucleation in the thin films surrounding a vapor core.

Bonjour and Lallemand (1998) reported flow patterns of R-113 boiling in a narrow space between two vertical surfaces. They noted that the Bond number effectively identifies the transition of flow patterns from conventional diameter tubes to minichannels. For smaller diameter channels, however, the gravitational forces become less important and Bond number is not useful in modeling the flow characteristics. The presence of nucleation followed by bubble growth was visually observed by Kandlikar and Stumm (1995), and Kandlikar and Spiesman (1997).

Table 5.2

Summary of investigations on evaporation in minichannels and Microchannels.

Author (year)	Fluid and ranges of parameters $G(\text{kg/m}^2\text{-s})$, $q''(\text{kW/m}^2)$	Channel size, D_h (mm) horizontal (unless otherwise stated)	Flow patterns	Remarks
Lazarek and Black (1982)	R-113, $G = 125\text{--}750$, $q'' = 14\text{--}380$	Circular, $D = 3.1$, $L = 123$ and 246	Not observed	Subcooled and saturated data, h almost constant in the two-phase region, dependent on q'' . Behavior similar to large diameter tubes
Cornwell and Kew (1992)	R-113, $G = 124\text{--}627$, $q'' = 3\text{--}33$	Rectangular, 75 channel 1.2×0.9 36 channel 3.25×1.1	Isolated bubble, confined bubble, annular slug	h was dependent on the flow pattern. Isolated bubble region, $h \sim q^{0.7}$, lower q effect in confined bubble region, convection dominant in annular slug region
Moriyama and Inoue (1992)	R-113, $G = 200\text{--}1000$, $q'' = 4\text{--}30$	Rectangular, $0.035\text{--}0.11$ gap, $w = 30$, $L = 265$	Flattened bubbles, with coalescence, liquid strips/film	Data in narrow gaps obtained and correlated with an annular film flow model. Nucleate boiling ignored, although h varied with q
Wambsganss <i>et al.</i> (1993)	R-113 $G = 50\text{--}100$, $q'' = 8.8\text{--}90.7$	Circular, $D = 2.92$ mm	Not reported	Except at the lowest heat and mass fluxes, both nucleate boiling and convective boiling components were present
Bowers and Mudawar (1994)	R-113, $0.28\text{--}1.1$ ml/s, $q'' = 1000\text{--}2000$	Minichannels and microchannels $D = 2.54$ and 0.51	Not studied	Minichannels and microchannels compared. Minichannels are preferable unless liquid inventory or weight constraints are severe
Mertz <i>et al.</i> (1996)	Water/R-141b $G = 50\text{--}300$ $q'' = 3\text{--}227$	Rectangular, 1, 2, and 3 mm wide, aspect ratio up to 3	Nucleate boiling, confined bubble and annular	Single- and multi-channel test sections. Flow boiling pulsations in multi-channels, reverse flow, nucleate boiling dominant
Ravigururajan <i>et al.</i> (1996)	R-124, $0.6\text{--}5$ ml/s, $20\text{--}400$ W	$270\text{ }\mu\text{m}$ wide, 1 mm deep, and 20.52 mm long,	Not studied	Experiments were conducted over $0\text{--}0.9$ quality and 5°C inlet subcooling. Wall superheat from 0°C to 80°C

(Continued)

Table 5.2

(Continued)

Author (year)	Fluid and ranges of parameters $G(\text{kg/m}^2\text{-s})$, $q''(\text{kW/m}^2)$	Channel size, D_h (mm) horizontal (unless otherwise stated)	Flow patterns	Remarks
Tran <i>et al.</i> (1996)	R-12, $G = 44\text{--}832$, $q'' = 3.6\text{--}129$	Circular, $D = 2.46$, Rectangular, $D_h = 2.4$	Not studied	Local h obtained up to $X = 0.94$. Heat transfer in nucleate boiling dominant and convective dominant regions obtained
Kasza <i>et al.</i> (1997)	Water, $G = 21$, $q'' = 110$	Rectangular, $2.5 \times 6.0 \times 500$	Bubbly, slug	Increased bubble activity on wall at nucleation sites in the thin liquid film responsible for high heat transfer
Tong <i>et al.</i> (1997)	Water, $G = 25\text{--}45 \times 10^3$, CHF $50\text{--}80 \text{ MW/m}^2$	Circular, $D = 1.05\text{--}2.44$	Not studied	Pressure drop measured in highly subcooled flow boiling, correlations presented for both single-phase and two-phase
Bonjour and Lallemand (1998)	R-113, $q'' = 0\text{--}20$	Rectangular, vertical $0.5\text{--}2 \text{ mm}$ gap, 60 mm wide, and 120 mm long	Three flow patterns with nucleate boiling	Nucleate boiling with isolated bubbles, nucleate boiling with coalesced bubbles and partial dryout, transition criteria proposed
Peng and Wang (1998)	Water, ethanol, and mixtures	Rectangular, $a = 0.2\text{--}0.4$, $b = 0.1\text{--}0.3$, $L = 50$; triangular, $D_h = 0.2\text{--}0.6$, $L = 120$	Not observed	No bubbles observed, propose a fictitious boiling. Microscope/high-speed video not used resulting in erroneous conclusions
Kamidis and Ravigururajan (1999)	R-113, $\text{Re} = 190\text{--}1250$; $25\text{--}700 \text{ W}$	Circular, $D = 1.59, 2.78, 3.97$, 4.62	Not studied	Extremely high h , up to $11 \text{ kW/m}^2\text{C}$ were observed. Fully developed sub-cooled boiling and CHF were obtained
Kuznetsov and Shamirzaev (1999)	R-318C, $G = 200\text{--}900$, $q'' = 2\text{--}110$	Annulus, $0.9 \text{ gap} \times 500$	Confined bubble, cell, annular	Capillary forces important in flow patterns, thin film suppresses nucleation, leads to convective boiling
Lin <i>et al.</i> (1999)	R-141b, $G = 300\text{--}2000$ $q'' = 10\text{--}150$	Circular, $D = 1$	Not studied	Heat transfer coefficient obtained as a function of quality and heat flux. Trends are similar to large tube data
Downing <i>et al.</i> (2000)	R-113, Ranges not clearly stated	Circular coils, $D_h = 0.23\text{--}1.86$, helix diameter $= 2.8\text{--}7.9$	Not studied	As the helical coil radius became smaller, pressure drop reduced – possibly due to rearrangement in flow patterns
Hetsroni <i>et al.</i> (2001)	Water, $\text{Re} = 20\text{--}70$, $q'' = 80\text{--}360$	Triangular, $\theta = 55^\circ$, $n = 21, 26$, $D_h = 0.129\text{--}0.103$, $L = 15$	Periodic annular	Periodic annular flow observed in microchannels. Significant enhancement noted in h during flow boiling

(Continued)

Table 5.2
(Continued)

Author (year)	Fluid and ranges of parameters G (kg/m ² -s), q'' -(kW/m ²)	Channel size, D_h (mm) horizontal (unless otherwise stated)	Flow patterns	Remarks
Kennedy <i>et al.</i> (2000)	Water, $G = 800\text{--}4500$, $q'' = 0\text{--}4000$	Circular, $D = 1.17$ and 1.45 , $L = 160$	Not studied	q'' at the OFI was 0.9 of q'' required for saturated vapor at exit Similarly, G at OFI was 1.1 times G for saturated exit vapor condition
Lakshmi-narasimhan, <i>et al.</i> (2000)	R-11, $G = 60\text{--}4586$,	Rectangular, $1 \times 20 \times 357$ mm,	Boiling incipience observed through LCD	Boiling front observed in laminar flow, not visible in turbulent flow due to comparable h before and after, flow boiling data correlated by Kandlikar (1990) correlation
Kandlikar <i>et al.</i> (2001)	Water, $G = 80\text{--}560$	Rectangular, 1/6 channels, 1×1 , $L = 60$	High-speed photography	Flow oscillations and flow reversal linked to the severe pressure drop fluctuations, leading to flow reversal during boiling
Khodabandeh and Palm (2001)	R-134a/ R-600a, G not measured, $q'' = 28\text{--}424$	Circular tube, 1.5 mm diameter	Not studied	h compared with 11 correlations. Mass flow rate not measured, assumed constant in all experiments – perhaps causing large discrepancies with correlations at higher h
Kim and Bang (2001)	R-22, $G = 384\text{--}570$, $q'' = 2\text{--}10$	Square tube, 1.66 mm, rectangular 1.32×1.78	Flow pattern observed in rectangular chain	Heat transfer coefficient somewhat higher than correlation predictions. Slug flow seen as the dominant flow pattern
Koo <i>et al.</i> (2001)	Water, 200 W heat sink	Parallel rectangular microchannels $50 \mu\text{m} \times 25 \mu\text{m}$	Thermal profile predicted on the chip and compared with experiments	Pressure drop using homogeneous flow model in good agreement with data. Kandlikar (1990) correlation predictions in good agreement with data
Lee and Lee (2001a, b)	R-113 $G = 50\text{--}200$, $q'' = 3\text{--}15$	Rectangular, $0.4\text{--}2$ mm high, 20 mm wide	Not reported	Pressure drop correlated using Martinelli-Nelson parameter, Heat transfer predicted will by Kandlikar (1990)

(Continued)

Table 5.2
(Continued)

Author (year)	Fluid and ranges of parameters $G(\text{kg/m}^2\text{-s})$, $q''\text{-(kW/m}^2\text{)}$	Channel size, D_h (mm) horizontal (unless otherwise stated)	Flow patterns	Remarks
				correlation for film $\text{Re} > 200$, new correlation developed using film flow model for film $\text{Re} < 200$
Serizawa and Feng (2001)	Air–water, $j_L = 0.003\text{--}17.52\text{ m/s}$, $j_G = 0.0012\text{--}295.3\text{ m/s}$.	Circular tubes, diameters of $50\text{ }\mu\text{m}$ for air–water and $25\text{ }\mu\text{m}$ for steam–water	Flow patterns identified over the ranges of of flow rates studied	Two new flow patterns identified: liquid ring flow and liquid lump flow. Steam–water ranges not given
Warrier <i>et al.</i> (2001)	FC-84, $G = 557\text{--}1600$, $q'' = 59.9$	Rectangular, dimensions not available, hydraulic diameter = 0.75 mm	Not studied	Overall pressure drop and local heat transfer coefficient determined. A constant value of $C = 38$ used in Eq. (1). Heat transfer coefficient correlated as a function of Boiling number alone

OFI: Onset of flow instability.
Adapted from Kandlikar (2002a).

Table 5.3
Available literature for evaporation of pure liquid flows in parallel minichannel and microchannel passages.

Author (year)	Fluid	D_h (mm)	Re	G (kg/m ² s)	(kW/m ²)	Type*	Vis.**
Lazarek and Black (1982)	R-113	3.150	57–340	125–750	14–380	O	N
Moriyama and Inoue (1992)	R-113	0.140–0.438	107–854	200–1000	4.0–30	O/L	Y
Wambsganss <i>et al.</i> (1993)	R-113	2.920	313–2906	50–300	8.8–90.75	L	N
Bowers and Mudawar (1994)	R-113	2.540 and 0.510	14–1714	20–500	30–2000	O	N
Peng <i>et al.</i> (1994)	Water	0.133–0.343	200–2000	500–1626	–	O	N
Cuta <i>et al.</i> (1996)	R-124	0.850	100–570	32–184	1.0–400	O	N
Mertz <i>et al.</i> (1996)	Water	3.100	57–210	50–300	10–110	O	N
Ravigururajan <i>et al.</i> (1996)	R-124	0.425	217–626	142–411	5.0–25	L	N
Tran <i>et al.</i> (1996)	R-12	2.400–2.460	345–2906	44–832	3.6–129	L	N
Kew and Cornwell (1997)	R-141b	1.390–3.690	1373–5236	188–1480	9.7–90	L	Y
Ravigururajan (1998)	R-124	0.850	11,115–32,167	3583–10,369	20–700	L	N
Yan and Lin (1998)	R-134a	2.000	506–2025	50–900	5.0–20	L	N
Kamidis and Ravigururajan (1999)	R-113	1.540–4.620	190–1250	90–200	50–300	L	N

(Continued)

Table 5.3
(Continued)

Author (year)	Fluid	D_h (mm)	Re	G (kg/m ² s)	(kW/m ²)	Type*	Vis.**
Lin <i>et al.</i> (1999)	R-141b	1.100	1591	568	—	L	N
Mudawar and Bowers (1999)	Water	0.902	16–49	2×10^4 – 1×10^5	1×10^3 – 2×10^5	O	N
Bao <i>et al.</i> (2000)	R-11/R-123	1.950	1200–4229	50–1800	5–200	L	N
Lakshminarasimhan <i>et al.</i> (2000)	R-11	3.810	1311– 11,227	60–4586	7.34–37.9	O	Y
Jiang <i>et al.</i> (2001)	Water	0.026	1541–4811	2×10^4 – 5×10^4	—	O	Y
Kandlikar <i>et al.</i> (2001)	Water	1.000	100–556	28–48	1–150	O	Y
Kim and Bang (2001)	R-22	1.660	1883–2796	384–570	2.0–10	L	Y
Koizumi <i>et al.</i> (2001)	R-113	0.500–5.000	67–5398	100–800	1.0–110	O	Y
Lee and Lee (2001c)	R-113	1.569–7.273	220–1786	52–209	2.98–15.77	L	N
Lin <i>et al.</i> (2001)	R-141b	1.100	536–2955	50–3500	1–300	L	N
Hetsroni <i>et al.</i> (2002)	Vertrel XF	0.158	35–68	148–290	22.6–36	L	Y
Qu and Mudawar (2002)	Water	0.698	338–1001	135–402	1–1750	N	N
Warrier <i>et al.</i> (2002)	FC-84	0.750	440–1552	557–1600	1.0–50	L	N
Yen <i>et al.</i> (2002)	R-123	0.190	65–355	50–300	5.46–26.9	L	Y
Yu <i>et al.</i> (2002)	Water	2.980	534–1612	50–200	50–200	L	N
Zhang <i>et al.</i> (2002)	Water	0.060	127	590	2.2×10^4	O	N
Faulkner and Shekarritz (2003)	Water	1.846–3.428	20,551– 41,188	3106–6225	250–2750	O	N
Hetsroni <i>et al.</i> (2003)	Water	0.103–0.161	8.0–42	51–500	80–220	O	Y
Kuznetsov <i>et al.</i> (2003)	R-21	1.810	148–247	30–50	3.0–25	L	N
Lee <i>et al.</i> (2003)	Water	0.036–0.041	22–51	170–341	0.2–301	O	Y
Lee and Garimella (2003)	Water	0.318–0.903	300–3500	260–1080	—	O	N
Molki <i>et al.</i> (2003)	R-134a	1.930	717–1614	100–225	14	L	N
Park <i>et al.</i> (2003)	R-22	1.660	1473–2947	300–600	10.0–20	L	N
Qu and Mudawar (2003)	Water	0.349	338–1001	135–402	10.0–1300	L	N
Wu and Cheng (2003)	Water	0.186	75–97	112	226	O	Y
Steinke and Kandlikar (2004)	Water	0.207	116–1218	157–1782	5–930	L	Y

Adapted from Steinke and Kandlikar (2004).
*O = overall, L = local; ** Visualization, Y = yes, N = no.

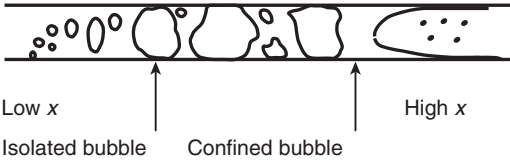


Fig. 5.4. Flow patterns observed by Cornwell and Kew (1992) during flow boiling of R-113 in 1.2 mm \times 0.9 mm rectangular channel.

The contribution of nucleate boiling to flow boiling heat transfer was clearly confirmed in the above studies, as well as a number of other studies reported in the literature, (e.g. Lazarek and Black, 1982; Wambsganss *et al.*, 1993; Tran *et al.*, 1996; Yan and Lin, 1998; Bao *et al.*, 2000; Steinke and Kandlikar, 2004). However, for microchannels, it was

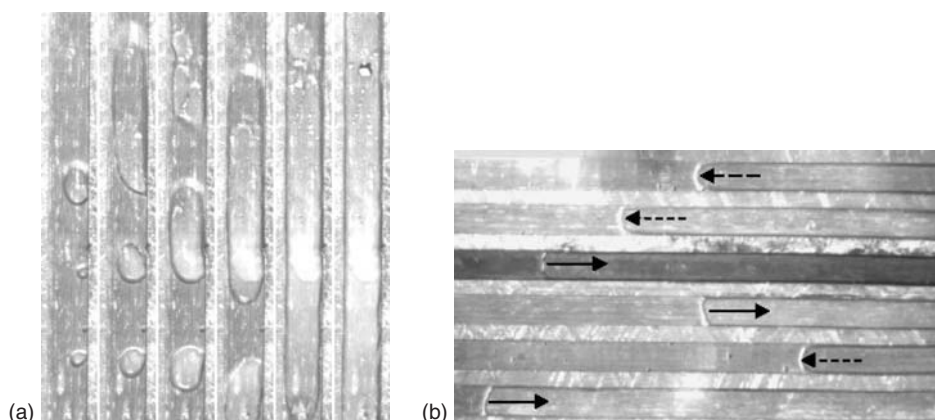


Fig. 5.5. Flow patterns in $200\ \mu\text{m} \times 1054\ \mu\text{m}$ parallel channels (a) expanding bubble flow pattern (Kandlikar *et al.*, 2005) each frame shows the progression of boiling in the same channel at 1 ms time intervals, and (b) a snapshot of interface movements in six parallel channels connected by common headers (Kandlikar and Balasubramanian, 2005).

also noted that the rapid evaporation and growth of a vapor bubble following nucleation caused major flow excursions, often resulting in reversed flow. Figure 5.5(a) shows a sequence of frames obtained by Kandlikar *et al.* (2005) for water boiling in $200\ \mu\text{m}$ square parallel channels. The images are taken at intervals of 1 ms and the flow direction is upward. The growth of bubbles and their expansion against the flow direction is clearly seen. Figure 5.5(b) shows the movement of the liquid–vapor interface in both directions as obtained by Kandlikar and Balasubramanian (2005). Similar observations have been made by a number of investigators, including Mertz *et al.* (1996), Kennedy *et al.* (2000), Kandlikar *et al.* (2001), Peles *et al.* (2001), Kandlikar (2002a, b), Zhang *et al.* (2002), Hetsroni *et al.* (2001; 2003), Peles (2003), Brutin and Tadrist (2003), Steinke and Kandlikar (2004), and Balasubramanian and Kandlikar (2005).

Flow instability poses a major concern for flow boiling in minichannels and microchannels. A detailed description of the flow boiling instabilities is provided by Kandlikar (2002a, b; 2005). Instabilities during flow boiling have been studied extensively in large diameter tubes. The excursive or Ledinegg and the parallel channel instabilities have been studied extensively in the literature. These instabilities are also present in small diameter channels as discussed by Bergles and Kandlikar (2005). Nucleation followed by an increase in the flow resistance due to two-phase flow in channels leads to a minimum in the pressure drop demand curve leading to instabilities. Parallel channel instabilities also occur at the minimum in the pressure drop demand curve. In a microchannel, in addition to these two instabilities, there is a phenomenon that comes into play due to rapid bubble growth rates that causes instability and significant flow reversal problems. Large pressure fluctuations at high frequencies have been reported by a number of investigators including Kew and Cornwell (1996), Peles (2003), and Balasubramanian and Kandlikar (2005) among others.

The stability of the flow boiling process has been studied analytically using linear and non-linear stability analyses. Some of the semi-empirical methods have yielded limited success (e.g. Peles *et al.*, 2001; Brutin *et al.*, 2002; Stoddard *et al.*, 2002; Brutin and

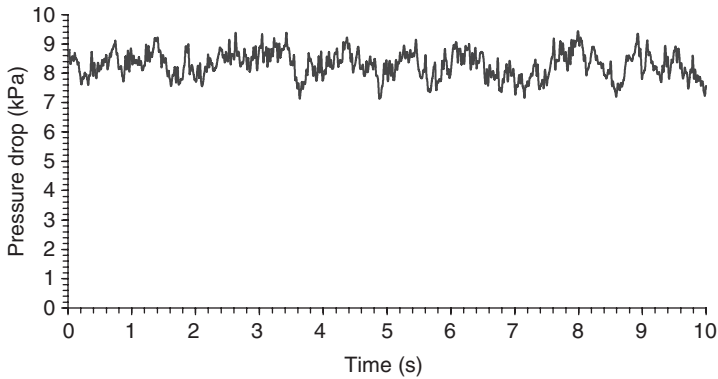


Fig. 5.6. Pressure fluctuations observed during flow boiling of water in $1054\ \mu\text{m} \times 197\ \mu\text{m}$ parallel minichannels (Balasubramanian and Kandlikar, 2005).

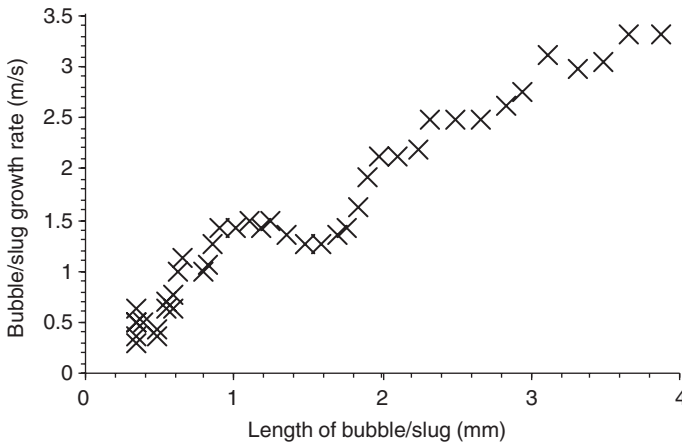


Fig. 5.7. Bubble/slug growth rates during flow boiling of water in $1054\ \mu\text{m} \times 197\ \mu\text{m}$ parallel minichannels (Balasubramanian and Kandlikar, 2005).

Tadrist, 2003). However, these models cannot be tested because of a lack of extensive experimental data under stable boiling conditions. It is expected that with the availability of such data sets, more rigorous models, similar to those available for flow boiling in conventional sized tubes, will be developed in the near future.

The pressure fluctuations associated with the flow boiling process were observed by many researchers as described earlier. Figure 5.6 shows a typical plot of the pressure drop fluctuations obtained during flow boiling in minichannels by Balasubramanian and Kandlikar (2005). A fast fourier transform analysis of the instantaneous pressure drop signal revealed that the dominant frequency was dependent on the wall temperature and was related to the nucleation activity within the channels. The growth rate of the growing bubbles was measured to be as high as 3.5 m/s. Figure 5.7 shows the growth rate of a slug in $1054\ \mu\text{m} \times 197\ \mu\text{m}$ parallel channels. As the bubbles reach the opposite channel wall, the growth rate stabilizes until the rapid evaporation from the walls causes the growth rate to

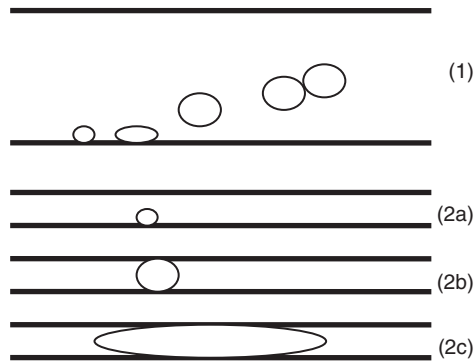


Fig. 5.8. Schematic representation of bubble growth in (1) large diameter tubes, and (2a–c) microchannels and minichannels.

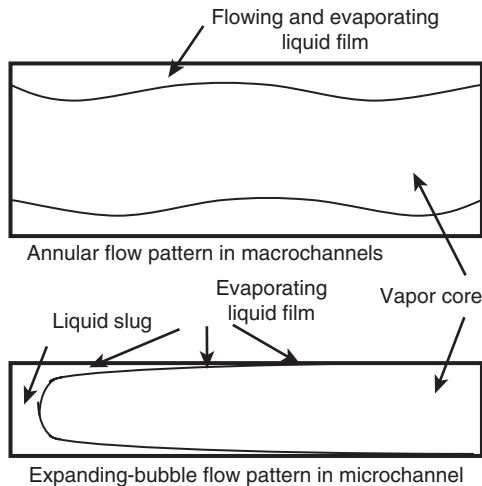


Fig. 5.9. Comparison of the annular flow pattern in macrochannels and the expanding-bubble flow pattern in microchannels and minichannels.

increase again. The numerical simulation by Mukherjee and Kandlikar (2004) confirmed the bubble growth observed in Fig. 5.7. Nucleation followed by rapid bubble growth is believed to be the cause of instabilities.

As a bubble grows under pool boiling conditions, the bubble growth rate is much higher immediately following its inception. The growth rate is initially proportional to time t and is controlled by the inertial forces. As the bubble grows, the growth rate slows down and follows a $t^{1/2}$ trend in the thermally controlled region. In large diameter channels (above 1–3 mm, depending on heat flux), the bubbles grow to sizes that are smaller than the channel diameter and leave the heater surface under inertia forces. In flow boiling in macrochannels, the bubble growth is similar to that in pool boiling, except that the flow causes the bubbles to depart early as shown in Fig. 5.8. These departing bubbles contribute to the bubbly flow. As more bubbles are formed, they coalesce and develop into slug and annular flows as shown in Fig. 5.9.

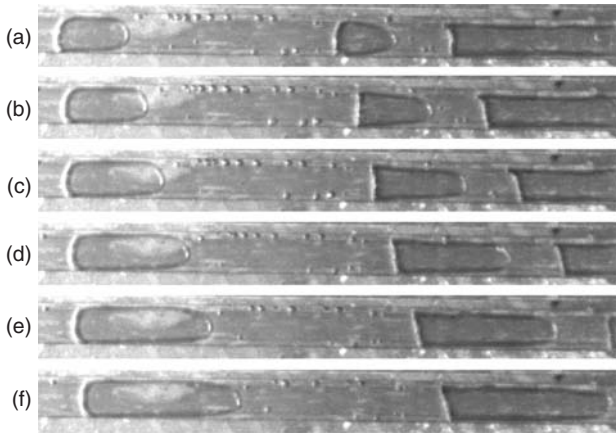


Fig. 5.10. The expanding-bubble flow pattern observed in a $197\ \mu\text{m} \times 1054\ \mu\text{m}$ channel, using water at atmospheric pressure, the time duration between successive images is $0.16\ \text{ms}$, $G = 120\ \text{kg/m}^2\ \text{s}$, $q'' = 317\ \text{kW/m}^2$, $T_s = 110.9^\circ\text{C}$, flow is from left to right (Kandlikar and Balasubramanian, 2005).

In microchannels and minichannels, as a bubble nucleates and initially grows in the inertia controlled region, it encounters the channel walls prior to entering the thermally controlled region found in the conventional channels. The large surface area to fluid volume ratio in the channel causes the liquid to heat up rapidly. Thus, the bubble encounters a superheated liquid as it continues to grow and spreads over the other areas of the channel wall. The availability of heat from the superheated layer and from the channel walls causes a rapid expansion of the bubble, leading to the expanding-bubble flow pattern shown in Fig. 5.8. The bubble occupies the entire channel cross-section and continues to grow as shown in Fig. 5.9. The expanding-bubble flow pattern differs from the annular flow pattern mainly in that the liquid on the wall acts similar to the film under a growing vapor bubble, rather than as a flowing film. This makes the heat transfer mechanism very similar to the nucleate boiling mechanism. A number of investigators have confirmed the strong heat flux dependence of the heat transfer coefficient during flow boiling in microchannels, which indicates the dominance of nucleate boiling.

Figure 5.10 shows the expanding-bubble flow pattern observed during flow boiling in a rectangular minichannel by Kandlikar and Balasubramanian (2005). Note the rapid interface movement on the right side of the bubbles (downstream). The liquid film is essentially stationary and occasionally dries out before the upstream liquid slug flows through and rewets the surface. At other times, severe flow reversal was observed at the same site, and the bubble interface moved upstream rapidly.

Mukherjee and Kandlikar (2004) performed a numerical simulation of the bubble growth process in a microchannel evaporator. The bubble initially nucleated from one of the walls and then grew to occupy the entire channel cross-section. The bubble shapes were compared with the experimental observations by Balasubramanian and Kandlikar (2005) for the same geometry of $197\ \mu\text{m} \times 1054\ \mu\text{m}$ with water in the expanding-bubble flow pattern region (Fig. 5.11). Their agreement validates numerical simulation as a powerful tool for analyzing the flow boiling phenomenon.

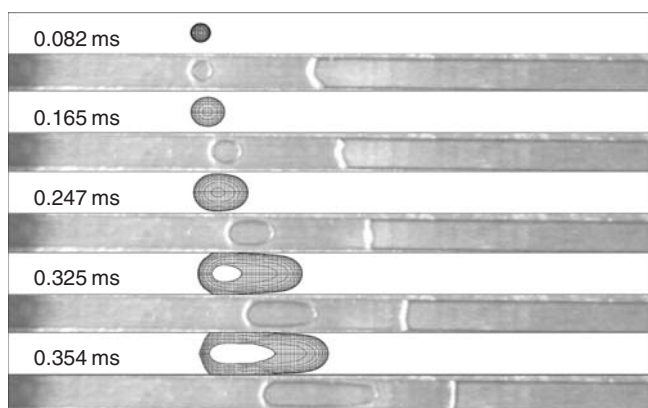


Fig. 5.11. Comparison of bubble shapes obtained from numerical simulation by Mukherjee and Kandlikar (2004) and experimental observations (Balasubramanian and Kandlikar, 2005).

5.5. CHF in microchannels

The two-phase flow and local wall interactions during flow boiling set a limit for the maximum heat flux that can be dissipated in microchannels and minichannels. In the electronics cooling application, the inlet liquid is generally subcooled, while a two-phase mixture under saturated conditions may be introduced if a refrigeration loop is used to lower the temperature of the evaporating liquid. Thus the CHF under both subcooled and saturated conditions is of interest.

Kandlikar (2001) modeled the CHF in pool boiling on the basis of the motion of the liquid–vapor–solid contact line on the heater surface. CHF was identified as the result of the interface motion caused by the evaporation momentum force at the evaporating interface near the heater surface. This force causes the “vapor-cutback” phenomenon separating liquid from the heater surface by a film of vapor. High-speed images of the interface motion under such conditions were obtained by Kandlikar and Steinke (2002). This phenomenon is also responsible in restoring the CHF conditions on subsequent rewetting of the heater surface. Extension of this pool boiling CHF model to microchannels and minichannels is expected to provide useful results.

Bergles (1963) and Bergles and Rohsenow (1964) provide extensive coverage on subcooled CHF in macrochannels. Under subcooled flow boiling conditions, the primary concern is the explosive growth of vapor bubbles upon nucleation. At the location where nucleation is initiated, the bulk liquid may have a low value of liquid subcooling. In some cases, the liquid may even be under superheated conditions. This situation arises when the proper nucleation sites are not available, and nucleation is initiated toward the exit end of the microchannels. This would result in an explosive bubble growth following nucleation as shown in Fig. 5.12(a). Since the bubble growth is quite rapid, it often results in a reverse flow in the entire channel. When such bubble growth occurs near the channel entrance, the vapor is pushed back into the inlet plenum as shown in Fig. 5.12(b). The vapor bubbles growing near the entrance region find the path of least resistance into the inlet plenum. The resulting instability leads to a CHF condition.

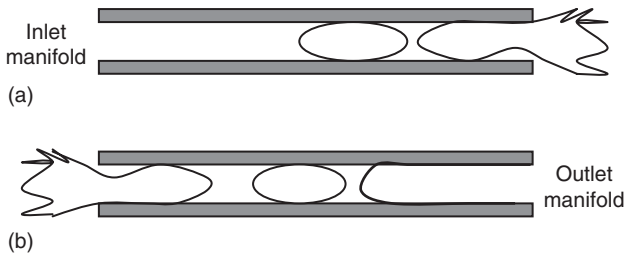


Fig. 5.12. Reverse flow of vapor into the inlet manifold leading to early CHF.

The unstable operating conditions are largely responsible for the low values of CHF reported in literature. It may be recalled that the CHF under pool boiling conditions is around 1.6 MW/m^2 , while the values reported for narrow channels are significantly lower than this value. For example, Qu and Mudawar (2004) reported CHF data with a liquid subcooling between 70°C and 40°C , and their CHF values (based on the channel area) are only 316.2 to 519.7 kW/m^2 . The main reason for such low values is believed to be the instabilities, which were reported by Qu and Mudawar in the same paper (see Fig. 5.12). Bergles and Kandlikar (2005) reviewed the available CHF data and concluded that all the available data in the literature on microchannels suffers from this instability.

The effect of mass flux on the CHF is seen to be quite significant. For example, Roach *et al.* (1999) obtained CHF data in 1.17- and 1.45-mm diameter tubes and noted that the CHF increased from 860 kW/m^2 (for a 1.15-mm diameter tube with $G = 246.6 \text{ kg/m}^2 \text{ s}$), to 3.699 MW/m^2 (for a 1.45-mm diameter tube with $G = 1036.9 \text{ kg/m}^2 \text{ s}$). It is suspected that the higher flow rate results in a higher inertia force and induces a stabilization effect. This trend is supported by the experimental results obtained by Kamidis and Ravigururajan (1999) with R-113 in 1.59, 2.78, 3.97, and 4.62 mm tubes, and by Yu *et al.* (2002) with water in a 2.98 mm diameter tube.

The influence of tube diameter is somewhat confusing in light of the instabilities. In general, the CHF decreased with the tube diameter, and in many cases the reduction was rather dramatic (e.g. Qu and Mudawar, 2004). The presence of flow instability, especially in small diameter tubes, needs to be addressed in obtaining reliable experimental data. Further research in this area is warranted.

5.6. Stabilization of flow boiling in microchannels

The reversed flow that leads to unstable operation poses a major concern in implementing flow boiling in practical applications. The rapid growth of a vapor bubble in a superheated liquid environment leads to flow reversal, which is identified as a major cause of instability.

The flow instability results from the reversed flow occurring in the parallel channels. Two methods for reducing the instabilities are discussed in this section.

5.6.1. Pressure drop element at the inlet to each channel

The parallel channels provide an effect similar to the upstream compressibility for each of the channels. Therefore, placing a flow restrictor in the flow loop prior to the inlet

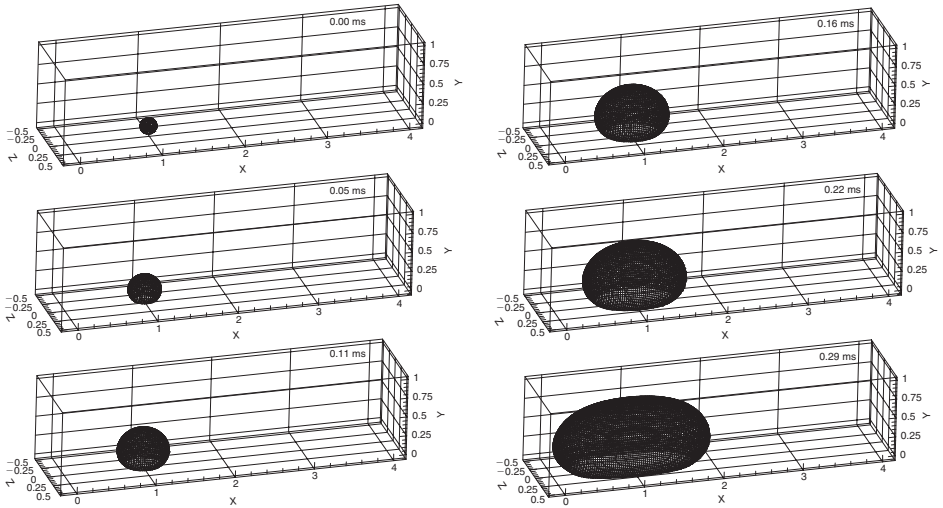


Fig. 5.13. Simulation of bubble growth in a microchannel with upstream to downstream flow resistance ratio, $R = 1$ (Mukherjee and Kandlikar, 2005).

manifold will not reduce the instability arising in each channel. To reduce the intensity and occurrence of reverse flow, a pressure drop element (essentially a flow constrictor or a length of reduced cross-sectional area) is placed at the entrance of each channel. This introduces an added resistance to fluid flow, but provides an effective way to reduce the flow instabilities arising from the reverse flow.

Mukherjee and Kandlikar (2004; 2005) conducted an extensive numerical analysis of bubble growth in a microchannel in an effort to study the effect of the pressure drop elements on flow stabilization. They utilized the level set method to define the interface and track its movement by applying conservation equations. Figure 5.13 shows the consecutive frames of a bubble growing in a microchannel. The resistance to flow in both the upstream and downstream directions was the same. The bubble growth is seen to be slow at the beginning, but becomes more rapid after the bubble touches the other heated channel walls. This leads to an extension of the inertia-controlled region, where the heat transfer is more efficient since it does not depend on the diffusion of heat across a thin layer surrounding the liquid–vapor interface.

Mukherjee and Kandlikar (2005) introduced a new parameter R to represent the upstream to downstream flow resistance ratio. In their simulation, they showed that increasing the upstream resistance reduced the intensity of the backflow. The results are shown in Fig. 5.14. In Fig. 5.14(a), the resistance in both directions is the same, while in Fig. 5.14(b), the inlet to outlet ratio is 0.25 indicating a four-fold higher flow resistance in the backward direction. The resulting bubble growth in Fig. 5.14(b) shows that reverse flow is completely eliminated in this case. As expected, the backflow characteristics were also found to be dependent on the heat flux and the local liquid superheat at the nucleation site.

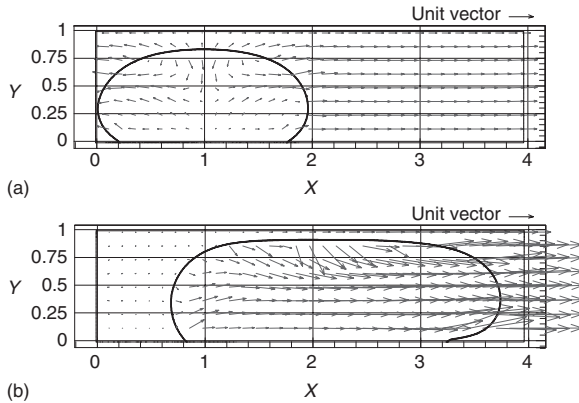


Fig. 5.14. Bubble growth with unequal flow resistances on the upstream and downstream flow directions, upstream to downstream flow resistance ratio (a) $R = 1$ and (b) $R = 0.25$ (Mukherjee and Kandlikar, 2005). Channel details, 200 μm square channel, X : channel length direction; Y : channel height direction.

5.6.2. Flow stabilization with nucleation cavities

Introducing artificial nucleation sites on the channel wall is another method for reducing the instability. Introducing nucleation cavities of the right size would initiate nucleation before the liquid attains a high degree of superheat. Kandlikar *et al.* (2005) experimentally observed nucleation behavior with the introduction of artificial cavities into the microchannel. Figure 5.15 shows nucleation on these cavities much earlier with significant reduction in the reverse flow and instabilities.

The flow pattern present after nucleation is initiated is an important feature of flow boiling in minichannels and microchannels. The bubbles expand to occupy the entire cross-section, with intermittent liquid slugs between successive expanding bubbles. Additional nucleation within the slugs further divides them. Figures 5.4, 5.5, and 5.10 show the two-phase structure with a vapor core surrounded by a film of liquid. This flow pattern is similar to the annular flow pattern, but with an important distinction. In an annular flow pattern, liquid flows in the thin film surrounding the vapor core. The velocity profile and flow rate in the film of the classical annular flow are determined from the well-known triangular relationship between the wall shear stress, pressure drop, and the liquid film flow rate.

The sizes of the nucleation cavities required to initiate nucleation are functions of local wall and bulk fluid temperatures, heat transfer coefficient, and heat flux. Examples 5.1 and 5.2 illustrate the size ranges of nucleating cavities under given flow and heat flux conditions.

Implementing cavities and pressure drop elements together was found to be most effective in reducing the instabilities. The placement of nucleation cavities and the area reduction at the inlet section are some of the design variables that need to be taken into account while designing a flow boiling system. Table 5.4 shows the effect of various configurations in reducing the flow boiling instabilities.

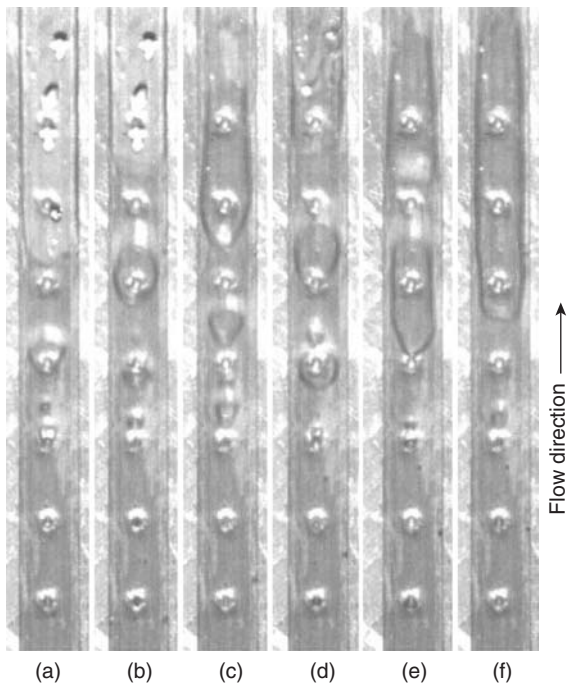


Fig. 5.15. Stabilized flow with large fabricated nucleation sites; successive frames from (a) to (f) taken at 0.83 ms time intervals illustrate stabilized flow in a single channel from a set of six parallel vertical microchannels; water, $G = 120 \text{ kg/m}^2 \text{ s}$, $q'' = 308 \text{ kW/m}^2$, $T_s = 114^\circ\text{C}$ (Kandlikar *et al.*, 2005).

Table 5.4
Effect of artificial nucleation sites and pressure drop elements on flow boiling stability in $1054 \mu\text{m} \times 197 \mu\text{m}$ channel (Kandlikar *et al.*, 2005).

Case	Average surface temperature ($^\circ\text{C}$)	Pressure drop (kPa)	Pressure fluctuation ($\pm \text{kPa}$)	Stability
Open header, 5–30 μm nucleation sites	113.4	12.8	2.3	Unstable
51% area PDEs, 5–30 μm nucleation sites	113.0	13.0	1.0	Partially stable
4% area PDEs, 5–30 μm nucleation sites	111.5	39.5	0.3	Completely stable

PDE: pressure drop element.

PDE, refers to pressure drop elements, placed at the inlet of each channel providing the specified cross-sectional area for flow. For the cases investigated, the pressure drop elements or artificial nucleation sites alone did not eliminate the instabilities as noted from the pressure drop fluctuations. The 4% PDEs are able to eliminate the instabilities completely, but they introduce a very large pressure drop. The effect of 51% area reduction

in conjunction with the artificial nucleation sites is interesting to note. There was little pressure drop increase due to area reduction as compared to the fully open channel. It is therefore possible to arrive at an appropriate area reduction in conjunction with the artificial nucleation sites with marginal increase in the pressure drop.

5.7. Predicting heat transfer in microchannels

Flow boiling heat transfer data was obtained by a number of investigators. Many of the researchers reported unstable operating conditions during their tests. Therefore, this data and the matching correlations should be used with some degree of caution. At the same time, it is recommended that experimental data under stable operating conditions be obtained by providing artificial nucleation sites and pressure drop elements near the inlet inside each channel.

A good survey of available experimental data and correlations is provided by Qu and Mudawar (2004), and Steinke and Kandlikar (2004). Table 5.3 is adapted from Steinke and Kandlikar (2004), and lists the ranges of experimental data available in the literature. It can be seen that the fluids investigated include: water, R-21, R-22, R-113, R-123, R-124, R-141b, FC-84, and Vertrel XF. The mass fluxes, liquid Reynolds numbers, and heat fluxes range from 20 to 6225 kg/m² s, 14 to 5236, and up to 2 MW/m², respectively. As the tube diameter decreases, the Reynolds number shifts toward a lower value.

In order to establish the parametric trends, the local flow boiling heat transfer data are needed. In the papers listed in Table 5.3, only those by Hetsroni *et al.* (2002), Yen *et al.* (2002), and Steinke and Kandlikar (2004) deal with tubes around 200 μ m and report local heat transfer data. Qu and Mudawar (2003) also report local data for parallel rectangular channels of 349 μ m hydraulic diameter.

The experimental data of Bao *et al.* (2000) for a 1.95 mm diameter tube indicates a strong presence of the nucleate boiling term, while Qu and Mudawar's data exhibits a strong influence of mass flux, indicating the presence of convective boiling. The decreasing trends in heat transfer coefficient with quality seen in Qu and Mudawar's data was also seen in Steinke and Kandlikar's (2004) data. A number of issues arise that make it difficult to assess the available experimental data accurately. Some of the factors are:

- (i) the presence of instabilities during the experiments,
- (ii) different ranges of parameters, especially heat flux and mass flux.

The influence of instabilities was discussed in the earlier sections. The ranges of mass fluxes employed in small diameter channels typically fall in the laminar range. The correlations developed for large diameter tubes are in a large part based on the turbulent flow conditions for Reynolds numbers based on all-liquid flow.

Some of the data available in literature was seen to be correlated by the all-nucleate boiling-type correlations, such as Lazarek and Black (1982), and Tran *et al.* (1996). However, recent data reported by Qu and Mudawar has very large errors (36.2% and 98.8%). Similar observations can be made with the Steinke and Kandlikar (2004) data. Some of the more recent correlations by Yu *et al.* (2002) and Warriar *et al.* (2002) employ only the heat flux dependent terms (similar to Lazarek and Black (1982), and Tran *et al.* (1996)) and correlate Qu and Mudawar's (2003) data well. However, the presence of both nucleate

boiling and convective boiling terms to a varying degree is reported by Kandlikar and Balasubramanian (2004). They recommend using the laminar flow equations for the all-liquid flow heat transfer coefficients in the Kandlikar (1990) correlation and cover a wide range of data sets.

The flow boiling correlation by Kandlikar (1990) utilizes the all-liquid flow, single-phase correlation. Since most of the available data was in the turbulent region, use of the Gnielinski correlation was recommended. However, later, Kandlikar and Steinke (2003), and Kandlikar and Balasubramanian (2004) introduced the laminar flow equation for laminar flow conditions based on Re_{LO} . The correlation based on the available data is given below:

For $Re_{LO} > 100$:

$$h_{TP} = \text{larger of } \begin{cases} h_{TP,NBD} \\ h_{TP,CBD} \end{cases} \quad (5.21)$$

$$h_{TP,NBD} = 0.6683Co^{-0.2}(1-x)^{0.8}h_{LO} + 1058.0Bo^{0.7}(1-x)^{0.8}F_{FI}h_{LO} \quad (5.22)$$

$$h_{TP,CBD} = 1.136Co^{-0.9}(1-x)^{0.8}h_{LO} + 667.2Bo^{0.7}(1-x)^{0.8}F_{FI}h_{LO} \quad (5.23)$$

where $Co = [(1-x)/x]^{0.8}(\rho_V/\rho_L)^{0.5}$ and $Bo = q''/Gh_{LV}$. The single-phase all-liquid flow heat transfer coefficient h_{LO} is given by:

$$\text{for } 10^4 \leq Re_{LO} \leq 5 \times 10^6 \quad h_{LO} = \frac{Re_{LO} Pr_L (f/2)(k_L/D)}{1 + 12.7(Pr_L^{2/3} - 1)(f/2)^{0.5}} \quad (5.24)$$

$$\text{for } 3000 \leq Re_{LO} \leq 10^4 \quad h_{LO} = \frac{(Re_{LO} - 1000) Pr_L (f/2)(k_L/D)}{1 + 12.7(Pr_L^{2/3} - 1)(f/2)^{0.5}} \quad (5.25)$$

$$\text{for } 100 \leq Re_{LO} \leq 1600 \quad h_{LO} = \frac{Nu_{LO} k}{D_h} \quad (5.26)$$

In the transition region between Reynolds numbers of 1600 and 3000, a linear interpolation is suggested for h_{LO} .

For Reynolds number below and equal to 100 ($Re \leq 100$) the nucleate boiling mechanism governs, and the following Kandlikar Correlation is proposed,

For $Re_{LO} \leq 100$,

$$h_{TP} = h_{TP,NBD} = 0.6683Co^{-0.2}(1-x)^{0.8}h_{LO} + 1058.0Bo^{0.7}(1-x)^{0.8}F_{FI}h_{LO} \quad (5.27)$$

The single-phase all-liquid flow heat transfer coefficient h_{LO} in Eq. (5.27) is found from Eq. (5.26).

The fluid surface parameter F_{FL} in Eqs. (5.22), (5.23), and (5.27) for different fluid surface combinations is given in Table 5.5. These values are for copper or brass surfaces. For stainless steel surfaces, use $F_{FL} = 1.0$ for all fluids. For silicon surfaces, no data is currently available. Use of the values listed in Table 5.5 for copper is suggested.

Table 5.5
Recommended F_{FI} (fluid surface parameter)
values in flow boiling correlation by Kandlikar
(1990; 1991).

Fluid	F_{FI}
Water	1.00
R-11	1.30
R-12	1.50
R-13B1	1.31
R-22	2.20
R-113	1.30
R-114	1.24
R-134a	1.63
R-152a	1.10
R-32/R-132	3.30
R-141b	1.80
R-124	1.00
Kerosene	0.488

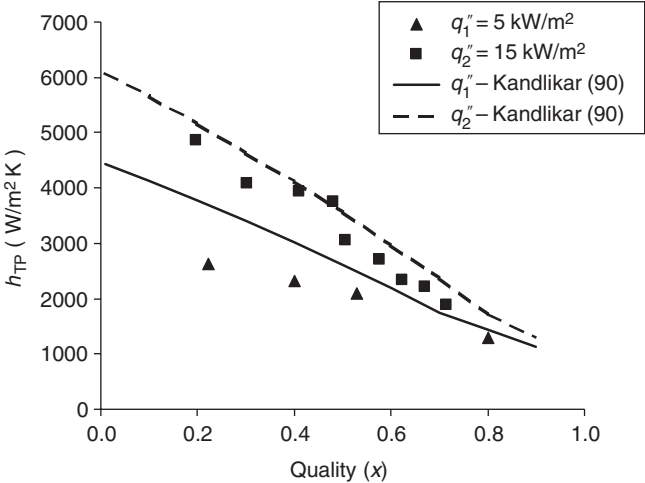


Fig. 5.16. Yan and Lin (1998) data points for R-134a compared to the correlation by Kandlikar and Balasubramanian (2004) using the laminar single-phase equation; $D_h = 2$ mm, $G = 50$ kg/m²s, $q'' = 5$ and 15 kW/m², $Re_{LO} = 506$.

The above correlation scheme is based on the data available in the literature. It has to be recognized that all of the data suffer from the instability condition to some extent. It is expected that the correlation will undergo some changes as new data under stabilized flow conditions become available.

A comparison of the correlation scheme described in Eqs. (5.21)–(5.27) with some of the experimental data available in the literature is shown in Figs 5.16–5.18. The decreasing

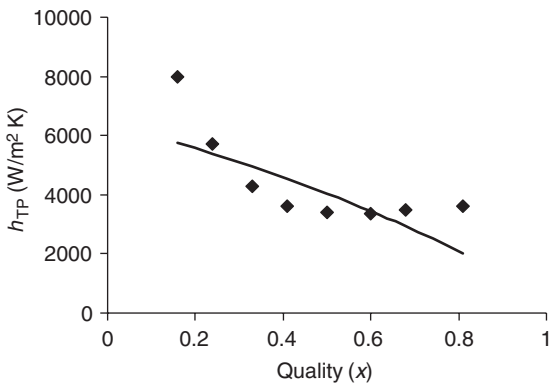


Fig. 5.17. Yen *et al.* (2002) data points for HCFC 123 compared to the correlation by Kandlikar and Balasubramanian (2004) using the laminar single-phase flow equation; $D_h = 0.19 \text{ mm}$, $G = 145 \text{ kg/m}^2\text{-s}$, $q'' = 6.91 \text{ kW/m}^2$, $p_{\text{avg}} = 151.8 \text{ kPa}$, $\text{Re}_{LO} = 86$.

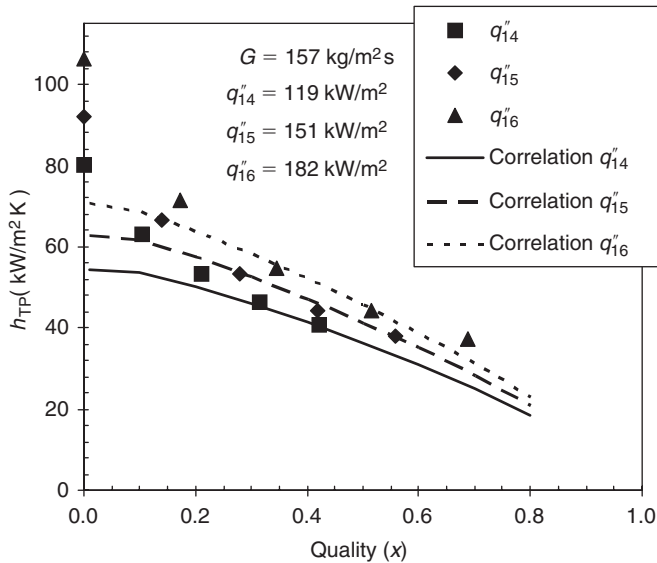


Fig. 5.18. Steinke and Kandlikar (2004) data points compared to the correlation by Kandlikar and Balasubramanian (2004) using the laminar flow equation with the nucleate boiling dominant term only; $D_h = 207 \mu\text{m}$, $G = 157 \text{ kg/m}^2\text{-s}$, $q'' = 119, 151 \text{ and } 182 \text{ kW/m}^2$, $\text{Re}_{LO} = 116$.

trend in the heat transfer coefficient with quality is evident in the data, indicating the dominance of the nucleate boiling mechanism. The complex nature of flow boiling in small diameter channels, including liquid–vapor interactions, presence of expanding bubbles with thin evaporating film, nucleation of bubbles in the flow as well as in the thin film, etc. make it difficult to present a comprehensive analytical model to account for the heat

transfer mechanisms during flow boiling. Further efforts with high-speed flow visualization techniques are recommended to provide the fundamental information on this topic.

5.8. Pressure drop during flow boiling in microchannels and minichannels

The pressure drop in a microchannel or a minichannel heat exchanger is the sum of the following components:

$$\Delta p = \Delta p_c + \Delta p_{f,1-ph} + \Delta p_{f,tp} + \Delta p_a + \Delta p_g + \Delta p_e \quad (5.28)$$

where subscripts c: contraction at the entrance; f,1-ph: single-phase pressure loss due to friction, including entrance region effects; f,tp: two-phase frictional pressure drop; a: acceleration associated with evaporation; g: gravitational; and e: expansion at the outlet. Equations for calculating each of these terms are presented in the following sections.

5.8.1. Entrance and exit losses

The inlet to the microchannel may be single-phase liquid or a two-phase mixture. It is common to have liquid at the inlet when a liquid pump and a condenser are employed in the cooling system. When the refrigeration system forms an integral part of the cooling system, the refrigerant is throttled prior to entry into the microchannels. With the need to incorporate pressure drop elements in each channel, liquid at the inlet in such cases is also possible.

The contraction losses in the single-phase liquid are covered in Chapter 3. The nature of the liquid's entry into the channels is another factor that needs to be taken into consideration. The channel floor may be flush with the manifold, or may be shallower or deeper than the manifold. Lee and Kim (2003) used a micro-PIV system to identify the entrance losses with sharp and smooth channel entrances.

For the two-phase entry and exit losses, Coleman (2003) recommends the following scheme proposed by Hewitt (2000).

The following equation is used to calculate the pressure loss due to a sudden contraction of a two-phase mixture using a separated flow model:

$$\Delta p_c = \frac{G^2}{2\rho L} \left[\left(\frac{1}{C_o} - 1 \right)^2 + 1 - \frac{1}{\sigma_c^2} \right] \psi_h \quad (5.29)$$

where G : mass flux, σ_c : contraction area ratio (header to channel > 1), C_o – contraction coefficient given by:

$$C_o = \frac{1}{0.639(1 - 1/\sigma_c)^{0.5} + 1} \quad (5.30)$$

and ψ_h : two-phase homogeneous flow multiplier given by:

$$\psi_h = [1 + x(\rho_L/\rho_V - 1)] \quad (5.31)$$

with x : local quality.

The exit pressure loss is calculated from the homogeneous model:

$$\Delta p_e = G^2 \sigma_e (1 - \sigma_e) \psi_s \quad (5.32)$$

where σ_e : area expansion ratio (channel to header < 1), and ψ_s : the separated flow multiplier given by:

$$\psi_s = 1 + \left(\frac{\rho_L}{\rho_V} - 1 \right) [0.25x(1 - x) + x^2] \quad (5.33)$$

The frictional pressure drop in the single-phase region prior to nucleation is calculated from the equations presented in Chapter 3. In the two-phase region, the following equations may be used to calculate the frictional, acceleration and gravity components of the pressure drop.

The local friction pressure gradient at any section is calculated with the following equation:

$$\left(\frac{dp_F}{dz} \right) = \left(\frac{dp_F}{dz} \right)_L \phi_L^2 \quad (5.34)$$

The two-phase multiplier ϕ_L^2 is given by the following equation by Chisholm (1983):

$$\phi_L^2 = 1 + \frac{C}{X} + \frac{1}{X^2} \quad (5.35)$$

The value of the constant C depends on whether the individual phases are in the laminar or turbulent region. Chisholm recommended the following values of C :

$$\text{Both phases turbulent} \quad C = 21 \quad (5.36a)$$

$$\text{Laminar liquid, turbulent vapor} \quad C = 12 \quad (5.36b)$$

$$\text{Turbulent liquid, laminar vapor} \quad C = 10 \quad (5.36c)$$

$$\text{Both phases laminar} \quad C = 5 \quad (5.36d)$$

The Martinelli parameter X is given by the following equation:

$$X^2 = \left(\frac{dp_F}{dz} \right)_L / \left(\frac{dp_F}{dz} \right)_V \quad (5.37)$$

Mishima and Hibiki (1996) found that the constant C depends on the tube diameter, and recommended the following equation for C :

$$C = 21(1 - e^{-319D_h}) \quad (5.38)$$

where D_h is in m. Mishima and Hibiki's correlation is used extensively and is recommended. English and Kandlikar (2005) found that their adiabatic air–water data in a 1-mm square channel was overpredicted by using Eq. (5.38). Upon further investigation, they found that

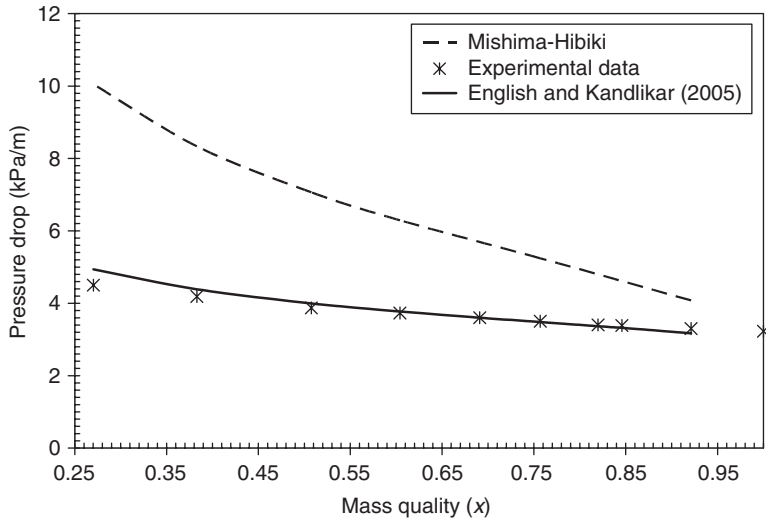


Fig. 5.19. Comparison of experimental data from English and Kandlikar (2005) with their correlation, and Mishima and Hibiki's correlation (1996).

the diameter correction recommended by Mishima and Hibiki (1996) should be applied to C in Eq. (5.35). Accordingly, the value of C will change depending on the laminar or turbulent flow of individual phases. Thus the following modified equation is recommended for frictional pressure drop calculation in microchannels and minichannels:

$$\phi_L^2 = 1 + \frac{C(1 - e^{-319D_h})}{X} + \frac{1}{X^2} \quad (5.39)$$

The value of C is obtained from Eqs. (5.36a)–(5.36d).

Figure 5.19 shows the agreement of experimental data obtained by English and Kandlikar (2005) during air–water flow in a 1-mm square channel. The average absolute deviation was found to be 3.5%, which was within the experimental uncertainties. Further validation of Eq. (5.39) is recommended.

The acceleration pressure drop is calculated from the following equation assuming homogeneous flow:

$$\Delta p_a = G^2 v_{LV} x_e \quad (5.40)$$

where v_{LV} : difference between the specific volumes of vapor and liquid phases $= v_V - v_L$. The above equation assumes the inlet flow to be liquid only and exit quality to be x_e . For a two-phase inlet flow, the x_e should be replaced with the change in quality between the exit and inlet sections.

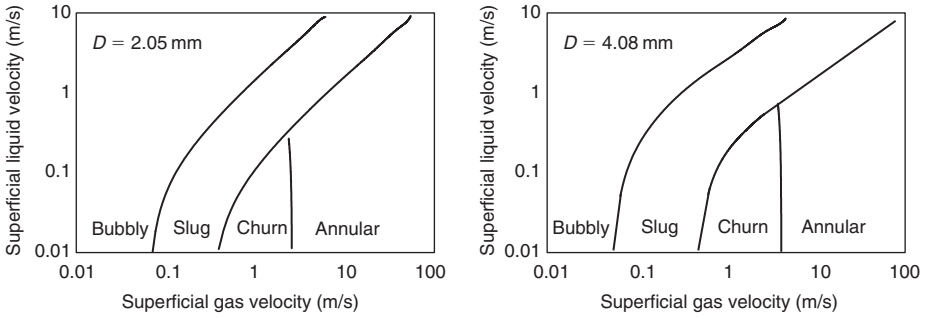


Fig. 5.20. Flow pattern map for minichannels derived from Mishima and Hibiki (1996).

The gravitational pressure drop will be a very small component. It can be calculated from the following equation based on the homogeneous flow model:

$$\Delta p_g = \frac{g(\sin \beta)L}{v_{LV}x_e} \ln \left(1 + x_e \frac{v_{LV}}{v_L} \right) \quad (5.41)$$

Equation (5.41) also assumes a liquid inlet condition. In case of two-phase inlet flow, the difference between the exit and inlet quality should be used in place of x_e .

5.9. Adiabatic two-phase flow

Adiabatic two-phase flow has been studied extensively in literature, especially with air–water flow. For small diameter channels, the work of Mishima and Hibiki (1996) is particularly noteworthy. Figure 5.20 shows their flow pattern map.

The effect of surfactants on the adiabatic two-phase flow pressure drop was studied by English and Kandlikar (2005) in a 1-mm square minichannel with air and water with superficial gas and liquid velocities of 3.19–10 m/s and 0.001–0.02 m/s, respectively. The resulting flow pattern was stratified (annular) in all cases, which is near the bottom right corner in Fig. 5.20. The pressure drop was not affected by variation in surface tension from 0.034 to 0.073 N/m. The reason for this is believed to be the absence of a three-phase line (such as would exist with discrete droplets sliding on the wall). The Mishima and Hibiki (1996) correlation for pressure drop was modified as shown in Fig. 5.19 using Eqs. (5.39) and (5.36).

5.10. Practical cooling systems with microchannels

Use of microchannels in a high heat flux cooling application using flow boiling systems was reviewed by Pokharna *et al.* (2004) for notebook computers and for server applications by Kandlikar (2005). The major issues that need to be addressed before implementation of flow boiling becomes practical are listed as follows (Kandlikar, 2005).

High heat flux cooling systems with flow boiling have lagged behind the single-phase liquid cooled systems because of some of the operational challenges that still remain to be resolved. These are listed below:

- (i) Need for low-pressure water or a suitable refrigerant to match the saturation temperature requirement for electronics cooling.
- (ii) Unstable operation due to rapid bubble expansion and occasional flow reversal.
- (iii) Unavailability of CHF data and a lack of fundamental understanding of the flow boiling phenomenon in microchannel passages.

The use of water is very attractive from a heat transfer performance perspective, but the positive pressure requirement may lead to a vacuum system, which is generally not desirable due to possible air leakage, which raises the saturation temperature in the system. Development of a suitable refrigerant suitable for this application is recommended.

The desirable characteristics of an ideal refrigerant in a flow boiling system may be listed as (Kandlikar, 2005):

- (a) saturation pressure slightly above the atmospheric pressure at operating temperatures;
- (b) high latent heat of vaporization;
- (c) good heat transfer and pressure drop related properties (high liquid thermal conductivity, low liquid viscosity, low hysteresis for ONB);
- (d) high dielectric constant if applied directly into the chip;
- (e) compatible with silicon (for direct chip cooling) and copper (for heat sink applications), and other system components;
- (f) low leakage rates through pump seals;
- (g) chemical stability under system operating conditions;
- (h) low cost;
- (i) safe for human and material exposure under accidental leakages.

The fundamental understanding of the flow boiling phenomenon is slowly emerging, and efforts to stabilize the flow using nucleating cavities and pressure drop elements is expected to help in making flow boiling systems as a viable candidate for high heat flux cooling application.

Another application for flow boiling in narrow channels is in compact evaporators. The evaporators used in automotive application currently do not employ some of the small channel configurations used in condenser application due to stability problems. Stabilized flow boiling, as described in Section 5.6, will enable practical implementation of microchannels and minichannels in a variety of compact evaporator applications.

5.11. Solved examples

Example 5.1

Water is used as the cooling liquid in a microchannel heat sink. The dimensions of one channel are $a = 1054 \mu\text{m} \times b = 50 \mu\text{m}$, where a is the unheated length in the three-sided heating case. The inlet temperature of the water is 70°C , and the Reynolds number in the channel is 600.

- (1) Calculate the insipient boiling location and cavity radius and plot the wall superheat and liquid subcooling at the ONB versus the cavity radius r_c . Also plot the predicted heat transfer coefficient as a function of quality for the following values of heat flux:
- (i) $q'' = 50 \text{ kW/m}^2$, (ii) $q'' = 340 \text{ kW/m}^2$, (iii) $q'' = 1 \text{ MW/m}^2$.
- (2) Calculate the pressure drop in the heat exchanger core for a heat flux of 1 MW/m^2 and a channel length of 20 mm.

Assumptions

Fully developed laminar flow Nusselt number; three-sided heating; properties of water are at saturation temperature at 1 atm; Receding contact angle is 40° .

Solution

Properties of water at 100°C : $h_{LV} = 2.26 \times 10^6 \text{ J/kg}$, $i_L = 4.19 \times 10^5 \text{ J/kg}$, $\rho_V = 0.596 \text{ kg/m}^3$, $v_L = 0.001044 \text{ m}^3/\text{kg}$, $v_g = 1.679 \text{ m}^3/\text{kg}$, $c_{p,L} = 4217 \text{ J/kg-K}$, $\mu_V = 1.20 \times 10^{-5} \text{ N-s/m}^2$, $\mu_L = 2.79 \times 10^{-4} \text{ N-s/m}^2$, $k_L = 0.68 \text{ W/m-K}$, $\sigma = 0.0589 \text{ N/m}$, $\text{Pr} = 1.76$ (Incropera and DeWitt, 2002). Properties of water at 70°C : $i_L = 2.93 \times 10^5 \text{ J/kg}$.

Part 1

(i) Heat flux is 50 kW/m^2

The fully developed Nusselt number is found using Table 3.3 with aspect ratio $\alpha_c = a/b = 1054 \mu\text{m}/50 \mu\text{m} = 21.08$. Since the aspect ratio is greater than 10, the Nusselt number for three-sided heating is 5.385. The hydraulic diameter and heated perimeter are:

$$D_h = \frac{4A_c}{P_w} = \frac{2ab}{(a+b)} = \frac{2 \times 1054 \times 10^{-6} \times 50 \times 10^{-6}}{(1054 + 50) \times 10^{-6}} = 9.547 \times 10^{-5} \text{ m} \\ = 95.47 \mu\text{m}$$

$$P = a + 2b = (2 \times 50 + 1054) \times 10^{-6} = 1.154 \times 10^{-3} \text{ m} = 1154 \mu\text{m}$$

The heat transfer coefficient is $h = k_L \text{Nu}/D_h = (0.68 \text{ W/m-K})(5.385)/(9.55 \times 10^{-5} \text{ m}) = 38,355 \text{ W/m}^2\text{-K}$.

Under the fully developed assumption, a value for the temperature difference between the wall temperature and the bulk liquid temperature can be found using the equation $q'' = h(\Delta T) = h(T_{\text{Wall}} - T_{\text{Bulk}}) = h(T_{\text{Wall}} - T_{\text{Sat}} + T_{\text{Sat}} - T_{\text{Bulk}}) = h(\Delta T_{\text{Sat}} + \Delta T_{\text{Sub}})$. Therefore, the sum of ΔT_{Sat} and ΔT_{Sub} can be found for a given heat flux as $q''/h = (\Delta T_{\text{Sat}} + \Delta T_{\text{Sub}}) = (50,000 \text{ W/m}^2)/(38,355 \text{ W/m}^2\text{-K}) = 1.30^\circ\text{C}$.

The wall superheat at the critical cavity radius is found by setting the expression under the radical in Eq. (5.16) equal to zero.

$$\sqrt{1 - [8.8\sigma T_{\text{Sat}}(\Delta T_{\text{Sat}} + \Delta T_{\text{Sub}})]/(\rho_V h_{LV} \delta_t \Delta T_{\text{Sat}}^2)} = 0$$

Noting that $\delta_t = k_L/h$, the equation $q'' = h(\Delta T_{\text{Sat}} + \Delta T_{\text{Sub}})$ can be written as $q'' = \frac{k_L}{\delta_t}(\Delta T_{\text{Sat}} + \Delta T_{\text{Sub}})$.

Solving this equation for δ_t :

$$\delta_t = k_L(\Delta T_{\text{Sat}} + \Delta T_{\text{Sub}})/q'' = (0.68 \times 1.3)/50,000 = 1.77 \times 10^{-5} \text{ m} = 17.7 \mu\text{m}$$

and substituting it into the expression under the radical in Eq. (5.16), the value for ΔT_{Sat} at the critical r_c can be obtained as:

$$\Delta T_{\text{Sat}} = \sqrt{\frac{8.8\sigma T_{\text{Sat}} q''}{\rho_V h_{LV} k_L}} = \sqrt{\frac{8.8 \times 0.0589 \times 373.15 \times 50,000}{0.596 \times 2.26 \times 10^6 \times 0.68}} = 3.25^\circ\text{C}$$

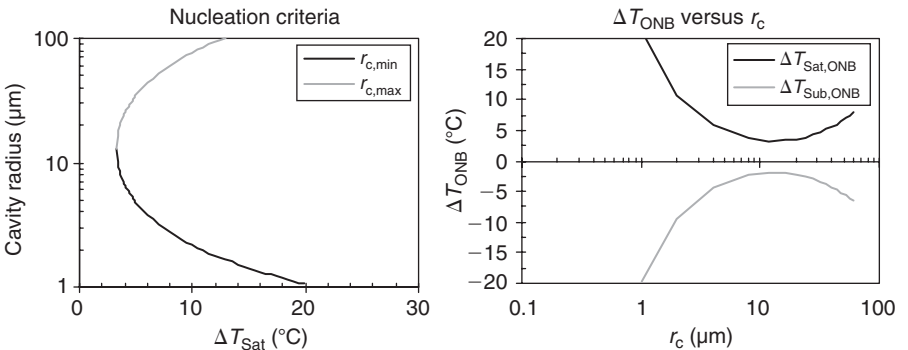
The cavity radius can be found by using Eq. (5.17):

$$r_{c,\text{crit}} = \left(\frac{\delta_t \sin \theta_r}{2.2} \right) \left(\frac{\Delta T_{\text{Sat}}}{\Delta T_{\text{Sat}} + \Delta T_{\text{Sub}}} \right) = \left(\frac{1.77 \times 10^{-5} \times \sin 40^\circ}{2.2} \right) \frac{3.25}{1.3} \\ = 12.9 \times 10^{-6} \text{ m} = 12.9 \mu\text{m}$$

Using Eq. (5.1) and the definitions of wall superheat and liquid subcooling given by Eqs. (5.8) and (5.9), the location where ONB occurs is found:

$$z = \frac{(T_{B,z} - T_{B,i}) \dot{m} c_p}{q'' P} = \frac{(375.1 - 343.15) \times 92.4 \times 10^{-6} \times 4217}{50,000 \times 1.15 \times 10^{-3}} \\ = 0.216 \text{ m} = 21.6 \text{ cm}$$

Realistically, this length is too large for a microchannel heat exchanger and the actual length is expected to be much shorter. Also, the heat flux is very low for a microchannel heat exchanger. Therefore, it will be operating under single-phase liquid flow conditions throughout. Plotting Eq. (5.16) as a function of ΔT_{Sat} illustrates the nucleation criteria for the given heat flux. The wall superheat at ONB is plotted as a function of the nucleation cavity radius (ΔT_{ONB} versus r_c) by using Eq. (5.20). The liquid subcooling is also presented on this plot. Note that the negative values of ΔT_{Sub} indicate that the bulk is superheated at the point of nucleation. This will lead to significant flow instabilities as discussed in the Section 5.4.



The Boiling number is calculated from Table 5.1:

$$Bo = \frac{q''}{Gh_{LV}} = \frac{q''D_h}{h_{LV} Re \mu_L} = \frac{50,000 \times 9.547 \times 10^{-5}}{2.26 \times 10^6 \times 600 \times 2.79 \times 10^{-4}} = 1.262 \times 10^{-5}$$

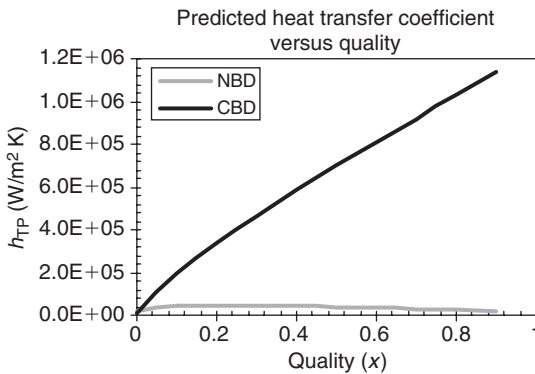
For a flow of higher Reynolds number, the value of h_{LO} would not be the same as the single-phase value of h , as can be seen with Eqs. (5.24)–(5.26). As the Reynolds number is 600, the heat transfer coefficient h_{LO} is equal to the single-phase value of h by Eq. (5.26), $h_{LO} = h = 38,355 \text{ W/m}^2 \text{ K}$.

The Convection number is a function of quality:

$$\begin{aligned} Co &= [(1-x)/x]^{0.8} [\rho_V/\rho_L]^{0.5} = [(1-x)/x]^{0.8} (0.596/957.9) \\ &= [(1-x)/x]^{0.8} \times 6.22 \times 10^{-4} \end{aligned}$$

From Eq. (5.21), the flow boiling h_{TP} is the larger of Eqs. (5.22) and (5.23), which can be plotted as functions of x as seen below using an F_{FI} of 1:

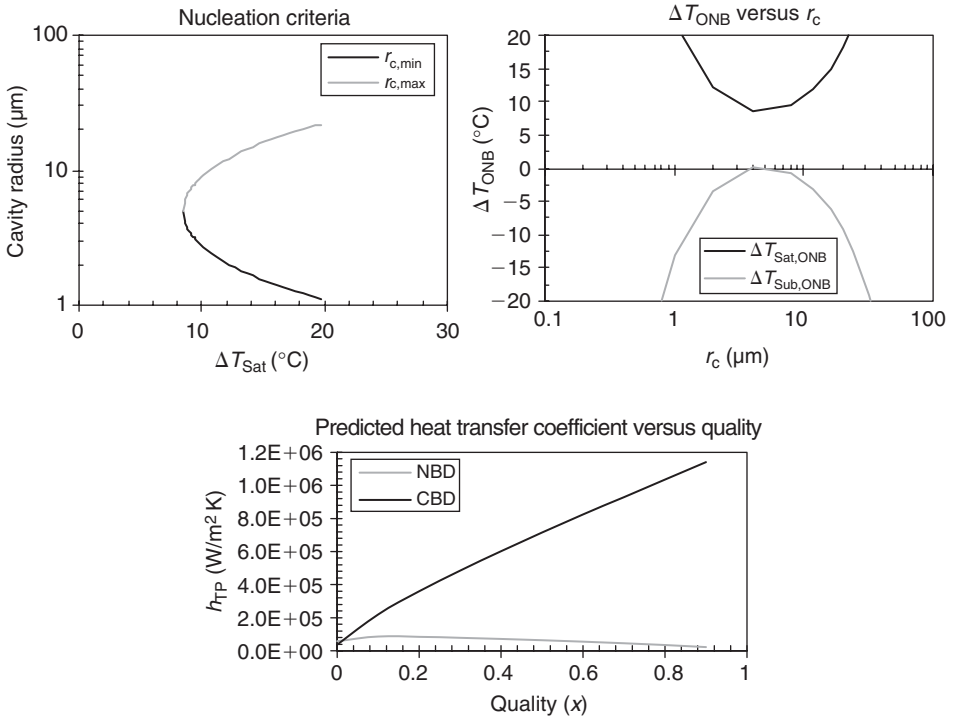
$$\begin{aligned} h_{TP} &= \text{larger of } \begin{cases} h_{TP,NBD} \\ h_{TP,CBD} \end{cases} \\ h_{TP,NBD} &= h_{LO} [0.6683 Co^{-0.2} (1-x)^{0.8} + 1058.0 Bo^{0.7} (1-x)^{0.8} F_{FI}] \\ &= 38,355 \{ 0.6683 [(1-x)/x]^{0.8} \times 6.22 \times 10^{-4} \}^{-0.2} (1-x)^{0.8} \\ &\quad + 1058.0 (1.262 \times 10^{-5})^{0.7} (1-x)^{0.8} \times 1 \} \\ h_{TP,CBD} &= h_{LO} [1.136 Co^{-0.9} (1-x)^{0.8} + 667.2 Bo^{0.7} (1-x)^{0.8} F_{FI}] \\ &= 38,355 \{ 1.136 [(1-x)/x]^{0.8} \times 6.22 \times 10^{-4} \}^{-0.9} (1-x)^{0.8} \\ &\quad + 667.2 (1.262 \times 10^{-4})^{0.7} (1-x)^{0.8} \times 1 \} \end{aligned}$$



Since $h_{TP,NBD}$ yields higher values than $h_{TP,CBD}$, it represents the flow boiling thermal conditions and should be used for the present case. Note that h_{TP} increases with quality for this case.

(ii) Heat flux is 340 kW/m²

$a = 1054 \mu\text{m}$; $b = 50 \mu\text{m}$; $T_i = 70^\circ\text{C}$; $\text{Re} = 600$; $\alpha_c = 21.08$; $h = 38,355 \text{ W/m}^2 \text{ K}$
 $(\Delta T_{\text{Sat}} + \Delta T_{\text{Sub}}) = 8.86^\circ\text{C}$; $\Delta T_{\text{Sat}} = 8.48^\circ\text{C}$; $r_{c,\text{crit}} = 5.0 \mu\text{m}$; $z = 2.9 \text{ cm}$

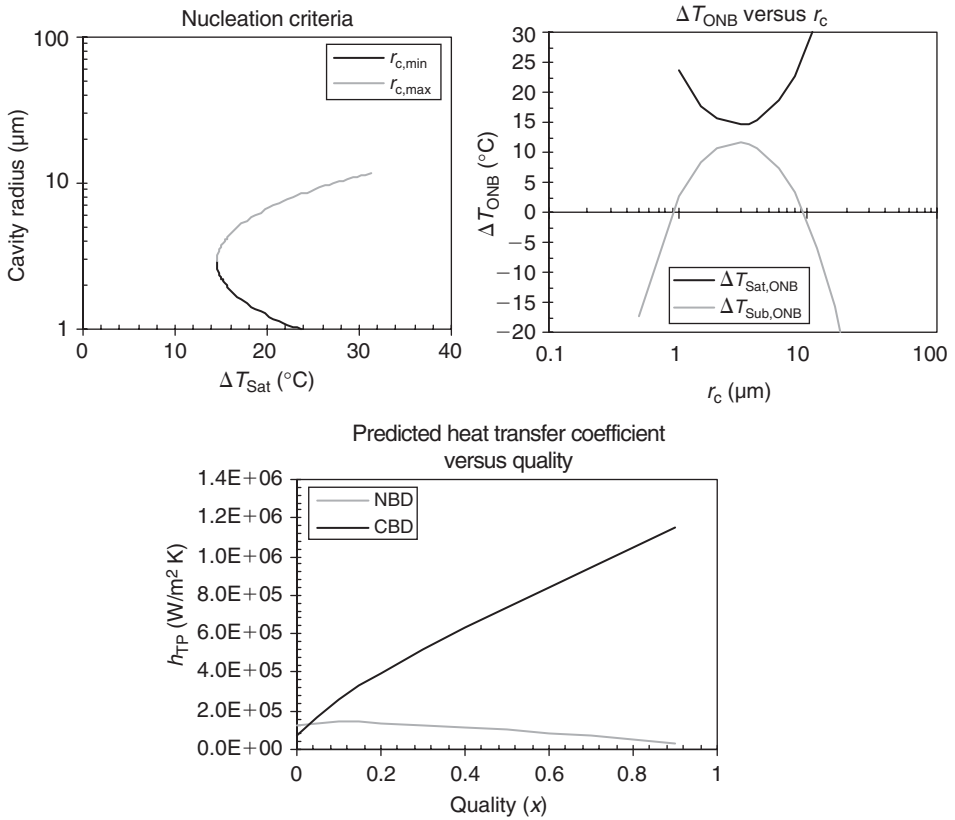


In plotting the heat transfer coefficient versus quality, it is seen that the nucleate boiling dominant prediction is actually higher than the convective dominant prediction for very low qualities (<0.1) and should be used in those cases. There is an increase in the nucleate boiling behavior in comparison to the lower heat flux case.

(iii) Heat flux is 1 MW/m²

$a = 1054 \mu\text{m}$; $b = 50 \mu\text{m}$; $T_i = 70^\circ\text{C}$; $\text{Re} = 600$; $\alpha_c = 21.08$; $h = 38,355 \text{ W/m}^2 \text{ K}$
 $(\Delta T_{\text{Sat}} + \Delta T_{\text{Sub}}) = 26.1^\circ\text{C}$; $\Delta T_{\text{Sat}} = 14.5^\circ\text{C}$; $r_{c,\text{crit}} = 2.9 \mu\text{m}$; $z = 0.6 \text{ cm}$

The nucleate boiling dominant prediction is higher than the convective boiling dominant for qualities lower than 0.4 and should be used for those cases. Note that a high wall superheat is needed to initiate nucleation (14.5°C). Also, the cavity sizes for nucleation become smaller as the heat flux increases. Thus a variety of different cavity sizes are needed on a surface to operate it at different heat flux conditions. Another point to note is that the saturation temperature of water at 1 atm is quite high for electronics cooling applications. Two options can be pursued: one is to use low-pressure steam, and the other is to use refrigerants. The next example illustrates the use of refrigerants.



Part 2

From **Part 1, (iii)**, it is found that the onset of nucleate boiling occurs at 0.6 cm from the entrance end. Therefore, the flow is single-phase up to 0.6 cm at which point it becomes two-phase flow. However, the bulk is subcooled at this location and so Eq. (5.1) is used to determine the location where the saturation temperature is reached:

$$z = \frac{(T_{B,z} - T_{B,i})\dot{m}c_p}{q''P} = \frac{(100 - 70) \times 92.4 \times 10^{-6} \times 4217}{1 \times 10^6 \times 1.15 \times 10^{-3}} = 0.0101 \text{ m} = 1.01 \text{ cm}$$

Using this approach simplifies the problem, but keep in mind that since ONB actually occurs before this location in the channel, the actual pressure drop in the core of the channel will be slightly higher due to the longer two-phase flow length.

The exit quality can be solved for by using the following equation to get $x_e = 0.055$, where A_T is the heated perimeter multiplied by the channel length:

$$q''A_T = \dot{m}[(i_{L,@T_{\text{Sat}}} + x_e h_{\text{LV},@T_{\text{Sat}}}) - i_{L,@T_{B,\text{in}}}]$$

$$\begin{aligned}
x_e &= \left(\frac{q'' A_T}{\dot{m}} + i_{L,@T_{B,in}} - i_{L,@T_{Sat}} \right) / h_{LV,@T_{Sat}} \\
&= \left(\frac{10,00,000 \times 1.15 \times 10^{-3} \times 0.02}{9.24 \times 10^{-5}} + 2.93 \times 10^5 - 4.19 \times 10^5 \right) / 2.26 \times 10^6 \\
&= 0.055
\end{aligned}$$

The total mass flux can be calculated from the Reynolds number and channel geometry:

$$G = \text{Re} \mu_L / D_h = (600 \times 2.79 \times 10^{-4}) / (9.547 \times 10^{-5}) = 1753 \text{ kg/m}^2\text{s}$$

The superficial Reynolds numbers of the liquid and vapor phases in the two-phase flow region are found by using the following equations. The average quality over the channel length is taken as half the exit quality.

$$\begin{aligned}
\text{Re}_V &= \frac{G \frac{x_e}{2} D_h}{\mu_V} = \frac{1753 \times \frac{0.055}{2} \times 9.547 \times 10^{-5}}{1.2 \times 10^{-5}} = 384 \\
\text{Re}_L &= \frac{G \left(1 - \frac{x_e}{2}\right) D_h}{\mu_L} = \frac{1753 \left(1 - \frac{0.055}{2}\right) 9.547 \times 10^{-5}}{2.79 \times 10^{-4}} = 583
\end{aligned}$$

The single-phase friction factors f_L and f_V are obtained by using Eq. (3.10) with the Reynolds numbers calculated above.

$$\begin{aligned}
\text{Po} = f \text{Re} &= 24(1 - 1.3553\alpha_c + 1.9467\alpha_c^2 - 1.7012\alpha_c^3 + 0.9564\alpha_c^4 - 0.2537\alpha_c^5) \\
&= 24(1 - 1.3553 \times 21.08 + 1.9467 \times 21.08^2 - 1.7012 \times 21.08^3 \\
&\quad + 0.9564 \times 21.08^4 - 0.2537 \times 21.08^5) \\
&= 22.56
\end{aligned}$$

The friction pressure gradients given in Eq. (5.37) are defined as:

$$\begin{aligned}
-\left(\frac{dp_F}{dz}\right)_L &= \frac{2f_L G^2 \left(1 - \frac{x_e}{2}\right)^2}{D_h \rho_L} \\
&= \frac{2 \left(\frac{22.56}{583}\right) 1753^2 \left(1 - \frac{0.055}{2}\right)^2}{9.547 \times 10^{-5} \times 957.9} = 2,458,697 \text{ Pa/m} = 2.46 \text{ MPa/m} \\
-\left(\frac{dp_F}{dz}\right)_V &= \frac{2f_V G^2 \left(\frac{x_e}{2}\right)^2}{D_h \rho_V} = \frac{2 \left(\frac{22.56}{384}\right) 1753^2 \left(\frac{0.055}{2}\right)^2}{9.547 \times 10^{-5} \times 0.5956} \\
&= 4,800,308 \text{ Pa/m} = 4.80 \text{ MPa/m} \\
X^2 &= \left(\frac{dp_F}{dz}\right)_L / \left(\frac{dp_F}{dz}\right)_V = \frac{2.46}{4.80} = 0.5125
\end{aligned}$$

The two-phase multiplier is calculated with Eq. (5.39):

$$\phi_L^2 = 1 + \frac{C(1 - e^{-319D_h})}{X} + \frac{1}{X^2} = 1 + \frac{5(1 - e^{-319 \times 9.547 \times 10^{-5}})}{\sqrt{0.5125}} + \frac{1}{0.5125} = 3.16$$

and the two-phase pressure drop per unit length is calculated with Eq. (5.34):

$$\left(\frac{dp_F}{dz}\right)_{TP} = \left(\frac{dp_F}{dz}\right)_L \phi_L^2 = 24,58,697 \times 3.16 = 7,769,482 \text{ Pa/m} = 7.77 \text{ MPa/m}$$

The frictional two-phase pressure drop is found by multiplying the frictional pressure gradient by the two-phase flow length ($0.02 \text{ m} - 0.0101 \text{ m} = 0.0099 \text{ m}$) to get 76.7 kPa.

The total pressure drop in the core is found by adding the pressure drop in the single-phase flow section length (0.0101 m) and the two-phase pressure drop:

$$\Delta p = \Delta p_{f,1-ph} + \Delta p_{f,tp} = 26,800 + 76,700 = 103,500 \text{ Pa} = 103.5 \text{ kPa} (15.0 \text{ psi})$$

Example 5.2

Microchannels are directly etched into the silicon chips to dissipate a heat flux of $13,000 \text{ W/m}^2$ from a computer chip. The geometry may be assumed similar to Fig. 3.19. Each of the parallel microchannels has a width $a = 200 \mu\text{m}$, height $b = 200 \mu\text{m}$, and length $L = 10 \text{ mm}$. Refrigerant-123 flows through the horizontal microchannels at an inlet temperature of $T_{B,i} = 293.15 \text{ K}$. The heated perimeter $P = b + a + b = 600 \times 10^{-6} \text{ m}$, and the cross-sectional area $A_c = a \times b = 40 \times 10^{-9} \text{ m}^2$. Assume θ_r from Fig. 5.1 is 20° , and $\text{Re} = 100$.

Solution

Properties of R-123 at $T_{\text{Sat}} = 300.9 \text{ K}$ and 1 atm : $\mu_L = 404.2 \times 10^{-6} \text{ N-s/m}^2$, $\mu_V = 10.8 \times 10^{-6} \text{ N-s/m}^2$, $\rho_L = 1456.6 \text{ kg/m}^3$, $\rho_V = 6.5 \text{ kg/m}^3$, $c_{p,L} = 1023 \text{ J/kg K}$, $k_L = 75.6 \times 10^{-3} \text{ W/m K}$, $k_V = 9.35 \times 10^{-3} \text{ W/m K}$, $\sigma_L = 14.8 \times 10^{-3} \text{ N/m}$, $h_{LV} = 170.19 \times 10^3 \text{ J/kg}$, $i_L = 228 \times 10^3 \text{ J/kg}$, $i_V = 398 \times 10^3 \text{ J/kg}$.

(i) Calculate the incipient boiling location and cavity radius (Answers: $z = 0.584 \times 10^{-3} \text{ m}$, and $r_{c,\text{crit}} = 2.23 \times 10^{-6} \text{ m}$)

From Eq. (5.18):

$$\begin{aligned} \Delta T_{\text{Sat,ONB}} &= \sqrt{8.8\sigma T_{\text{Sat}} q'' / (\rho_V h_{LV} k_L)} \\ &= \sqrt{8.8(14.8 \times 10^{-3})(300.9)(13,000) / (6.5)(170.19 \times 10^3)(75.6 \times 10^{-3})} \\ &= 2.47 \text{ K} \end{aligned}$$

Calculate the hydraulic diameter:

$$D_h = \frac{4A_c}{P_w} = a = b = 200 \times 10^{-6} \text{ m}$$

From Table 3.3, $\text{Nu}_{\text{fd},3} = 3.556$, and note that:

$$h = \frac{\text{Nu}_L k_L}{D_h} = \frac{(3.556)(0.0756)}{(200 \times 10^{-6})} = 1344 \text{ W/m}^2 \text{ K}$$

From Eq. (5.19):

$$\Delta T_{\text{Sub,ONB}} = \frac{q''}{h} - \Delta T_{\text{Sat,ONB}} = \frac{13,000}{1344} - 2.47 = 7.2 \text{ K}$$

From Eq. (5.8), T_B at the onset of nucleate boiling is:

$$T_{\text{B,ONB}} = T_{\text{Sat}} - \Delta T_{\text{Sub,ONB}} = 300.9 - 7.2 = 293.7 \text{ K}$$

Calculate the flow velocity using the Reynolds number:

$$V = \frac{\text{Re} \mu_L}{\rho D_h} = \frac{(100)(404.2 \times 10^{-6})}{(1456.6)(200 \times 10^{-6})} = 0.139 \text{ m/s}$$

Calculate the mass flow rate:

$$\dot{m} = \rho V A_c = (1456.6)(0.139)(40 \times 10^{-9}) = 8.09 \times 10^{-6} \text{ kg/s}$$

Calculate the mass flux:

$$G = \frac{\dot{m}}{A_c} = \frac{8.09 \times 10^{-6}}{40 \times 10^{-9}} = 202 \text{ kg/m}^2 \text{ s}$$

The incipient boiling location can be calculated by rearranging Eq. (5.1):

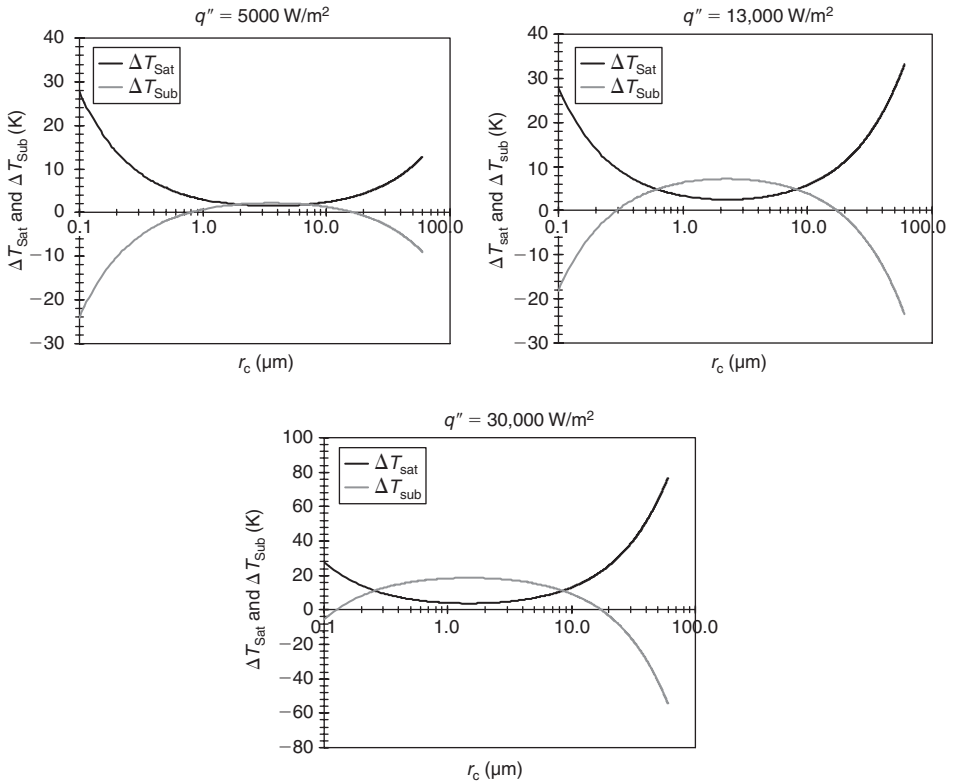
$$\begin{aligned} z &= (T_{\text{B,ONB}} - T_{\text{B,i}}) \left(\frac{\dot{m} c_{p,L}}{q'' P} \right) \\ &= (293.7 - 293.15) \left(\frac{(8.09 \times 10^{-6})(1023)}{(13,000)(600 \times 10^{-6})} \right) \\ &= 0.584 \times 10^{-3} \text{ m} \end{aligned}$$

To find the cavity radius, substitute Eqs. (5.3) and (5.19) into Eq. (5.17) we get

$$r_{\text{c,crit}} = \frac{k_L \sin \theta_r \Delta T_{\text{Sat,ONB}}}{2.2 q''} = \frac{(75.6 \times 10^{-3})(\sin 20^\circ)(2.47)}{2.2(13,000)} = 2.23 \times 10^{-6} \text{ m}$$

(ii) Plot the wall superheat and liquid subcooling versus nucleating cavity radius for $q'' = 5, 13, \text{ and } 30 \text{ kW/m}^2$.

Equations (5.19) and (5.20) are used to plot the following figures.



(iii) Calculate the pressure drop in the test section (Answer: 426 Pa)

For fully developed laminar flow, the hydrodynamic entry length may be obtained using Eq. (3.11):

$$L_h = 0.05 \text{Re} D_h = 0.05(100)(0.200) = 1.0 \text{ mm}$$

Since $L > L_h$, the fully developed flow assumption is valid.

From Eq. (5.1):

$$\begin{aligned} z &= (T_{B,z} - T_{B,i}) \left(\frac{\dot{m} c_{p,L}}{q'' P} \right) = (300.97 - 293.15) \left(\frac{(8.09 \times 10^{-6})(1023)}{(13,000)(600 \times 10^{-6})} \right) \\ &= 8.29 \times 10^{-3} \text{ m} \end{aligned}$$

Note that z is the location where two-phase boiling begins. So, we need to find the single-phase pressure drop until z and then add to that the value of the two-phase pressure drop from z to L .

The total pressure drop can be found using Eq. (5.28):

$$\Delta p = \Delta p_c + \Delta p_{f,1\text{-ph}} + \Delta p_{f,tp} + \Delta p_a + \Delta p_g + \Delta p_e$$

To find the single-phase pressure drop, the f Re term can be obtained using Eq. (3.10) and using an aspect ratio of one:

$$\alpha_c = a/b = 200/200 = 1$$

$$\begin{aligned} f \text{ Re} &= 24(1 - 1.3553\alpha_c + 1.9467\alpha_c^2 - 1.7012\alpha_c^3 + 0.9564\alpha_c^4 - 0.2537\alpha_c^5) \\ &= 24(1 - 1.3553 \times 1 + 1.9467 \times 1^2 - 1.7012 \times 1^3 + 0.9564 \times 1^4 \\ &\quad - 0.2537 \times 1^5) = 14.23 \end{aligned}$$

The single-phase core frictional pressure drop can be calculated using Eq. (3.14):

$$\Delta p_{f,1-ph} = \frac{2(f \text{ Re})\mu_L U_m z}{D_h^2} + K(\infty) \cdot \frac{\rho_L U_m^2}{2} \quad \text{where } K(\infty) \text{ is given by Eq. (3.18)}$$

$$\begin{aligned} K(\infty) &= (0.6796 + 1.2197\alpha_c + 3.3089\alpha_c^2 - 9.5921\alpha_c^3 \\ &\quad + 8.9089\alpha_c^4 - 2.9959\alpha_c^5) \\ &= 1.53 \end{aligned}$$

$$\begin{aligned} \Delta p_{f,1-ph} &= \frac{2(14.23)(0.404 \times 10^{-3})(0.139)(0.00829)}{(200 \times 10^{-6})^2} \\ &\quad + (1.53) \frac{(1456.6)(0.139)^2}{2} \\ &= 353 \text{ Pa} \end{aligned}$$

Note that Δp_c , Δp_g and Δp_e can be neglected because we are calculating the core pressure drop in horizontal microchannels.

The following Eqs. (9.1-12, 14, 35, 36, 37, 39 and 40) are from Chapter 9 of Handbook of Phase Change (Kandlikar *et al.*, 1999). Assuming that the liquid pressure is 1 atm, then $i_{IN} = 228 \times 10^3 \text{ J/kg}$. The heated area in the two-phase region is:

$$\begin{aligned} A_{h,tp} &= (b + a + b)(L - z) = (200 \times 10^{-6} + 200 \times 10^{-6} + 200 \times 10^{-6}) \\ &\quad \times (10 \times 10^{-3} - 8.29 \times 10^{-3}) \\ &= 1.026 \times 10^{-6} \text{ m}^2 \end{aligned}$$

From Eq. (9.1-12):

$$i_{TP} = i_{IN} + \frac{q'' A_{h,tp}}{G A_c} = 228 \times 10^3 + \frac{(13,000)(1.026 \times 10^{-6})}{(8.09 \times 10^{-6})} = 229.6 \times 10^3 \text{ J/kg}$$

From Eq. (9.1-14):

$$x_e = \frac{i_{TP} - i_L}{h_{LV}} = \frac{(229.6 \times 10^3 - 228 \times 10^3)}{(170.19 \times 10^3)} = 0.0094$$

Use the average thermodynamic quality between 0 and x_e , $x_{\text{avg}} = 0.0047$. From Eq. (9.1-39):

$$\text{Re}_V = \frac{Gx D_h}{\mu_V} = \frac{(202)(0.0047)(200 \times 10^{-6})}{(10.8 \times 10^{-6})} = 17.58$$

From earlier the vapor friction factor is:

$$f_V = \frac{14.23}{\text{Re}_V} = \frac{14.23}{17.58} = 0.809$$

From Eq. (9.1-35):

$$-\left(\frac{dp_F}{dz}\right)_V = \frac{2f_V G^2 x^2}{D_h \rho_V} = \frac{2(0.809)(202)^2(0.0047)^2}{(200 \times 10^{-6})(6.5)} = 1122 \text{ Pa/m}$$

From Eq. (9.1-40):

$$\text{Re}_L = \frac{G(1-x) D_h}{\mu_L} = \frac{(202)(1-0.0047)(200 \times 10^{-6})}{(0.4042 \times 10^{-3})} = 99.48$$

$$f_L = \frac{14.23}{\text{Re}_L} = \frac{14.23}{99.48} = 0.143$$

From Eq. (9.1-36):

$$-\left(\frac{dp_F}{dz}\right)_L = \frac{2f_L G^2 (1-x)^2}{D_h \rho_L} = \frac{2(0.143)(202)^2(1-0.0047)^2}{(200 \times 10^{-6})(1456.6)} = 39,683 \text{ Pa/m}$$

From Eq. (5.37):

$$X^2 = \left(\frac{dp_F}{dz}\right)_L / \left(\frac{dp_F}{dz}\right)_V = \frac{39,683}{1122} = 35.37$$

Assuming both phases are laminar, from Eq. (5.36d), $C = 5$.

Using Eq. (5.39):

$$\phi_L^2 = 1 + \frac{C(1 - e^{-319 D_h})}{X} + \frac{1}{X^2} = 1 + \frac{5(1 - e^{-319(200 \times 10^{-6})})}{\sqrt{35.37}} + \frac{1}{35.37} = 1.08$$

From Eq. (5.34) $\Delta p_{f,\text{tp}} = \left(\frac{dp_F}{dz}\right) = \left(\frac{dp_F}{dz}\right)_L \phi_L^2 = (39,683)(1.08) = 42,858 \text{ Pa/m}$

The acceleration pressure drop is calculated from Eq. (5.40):

$$\Delta p_a = G^2 v_{LV} x_e = (202)^2 (0.00069)(0.0094) = 0.26 \text{ Pa}$$

The value of the acceleration pressure drop is negligible, and hence the total pressure drop is

$$\Delta p = \Delta p_{f,1-ph} + \Delta p_{f,tp} = (353) + (42,858)(0.01 - 0.00829) = 426 \text{ Pa}$$

(iv) Plot the predicted heat transfer coefficient as a function of quality

From Table 5.1, the Boiling number is:

$$Bo = \frac{q''}{Gh_{LV}} = \frac{(13,000)}{(202)(170.19 \times 10^3)} = 0.378 \times 10^{-3}$$

From Table 5.1, the convection number is:

$$\begin{aligned} Co &= [(1-x)/x]^{0.8} [\rho_V/\rho_L]^{0.5} = [(1-x)/x]^{0.8} (6.5/1456.6)^{0.5} \\ &= 0.0668[(1-x)/x]^{0.8} \end{aligned}$$

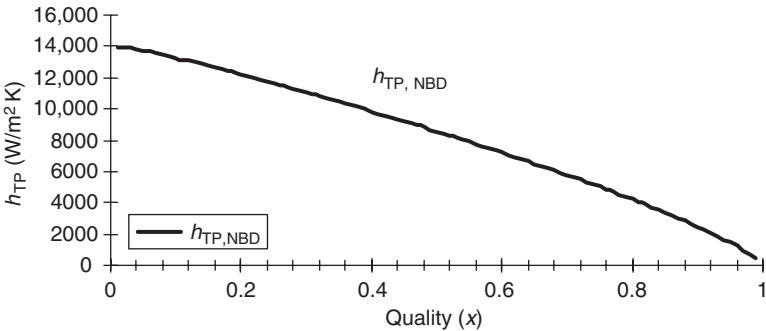
For $Re_{LO} \leq 100$, from Eqs. (5.26) and (5.27):

$$h_{LO} = \frac{Nuk_L}{D_h} = \frac{(3.556)(0.0756)}{(200 \times 10^{-6})} = 1344 \text{ W/m}^2 \text{ K}$$

From Table 3 in page 391 of Handbook of Phase Change (Kandlikar *et al.*, 1999), assume $F_{FI} = 1.3$.

For $Re_{LO} \leq 100$, $h_{TP} = h_{TP,NBD}$ and we can plot the predicted heat transfer coefficient as a function of quality using Eq. (5.27). This is very similar to the method followed in the previous example, but only the nucleate boiling dominant prediction is used from Eq. (5.27):

$$\begin{aligned} h_{TP} &= h_{TP,NBD} = h_{LO} \{ 0.6683 Co^{-0.2} (1-x)^{0.8} + 1058.0 Bo^{0.7} (1-x)^{0.8} F_{FI} \} \\ &= 1344 \{ 0.6683 (0.0668 [(1-x)/x]^{0.8})^{-0.2} (1-x)^{0.8} \\ &\quad + 1058.0 (0.378 \times 10^{-3})^{0.7} (1-x)^{0.8} F_{FI} \} \end{aligned}$$



The total frictional pressure drop has to consider the minor losses because the actual Δp is higher than the core frictional pressure drop. Due to the laminar conditions and the dominance of nucleate boiling effects, note the decreasing trend in h_{TP} as a function of quality.

5.12. Practice problems

1. A microchannel with dimensions of $120\ \mu\text{m} \times 400\ \mu\text{m}$ and 3 mm length operates at an inlet pressure of 60 kPa. The inlet liquid is at saturation temperature. A heat flux of $600\ \text{kW/m}^2$ is applied to the three sides of the channel walls:
 - (i) Calculate the mass flux to provide an exit quality of 0.1 from this channel. Assuming that cavities of all sizes are available, calculate the distance at which ONB occurs. What is the nucleating cavity diameter at this location?
 - (ii) Calculate the pressure drop in the channel.
 - (iii) Plot the variation of heat transfer coefficient with channel length assuming an evaporator pressure to be mean of the inlet and exit pressures.
2. R-123 is used to cool a microchannel chip dissipating 400 W from a chip $12\ \text{mm} \times 12\ \text{mm}$ surface area. Assuming an allowable depth of $300\ \mu\text{m}$, design a cooling system to keep the channel wall temperature below 70°C . Calculate the associated pressure drop in the channel.
3. A copper heat sink has a $60\ \text{mm} \times 120\ \text{mm}$ base. It is desired to dissipate 10 kW of heat while keeping the plate temperature below 130°C with a flow boiling system using water. Design a suitable cooling channel configuration and water flow rate to accomplish the design.
4. Flow boiling instability in microchannels arises due to rapid bubble growth, especially near the inlet of the channels. Identify the relevant parameters that affect the resulting instability and develop an analytical model to predict the instability condition.

References

- Balasubramanian, P. and Kandlikar, S. G., An experimental study of flow patterns, pressure drop and flow instabilities in parallel rectangular minichannels, *Heat Transfer Eng.*, **26**(3), 20–27, 2005.
- Bao, Z. Y., Fletcher, D. F., and Haynes, B. S., Flow boiling heat transfer of freon R11 and HCFC123 in narrow passages, *Int. J. Heat Mass Transfer*, **43**, 3347–3358, 2000.
- Bergles, A. E., Forced convection surface boiling heat transfer and burnout in tubes of small diameter, Doctoral Dissertation, Massachusetts Institute of Technology, Cambridge, Massachusetts, 1962.
- Bergles, A. E., Subcooled burnout in tubes of small diameter, ASME Paper No. 63-WA-182, 1963.
- Bergles, A. E. and Kandlikar, S. G., On the nature of critical heat flux in microchannels, *J. Heat Transfer*, **127**(1), 101–107, 2005.
- Bergles, A. E. and Rohsenow, W. M., Forced convection surface boiling heat transfer and burnout in tubes of small diameter, M.I.T. Engineering Projects Laboratory Report No. DSR 8767-21, 1962.
- Bergles, A. E. and Rohsenow, W. M., The determination forced-convection surface boiling heat transfer, *J. Heat Transfer*, **86**, 365–272, 1964.

- Bonjour, J. and Lallemand, M., Flow patterns during boiling in a narrow space between two vertical surfaces, *Int. J. Multiphase Flow*, **24**, 947–960, 1998.
- Bowers, M. B. and Mudawar, I., High flux boiling in low flow rate, low pressure drop mini-channel and micro-channel heat sinks, *Int. J. Heat and Mass Transfer*, **37**(2), 321–334, 1994.
- Brutin, D. and Tadrist, F., Experimental study of unsteady convective boiling in heated minichannels, *Int. J. Heat Mass Transfer*, **46**, 2957–2965, 2003.
- Brutin, D., Topin, F., and Tadrist, L., Experimental study on two-phase flow and heat transfer in capillaries, in *Proceedings of the Twelfth International Heat Transfer Conference*, France, pp. 789–784, 2002.
- Chisholm, D., *Two-Phase Flow in Pipelines and Heat Exchangers*, New York: Godwin, 1983.
- Coleman, J. W., An experimentally validated model for two-phase sudden contraction pressure drop in microchannel tube headers, in *Proceedings of the First International Conference on Microchannels and Minichannels*, ASME Paper No. ICMM2003-1026, April 24–25, Rochester, New York, USA, pp. 241–248, 2003.
- Cornwell, K. and Kew, P. A., Boiling in small parallel channels, in *Proceedings of CEC Conference on Energy Efficiency in Process Technology*, Athens, October 1992, Paper 22, Elsevier Applied Sciences, pp. 624–638, 1992.
- Cuta, J. M., McDonald, C. E., and Shekarriz, A., Forced convection heat transfer in parallel channel array microchannel heat exchanger, ASME PID-Vol. 2/HTD-Vol. 338, in *Advances in Energy Efficiency, Heat and Mass Transfer Enhancement*, ASME, New York, pp. 17–22, 1996.
- Davis, E. J. and Anderson, G. H., The incipience of nucleate boiling in forced convection flow, *AIChE J.*, **12**(4), 774–780, 1966.
- Downing, R. S., Meinecke, J., and Kojasoy, G., The effects of curvature on pressure drop for single and two-phase flow in miniature channels, in *Proceedings of NHTC2000: 34th National Heat Transfer Conference*, Paper No. NHTC2000-12100, August 20–22, Pittsburgh, PA, 2000.
- English, N. J. and Kandlikar, S. G., An experimental investigation into the effect of surfactants on air-water two-phase flow in minichannels, in *proceedings of the Third International Conference on Microchannels and Minichannels*, ASME Paper No. ICMM2005-75110, June 13–15, Toronto, Canada, p. 8, 2005.
- Faulkner, D. J. and Shekarriz, R., Forced convective boiling in microchannels for kW/cm^2 electronics cooling, in *Proceedings of ASME Summer Heat Transfer Conference*, Paper No. HT2003-47160, July 21–23, Las Vegas, USA: ASME Publications, 2003.
- Hetsroni, G., Segal, Z., and Mosyak, A., Nonuniform temperature distribution in electronic devices cooled by flow in parallel microchannels, in *Packaging of Electronic and Photonic Devices*, IEEE Transactions on Components and Packaging Technologies, **24**(1), pp. 16–23, 2001.
- Hetsroni, G., Mosyak, A., Segal, Z., and Ziskind, G., A uniform temperature heat sink for cooling of electronic devices, *Int. J. Heat Mass Transfer*, **45**, 3275–3286, 2002.
- Hetsroni, G., Klein, D., Mosyak, A., Segal, Z., and Pogrebnyak, E., Convective boiling in parallel microchannels, in *Proceeding of the First International Conference on Microchannels and Minichannels*, ASME Paper No. ICMM2003-1006, April 24–25, Rochester, New York, pp. 59–68, 2003.
- Hewitt, G. F., Fluid mechanics aspects of two-phase flow, Chapter 9, in *Handbook of Boiling and Condensation*, S. G., Kandlikar, M., Shoji, V. K., Dhir, New York, NY, USA: Taylor and Francis, 2000.
- Hsu, Y. Y., On the size range of active nucleation cavities on a heating surface, *J. Heat Transfer*, **84**, 207–216, 1962.
- Hsu, Y. Y. and Graham, R., An analytical and experimental study of the thermal boundary layer and ebullition cycle in nucleate boiling, NASA TN-D-594, 1961.
- Incropera, F. P. and DeWitt, D. P., *Fundamentals of Heat and Mass Transfer*, 5th Edn., New York: John Wiley and Sons, 2002.

- Jiang, L., Wong, M., and Zohar, Y., Phase change in microchannel heat sinks with integrated temperature sensors, *J. Microelectromech. Sys.*, **8**, 358–365, 1999.
- Jiang, L., Wong, M., and Zohar, Y., Forced convection boiling in a microchannel heat sink, *J. Microelectromech. Sys.*, **10**(1), 80–87, 2001.
- Kamidis, D. E. and Ravigururajan, T. S., Single and two-phase refrigerant flow in mini-channels, in *Proceedings of 33rd National Heat Transfer Conference*, Paper No. NHTC99-262, August 15–17, Albuquerque, NM: ASME Publications, 1999.
- Kandlikar, S. G., A general correlation for two-phase flow boiling heat transfer inside horizontal and vertical tubes, *J. Heat Transfer*, **112**, 219–228, 1990.
- Kandlikar, S. G., A model for flow boiling heat transfer in augmented tubes and compact evaporators, *J. Heat Transfer*, **113**, 966–972, 1991.
- Kandlikar, S. G., A theoretical model to predict pool boiling CHF incorporating effects of contact angle and orientation, *J. Heat Transfer*, **123**, 1071–1079, 2001.
- Kandlikar, S. G., Fundamental issues related to flow boiling in minichannels and microchannels, *Exp. Therm. Fluid Sci.*, **26**(2–4), 389–407, 2002a.
- Kandlikar, S. G., Two-phase flow patterns, pressure drop, and heat transfer during flow boiling in minichannel flow passages of compact heat evaporators, *Heat Transfer Eng.*, **23**(5), 5–23, 2002b.
- Kandlikar, S. G., Heat transfer mechanisms during flow boiling in microchannels, *J. Heat Transfer*, **126**, 8–16, 2004.
- Kandlikar, S. G., High flux heat removal with microchannels – a roadmap of opportunities and challenges, in *Proceedings of the Third International Conference on Microchannels and Minichannels*, Keynote Paper, ASME Paper No. 75086, June 13–15, Toronto, Canada, 2005.
- Kandlikar, S. G. and Balasubramanian, P., An extension of the flow boiling correlation to transition, laminar and deep laminar flows in minichannels and microchannels, *Heat Transfer Eng.*, **25**(3), 86–93, 2004.
- Kandlikar, S. G. and Balasubramanian, P., Effect of gravitational orientation on flow boiling of water in 1054×197 micron parallel minichannels, in *Proceedings of the Second International Conference on Microchannels and Minichannels*, ASME Paper No. ICMM 2004-2379, June 17–19, 2004, Rochester, NY, USA, pp. 539–550, 2005 (also to appear in *J. Heat Transfer*, 2005).
- Kandlikar, S. G. and Spiesman, P. H., Effect of surface characteristics on flow boiling heat transfer, *Paper presented at the Engineering Foundation Conference on Convective and Pool Boiling*, May 18–25, Irsee, Germany, 1997.
- Kandlikar, S. G. and Steinke, M. E., Contact angles and interface behavior during rapid evaporation of liquid on a heated surface, *Int. J. Heat Mass Transfer*, **45**, 3771–3780, 2002.
- Kandlikar, S. G. and Steinke, M. E., Predicting heat transfer during flow boiling in minichannels and microchannels, *ASHRAE Trans.*, **109**(1), 1–9, 2003.
- Kandlikar, S. G. and Stumm B. J., A control volume approach for investigating forces on a departing bubble under subcooled flow boiling, *J. Heat Transfer*, **117**, 990–997, 1995.
- Kandlikar, S. G., Cartwright, M. D., and Mizo, V. R., A photographic study of nucleation characteristics of cavities in flow boiling, in *Convective Flow Boiling, Proceedings of Convective Flow Boiling, an International Conference held at the Banff Center for Conferences*, April 30–May 5, Banff, Alberta, Canada: Taylor and Francis, pp. 73–78, 1995.
- Kandlikar, S. G., Mizo, V. R., Cartwright, M. D., and Ikenze, E., Bubble nucleation and growth characteristics in subcooled flow boiling of water, HTD-Vol. 342, *ASME Proceedings of the 32nd National Heat Transfer Conference*, **4**, pp. 11–18, 1997.
- Kandlikar, S.G., Dhir, V.K., and Shoji, M., *Handbook of Phase Change*, Taylor and Francis, New York, 1999.

- Kandlikar, S. G., Steinke, M. E., Tian, S., and Campbell, L. A., High-speed photographic observation of flow boiling of water in parallel mini-channels, *Paper presented at the ASME National Heat Transfer Conference*, June, ASME, 2001.
- Kandlikar, S. G., Willistein, D. A., and Borrelli, J., Experimental evaluation of pressure drop elements and fabricated nucleation sites for stabilizing flow boiling in microchannels, in *Proceedings of the Third International Conference on Microchannels and Minichannels*, ASME Paper No. ICMM2005-75197, June 13–15, Toronto, Canada, 2005 (Also submitted to Journal of Heat Transfer).
- Kasza, K. E., Didascalou, T., and Wambsganss, M. W., Microscale flow visualization of nucleate boiling in small channels: mechanisms influencing heat transfer, in *Proceedings of the International Conference on Compact Heat Exchanges for the Process Industries*, R. K. Shah (ed.), New York: Begell House, Inc., pp. 343–352, 1997.
- Kennedy, J. E., Roach Jr, G. M., Dowling, Abdel-Khalik, S. I., Ghiaasiaan, S. M., Jeter, S. M., and Quershi, Z. H., The onset of flow instability in uniformly heated horizontal microchannels, *J. Heat Transfer*, **122**(1), 118–125, 2000.
- Kenning, D. B. R. and Cooper, M. G., Flow patterns near nuclei and the initiation of boiling during forced convection Heat Transfer, *Paper presented at the Symposium on Boiling heat Transfer in Steam Generating Units and Heat Exchangers held in Manchester*, September, 15–16, London: IMechE, 1965.
- Kew, P. A. and Cornwell, K., On pressure drop fluctuations during boiling in narrow channels, *2nd European Thermal Sciences and 14th UIT National Heat Transfer Conference*, G. P. Celata, P. Di Marco, and A. Mariani, eds., Edizioni, Pisa, Italy, pp. 1323–1327, 1996.
- Kew, P. A. and Cornwell, K., Correlations for the prediction of boiling heat transfer in small-diameter channels. *App. Therm. Eng.*, **17**(8–10), 705–715, 1997.
- Khodabandeh, R. and Palm, B., Heat transfer coefficient in the vertical narrow channels of the evaporator of an advanced thermosyphon loop, in *Proceedings of the Fourth International Conference on Multiphase Flow*, May 27–June 1, New Orleans: ASME, 2001.
- Kim, J. and Bang, K., Evaporation heat transfer of refrigerant R-22 in small hydraulic-diameter tubes, in *4th Proceedings of International Conference on Multiphase Flow*, Paper no. 869, May 27–June, New Orleans, LA. E. E. Michaelides, Ed., 2001.
- Koizumi, Y., Ohtake, H., and Fujita, Y., Heat transfer and critical heat flux of forced flow boiling in vertical–narrow–annular passages, in *Proceedings of the ASME International Mechanical Engineering Congress and Exposition*, Paper No. HTD-24219, November 11–16, New York, NY: ASME, 2001.
- Koo, J. M., Jiang, L., Zhang, L., Zhou, L., Banerjee, S. S., Kenny, T. W., Santiago, J. G., and Goodson, K. E., Modeling of two-phase microchannel heat sinks for VLSI chips, in *Proceedings of the IEEE 14th International MEMS Conference*, January, Interlaken, Switzerland, IEEE, 2001.
- Kuznetsov, V. V. and Shamirzaev, A. S., Two-phase flow pattern and flow boiling heat transfer in noncircular channel with a small gap, in *Two-phase Flow Modeling and Experimentation*, pp. 249–253, 1999.
- Kuznetsov, V. V. and Vitovsky, O. V., Flow pattern of two-phase flow in vertical annuli and rectangular channel with narrow gap, in *Two-Phase Flow Modelling and Experimentation 1995*, G. P. Celata and R. K. Shah eds., Edizioni, Pisa, Italy, 1995.
- Kuznetsov, V. V., Dimov, S. V., Houghton, P. A., Shamirzaev, A. S., and Sunder, S., Upflow boiling and condensation in rectangular minichannels, in *Proceedings of the First International Conference on Microchannels and Minichannels*, Paper No. ICMM2003-1087, April 24–25, Rochester, New York, USA: ASME Publications, 2003.

- Lakshminarasimhan, M. S., Hollingsworth, D. K., and Witte, L. C., Boiling Incipience in Narrow Channels, HTD-Vol. 366-4, in *Proceedings of the ASME Heat Transfer Division 2000*, Vol. 4, ASME IMECE 2000, pp. 55–63, 2000.
- Lazarek, G. M. and Black, S. H., Evaporative heat transfer, pressure drop and critical heat flux in a small diameter vertical tube with R-113, *Int. J. of Heat and Mass Transfer*, **25**(7), 945–960, 1982.
- Lee, H. J. and Lee, S. Y., Pressure drop correlations for two-phase flow within horizontal rectangular channels with small heights, *Int. J. Multiphase Flow*, **27**, 783–796, 2001a.
- Lee, H. J. and Lee, S. Y., Pressure drop and heat transfer characteristics of flow boiling in small rectangular horizontal channels, in *proceedings of the International Conference on Multiphase Flow*, ASME Fluid Mechanics Division, New Orleans, LA, 2001b.
- Lee, H. J. and Lee, S. Y., Heat transfer correlation for boiling flows in small rectangular horizontal channels with low aspect ratios, *Int. J. Multiphase Flow* **27**, 823–827, 2043–2062, 2001e.
- Lee, P. C., Li, H. Y., Tseng, F. G., and Pan, C., Nucleate boiling heat transfer in silicon-based microchannels, in *Proceedings of ASME Summer Heat Transfer Conference, Paper No. HT2003-47220* July 21–23, Las Vegas, USA: ASME Publications, 2003.
- Lee, S. and Kim, G., Analysis of flow resistance inside microchannels with different inlet configurations using micro-PIV System, ASME Paper No. ICMM2003-1108, in *Proceedings of the First International Conference on Microchannels and Minichannels*, April 24–25, Rochester, New York, USA, pp. 823–827, 2003.
- Lee, P. S. and Garimella, S. V., Experimental investigation of heat transfer in microchannels. In *Proceedings of ASME Summer Heat Transfer Conference, Paper No. HT2003-47293*. July 21–23, Las Vegas, USA: ASME Publications, 2003.
- Lin, S., Kew, P. A., and Cornwell, K., Two-phase flow regimes and heat transfer in small tubes and channels, in *Heat Transfer 1998, Proceedings of 11th International Heat Transfer Conference*, Vol. 2, Kyongju, Korea, pp. 45–50, 1998.
- Lin, S., Kew, P. A., and Cornwell, K., Two-phase evaporation in a 1 mm diameter tube, in *Proceedings of the 6th UK Heat Transfer Conference in Edinburgh*, September, 1999.
- Lin, S., Kew, A., and Cornwell, K., Flow boiling of refrigerant R141B in small tubes, in *Chemical Engineering Research and Design*, **79**(4), May, pp. 417–424, 2001.
- Mertz, R., Wein, A., and Groll, M., Experimental investigation of flow boiling heat transfer in narrow channels, *Calore Technol.*, **14**(2), 47–54, 1996.
- Mishima, K. and Hibiki, T., Some characteristics of air–water two-phase flow in small diameter vertical tubes, *Int. J. Multiphase Flow*, **22**(4), 703–712, 1996.
- Molki, M., Mahendra, P., and Vengala, V. Flow boiling of R-134A in minichannels with transverse ribs. in *Proceedings of the First International Conference on Microchannels and Minichannels Paper no. ICMM2003-1074* April 24–25, Rochester, New York, USA. ASME Publications, 2003.
- Moriyama, K. and Inoue, A., The thermodynamic characteristics of two-phase flow in extremely narrow channels (the frictional pressure drop and heat transfer of boiling two-phase flow, analytical model), *Heat Transfer Jpn. Res.*, **21**(8), 838–856, 1992.
- Mukherjee, A. and Kandlikar, S. G., Numerical study of growth of a vapor bubble during flow boiling of water in a microchannel, ASME Paper No. ICMM 2004-2382, in *Proceedings of the Second International Conference on Microchannels and Minichannels 2004*, Rochester, New York, pp. 565–572, 2004.
- Mukherjee, A. and Kandlikar, S. G., Numerical study of the effect of inlet constriction on flow boiling stability in microchannels, ASME Paper No. ICMM2005-75143, in *Proceedings of the Third International Conference on Microchannels and Minichannels*, June 13–15, Toronto, Canada, 2005.

- Mudawar, I. and Bowers, M. B., Ultra-high critical heat flux (CHF) for subcooled water flow boiling-I: CHF data and parametric effects for small diameter tubes, *Int. J. Heat Mass Transfer*, **42**, 1405–1428, 1999.
- Park, K. S., Choo, W. H., and Bang K.H., Flow boiling heat transfer of R-22 in small-diameter horizontal round tubes. in *Proceedings of the First International Conference on Microchannels and Minichannels, Paper no.ICMM2003-1073* April 24–25, Rochester, New York, USA: ASME Publications, 2003.
- Peles, Y., Two-phase boiling flow in microchannels – instabilities issues and flow regime mapping, in *Proceeding of the First International Conference on Microchannels and Minichannels, ASME Paper No. 2003-1069*, April 24–25, Rochester, New York, pp. 559–566, 2003.
- Peles, Y., Yarin, L. P., and Hetsroni, G., Steady and unsteady flow in a heated capillary, *Int. J. Multiphase Flow*, **27(4)**, 577–598, 2001.
- Peng, X. F. and Wang, B. X., Forced convection and boiling characteristics in microchannels, in *Heat Transfer 1998, Proceedings of 11th IHTC*, Vol. 1 August 23–28, Kyongju, Korea, pp. 371–390, 1998.
- Peng, X. F., Peterson, G. P., and Wang, B. X., Heat transfer characteristics of water flowing through microchannels. *Exp. Heat Transfer*, **7(4)**, pp. 265–283, 1994.
- Pokharna, H., Masahiro, K., DiStefanio, E., Mongia, R., Barry, J., Crowley, Chen, W., and Izenzon, M., Microchannel cooling in computing platforms: performance needs and challenges in implementation, Keynote Paper, ASME Paper No. ICMM2004-2325, in *Proceedings of the Second International Conference on Microchannels and Minichannels*, June 17–19, Rochester, New York, pp. 109–118, 2004.
- Qu, W. and Mudawar, I., Prediction and measurement of incipient boiling heat flux in micro-channel heat sinks, *Int. J. Heat Mass Transfer*, **45**, 3933–3945, 2002.
- Qu, W. and Mudawar, I., Measurement and correlation of critical heat flux in two-phase micro-channel heat sinks, *Int. J. Heat Mass Transfer*, **47**, 2045–2059, 2004.
- Qu, W. and Mudawar, I., Flow boiling heat transfer in two-phase micro-channel heat sinks Part-I. Experimental investigation and assessment of correlation methods, *Int. J. Heat Mass Transfer*, **46**, 2755–2771, 2003.
- Ravigururajan, T. S., Cuta, J., McDonald, C. E., and Drost, M. K., Effects of heat flux on two-phase flow characteristics of refrigerant flows in a micro-channel heat exchanger, HTD-Vol. 329, in *Proceedings of the National Heat Transfer Conference*, Vol. 7, ASME, pp. 167–178, 1996.
- Ravigururajan, T. S., Impact of channel geometry on two-phase flow heat transfer characteristics of refrigerants in microchannel heat exchangers. *J. Heat Transfer* **120**, 485–491, 1998.
- Roach, G. M., Abdel-Khalik, S. I., Ghiaasiaan, S. M., Dowling, M. F., and Jeter, S. M., Low-flow critical heat flux in heated microchannels, *Nucl. Sci Eng.*, **131**, 411–425, 1999.
- Sato, T. and Matsumura, H., On the condition of incipient subcooled boiling with forced convection, *Bull. JSME*, **7(26)**, 392–398, 1964.
- Serizawa, A. and Feng, Z. P., Two-phase flow in microchannels, in *Proceedings of the Fourth International Conference on Multiphase Flow*, May 27–June 1 New Orleans: ASME, 2001.
- Steinke, M. E. and Kandlikar, S. G., An experimental investigation of flow boiling characteristics of water in parallel microchannels, *J. Heat Transfer*, **126(4)**, 518–526, 2004.
- Stoddard, R. M., Blasick, A. M., Ghiaasiaan, S. M., Abdel-Khalik, S. I., Jeter, S. M., and Dowling, M. F., Onset of flow instability and critical heat flux in thin horizontal annuli, *Exp. Thermal Fluid Sci.*, **26**, 1–14, 2002.
- Tong, W., Bergles, A. E., and Jensen, M. K., Pressure drop with highly subcooled flow boiling in small-diameter tubes, *Exp. Thermal Fluid Sci.* 1997, Elsevier Science Inc., **15**, 202–212, 1997.
- Tran, T. N., Wambsganss, M. W., and France, D. M., Small circular- and rectangular-channel boiling with two refrigerants, *Int. J. Multiphase Flow*, **22(3)**, 485–498, 1996.

- Wambsganss, M. W., France, D. M., Jendrzeczyk, J. A., and Tran, T. N., Boiling heat transfer in a horizontal small-diameter tube, *J. Heat Transfer*, **115**(4), 963–972, 1993.
- Warrier, G. R., Pan, T., and Dhir, V. K., Heat transfer and pressure drop in narrow rectangular channels, in *Proceedings of the Fourth International Conference on Multiphase Flow*, May 27–June 1, New Orleans: ASME, 2001.
- Warrier, G. R., Pan, T., and Dhir, V. K., 2002, Heat transfer and pressure drop in narrow rectangular channels, *Exp. Thermal Fluid Sci.*, **26**, 53–64, 2002.
- Wu, H. Y. and Cheng, P., Liquid/two-phase/vapor alternating flow during boiling in microchannels at high heat flux. *Int. Communi. Heat Mass Transfer* **30**(3), 295–302, 2003.
- Yan, Y. and Lin, T., Evaporation heat transfer and pressure drop of refrigerant R-134a in a small pipe, *Int. J. heat Mass Transfer*, **42**, 4183–4194, 1998.
- Yen, T. H., Kasagi, N., and Suzuki, Y., Forced convective boiling heat transfer in microtubes at low mass and heat fluxes, in *Symposium on Compact Heat Exchangers on the 60th Birthday of Ramesh K. Shah*, August 24, Grenoble France, pp. 401–406, 2002.
- Yu, W., France, D. M., Wambsganss, M. W., and Hull, J. R., Two-phase pressure drop, boiling heat transfer, and critical heat flux to water in a small-diameter horizontal tube. *Int. J. Multiphase Flow* **28**, 927–941, 2002.
- Zhang, L., Koo, J.- M., Jiang, L., and Asheghi. M., Measurements and modeling of two-phase flow in microchannels with nearly constant heat flux boundary conditions, *J. Microelectromech. Syst.*, **11**(1), 12–19, 2002.

Chapter 6

CONDENSATION IN MINICHANNELS AND MICROCHANNELS

Srinivas Garimella

George W. Woodruff School of Mechanical Engineering, Georgia Institute of Technology, Atlanta, GA, USA

6.1. Introduction

6.1.1. Microchannel applications

Microchannels are increasingly being used in industry to yield compact geometries for heat transfer in a wide variety of applications. Considerable literature exists on single-phase flow, pressure drop, and heat transfer in such channels, as has been documented elsewhere in this book and can be seen in some recent reviews of the literature (Sobhan and Garimella, 2001; Garimella and Sobhan, 2003; Garimella and Singhal, 2004; Liu and Garimella, 2004). Similarly, boiling and evaporation in microchannels have also been studied due to the electronics cooling industry's need to remove high heat fluxes through vaporization from compact devices that must be maintained at relatively low temperatures while being not readily accessible or conducive to the installation of large and complex cooling systems. In addition to high heat flux applications like electronics cooling, microchannels have also seen increasing use for the purpose of reducing inventories of hazardous fluids in components and for reducing material consumption for component fabrication. Ultimately, in these applications, microchannels are viewed as being responsible for the mitigation of ozone depletion by enabling the use of smaller amounts of environmentally harmful fluids, and also reducing greenhouse gas emissions by improving component and system energy efficiencies. Utilization in micro-sensors and micro-actuators, and in biological diagnostic devices are other candidate applications.

The art of the utilization of microchannels for achieving high heat transfer rates is in fact much farther ahead than the science of obtaining a comprehensive understanding of phase change in these channels. For example, the large heat transfer coefficients in microchannels, and the large surface area-to-volume ratios they offer, has led to their use in compact

E-mail: sgarimella@me.gatech.edu

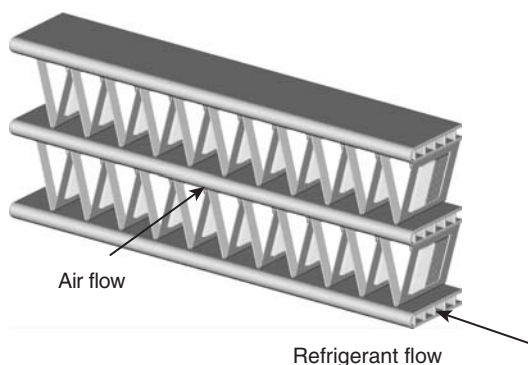


Fig. 6.1. Schematic of a microchannel tube, multilouver fin condenser.

condensers for the air-conditioning systems in automobiles for many years. These condensers consist of rectangular tubes with multiple parallel microchannels (Fig. 6.1) cooled by air flowing across multilouver fins. The microchannels used in these condenser designs typically have hydraulic diameters in the 0.4–0.7 mm range, although an understanding of the fundamental phase-change phenomena in these heat exchangers is just beginning to emerge. Garimella and Wicht (1995) demonstrated that substantial reductions in condenser sizes can be achieved for small (~ 18 kW) condensers for ammonia–water absorption space-conditioning systems for residential application by using microchannel condensers instead of conventional round-tube, flat-fin designs. This compactness was attributed to large condensation heat transfer coefficients, high surface-to-volume ratios, and reduced air-side pressure drops due to the use of multilouver fins. Noting the potential enhancements due to the use of microchannels, Webb and Ermis (2001) investigated condensation of R134a in extruded aluminum tubes with multiple parallel microchannels with and without microfins, and with hydraulic diameter $0.44 < D_h < 1.564$ mm. Their work documented that heat transfer coefficients and pressure gradients increase with decreasing hydraulic diameter. Webb and Lee (2001) investigated the use of these microchannel condensers as replacements for 2-row, round-tube condensers with 7-mm diameter tubes. They noted material cost reductions of up to 55% over the conventional geometries due to a combination of air-side and tube-side improvements. Other advantages such as air-side pressure drop (in part, due to form drag reduction over flat tubes) and material weight reduction were also noted due the use of microchannel condensers, depending on the specific tube and fin geometry parameters. Jiang and Garimella (2001) demonstrated the implementation of microchannel tubes for residential air-conditioning systems. They compared conventional round-tube, flat-fin geometries to systems with air-coupled microchannel evaporators and condensers as well as systems that coupled refrigerant heat exchange to intermediate glycol–water solution loops. Their work showed that indoor and outdoor units of air-coupled microchannel systems can be packaged in only one-half and one-third the space required for a conventional system, respectively. Furthermore, they showed that significant additional compactness can be achieved through hydronic coupling, because of the high heat transfer coefficients on both sides of the liquid-coupled heat exchangers, and the counterflow orientation, which is more suitable in the presence of a temperature glide.

It was also shown that the refrigerant charge of the microchannel air-coupled system is 20% less than that of the round-tube heat pump. For the hydronically coupled system, the refrigerant charge is only 10% of the charge in the round-tube heat pump, yielding significant benefits pertaining to the reduction of the environmental impact of air-conditioning systems. These representative studies clearly demonstrate the wide-ranging benefits that can be obtained by the use of microchannels in phase-change applications.

6.1.2. Microchannel phenomena

Researchers have discussed the term “microchannel” at some length in the literature and elsewhere in this book. One extreme of the size range (sub-micron size channels) is where continuum phenomena do not apply, and properties such as viscosity, ice point, and others change due to molecular and electrokinetic forces, but not much information is available for that size range, and there are few practical phase-change applications at that range. However, such non-continuum phenomena do not have to be present for there to be differences in flow and heat transfer phenomena from conventional, larger diameter channels. One simple way of looking at microchannels is the existence of deviations in pressure gradients and heat transfer coefficients from widely available models, which is sufficient to warrant studies that understand and account for the different flow phenomena. In boiling applications, for example, the microchannel designation may be applied when the channel size approaches the bubble departure diameter, which would lead to differences from macrochannel phenomena. Essentially, when channel size affects flow, pressure gradients and heat transfer in a manner that are not accounted for by models developed for the larger channels, it warrants a different treatment. Thus, microchannel phase change differs from its counterpart in macrochannels due to differences in the relative influences of gravity (whose effects are less prominent at small scales), shear, and surface tension, the latter playing a dominant role. The microchannel behavior, therefore, depends on phenomena that do not exist or are not prominent at the larger scales, or phenomena that are suppressed at the small scales. As these phenomena would depend on the liquid and vapor phase properties of the fluid under consideration, a rigorous definition of the term microchannel would necessarily depend on the fluid in question. Serizawa *et al.* (2002), who conducted air–water and steam–water flow visualization studies in 50- μm channels, recommend the Laplace constant $L > D_h$ (also referred to as the capillary length scale) as the criterion for determining whether a channel should be considered to be a microchannel:

$$L = \sqrt{\frac{\sigma}{g(\rho_l - \rho_v)}} \quad (6.1)$$

The Laplace constant represents the ratio of surface tension and gravity forces, and has been interpreted as the dimension at which influence of surface tension becomes more important than the stratifying effect of gravity (Fukano and Kariyasaki, 1993). This criterion implies that for a high surface tension fluid pair like air–water at standard temperature and pressure, a channel with $D_h < 2.7$ mm would be a microchannel, while for R-134a at 1500 kPa, the corresponding value is $D_h < 0.66$ mm. Another interpretation of a different form of this same quantity is provided in terms of the confinement of bubbles in channels (Kew

and Cornwell, 1997). Thus, typically, microchannel two-phase flows are characterized by “confined” single elongated bubbles occupying much of the channel (as will be discussed at length in a subsequent section), whereas multiple bubbles may occupy the cross-section in macrochannels. Also, typical bubble sizes decrease as the pressure increases, affecting how the channel may be viewed in relation to the bubble size. Based on this interpretation, Kew and Cornwell (1997) recommend the use of the confinement number ($Co > 0.5$) as the transition criterion (for boiling applications) beyond which microchannel effects are present:

$$Co = \frac{\sqrt{\sigma/(g(\rho_l - \rho_v))}}{D_h} \quad (6.2)$$

Thus, $Co = L/D_h$, and the transition D_h value is 1.32 mm, that is double the value recommended by Serizawa *et al.* (2002). However, the practical value of such a categorization is somewhat limited – even a change in operating temperature would affect whether the channel should be treated as a microchannel through the influence of temperature on surface tension. What is more important is to recognize and account for the respective flow phenomena in the development of pressure drop and heat transfer models. For example, substantial differences due to channel size have been documented by several researchers at hydraulic diameters of a few millimeters, as noted by Palm (2001).

It is also clear that the increase in surface area associated with the use of microchannels increases the importance of surface forces over that of body forces, as noted by Serizawa and Feng (2004). Thus, surface phenomena, and in some cases, surface characteristics, become more prominent in these small channels, and the interactions between the fluid and wall increase in importance. This is another rationale for the commonly noted observation that in microchannels, surface tension and viscous forces dominate over gravitational forces. As will also become clear in the following sections, neither the same measurement techniques nor the same modeling approaches used for the larger scale channels are adequate for addressing these phenomena that are specific to microchannels.

6.1.3. Chapter organization and contents

The focus of this chapter is condensation in microchannels. Compared to single-phase flow and boiling in such channels, condensation has received less attention. Part of this is because researchers have concentrated primarily on the removal of heat from small and inaccessible surfaces such as high-flux electronics components, using single-phase and boiling processes. Condensation has thus far been generally coupled with air: the dominant air-side resistance in such situations may be one reason for the relatively smaller attention to condensation. However, liquid coupling, condensation in heat pipes, fluid charge minimization, and other factors are making this process more prominent. The heat *removed* from the sources must also be *rejected*, requiring innovative compact designs and a better understanding of condensation in microchannels.

This chapter presents the available information in an emerging field for which directly relevant literature is limited; therefore, it is by no means a comprehensive treatment of all aspects of condensation in microchannels. The chapter is written with the primary

application of refrigerant condensation and condensers as the basis, but can be extended as necessary to other related applications. Heat transfer coefficients and pressure drops for condensation inside microchannels are strongly dependent on the different flow patterns that are established as the fluid undergoes a transition from vapor to liquid. Methods to predict flow regimes as a function of flow-related parameters such as mass flux, quality, and fluid properties are therefore presented first. Where possible, the differences between the flow patterns in large channels and microchannels are discussed. This is followed by a brief discussion of void fraction in condensing flows. The void fraction is almost invariably required for the modeling of pressure drop and heat transfer in two-phase flow. (Once again, it is noted that void fractions in microchannels have proved to be difficult to measure due to issues such as optical access, and the dynamic and sometimes indeterminate nature of the vapor–liquid interface.) Models for the prediction of pressure drops in the different flow regimes are then presented along with a comparison of the predicted pressure drops from the different models. This is followed by a presentation of the corresponding models for condensation heat transfer in microchannels. Finally, areas of critical research needs for furthering the understanding of condensation in microchannels are pointed out. At the time of this writing, there is ongoing research in this field at several laboratories around the world, and the information presented here will no doubt need to be updated on a continuous basis.

6.2. Flow regimes

The first step in understanding condensation in microchannels is the characterization of how the condensing fluid flows through the channels, because this forms the basis for the associated pressure drop and heat transfer. As the fluid condenses in the channel and progresses from the vapor phase toward the liquid phase over a range of qualities, different flow patterns are established at different regions of the condenser. The progression of flow regimes, and in particular, the transitions between the different flow mechanisms, is different in microchannels than those in larger diameter tubes, primarily due to differences in relative magnitudes of gravity, shear, viscous, and surface tension forces. Similar differences exist between flow regimes and transitions in circular and non-circular microchannels. Therefore, extrapolation of large round-tube correlations to smaller diameters and non-circular geometries could introduce errors into pressure drop and heat transfer predictions. Also, the design of optimal condensers often requires the provision of varying tube-side flow area. If a constant tube-side cross-sectional area is provided, the high velocities in the initial portion of the condenser would result in excessive pressure drops with a corresponding decrease in saturation temperature and driving temperature difference, while the low velocities toward the end of the condenser would result in very low heat transfer coefficients. A gradually decreasing flow cross-section through the use of varying numbers of tubes per pass is therefore desirable for optimal condenser design. The selection of tube sizes and pass arrangements for a given application would require not just an average condensation coefficient, but rather an understanding of the variation in heat transfer coefficient and pressure drop with quality, phase velocities, and flow patterns.

Unfortunately, the bulk of the literature on two-phase flow regimes is on adiabatic flows, in which air–water, nitrogen–water, and air–oil mixtures, typically in the absence of heat

transfer, are used to simulate condensing flows. The obvious reason for this approach is the substantial simplification in experimental facilities that it offers. Thus, the requisite vapor–liquid “quality” can simply be “dialed in” by independently controlling the air and liquid flow rates entering the test section, whereas this must be achieved indirectly though upstream and downstream conditioning of a condensing fluid through pre- and post-heating/cooling, as appropriate. In addition, experiments on refrigerants require closed loops, whereas a nitrogen–water or air–water experiment can be conducted in a once-through manner, with the exiting fluid streams simply being exhausted and drained. Finally, several fluids (most refrigerants), at condensing temperatures of interest, are at pressures much higher than atmospheric, which presents challenges in providing optical access during the condensation process. On the other hand, air–water experiments are typically conducted at or near atmospheric pressure.

The properties of the air–water fluid pair are significantly different from those of refrigerant vapor–liquid mixtures; therefore, application of the results from air–water studies and extrapolation to condensing flows must be done with appropriate caution. Also, the absence of the heat of condensation during air–water experiments must be recognized while applying these studies to condensation in microchannels. Nevertheless, due to the preponderance of adiabatic air–water studies in the literature, and the relative scarcity of condensation studies, a discussion of the significant studies on adiabatic two-phase flow is provided here first, followed by studies on condensation (Table 6.1).

6.2.1. Adiabatic flow

6.2.1.1. Conventional tubes

Early attempts at flow regime mapping were conducted on relatively large tubes using air–water or air–oil mixtures (Alves, 1954; Baker, 1954; Govier and Omer, 1962). Alves (1954) recognized several different flow patterns for air–water and air–oil flows corresponding to different gas and liquid superficial velocities in a 25.4-mm tube. Through comparisons of pressure drop data with the Lockhart–Martinelli (1949) correlation, he suggested that it was necessary to take flow regimes into account while computing two-phase pressure drops. Baker (1954) developed a flow regime map with flow pattern transitions based on functions of the mass flux of the gas phase and the liquid-to-gas ratio. Flow patterns such as bubble, plug, stratified, wavy, slug, annular, and spray were observed for oil and gas flow in 25.4–102-mm tubes, and combined with the data of Jenkins (1947), Alves (1954), and others to develop the map. He found that pressure drops for the large pipes (>200 mm) were 40–60% less than those predicted by the Lockhart–Martinelli (1949) correlation. He also found that the onset of slug flow occurred at lower values of the Lockhart–Martinelli parameter, X , in the larger pipes, and that the pipe diameter affects the two-phase multiplier. Thus, the influence of pipe diameter on flow patterns has been acknowledged for quite some time. The importance of tube diameter was also recognized and quantified by Govier *et al.* (1957) and Govier and Short (1958), particularly for upward flow of air–water mixtures, even though their work was limited to a relatively larger diameter range (16.00–63.50 mm). Mandhane *et al.* (1974) tested the available flow maps with data representing a wide range of flow conditions for pipe diameters ranging from 12.7 to 165.1 mm. They

Table 6.1

Summary of flow regime studies.

Investigators	Hydraulic diameter	Fluids	Orientation/ conditions	Range/ applicability	Techniques, basis, observations
Adiabatic flow: conventional tubes					
Taitel and Dukler (1976)		Air–water			<ul style="list-style-type: none"> Devised theoretical approach to flow regime mapping using a momentum balance on a stratified flow pattern
Mandhane <i>et al.</i> (1974)	12.7–165.1 mm	Air–water	Horizontal	$0.043 < j_G < 170.7 \text{ m/s}$ $0 < j_L < 7.315 \text{ m/s}$	<ul style="list-style-type: none"> “Best fit” map from available flow regime maps Introduced physical property corrections
Adiabatic flow: small circular channels					
Suo and Griffith (1964)	1–6 mm	Air–water	Horizontal adiabatic	$\rho_l/\rho_g \gg 1$ $\mu_l/\mu_g > 25$	<ul style="list-style-type: none"> Transition from elongated bubble to annular and bubbly flow Criterion to determine when buoyancy effects can be neglected
Barnea <i>et al.</i> (1983)	4–12 mm	Air–water	Horizontal	$T = 25^\circ\text{C}$ $P_{\text{exit}} = 1 \text{ atm}$ $0.001 < j_L < 10 \text{ m/s}$ $0.01 < j_G < 100 \text{ m/s}$	<ul style="list-style-type: none"> Recommended Taitel and Dukler (1976) model for all transitions except stratified to non-stratified Modified stratified-to-intermittent transition boundary of Taitel and Dukler (1976)
Damianides and Westwater (1988)	1–5 mm	Air–water	Horizontal	$P \sim 5 \text{ atm}$ $T \sim 15\text{--}20^\circ\text{C}$ $0.001 < j_L < 10 \text{ m/s}$ $0.01 < j_G < 100 \text{ m/s}$	<ul style="list-style-type: none"> Documented effect of hydraulic diameter Some agreement for 5 mm with Taitel and Dukler (1976), but poor agreement for 1 mm 1-mm tube showed large intermittent flow region Increasingly small stratified flow region in small diameter tubes
Fukano <i>et al.</i> (1989)	1–4.9 mm	Air–water	Horizontal adiabatic	$P_{\text{exit}} = 1 \text{ atm}$ $0.04 < j_G < 40 \text{ m/s}$ $0.2 < j_L < 4 \text{ m/s}$	<ul style="list-style-type: none"> Results agreed with Barnea <i>et al.</i> (1983) but not with Damianides and Westwater (1988) Mandhane <i>et al.</i> (1974) cannot predict transitions in small tubes Taitel and Dukler (1976) and Weisman <i>et al.</i> (1979) not reliable for small diameters
Brauner and Maron (1992)	4–25.2 mm	Air–water	Horizontal	$0.01 < j_G < 40 \text{ m/s}$ $0.001 < j_L < 0.3 \text{ m/s}$	<ul style="list-style-type: none"> Incorporated the stabilizing effect of surface tension associated with practically finite wavelengths Transition criteria based on Eotvos number

(Continued)

Table 6.1
(Continued)

Investigators	Hydraulic diameter	Fluids	Orientation/ conditions	Range/ applicability	Techniques, basis, observations
Ide <i>et al.</i> (1995)	0.5–6 mm	Air–water	Vertical upwards		<ul style="list-style-type: none"> • Studied “liquid lumps” formed in vertically upward flow • Velocity characteristics of liquid lumps used to interpret flow pattern with corresponding maps by Fukano <i>et al.</i> (1989)
Mishima and co-workers (Mishima and Hibiki, 1996; Mishima <i>et al.</i> , 1997; Mishima and Hibiki, 1998)	1–4 mm	Air–Water	Vertical upwards	$0.0896 < j_G < 79.3 \text{ m/s}$ $0.0116 < j_L < 1.67 \text{ m/s}$	<ul style="list-style-type: none"> • Neutron radiography for flow visualization and void fractions • Recommended transition criteria of Mishima and Ishii (1984)
Coleman and Garimella (1999)	5.5-, 2.6-, 1.75-, 1.3-mm circular $D_h = 5.36 \text{ mm}$ ($\alpha = 0.725$) rectangular	Air–water	Horizontal	$0.1 < j_G < 100 \text{ m/s}$ $0.01 < j_L < 10 \text{ m/s}$	<ul style="list-style-type: none"> • Diameter has significant effect on flow regime transitions • Intermittent flow regime increases in small diameter tubes • Comparisons with the criteria of Damianides and Westwater (1988), Fukano <i>et al.</i> (1989) and Weisman <i>et al.</i> (1979)
Triplett <i>et al.</i> (1999b)	1.1- and 1.45-mm circular; semi-triangular 1.09 and 1.49 mm	Air–water	Horizontal adiabatic	$0.02 < j_G < 80 \text{ m/s}$ $0.02 < j_L < 8 \text{ m/s}$	<ul style="list-style-type: none"> • Observed bubbly, churn, slug, slug-annular and annular flow • No stratified flow • Maps agreed with Damianides and Westwater (1988), Fukano <i>et al.</i> (1989) and Fukano and Kariyasaki (1993) • Poor agreement with analytically derived criteria (Suo and Griffith, 1964; Taitel and Dukler, 1976)
Zhao and Bi (2001a)	Triangular channels $D_h = 2.886, 1.443,$ and 0.866 mm	Air–water	Vertical upward	$0.1 < j_G < 100 \text{ m/s};$ For $D_h = 2.886, 1.443$ $0.08 < j_L < 6 \text{ m/s}$ For $D_h = 0.866$ $0.1 < j_L < 10 \text{ m/s}$	<ul style="list-style-type: none"> • Dispersed bubbly flow not observed in smallest channel, but capillary bubble flow pattern seen • Trends agreed well with several investigators (Barnea <i>et al.</i>, 1983; Galbiati and Andreini, 1992a; Mishima and Hibiki, 1996; Ide <i>et al.</i>, 1997), but not with Taitel and Dukler (1976) and Mishima and Ishii (1984)
Yang and Shieh (2001)	1, 2, and 3 mm	Air–water	Horizontal adiabatic	$T = 25\text{--}30^\circ\text{C}$ $0.016 < j_G < 91.5 \text{ m/s}$ $0.006 < j_L < 2.1 \text{ m/s}$	<ul style="list-style-type: none"> • Transitions difficult to distinguish for air–water, but clear for R-134a • Lower σ of R-134a compared to air–water led to differences • R-134a transitions agreed with Hashizume (1983) and Wang <i>et al.</i> (1997a)
		R-134a		$300 < G < 1600 \text{ kg/m}^2\text{-s}$ $T = 30^\circ\text{C}$	

Tabatabai and Faghri (2001)	4.8–15.88-mm condensation 12.3–1-mm air–water	Water R-12 R-113 R-22 R-134a	Horizontal		<ul style="list-style-type: none"> Flow regime maps based on relative effects of surface tension, shear, and buoyancy forces Better agreement with available data in shear-dominated regions Predicts movement of boundaries with channel size
Adiabatic flow: narrow, high-aspect ratio, rectangular channels					
Troniewski and Ulbrich (1984)	Rectangular $0.09 < \alpha < 10.10$ $7.45 < D_h < 13.1$	Air–water	Horizontal	$T = 25\text{--}35^\circ\text{C}$ $0.6 < j_G < 43 \text{ m/s}$ $200 < j_L < 1600 \text{ m/s}$ $T = 25\text{--}35^\circ\text{C}$ $0.7 < \mu_L < 40 \times 10^{-3} \text{ Pa s}$ $995 < \rho_L < 1150 \text{ kg/m}^3$	<ul style="list-style-type: none"> Corrections to axes of Baker (1954) map based on single-phase velocity profiles
Wambsganss <i>et al.</i> (1991; 1994)	Rectangular $\alpha = 6, 0.167$ $D_h = 5.44 \text{ mm}$	Air–water	Horizontal adiabatic	$0.0001 < x < 1$ $50 < G < 2000 \text{ kg/m}^2\text{-s}$	<ul style="list-style-type: none"> Flow visualization and dynamic pressure measurements Qualitative agreement with large circular channels but quantitative differences Transition criteria for bubble or plug flow to slug flow based on root-mean-square pressure changes
Xu and co-workers (Xu, 1999; Xu <i>et al.</i> , 1999)	Rectangular gap = 0.3, 0.6, and 1 mm	Air–water	Vertical adiabatic	$P_{\text{exit}} = 1 \text{ atm}$ $0.01 < j_G < 10 \text{ m/s}$ $0.01 < j_L < 10 \text{ m/s}$	<ul style="list-style-type: none"> Bubbly, slug, churn, and annular flow in 0.6- and 1-mm channels Bubbly flow absent in 0.3-mm channel Extended criteria of Mishima and Ishii (1984) for application to narrow rectangular geometry
Hibiki and Mishima (2001)	Rectangular channels with gap 0.3–17 mm	Air–water, steam–water	Vertical upward	Air–water data (from Sadatomi <i>et al.</i> , 1982; Lowry and Kawaji, 1988; Ali <i>et al.</i> , 1993; Mishima <i>et al.</i> , 1993; Wilmarth and Ishii, 1994; Xu, 1999) Steam–water data (from Hosler, 1968)	<ul style="list-style-type: none"> Criteria specifically for narrow rectangular channels based on Mishima and Ishii (1984) criteria Collision/coalescence of bubbles increase when maximum distance between bubbles < projected bubble diameter

(Continued)

Table 6.1
(Continued)

Investigators	Hydraulic diameter	Fluids	Orientation/ conditions	Range/ applicability	Techniques, basis, observations
Adiabatic flow: microgravity					
Rezkallah <i>et al.</i> (Rezkallah, 1995; Rezkallah and Zhao, 1995; Lowe and Rezkallah, 1999)	9.525 mm	Air–water Air–glycerin/ water	Microgravity	$0.09 < j_G < 30$ m/s $0.015 < j_L < 3.5$ m/s $0.6 < j_G < 12$ m/s $0.7 < j_L < 2$ m/s	<ul style="list-style-type: none"> • Slug at μg different from “Taylor bubble” profile seen at 1-g • Annular flow regime similar to 1-g • Little effect of μ_L on transitions • Later verified and modified based on 6–40-mm tubes
Adiabatic flow: $D \ll 1$ mm					
Kawahara <i>et al.</i> (2002)	100 μm	Nitrogen–water	Horizontal	$0.1 < j_G < 60$ m/s $0.02 < j_L < 4$ m/s	<ul style="list-style-type: none"> • Low Re at small D_h implies greater effects of wall shear and surface tension • Observed liquid slug, gas core with smooth-thin liquid film, gas core with smooth-thick liquid film, gas core with ring-shaped liquid film, and gas core with deformed interface • No gravitational effects, absence of bubbly flow (no bubble breakup due to absence of liquid phase turbulence at low Re) • Flow conditions determine likely, but not unique patterns • Map based on probability of occurrence of patterns • Four flow regimes (slug-ring, ring-slug, semi-annular, and multiple), which are combinations of flow mechanisms
Chung and Kawaji (2004)	530, 250, 100, and 50 μm	Nitrogen–water	Horizontal	$0.02 < j_G < 73$ m/s $0.01 < j_L < 5.77$ m/s	<ul style="list-style-type: none"> • Extended work of Kawahara <i>et al.</i> (2002) for effect of diameter • 530- and 250-μm flow similar to ~ 1-mm flow • Slug flow in small channels; absence of bubbly, churn, slug-annular, and annular flow
Chung <i>et al.</i> (2004)	96- μm square 100- μm circular	Nitrogen–water	Horizontal	Circular data (from Chung and Kawaji, 2004)	<ul style="list-style-type: none"> • Negligible effect of channel shape
Serizawa <i>et al.</i> (2002)	20-, 25-, and 100- μm circular	Air–water, steam (only 50 μm)	Horizontal	$0.0012 < j_G < 295.3$ m/s $0.003 < j_L < 17.52$ m/s	<ul style="list-style-type: none"> • Results different from other investigators of $D \ll 1$-mm channels • Numerous terms to define flow patterns • Bubbly flow in 25-μm channel

Condensing flow

Traviss and Rohsenow (1973)	8 mm	R-12	Horizontal condensing	$100 < G < 990 \text{ kg/m}^2\text{-s}$ $10 < T < 40.6^\circ\text{C}$	<ul style="list-style-type: none"> • High capillary pressure at small bubble interface keeps bubble spherical and prevents coalescence • Slug flow due to entrance phenomenon, not bubble coalescence • Liquid ring flow due to rupture of liquid bridges between bubbles at high gas velocities • Surface tension prevents liquid slugs from spreading as film, leads to dry patches, liquid “lumps” • State that air–water and steam–water patterns in 25-μm channel similar; photographs presented seem dissimilar • Surprisingly state that flow map agrees with large channel Mandhane <i>et al.</i> (1974) map, but graphs indicate otherwise
Breber <i>et al.</i> (1980)	4.8–50.8 mm	R-11, R-12, R-113, steam, <i>n</i> -pentane	Horizontal condensing	$108.2 < P < 1250 \text{ kPa}$ $17.6 < G < 990 \text{ kg/m}^2\text{-s}$	<ul style="list-style-type: none"> • Disperse, annular, semi-annular, and slug flow observed • Froude number as basis for condensation mode • von Karman velocity profile to describe film velocity • Taitel and Dukler (1976) map to develop simple criteria for condensation in horizontal tubes • Criteria based on ratio of shear to gravity forces • All map boundaries vertical and horizontal lines – easy to use • Defined transition regions, rather than abrupt transitions
Sardesai <i>et al.</i> (1981)	24.4 mm	R-113, steam, propane, methanol, <i>n</i> -pentane	Horizontal condensing		<ul style="list-style-type: none"> • Investigated annular–stratified/wavy transition • Taitel and Dukler (1976) annular–stratified/wavy transition criterion as basis to develop transition criterion from data
Soliman (1982; 1986)	$4.8 < D < 15.9 \text{ mm}$	R-12, R-113, steam	Condensing		<ul style="list-style-type: none"> • Annular–wavy Froude number transition criterion based on data from different sources • Mist–annular Weber number transition criterion
Tandon <i>et al.</i> (1982; 1985a)	$4.8 < D < 15.9 \text{ mm}$	R-12, R-113, R-22	Condensing	$0.01 < j_g^* < 20$ $0.001 < 1 - \alpha/\alpha < 3$	<ul style="list-style-type: none"> • Simple transition criteria, good agreement with data for annular, semi-annular, and wavy flows
Hashizume <i>et al.</i> (Hashizume, 1983; Hashizume <i>et al.</i> , 1985; Hashizume and Ogawa, 1987)	10 mm	R-12, R-22	Horizontal condensing	$570 < p < 1960 \text{ kPa}$	<ul style="list-style-type: none"> • Refrigerant flow patterns different from air–water • Modified property corrections of Baker (1954) map proposed by Weisman <i>et al.</i> (1979) to make them applicable to R-12 and R-22

(Continued)

Table 6.1
(Continued)

Investigators	Hydraulic diameter	Fluids	Orientation/ conditions	Range/ applicability	Techniques, basis, observations
Wang <i>et al.</i> (1997a, b)	6.5 mm	R-22, R-134a, R-407C	Horizontal	$50 < G < 700 \text{ kg/m}^2\text{-s}$ $T_{\text{sat}} = 2, 6, \text{ and } 20^\circ\text{C}$	<ul style="list-style-type: none"> At low G, intermittent and stratified flow; at high G, annular Agreed with modified Baker (1954) map of Hashizume <i>et al.</i> (Hashizume, 1983; Hashizume <i>et al.</i>, 1985; Hashizume and Ogawa, 1987)
Dobson and co-workers (Dobson, 1994; Dobson <i>et al.</i> , 1994; Dobson and Chato, 1998)	3.14, 4.6, and 7.04 mm	R-12, R-134a, R-22, R32/R125	Horizontal	Condensing $25 < G < 800 \text{ kg/m}^2\text{-s}$ $T = 35\text{--}60^\circ\text{C}$	<ul style="list-style-type: none"> Good agreement with Mandhane <i>et al.</i> (1974) map after axis transformation Primary distinction between gravity and shear-controlled flows Criteria based on modified Soliman number and mass flux
Coleman and Garimella (2000 a, b; 2003), Garimella (2004)	Round: 4.91 mm; Square: 4, 3, 2, 1 mm; Rectangular: 4×6 ; 6×4 ; 2×4 ; $4 \times 2 \text{ mm}$	R-134a	Horizontal condensing	$P = 1379\text{--}1724 \text{ kPa}$ $150 < G < 750 \text{ kg/m}^2\text{-s}$	<ul style="list-style-type: none"> Flow regimes subdivided into flow patterns, G-x based transition criteria D_h more important than shape, aspect ratio for transition criteria Intermittent and annular flow increases as D_h decreases Wavy flow non-existent in 1-mm channel
Cavallini <i>et al.</i> (2001; 2002a, b)	8 mm	R-22, R-134a, R-125, R-32, R-236ea, R-407C, and R-410A	Condensation, horizontal tubes	$30 < T_{\text{sat}} < 50^\circ\text{C}$ $100 < G < 750 \text{ kg/m}^2\text{-s}$	<ul style="list-style-type: none"> Criteria similar to Breber <i>et al.</i> (1979; 1980) for primary flow regimes (annular, stratified, wavy, and slug) Recommended Kosky and Staub (1971) model for annular flow
El Hajal <i>et al.</i> (2003)	$3.14 < D < 21.4 \text{ mm}$	R-22, R-134a, R-125, R-32, R-236ea, R-410a	Horizontal condensing	$16 < G < 1532 \text{ kg/m}^2\text{-s}$ $0.02 < p_r < 0.8$ $76 < (\text{We}/\text{Fr})_L < 884$	<ul style="list-style-type: none"> Transitions between stratified, wavy, intermittent, annular, mist and bubbly flow on G-x coordinates, adapting boiling map of Kattan <i>et al.</i> (1998a, b; 1998c) with updates by Zurcher <i>et al.</i> (1999) Void fraction for map construction deduced from heat transfer database, subsequently averaged with homogeneous value

developed a “best fit” map from the different flow regime maps available at the time, and also introduced physical property corrections for gas and liquid density, gas and liquid viscosity, and surface tension to be applied to the transition lines. However, these corrections did not yield a significant improvement in flow pattern prediction. A theoretical model of pressure drop for slug flows in horizontal and near-horizontal tubes was developed by Dukler and Hubbard (1975) with the two main contributions to pressure drop being the acceleration of the liquid to the slug velocity, and the pressure drop due to wall shear at the back of the slug. This model was validated using pressure–time traces and individual phase velocity measurements. Nicholson *et al.* (1978) extended this model to include elongated bubble flows by using a constant slug length, and also used the model to predict flow regime transitions. Taitel and Dukler (1976) devised a theoretical approach to flow regime mapping for air–water mixtures using a momentum balance on a stratified flow pattern. A set of four non-dimensional parameters was used to define instability-driven transitions from the stratified to annular or intermittent flows, and to distinguish between stratified smooth and stratified wavy flows. This theoretical model showed good agreement with the experimentally developed flow map of Mandhane *et al.* (1974). The effects of fluid properties (liquid viscosity, surface tension, gas density) and pipe diameter on two-phase horizontal flow patterns were investigated by Weisman *et al.* (1979) for pipe diameters ranging from 11.5 mm to 51 mm. Using data from other investigators as well as new flow visualization and pressure fluctuation data, modifications to existing correlations were developed for the flow-regime transitions. It was concluded that for the range of diameters tested, the pipe diameters and fluid properties have only moderate influences on the transition lines.

Some investigators (Moore and Turley, 1983; Cai *et al.*, 1996) have used statistical approaches to better define the transitions between flow regimes (plug or bubble to slug flow, annular to annular–mist flow) that are difficult to distinguish visually. This approach utilizes the root mean square and fluctuations in the pressure/time signals, frictional pressure gradients, and chaos theory to provide an objective means to interpret flow pattern transitions. Annunziato and Girardi (1987) used differential pressure measurement and local void fraction probes to measure the temporal fluctuations in a 89-mm diameter tube.

6.2.1.2. Small circular channels

Among the studies on flow regime maps for microchannels using adiabatic air–water mixtures, Suo and Griffith (1964) correlated the transition from elongated bubble to annular and bubbly flow in capillary tubes ($1.0 < D < 1.6$ mm) by using the average volumetric flows of the liquid and gas phases, and the velocity of the bubbles. They also provided a criterion which determines when buoyancy effects can be neglected in terms of the parameter $\rho_l g D^2 / \sigma$. However, it must be noted that they restrict their analysis to situations where $\rho_l / \rho_g \gg 1$ and $\mu_l / \mu_g > 25$. While they explicitly state these restrictions in their paper, several other air–water adiabatic flow papers do not establish such explicit restrictions; therefore, caution is advised when applying these air–water based criteria to refrigerant condensation. For example, for refrigerant R-134a condensing at 1500 kPa, the density ratio is 14, while the viscosity ratio is 9.7. For the air–water pair at standard conditions, the corresponding ratios are $\rho_l / \rho_g = 839$ and $\mu_l / \mu_g = 49$. Similarly, the surface tension of the air–water pair is 17 times higher than that of R-134a.

Barnea *et al.* (1983) classified two-phase flow patterns in small horizontal tubes ($4 < D < 12$ mm) into four major regimes (dispersed, annular, intermittent and stratified). They found that all transitions except the stratified to non-stratified transition were satisfactorily described by the Taitel–Dukler (1976) model. Therefore, they modified the stratified-to-intermittent flow transition boundary predicted by Taitel and Dukler (1976) by accounting for surface tension in terms of the gas-phase height in the channel as follows:

$$h_G \leq \frac{\pi}{4} \sqrt{\frac{\sigma}{\rho g \left(1 - \frac{\pi}{4}\right)}} \quad (6.3)$$

Even though the above equation includes surface tension and gravitational terms, they commented that for small channels, this condition is always satisfied, which leads to a further simplification of the criterion, namely, $h_G \leq \frac{\pi}{4} D$. They also provided different interpretations for the formation of intermittent flow from stratified flows. In large channels, they attribute the transition to the Kelvin–Helmholtz instability, whereas in small tubes with wetting liquid, wetting of the wall due to capillary forces causes the film to climb and form a bridge, which leads to intermittent flow.

Damianides and Westwater (1988) developed individual flow regime maps for air–water mixtures for $1 < D_h < 5$ mm to document the effect of diameter on the flow regime transitions. They found some agreement between their results and the transition criteria of Taitel and Dukler (1976) for the 5-mm case, but the agreement was poor for 1-mm tubes. The 1-mm tube showed a large intermittent flow region, with the transition from annular flow attributed to the generation of roll waves. For the larger diameter tubes, they reported the existence of an increasingly large region of stratified wavy flow, with the waves creeping up to form annular flow at larger gas velocities. The agglomeration of plugs of gas led to slug flow, rather than the growth of a finite amplitude wave, which meant that the Kelvin–Helmholtz instability could not be used to predict the onset of slugging. As observed by almost all investigators, they also stated increasingly important role of surface tension at the smaller channel diameters. They noted that the intermittent-to-disperse flow transition occurred at larger liquid flow rates in the larger tubes, and that the intermittent-to-annular transition occurred at larger gas flow rates in smaller tubes. The stratified flow region was essentially non-existent in the 1-mm tube.

Fukano *et al.* (1989) also investigated air–water flow patterns in tubes with $1 < D_h < 4.9$ mm and recorded bubbly, annular, plug, and slug flows, the latter two being combined into one intermittent region for pressure drop analyses. Their results agreed with the work of Barnea *et al.* (1983), and while there is some disagreement between the results reported by Fukano *et al.* (1989) and Damianides and Westwater (1988), these studies do point out that the flow regime map presented by Mandhane *et al.* (1974) cannot sufficiently predict the flow regime transitions in small diameter tubes. Also, it appears that the theoretical predictions of Taitel and Dukler (1976) and the correlations presented by Weisman *et al.* (1979) are not reliable for small diameters.

Brauner and Maron (1992) noted that several previous researchers had based their flow regime transition analyses on single stability criteria of infinitely long waves. Therefore, they incorporated the stabilizing effects of surface tension associated with practically finite

wavelengths, and were able to predict the transition from stratified flow over a wide range of channel sizes. This resulted in a transition criterion based on the Eotvos number:

$$\text{Eö} = \frac{(2\pi)^2 \sigma}{(\rho_l - \rho_g) D^2 g} > 1 \quad (6.4)$$

Ide *et al.* (1995) studied the “liquid lumps” formed during vertical upward air–water flow in six tubes with $0.5 < D < 6.0$ mm, including the velocity of the lumps, the corresponding disturbance wave and the base film. A momentum-averaged mean velocity of liquid lumps was used to characterize the flow for cases with large liquid lumps and many small waves. The liquid lump velocity characteristics were then used to interpret the flow patterns with corresponding maps (Fukano *et al.*, 1989) for horizontal capillary tubes.

Mishima and Hibiki (1996) investigated flow patterns for upward flow of air–water mixtures in vertical tubes (an orientation that is not particularly relevant for condensation applications) with $1 < D < 4$ mm. Some variants of flow patterns typically seen in larger tubes were observed, but the transitions were in reasonable agreement with Mishima and Ishii’s (1984) transition criteria. Mishima *et al.* (1997; 1998) used neutron radiography, which uses the fact that thermal neutrons easily penetrate heavy materials such as metals, but are attenuated by light materials containing hydrogen, that is water, to non-intrusively investigate qualitative and quantitative two-phase flow phenomena. Thus, the incident neutron beam is attenuated in proportion to the liquid phase thickness, allowing projection of the image of the two-phase flow, which is then converted to an optical image by the scintillator. The image is intensified and enlarged, and detected by a high-speed video camera. Air–water vertical upward flow was visualized to identify the prevailing flow regime, rising velocity of bubbles, and wave height and interfacial area in annular flow. Representative images of slug flow before and after processing are shown in Fig. 6.2. Void profiles and void fraction variations were also recorded as discussed in a subsequent section. By utilizing attenuation characteristics of neutrons in materials, measurements of void profile and average void fraction were performed. This technique enables flow visualization in situations without optical access and where X-ray radiography is not applicable.

Coleman and Garimella (1999) investigated the effect of tube diameter and shape on flow patterns and flow regime transitions for air–water flow in circular tubes of 5.5-, 2.6-, 1.75-, and 1.3-mm diameter, and a rectangular tube with $D_h = 5.36$ mm and aspect ratio $\alpha = 0.725$. Gas and liquid superficial velocities were varied from $0.1 \text{ m/s} < U_{SG} < 100 \text{ m/s}$, and $0.01 \text{ m/s} < U_{SL} < 10.0 \text{ m/s}$, respectively. Bubble, dispersed, elongated bubble, slug, stratified, wavy, annular–wavy, and annular flow patterns were observed (Fig. 6.3). This figure also shows their attempt to bring some uniformity to the terminology used to describe these flow mechanisms by the various investigators cited above. Thus, they divided the mechanisms into four major *regimes* (stratified, intermittent, annular, and dispersed) and subdivided these major regimes further into the applicable *patterns*. Thus, when comparing with the results of various investigators, the nomenclature for at least the major regimes would be somewhat uniform. The tube diameter had a significant effect on the transitions. As the tube diameter is decreased, the transition from the intermittent regime to the dispersed or bubbly regime occurred at progressively higher U_{SL} . Also, the transition from intermittent to annular flow occurs at a nearly constant U_{SL} , for a given tube, with the

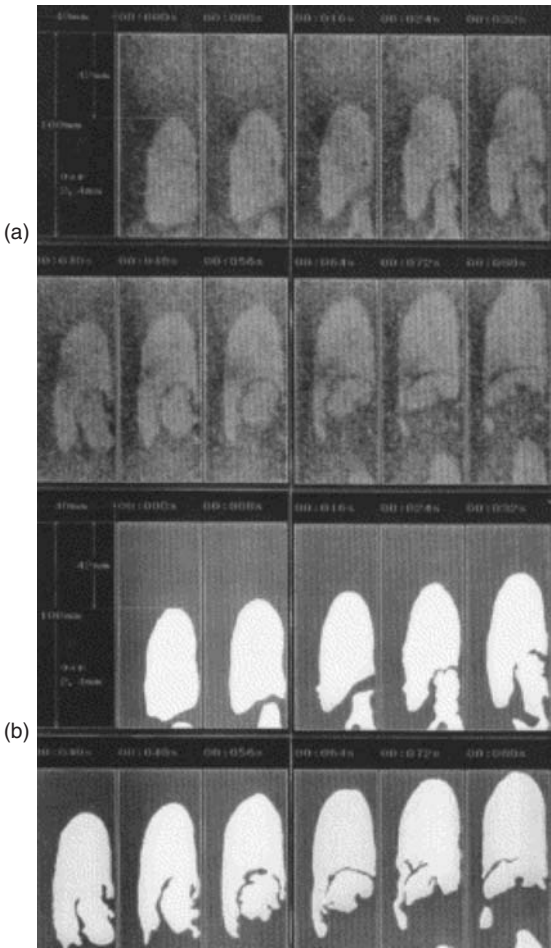
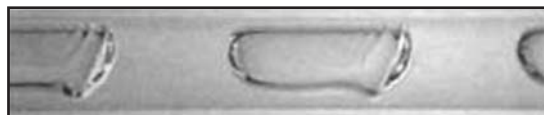


Fig. 6.2. Raw and processed images of slug flow in vertical upward air–water flow. Reprinted from Mishima, K., Hibiki, T. and Nishihara, H., Visualization and measurement of two-phase flow by using neutron radiography, *Nuclear Engineering and Design*, **175**(1–2), pp. 25–35 (1997) with permission from Elsevier.

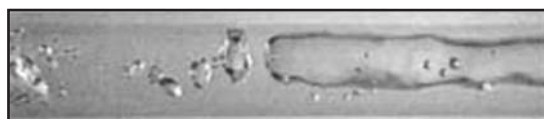
transition U_{SL} increasing as the diameter first decreases from 5.5 mm, but approaching a limiting value as the diameter decreases further to 1.75 and 1.30 mm. The size of the intermittent regime increases in small diameter tubes. The primary difference in their results for round and rectangular channels of approximately the same D_h was that the rectangular tube showed a transition to disperse flows at higher U_{SL} , presumably because it is more difficult to dislodge the liquid from the corners of the rectangular tube due to the surface tension forces. As with other investigators, they found that very few points for the 5.5-mm tube were in the stratified regime, whereas the Taitel–Dukler (1976) criteria predicted the existence of a stratified region for these conditions. The agreement with the intermittent-to-disperse and the annular-to-disperse transitions was somewhat better. However, the assumptions inherent in the Taitel–Dukler analyses were not considered applicable to the small diameter channels. The agreement with the data of Damianides and Westwater (1988)



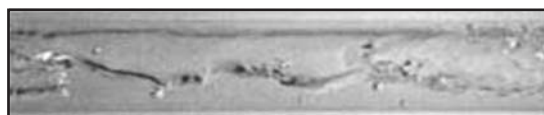
Stratified regime: wavy flow pattern



Intermittent regime: elongated bubble pattern



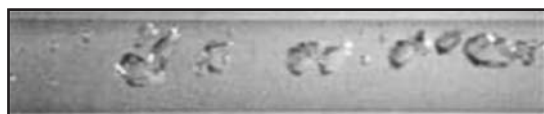
Intermittent regime: slug flow pattern



Annular regime: wavy-annular pattern



Annular regime: annular pattern



Dispersed regime: bubble flow pattern



Dispersed regime: dispersed flow pattern

Fig. 6.3. Air–water flow patterns in circular and rectangular tubes. Reprinted from Coleman, J. W. and Garimella, S., Characterization of two-phase flow patterns in small diameter round and rectangular tubes, *International Journal of Heat & Mass Transfer*, **42(15)**, pp. 2869–2881 (1999) with permission from Elsevier.

was much better. The transition to the dispersed region (including the effect of diameter) was also in good agreement with the results of Fukano *et al.* (1989). The transition correlations presented by Weisman *et al.* (1979) were only in agreement for the largest tube studied by Coleman and Garimella, with the agreement deteriorating as D_h decreased.

Triplett *et al.* (1999b) conducted an investigation similar to that of Coleman and Garimella (1999) of flow regimes in adiabatic air–water flows through circular microchannels of 1.1- and 1.45-mm diameter, and in semi-triangular microchannels with $D_h = 1.09$ and 1.49 mm. They identified bubbly, churn, slug, slug–annular, and annular flow patterns (stratified flow was not observed as was the case with many other investigators), and plotted the data on gas and liquid superficial velocity axes. The progression between the respective regimes as the gas and liquid velocities are changed is shown in Fig. 6.4. Bubbly flow undergoes a transition to slug flow when the gas superficial velocity U_{GS} increases due to the corresponding rise in the void fraction and the coalescence of bubbles. At high superficial liquid velocities U_{LS} , as the overall mass flux is increased, churn flow is established due to the disruption of slugs. Churn flow also occurred when large waves disrupted wavy–annular flows. Slug–annular flow is established at low U_{GS} and U_{LS} , and changes to annular flow when U_{GS} increases. The flow regime maps for all channels tested were substantially similar. Their maps agreed in general with the results of Damianides and Westwater (1988) and Fukano and Kariyasaki (1993), but the agreement with almost all analytically derived transition criteria (Suo and Griffith, 1964; Taitel and Dukler, 1976) was poor.

Zhao and Bi (2001a) investigated flow patterns for co-current upward air–water flow in vertical equilateral triangular channels with $D_h = 2.886$, 1.443, and 0.866 mm. The flow patterns encountered included dispersed bubbly flow, slug flow, churn flow and annular flow for $D_h = 2.886$ and 1.443 mm. For $D_h = 0.866$ mm, dispersed bubbly flow was not observed, but a capillary bubbly flow pattern, consisting of a succession of ellipsoidal bubbles, spanned the cross-section of the channel (Fig. 6.5) at low gas flow rates. Long slugs were seen at high superficial gas velocities in the slug flow regime. Churn and annular flows occurred at higher superficial gas velocities as the channel size decreased. These trends were in agreement with the results of other investigators (Barnea *et al.*, 1983; Galbiati and Andreini, 1992a; Mishima and Hibiki, 1996; Ide *et al.*, 1997) for small circular tubes. However, occurrence of the churn–annular transition line at higher gas velocities with decreasing channel diameter did not agree with the findings of Taitel *et al.* (1980) and Mishima and Ishii (1984), who predicted the opposite trend for conventional tubes. The significant discrepancies between the data and the Taitel *et al.* and the Mishima–Ishii transition criteria were attributed to the large difference in channel size and the meniscus effect due to the triangular shape.

Yang and Shieh (2001) observed bubbly, plug, wavy, slug, annular, and dispersed regimes during air–water and R-134a (adiabatic) flow through 1-, 2-, and 3-mm horizontal tubes. Transitions between the regimes, especially slug-to-annular, were difficult to distinguish in air–water flow, while all the R-134a transitions were clear. In a manner much like the study by Coleman and Garimella (1999), they plotted their flow regime maps for the different tubes versus the transition lines of Taitel and Dukler (1976), Barnea *et al.* (1983), and Damianides and Westwater (1988). The results were in generally good agreement with those of the latter two investigators, but as pointed out by numerous other investigators, the stratified–intermittent transition predicted by Taitel and Dukler (1976) was not seen, due to the inapplicability of the basis for this transition to the smaller tubes. The slug–annular transition for R-134a occurred at lower gas velocities, while the intermittent–bubbly transition occurred at higher liquid velocities, both attributed to the lower surface tension of R-134a compared to the air–water pair. The R-134a transitions were in good agreement with the

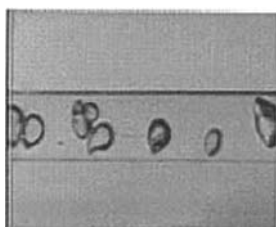
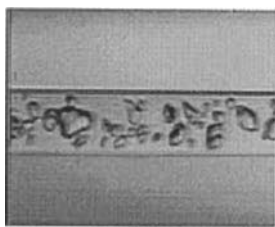
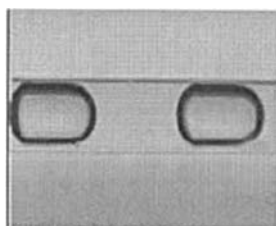
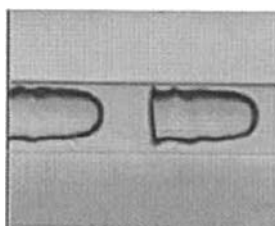
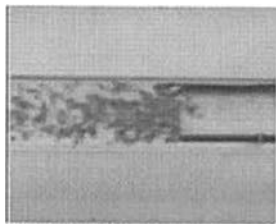
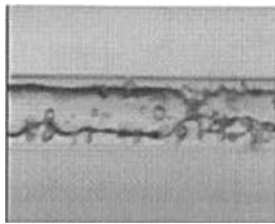
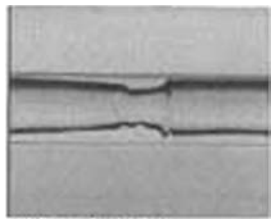
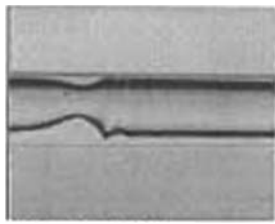
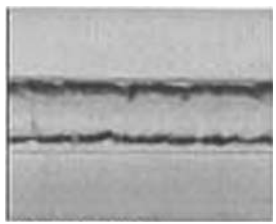
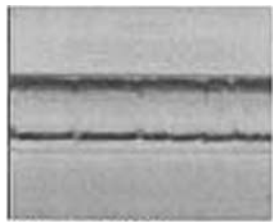
(a) $U_{LS} = 3.021$ m/s, $U_{GS} = 0.083$ m/s(b) $U_{LS} = 5.997$ m/s, $U_{GS} = 0.396$ m/s(c) $U_{LS} = 0.213$ m/s, $U_{GS} = 0.154$ m/s(d) $U_{LS} = 0.608$ m/s, $U_{GS} = 0.498$ m/s(e) $U_{LS} = 0.661$ m/s, $U_{GS} = 6.183$ m/s(f) $U_{LS} = 1.205$ m/s, $U_{GS} = 4.631$ m/s(g) $U_{LS} = 0.043$ m/s, $U_{GS} = 4.040$ m/s(h) $U_{LS} = 0.082$ m/s, $U_{GS} = 6.163$ m/s(i) $U_{LS} = 0.082$ m/s, $U_{GS} = 73.30$ m/s(j) $U_{LS} = 0.271$ m/s, $U_{GS} = 70.42$ m/s

Fig. 6.4. Flow regimes for adiabatic air–water flow through 1.09-mm circular channels. Reprinted from Triplett, K. A., Ghiaasiaan, S. M., Abdel-Khalik, S. I. and Sadowski, D. L., Gas–liquid two-phase flow in microchannels, Part I: Two-phase flow patterns, *International Journal of Multiphase Flow*, **25**(3), pp. 377–394 (1999) with permission from Elsevier.

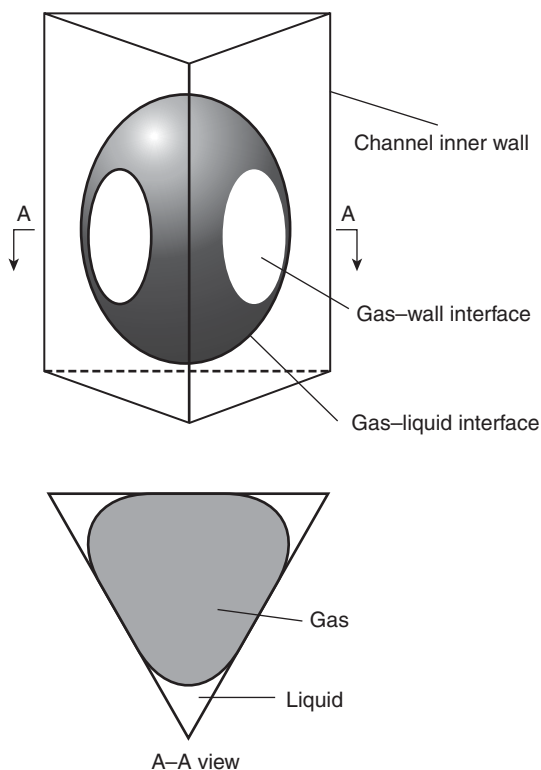


Fig. 6.5. Capillary bubble in triangular channel. Reprinted from Zhao, T. S. and Bi, Q. C. Co-current air–water two-phase flow patterns in vertical triangular microchannels, *International Journal of Multiphase Flow*, **27**(5), pp. 765–782 (2001) with permission from Elsevier.

results of Wang *et al.* (1997a) and Hashizume (1983), although these two investigations focused on lower mass fluxes than those studied by Yang and Shieh (2001).

Tabatabai and Faghri (2001) developed a flow regime map for microchannels with particular attention to the influence of surface tension. They noted that in two-phase flow, ripples are generated on the annular layer with an increase in gas-phase velocity, which in turn leads to the formation of collars and bridges. They distinguish slug, plug, and bubble regimes based on the size and gap between the bridges. As with other investigators, they state that in large tubes, gravitational forces pull the liquid film down, preventing bridge formation. Their map is based on the relative effects of surface tension, shear, and buoyancy forces. The map uses the ratio of pressure difference due to surface tension and that due to shear forces as one axis, while the ratio of superficial velocities $V_{G,S}/V_{L,S}$ forms the other axis. The void fraction model of Smith (1969) is used to compute the required vapor or gas-core flow area and interfacial surface area. The three terms in the force balance per unit length of the region of interest are given by:

$$\frac{F_{\text{surface tension}}}{L} = 2\sigma(1 - \alpha)^{0.5} \quad (6.5)$$

$$\frac{F_{\text{shear}}}{L} = \pi D \alpha f_1 \left(\frac{\rho_l u_1^2}{4} \right) \quad (6.6)$$

$$\frac{F_{\text{buoyancy}}}{L} = g(\rho_l - \rho_g) A_g \quad (6.7)$$

where the void fraction α appears in each of the three equations above (indirectly through the gas phase area in the buoyancy term). This establishes a condition for the surface tension forces being dominant:

$$|F_{\text{surface tension}}| > |F_{\text{shear}}| + |F_{\text{buoyancy}}| \quad (6.8)$$

which then yields a criterion for the transition from surface-tension-dominated regions to shear-dominated regions:

$$u_1 < B = \left[\frac{2\sigma(1 - \alpha)^{0.5} - g(\rho_l - \rho_g) A_g}{\left(\frac{\pi D \alpha \rho_l f_1}{4} \right)} \right]^{0.5} \quad (6.9)$$

Relating the actual phase velocities to the corresponding superficial velocities results in the following form of the transition criterion:

$$\frac{V_{\text{SG}}}{V_{\text{SL}}} > \frac{V_{\text{SG}}}{(1 - \alpha)B} \quad (6.10)$$

For the annular-to-intermittent transition, they used the following criterion for the liquid volume fraction m proposed by Griffith and Lee (1964), which is based on collars forming in annular flow due to instabilities at a wavelength of $5.5 \times D$, with the collar ultimately forming bridges and slugs:

$$m = \frac{(\pi r^2)2r - \frac{4}{3}\pi r^3}{\pi r^2(5.5)2r} = 0.06 \quad (6.11)$$

where the numerator is the total liquid volume per slug and the denominator is the total volume of the slug at the most unstable wavelength of 5.5. Tabatabai and Faghri compared this flow regime map with data in the literature for condensation of steam and refrigerants in tubes with $D > 4.8$ mm, and for air–water flow in smaller diameter tubes, and stated that better agreement was obtained in the surface-tension-dominated regions, and also that the map is able to predict the movement of the boundaries with channel size.

6.2.1.3. Narrow, high aspect ratio, rectangular channels

Most of the research on two-phase flow in small hydraulic diameter rectangular channels uses tubes of either small ($\alpha < 0.50$) or large ($\alpha > 2.0$) aspect ratios (Hosler, 1968; Jones Jr. and Zuber, 1975; Lowry and Kawaji, 1988; Wilmarth and Ishii, 1994). In a study on flow regime maps for $0.125 < \alpha < 0.50$ and $11.30 < D_h < 33.90$ mm, Richardson (1959) showed that the smaller aspect ratio suppressed the stratified and wavy flow regimes and promoted the onset of elongated bubble and slug flows. Troniewski and Ulbrich (1984) proposed

corrections to the axes of the Baker (1954) map based on the single-phase velocity profiles in rectangular channels for horizontal and vertical channels with $0.09 < \alpha < 10.10$ and $7.45 < D_h < 13.10$ mm. Lowry and Kawaji (1988) studied rectangular geometries with $D_h < 2.0$ mm and $40 < \alpha < 60$ in vertical upward flows and concluded that the Taitel and Dukler (1976) model was not valid for narrow channel flow. Wambsganss *et al.* (1991) reported flow patterns and flow regime transitions in a single rectangular channel with aspect ratios of 6.0 and 0.167 and $D_h = 5.45$ mm through flow visualization and dynamic pressure measurements. They found qualitative agreement with the corresponding flow regime maps for circular channels and larger rectangular channels, but noted quantitative differences between those maps and their results for the relatively smaller rectangular channels. Wambsganss *et al.* (1994) extended this work to develop criteria for transition from bubble or plug flow to slug flow based on root-mean-square pressure changes. The transition was identified from a distinct change in the slope or a local peak in the pressure drop versus Martinelli parameter X or quality x -graph.

Xu (1999) investigated adiabatic air/water flow in vertical rectangular channels with gaps of 0.3, 0.6, and 1.0 mm. The flow regimes (bubbly, slug, churn, and annular) in the 1 and 0.6 mm channels were found to be similar to those reported in other studies. At smaller gaps, the bubbly–slug, slug–churn and churn–annular flow transitions occurred at lower superficial gas velocities, due to the squeezing of the gas phase along the width of the narrow channels, which was believed to facilitate these transitions. In the 0.3-mm channel, bubbly flow was absent, but cap-bubbly flow was seen, characterized by two-dimensional (2-D) semi-circular tops and flat bottoms. In addition, the presence of droplets together with slug and annular flows (attributed to the increased influence of surface tension and shear) led him to add slug-droplet and annular-droplet regimes to the others found in the bigger channels. Xu *et al.* (1999) later extended the transition criteria developed by Mishima and Ishii (1984) for application to the narrow rectangular geometry. Although this orientation and the corresponding physical considerations are not particularly relevant to condensation, their approach can be modified to yield analogous transition criteria for some of the transitions encountered in condensing flows. They based the bubbly-to-slug transition on the increasing probability of bubble collision and coalescence, which would lead to slug flow, with this transition occurring in the range of void fractions $0.1 < \alpha < 0.3$, as suggested by Mishima and Ishii (1984). The slug–churn transition was also adapted from the work of Mishima and Ishii (1984), based on the flow becoming unstable when two neighboring slugs start to touch each other as the channel mean void fraction increases. The transition to annular flow was assumed to occur somewhat arbitrarily for void fractions > 0.75 . They justified this based on the findings of Armand (1946), who found that the void fraction is related to the volumetric quality β through a simple linear relationship $\alpha = 0.833\beta$ for $\beta < 0.9$, but increased sharply when $\beta > 0.9$, signifying annular flow due to the uninterrupted gas core. Although these investigators applied some reasonable physical insights to the development of the transition criteria, the agreement was only acceptable with the 1-mm channel data, yielding poor agreement with the 0.6- and 0.3-mm data.

Using much the same approach as Xu *et al.* (1999), Hibiki and Mishima (2001) adapted Mishima and Ishii's (1984) model for round tubes to develop a flow regime map and transition criteria specifically for narrow rectangular cross-sections with vertical upflow. Their map consisted of bubbly, slug, churn, and annular flows. The bubbly-to-slug

transition was based on fluctuations of bubbles distributed in a square lattice pattern. They postulated that collisions and coalescences of bubbles increase significantly when the maximum distance between bubbles is less than the projected diameter of a flat bubble. The bubble spacing was related to void fraction, which yielded the transition criterion in terms of the void fraction. The slug-to-churn transition was based on the pressure gradients around the bubble and in the liquid film surrounding it, while the churn flow-to-annular flow criterion was based on flow reversal considerations or the destruction of liquid slugs due to deformation or entrainment. Their transition criteria were in reasonable agreement with data for air–water flows in rectangular channels with gaps of 0.3–17 mm, and with some high-pressure water boiling data.

6.2.1.4. Insights from relevant microgravity work

Based on the relatively small influence of gravity on two-phase flow in microchannels, insights into these flows can also be obtained from related work on similar flows in reduced gravity environments. Rezkallah *et al.* (Rezkallah, 1995; Rezkallah and Zhao, 1995) recorded two-phase flow patterns aboard the NASA KC-135 aircraft using air–water and air–glycerin/water (to obtain different viscosities) in a 9.525-mm tube. They classified the flows into three regimes (Fig. 6.6): surface-tension-dominated bubbly and slug flows, an intermediate frothy slug–annular region, and inertia-dominated annular flow and plotted the flow regimes on liquid- and gas-phase Weber number (We_{SG} , We_{SL}) (where $We = \rho V_s^2 D / \sigma$) coordinates based on the respective superficial velocities. They noted that slug flow under these conditions was different from the “Taylor bubble” profile typically seen at earth normal gravity: the fore and aft portions of the slug were smooth and half-spherical, with little entrainment of small bubbles – similar observations will be described

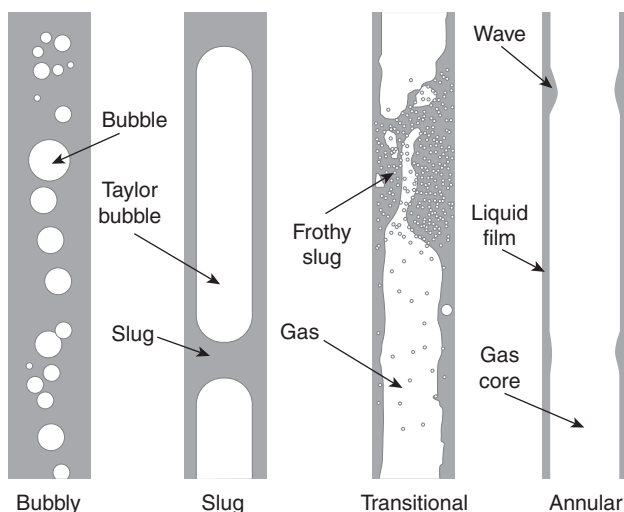


Fig. 6.6. Microgravity flow patterns documented by Lowe and Rezkallah (1999). Reprinted from Lowe, D. C. and Rezkallah, K. S., Flow regime identification in microgravity two-phase flows using void fraction signals, *International Journal of Multiphase Flow*, **25**(3), pp. 433–457 (1999) with permission from Elsevier.

for microchannel flows in a subsequent part of this section. The annular flow regime was similar to what is observed at 1-g, except that the film thickness was larger. The transition from bubbly/slug flow to intermediate flow occurred at Weber number (based on the gas superficial velocity) of $We_{SG} \cong 1$, while the transition to annular flow started at $We_{SG} \cong 20$. The bubbly-to-slug flow transition occurred at the ratio of superficial liquid and gas velocities $V_{SL} = C \cdot V_{SG}$ ($1.2 < C < 4.6$). Based on their own additional work, void fraction information, and data from other investigators comprising data for $6 < D < 40$ mm, they later (Rezkallah, 1996) modified the first transition to $We = 2$, and also recommended that the Weber numbers based on actual phase velocities, rather than superficial velocities be used as coordinates for the flow regime map. Liquid viscosity was found to have little effect on the transitions. These transition criteria were also subsequently (Lowe and Rezkallah, 1999) validated through very detailed measurements and analyses of the void fraction signals in the various regimes. Galbiati *et al.* (1992a, b; 1994) investigated flow patterns in horizontal and vertical two-phase flow of air–water mixtures in capillary tubes, and developed transition criteria between these patterns. The Taitel–Dukler (1976) stratified-to-annular flow transition criteria were modified to account for the influence of surface tension. They also pointed out that inlet mixing effects are significant in establishing fully developed flow. Two-phase flow in capillary tubes was treated as analogous to microgravity situations.

6.2.1.5. Channels with $D \ll 1$ mm

Flow regimes in two-phase flow through microchannels with $D \ll 1$ mm have only recently been investigated. One of the first groups of investigators of such flows include Feng and Serizawa (1999; 2000) and Serizawa and Feng (2001), who studied air–water and steam–water flow through 25- and 50- μ m channels. Their use of the term “liquid ring flow” for such small microchannels has since been used by other investigators in several different forms, as discussed throughout this section. Essentially, as the gas flow rate increases, the liquid bridge between adjacent gas slugs in slug flow becomes unstable, and transitions to this so-called liquid ring flow pattern. Kawahara *et al.* (2002) then conducted a comprehensive study of flow regimes, void fraction and pressure drop for horizontal nitrogen–water flow in 100- μ m circular channels. These authors contend that, in comparison with flow in channels in the 1-mm diameter range, the order of magnitude reduction in channel diameter results in lower Reynolds numbers and greater effects of wall shear and surface tension, which are manifested in different types of flow patterns. Although they stated the need for refractive index matching to remove the effects of optical distortion arising due to the small radius of curvature, they chose to conduct the experiments without such apparatus. This is because they felt that the near-wall phenomena, although distorted, could be viewed in more detail without optical correction, and the effects of distortion could be accounted for during the analysis phase. They observed five different flow mechanisms: liquid alone (liquid slug), gas core with smooth-thin liquid film, gas core with smooth-thick liquid film, gas core with ring-shaped liquid film, and gas core with a deformed interface. These flow regimes are shown in Fig. 6.7 for various combinations of liquid and gas velocities. The axi-symmetric (non-stratified) flow patterns clearly demonstrated the absence of gravitational effects. Similarly, the absence of small, dispersed bubbles (bubbly flow) was attributed to the liquid phase Re , being very low; thus, no bubble breakup induced

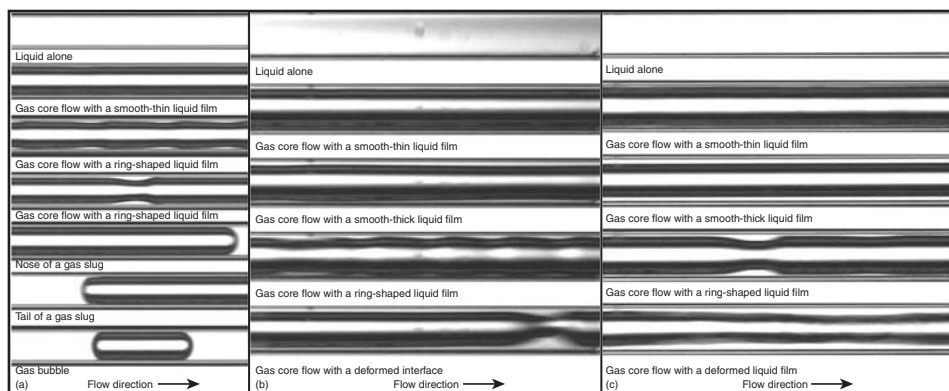


Fig. 6.7. Air–water flow regimes in 100- μm channels. (a) $U_L = 0.15$ m/s, $U_G = 6.8$ m/s; (b) $U_L = 0.56$ m/s, $U_G = 20.3$ m/s; (c) $U_L = 3.96$ m/s, $U_G = 19.0$ m/s. Reprinted from Kawahara, A., Chung, P.M.-Y. and Kawaji, M. Investigation of two-phase flow pattern, void fraction and pressure drop in a microchannel, *International Journal of Multiphase Flow*, **28**(9), pp. 1411–1435 (2002) with permission from Elsevier.

by liquid phase turbulence could occur. They also recognized that a given combination of liquid and gas phase velocities does not always result in a unique flow pattern – it simply establishes the more likely patterns. Other investigators such as Coleman and Garimella (2000a; 2003) have addressed this issue by defining “overlap zones” in their flow regime maps, in which the flow could transition from one regime to another at the same conditions. Therefore, they developed a flow regime map based on the probability of occurrence of the different patterns at the different conditions. These probability analyses led them to define four flow regimes (slug-ring, ring-slug, semi-annular, and multiple), which were combinations of the flow mechanisms mentioned above. At low liquid flow rates, flows with a gas core surrounded by a smooth-thin liquid film occurred at low gas flow rates, while the gas core was accompanied with a ring-shaped liquid film at high gas flow rates. At high liquid flow rates, the gas core was surrounded by a thick liquid film, or the gas core moved through a deformed film in serpentine manner. At a combination of high gas and liquid flow rates, several combinations of flows occurred to yield the “multiple” flow pattern.

Chung and Kawaji (2004) extended the work of Kawahara *et al.* (2002) to investigate the effect of channel diameter, by conducting experiments on nitrogen–water flow through 530-, 250-, 100-, and 50- μm channels. They found that the two-phase flow characteristics in the 530- and 250- μm channels were similar to those reported for channels of ~ 1 -mm diameter, for example by Triplett *et al.* (1999b). For channels smaller than these, only slug flow was observed, with the absence of bubbly, churn, slug–annular and annular flow attributed to the greater viscous and surface tension effects. From a combination of flow visualization and void fraction and pressure drop analyses, they interpreted slug flow as the rapid motion of a gas slug through a relatively quiescent liquid film retarded by the wall. Based on the values of the pertinent dimensionless parameters, they observed that the relevant forces for these channels were inertia, surface tension, viscous force, and gravity, in decreasing order of importance. Furthermore, with decreasing channel size, the Bond number, the superficial Reynolds numbers, the Weber number, and the capillary number

all decrease, which implies that the influence of gravitational and inertia forces decreases, while the importance of surface tension and viscous forces increases.

Chung *et al.* (2004) also investigated the effect of channel shape on flow patterns, void fraction, and pressure drop by conducting similar tests on a 96- μm square, and a 100- μm circular, microchannel. The flow regime maps for the two channels were substantially similar, except that the square channel did not exhibit the ring-slug flow pattern that was present in the circular channel. They reasoned that whereas in the circular channel, the liquid film must increase in thickness or develop into thicker rings periodically, in the square channel, it accumulates in the corners of the square channel, which was also supported by the analyses of Kolb and Cerro (1991; 1993). Kawahara *et al.* (2005) subsequently also investigated water/nitrogen and ethanol–water/nitrogen mixtures in 50-, 75-, 100-, and 251- μm circular channels to demonstrate that fluid properties have little effect on flow patterns in these channels.

Serizawa *et al.* (2002) also conducted a study similar to that of Kawahara *et al.* (2002) on air–water flow in circular tubes of 20-, 25- and 100- μm diameter, and steam–water flow in a 50- μm circular tube. Representative flow patterns recorded by them are shown in Fig. 6.8. It must be noted that they develop a particularly imaginative and varied set of terms that lead to further proliferation (and perhaps confusion) about the descriptors for

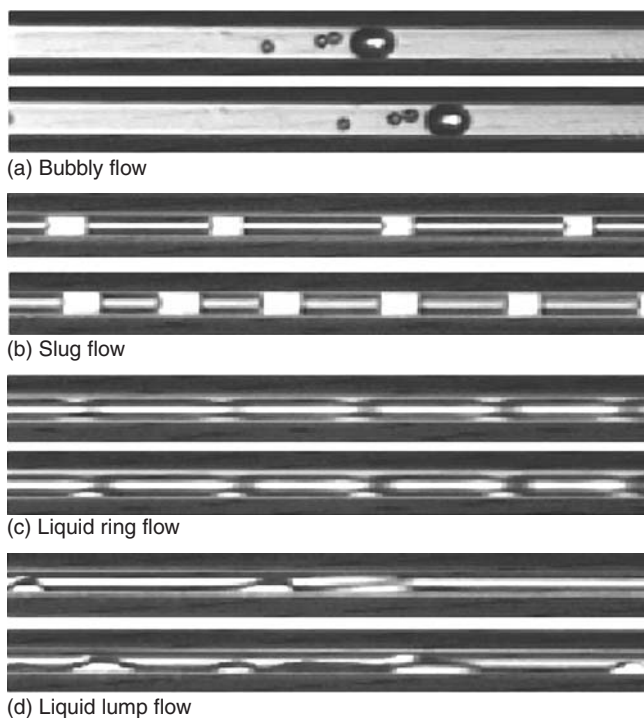


Fig. 6.8. Air–water flow patterns in 25- μm circular channel. Reprinted from Serizawa, A., Feng, Z. and Kawara, Z. Two-phase flow in microchannels, *Experimental Thermal & Fluid Science*, **26**(6–7), pp. 703–714 (2002) with permission from Elsevier.

the observed flow mechanisms. Thus, the terms they use include: dispersed bubbly flow, gas slug flow, liquid ring flow, liquid lump flow, skewed barbecue (Yakitori) shaped flow, annular flow, frothy or wispy annular flow, rivulet flow, and liquid droplets flow. Unlike the findings of Kawahara *et al.* (2002), they observed bubbly flow in the 25- μm channel, often bubbles almost the size of the channel closely followed by much smaller, finely dispersed bubbles. They noted that the capillary pressure at the small 5- μm bubble interface was as high as 0.3 bar, which kept the bubble from distorting from a spherical shape or from coalescing. They explained that slug flow occurs not due to bubble coalescence, but rather because of an entrance phenomenon, whereby gas at a high flow rate enters the channel, but the gas bubble velocity is not high enough to overcome the surface tension of the liquid bridge. This is an explanation quite different from most other investigators, and requires further study. They also state that surface tension prevents the liquid slug from spreading as a film, and coupled with the high pressure of the gas bubble, which pushes it to expand across the entire cross-section, leads to dry spots and patches. Liquid ring flow originates from liquid bridges between slugs that are ruptured when the gas velocity is very high. Liquid ring motion is governed by a balance between viscous forces at the wall and shear at the gas interface: viscous forces dominate up to a certain threshold thickness, beyond which the shear from the gas core pushes the liquid ring. Liquid lumps are formed at even higher gas velocities, when liquid is entrained and oscillates, but surface tension prevents it from spreading as a film. Liquid lumps are considered by them to be “partially continuous films” rather than the term rivulet that is often used in the literature. They also present steam–water flow regimes that include bubbly, slug, liquid ring and liquid droplet flows, and state that these flow mechanisms are similar to those shown for air–water in a 25- μm tube (Fig. 6.8). However, given the degree of distinction they make in this work between small variations in flow mechanisms, it does not appear that the steam–water and air–water flow patterns are all that similar. Several of their photographs show large gas bubbles appearing together with adjoining small bubbles, and detailed explanations are provided based on the prominence of surface effects in small channels.

Given the above emphasis on the uniqueness of microchannel two-phase flow, one of their more surprising findings is that their flow regime map is deemed to agree with the map of Mandhane *et al.* (1974), which is one of the more widely quoted flow maps for *much larger* conventional channels. No real explanation is given for this stated agreement with such a map, although a quick look at the map and their data reveals that the agreement is not as good as they state.

6.2.1.6. Dependence on contact angle and surface properties

Barajas and Panton (1993) studied the effect of contact angle on air–water flow by using 1.6-mm diameter horizontal pyrex, polyethylene, polyurethane, and fluoropolymer resin tubes. These tubes constituted three partially wetting and one non-wetting combination with contact angles of 34°, 61°, 74°, and 106°. Similar flow maps were found for the partially wetting tubes, except for the existence of rivulet flow, which replaces wavy flow when the contact angle becomes large. The transitions for the non-wetting system (except for the plug–slug transition) were considerably different. The transitions between slug and rivulet flow and those between slug and annular flow shift to

lower gas velocities. The non-wetting systems facilitate movement of liquid due to shear forces, causing the transition to rivulet or annular flow at lower gas velocities. Serizawa and Kawahara (2001) pointed out that surface wettability effects on flow patterns are more significant in smaller tubes due to the proportionately larger influence of surface forces in these tubes. This was confirmed by conducting tests with very carefully cleaned tubes, followed by tests using only cleaning with ethanol, as also mentioned in Serizawa *et al.* (2002).

6.2.2. Condensing flow

Compared to the number of investigations on adiabatic two-phase flows, there are few particularly relevant studies on condensing flows in small diameter channels. A few of the key investigations toward the low end of the hydraulic diameter range from among the available studies are summarized here.

One of the earlier, well-cited investigations of flow patterns during condensation of refrigerants was conducted by Traviss and Rohsenow (1973), who studied condensation of R-12 in an 8-mm diameter tube. A wide range of qualities, mass fluxes ($100 < G < 990 \text{ kg/m}^2\text{-s}$), and saturation temperatures ($10^\circ\text{C} < T < 40.6^\circ\text{C}$) was tested. Disperse, annular, semi-annular (referred to by many as wavy, with a thin liquid film at the top and a thicker film at the bottom of the tube), and slug flows were observed. Their main focus, as is the case with most of the studies on tubes with $D > \sim 5 \text{ mm}$, was the transition between shear-dominated annular flow and gravity-dominated stratified flow. They used the Froude number $\text{Fr}_1^2 = \bar{V}_1^2/g\delta$, where \bar{V}_1 is the average velocity of the liquid film and δ is the film thickness, as the basis for determining the applicable mode of condensation. They used the von Karman universal velocity profile to describe the film velocity. Using this velocity profile, and expressing the wall shear stress in terms of the two-phase frictional pressure drop (which was computed using a two-phase multiplier to the vapor-phase pressure drop), they developed expressions for the film Reynolds number $\text{Re}_1 = G(1-x)D/\mu_1$ in terms of Fr_1 , the Galileo number $\text{Ga}_1 = gD^3/\nu_1^2$, and the Martinelli parameter X_{tt} . By plotting their data on a Re_1 versus X_{tt} graph, they proposed that the annular to semi-annular transition occurs at a constant Fr_1 of 45. They further state that this boundary may be used to distinguish between non-stratified disperse and annular flows and “stratified” semi-annular, wavy, slug and plug flows. This development is widely available in the relevant textbooks, and the details are not presented here.

Breber *et al.* (1980) used the Taitel–Dukler (1976) map discussed in the previous section to develop simple transition criteria for condensation in horizontal tubes, once again basing them on the ratio of shear forces to gravity forces on the liquid film, which are quantified through the Wallis dimensionless gas velocity j_g^* :

$$j_g^* = \frac{G_{tx}}{\sqrt{Dg\rho_v(\rho_l - \rho_v)}} \quad (6.12)$$

in addition to the ratio of liquid volume to vapor volume. In the absence of a reliable way to predict the slip between the phases, the Martinelli parameter X is used to quantify this:

$$X = \sqrt{\frac{\Delta P_l}{\Delta P_v}} = \left(\frac{1-x}{x}\right)^{0.9} \left(\frac{\rho_v}{\rho_l}\right)^{0.5} \left(\frac{\mu_l}{\mu_v}\right)^{0.1} \quad (6.13)$$

They applied these criteria to data from a variety of studies on fluids such as R-12, R-113, steam, and *n*-pentane flowing through $4.8 < D < 22.0$ -mm tubes, at $108 < p < 1249$ kPa, and $18 < G < 990$ kg/m²-s. On the basis of the comparisons between these data and the aforementioned coordinate axes, they recommended the following simplified transition criteria:

Annular flow	$j_g^* > 1.5; X < 1.0$
Wavy/stratified flow	$j_g^* < 0.5; X < 1.0$
Slug (intermittent) flow	$j_g^* < 1.5; X > 1.5$
Disperse (bubbly) flow	$j_g^* > 1.5; X > 1.5$

One advantage of these criteria is the simplicity they afford: the transition lines appear as horizontal or vertical lines, helping in the clear bracketing of the various regimes. The existence of a transition band between the respective regimes also allows for the more realistic accounting of overlap zones through linear interpolation of heat transfer coefficients and other performance parameters. The authors do note, however, that its predictive capabilities are the weakest for the wavy–slug transition (which happens to be of considerable interest in small diameter and microchannels).

Sardesai *et al.* (1981) also investigated the annular-to-stratified/wavy transition for a variety of fluids (R-113, steam, propanol, methanol, and *n*-pentane) condensing in horizontal 24.4-mm diameter tubes. They instrumented their test section with thermocouples around the circumference on the tube at several axial locations to determine the circumferential variation of heat transfer coefficients, which enabled them to compute the ratio of the heat transfer coefficient at the top and bottom of the tube. They used the Taitel–Dukler (1976) annular–stratified/wavy transition criterion (representing a ratio of the axial shear force to the circumferential gravity force in the liquid film) as the basis for developing their experimentally derived transition criterion. Thus, they used the data to find a multiplier β to this transition line $\beta(F, X) = \text{constant}$, which would result in a line parallel to the Taitel–Dukler transition line. The data showed that the heat transfer coefficient ratio stayed close to unity (signifying axi-symmetric annular flow) down to $\beta = 1.75$, below which it decreased rapidly, signifying gravity-driven condensation. An empirical fit derived from the square root of the two-phase frictional multiplier of Chisholm and Sutherland (1969–70) was used such that $\phi_g^2 F = 1$ is used as the upper limit of gravity-controlled condensation, while $\phi_g^2 F = 1.75$ is used as the lower limit for annular flow, with $\phi_g^2 = 0.7X^2 + 2X + 0.85$. Here, F is the modified Froude number given by:

$$F = \sqrt{\frac{\rho_g}{\rho_l - \rho_g}} \frac{U_{GS}}{\sqrt{Dg}} \quad (6.14)$$

and U_{GS} is the superficial gas phase velocity.

Soliman (1982) also proposed an annular-wavy transition criterion based on data from different sources that included R-12, R-113, and steam flowing through $4.8 < D < 15.9$ -mm tubes for $28^\circ\text{C} < T < 110^\circ\text{C}$. During the progression from vapor to liquid, the increase in the liquid volume and the significance of gravity, coupled with the decreasing velocity, and thus the inertial effects, were quantified based on the decrease in the Froude number. Using the liquid film thickness expressions of Kosky (1971), the Martinelli parameter X_{tt} , and the

Azer *et al.* (1972) equation $\phi_G = 1 + 1.09X_{tt}^{0.039}$, he developed the following expressions for the film Reynolds number:

$$\begin{aligned} Re_l &= 10.18Fr^{0.625}Ga^{0.313}(\phi_G/X_{tt})^{-0.938} & \text{for } Re_l \leq 1250 \\ Re_l &= 0.79Fr^{0.962}Ga^{0.481}(\phi_G/X_{tt})^{-1.442} & \text{for } Re_l > 1250 \end{aligned} \quad (6.15)$$

The data from the various sources were then used to determine that the annular-to-wavy and intermittent transition occurs when $Fr = 7$ in the above expressions, irrespective of the diameter or fluid under consideration.

Subsequently, Soliman (1986) also developed a correlation for the mist–annular transition. Mist flow occurs in the entrance region of the condenser, with the liquid phase flowing as entrained droplets without any visible liquid film at the wall. He used the large discrepancies between experimentally determined heat transfer and pressure drop values and predictions typically using annular flow models as the rationale to propose that mist flow must be treated separately. He reasoned that entrainment occurs due to the inertia of the vapor phase ($\rho_G V_G^2$) shearing droplets from the surface of the liquid film, while viscous ($\mu_L V_L/\delta$) and surface tension (σ/D) forces tend to stabilize the liquid film, with the balance between them being represented by the Weber number, for which the following expressions were derived:

$$\begin{aligned} We &= 2.45Re_{GS}^{0.64} \left(\frac{\mu_G^2}{\rho_G \sigma D} \right)^{0.3} \phi_G^{-0.4} & \text{for } Re_{LS} \leq 1250 \\ We &= 0.85Re_{GS}^{0.79} \left(\frac{\mu_G^2}{\rho_G \sigma D} \right)^{0.3} \left[\left(\frac{\mu_G}{\mu_L} \right)^2 \left(\frac{\rho_L}{\rho_G} \right) \right]^{0.084} (X_{tt}/\phi_G^{2.55})^{0.157} & (6.16) \\ &\text{for } Re_{LS} > 1250 \end{aligned}$$

Based on the above definitions and comparison with the database mentioned above, the following criteria were established:

$$\begin{aligned} We < 20 & \quad \text{always annular} \\ We > 30 & \quad \text{always mist} \end{aligned} \quad (6.17)$$

Tandon *et al.* (1982) also used data for R-12 and R-113 from several sources for the range $4.8 < D < 15.9$ mm, and proposed a flow regime map with dimensionless gas velocity j_G^* as the ordinate and $(1 - \alpha)/\alpha$ as the abscissa, which resulted in simple transition equations and good agreement with the data for annular, semi-annular, and wavy flows. The correlation by Smith (1969) was used to compute the void fraction α . Similar to the Breber *et al.* (1980) criteria, their transition criteria, given below, also result in horizontal and vertical transition lines on the map. Thus:

$$\begin{aligned} \text{Spray} & & 6 < j_G^* & \quad \text{and} & \quad \frac{1 - \alpha}{\alpha} \leq 0.5 \\ \text{Annular/semi-annular} & & 1 \leq j_G^* \leq 6 & \quad \text{and} & \quad \frac{1 - \alpha}{\alpha} \leq 0.5 \\ \text{Wavy} & & j_G^* \leq 1 & \quad \text{and} & \quad \frac{1 - \alpha}{\alpha} \leq 0.5 \end{aligned} \quad (6.18)$$

$$\begin{array}{ll} \text{Slug} & 0.01 \leq j_G^* \leq 0.5 \quad \text{and} \quad \frac{1-\alpha}{\alpha} \geq 0.5 \\ \text{Plug} & j_G^* \leq 0.01 \quad \text{and} \quad \frac{1-\alpha}{\alpha} \geq 0.5 \end{array}$$

Subsequently, Tandon *et al.* (1985a) also demonstrated good agreement with their own data on condensation of R-12, R-22, and mixtures of the two fluids flowing through 10-mm tubes.

Hashizume and co-workers (Hashizume, 1983; Hashizume *et al.*, 1985; Hashizume and Ogawa, 1987) conducted a three-part study on flow patterns, void fraction, and pressure drop for refrigerant (R-12 and R-22) flows in 10-mm diameter horizontal tubes. Tests were conducted at saturation pressures in the range $570 < p < 1960$ kPa, corresponding to saturation temperatures in the range $20^\circ\text{C} < T < 72^\circ\text{C}$ for R12 and $4^\circ\text{C} < T < 50^\circ\text{C}$ for R-22, and it was shown that these flow patterns for refrigerants are quite different from those for the air–water system. The flows were analyzed using simplified models for annular and stratified flow, and the velocity profiles in the liquid and gas phases were described using the Prandtl mixing length. They modified the property corrections to the Baker map (1954) proposed by Weisman *et al.* (1979) (specifically, they decreased the surface tension exponent in $\psi = (\sigma_W/\sigma)^1 [(\mu_L/\mu_W)(\rho_W/\rho_L)^2]^{1/3}$ from 1 to 0.25) to make those maps applicable for R-12 and R-22.

Wang *et al.* (1997a,b) investigated two-phase flow patterns for refrigerants R-22, R-134a, and R-407C in a 6.5-mm circular tube over the mass flux range $50 < G < 700$ kg/m²-s, for saturation temperatures of 2°C , 6°C and 20°C . They noted, as did Wambsganss *et al.* (1991), that prior flow pattern studies had focused on diameters in the range $9.5 < D < 75.0$ mm, and had been conducted at high mass fluxes ($G > 300$ kg/m²-s), which are not particularly applicable to refrigeration and air-conditioning applications. At $G = 100$ kg/m²-s, plug, slug, and stratified flow patterns were observed, with no occurrence of annular flow. As the mass flux increased to 200 and 400 kg/m²-s, annular flow appeared, and dominated the map at higher mass fluxes. They found the transitions in their study to be in good agreement with the modified Baker map of Hashizume (Hashizume, 1983; Hashizume *et al.*, 1985; Hashizume and Ogawa, 1987), with the transitions occurring at somewhat lower mass fluxes, which they attributed to the smaller diameter used in their study. The slug-to-wavy and wavy-to-annular flow regime transitions for the refrigerant blend R-407C occurred at higher G and x than for the pure fluids. The higher phase densities and the consequent lower gas- and liquid-phase velocities for R-407C compared to R-22, and the higher liquid-phase viscosity of the constituents of R-407C were assumed to be the cause for this lagging behavior of the refrigerant flow transitions.

One of the more exhaustive studies of refrigerant condensation in small diameter ($D = 3.14, 4.6$, and 7.04 mm) tubes was conducted by Dobson and Chato (1998) using refrigerants R-12, R-22 R-134a, and two different compositions of a near-azeotropic blend of R-32/R-125 over the mass flux range $25 < G < 800$ kg/m²-s. The authors provide a good overview of the various studies on condensation, including a step-by-step description of the progression of flows from one regime to another as the quality changes at different mass fluxes. At the lowest mass flux of 25 kg/m²-s, the flow was entirely smooth stratified for all qualities, while wavy flow was observed at 75 kg/m²-s. As the mass flux was increased to 150 – 300 kg/m²-s, condensation occurred over annular, wavy–annular, wavy and slug flow

as the quality decreased. Fluid properties and tube diameter affected the flow transitions the most at these mass fluxes. At the highest mass fluxes, (500, 650, and 800 kg/m²-s), the flow progressed from annular-mist (indicating entrainment) at high qualities to annular, wavy-annular and slug flow with decreasing quality. With tests conducted at $T = 35$ and 45°C , they commented that the decreasing difference in vapor and liquid properties with an approach toward the critical pressure (increasing reduced pressure) explained the changes in the flow patterns. Thus, annular flow was seen over a larger portion of the map at lower reduced pressures; for example, annular flow was established in R-134a at 35°C at qualities as low as 15% at $G = 600 \text{ kg/m}^2\text{-s}$. Also, the R-32/R-125 blend showed transitions to annular flow at much higher qualities than the other fluids, with a significant amount of stratification seen at the high temperature case even at $G = 600 \text{ kg/m}^2\text{-s}$. It was also shown that the slug flow region increases at higher reduced pressures. As the tube diameter decreased, the transition from wavy flow to wavy-annular flow, and from wavy-annular to annular flow moved to lower qualities. They found very good agreement with the Mandhane *et al.* (1974) map after correcting the superficial vapor velocity with the factor $\sqrt{\rho_g/\rho_a}$ to account for the fact that the Mandhane *et al.* map was based primarily on air-water data, where the gas phase density is drastically lower than refrigerant vapor density. This correction accounts for the different gas-phase kinetic energies better than the original map. Since their stated objective was to primarily develop flow-regime-based heat transfer correlations, they divided the above-mentioned flow regimes into gravity-dominated and shear-controlled regimes (as done by the many other researchers cited above), and did not provide detailed transition criteria between each of the flow regimes observed. Instead, in their prior work (Dobson, 1994; Dobson *et al.*, 1994), they established that the wavy-annular to annular flow transition would occur at a Soliman-modified Froude number Fr_{so} of 18, instead of $\text{Fr}_{\text{so}} = 7$ recommended by Soliman (1982). In the heat transfer correlations also developed in this work, and to be discussed in a subsequent section of this chapter, they recommend that the shear-controlled annular flow correlation be used for $G \geq 500 \text{ kg/m}^2\text{-s}$ for all x , while for $G < 500 \text{ kg/m}^2\text{-s}$, the annular flow correlation should be used for $\text{Fr}_{\text{so}} > 20$, and the gravity-driven correlation should be used for $\text{Fr}_{\text{so}} < 20$.

The studies by Coleman and Garimella (2000a, b; 2003) and Garimella (2004) are perhaps the only investigations to date that address specifically all the aspects of the subject at hand. Thus, several studies cited above either report detailed flow regimes in microchannels as small as $25 \mu\text{m}$, but for adiabatic air-water flow, or those that study flow regimes in condensing flows are typically restricted to $D > \sim 5 \text{ mm}$, with the exception of the one 3.14-mm tube studied by Dobson and Chato (1998) and discussed above. The work of Coleman and Garimella simultaneously addressed: (a) small diameters, (b) condensing instead of adiabatic flow, (c) flow visualization during condensation, (d) temperatures representative of practical condensation processes, and (e) a wide range of mass fluxes and qualities. They conducted flow visualization studies for refrigerant R-134a in nine different tubes of round, square, and rectangular cross-section tubes with $1 < D_h < 4.91 \text{ mm}$ over the mass flux range $150 < G < 750 \text{ kg/m}^2\text{-s}$, and quality range $0 < x < 1$. The channels studied by them are shown in Fig. 6.9. In their studies, refrigerant of a desired quality was supplied to the test section by pre-condensing a superheated vapor. Visualization was conducted in a counterflow heat exchanger, with refrigerant flowing through an inner glass tube of the cross-section of interest, and air flowing through the space between this inner tube and another transparent outer Plexiglas tube, thus enabling visualization of the respective flow regimes.

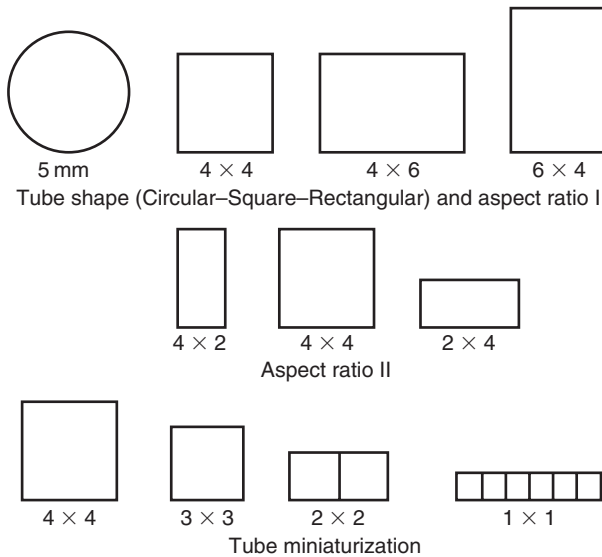


Fig. 6.9. Flow visualization geometries of Coleman and Garimella (2000a, b; 2003).

Heat transfer between the cold air and refrigerant causes condensation. Compressed air flowing in the annulus provided a low differential pressure for the glass microchannel, making it possible to conduct tests at saturation pressures as high as 1379–1724 kPa. Post condensers/subcoolers completed the closed loop facility. They recorded flow patterns for each mass flux at nominally 5–10% quality increments for a total of about 50 data per tube, to provide a fine resolution in the variation of flow patterns along the condensation process.

Four major flow *regimes*, including annular, intermittent, wavy, and dispersed flow were identified, with the regimes further subdivided into flow *patterns* (Fig. 6.10). In the annular flow regime, the vapor flows in the core of the tube with a few entrained liquid droplets, while liquid flows along the circumference of the tube wall. The flow patterns within this regime (mist, annular ring, wave ring, wave packet, and annular film) show the varying influences of gravity and shear forces as the mass flux and quality changes. Flow patterns with a significant influence of gravity (vapor flowing above the liquid, or a noticeable difference in film thickness at the top and bottom of the tube) and a wavy interface were assigned to the wavy flow regime. The waves at the liquid–vapor interface are caused by interfacial shear between the two phases moving at different velocities. Thus, this regime was subdivided into discrete waves of larger structure moving along the phase interface, and disperse waves with a large range of amplitudes and wavelengths superimposed upon one another, as shown in Fig. 6.10. The other flow regimes shown in the figure have already been described in detail in this chapter. In some cases, the flow mechanisms corresponded to more than one flow regime, typically indicating a transition between the respective regimes. A typical flow regime map for the 4.91-mm circular tube plotted using the mass flux G , and quality x -coordinates is shown in Fig. 6.11. A major portion of this map is occupied by the wavy flow regime with a small region where the plug, slug, and discrete wave flow patterns coexist. The waves become increasingly disperse as the quality and mass flux is increased (shown by the arrow in Fig. 6.11). The approximate demarcation


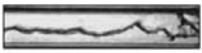








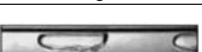
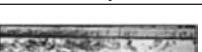
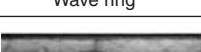
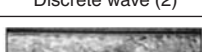
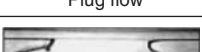
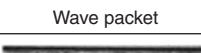
	Flow regimes			
	Annular	Wavy	Intermittent	Dispersed
Flow patterns	 Mist flow	 Discrete wave (0)	 Slug flow	 Bubbly flow
	 Annular ring	 Discrete wave (1)	 Slug flow	 Bubbly flow
	 Wave ring	 Discrete wave (2)	 Plug flow	 Bubbly flow
	 Wave packet	 Disperse wave (3)	 Plug flow	
	 Annular film	Note: Numbers above denote intensity of secondary waves		

Fig. 6.10. Condensation flow regimes and patterns ($1 < D_h < 4.9$ mm). Reprinted from Coleman, J. W. and Garimella, S., Two-phase flow regimes in round, square and rectangular tubes during condensation of Refrigerant R134a, *International Journal of Refrigeration*, **26**(1), pp. 117–128 (2003) with permission from Elsevier and International Institute of Refrigeration (iifir@iifir.org or www.iifir.org).

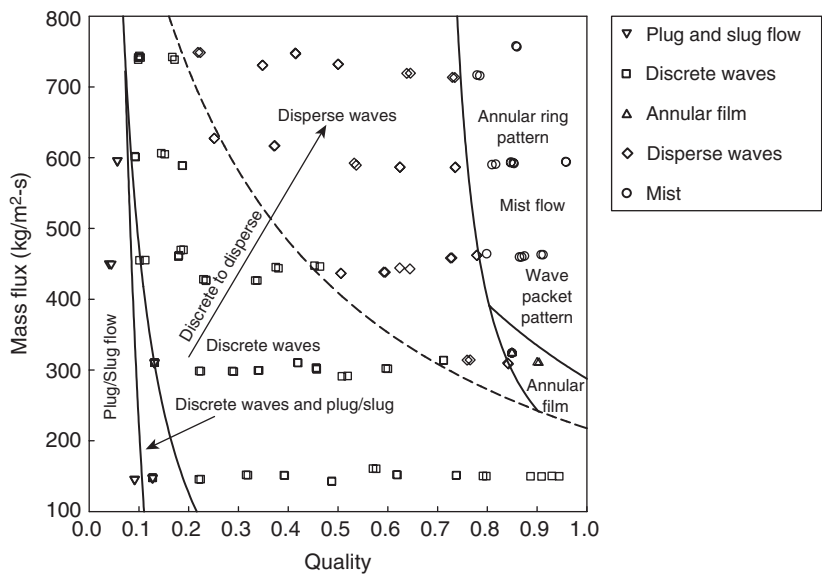


Fig. 6.11. Condensation flow regime map (4.91 mm). Reprinted from Coleman, J. W. and Garimella, S., Two-phase flow regimes in round, square and rectangular tubes during condensation of Refrigerant R134a, *International Journal of Refrigeration*, **26**(1), pp. 117–128 (2003) with permission from Elsevier and International Institute of Refrigeration (iifir@iifir.org or www.iifir.org).

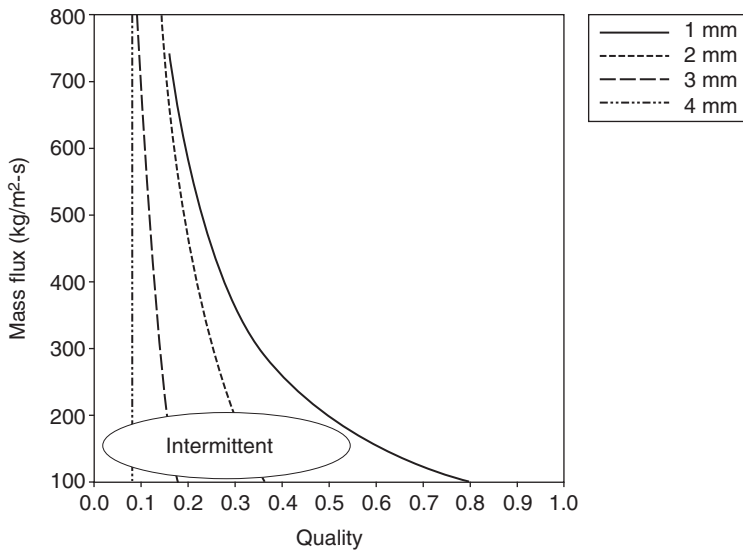


Fig. 6.12. Effect of D_h on intermittent flow regime. From Garimella, S., Condensation flow mechanisms in microchannels: Basis for pressure drop and heat transfer models, *Heat Transfer Engineering*, **25**(3), pp. 104–116 (2004).

between discrete and disperse waves is shown by the dashed line in this figure, although this transition occurs gradually.

The effect of hydraulic diameter on the flow regime maps is shown in Figs. 6.12 and 6.13. Figure 6.12, which depicts the transition from the intermittent regime for the four square tubes investigated, shows that the size of the intermittent regime increases as D_h decreases, with this effect being greater at the lower mass fluxes. The large increase in the size of the intermittent regime in the smaller hydraulic diameter tubes is because surface tension achieves a greater significance in comparison with gravitational forces at these dimensions. This also occurs because in square channels, it is easier for the liquid to be held in the sharp corners, counteracting to some extent, the effects of gravity. This facilitates plug and slug flow at higher qualities as the hydraulic diameter is decreased. Figure 6.13 shows that the 4-mm tube map is dominated by the wavy flow regime (with an absence of the annular film flow pattern). As D_h is decreased, the annular flow regime appears and occupies an increasing portion of the map. Thus, for the 4-mm tube, the effects of gravity dominate, resulting in most of the flow regime map being covered by the wavy flow regime. As the hydraulic diameter decreases, the effects of surface tension increasingly counteract the effects of gravity, promoting and extending the size of the annular film flow pattern region instead of the more stratified wavy flow regime. Thus, as D_h decreases, the wavy flow regime is increasingly replaced by the annular flow regime, and is non-existent in the $D_h = 1$ -mm tube. Furthermore, surface tension stabilizes the waves, which leads to more discrete waves at small diameters.

The effect of tube shape was investigated using maps for circular, square, and rectangular tubes of approximately the same $D_h \sim 4$ –4.9 mm (Fig. 6.14). This figure shows that the

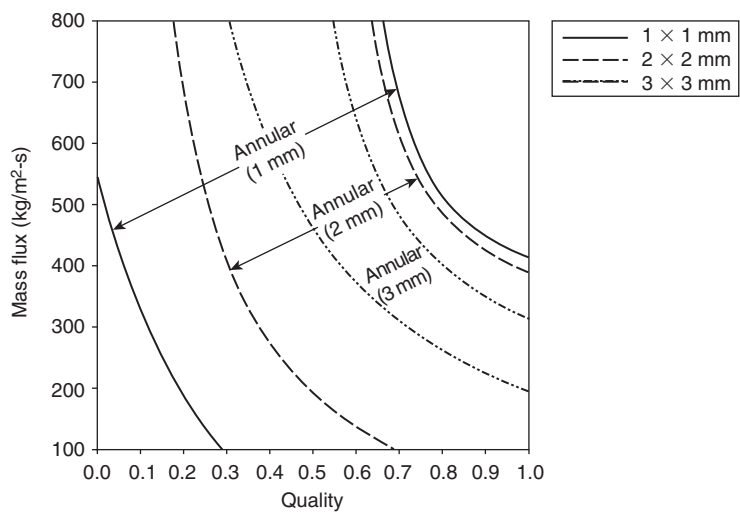
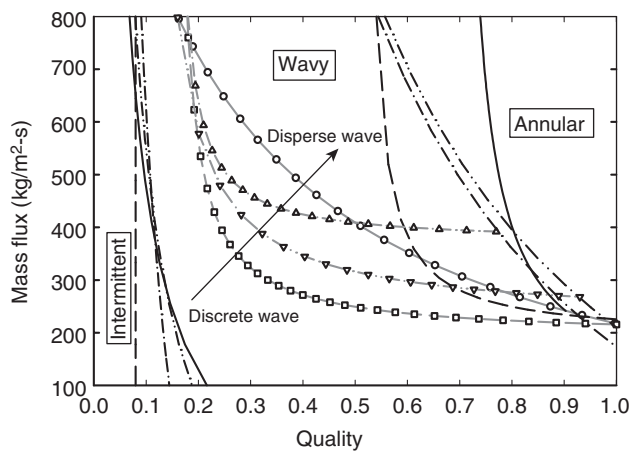


Fig. 6.13. Effect of D_h on annular flow regime. From Garimella, S., Condensation flow mechanisms in microchannels: Basis for pressure drop and heat transfer models, *Heat Transfer Engineering*, **25**(3), pp. 104–116 (2004).



Major transitions	Discrete-to-disperse wave
— Round (4.91 mm)	—○—
— Square (4 × 4 mm)	—□—
— Rectangular 4 (H) × 6 (W) mm	—△—
— Rectangular 6 (H) × 4 (W) mm	—▽—

Fig. 6.14. Effect of tube shape on flow regime transitions. From Garimella, S., Condensation flow mechanisms in microchannels: Basis for pressure drop and heat transfer models, *Heat Transfer Engineering*, **25**(3), pp. 104–116 (2004).

intermittent regime is larger in the round tube than in the square tube at lower mass fluxes and approximately the same at higher mass fluxes. The extent of the intermittent regime for the rectangular tubes is in between that of the circular and square tubes. The wavy flow regime is also larger in the round tube. The square and rectangular channels help liquid retention in the corners and along the entire circumference of the tube leading to annular flow, rather than preferentially at the bottom of the tube as would be the case in the wavy flow regime. In the 4×6 -mm and 6×4 -mm tubes, the larger aspect ratio results in a slight increase in the size of the intermittent regime at the lower mass fluxes, and a small reduction in the size of this regime at the higher mass fluxes. However, these effects are small, and it can be concluded that this transition line is only weakly dependent on the aspect ratio. The smaller aspect ratio also results in a larger annular film flow pattern region, which is to be expected because of the reduced influence of gravity for the tubes with the smaller height. Discrete waves are more prevalent in the round tube compared to the square and rectangular tubes. It was also found that the smaller aspect ratio results in a smaller wavy flow regime but with a larger fraction of discrete waves. At the higher mass fluxes, the effect of the aspect ratio is negligible. The increase in the annular film flow pattern region was more pronounced in the smaller hydraulic diameter tubes tested by them, perhaps due to the greater influence of surface tension. Thus, while tube shape had some effect on the transitions between the various flow regimes, the influence of hydraulic diameter was found to be far more significant.

A two-part study on flow regimes and heat transfer during condensing flows in channels with $3.14 < D < 21$ mm has also appeared recently (El Hajal *et al.*, 2003; Thome *et al.*, 2003). Although this work is primarily on large channels, the comprehensive nature of the database used for model development warrants discussion in this chapter. However, due to the highly coupled nature of the flow regime (El Hajal *et al.*, 2003) and heat transfer parts (Thome *et al.*, 2003), it is presented in a subsequent section on heat transfer.

6.2.3. Summary observations and recommendations

The above discussion has shown that numerous studies have been conducted to understand two-phase flow in small diameter channels. The preponderance of studies is on adiabatic air–water flows. While these flows have historically provided some understanding of condensation phenomena, many of the discrepancies between the behavior observed in these studies and the actual flow regimes during the condensation process can be attributed to the substantially different properties of the air–water pair compared to refrigerant vapor/liquid pair. It also appears that video recording technology is affording investigators the ability to capture every nuance of two-phase flow in great detail. High-speed video presents the investigator with a plethora of images separated in time by very small increments. While this is certainly advantageous in understanding the intricacies of two-phase flow, it has led to the further proliferation of creative, confusing, and vague definitions of flow patterns. Just the number of flow patterns cited in this chapter alone would approach about 50! There are many *definitions* with relatively less *distinction*. Flow patterns from different investigators can be as easily thought to agree as not, depending on the interpretation of these terms. As one who has himself pored over numerous frames of high-speed video, it is easy to understand how each researcher attempts to capture every nuance of a dynamic

bubble or a wave in a description of the pattern. It is not clear whether such detailed descriptions have led to a significant advancement in the quantification of the relevant physical phenomena that are responsible for these mechanisms in the first place. These minute distinctions between flow patterns would only be useful if they lead to quantitative models of essential features such as interfacial area, shear, slip, void fraction, momentum coupling, and ultimately, heat transfer and pressure drop.

The summary evaluation of the above-mentioned studies is as follows:

- (1) Adiabatic flow patterns are now available for a wide range of microchannels, mostly using air or nitrogen/water mixtures, all the way down to 25 μm . Extrapolation of air–water flow patterns to condensing refrigerant applications must be done with caution, however.
- (2) Many of the studies on small circular and narrow rectangular channels were conducted on co- or countercurrent vertical upflow, which is an orientation seldom used in condensation.
- (3) It has now been very well documented that gravitational forces have little significance in the small channels ($D < \sim 1$ mm) of interest in this book. This has been validated through observations of symmetric films, bubbles and slugs, and also flow patterns independent of channel orientation.
- (4) In the channels with $1 < D < 10$ mm, the flow patterns can broadly be classified as disperse, annular, wavy, and intermittent. Most of the phase-change studies in this size range have focused on channels with $D > 3$ mm, and the primary focus of most of these investigations has been to understand gravity-dominated versus shear-controlled condensation.
- (5) In channels with $D < 1$ mm, it appears that the primary patterns are some kind of slug/plug flow, a transition region designated as liquid ring by some investigators, and annular flow (with some mist flow at high qualities and mass fluxes).
- (6) Maps and transition criteria such as those by Taitel–Dukler (1976) are tempting to use because of their analytical basis; however, rarely do they predict condensation phenomena in microchannels – the original investigators perhaps never intended for them to be applied in this manner.
- (7) For the ~ 5 -mm channels, simple criteria such as those by Breber *et al.* (1980), Tandon *et al.* (1982), and Soliman (1982; 1986) may suffice, with minor modifications to match the application under consideration to distinguish between gravity and shear-controlled condensation. The more recent descriptive reporting of flow patterns by Dobson and Chato (1998) may also be used to obtain qualitative insights.
- (8) While flow pattern descriptions are available for channels with $D < \sim 5$ mm, and even for channels in the 50–250 μm range, explicit equations that quantify the transition criteria are still missing. A combination of the analytical approaches of Tabatabai and Faghri (2001), some of the analyses of Mishima and Ishii (1996), and the ongoing work of Kawahara, Kawaji, and others (Kawahara *et al.*, 2002; Chung and Kawaji, 2004) can be brought to bear to obtain such criteria.
- (9) In addition, transition criteria that are applicable over a wide range of fluid properties, operating conditions, and channel sizes must be developed based on the underlying forces and validated by the detailed experimentally obtained phase-change maps such as those of Coleman and Garimella (2000a, b; 2003) and Garimella (2004).

- (10) Similarly, the investigators of microchannels with $D \ll 1$ mm should also test condensation processes to supplement the information gathered from adiabatic flow visualization studies.

The assignment of flow regimes for nine representative cases (combinations of mass fluxes and qualities) for condensation of refrigerant R-134a in a 1-mm diameter channel using several of the prominent transition criteria is illustrated in Example 6.1.

6.3. Void fraction

6.3.1. Conventional tubes

An important parameter for the calculation of heat transfer coefficients, and more so pressure drops, is the void fraction in two-phase flow. The void fraction also determines the amount of fluid to be charged into a closed loop system such as a refrigeration cycle. Void fraction is simply the ratio of the cross-sectional area A_g occupied by the gas, to the total cross-sectional area of the channel (see Table 6.2):

$$\alpha = \frac{A_g}{A} \quad (6.19)$$

The calculation of this parameter is an essential step and provides closure to the set of equations that must be solved to estimate the pressure drop and heat transfer in two-phase flow. While the vapor quality x is a thermodynamic quantity determined by the state of the two-phase mixture, the void fraction depends on the characteristics of the flow, and has been the subject of several investigations. The slip, that is, the ratio of the velocities of the two phases, is required to enable computation of the void fraction. The simplest assumption that can be made is of homogeneous flow, where it is assumed that the vapor- and liquid-phase velocities are equal, and that the two phases behave like a single, uniform mixture that has representative average properties, which yields the following expression:

$$\alpha = \frac{x\rho_v}{(1-x)/\rho_l + x/\rho_v} \quad (6.20)$$

While the homogeneous model is in fact quite arbitrary, and serves as a starting point for the more representative models of void fraction, it has gained some acceptance for the modeling of microchannels, as will be discussed later. Void fraction models for conventional channels are readily available in textbooks such as those by Carey (1992), Collier and Thome (1994), and Hewitt *et al.* (1994); therefore, the more prominent correlations are simply presented here without discussion. While the details of the flow patterns must be taken into account to obtain models based on the physical phenomena, several of the more widely used correlations often assume annular flow and relate the void fraction to a parameter that resembles the Martinelli parameter X , often X_{tt} (which assumes turbulent flow in both phases). Incorporating the appropriate expressions for the pressure drops in the two phases, these expressions can be represented by the following generic expression (Butterworth, 1975):

$$\alpha = \left[1 + B_B \left(\frac{1-x}{x} \right)^{n_1} \left(\frac{\rho_v}{\rho_l} \right)^{n_2} \left(\frac{\mu_l}{\mu_v} \right)^{n_3} \right]^{-1} \quad (6.21)$$

Table 6.2

Summary of void fraction studies.

Investigator	Hydraulic diameter	Fluids	Orientation	Range/ applicability	Techniques, basis, observations
Conventional tubes					
Premoli <i>et al.</i> (1971)					<ul style="list-style-type: none"> • Slip ratio-based correlation
Smith (1969)	6 mm	Boiling heavy water	Vertical	$0.7 < p < 5.9 \text{ MPa}$ $0 < x < 0.38$ $650 < G < 2050 \text{ kg/m}^2\text{-s}$ $380 < q'' < 1200 \text{ kW/m}^2$	<ul style="list-style-type: none"> • Semi-empirical model • Assumed stratified annular flow (liquid-phase) with liquid entrainment in vapor-phase (homogeneous mixture phase), equal velocity head in both phases
	38 mm	Boiling water	Horizontal, vertical	$1.725 < p < 14.5 \text{ MPa}$ $0.003 < x < 0.17$ $750 < G < 1950 \text{ kg/m}^2\text{-s}$ $20 < q'' < 140 \text{ kW/m}^2$	<ul style="list-style-type: none"> • States that is model independent of flow regime, p, G, x; applicable to horizontal and vertical co-current flow • For $K = 0.4$, applicability assumed only for circular tubes • Not recommended for $x < 0.01$ in boiling flow (due to thermal inequilibrium)
	11 mm	Air–water	Vertical	Atmospheric pressure $0.005 < x < 0.525$ $50 < G < 1330 \text{ kg/m}^2\text{-s}$	
Zivi (1964)	Several	Steam–water	Horizontal, vertical		<ul style="list-style-type: none"> • Analytical void fraction model (assuming annular flow), minimizes rate of energy dissipation • Three models: (I) without liquid entrainment and wall friction, (II) with wall friction, and (III) with liquid entrainment • Data show wall friction effect \ll effect of liquid entrainment • As p increases, model (I) approaches homogeneous model • Simplest model (I) widely used, does not rely on data
Tandon <i>et al.</i> (1985b)	6.1 mm	Boiling heavy water	Vertical	$0.7 < p < 6 \text{ MPa}$, $x < 0.41$ $650 < G < 2050 \text{ kg/m}^2\text{-s}$ $380 < q'' < 1200 \text{ kW/m}^2$ $0.24 < \alpha < 0.92$	<ul style="list-style-type: none"> • Semi-empirical void fraction model • Assumed annular flow without liquid entrainment in vapor-phase and turbulent flow in both phases • State that model performs as well as Smith's model (1969) and better than Wallis' (1969) and Zivi's (1964) correlations
	22 mm	Steam–water		Atmospheric pressure $x < 0.04$	

Yashar <i>et al.</i> (2001)	<ul style="list-style-type: none"> • Microfin tubes: 0.2-mm fin height • 7.3, 8.9 mm (evaporation) • 8.9 mm (condensation) 	R-134a, R-410A	Horizontal	$75 < G < 700 \text{ kg/m}^2\text{-s}$ $0.05 < x < 0.8$	<ul style="list-style-type: none"> • Measurements in condensing microfin tubes (uncertainty 10%) • Similar trends for microfin and smooth tubes • Lower void fractions compared to evaporation, for same G, x • No effect of fin arrangement (helix angle)
El Hajal <i>et al.</i> (2003)	8 mm	R-22, R-134a, R-236ea, R-125, R-32, R-410A	Horizontal (condensing)	$65 < G < 750 \text{ kg/m}^2\text{-s}$ $0.22 < p_s < 3.15 \text{ MPa}$ $0.15 < x < 0.88$	<ul style="list-style-type: none"> • Used earlier boiling maps (Kattan <i>et al.</i>, 1998a, b, c; Zurcher <i>et al.</i>, 1999) as basis • Deduced void fractions for annular flow from heat transfer database (Cavallini <i>et al.</i>, 2001; 2002a, b) and film thickness considerations • Logarithmic mean of homogeneous and Steiner (1993) models
Koyama <i>et al.</i> (2004)	7.52 mm (smooth) 8.86 mm (microfin)	R-134a	Horizontal (adiabatic)	$0.01 < x < 0.96$ $p = 0.8, 1.2 \text{ MPa}$ $G = 125, 250 \text{ kg/m}^2\text{-s}$ (smooth) $G = 90, 180 \text{ kg/m}^2\text{-s}$ (microfin)	<ul style="list-style-type: none"> • Void fraction increases as pressure decreases (smooth and microfin) • Smooth-tube data agree with Smith's (1969) and Baroczy's (1965) models • Microfin tube data lower than smooth tube values • Results different from Yashar <i>et al.</i> (2001), who reported similar values for both tube types • Yashar <i>et al.</i> (2001) correlation overpredicts microfin tube data • α in microfin tubes increases with increasing G, at low p, x • Model for stratified–annular and annular flow; reasonable agreement with data, especially at high x
Small channels					
Armand (1946)		Air–water	Horizontal	$\beta < 0.9$ atmospheric pressure	<ul style="list-style-type: none"> • Empirical correlation
Kariyasaki <i>et al.</i> (1991)	1, 2.4, 4.9 mm	Air–water	Horizontal	$0.1 < j_G < 25 \text{ m/s}$ $0.03 < j_L < 2 \text{ m/s}$	<ul style="list-style-type: none"> • Numerous curve-fits to match data without physical considerations
Mishima and Hibiki (1996)	1–4 mm	Air–water	Vertical	$0.0896 < j_G < 79.3 \text{ m/s}$ $0.0116 < j_L < 1.67 \text{ m/s}$	<ul style="list-style-type: none"> • Image processing from neutron radiography for non-intrusively measuring void fraction • Correlated void fraction using drift-flux model with empirical parameters for vertical bubbly and slug flow

(Continued)

Table 6.2
(Continued)

Investigator	Hydraulic diameter	Fluids	Orientation	Range/ applicability	Techniques, basis, observations
Hibiki and Mishima (1996)	1–4 mm	Air–water	Vertical	$j < 19 \text{ m/s}$	<ul style="list-style-type: none"> • Distribution parameter function of D, larger values for small channels than reported by Ishii (1977) for larger tubes • Agreed with Kariyasaki <i>et al.</i> (1992) correlation
Hibiki <i>et al.</i> (1997)	3.9 mm	Air–water	Vertical upward	$j_G = 0.131 \text{ m/s}$ $j_L = 0.0707 \text{ m/s}$	<ul style="list-style-type: none"> • Best agreement with 1-mm data • Technique also works for annular flow at high α in larger tubes • Correlation for radial void fraction profile for vertical slug flow
Mishima <i>et al.</i> (1997)	2.4 mm	Air–water	Vertical upward	$j < 8 \text{ m/s}$	<ul style="list-style-type: none"> • Neutron radiography image processing for variation of void fraction along channel length for slug flow • Rise of bubble tracked using high void fraction region • Merging of void fraction peaks indicated bubble coalescence
Kureta <i>et al.</i> (2001; 2003)	3, 5 mm	Steam–water	Vertical upward	$240 < G < 2000 \text{ kg/m}^2\text{-s}$	<ul style="list-style-type: none"> • Instantaneous and time-averaged 2-D α for subcooled boiling (at low α)
Triplett <i>et al.</i> (1999a)	1.1, 1.45 mm	Air–water	Horizontal (adiabatic)	$0.02 < j_G < 80 \text{ m/s}$ $0.02 < j_L < 8 \text{ m/s}$	<ul style="list-style-type: none"> • Volumetric void fraction from still photographs (rotational symmetry assumed, uncertainty $\sim 15\%$) • Void fraction increases with increasing gas velocity and decreases with increasing superficial liquid velocity • Homogeneous model best for slug and bubble flow, Premoli <i>et al.</i> (1971), Chexal <i>et al.</i> (Chexal and Lellouche, 1986; Chexal <i>et al.</i>, 1992; Chexal <i>et al.</i>, 1997), Lockhart–Martinelli (1949), Baroczy (1965) overpredict for annular and churn flow
Microgravity					
Elkow and Rezkallah (1997a, b)	9.525 mm	Air–water	Vertical upward (adiabatic)	$0.1 < j_G < 18 \text{ m/s}$ $0.07 < j_L < 2.5 \text{ m/s}$ $0.1 < \alpha < 0.9$	<ul style="list-style-type: none"> • PDF of void fluctuations at 1-g, μ-g with capacitance sensor • Average α in slug flow $\sim 10\%$ higher at μ-g • Larger α fluctuations in bubble and slug flow at 1-g • Fluctuations decreased in transitional and annular flow, due to increasing dominance of inertia forces • Compared with drift-flux model, at 1-g: power law distribution in slug flow, saddle-shaped distribution in bubbly flow; at μ-g, power law distribution for both flows

Lowe and Rezkallah (1999)	9.525 mm	Air–water	Vertical upward	$0.09 < j_G < 20.94$ m/s $0.04 < j_L < 3.03$ m/s $p = 89$ kPa, μ -g, 1-g	<ul style="list-style-type: none"> Capacitance sensor to measure α, identify flow regimes using time trace and PDF
Microchannels					
Serizawa <i>et al.</i> (2002)	20, 25, 100, 50 μ m	Air–water (steam–water)	Horizontal	$0.0012 < j_G < 295.3$ m/s $0.003 < j_L < 17.52$ m/s	<ul style="list-style-type: none"> α in bubbly and slug flow from video analysis Follows Armand (1946) and Kariyasaki <i>et al.</i> (1991) correlations
Kawahara <i>et al.</i> (2002)	100 μ m	Nitrogen–water	Horizontal	$0.1 < j_G < 60$ m/s $0.02 < j_L < 4$ m/s	<ul style="list-style-type: none"> Time-averaged void fraction and curve-fit from video analysis α increases with increasing homogenous void fraction. Very low α for $\beta < 0.8$, rapid increase for $\beta > 0.8$ Different from Serizawa <i>et al.</i> (2002) who found linear correlation to homogeneous α for similar diameters Low α at high gas flow rates indicates large slip ratios and weak momentum coupling between phases
Chung and Kawaji (2004)	50, 100, 250, 530 μ m	Nitrogen–water	Horizontal	$T = 22.9\text{--}29.9^\circ\text{C}$ $0.02 < j_G < 72.98$ m/s $0.01 < j_L < 5.77$ m/s	<ul style="list-style-type: none"> 530 μm: homogeneous model, 250 μm: Armand (1946) correlation, 50, 100 μm: Kawahara <i>et al.</i> (2002) correlation Slightly different constants for 50-μm channel
Chung <i>et al.</i> (2004)	96- μ m square	Nitrogen–water	Horizontal (adiabatic)	$0.000310 < Bo < 0.000313$ $0.00010 < We_{LS} < 25$ $0.000019 < We_{GS} < 9$ $1 < Re_{LS} < 438$ $1 < Re_{GS} < 612$	<ul style="list-style-type: none"> Kawahara <i>et al.</i> (2002) correlation holds for 96 μm square channel
Kawahara <i>et al.</i> (2005)	50, 75, 100, 251 μ m	Water–Nitrogen, Ethanol–water/nitrogen	Horizontal	$0.08 < j_G < 70$ m/s $0.02 < j_L < 4.4$ m/s	<ul style="list-style-type: none"> No effects of fluid properties 50-, 75-, 100 μm data follow Kawahara <i>et al.</i> (2002) correlation, 251 μm data follow linear Armand (1946) correlation Used to demarcate micro-/minichannels (100–251 μm)

A convenient tabulation of the leading coefficient B_B and the exponents $n_1 \dots n_3$ for this model appears in Carey (1992) for the Zivi (1964) entropy minimization model, the Wallis (1969) separated cylinder model, the Lockhart–Martinelli (1949) model, the Thom (1964) correlation, and the Baroczy (1965) correlation. Hewitt *et al.* (1994) also provide the following correlation developed by Premoli *et al.* (1971) based on the slip ratio u_G/u_L :

$$S = 1 + E_1 \left[\left(\frac{y}{1 + yE_2} \right) - yE_2 \right]^{1/2} \quad (6.22)$$

where $y = \beta/1 - \beta$, and β is the volume ratio (also equivalent to the homogeneous void fraction):

$$\beta = \frac{x\rho_L}{x\rho_L + (1 - x)\rho_G} \quad (6.23)$$

The parameters E_1 and E_2 are given by:

$$\begin{aligned} E_1 &= 1.578 \text{Re}_{\text{LO}}^{-0.19} \left(\frac{\rho_L}{\rho_G} \right)^{0.22} \\ E_2 &= 0.0273 \text{We}_{\text{LO}} \text{Re}_{\text{LO}}^{-0.51} \left(\frac{\rho_L}{\rho_G} \right)^{-0.08} \end{aligned} \quad (6.24)$$

where $\text{Re}_{\text{LO}} = GD/\mu_L$ and $\text{We}_{\text{LO}} = G^2 D/\sigma\rho_L$. Once the slip ratio is calculated using the above equations, the void fraction is obtained as follows:

$$\alpha = \frac{x}{x + S(1 - x)\rho_G/\rho_L} \quad (6.25)$$

Several investigators have also used the void fraction by Smith (1969), which was based on an annular flow assumption, and also assumed equal velocity heads of the core and annular film flows. Smith stated that this correlation, given below, can be used irrespective of flow regime, pressure, mass flux, quality, and other parameters:

$$\alpha = \left\{ 1 + \left(\frac{\rho_G}{\rho_L} \right) \left(\frac{1 - x}{x} \right) \times \left[0.4 + 0.6 \sqrt{\frac{\left(\frac{\rho_L}{\rho_G} \right) + 0.4 \left(\frac{1 - x}{x} \right)}{1 + 0.4 \left(\frac{1 - x}{x} \right)}} \right] \right\}^{-1} \quad (6.26)$$

Tandon *et al.* (1985b) developed an analytical model for the void fraction in annular flows. They assumed an axi-symmetric annular film and a core with no liquid entrainment, and turbulent flow in both phases, which was justified based on Carpenter and Colburn's (1951) finding that at high gas velocities, the liquid phase laminar–turbulent transition could occur at $\text{Re}_L \sim 240$. Frictional pressure drops were computed using the Lockhart–Martinelli (1949) method, and the von Karman universal velocity profile was used to represent the velocity distribution in the liquid film. They found good agreement with data from Isbin *et al.* (1957) for steam–water flow through a 22-mm tube, and Rouhani and Becker (1963) for boiling of steam in 6.1-mm vertical tubes, and also with the correlation of Smith *et al.*

(1969). The void fraction is related to the liquid film Reynolds number and the Martinelli parameter as follows:

$$\alpha = \begin{cases} 1 - 1.928 \text{Re}_L^{-0.315} [F(X_{tt})]^{-1} + 0.9293 \text{Re}_L^{-0.63} [F(X_{tt})]^{-2} & 50 < \text{Re}_L < 1125 \\ 1 - 0.38 \text{Re}_L^{-0.088} [F(X_{tt})]^{-1} + 0.0361 \text{Re}_L^{-0.176} [F(X_{tt})]^{-2} & \text{Re}_L > 1125 \end{cases} \quad (6.27)$$

where $F(X_{tt}) = 0.15[X_{tt}^{-1} + 2.85X_{tt}^{-0.476}]$.

A review of the applicability of several different void fraction models appears in Rice (1987), who pointed out that the choice of the void fraction model affects refrigerant charge prediction to a significant degree, and that models based on non-refrigerant fluids, geometries, and flow conditions yield high levels of uncertainty when applied to refrigerants. Improper charge prediction can lead to problems in off-design and transient performance.

Yashar *et al.* (2001) pointed out that commonly used void fraction models (Smith, 1969; Wallis, 1969; Premoli *et al.*, 1971) are best suited for evaporation applications due to their basis in air–water flows or in water boiling applications. As stated previously in this chapter, air–water and steam–water mixtures are characterized by low gas-phase densities, whereas in condensation, particularly of refrigerants, the vapor-phase density is much higher due to the higher pressures involved. Due to these higher vapor-phase densities, the vapor velocities are lower, which favors stratified flows, and leads to a dependence of the void fraction on mass flux – a feature that is often not included in several of the widely used models. Noting that transitions between stratified and annular regions are in fact gradual due to the movement of the liquid film up around the circumference of the tube with increasing velocities, Hurlburt and Newell (1999) developed a model for the non-uniform film thickness during this stratified–annular transition. (It was pointed out in the previous section that other investigators have refereed to this region as semi-annular or wavy flow.) Graham *et al.* (1999) attempted to account for the dependence of the void fraction on the non-uniform film thickness by using the Froude rate (Yashar *et al.* 2001), a parameter that compares the vapor kinetic energy to the energy required to move the liquid phase upward along the circumference. Thus, the Froude rate parameter is the Froude number multiplied by the square root of the vapor-to-liquid mass flow rate ratio:

$$\text{Ft} = \left[\frac{G^2 x^3}{(1-x) \rho_g^2 g D} \right]^{0.5} \quad (6.28)$$

They reasoned that variation of the void fraction during the transition from stratified to annular flow would be accounted for by this parameter (vapor kinetic energy/gravitational drag) combined with the Lockhart–Martinelli parameter (viscous drag/vapor kinetic energy), and proposed the following expression:

$$\alpha = \left[1 + \frac{1}{\text{Ft}} + X_{tt} \right]^{-0.321} \quad (6.29)$$

In the above expression, both phenomena are assumed to act independently. Yashar *et al.* (2001) measured void fractions during condensation in microfin (0.2-mm fin height) tubes

of 8.9-mm diameter. Essentially, linked shutoff valves were actuated during tests to isolate the inventory of the two-phase mixture in the test section, which provided the volume-averaged void fraction for the given test condition. (It should be noted that this technique, used by many investigators, does not provide the area fraction at a cross-section of the tube, which is the more relevant parameter, but rather a volumetric average.) These tests showed that the trends for smooth and microfin tubes were similar and that for evaporation, the void fraction was relatively insensitive to mass flux. However, mass flux effects were seen in condensation, particularly at low mass fluxes ($G < 200 \text{ kg/m}^2\text{-s}$), presumably due to the larger vapor densities at condensing conditions.

Koyama *et al.* (2004) investigated void fractions for the adiabatic flow of R-134a in horizontal 7.52-mm smooth and 8.86-mm microfin tubes over the quality range $0.01 < x < 0.96$ using quick closing valves, an approach similar to that used by Yashar *et al.* (2001). The void fractions in the smooth tube agreed well with the Smith (1969) and Baroczy (1965) correlations. The void fractions were lower at the higher pressures, whereas the effect of mass flux was minimal. They also found that the void fractions in the microfin tube were lower than those in the smooth tube; thus the smooth-tube void fraction models were unable to predict the experimental values for the microfin tube. They stated that because of the higher pressure drop in the microfin tubes, the mean liquid velocity is lower and the liquid occupies a larger portion of the cross-section, which leads to lower void fractions in the microfin tubes. The void fraction in microfin tubes was found to increase with an increase in mass flux, particularly at low pressures and qualities. They also developed models for the void fraction in microfin tubes for stratified-annular and annular flow. They assumed that the liquid flows at the bottom of the tube and also fills the grooves around the whole circumference in stratified-annular flow. For annular flow, they assumed that the grooves were filled uniformly. Using these assumptions, they iteratively solved simple momentum balance equations between the vapor and liquid regions to obtain the void fraction for the experimental conditions. They found reasonably good agreement between the experimental and numerically predicted values, especially at high vapor qualities.

6.3.2. Small channels

For the small diameter range, Kariyasaki *et al.* (1991) measured void fraction in 1-, 2.4-, and 4.9-mm tubes and proposed several empirical curve-fits to the measured void fractions in small regions as a function of the homogeneous volume fraction (see Table 6.2):

$$\begin{array}{ll}
 \beta < \beta_A: & \alpha = \beta \\
 \beta_B < \beta < 0.6 \text{ (intermittent flow):} & \alpha = 0.833\beta \\
 \beta_B < \beta, 0.6 < \beta < 0.95 \text{ (intermittent flow):} & \alpha = 0.69\beta + 0.0858 \\
 \beta_B < \beta, 0.95 < \beta \text{ (annular and intermittent flow):} & \alpha = 0.83 \log(1 - \beta) + 0.633
 \end{array} \tag{6.30}$$

where β_A and β_B are also empirically derived transition points. While the above correlation matched their data, it appears to have been derived simply based on statistical curve-fits to follow the data closely, and the trends exhibited show numerous unrealistic discontinuities, changes in slope and inflections for which no physical rationale is provided. The first intermittent flow correlation above is the so-called Armand (1946) correlation.

Mishima and Hibiki (1996) used neutron radiography to conduct flow visualization studies on air–water flows in 1–4-mm diameter tubes. The void fraction was correlated well by the drift-flux model with a new equation for the distribution parameter as a function of inner diameter. The drift-flux model was used to correlate the void fraction as follows:

$$u_G = j_G/\alpha = C_0 j + U_{Gj} \quad (6.31)$$

where u_G is the gas velocity, j is the mixture volumetric flux, $j = j_G + j_L$, C_0 is the distribution parameter, and U_{Gj} is the drift velocity. For each regime (bubbly, slug, annular and churn), the required distribution parameter was taken from Ishii (1977). However, in accordance with the findings of several other researchers (Gibson, 1913; Zukoski, 1966; Tung and Parlange, 1976; Kariyasaki *et al.*, 1992), the drift velocity in slug and bubbly flows was assumed to be zero, and the distribution parameter was fit to the following equation based on the data:

$$C_0 = 1.2 + 0.510e^{-0.691D} \quad (6.32)$$

where the tube diameter D is in mm. These findings were in good agreement with the results of Kariyasaki *et al.* (1992), who modeled their data in terms of the volumetric void fraction $\beta = j_G/(j_G + j_L)$. The distribution parameters resulting from the data and the above equation for the small diameter channels are larger than those reported by Ishii (1977) for larger channels. Mishima *et al.* (1993) also found this increase in C_0 for narrow rectangular channels, and attributed this trend to the centralized void profile and the laminarization of flow in these smaller and narrower channels. Hibiki and Mishima (1996) developed an approximate method for the processing of images obtained from neutron radiography, which was then used for non-intrusively measuring void fractions in air–water flows in tubes with $1 < D < 4$ mm. The agreement between the data and the predictions of the radiography technique was best at 1 mm, but the technique was deemed to be acceptable for annular flows with large void fractions in the larger tubes also. Hibiki *et al.* (1997) then used the neutron radiography method to measure radial void fraction distributions in vertical upward air–water flow in a 3.9-mm channel. An assumed power law or saddle-shaped void fraction profile was subsequently verified using measured integrated variations in the void fraction profile along the channel axis. A triple-concentric-tube apparatus with some channels filled with water or gas in different combinations provided baseline attenuations and ensured calibration of the experimental results. The method was demonstrated by developing the following equation for void fraction in slug flow:

$$\alpha_r = 0.8372 + \left[1 - \left(\frac{r}{r_w} \right)^{7.316} \right] \quad (6.33)$$

The variation in void fraction along channel length in slug flow was determined by Mishima *et al.* (1997), who used the images shown in the previous section on flow patterns (Fig. 6.2) to compute the void profile across the channel at intervals of 6.45 mm (Fig. 6.15). This figure shows that the high void fraction region moves upward with the rise of the slug bubble. Also, the merging of two peaks into one peak is illustrated, corresponding to the coalescence of two bubbles. Unesaki *et al.* (1998) later conducted Monte Carlo simulations for the triple-concentric-tube apparatus described above to further validate the technique.

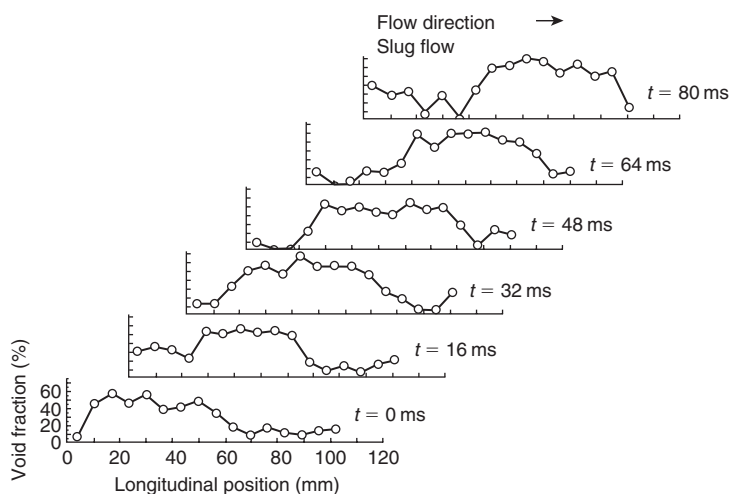


Fig. 6.15. Progression of void fraction profiles with time. Reprinted from Mishima, K., Hibiki, T. and Nishihara, H., Visualization and measurement of two-phase flow by using neutron radiography, *Nuclear Engineering and Design*, **175**(1–2), pp. 25–35 (1997) with permission from Elsevier.

This group (Kureta *et al.*, 2001; 2003) also measured instantaneous and time-averaged void fractions for subcooled boiling of water (at low void fractions) in narrow rectangular channels (3- and 5-mm gap) using neutron radiography in the mass flux range $240 < G < 2000 \text{ kg/m}^2\text{-s}$. Although their primary objective was to determine the point of net vapor generation and its effect on critical heat flux, their technique and results demonstrate the feasibility of non-intrusively obtaining temporally (0.89 ms) and spatially (2-D) resolved void fractions in two-phase flows in minichannels. A representative distribution of instantaneous void fractions obtained by them is shown in Fig. 6.16. Such temporal resolution is particularly helpful for flows more prevalent in minichannels (such as slug flows) with large temporal variations in void fraction. Fig. 6.17 shows void fraction profiles computed by averaging instantaneous values over 2 s (2250 images). Such techniques could also be applied to gain detailed insights into condensing flows.

Triplett *et al.* (1999a, b) used still photographs of flow patterns in 1.1- and 1.45-mm horizontal circular channels (although, as noted in the previous section, flow patterns were also recorded for semi-triangular channels) to obtain the volumetric void fraction. Bubbles in the bubbly flow pattern were assumed to be spheres or ellipsoids, while the bubbles in slug flow were assumed to consist of cylinders and spherical segments. Annular flow void fractions were estimated by averaging cylindrical segments of the vapor core. The estimated uncertainties in these void fractions were relatively high, 15%. Also, they were unable to reliably measure void fractions in slug-annular and churn flow, and assigned a void fraction of 0.5 to the portion of churn flow in which the gas phase was dispersed. In general they found that the void fraction increases with increasing gas superficial velocity, U_{GS} at a constant liquid superficial velocity, U_{LS} , and decreases with increasing U_{LS} for constant U_{GS} . They compared their results with the void fraction correlations of Butterworth (1975), Premoli *et al.* (1971), and the correlation of Chexal *et al.* (Chexal and Lellouche, 1986; Chexal *et al.*, 1992; Chexal *et al.*, 1997), which is based on the drift-flux model of Zuber

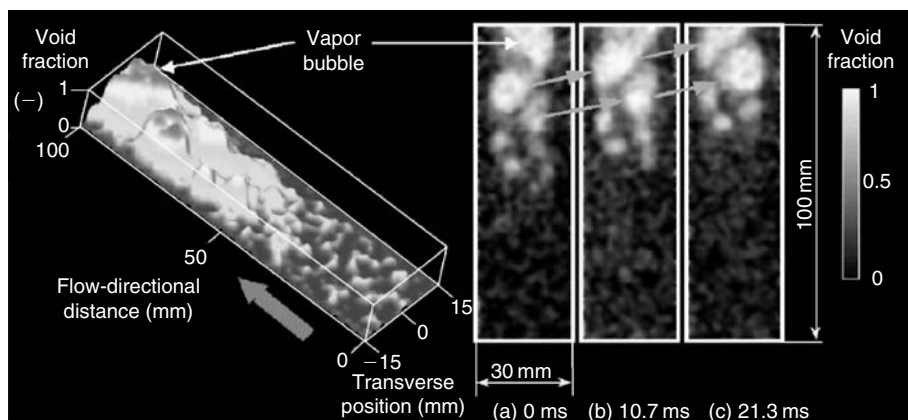


Fig. 6.16. Instantaneous 2-D void fraction profiles in narrow rectangular channels. Reprinted from Kureta, M., Hibiki, T., Mishima, K. and Akimoto, H., Study on point of net vapor generation by neutron radiography in sub-cooled boiling flow along narrow rectangular channels with short heated length, *International Journal of Heat and Mass Transfer*, **46**(7), pp. 1171–1181 (2003) with permission from Elsevier.

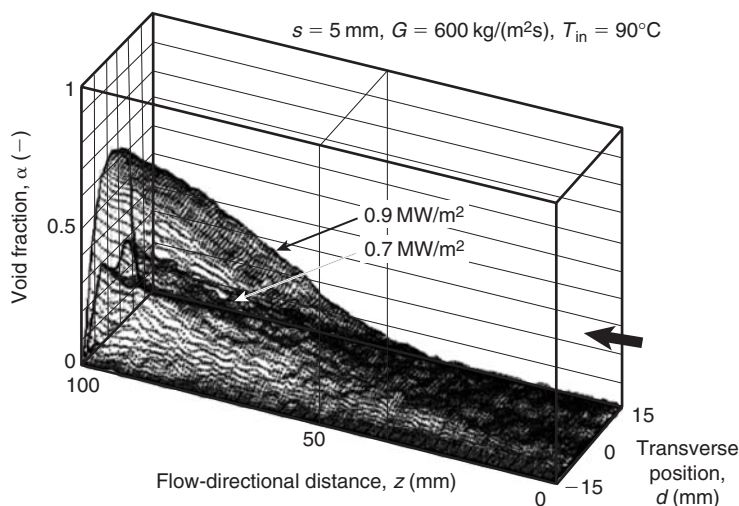


Fig. 6.17. Time-averaged 2-D void fraction in narrow rectangular channels. Reprinted from Kureta, M., Hibiki, T., Mishima, K. and Akimoto, H., Study on point of net vapor generation by neutron radiography in sub-cooled boiling flow along narrow rectangular channels with short heated length, *International Journal of Heat and Mass Transfer*, **46**(7), pp. 1171–1181 (2003) with permission from Elsevier.

and Findley (1965). They found that the homogeneous flow model was the best predictor of the measured void fractions in bubbly and slug flow, that is, at low U_{GS} values. For annular and churn flow, however, the homogeneous model and other empirical models significantly overpredicted the experimental values. They believe that this overprediction by the empirical correlations, typically based on annular flow in large channels, is due to the slip being greater in the larger channels than in microchannels.

6.3.3. Microgravity

As mentioned in the previous section on flow regimes, Rezkallah and co-workers have conducted investigations on two-phase flow in microgravity environments that pertains to flows in small diameter channels due to the decreased influence of gravity. Elkow and Rezkallah (1997a, b) conducted detailed measurements of void fraction fluctuations in earth normal (vertical upward) and microgravity conditions for air–water flow in a 9.53-mm tube. Such fluctuations were also measured by Jones and Zuber (1975) using signals from gamma densitometers, by Weisman *et al.* (1979) (discussed in the previous section) using pressure signals, by Das and Pattanayak (1993; 1994a, b; 1995a, b; 1996) and Matuszkiewicz *et al.* (1987) using impedance and conductivity probes, respectively, and by Geraets and Borst (1988) and Keska *et al.* (1992) using capacitance probes. Probability density functions (PDFs) of the void fraction fluctuations were larger in the bubble and slug flow regimes at 1-g compared to those at microgravity. This difference decreased as inertia forces became more predominant in transitional and annular flows. They inferred that at microgravity conditions, the slip velocity in bubble flow is almost zero – an observation made by several others cited in this chapter, and the bubble movement and liquid turbulence are highly suppressed. In slug flow, the average void fraction values at 1-g were found to be $\sim 10\%$ lower than those at microgravity. The void fraction signal fluctuated from high to low values, based on whether the channel was occupied by the liquid or the gas phase. At 1-g, bubbles coalesce readily due to contact between Taylor bubbles, leading to fluctuations in the void fraction (0–0.75), while at microgravity, Taylor bubbles did not interact with each other, resulting in much smaller void fraction fluctuations (0.3–0.55). The relationship between the volumetric void fraction β and the area-based void fraction α can be expressed as follows (see Table 6.2):

$$\frac{\langle \beta \rangle}{\langle \alpha \rangle} = C_0 + \frac{\langle \alpha U_{Gj} \rangle}{\langle \alpha \rangle \langle j \rangle} \quad (6.34)$$

where U_{Gj} is the previously defined drift velocity and j is the volumetric flux, ($j = U_{SG} + U_{SL}$). The distribution coefficient $C_0 = \langle \alpha j \rangle / (\langle \alpha \rangle \langle j \rangle)$ accounts for the non-uniform distribution of the void fraction over the cross-section of the tube, and depends on the flow regime and the void fraction profile. In microgravity flow, the second term above (drift velocity) was neglected (as was the case with other investigators discussed above), which yielded a distribution coefficient of 1.25 in bubbly and slug flow (centerline void fraction > wall void fraction). The distribution coefficient being the same for bubbly and slug flows at zero gravity is because of the slip between the two phases being negligible in both types of flow. While C_0 at 1-g in slug flow was close to this value ($C_0 = 1.17$), in bubbly flow, it was found to be 0.61, indicating a saddle-shaped void fraction profile, with a higher void fraction at the wall than at the center.

Lowe and Rezkallah (1999) developed this technique further, using a concave parallel plate capacitance sensor to measure void fractions for identifying flow regimes. They were able to define objective criteria for flow regime identification based on the void fraction PDF in conjunction with high-speed video images. An illustration of the different signals and PDFs for the three primary flow regimes of interest in microchannels is shown in

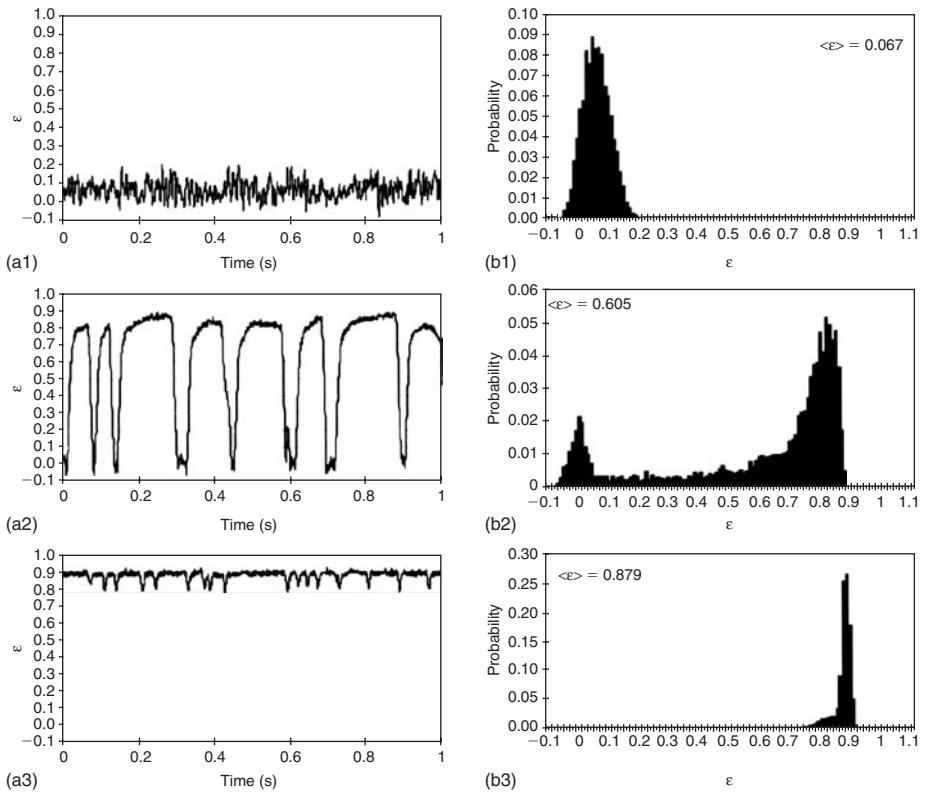


Fig. 6.18. Void fraction signals and PDF. Reprinted from Lowe, D. C. and Rezkallah, K. S., Flow regime identification in microgravity two-phase flows using void fraction signals, *International Journal of Multiphase Flow*, **25**(3), pp. 433–457 (1999) with permission from Elsevier.

Fig. 6.18. A low average void fraction signal with small fluctuations corresponding to the passage of the bubbles, and a PDF with a single narrow peak at the low end of the void fraction range characterizes bubbly flow. A void fraction signal with large fluctuations between high and low values corresponding to the passage of gas bubbles and liquid slugs characterizes slug flow. The corresponding PDF has two peaks. Annular flow exhibits a relatively constant void fraction of about 0.80–0.90, with the PDF showing a very narrow peak. Small dips in the void fraction trace correspond to the passage of disturbance waves. Such traces and PDFs were also used to identify transitions between the respective regimes. Packing densities of spherical and elongated bubbles were used to interpret the locations of the transitions from slug-annular flow.

6.3.4. Microchannels

Serizawa *et al.* (2002) studied air–water flow in microchannels (20, 25, and 100 μm) and steam–water flow in a 50- μm tube. Although a variety of flow regimes (discussed in

the previous section) were identified by them, cross-sectional-averaged void fractions were calculated from high-speed video pictures only for the bubbly and slug flow regimes (liquid ring flow was not included for void fraction analysis). The Armand (1946) correlation $\alpha = 0.833\beta$, discussed above in connection with the work of Kariyasaki *et al.* (1991), was recommended for these regimes (Table 6.2).

Kawahara *et al.* (2002) measured void fractions for nitrogen–water flow in a 100- μm tube by analyzing video frames and assigning a void fraction of 0 to the liquid slug, and a void fraction of 1 to a frame with a gas core surrounded by a smooth-thin liquid film or ring-shaped liquid film. Time-averaged void fractions were then calculated over several frames. For high liquid flow rates, gas-core flow with a thick liquid film was assigned a void fraction ($0 < \alpha < 1$), thus accounting for a finite film thickness surrounding the core in such flows. They found that the void fraction is not strongly dependent on j_L , and developed the following empirical fit for the void fraction in terms of the homogeneous void fraction:

$$\alpha = \frac{0.03\beta^{0.5}}{1 - 0.97\beta^{0.5}}$$

(6.35)

This variation of void fraction (Fig. 6.19) is significantly different from the linear relationship with the homogeneous void fraction described above. Thus, void fractions remain

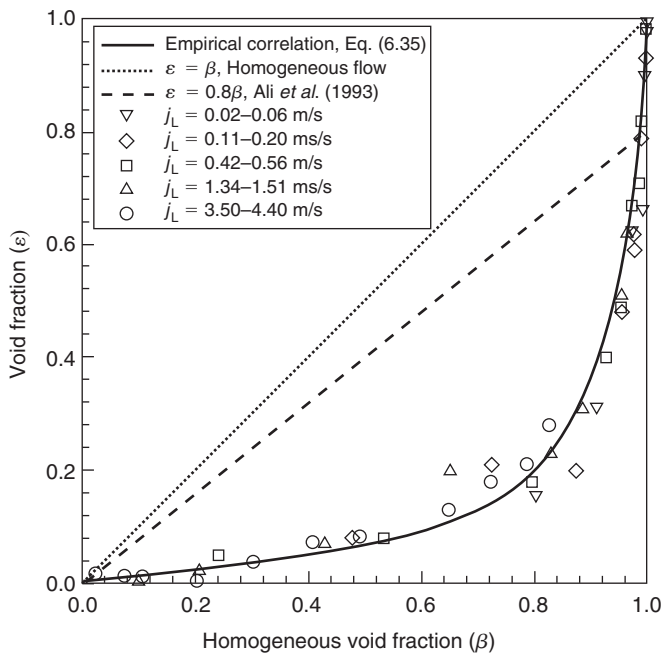


Fig. 6.19. Void fractions for air–water flow in 100- μm channels. Reprinted from Kawahara, A., Chung, P. M. -Y. and Kawaji, M. Investigation of two-phase flow pattern, void fraction and pressure drop in a microchannel, *International Journal of Multiphase Flow*, **28**(9), pp. 1411–1435 (2002) with permission from Elsevier.

low even at high values of β ($\beta < 0.8$), and increase steeply for $0.8 < \beta < 1$. They attributed this phenomenon to the observation that single-phase liquid flow occurred most frequently at high liquid flow rates for all gas flow rates, and also at low liquid and gas flow rates. Wall shear and surface tension resulted in channel bridging under such conditions, and the associated low average void fractions. At low liquid and high gas flow rates, gas-core flow surrounded by a liquid film with weak momentum coupling was seen. While the liquid flow was governed by wall shear and surface tension, the gas phase flowed without significant resistance due to the undeformed shape characteristic of the flow in such small channels observed by them. The nonlinear dependence of the area-based void fraction on the volumetric void fraction implies that slip ratios are much higher (as high as 16) in these channels compared to the much lower values seen in channels with $D_h > 1$ mm. It should be noted that these results contradict the results of Serizawa *et al.* (2002), who reported the adequacy of the Armand correlation for a similar range of D_h .

Chung and Kawaji (2004) investigated the effect of channel diameter on void fraction for the flow of nitrogen–water mixtures in circular 530-, 250-, 100-, and 50- μm channels. For the larger channels (530 and 250 μm), multiple images at each data point were analyzed by estimating the gas fraction volume as a combination of symmetrical shapes. For the smaller channels, the void fraction was estimated as described above in Kawahara *et al.* (2002). They found that the void fraction for the 530- μm channel was predicted well by the homogeneous flow model, and the void fraction for the 250- μm channel agreed well with the Armand-type correlation. However, the 100- and 50- μm channel void fractions followed the slow linear increase up to $\beta = 0.8$, followed by a steep exponential increase captured by Eq. (6.35) above that was developed by them earlier (Kawahara *et al.*, 2002). (Based on this latter work, however, they modified the leading constants for the 50- μm channel to 0.02 and 0.98 in the numerator and denominator, respectively.) They attributed the departure from homogeneous flow at high volumetric void fractions to a larger slip between the phases. This modified equation indicates a further decrease from the homogeneous model, even compared to the values for the 100- μm channel. They argued that in the larger (mini) channels, the wavy and deformed gas–liquid interface leads to more momentum exchange between the gas and liquid phases, which slows the flow of the gas bubbles, keeping the void fraction high. On the other hand, according to them, the lack of this momentum exchange in the microchannels leads to a lower void fraction. Chung *et al.* (2004) later confirmed that the coefficients in the void fraction correlation for circular 100- μm channels ($C_1 = 0.03$, and $C_2 = 0.97$) would apply to square channels with $D_h = 96 \mu\text{m}$.

Kawahara *et al.* (2005) further investigated the effect of fluid properties and diameter on void fraction. They tested the two-phase flow of water–nitrogen and ethanol–water/nitrogen gas mixtures (of varying ethanol concentrations) in 50-, 75-, 100-, and 251- μm circular channels. Their results showed that the void fraction was not sensitive to fluid properties over the range of diameters studied. The void fraction data for the 50-, 75-, and 100- μm channels agreed with the correlation of Kawahara *et al.* (2002), but the data for the 251- μm diameter channel followed the homogeneous flow type model of Armand (1946). They interpreted these results to imply that the boundary between “microchannels” and “minichannels” would lie between 100 and 251 μm .

6.3.5. Summary observations and recommendations

The above discussion has shown that void fraction models for conventional tubes have been developed on the basis of an assumption of homogeneous flow, or as a function of slip ratio, the Lockhart–Martinelli parameter, and those that incorporate some dependence on the mass flux. Many of these models assume annular flow regardless of the flow conditions. Also, several of these models were developed using data from air–water adiabatic flow, or evaporating flows, although in practice, they are routinely used for condensation also. Yashar *et al.* (2001) acknowledged the higher vapor phase densities in condensing flows compared to air–water or evaporating flows, and pointed out that this leads to lower vapor velocities, more stratified flows, and a dependence of the void fraction on mass flux. This group (Graham *et al.*, 1999) also used a Froude Rate parameter and developed a simple model for the changing void fraction from stratified to annular flows by accounting for the ratio of the vapor kinetic energy to the gravitational drag, combined with the Lockhart–Martinelli parameter, which accounts for the ratio of the viscous drag to the vapor kinetic energy. Linked shutoff valves were used by this group as well as by Koyama *et al.* (2004) to measure the vapor trapped in the test section, which yields the volumetric void fraction, but not the cross-sectional void fraction.

Mishima, Hibiki, and co-workers (Mishima *et al.*, 1993; Hibiki and Mishima, 1996; Mishima and Hibiki, 1996; Hibiki *et al.*, 1997; Mishima *et al.*, 1997; Kureta *et al.*, 2001; Kureta *et al.*, 2003) have used neutron radiography to measure the distribution of void fractions in 2-D in small channels, as well as the temporal evolution of the void fraction, for example, as the vapor and liquid phases in slug flow pass through the region of interest. Triplett *et al.* (1999a, b) have used image analysis to measure void fractions in these channels, while Rezkallah and co-workers (Elkow and Rezkallah, 1997a, b; Clarke and Rezkallah, 2001) have focused on non-intrusive measurement of void fraction using capacitance sensors in microgravity environments. Their work has also identified the use of time traces and PDF of the void fraction as signatures for the different kinds of flow regimes and transitions between them. Kawaji, Kawahara, and co-workers (Kawahara *et al.*, 2002; Chung and Kawaji, 2004; Chung *et al.*, 2004; Kawahara *et al.*, 2005) have used image analysis to obtain void fraction models for the <1 -mm range. Their work shows that the void fraction for channels of ~ 1 -mm diameter follows the homogeneous flow model, while smaller channels ($D < 250\ \mu\text{m}$) show much lower void fractions at volumetric void fraction $\beta < 0.8$, beyond which the void fraction sharply rises to the homogeneous value. Serizawa *et al.* (2002), on the other hand, found a variant of the homogeneous flow model to apply to smaller geometries.

As was the case for the identification of flow regimes and transition criteria, much of the work on void fractions has been conducted using adiabatic air–water flow. The few studies on void fractions in condensation are for larger diameters (~ 7 – 8 mm). Clearly, much additional research on void fractions in different flow regimes during condensation in microchannels is required.

Void fractions computed for representative conditions for R-134a condensing in a 1-mm tube at a pressure of 1500 kPa, at different mass fluxes and qualities using a wide variety of correlations are illustrated in Example 6.2. A comparison of the resulting void fractions is shown in Fig. 6.20.

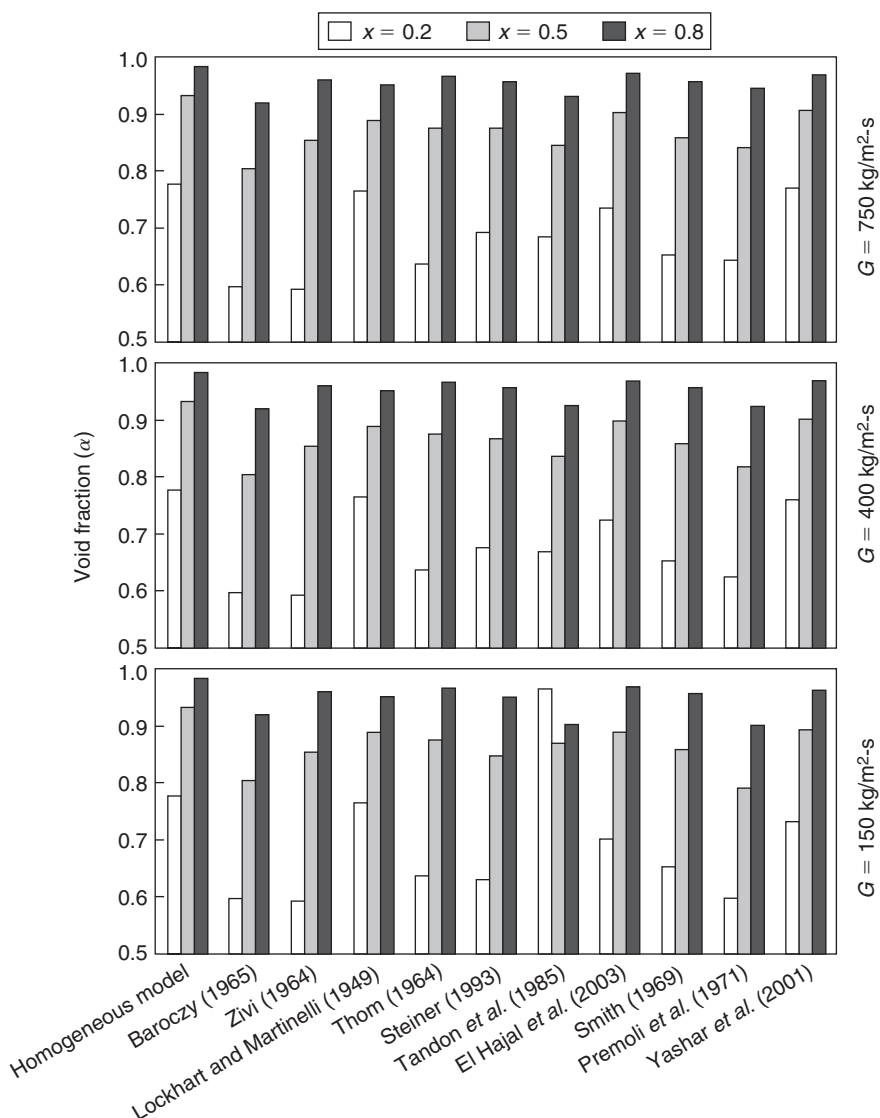


Fig. 6.20. Void fractions for R-134a condensing in a 1-mm tube.

6.4. Pressure drop

As was noted in the preceding sections, there is relatively little information on flow regimes and void fraction in condensing flows through microchannels. This is particularly true for pressure drops during condensation. Therefore, the available relevant information on pressure drops in condensing flows through relatively small channels and primarily adiabatic flows through microchannels is presented here (Table 6.3).

Table 6.3

Summary of pressure drop studies.

Investigator	Hydraulic diameter (mm)	Fluids	Orientation/ conditions	Range/ applicability	Techniques, basis, observations
Classical correlations					
Lockhart and Martinelli (1949)	1.5–26 mm	Air and benzene, kerosene, water, and various oils	Adiabatic		<ul style="list-style-type: none"> • ΔP correlated based on whether gas and liquid phases are laminar or turbulent • ΔP related in terms of two-phase multiplier ϕ^2 to corresponding liquid-or gas-phase pressure drop • Chisholm (1967) correlated ϕ_L^2 in terms of X_{tt}
Chisholm (1973)		Steam			<ul style="list-style-type: none"> • Modified procedure and equation developed by Baroczy (Baroczy and Sanders, 1961; Baroczy, 1966) to develop correlation based on liquid only ΔP
Friedel (1979; 1980)	$D > 1$ mm		Adiabatic	$\mu_l/\mu_v < 1000$	<ul style="list-style-type: none"> • Developed ϕ_{LO}^2 correlation from database of 25,000 points • Includes surface tension effects
Condensation or adiabatic liquid–vapor studies ($\sim 2 < D_h < \sim 10$ mm)					
Hashizume <i>et al.</i> (1985)	10 mm	R-12, R-22	Horizontal condensing	$570 < p < 1960$ kPa	<ul style="list-style-type: none"> • ΔP expressions for annular and stratified flow, liquid-and gas-phase velocity in terms of Prandtl mixing length • Stratified flow modeled as flow between parallel plates
Wang <i>et al.</i> (1997b)	6.5 mm	R-22, R-134a, R-407C	Horizontal adiabatic	$50 < G < 700$ kg/m ² -s $T = 2^\circ\text{C}, 6^\circ\text{C}, \text{ and } 20^\circ\text{C}$	<ul style="list-style-type: none"> • Modified Chisholm (1967) C for ϕ_L^2 for $G > 200$ kg/m²-s • Empirical correlation for ϕ_G^2, for $G < 200$ kg/m²-s
Hurlburt and Newell (1999)	3–10 mm	R-22, R-134a (Dobson, 1994) R-11, R-12, R-22 (Sacks, 1975)	Horizontal	$0.2 < x < 0.9$ $200 < G < 650$ kg/m ² -s	<ul style="list-style-type: none"> • Scaling equation to predict ΔP at new condition from available information at a different condition • Assumed bulk of condensation occurs in annular flow • Turbulent vapor and liquid films, law of wall assumed
Chen <i>et al.</i> (2001)	1.02, 3.17, 5.05, 7.02 mm 3.17, 5.05, 7.02, 9 mm	Air–water R-410A	Horizontal	Room temperature $50 < G < 3000$ kg/m ² -s $0.001 < x < 0.9$ 5°C and 15°C $50 < G < 600$ kg/m ² -s $0.1 < x < 0.9$	<ul style="list-style-type: none"> • Accounted for increased σ influence, decreased g influence • Poor agreement with Chisholm (1967), Friedel (1979; 1980), and homogeneous flow models • Modified homogeneous model to include Bo and We to account for effect of surface tension and mass flux

Wilson <i>et al.</i> (2003)	$D_h = 7.79, 6.37,$ 4.40, and 1.84	R-134a R-410A	Horizontal condensing	$T = 35^\circ\text{C}$ $75 < G < 400 \text{ kg/m}^2\text{-s}$	<ul style="list-style-type: none"> Flattened round smooth, axial, and helical microfin tubes ΔP increases as tube approaches rectangular shape
Souza <i>et al.</i> (1993)	10.9 mm	R-12 R-134a	Horizontal	$P_r = 0.07\text{--}0.12$ $200 < G < 600 \text{ kg/m}^2\text{-s}$ $0.1 < x < 0.9$	<ul style="list-style-type: none"> New correlation for ϕ_{LO}^2 Demonstrated effect of oil in refrigerant on pressure drop
Cavallini <i>et al.</i> (2001; 2002a, b)	8 mm	R-22, R-134a, R-125, R-32, R-236ea, R-407C, and R-410A	Horizontal tubes	$30 < T_{\text{sat}} < 50^\circ\text{C}$ $100 < G < 750 \text{ kg/m}^2\text{-s}$	<ul style="list-style-type: none"> Modified Friedel (1979) correlation to apply only to annular flow, whereas it had originally been intended for annular and stratified regimes
Air–water studies ($\sim 1 < D_h < \sim 10 \text{ mm}$)					
Zhao and Rezkallah (1995)	9.525 mm	Air–water	Vertical upward 1-g, μ -g	$0.1 < j_G < 18 \text{ m/s}$ $0.1 < j_L < 2.5 \text{ m/s}$	<ul style="list-style-type: none"> ΔP about the same for 1-g and μ-g, especially in annular flow Relatively good agreement with homogeneous, Lockhart and Martinelli (1949) and Friedel (1979; 1980) correlations
Fukano <i>et al.</i> (1989)	1, 2.4, and 4.9 mm	Air–water	Horizontal isothermal	$P_{\text{exit}} = 1 \text{ atm}$ $0.04 < j_G < 40$ $0.2 < j_L < 4$	<ul style="list-style-type: none"> Correlation for ΔP in bubbly, slug, plug, and annular flow Proposed a new slug flow model accounting for slug/bubble velocity ratios for different gas- and liquid-phase regimes, and for expansion losses as liquid flowed from the annular film surrounding the gas bubble into liquid slug region
Mishima and Hibiki (1996)	1–4 mm	Air–water	Vertical upwards	$0.0896 < j_G < 79.3 \text{ m/s}$ $0.0116 < j_L < 1.67 \text{ m/s}$	<ul style="list-style-type: none"> C in Chisholm (1967) correlation decreases for small D, proposed new correlation for C based on D_h
Triplett <i>et al.</i> (1999a)	Circular 1.1 and 1.45 mm, semi-triangular 1.09 and 1.49 mm	Air–water	Horizontal adiabatic	$0.02 < j_G < 80 \text{ m/s}$ $0.02 < j_L < 8 \text{ m/s}$	<ul style="list-style-type: none"> Homogeneous model predicted bubbly and slug flow data well at high Re_L Poor agreement in slug–annular and annular region, also in slug flow at very low Re_L Friedel (1979; 1980) correlation resulted in large deviations
Tran <i>et al.</i> (2000)	Circular 2.46 and 2.92 mm, rectangular $4.06 \times 1.7 \text{ mm}$	R-134a, R-12, R-113	Boiling	$138 < P < 856 \text{ kPa}$ $33 < G < 832 \text{ kg/m}^2\text{-s}$	<ul style="list-style-type: none"> Developed correlation for ΔP during boiling of refrigerants Trends similar to large-diameter tubes Proposed modified version of Chisholm (1973) correlation to account for surface tension effects

(Continued)

Table 6.3
(Continued)

Investigator	Hydraulic diameter (mm)	Fluids	Orientation/ conditions	Range/ applicability	Techniques, basis, observations
Zhao and Bi (2001b)	Equilateral triangular channels $D_h = 0.866$, 1.443, and 2.886 mm	Air–water	Vertical upward co-current	$0.1 < j_G < 100$ m/s For $D_h = 2.886$, 1.443 mm $0.08 < j_L < 6$ m/s For $D_h = 0.866$ mm $0.1 < j_L < 10$ m/s	<ul style="list-style-type: none"> Frictional ΔP correlated using Lockhart and Martinelli (1949) approach
Lee and Lee (2001)	Rectangular 20 mm wide Gap 0.4–4 mm	Air–water	Horizontal	$175 < Re_{LO} < 17700$ $0.303 < X < 79.4$	<ul style="list-style-type: none"> Commented on weaker coupling between phases in smaller channels, correlated parameter C in the two-phase multiplier (Chisholm, 1967) in terms of non-dimensional parameters to include surface tension effects
Condensation studies ($\sim 0.4 < D_h < \sim 5$ mm)					
Yang and Webb (1996b)	Rectangular plain: $D_h = 2.64$, Microfin: $D_h = 1.56$	R-12	Horizontal adiabatic	$400 < G < 1400$ kg/m ² -s $0.1 < x < 0.9$	<ul style="list-style-type: none"> ΔP in microfin tube higher than in plain tube Equivalent Re-based model for ΔP Concluded surface tension does not affect ΔP
Yan and Lin (1999)	2 mm	R-134a	Horizontal	$T = 40\text{--}50^\circ\text{C}$	<ul style="list-style-type: none"> Used Akers <i>et al.</i> (1959) equivalent mass velocity concept to correlate condensation ΔP

Zhang and Webb (2001)	3.25 and 6.25 mm Multiport extruded Al $D_h = 2.13$ mm	R-134a, R-22 R-404A	Adiabatic	$T = 20\text{--}65^\circ\text{C}$ $200 < G < 1000$ kg/m ² -s	<ul style="list-style-type: none"> Friedel (1979; 1980) correlation did not predict data well ΔP function of reduced pressure rather than density or viscosity ratio; proposed new correlation for ϕ_{LO}^2
Garimella <i>et al.</i> (2002; 2003a, b; 2005)	0.5–4.91 mm	R-134a	Horizontal	$T \sim 52^\circ\text{C}$ $0 < x < 1$ $150 < G < 750$ kg/m ² -s	<ul style="list-style-type: none"> Flow regime based models for intermittent and annular/mist/disperse flow regimes Intermittent flow model treats ΔP as combination of ΔP due to liquid slug, film–bubble interface, and transitions between slug and bubble, slug frequency deduced from ΔP data Annular flow model: interfacial friction factor derived from measured pressure drops correlated with Re_L, f_L, X, and surface tension parameter Combined model ensures smooth transitions across regimes
Air–Water Studies ($D_h < \sim 500$ μm)					
Kawahara <i>et al.</i> (2002)	100 μm	Nitrogen–water	Horizontal	$0.1 < j_G < 60$ m/s $0.02 < j_L < 4$ m/s	<ul style="list-style-type: none"> Homogeneous correlations did not predict data well Lockhart and Martinelli (1949) approach with Chisholm (1967) coefficient significantly overpredicted data Proposed new values for parameter C based on data
Chung and Kawaji (2004)	530, 250, 100, and 50 μm	Nitrogen–water	Horizontal	$T = 22.9\text{--}29.9^\circ\text{C}$ $0.02 < j_G < 72.98$ m/s $0.01 < j_L < 5.77$ m/s	<ul style="list-style-type: none"> Effect of diameter investigated New slug flow model based on work of Garimella <i>et al.</i> (2002; 2003a, b; 2005) for 50- and 100-μm tubes

6.4.1. Classical correlations

Pressure drops in conventional channels have long been calculated using three well-known correlations by Lockhart and Martinelli (1949), Chisholm (1973), and Friedel (1979; 1980), sometimes with modifications to account for the specific geometry or flow conditions under investigation. The Lockhart–Martinelli (1949) correlation was based on adiabatic flow of air and benzene, kerosene, water, and various oils flowing through 1.5–26-mm pipes, and the pressure drops were correlated based on whether the individual liquid and gas phases were considered to be in laminar or turbulent flow. As many of the separated flow correlations for small channels are also based on this basic methodology, a brief overview is presented here. The two-phase pressure drop is expressed in terms of two-phase multipliers to the corresponding single-phase liquid or gas-phase pressure drop:

$$\phi_L^2 = \frac{(dP_F/dz)}{(dP_F/dz)_L} \quad (6.36)$$

$$\phi_G^2 = \frac{(dP_F/dz)}{(dP_F/dz)_G} \quad (6.37)$$

$$\phi_{LO}^2 = \frac{(dP_F/dz)}{(dP_F/dz)_{LO}} \quad (6.38)$$

where ϕ^2 is the two-phase multiplier, the subscripts L and G refer to the flow of the liquid and gas phases flowing through the whole channel, and LO refers to the entire fluid flow occurring as a liquid phase through the channel. These multipliers are in turn most often correlated in terms of the Martinelli parameter $X = \left[\frac{(dP_F/dz)_L}{(dP_F/dz)_G} \right]^{0.5}$ (which has been referred to in the previous sections). Chisholm (1967) developed the following correlations for the two-phase multipliers of Lockhart and Martinelli:

$$\phi_L^2 = 1 + \frac{C}{X} + \frac{1}{X^2} \quad (6.39)$$

$$\phi_G^2 = 1 + CX + X^2 \quad (6.40)$$

where C depends on the flow regime of the liquid and gas phases. While these (Lockhart and Martinelli, 1949; Chisholm, 1967) correlations have shown considerable deviations from the data for small channels with phase-change flows, they continue to be the basis for many of the more recent correlations, as will be seen later in this section.

Chisholm (1973) modified the procedure and equations developed by Baroczy (Baroczy and Sanders, 1961; Baroczy, 1966) that account for fluid properties, quality, and mass flux based on steam, water/air, and mercury/nitrogen data to develop the following correlation:

$$\phi_{LO}^2 = 1 + (Y^2 - 1) [Bx^{(2-n)/2} (1-x)^{(2-n)/2} + x^{2-n}] \quad (6.41)$$

where n is the exponent for Reynolds number in the turbulent single-phase friction factor correlation, for example, $n = 0.5$ for the Blasius equation. The parameter Y is the Chisholm parameter:

$$Y = \left[\frac{(dP_F/dz)_{GO}}{(dP_F/dz)_{LO}} \right]^{0.5} \quad (6.42)$$

and B is given by:

$$\begin{aligned} B &= \frac{55}{G^{0.5}} & 0 < Y < 9.5 \\ &= \frac{520}{(YG^{0.5})} & 9.5 < Y < 28 \\ &= \frac{15,000}{(Y^2 G^{0.5})} & 28 < Y \end{aligned} \quad (6.43)$$

Friedel (1979; 1980) developed the following correlation based on a database of 25,000 points for adiabatic flow through channels with $d > 1$ mm:

$$\phi_{LO}^2 = E + \frac{0.324FH}{Fr^{0.045}We^{0.035}} \quad (6.44)$$

where

$$E = (1 - x)^2 + x^2 \left(\frac{\rho_L f_{GO}}{\rho_G f_{LO}} \right) \quad (6.45)$$

$$F = x^{0.78} (1 - x)^{0.24} \quad (6.46)$$

$$H = \left(\frac{\rho_L}{\rho_G} \right)^{0.91} \left(\frac{\mu_G}{\mu_L} \right)^{0.19} \left(1 - \frac{\mu_G}{\mu_L} \right)^{0.7} \quad (6.47)$$

and $Fr = G^2/gD\rho_{TP}^2$ and $We = G^2D/\rho_{TP}\sigma$, and f_{LO} and f_{GO} are the single-phase friction factors for the total fluid flow occurring as liquid and gas respectively. The two-phase mixture density is calculated as follows:

$$\rho_{TP} = \left(\frac{x}{\rho_G} + \frac{1-x}{\rho_L} \right)^{-1} \quad (6.48)$$

The above correlation is the more widely used correlation for vertical upward and horizontal flow, and is recommended by Hewitt *et al.* (1994) for situations where surface tension data are available, and by Hetsroni (1982) for $\mu_l/\mu_v < 1000$.

While these correlations have been used widely, often their predictive capabilities are not particularly good, primarily because investigators have tried to use them beyond their originally intended range of applicability, and also because these models do not account for the flow regimes that are established over these diverse ranges of conditions and geometries.

6.4.2. Condensation or adiabatic liquid–vapor studies ($\sim 2 < D_h < \sim 10$ mm)

Hashizume *et al.* (1985) conducted flow visualization and pressure drop experiments on refrigerants R-12 and R-22 flowing through horizontal 10-mm tubes over the range $20^\circ\text{C} < T < 50^\circ\text{C}$. They developed pressure drop expressions for annular and stratified flow, describing the liquid- and gas-phase velocity profiles in terms of the Prandtl mixing length. The pressure drop was modeled as $dP/dL = (4(\text{Re}^+)^2 \mu_L^2 / \rho_L D^3)$ where Re^+ is the friction Reynolds number. Stratified flow was modeled as flow between parallel plates with the liquid pool forming one of the parallel plates, with an equivalent gap between the plates derived in terms of the tube diameter, quality, and mass flux. Transition (wavy) region pressure drops were calculated by interpolating between the annular and stratified regions, with the corresponding transitions established by the modified Baker map developed by them (Hashizume, 1983). They later (Hashizume and Ogawa, 1987) tried to extend this work to air–water and steam–water flows, but found that the best agreement was with refrigerant data, and not with air–water or steam–water mixtures.

Wang *et al.* (1997b) measured pressure drops during the adiabatic flow of refrigerants R-22, R-134a, and R-407C in a 6.5-mm tube for the mass flux range $50 < G < 700$ kg/m²-s. They computed two-phase multipliers ϕ_G^2 analogous to the Lockhart–Martinelli (1949) correlation from the measured pressure drops, and tried to obtain the best fit for the C parameter in Chisholm's (1967) equation for the multiplier, because they found that C was strongly dependent on the flow pattern. For R-22 and R-134a, the intermittent flow data were predicted well with $C = 5$. For $G > 200$ kg/m²-s, wavy-annular flow was observed with the two-phases being turbulent, and the multipliers did not depend on the mass flux. For $G = 50$ and 100 kg/m²-s, there was a pronounced influence of the mass flux. They stated that for $G = 100$ kg/m²-s, the flow is not shear dominated, thus the waves do not reach the top of the tubes, and the pressure drop would therefore depend on the wetted perimeter, which in turn depends on the mass flux. However, for $G > 200$ kg/m²-s, even though the flow continues to be wavy (with a thicker film at the bottom), the waves do reach the top of the tube and render the tube completely wet, which makes the wetted perimeter relatively constant as the mass flux varies. Based on these considerations, they developed the following equations for the two-phase multiplier:

For $G > 200$ kg/m²-s:

$$\phi_G^2 = 1 + 9.4X^{0.62} + 0.564X^{2.45} \quad (6.49)$$

and for $G < 200$ kg/m²-s, the C parameter in the Chisholm (1967) correlation for the Lockhart–Martinelli (1949) multiplier was modified to include a mass flux dependence as follows:

$$C = 4.566 \times 10^{-6} X^{0.128} \text{Re}_{\text{LO}}^{0.938} \left(\frac{\rho_L}{\rho_G} \right)^{-2.15} \left(\frac{\mu_L}{\mu_G} \right)^{5.1} \quad (6.50)$$

Hurlburt and Newell (1999) developed scaling equations for condensing flows that would enable the prediction of void fraction, pressure drop, and heat transfer for a refrigerant at a given condition and tube diameter from the available results for another similar fluid (R-11,

R-12, R-22, and R-134a) operating at a different condition in the diameter range 3–10 mm. To achieve this, they assumed that the bulk of the condensation process occurs under annular flow conditions, and that even though in reality, the condensing film is non-uniform around the circumference, an equivalent average film thickness would suffice for the prediction of shear stress. They further considered that the primary resistance to heat transfer occurs in the viscous and buffer layers of the film, regardless of the actual thickness. The approach used for modeling the film and core flows was similar to that of Rohsenow *et al.* (Rohsenow *et al.*, 1957; Bae *et al.*, 1971; Traviss *et al.*, 1973), assuming turbulent vapor and liquid films and law-of-the-wall universal velocity and temperature profiles. (The liquid film was assumed to be turbulent even at low Re ($Re > 240$) due to interactions with the turbulent vapor core, based on the work of Carpenter and Colburn (1951).) They used the interfacial shear stress, rather than the void fraction, as an input to determine the liquid film thickness, which enabled them to capture the dependence of void fraction on mass flux. They used void fraction, pressure drop, and heat transfer data of Sacks (1975) for R-11, R-12, and R-22, and the R-22 and R-134a data of Dobson (1994) to validate their model. Using these considerations, they developed the following scaling equation for pressure drop prediction:

$$\begin{aligned} \Delta P_2 / \Delta P_1 = & (\rho_{g2} / \rho_{g1})^{-0.75} (\rho_{L2} / \rho_{L1})^{-0.25} (\mu_{g2} / \mu_{g1})^{-0.15} (\mu_{L2} / \mu_{L1})^{0.125} \\ & \times (D_2 / D_1)^{-1.0} (G_2 / G_1)^2 (x_2 / x_1)^{1.65} \left(\frac{1 - x_2}{1 - x_1} \right)^{0.38} \end{aligned} \quad (6.51)$$

This equation predicts a five-fold increase in pressure drop between R-22 and R-11, primarily due to the drastic difference in saturation pressure at 40°C (959 kPa for R-22, 175 kPa for R-11), which leads to a much higher vapor-phase density for R-22 (65.7 kg/m³) than for R-11 (9.7 kg/m³). This approach was considered to be valid for the quality range $0.2 < x < 0.8$, where annular flow prevails in general. Although there were some disagreements between the trends predicted by this equation and the experimental data, particularly in the effect of mass flux, the approach provides some general guidance for the modeling of annular flows.

Chen *et al.* (2001) attempted to account for the increased influence of surface tension and the decreased influence of gravity in tubes with $D < 10$ mm for fluids encompassing a wide range of properties, air–water (in 1.02-, 3.17-, 5.05-, 7.02 mm tubes) and R-410A (in 3.17-, 5.05-, 7.02-, 9.0 mm tubes). The air–water tests were conducted at room temperature, while the R-410A tests were conducted at 5°C and 15°C, somewhat lower than typical condensation temperatures of interest. Poor agreement was found between their pressure drop data and the predictions of the Chisholm (1967), Friedel (1979), and homogeneous flow (with average viscosity (Beattie and Whalley, 1982)) models. Therefore, they modified the homogeneous flow model by including the Bond number and the Weber number to account for the effects of surface tension and mass flux:

$$\begin{aligned} \frac{dP}{dz} = \frac{dP}{dz} \Big|_{\text{hom}} \Omega_{\text{hom}} \\ \Omega_{\text{hom}} = \begin{cases} 1 + (0.2 - 0.9 \exp(-Bo)) & Bo < 2.5 \\ 1 + (We^{0.2} / \exp(Bo^{0.3})) - 0.9 \exp(-Bo) & Bo \geq 2.5 \end{cases} \end{aligned} \quad (6.52)$$

where $We = G^2 D / \sigma \rho_m$ and $Bo = g(\rho_L - \rho_G) ((d/2)^2 / \sigma)$. They also developed a similar modification to the Friedel (1979) correlation using the rationale that, when used for small tubes, this correlation does not emphasize surface tension (We) enough, and may emphasize gravity (Fr) too much. The resulting modification is as follows:

$$\frac{dP}{dz} = \left. \frac{dP}{dz} \right|_{\text{Friedel}} \Omega \quad (6.53)$$

$$\Omega = \begin{cases} \frac{0.0333 \text{Re}_{\text{LO}}^{0.45}}{\text{Re}_G^{0.09} (1 + 0.4 \exp(-Bo))} & Bo < 2.5 \\ \frac{We^{0.2}}{(2.5 + 0.06Bo)} & Bo \geq 2.5 \end{cases}$$

These modifications improved the predictive capabilities of the homogeneous and Friedel correlations from deviations of 53.7% and 218.0% to 30.9% and 19.8%, respectively. In addition, these equations also agreed reasonably well with the pressure drop data of Hashizume (1983) for R-12 and R-22 in 10-mm tubes.

Wilson *et al.* (2003) studied the effect of progressively flattening 8.91-mm round smooth tubes and tubes with axial and helical microfin tubes on void fraction, pressure drop, and heat transfer during condensation of refrigerants R-134a and R-410A at 35°C. The hydraulic diameters of the tubes tested were 7.79, 6.37, 4.40, and 1.84 mm, with the microfin tubes having 60 fins of 0.2 mm height for a surface area increase of 60% over a smooth tube. The pressure drop at a given mass flux and quality increased as the tube approached a rectangular shape. They found that the following circular tube liquid-only two-phase multiplier correlation of Jung and Radermacher (1989) predicted their results within 40%:

$$\phi_{\text{LO}}^2 = 12.82 X_{\text{tt}}^{-1.47} (1 - x)^{1.8} \quad (6.54)$$

Similarly, the following annular and stratified flow correlation of Souza *et al.* (1993) with the D_h of the flattened tube as the characteristic dimension, also predicted their data within 40%:

$$\phi_L^2 = 1.376 + C_1 X_{\text{tt}}^{-C_2}$$

$$\text{Fr}_1 < 0.7:$$

$$C_1 = 4.172 + 5.48 \text{Fr}_1 - 1.564 \text{Fr}_1^2$$

$$C_2 = 1.773 - 0.169 \text{Fr}_1 \quad (6.55)$$

$$\text{Fr}_1 > 0.7:$$

$$C_1 = 7.242; \quad C_2 = 1.655$$

where $\text{Fr}_1 = G / (\rho_L \sqrt{gD})$. The corresponding single-phase friction factor was calculated using the Colebrook (1939) equation and an expression for the relative roughness of the microfin tubes developed by Cavallini *et al.* (2000). Wilson *et al.* (2003) deemed this 40% agreement to be adequate and did not develop a new correlation specifically for flat (flattened) tubes.

6.4.3. Air–water studies ($\sim 1 < D_h < \sim 10$ mm)

Zhao and Rezkallah (1995) measured pressure drops for upward air–water flow data in a 9.5-mm tube at 1-g and microgravity conditions and found that the pressure drops were about the same at both environments. In addition, the data were in relatively good agreement with the homogeneous, Lockhart–Martinelli (1949) and Friedel (1979) correlations, although Friedel's correlation was found to overestimate the data. They reasoned that at reduced gravity, annular flow pressure drops would not be affected due to the dominance of inertia forces. In bubble and slug flows, the slip between the two phases decreases due to a decrease in gas-phase velocity, leading to a higher void fraction, and therefore increasing the liquid phase pressure drop due to the reduced liquid flow area. However, in bubbly flow, the decrease in turbulence at reduced gravity due to the similar velocities of the gas and liquid phases would lead to lower pressure drops. The difference in pressure drop at 1-g and μ -g would be due to a trade-off between these competing influences. However, at the relatively high velocities and fully turbulent flows they tested, small changes in bubble velocity due to the change in gravity were not deemed to be very significant in altering the pressure drop.

Fukano *et al.* (1989) proposed correlations for pressure drop in bubbly, slug, plug, and annular flow based on experiments with air–water flow in 1-, 2.4-, and 4.9-mm tubes. In slug flow, sequential photographs showed that the velocity of the large gas bubble can be correlated as $u_S = 1.2 (j_G + j_L)$ where $j_G + j_L$ is the liquid slug velocity. From this, the relative velocity between the gas bubble and the liquid in the slug is given by $u_r = 0.2 (j_G + j_L)$. From photographic observations, it was also established that the liquid slug length is given by:

$$L_L / (L_L + L_G) = K j_L / (j_L + j_G) \quad (6.56)$$

where the constant of proportionality K varied from 0.9 at 1 mm to 0.72 at 4.9 mm. Assuming that in slug and plug flows, the pressure drop occurs in the liquid slug only, while in annular and bubbly regions, it occurs over the entire length of the channel, they developed the following equations for the two-phase multiplier:

$$\phi_L^2 \propto K \left(\frac{\rho_T}{\rho_L} \right) \left(\frac{v_L}{v_T} \right)^n \left(\frac{j_G + j_L}{j_L} \right)^{n+c+1} \text{Re}_L^{n-m} \quad (6.57)$$

where $c = 0$ for intermittent flow and $c = 1$ for annular and bubbly flows, subscript T refers to the two-phase mixture, and m and n refer to the Re exponent in the single-phase friction factor for the liquid and two-phase flows, respectively, dependent on whether the flow is laminar or turbulent. As the experimental ϕ_L^2 values were larger than those predicted by this treatment, they proposed a new slug flow model that accounts for the expansion losses (loss coefficient = 1) as the liquid flowed from the annular film surrounding the gas bubble into the liquid slug region. This additional contribution of the expansion losses was shown to be significant, and led to much better agreement between the measured and predicted values. The analysis also showed that for a 2.4-mm channel, the expansion losses could in fact be larger than the frictional losses in the slug. The expansion losses were found to first increase with increasing j_G because the liquid slug length decreases, presumably

leading to more expansion events; but further increases in j_G make the expansion losses less significant because at very high j_G , the frictional losses increase rapidly.

Mishima and Hibiki (1996) (whose work was discussed in the previous sections on flow regimes and void fraction) measured frictional pressure drops in air–water flows through 1–4-mm tubes. By comparing their results with the Lockhart–Martinelli (1949) correlation, they noticed that the parameter C in Chisholm's (1967) curve-fit (Eq. (6.39) above) to the multiplier decreased with a decrease in tube diameter. Similar trends were also observed by Sugawara *et al.* (1967) for air–water flow in horizontal 0.7–9.1-mm round tubes, Ungar and Cornwell (1992) for the flow of ammonia in horizontal 1.46–3.15-mm round tubes, Mishima *et al.* (1993) for vertical upward flow of air–water in rectangular 1.07×40 -, 2.45×40 -, and 5.00×40 -mm channels, Sadatomi *et al.* (1982) for vertical upward flow of air–water through rectangular $(7-17) \times 50$ - and 7×20.6 -mm channels, and by Moriyama *et al.* (1992a,b) for the flow of R113-nitrogen through horizontal rectangular $(0.007-0.098) \times 30$ -mm channels. Including the data from these investigators and their own data, they developed the following equation for the parameter C :

$$C = 21(1 - \exp(-0.319D_h)) \quad (6.58)$$

where D_h is in mm. They state that this equation is valid for vertical and horizontal round tubes as well as rectangular ducts (although the predictions did not agree well with the ammonia vapor data of Ungar and Cornwell (1992)).

It should be noted that several investigators have shown that the homogeneous flow model is reasonably successful in predicting pressure drop during adiabatic flow and boiling in channels with a diameter of a few mm. These include the previously mentioned work of Ungar and Cornwell (1992) on the flow of ammonia in horizontal 1.46–3.15-mm round tubes, and Kureta *et al.* (1998) on the boiling of water in 2–6-mm channels at atmospheric pressure over a wide range of mass fluxes. Similarly, Triplett *et al.* (1999a) found that this model was able to predict some of their data on adiabatic flow of air–water mixtures through 1.1- and 1.45-mm circular, and 1.09- and 1.49-mm semi-triangular channels. In particular, the homogeneous model predicted the data in the bubbly and slug flow regimes well at high Re_L . The agreement in the slug-annular and annular flow regions was poor, as was the agreement with the slug flow data at very low Re_L . Also, the Friedel (1979) correlation resulted in larger deviations from the data, especially at low Re_L values. This same group (Ekberg *et al.*, 1999) also investigated air–water flow in two narrow, concentric annuli with inner and outer diameters of 6.6 and 8.6 mm for one annulus, and 33.2 and 35.2 mm for the second annulus, respectively. The measured pressure drops did not show particularly good agreement with any of the available models, and even the Friedel correlation, which they state provided the best agreement, had deviations of over 50%.

Tran *et al.* (2000) developed a correlation for pressure drop during boiling of refrigerants in circular (2.46 and 2.92 mm) and rectangular (4.06×1.7 mm) channels. Their tests did not record local pressure drops – the pressure drop was measured from the inlet at nominally zero quality to a varying exit quality. For the tests with large exit qualities, therefore, the measured pressure drops could be the result of considerably varying local pressure drops as the flow regimes change along the test section. Although they found that the trends in the data (in terms of the effect of mass flux, quality and saturation pressure) were similar

to those found in large tubes (Eckels *et al.*, 1994), the large tube correlations (Chisholm, 1967, 1973; Friedel, 1979; Jung and Radermacher, 1989; Souza and Pimenta, 1995) typically underpredicted the data, with the discrepancy increasing at large qualities and mass fluxes. The reason for the higher pressure drop in small tubes was thought to be the fact that coalesced bubbles in small channels are confined, elongated, and slide over a thin liquid film, whereas in large tubes, the bubbles may grow and flow unrestricted through the tubes. In view of this, they proposed a modified version of the Chisholm (1973) correlation that accounted for the role of surface tension through the confinement number (defined in a previous section of this chapter) introduced by Cornwell and Kew (1993) as follows:

$$\Delta P_f = \Delta p_{fLO} \left\{ 1 + (4.3Y^2 - 1) [N_{\text{conf}} x^{0.875} (1 - x)^{0.875} + x^{1.75}] \right\} \quad (6.59)$$

where Y is the ratio of the gas- and liquid-only pressure drops defined in Eq. (6.42) above.

Zhao and Bi (2001b) measured pressure drops for upward co-current air–water flow through equilateral triangular channels with $D_h = 0.866, 1.443, \text{ and } 2.886$ mm. They found that the void fraction could be simply represented by $\alpha = 0.838\beta$, which is very similar to the Armand (1946) correlation and was used to compute acceleration losses in two-phase flow. The frictional component was then correlated using the Lockhart–Martinelli (1949) approach. For this, they computed the required single-phase friction factor by replacing the laminar and turbulent friction factors in the comprehensive laminar-transition-turbulent correlation of Churchill (1977) with the corresponding expressions for triangular channels. This modification yielded two-phase multipliers that were between the values predicted by the Chisholm (1967) expression using $C = 5$ and $C = 20$.

Lee and Lee (2001) investigated pressure drop for air–water flow through 20-mm wide horizontal rectangular channels with gaps of 0.4–4 mm. They recalled that the original basis for the Chisholm (1967) correlation of the two-phase multiplier in the Lockhart–Martinelli (1949) correlation consisted of accounting for the pressure drop due to (a) gas phase, (b) liquid phase, and (c) interactions between the two phases. The parameter C in Chisholm's correlation represents this interaction term; which in turn depends on the flow regimes of the two phases. Therefore, they proposed different values for C , accounting for the gap size as well as the phase flow rates. They reasoned that as the gap size decreases, the flow tends more and more to plug and slug flow, with an increasing effect of surface tension due to the curved gas/liquid interface at the edge of the bubble. In such surface-tension-dominated flows, they stated that of the several dimensionless parameters identified by Suo and Griffith (1964) for capillary tubes, the Reynolds number of the liquid slug, $Re = (\rho_L j D_h) / \mu_L$, the ratio of viscous and surface tension effects, $\psi = \mu_L j / \sigma$, and a combination of parameters independent of the liquid slug velocity, $\lambda = \mu_L^2 / (\rho_L \sigma D_h)$, were the relevant ones. Lee and Lee then used their data to obtain individual values of the constant A and exponents q , r , and s for each combination of liquid and gas flow regimes in the following equation for the parameter C in the two-phase multiplier:

$$C = A \lambda^q \psi^r Re_{LO}^s \quad (6.60)$$

Regression analysis showed that the dependence on parameters λ and ψ above, that is, surface tension effects, was only significant when both phases were laminar, with C being

simply a function of Re_{LO} when either or both phases were in the turbulent regime. This approach predicted their data within $\pm 10\%$, and also predicted the data of Wambsganss *et al.* (1992) and Mishima *et al.* (1993) within 15% and 20%, respectively. This correlation is valid for $175 < Re_{LO} < 17700$ and $0.303 < X < 79.4$.

6.4.4. Condensation studies ($\sim 0.4 < D_h < 5 \text{ mm}$)

Yang and Webb (1996b) measured pressure drops in single- and adiabatic two-phase flows of refrigerant R-12 in rectangular plain and microfin tubes with $D_h = 2.64$ and 1.56 mm , respectively. The measurements were conducted at somewhat higher mass fluxes ($400 < G < 1400 \text{ kg/m}^2\text{-s}$) than those of interest for refrigeration and air-conditioning applications. Their single-phase friction factors were correlated by $f_{\text{smooth}} = 0.0676 Re_{D_h}^{-0.22}$ and $f_{\text{microfin}} = 0.0814 Re_{D_h}^{-0.22}$. The pressure gradient in the microfin tube was higher than that of the plain tube. They tried to model the two-phase pressure drops using the Lockhart–Martinelli (1949) approach and curve-fitting the two-phase multiplier ϕ_v^2 , but this did not lead to a satisfactory correlation. The equivalent mass velocity concept of Akers *et al.* (1959) was then attempted to develop a correlation. Thus, the single-phase friction factor is first calculated using the aforementioned equations at the Reynolds number Re_{D_h} for the liquid phase flowing alone. The equivalent Reynolds number for two-phase flow is then calculated as follows:

$$Re_{\text{eq}} = \frac{G_{\text{eq}} D_h}{\mu_l}; \quad G_{\text{eq}} = G \left[(1 - x) + x \left(\frac{\rho_l}{\rho_v} \right)^{1/2} \right] \quad (6.61)$$

The equivalent friction factor is therefore based on an equivalent all-liquid flow that yields the same frictional pressure drop as the two-phase flow. Based on their data, the two-phase friction factor at this equivalent Reynolds number was fit to the following equation:

$$\frac{f}{f_l} = 0.435 Re_{\text{eq}}^{0.12} \quad (6.62)$$

Finally, the two-phase pressure drop is calculated as follows:

$$\Delta P_f = f \frac{Re_{\text{eq}}^2 \mu_l^2}{2 \rho_l} \frac{4L}{D_h^3} \quad (6.63)$$

This approach was able to predict both plain and microfin tube data within $\pm 20\%$. It should be noted that this approach collapses both the single- and two-phase pressure gradients for each tube on the same line, when plotted against the Re_{eq} . From their data, Yang and Webb (1996b) also concluded that surface tension did not play a role in determining the pressure drop in these tubes, although in related work (Yang and Webb, 1996a), they found surface tension to be significant for the heat transfer coefficient, especially at low G and high x .

Subsequently, Yan and Lin (1999) used the same Akers *et al.* (1959) equivalent mass velocity concept that was used by Yang and Webb (1996b) to correlate condensation

pressure drop of R-134a in a 2-mm circular tube. They arranged 28 such copper tubes in parallel held between copper blocks, to which were soldered similar cooling channels to form a crossflow heat exchanger that served as the test section. The resulting friction factor correlation is as follows:

$$f = 498.3 \text{Re}_{\text{eq}}^{-1.074} \quad (6.64)$$

It should be noted that this is considerably different from the results of Yang and Webb cited above; however, Yan and Lin's single-phase friction factors were significantly higher than the predictions of the Blasius equation. They attributed this to the influence of entrance lengths and tube roughness, but this discrepancy may explain the substantial differences between the two studies.

Zhang and Webb (2001) measured adiabatic two-phase pressure drops for R-134a, R-22, and R-404A flowing through 3.25- and 6.25-mm circular tubes and through a multi-port extruded aluminum tube with a hydraulic diameter of 2.13 mm. They noted that the Friedel (1979) correlation, although recommended widely for larger tubes, was developed from a database with $D > 4$ mm, and therefore did not predict their data well, especially at the higher reduced pressures ($T_{\text{sat}} = 65^\circ\text{C}$). Since the dependence of the Friedel correlation on Weber number and Froude number was weak, they decided not to include them as variables while correlating their data. Also, based on the work of Wadekar (1990) for convective boiling, they postulated that the pressure drop would be a function of the reduced pressure rather than the density and viscosity ratios. Using these considerations, and additional data from a previous study on multi-port tubes with round 1.45- and 0.96-mm ports, and 1.33-mm rectangular ports, they developed the following modified version of the Friedel correlation:

$$\phi_{\text{LO}}^2 = (1 - x)^2 + 2.87x^2 (p/p_{\text{crit}})^{-1} + 1.68x^{0.8} (1 - x)^{0.25} (p/p_{\text{crit}})^{-1.64} \quad (6.65)$$

Garimella *et al.* developed experimentally validated models for pressure drops during condensation of refrigerant R-134a in intermittent flow through circular (Garimella *et al.*, 2002) and non-circular (Garimella *et al.*, 2003b) microchannels (Fig. 6.21) with $0.4 < D_h < 4.9$ mm. In addition, they developed a model for condensation pressure drop in annular flow (Garimella *et al.*, 2003a), and further extended it to a comprehensive multi-regime pressure drop model (Garimella *et al.*, 2005) for microchannels for the mass flux range $150 < G < 750$ kg/m²-s. For $D_h < 3.05$ mm, they used flat tubes with multiple extruded parallel channels to ensure accurately measurable flow rates and heat balances. Three such tubes were brazed together (Fig. 6.21), with refrigerant flowing through the center tube, and coolant (air) flowing in counterflow through the top and bottom tubes. The low thermal capacity and heat transfer coefficients of air maintained small changes in quality in the test section, which in turn enabled the measurement of the pressure drop variation as a function of quality with high resolution. The measurement techniques were first verified by conducting single-phase pressure drop measurements for each tube in the laminar and turbulent regimes for both the superheated vapor and subcooled liquid cases. The single-phase pressure drops were in excellent agreement with the values predicted by the Churchill (1977) correlation.

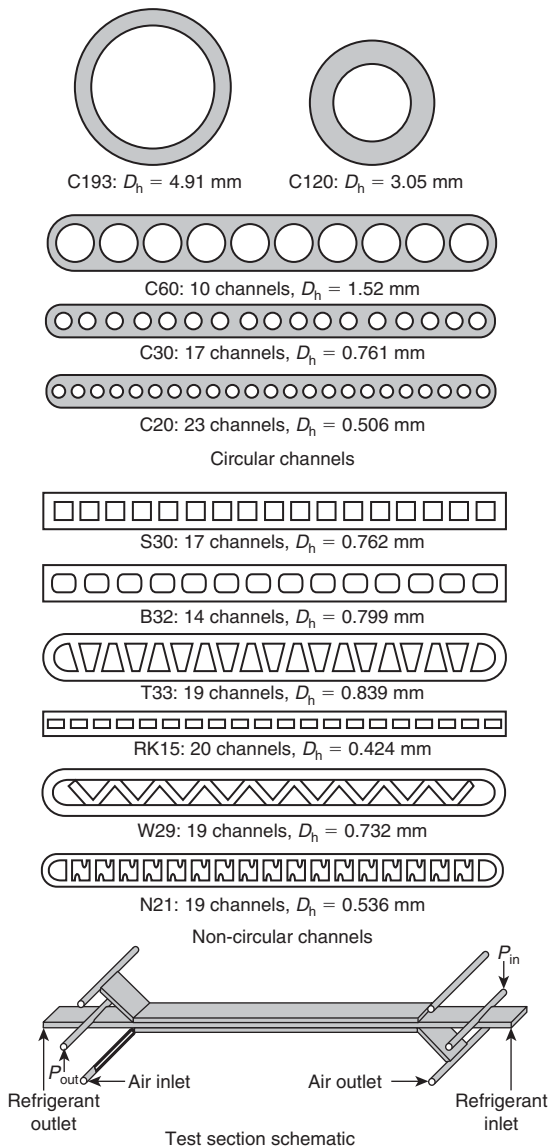


Fig. 6.21. Refrigerant condensation geometries of Garimella. From Garimella, S., Agarwal, A. and Killion, J. D., Condensation Pressure Drop in Circular Microchannels, *Heat transfer Engineering*, **26**(3), pp. 1–8 (2005).

The measured pressure drops included expansion and contraction losses due to the headers at both ends of the test section, and the pressure change due to deceleration caused by the changing vapor fraction as condensation takes place, and was represented as follows:

$$\Delta P_{\text{measured}} = \Delta P_{\text{frict}} + \Delta P_{\text{exp+contr}} + \Delta P_{\text{decel}} \tag{6.66}$$

The pressure drop due to contraction was estimated using a homogeneous flow model recommended by Hewitt *et al.* (1994):

$$\Delta P_{\text{contr}} = \frac{G^2}{2\rho_L} \left[\left(\frac{1}{C_c} - 1 \right)^2 + 1 - \gamma^2 \right] \left[1 + x \left(\frac{\rho_L}{\rho_G} - 1 \right) \right] \quad (6.67)$$

where γ is the area ratio ($A_{\text{test-section}}/A_{\text{header}}$) and C_c is the coefficient of contraction, which is in turn a function of this area ratio as given by Chisholm (1983):

$$C_c = \frac{1}{0.639(1 - \gamma)^{0.5} + 1} \quad (6.68)$$

For the expansion into the header from the test section, the following separated flow model recommended by Hewitt *et al.* (1994) was used:

$$\Delta P_{\text{expansion}} = \frac{G^2 \gamma (1 - \gamma) \psi_S}{\rho_L} \quad (6.69)$$

where ψ_S , the separated flow multiplier, is also a function of the phase densities and the quality. These estimates were validated using pressure drop measurements on a “near-zero” length test section, in which the measured pressure drops (with small frictional pressure drops) showed excellent agreement with the contraction/expansion contributions calculated as shown above. Contraction and expansion loss contributions were less than 5% of the total measured pressure drop for all their data. The pressure change due to acceleration (deceleration) of the fluid (due to the change in quality across the test section) was estimated as follows (Carey, 1992):

$$\Delta P_{\text{acceleration}} = \left[\frac{G^2 x^2}{\rho_V \alpha} + \frac{G^2 (1 - x)^2}{\rho_L (1 - \alpha)} \right]_{x=x_{\text{out}}} - \left[\frac{G^2 x^2}{\rho_V \alpha} + \frac{G^2 (1 - x)^2}{\rho_L (1 - \alpha)} \right]_{x=x_{\text{in}}} \quad (6.70)$$

where the void fraction was evaluated using the Baroczy (1965) correlation. For almost all their data, the deceleration term was extremely small compared to the overall pressure drop. These estimates were also corroborated by adiabatic flow and condensation tests at the same nominal conditions. The residual frictional component of the two-phase pressure drop, which generally was at least an order of magnitude larger than these minor losses, was used for developing condensation pressure drop models for the respective flow regimes.

To develop flow regime-based pressure drop models, transition from the intermittent to the other flow regimes (based on their earlier flow visualization work) was determined as follows:

$$x \leq \frac{a}{G + b} \quad (6.71)$$

where a and b are geometry-dependent constants given by:

$$a = 69.57 + 22.60 \times \exp(0.259 \times D_h) \quad (6.72)$$

$$b = -59.99 + 176.8 \times \exp(0.383 \times D_h)$$

(6.73)

where D_h is in mm. On a mass-flux versus quality map, these transition lines appear in the lower left corner, as shown in Fig. 6.22. For pressure drop model development, they broadly categorized the flow into the primary regimes, intermittent (lower left) and annular film/mist/disperse patterns of the annular flow regime (upper right). The very few data that were in the wavy regime in these small channels were incorporated into the annular or intermittent regimes, as appropriate. The overlap region in Fig. 6.22 accounts for the gradual transition between the primary regimes, during which the flow switches back and forth between the respective regimes. Pressure drop models for these regimes are described below.

The unit cell for the development of the intermittent model is shown in Fig. 6.23, in which the vapor-phase travels as long solitary bubbles surrounded by an annular liquid film

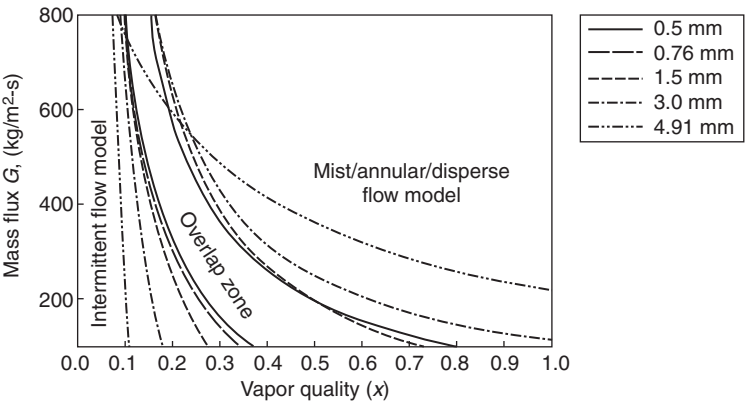


Fig. 6.22. Flow regime assignment. From Garimella, S., Agarwal, A. and Killion, J. D., Condensation Pressure Drop in Circular Microchannels, *Heat transfer Engineering*, **26**(3), pp. 1–8 (2005).

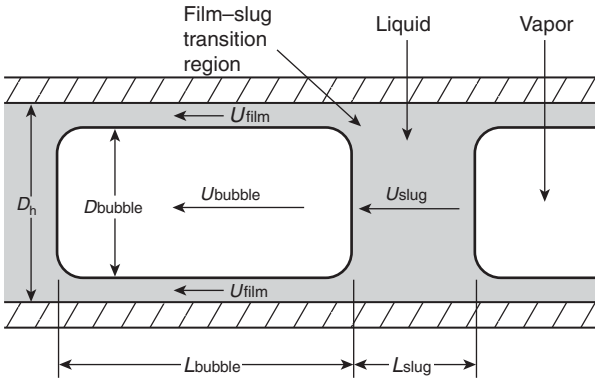


Fig. 6.23. Unit cell for intermittent flow. Reprinted from Garimella, S., Killion, J. D. and Coleman, J. W. An experimentally validated model for two-phase pressure drop in the intermittent flow regime for circular microchannels, *Journal of Fluids Engineering*, **124**(1), pp. 205–214 (2002) with permission from the American Society of Mechanical Engineers.

and separated by liquid slugs. Based on the recorded flow patterns, it was assumed that the bubble is cylindrical, and that there is no entrainment of vapor in the slug, or liquid in the bubble. Further, for any given condition, it was assumed that the length/frequency/speed of bubbles/slugs is constant, with no bubble coalescence, and a smooth bubble/film interface. The total pressure drop for this flow pattern includes contributions from: the liquid slug, the vapor bubble, and the flow of liquid between the film and slug as follows:

$$\Delta P_{\text{total}} = \Delta P_{\text{slug}} + \Delta P_{\text{f/b}} + \Delta P_{\text{transitions}} \quad (6.74)$$

A simple control volume analysis (Garimella *et al.*, 2002; 2003b) similar to that performed by Suo and Griffith (1964) was used to calculate the liquid slug velocity from the superficial phase velocities, in turn calculated from the overall mass flux and the quality. Thus, $U_{\text{slug}} = j_V + j_L$, which yielded the slug Reynolds number $\text{Re}_{\text{slug}} = (\rho_L U_{\text{slug}} D_h) / \mu_L$. This Re_{slug} was used to calculate the pressure gradient in the slug from an appropriate single-phase friction factor correlation from the literature. The results of several investigations (Suo and Griffith, 1964; Dukler and Hubbard, 1975; Fukano *et al.*, 1989) discussed in this chapter suggested that $U_{\text{bubble}} = 1.2 U_{\text{slug}}$. Unlike air–water studies, where many of these investigators have neglected the pressure drop in the film–bubble region, since the ratio of the liquid to vapor densities for R-134a is much lower (approximately 16:1 versus 850:1 for air–water) as is the ratio of liquid and vapor viscosities (approximately 10:1 versus 50:1), the contribution of the film/bubble region was not neglected. Based on the data, the film was assumed to be laminar, while the gas bubble was turbulent. The respective Reynolds numbers were defined as follows:

$$\text{Re}_{\text{film}} = \frac{\rho_L U_{\text{film}} (D_h - D_{\text{bubble}})}{\mu_L} \quad \text{Re}_{\text{bubble}} = \frac{\rho_V (U_{\text{bubble}} - U_{\text{interface}}) D_{\text{bubble}}}{\mu_V} \quad (6.75)$$

The film flow was assumed to be driven by the combination of the pressure gradient in the film/bubble region and shear at the film/bubble interface. The velocity profile for combined Couette–Poiseuille flow through an annulus where the inner surface moves at the interface velocity, $U_{\text{interface}}$, is represented by the superposition of the pressure-driven and the shear-driven components:

$$u_{\text{film}}(r) = \frac{-\left(\frac{dP}{dx}\right)_{\text{f/b}}}{4\mu_L} \left[R_{\text{tube}}^2 - r^2 - (R_{\text{tube}}^2 - R_{\text{bubble}}^2) \frac{\ln(R_{\text{tube}}/r)}{\ln(R_{\text{tube}}/R_{\text{bubble}})} \right] + U_{\text{interface}} \frac{\ln(R_{\text{tube}}/r)}{\ln(R_{\text{tube}}/R_{\text{bubble}})} \quad (6.76)$$

The bubble velocity, assuming a power law profile ($n = 7$) is given by:

$$u_{\text{bubble}}(r) = \frac{(n+1)(2n+1)}{2n^2} (U_{\text{bubble}} - U_{\text{interface}}) \left(1 - \frac{r}{R_{\text{bubble}}} \right)^{1/n} + U_{\text{interface}} \quad (6.77)$$

A shear balance at the film–bubble interface yields the interface velocity:

$$U_{\text{interface}} = \frac{-(dP/dx)_{\text{f/b}}}{4\mu_L} (R_{\text{tube}}^2 - R_{\text{bubble}}^2) \quad (6.78)$$

With a parabolic velocity profile in the film, the average film velocity can also be calculated. Also, with the film pressure gradient calculated using a single-phase friction factor for the gas phase, continuity yields:

$$U_{\text{slug}} = U_{\text{bubble}} \left(\frac{R_{\text{bubble}}}{R_{\text{tube}}} \right)^2 + U_{\text{film}} \left(1 - \left(\frac{R_{\text{bubble}}}{R_{\text{tube}}} \right)^2 \right) \quad (6.79)$$

These calculations yield $0.899 < R_{\text{bubble}}/R_{\text{tube}} < 0.911$; that is, the bubble diameter is $\sim 90\%$ of the tube diameter. With the pressure drop/length known in the slug and the film/bubble regions, the frictional pressure drop was calculated using the relationship proposed by Fukano *et al.* (1989) for the length of the slug (Eq. (6.56)):

$$\begin{aligned} \Delta P_{\text{friction only}} = L_{\text{tube}} & \left[\left(\frac{dP}{dx} \right)_{\text{f/b}} \left(1 - \frac{L_{\text{slug}}}{L_{\text{slug}} + L_{\text{bubble}}} \right) \right. \\ & \left. + \left(\frac{dP}{dx} \right)_{\text{slug}} \left(\frac{L_{\text{slug}}}{L_{\text{slug}} + L_{\text{bubble}}} \right) \right] \end{aligned} \quad (6.80)$$

The remaining contribution to the total pressure drop is the loss associated with the flow of liquid between the film and the slug. As the film moves slowly, the front of the liquid slug is constantly taking up fluid from the film. A pressure loss is associated with the acceleration and subsequent mixing of this liquid, with the total pressure loss from these transitions given by $\Delta P_{\text{film/slug transitions}} = N_{\text{UC}} \times \Delta P_{\text{one transition}}$, where N_{UC} is the number of cells per unit length. The pressure drop for one transition is based on the force to accelerate the portion of the liquid film overtaken by the rear of the bubble from the average film velocity to the average slug velocity (Dukler and Hubbard, 1975):

$$\Delta P_{\text{one transition}} = \rho_L \left(1 - \left(\frac{R_{\text{bubble}}}{R_{\text{tube}}} \right)^2 \right) (U_{\text{slug}} - U_{\text{film}})(U_{\text{bubble}} - U_{\text{film}}) \quad (6.81)$$

These components of the total pressure drop are shown below:

$$\frac{\Delta P}{L} = \left(\frac{dP}{dx} \right)_{\text{film bubble}} \left(\frac{L_{\text{bubble}}}{L_{\text{UC}}} \right) + \left(\frac{dP}{dx} \right)_{\text{slug}} \left(\frac{L_{\text{slug}}}{L_{\text{UC}}} \right) + \Delta P_{\text{one transition}} \left(\frac{N_{\text{UC}}}{L} \right) \quad (6.82)$$

A depiction of these various contributions to the measured pressure drop for circular channels is shown in Fig. 6.24. The number of unit cells per unit length required for closure of the model was computed from the slug frequency ω , which was correlated based on slug Re and D_h :

$$a (\text{Re}_{\text{slug}})^b = \omega \frac{D_h}{U_{\text{bubble}}} = D_h \left(\frac{N_{\text{UC}}}{L_{\text{tube}}} \right) = \left(\frac{D_h}{L_{\text{UC}}} \right) \quad (6.83)$$

The coefficients a and b were fit using the difference between the measured pressure drop and the pressure drop calculated as described above for the slug and bubble/film regions; that is, the net pressure drop due to transitions. The correlation yielded $a = 2.437$, $b = -0.560$ for both circular and non-circular (except triangular, for which different

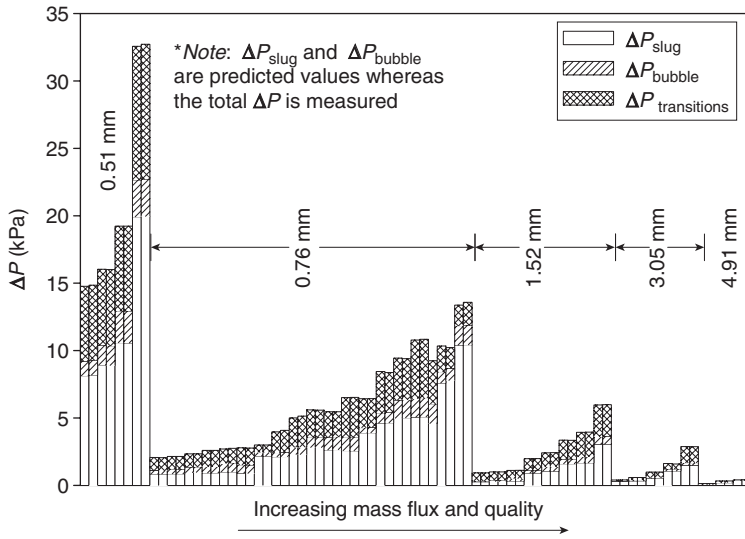


Fig. 6.24. Contribution of each pressure drop mechanism to total pressure drop. Reprinted from Garimella, S., Killion, J. D. and Coleman, J. W. An experimentally validated model for two-phase pressure drop in the intermittent flow regime for circular microchannels, *Journal of Fluids Engineering*, **124**(1), pp. 205–214 (2002) with permission from the American Society of Mechanical Engineers.

coefficients were necessary, as discussed in Garimella *et al.* (2003b)) channels. For circular channels (0.5–4.91 mm), the predicted pressure drops were on average within $\pm 13.5\%$ of the measured values.

The intermittent model was also extended to the discrete wave flow region by Garimella *et al.* (2005). This is because as the progression from the intermittent region to the discrete wave region occurs, the gas bubbles start disappearing, to be replaced by stratified, well-defined liquid and vapor layers. Within the discrete wave region, traversing from the intermittent flow boundary toward the annular flow boundary, the bubbles disappear completely, with the number of unit cells per unit length approaching zero. Based on this conceptualization of the intermittent and discrete flow regions, the slug frequency model developed by Garimella *et al.* (2002; 2003b) for intermittent flow was modified to include data from the discrete wave flow region, resulting in the following combined model for the two regions:

$$N_{UC} \left(\frac{D_h}{L_{tube}} \right) = \left(\frac{D_h}{L_{UC}} \right) = 1.573 (\text{Re}_{slug})^{-0.507} \quad (6.84)$$

Garimella *et al.* (2003a; 2005) also developed pressure drop models for annular flow condensation in microchannels, assuming equal pressure gradients in the liquid and gas core at any cross-section, uniform film thickness, and no entrainment of the liquid in the gas core. The measured pressure drops were used to compute the Darcy form of the interfacial friction factor to represent the interfacial shear stress as follows:

$$\frac{\Delta P}{L} = \frac{1}{2} \times f_i \rho_g V_g^2 \times \frac{1}{D_i} \quad (6.85)$$

The above equation uses the interface diameter, D_i . This same expression can be represented in terms of the more convenient tube diameter, D , by using the Baroczy (1965) void fraction model:

$$\frac{\Delta P}{L} = \frac{1}{2} \times f_i \frac{G^2 \times x^2}{\rho_g \times \alpha^{2.5}} \times \frac{1}{D} \quad (6.86)$$

The ratio of this interfacial friction factor (obtained from the experimental data) to the corresponding liquid-phase Darcy friction factor was then computed and correlated in terms of the Martinelli parameter and the surface tension parameter $\psi = j_L \mu_L / \sigma$ introduced by Lee and Lee (2001):

$$\frac{f_i}{f_l} = A \times X^a \text{Re}_l^b \psi^c \quad (6.87)$$

where $j_L = \frac{G(1-x)}{\rho_l(1-\alpha)}$ is the liquid superficial velocity. The phase Reynolds numbers required above and for the Martinelli parameter were defined in terms of the flow areas of each phase:

$$\text{Re}_l = \frac{GD(1-x)}{(1+\sqrt{\alpha})\mu_l} \quad \text{Re}_g = \frac{GxD}{\mu_g\sqrt{\alpha}} \quad (6.88)$$

The friction factors were computed using $f = 64/\text{Re}$ for $\text{Re} < 2100$ and the Blasius expression $f = 0.316 \times \text{Re}^{-0.25}$ for $\text{Re} > 3400$. Regression analysis on data grouped into two regions based on Re_l yielded:

$$\text{Laminar region } (\text{Re}_l < 2100): A = 1.308 \times 10^{-3} \quad a = 0.427 \quad b = 0.930 \quad c = -0.121 \quad (6.89)$$

$$\text{Turbulent region } (\text{Re}_l > 3400): A = 25.64 \quad a = 0.532 \quad b = -0.327 \quad c = 0.021 \quad (6.90)$$

Interpolations based on G and x are used to compute the pressure drop for the transition region. This model predicted 87% of the data within $\pm 20\%$. These predictions include not only the annular flow region, but also the mist and disperse-wave flow data, although the model development uses a physical representation where the liquid forms an annular film around a gas core. Garimella *et al.* (2005) explained this based on the fact that the annular flow regime increases in extent for smaller tubes, causing several data classified into the wavy and mist flow regions using $D_h = 1$ mm transition criteria to be in fact in the annular flow regime. Representative pressure drop trends predicted by this model are shown in Fig. 6.25.

6.4.5. Air–water studies ($D_h < \sim 500 \mu\text{m}$)

Kawahara *et al.* (2002) measured pressure drops for air–water flow through a 100- μm circular tube (the corresponding results on flow patterns and void fractions were discussed

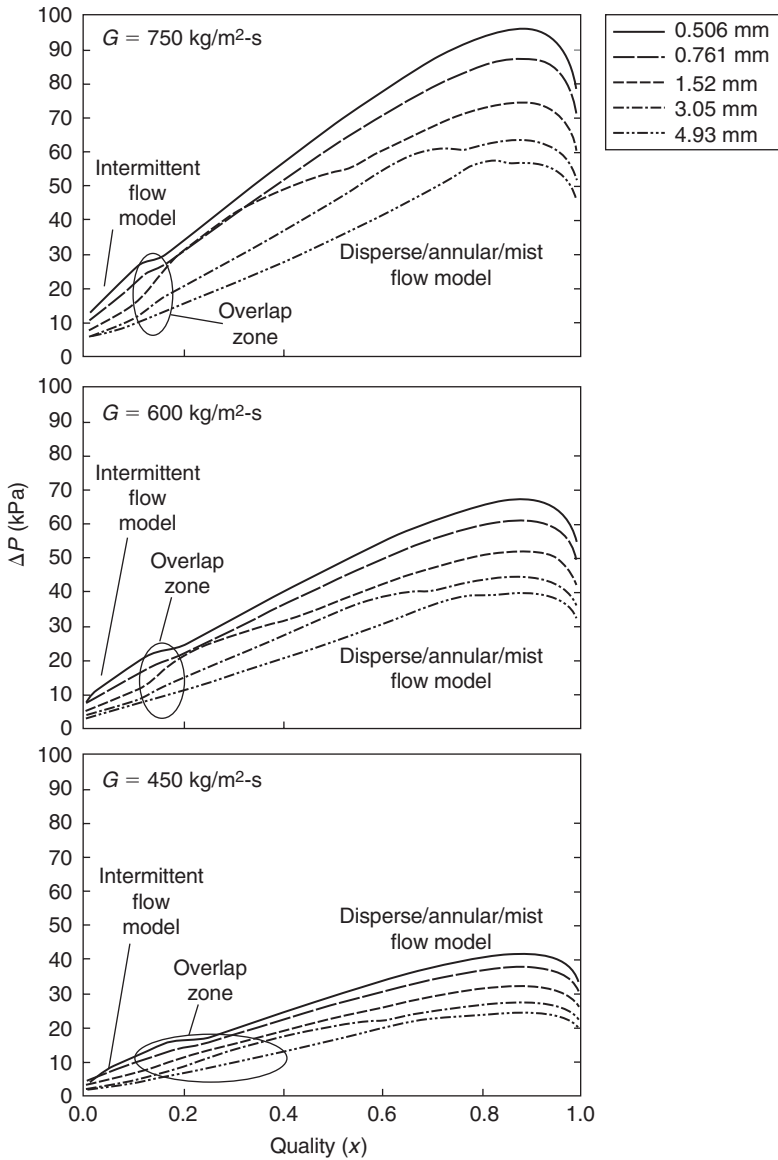


Fig. 6.25. Predictions of Garimella *et al.* (2005) multiple-flow-regime model for refrigerant condensation pressure drops in microchannels. From Garimella, S., Agarwal, A., and Killion, J. D. Condensation pressure drop in circular microchannels, *Heat Transfer Engineering*, **26**(3), pp. 1–8 (2005).

in previous sections). Test section entrance (contraction) losses, and acceleration losses due to the reduction in density across the test section were removed from the measured pressure drop in a manner similar to that discussed in connection with the work of Garimella *et al.* (2005) above. The void fraction required for the acceleration losses was evaluated using

Eq. (6.35) developed from their image analysis work. The contributions of these contraction and acceleration losses to the total pressure drop were found to be 0.05–9% and 0–4.5%, respectively, of the measured pressure drop. Although their flow pattern and void fraction results showed that the flow was not well represented by a homogeneous model, based on the success of others in using this model for small channels (Ungar and Cornwell, 1992; Triplett *et al.*, 1999a), they compared their results with homogeneous model using the homogeneous density and homogeneous viscosity models of Owens (1961), McAdams (1954), Cicchitti *et al.* (1960), Dukler *et al.* (1964), Beattie and Whalley (1982), and Lin *et al.* (1991). They found that none of these models were able to predict their data adequately (the Dukler *et al.* (1964) model, $\mu_H = \beta\mu_G + (1 - \beta)\mu_L$, provided somewhat reasonable predictions). When a Lockhart–Martinelli (1949) type two-phase multiplier approach was used, the Chisholm (1967) coefficient of $C = 5$ significantly overpredicted the data, while a C value of 0.66 from Mishima and Hibiki's (1996) work resulted in a 10% overprediction, and agreement within $\pm 10\%$ was achieved using Lee and Lee's (2001) correlation for C . Therefore, they conducted a regression analysis of the data to obtain a value of $C = 0.24$, which also yielded a $\pm 10\%$ agreement. In later work on a 96 μm square channel (Chung *et al.*, 2004), they noted that channel shape did not have any appreciable effect on two-phase pressure drop, and provided revised values of $C = 0.22$ for circular channels and $C = 0.12$ for square channels for the C coefficient in Chisholm's (1967) model.

Chung and Kawaji (2004) also investigated the effects of channel diameter on pressure drop during adiabatic flow of nitrogen–water through 530-, 250-, 100-, and 50 μm circular channels. In this study, they found that the Dukler *et al.* (1964) viscosity model (when used assuming homogeneous flow) did not predict the pressure drops for the 530- and 250- μm channels, although the agreement was within $\pm 20\%$ for the 100- and 50- μm data. Beattie and Whalley's (1982) mixture viscosity model showed the opposite trends, succeeding somewhat in predicting the 530- and 250- μm channel data, but significantly overpredicting the 100- and 50- μm channel data. They attributed this to the fact that Beattie and Whalley's (1982) model yields a higher mixture viscosity than that of Dukler *et al.* (1964), resulting in better agreement with the larger channel data because of the additional mixing losses in the bubbly and churn flows in these channels. When predominated by the more laminar slug flow with weak momentum coupling of the phases, however, as is the case in the smaller channels, the lower viscosities predicted by Dukler *et al.* (1964) model are more appropriate. When attempting the use of a two-phase multiplier approach as discussed above, they noted a mass flux effect on the friction multiplier for the 530- and 250- μm channels. The data at different mass fluxes for the 100- and 50- μm channels, however, were predicted well by a single C value ($C = 0.22$ for 100 μm , $C = 0.15$ for 50 μm). This decrease in C value (based on the above discussion of Lee and Lee's (2001) work) with a decrease in channel diameter implies a decrease in momentum coupling of the two phases; that is, completely separated laminar flow of gas and liquid, as also noted by Ali *et al.* (1993).

Based on the somewhat inadequate predictions of the homogeneous and two-phase multiplier approaches, they adapted the intermittent flow model of Garimella *et al.* (2002) to calculate the pressure drops in the 50- and 100- μm channels, which have predominantly intermittent flows. They also used the unit-cell concept consisting of gas bubbles surrounded by a liquid film and flowing through slower moving liquid slugs. Although in accordance with the model of Garimella *et al.* (2002), they represented the total pressure

drop as the summation of the frictional pressure drop in each of these regions, they ignored the mixing losses at the transitions between these regions. The rationale used was that in these smaller channels, the liquid flow is typically laminar, with suppressed mixing leading to negligibly small transition losses. For the single-phase liquid region, they computed the average liquid velocity $U_L = j_L / (1 - \alpha)$, which yielded $Re_L = (\rho_L U_L D) / \mu_L$. Laminar or turbulent single-phase friction factors were calculated based on Re_L . To compute the pressure drop in the film/bubble region, they assumed the average velocity of the gas phase and the gas bubble to be equal, $U_G = U_B$, where $U_G = j_G / \alpha$. This assumption is different from the assumption by Garimella *et al.* (2002) that $U_B = 1.2 U_S$, which, according to Chung and Kawaji (2004), is equivalent to assuming that the Armand (1946) correlation for void fraction approximately holds. Instead, they used the nonlinear expression for void fraction derived by them and discussed here in the previous section. Defining the bubble Re_B in terms of the relative velocity between the bubble and the interface, the computation of the pressure drop in the film–bubble region develops much like that in Garimella *et al.* (2002), with an assumption that $D_B = 0.9D$. The interface velocity, the film–bubble pressure gradient, and the bubble Reynolds number are then obtained iteratively. To calculate the relative lengths of the bubble and slug regions, they relied on the void fraction measured by them. Thus, treating the bubble as a cylinder with flat ends, the bubble length is given by:

$$\frac{L_B}{L_{UC}} = \alpha \left(\frac{D}{D_B} \right)^2 \quad (6.91)$$

Finally, the total pressure drop in the two regions is given by:

$$\left(\frac{dP_f}{dz} \right)_{TP} = \left(\frac{dP}{dz} \right)_{F/B} \frac{L_B}{L_{UC}} + \left(\frac{dP}{dz} \right)_L \frac{L_L}{L_{UC}} \quad (6.92)$$

The model was shown to agree better with the 50- and 100- μm channel pressure drop data than the homogeneous and two-phase multiplier approaches. Also, the predictions of the 50- μm channel data were better than those of the 100- μm data, presumably because the smaller channel exclusively exhibits slug flow, while the larger channel may have some regions of other kinds of flow. This also points out that this model should not be applied to larger ($D_h > 100 \mu\text{m}$) channels where the flow is not exclusively intermittent.

6.4.6. Summary observations and recommendations

The available information on pressure drop in two-phase flows was discussed above. One overall observation is that most of the studies continue to rely on the classical works of Lockhart and Martinelli (1949), Chisholm (1967), and Friedel (1979) for the evaluation of separated flow pressure drops. As in the case of flow regime and void fraction evaluation, most of the work in the small channels has been on adiabatic flows of air–water mixtures. It appears that the original two-phase multipliers proposed in these studies have been modified by the latter investigators (specifically the C coefficient in the Chisholm (1967) model of

the Lockhart–Martinelli (1949) multiplier) to match the data on the smaller channels. This indicates that of the liquid-phase, gas-phase, and gas–liquid interaction parameters, the gas–liquid interaction parameter has required the most modification to make it suitable for small channels. Examples include the work of Mishima and Hibiki (1996) and Lee and Lee (2001). As the channel approaches the smaller dimensions, Kawahara *et al.* (2002), Chung and Kawaji (2004), and others have found that the pressure drop predictions in the 530- and 250- μm channels and those for 100- and 50- μm channels required different mixture viscosity models to make the homogeneous flow models work. The standard two-phase flow multiplier approach with much smaller values of the C coefficient also yielded some success. However, it seems that for the plug/slug flows in the small channels, an approach that recognizes the intermittent nature of the flow, and accounts for the pressure drops in the liquid slug, the gas bubble, and in some cases, the mixing losses between the bubbles and slugs, as proposed by Garimella *et al.* (2002; 2003b) and later adapted by Chung and Kawaji (2004) is the best approach. Accounting for the range of flow regimes encountered in microchannels; that is, intermittent, annular, and to a certain extent, mist flow, has just recently been attempted. One multi-region model that accounts for the flow mechanisms in each of these regimes and results in smooth transitions between these regimes for condensing flows in the $0.4 < D_h < 5$ mm range is the model by Garimella *et al.* (2005).

The various techniques for predicting pressure drops in microchannels are illustrated in Example 6.3.

6.5. Heat transfer coefficients

In the above sections, the available information on flow regimes, void fractions, and pressure drop in two-phase flow was presented, including adiabatic flow of air–water mixtures and condensing flows. This is because the large body of work on adiabatic two-phase flows can be used as a starting point to understand the corresponding phenomena during phase change. However, for the evaluation of heat transfer coefficients, only the literature on condensing flows is relevant. The measurement and understanding of heat transfer in the really small channels ($D_h < 1$ mm) has proved to be particularly challenging in view of the confined spaces for measurement probes, the small flow rates in microchannels that correspond to small heat transfer rates that are therefore difficult to measure accurately, and the large heat transfer coefficients that lead to very small temperature differences, which are also difficult to measure. There would be little work to report, indeed, if the scope is restricted to channels with $D_h < 1$ mm (not much information is available even for channels with $D_h < \sim 7$ mm.) Therefore, in this section, an overview of the classical models of condensation is presented first to serve as a background for the work on the relatively smaller channels. Gravity-driven, shear-driven (which are the two idealized modes that have been studied the most) and multi-regime models are addressed, followed by a presentation of the limited information on channels in the 400 μm to 3 mm range, that have loosely been referred to as microchannels by the air-conditioning and refrigeration industry. The focus here is on condensation inside *horizontal* tubes (Table 6.4).

Table 6.4

Summary of heat transfer studies.

Investigator	Hydraulic diameter (mm)	Fluids	Orientation/ condition	Range/applicability	Techniques, basis, observations
Conventional channel models and correlations: gravity-driven condensation					
Chato (1962)	27.94 mm 14.53 mm	Air–water R-113	Horizontal, inclined	$Re_V < 35,000$	<ul style="list-style-type: none"> Analyzed stratified-flow condensation inside horizontal and inclined tubes under low vapor shear conditions Heat transfer in the liquid pool neglected
Rosson and Myers (1965)	9.53 mm	Methanol, acetone	Horizontal	Atmospheric pressure $2000 < Re_{SV} < 40,000$ $60 < Re_{SL} < 1500$	<ul style="list-style-type: none"> Measured circumferential variation of h during stratified condensation $h \sim$ constant at top of tube ($\theta < 10^\circ$), then decreased linearly to point where it again became approximately constant
Rufer and Kezios (1966)	9.75, 15.875 mm	R-22, Air–water	Horizontal, inclined	$T = 43.3^\circ\text{C}$ for R-22	<ul style="list-style-type: none"> Analyzed stratified condensation in horizontal/inclined tubes Predicted liquid levels to find area for film condensation in the upper portion of tube, and therefore, overall effective h Liquid pool depths and axial variation different from open-channel hydraulics results of Chato (1962)
Chen and Kocamustafaogullari (1987)	10.8–16.6 mm	R-12, R-113, water, methanol, acetone, propane	Horizontal		<ul style="list-style-type: none"> Numerical model for stratified condensation in smooth horizontal tube Effects of interfacial shear on condensing film and liquid pool, axial ΔP, T_{sat}, wall-to-saturation ΔT and variation of liquid pool height taken into account Analytical expression based on dimensional analysis also presented
Singh <i>et al.</i> (1996)	11 mm	R-134a	Horizontal	$T = 35^\circ\text{C}$ $50 < G < 300 \text{ kg/m}^2\text{-s}$	<ul style="list-style-type: none"> Strong mass flux dependence for h in wavy–annular and annular flow, less in stratified wavy regime Traviss <i>et al.</i> (1973), Shah (1979), Dobson <i>et al.</i> (1994), Chato (1962), and Akers <i>et al.</i> (1959) correlations underpredicted data Accounted for forced convection in liquid pool
Guo and Anand (2000)	Rectangular $12.7 \times 25.4 \text{ mm}$	R-410A	Horizontal (long side vertical)	$T = 7.8\text{--}36.7^\circ\text{C}$ $30 < G < 2200 \text{ kg/m}^2\text{-s}$	<ul style="list-style-type: none"> Analytical model for stratified condensation Area-weighted average of the top, bottom, and vertical wall h Accounted for axial vapor shear on film condensation

(Continued)

Table 6.4
(Continued)

Investigator	Hydraulic diameter (mm)	Fluids	Orientation/condition	Range/applicability	Techniques, basis, observations
Conventional channel models and correlations: shear-driven condensation					
Carpenter and Colburn (1951)	11.66 mm	Steam, methanol, ethanol, toluene, trichloroethylene	Vertical		<ul style="list-style-type: none"> • Data for local and average h • Thin condensate film becomes turbulent at $Re_1 \sim 240$ • Considered vapor shear, gravity, and momentum change due to condensation acting upon condensate layer • Major thermal resistance in laminar sublayer • von Karman velocity profile for liquid film to obtain local h as function of film thickness and sum of forces on condensate • Condensation divided into: laminar condensate entrance region, turbulent condensate, laminar vapor exit (Nusselt analysis)
Akers <i>et al.</i> (1959)				$Re_1 > 5000$ $Re_v \left(\frac{\mu_v}{\mu_l} \right) \left(\frac{\rho_l}{\rho_v} \right)^{0.5} > 20,000$	<ul style="list-style-type: none"> • Equivalent all-liquid mass flux to replace vapor core, and provided same h for condensing annular flow • Enables single-phase flow treatment
Akers and Rosson (1960)	15.88 mm	Methanol, R-12	Horizontal	$1000 < \frac{DG_v}{\mu_l} \left(\frac{\rho_l}{\rho_v} \right)^{0.5} < 100,000$	<ul style="list-style-type: none"> • Three different experimentally validated correlations for “semi-stratified” flow, laminar, and turbulent annular flow • Multipliers to single-phase Nu based on data
Soliman <i>et al.</i> (1968)	$7.44 < D < 11.66$ mm	Steam, R-113, ethanol, methanol, toluene, trichloroethylene, R-22	Horizontal vertical downward	$1 < Pr < 10$, $6 < U_v < 300$ m/s, $0.03 < x < 0.99$	<ul style="list-style-type: none"> • Modifications to Carpenter and Colburn (1951) shear stress • Wall shear stress combination of friction, momentum, and gravity contributions • Wall shear stress used to develop model for h for annular flow • Parametric analyses to highlight importance of different forces
Traviss <i>et al.</i> (1973)	8-mm tube	R-12 and R-22	Horizontal	$T = 25\text{--}58.3^\circ\text{C}$ $161 < G < 1533$ kg/m ² -s	<ul style="list-style-type: none"> • Heat–momentum analogy and von Karman velocity profile in liquid film to correlate Nu in annular flow • Frictional term from two-phase multiplier • Three-region turbulent film model

Shah (1979)	$7 < D < 40$ mm	R-11, R-12, R-22, R-113, methanol, ethanol, benzene, toluene, trichloro-ethylene	Horizontal, inclined and vertical tubes, annulus	$11 < G < 211$ kg/m ² -s $21 < T < 310^{\circ}\text{C}$ $3 < U_v < 300$ m/s $0.002 < \text{Pr} < 0.44$ $1 < \text{Pr}_l < 13$ $\text{Re}_l > 350$	<ul style="list-style-type: none"> Widely used general purpose empirical correlation Large database from 21 sources Basis: condensation h similar to evaporative h in absence of nucleate boiling Two-phase multiplier in terms of p_r and x
Soliman (1986)	$7.4 < D < 12.7$ mm	Steam, R-113, and R-12	Horizontal vertical	$21 < T < 310^{\circ}\text{C}$ $80 < G < 1610$ kg/m ² -s $0.20 < x < 0.95$ $8 < \text{We} < 140$ $1 < \text{Pr}_l < 7.7$	<ul style="list-style-type: none"> Correlation for annular-mist flow Heat-momentum analogy for single-phase turbulent flow used as starting point Homogeneous flow in thermodynamic equilibrium Mixture viscosity basis
Chen <i>et al.</i> (1987)			Co-current annular film in vertical and horizontal tube		<ul style="list-style-type: none"> Film condensation correlation based on analytical and empirical approach to asymptotically combine values at limits Interfacial shear, interface waviness, and turbulent transport Included effects of interfacial shear, interface waviness, and turbulent transport Average and local Nu from asymptotic limits
Tandon <i>et al.</i> (1995)	10 mm	R-12, R-22	Horizontal	$20 < T < 40^{\circ}\text{C}$ $175 < G < 560$ kg/m ² -s	<ul style="list-style-type: none"> At same G_v, h for R-22 higher than for R-12 h trends slope change at $\text{Re}_v \sim 3 \times 10^4$; based on transition, proposed wavy, and annular/semi-annular flow correlations
Chitti and Anand (1995; 1996)	8 mm	R-22, R-32/R-125 with oil	Horizontal	$32.2 < T < 51.7^{\circ}\text{C}$ $148 < G < 450$ kg/m ² -s	<ul style="list-style-type: none"> Analytical model for annular condensation Used Prandtl mixing length theory with van Driest's (1956) hypothesis (law of wall) to obtain ε_m, $\text{Pr}_t = 0.9$ h for R-32/R-125 15% higher than for R-22, effect of oil minimal
Moser <i>et al.</i> (1998)	$3.14 < D < 20$ mm	R-22, R-134a, R-410a, R-12, R-125, R-11			<ul style="list-style-type: none"> Akers <i>et al.</i> (1959) G_{eq} model consistently underpredicts data Akers assumptions of constant and equal f_v, f_l not correct, also ΔT of Akers <i>et al.</i> not correct New Re_{eq} with Friedel (1979) ϕ_{10}^2, boundary layer analysis to obtain equivalent Nu
Hurlburt and Newell (1999)	3–10 mm	R-22, R-134a, R-11, R-12, R-22	Horizontal	$0.2 < x < 0.9$ $200 < G < 650$ kg/m ² s	<ul style="list-style-type: none"> Scaling equations to translate between α, ΔP, h for different refrigerants at different conditions and geometries

(Continued)

Table 6.4
(Continued)

Investigator	Hydraulic diameter (mm)	Fluids	Orientation/condition	Range/applicability	Techniques, basis, observations
Conventional channel models and correlations: multi-regime condensation					
Jaster and Kosky (1976)	12.5 mm	Steam	Horizontal	$2 \times 10^4 < P < 1.7 \times 10^5$ $12.6 < G < 145 \text{ kg/m}^2\text{-s}$	<ul style="list-style-type: none"> Algebraic expression for film thickness facilitates computations Stress ratio to distinguish between annular/stratified regimes Heat–momentum transfer analogy (annular flow) with two-phase multiplier for shear stress For stratified flow, related liquid pool angle to void fraction Linear interpolation for transition region
Breber <i>et al.</i> (1979; 1980)	4.8–50.8 mm	R-11, R-12, R-113, steam, <i>n</i> -pentane	Horizontal	$108.2 < P < 1250 \text{ kPa}$ $17.6 < G < 990 \text{ kg/m}^2\text{-s}$	<ul style="list-style-type: none"> Forced-convective correlation with two-phase multiplier for annular, intermittent and bubbly flow Nusselt-type equation for stratified–wavy Interpolations in transition zones
Nitheanandan <i>et al.</i> (1990)	7.4–15.9 mm	R-12, R-113, and steam		Data from various sources	<ul style="list-style-type: none"> Evaluation of correlations in literature Mist flow ($We \geq 40$, $Fr \geq 7$): Soliman (1986) Annular flow ($We < 40$, $Fr \geq 7$): Shah (1979) Wavy flow ($Fr < 7$): Akers and Rosson (1960)
Dobson <i>et al.</i> (1994)	4.57 mm	R-12, R-134a	Horizontal	$75 < G < 500 \text{ kg/m}^2\text{-s}$ $T = 35^\circ\text{C}$ and 60°C	<ul style="list-style-type: none"> Annular flow: h increased with G, x due to increased shear and thinning of liquid film – used two-phase multiplier Wavy flow: h independent of G, slight increase with x – Chato (1962) with leading constant changed to function of X_{tt}
Dobson and Chato (1998)	31.4, 4.6, and 7.04 mm	R-12, R-134a, R-22, Near azeotropic blends of R-32/ R-125	Horizontal	$25 < G < 800 \text{ kg/m}^2\text{-s}$ $T = 35\text{--}60^\circ\text{C}$	<ul style="list-style-type: none"> Extended Dobson <i>et al.</i> (1994) – additional tubes, fluids Fluid properties effect not very significant No significant effect of diameter reduction Wavy and annular correlations updated, forced convection in liquid pool and film condensation at the top, void fraction for pool depth estimate Fr_{so} and G used to separate regimes
Wilson <i>et al.</i> (2003)	$D = 7.79, 6.37, 4.40$, and 1.84	R-134a and R-410A	Horizontal	$T = 35^\circ\text{C}$ $75 < G < 400 \text{ kg/m}^2\text{-s}$	<ul style="list-style-type: none"> Progressively flattened 8.91 mm round smooth/microfin tubes h increases with flattening, h highest for helical microfins No predictive models or correlations

Cavallini <i>et al.</i> (2001; 2002a; 2002b)	8 mm	R-22, R-134a, R-125, R-32, R-236ea, R-407C, and R-410A	Horizontal	$30 < T < 50^{\circ}\text{C}$ $100 < G < 750 \text{ kg/m}^2\text{-s}$	<ul style="list-style-type: none"> • Breber <i>et al.</i> (1979; 1980) type approach for h recommendations • Own data and database from others used for correlations • Kosky and Staub (1971) for annular h with modified Friedel (1979; 1980) for shear stress • Stratified: film condensation and forced convection in pool • Interpolations for other regimes, bubbly treated as annular • Mass flux criterion for wavy–slug transition
Thome <i>et al.</i> (2003)	$3.1 < D < 21.4 \text{ mm}$	R-11, R-12, R-113, R-32/ R-125, propane, <i>n</i> -butane, iso-butane, and propylene	Horizontal	$24 < G < 1022 \text{ kg/m}^2\text{-s}$ $0.02 < p_r < 0.8$ $0.03 < x < 0.97$	<ul style="list-style-type: none"> • Curve-fitting from large database • h data used to refine void fraction model, which is used to predict transitions, in turn used to predict tuned blend of stratified–convective heat transfer coefficients • Stratified pool spread out as partial annular film • Includes effect of interfacial waves on heat transfer • Smoothly varying h across regimes through interpolations • No new intermittent, bubbly, or mist models; treated as annular
Goto <i>et al.</i> (2003)	Helical, herringbone grooved tubes, 8.00 mm	R-410A and R-22	Horizontal	$30 < T < 40^{\circ}\text{C}$ $130 < G < 400 \text{ kg/m}^2\text{-s}$	<ul style="list-style-type: none"> • h tests in complete vapor compression system • h of herringbone grooved tube $\sim 2 \times$ helical grooved tubes • Modified Koyama and Yu's (1996) correlation for stratified and annular condensation, new expressions for annular flow part
Condensation in small channels					
Yang and Webb (1996a)	Rectangular plain $D_h = 2.64$, microfin tubes $D_h = 1.56 \text{ mm}$	R-12	Horizontal	$T = 65^{\circ}\text{C}$ $400 < G < 1400 \text{ kg/m}^2\text{-s}$	<ul style="list-style-type: none"> • Shah (1979) significantly overpredicted data, Akers <i>et al.</i> (1959) better agreement, except at high G • Enhancement due to microfins decreased with increasing G • h showed heat flux dependence • Surface tension drainage rationale for microfin enhancement • Yang and Webb (1996b) concluded surface tension did not play role in ΔP in these same tubes

(Continued)

Table 6.4
(Continued)

Investigator	Hydraulic diameter (mm)	Fluids	Orientation/ condition	Range/applicability	Techniques, basis, observations
Yang and Webb (1997)	Extruded microchannels ($D_h = 1.41$ and 1.56 mm) with microfins	R-12, R-134a			<ul style="list-style-type: none"> • $G = 400$ kg/m²-s and $x > 0.5$, surface tension contribution equals and exceeds vapor shear term • $G = 1400$ kg/m²-s, surface tension contribution very small • h model based on shear and surface tension drainage (flooded and unflooded parts) • Small fin tip radius enhanced h, large inter-fin drainage area activated surface tension effect at lower x
Kim <i>et al.</i> (2003)	$D_h = 1.41$ smooth, 1.56 mm microfin	R-22 and R-410A	Horizontal	$T = 45^\circ\text{C}$ $200 < G < 600$ kg/m ² -s	<ul style="list-style-type: none"> • In smooth tubes, R-410A h slightly higher than R-22, opposite true for microfin tubes • Many qualitative explanations for varying enhancement trends • Recommend Moser <i>et al.</i> (1998) model with modified two-phase multiplier for smooth tubes, and Yang and Webb's (1997) model with minor modifications for microfin tubes
Yan and Lin (1999)	2 mm	R-134a	Horizontal	$T = 40\text{--}50^\circ\text{C}$	<ul style="list-style-type: none"> • Condensation h higher at lower T_{sat}, especially at higher x • h decreased significantly as q'' increased, particularly at high x; some unusual trends in data • Re_{eq} based h correlation
Wang <i>et al.</i> (2002)	Rectangular $D_h = 1.46$ mm (1.50×1.40 mm)	R-134a	Horizontal	$T = 61.5\text{--}66^\circ\text{C}$ $75 < G < 750$ kg/m ² -s	<ul style="list-style-type: none"> • Large variations in x across test section • Stratification seen even at such small D_h • Akers <i>et al.</i> (1959) Re_{eq} agreed with annular data, Jaster and Kosky (1976) agreed best with stratified flow data • Breber <i>et al.</i> (1980) and Soliman (1982; 1986) transition criteria • Curve-fits for two-phase multiplier, dimensionless temperature • Stratified and annular flow correlations with interpolations

Koyama <i>et al.</i> (2003b)	Multi-port extruded al tubes	R-134a	Horizontal	$T = 60^{\circ}\text{C}$ $100 < G < 700 \text{ kg/m}^2\text{-s}$	<ul style="list-style-type: none"> Local h measured every 75 mm of using heat flux sensors Combination of convective and film condensation terms. Annular and stratified terms from Haraguchi <i>et al.</i> (1994a, b), two-phase multiplier replaced by Mishima and Hibiki (1996)
Wang, Rose, and co-workers (Wang and Rose, 2004; Wang <i>et al.</i> , 2004)	Triangular (Wang and Rose, 2004) $D_h = 0.577 \text{ mm}$ Square (Wang <i>et al.</i> , 2004)	R-134a	Horizontal	$T = 50^{\circ}\text{C}$ $100 < G < 1300 \text{ kg/m}^2\text{-s}$	<ul style="list-style-type: none"> Wang and Rose (2004) numerical analyses to predict varying condensate flow pattern across cross-section and length Wang <i>et al.</i> (2004) model for film condensation of R-134a in square, horizontal, 1-mm microchannels Surface tension, gravity, and shear terms can be turned on or off to demonstrate individual effects
Cavallini <i>et al.</i> (2005)	Multiple parallel 1.4-mm channels	R-134a R-410A		$T = 40^{\circ}\text{C}$ $200 < G < 1000 \text{ kg/m}^2\text{-s}$	<ul style="list-style-type: none"> h from T_{wall} measurements, available models (Akers <i>et al.</i>, 1959; Moser <i>et al.</i>, 1998; Zhang and Webb, 2001; Cavallini <i>et al.</i>, 2002a; Wang <i>et al.</i>, 2002; Koyama <i>et al.</i>, 2003a) underestimate results Mist flow in experiments might lead to high h
Shin and Kim (2005)	Circular and square channels $0.5 < D_h < 1 \text{ mm}$	R-134a	Horizontal	$T = 40^{\circ}\text{C}$ $100 < G < 600 \text{ kg/m}^2\text{-s}$	<ul style="list-style-type: none"> Technique matched T_{out} of electrically heated air stream with similar air stream heated by condensing refrigerant R-134a Measured small, local condensation Q Most available models and correlations (Akers <i>et al.</i>, 1959; Soliman <i>et al.</i>, 1968; Traviss <i>et al.</i>, 1973; Cavallini and Zecchin, 1974; Shah, 1979; Dobson, 1994; Moser <i>et al.</i>, 1998) underpredict data at low G At lower G, square channels had higher h than circular channels, reverse was true for high G
Garimella and Bandhauer (2001); Bandhauer <i>et al.</i> (2005)	$0.4 < D_h < 4.9 \text{ mm}$	R-134a	Horizontal	$150 < G < 750 \text{ kg/m}^2\text{-s}$	<ul style="list-style-type: none"> Thermal amplification technique for accurate h measurement h model for circular tubes based on Traviss <i>et al.</i> (1973) boundary-layer analyses Two-region dimensionless film temperature Interfacial shear stress from models developed specifically for microchannels Addresses annular, mist, and disperse wave regimes

6.5.1. Conventional channel models and correlations

6.5.1.1. Gravity-driven condensation

Gravity-driven condensation is expected to be less important in microchannel two-phase flows than in conventional channels; however, various authors have assumed that condensation occurs either in a gravity-driven mode or a shear-driven mode, even in channels as small as ~ 3 mm. The relative prevalence of these modes is governed by flow conditions and channel size, as discussed at length in the previous sections. A brief overview of the treatment of gravity-driven condensation is provided here.

Much of the early work on condensation heat transfer is based upon the falling-film condensation analysis of Nusselt (1916), who assumed that a thin laminar condensate film formed on an isothermal flat plate with a surface temperature less than the saturation temperature, surrounded by a stationary vapor at the saturation temperature. The condensate flows under the influence of gravity and the film thickens as it moves down the plate. Nusselt further assumed that heat transfer is due to conduction across the film only. In addition, he assumed constant film properties, negligible film subcooling, and a smooth liquid–vapor interface. After conducting an energy balance around a film element and integrating with appropriate relationships for the mass flow rate, the relationship for film thickness is found, which is used to derive the following relationship for the average Nusselt number along a plate with length L :

$$\overline{\text{Nu}}_L = \frac{\bar{h}_l L}{k_l} = 0.943 \left[\frac{\rho_l (\rho_l - \rho_v) g \times h_{lv} \times L^3}{k_l \times \mu_l (T_{\text{sat}} - T_{\text{wall}})} \right]^{1/4} \quad (6.93)$$

This result provides the foundation for much of the literature on gravity-driven condensation heat transfer. Rohsenow (1956) presented the solution for the temperature distribution for the condensate film in falling-film condensation, which was employed in Rohsenow *et al.* (1956) to account for the nonlinearity in film temperature. The analysis was similar to Nusselt's falling-film condensation model, except that the net enthalpy change in the fluid was accounted for in the energy balance. Therefore, a modified enthalpy of vaporization, as shown below, was introduced to account for film subcooling:

$$h'_{lv} = h_{lv} (1 + 0.68 Ja_1) \quad (6.94)$$

Chato (1962) analyzed stratified-flow condensation inside horizontal and inclined tubes under low vapor shear conditions using similarity solutions, and validated the analyses using data on air/water mixtures flowing inside a 27.94-mm tube, and R-113 condensing inside a 14.53-mm tube at various inclinations. He showed that for several applications, heat transfer in the liquid pool can be neglected, and through measurements and analysis, found that the mean vapor angle in the tube was relatively constant at about 120° . He also found that heat transfer coefficients increase when the tube is inclined; however, they decrease upon further increases in the inclination to yield an optimum inclination angle of 10 – 20° . Due to the significant influence of vapor shear on liquid pool shape, his work is only applicable for the entrance vapor Reynolds number $\text{Re}_v < 35,000$. The following

equation yields satisfactory agreement with the results for all but fluids of low liquid Prandtl numbers:

$$\text{Nu} = \frac{hD}{k_l} = 0.468 \times K \left[\frac{\rho_l(\rho_l - \rho_v)g \times h'_{lv} \times D^3}{k_l \times \mu_l (T_{\text{sat}} - T_{\text{wall}})} \right]^{1/4} \quad (6.95)$$

The constant K (a correction for the liquid Prandtl number) was presented graphically, and a nominal value of $0.555 = 0.468K$ may be used. This result for the Nusselt number for condensation inside tubes is very similar to Nusselt's (1916) result for falling-film condensation on a flat plate with Rohsenow's (1956) correction for film subcooling. However, the constant multiplier was lower in Chato's analysis, primarily due to the increased thermal resistance resulting from the thicker liquid pool of condensate at the bottom of the tube.

Rosson and Myers (1965) measured the circumferential variation of heat transfer coefficients during stratified condensation of methanol and acetone at atmospheric pressure in a 3/8" (9.53 mm) nominal stainless steel pipe with a 1/8" (3.175 mm) wall thickness. They found that the condensation heat transfer coefficient was nearly constant at the top of the tube ($\theta < 10^\circ$), then decreased linearly to a point where it again became approximately constant. Based on this result, for the top portion, they suggested a leading coefficient of $0.31\text{Re}_v^{0.12}$ to the Nusselt condensation equation to account for vapor shear. For the bottom portion of the tube, the liquid pool heat transfer was not neglected, and the von Karman analogy between heat transfer and momentum was used. By assuming the wall shear was approximately equal to the buffer layer shear and turbulent $\text{Pr}_t = 1$, a relationship between the Nusselt number and wall shear stress was obtained. After assuming that the average shear was equal to the local shear and employing the Lockhart and Martinelli (1949) method for shear stress, the following Nusselt number correlation for the bottom portion of the tube was obtained:

$$\text{Nu} = \frac{\phi_l \sqrt{8\text{Re}_l}}{5 + 5\text{Pr}_l^{-1} \ln(1 + 5\text{Pr}_l)} \quad (6.96)$$

They also defined an interpolation scheme for regions between the top and the bottom. The linear interpolation was based on the circumferential location at which the heat transfer coefficient is the arithmetic mean of the top and bottom heat transfer coefficients, which was related to the vapor and liquid Reynolds numbers and the Galileo number, and the slope of the heat transfer coefficient at this location.

Rufer and Kezios (1966) also analyzed stratified condensation in horizontal and inclined tubes using an analytical approach; however, their results about the liquid pool depth were different from those of Chato (1962), prompting an interesting discussion between these authors in their paper about the validity of these two models. They model laminar condensation occurring in the upper portion of the tube akin to the Nusselt analysis, combined with a pool of liquid of varying depth at the bottom. They questioned the open-channel hydraulics basis used in Chato's paper and in the work of Chaddock (1957), in which it is assumed that the energy required to overcome friction and accelerate the liquid is supplied by the hydraulic gradient. They also stated that unlike Chato and Chaddock's treatments, the angle subtended by the liquid pool should not be affected by the exit

condition. While they neglected the effect of vapor shear on the laminar condensing film, for the liquid pool and the interface, they accounted for the forces represented by the two-phase pressure gradient, and changes in momentum, hydrostatic, gravity, and wall friction forces. They compared the resulting variation of the liquid level along the condensation path with the vapor holdup (void fraction) correlations of several authors, and found that the Hughmark (1962) model provided the best agreement. Similar to the findings of Chato, they also found that the liquid level decreases steeply (thus increasing heat transfer) with tube inclination at small angles of inclination, with this effect being less prominent as the inclination is increased further. Contrary to the findings of Chato, they found that the flow level angle (and therefore the liquid pool depth) increases as the condensation proceeds in the tube. Also, they found that at low mass fluxes, the liquid level did not change much as quality changed, while at high mass fluxes, the liquid level increased considerably toward the exit of the condenser. At a given quality, the liquid level increased as the mass flux was increased. Based on the manner in which the condensation model is developed, the prediction of these liquid levels directly determines the surface area available for the Nusselt film condensation in the upper portion of the tube, and therefore the overall effective heat transfer coefficient. A considerable amount of discussion on the contradictory trends predicted by Rufer and Kezios (1966) and Chato (1962) appears at the end of the former paper. This discussion is primarily about whether the liquid level should in fact rise or fall as the condensation proceeds, about whether the tube should be filled with liquid at the end of the condensation process, and about whether exit conditions should govern the holdup in the tube. The interested reader is referred to the paper by Rufer and Kezios (1966) for further elaboration.

Chen and Kocamustafaogullari (1987) presented a numerical model for stratified condensation inside a smooth horizontal tube, in which a condensate film formed on the top portion of the tube and drained to a condensate pool at the bottom, where it moved axially. The effects of interfacial shear on the thin condensing film and the condensate pool, axial pressure gradient, saturation temperature, wall-to-saturation temperature difference, and the variation of the liquid pool height were taken into account. Continuity, momentum, and energy equations were applied to the vapor core and laminar falling film, and the film region was solved assuming a thin film so that the effect of curvature could be neglected. The interfacial shear was computed based on the pressure gradient in the vapor core. Heat transfer coefficients were calculated for the laminar falling film and the condensate pool, with the total heat transfer coefficient being a function of both of these and the subtended liquid pool level angle:

$$h(z) = [\phi_m h_c(z) + (\pi - \phi_m) h_l(z)]/\pi \quad (6.97)$$

where h_c refers to the film heat transfer coefficient, while h_l is the heat transfer coefficient in the liquid pool, and ϕ_m is the angle subtended by the pool to the vertical. The film heat transfer coefficient was an integrated average of the local value, which was calculated from the numerically determined film thickness. The condensate pool heat transfer was found by using the expression developed by Rosson and Myers (1965) (discussed above), which is based on the von Karman analogy between momentum and heat transfer. This method yielded reasonable agreement with an existing condensation heat transfer database,

which includes diameters ranging from 10.8 to 16.6 mm, and the fluids R-12, R-113, water, methanol, acetone, and propane. They also conducted a dimensional analysis to develop an approximate equation for the heat transfer coefficient from the results of their numerical analysis for design purposes. They noted that since the liquid pool heat transfer is a small fraction of the total heat transfer, the appropriate dimensionless parameters could be obtained from the film condensation region alone, resulting in the following equation:

$$\overline{Nu} = 0.492 Ku^{-0.27} Pr^{0.25} Ga^{0.73} (l/D)^{-0.03} Re_{g,si}^{0.05} (1 + Re_{l,si})^{-0.01} \quad (6.98)$$

where Ku is the Kutateladze number $Ku = C_p \Delta T / h_{fg}$, Ga is the Galileo number $Ga = D(g \Delta \rho / \rho v^2)^{1/3}$, and $Re_{g,si}$ and $Re_{l,si}$ are the superficial gas and liquid phase velocities at the inlet, respectively. This correlation was within 2.8% of the numerical solution.

Singh *et al.* (1996) conducted experiments on R-134a condensing at 35°C inside a 11-mm tube for the mass flux range $50 < G < 300 \text{ kg/m}^2\text{-s}$. The data were found to be in the stratified-wavy, wavy-annular, and annular flow regimes. In the latter two regimes, a strong mass flux dependence was found for the heat transfer coefficient, while in the stratified-wavy regime, the dependence was less, although not negligible. They found that the Traviss *et al.* (1973), Shah (1979), Dobson *et al.* (1994), Chato (1962), and Akers *et al.* (1959) correlations underpredicted the data. Therefore, they proposed a correlation that uses the Chato (1962) correlation (with a much lower leading constant of 0.0925) for the top portion of the tube (i.e. film condensation). For the forced convective heat transfer through the condensate at the bottom portion of the tube, they used a two-phase multiplier correction to the Gnielinski (1976) single-phase correlation for $Re > 2300$:

$$h_{fo} = h_l \left(1 + \frac{0.2332}{X_{tt}^{1.4020}} \right) \quad (6.99)$$

and a modification to the Dittus-Boelter (1930) correlation for $Re < 2300$:

$$h_l = \frac{k_l}{D} 0.2339 Re_l^{0.5000} Pr_l^{0.33} \quad (6.100)$$

The top and bottom portions of the heat transfer coefficient were combined in the usual manner, $h = \theta h_{fo} + (2\pi - \theta) h_{fl}$, with the subtended angle given by $\theta \approx 2\cos^{-1}(2\alpha - 1)$, where the void fraction α is calculated using the Zivi (1964) correlation. The flow regimes were distinguished using the modified Froude number criterion proposed by Dobson *et al.* (1994):

$$\begin{aligned} Re_l \leq 1250 \quad Fr_m &= 0.025 \left(\frac{Re_l^{1.59}}{Ga^{0.5}} \right) \left(\frac{1 + 1.09 X_{tt}^{0.039}}{X_{tt}} \right)^{1.5} \\ Re_l > 1250 \quad Fr_m &= 1.26 \left(\frac{Re_l^{1.04}}{Ga^{0.5}} \right) \left(\frac{1 + 1.09 X_{tt}^{0.039}}{X_{tt}} \right)^{1.5} \end{aligned} \quad (6.101)$$

Thus, the flow was considered stratified-wavy for $Fr_m \leq 7$ and annular for $Fr_m > 7$. It should be noted that even though their data showed a transition (wavy-annular) region, for the model development, an abrupt transition was chosen.

More recently, Guo and Anand (2000) presented an analytical model for stratified condensation of R-410A (50/50 mixture of R-32 and R-125) at $30 < G < 2200 \text{ kg/m}^2\text{-s}$ in a $12.7 \times 25.4\text{-mm}$ horizontal rectangular channel, with the long side vertical. The heat transfer coefficient was the area-weighted average of the top, bottom, and vertical wall heat transfer coefficients. For the top wall, the von Karman analogy between heat transfer and momentum was applied. The energy equation was integrated across the film laminar and buffer layers, with the shear in the buffer layer assumed to equal the wall shear, and also with the assumption of $\text{Pr}_t = 1$. The shear stress was calculated using the Lockhart and Martinelli (1949) two-phase multiplier approach, resulting in the following expression for the Nusselt number at the top:

$$\text{Nu}_{\text{top}} = \frac{\phi_l \text{Re}_l \sqrt{f_{ls}/2}}{5 + \frac{5}{\text{Pr}_l} \ln(5\text{Pr}_l + 1)} \quad (6.102)$$

where f_{ls} represents the superficial liquid phase friction factor. For the side walls, they paid particular attention to the combined effects of Nusselt-type gravity-driven condensation and the vapor shear in the axial direction. A mass, momentum, and energy balance was conducted across a two-dimensional element (vertical and horizontal axes), which was used to obtain the film thickness dependent on the axial and vertical direction. The resulting quasi-linear, first-order partial differential equation was solved numerically to get the film thickness and the average heat transfer coefficient for the vertical walls. Heat transfer through the bottom wall was assumed to be solely due to conduction across the liquid pool, which in turn represented the accumulated condensate from condensation at the top and vertical walls. Their results showed that the film thickness on the vertical walls was larger as the vapor velocities decreased along the flow direction (at decreasing qualities), with lower interfacial shear leading to a thicker film. The film thickness decreased with higher mass fluxes due to the increased velocities. The decrease in the heat transfer coefficient in the axial flow direction was illustrated through graphs of increasing film thickness, which constituted an increasing thermal resistance. Also, the slower growth of the film thickness along the length represented the lower condensation rates toward the end of the condensation process due to the lower heat transfer coefficients. These analytical and numerical results agreed well with the data of Guo (1998) (mean deviation of 6.75%), but not the correlations of Rosson and Myers (1965) and Dobson (1994). This could be because condensation on the bottom pool was neglected by Guo and Anand (2000), and also due to differences between the circular and rectangular geometries.

6.5.1.2. Shear-driven condensation

Carpenter and Colburn (1951) obtained data for local and average heat transfer coefficients for the condensation of steam, methanol, ethanol, toluene, and trichloroethylene inside a vertical 11.66-mm ID tube. The data were compared with the Nusselt equation, which underpredicted the values due to the influence of vapor shear. Carpenter and Colburn stated that the thin condensate layer for annular flow might become turbulent at very low liquid Reynolds numbers (~ 240). They considered vapor shear, gravity, and the momentum change due to condensation acting upon this condensate layer. The major thermal

resistance was considered to be due to the laminar sublayer. Using the von Karman universal velocity profile for the liquid film, a relationship for the local condensation heat transfer coefficient was derived, which was a function of the film thickness (i.e. the laminar sublayer thickness), fluid properties, and the sum of the forces acting on the condensate. The gravity force was deemed to be unimportant, which is the case for annular flow. The vapor friction force was determined from an equivalent vapor friction factor, which was higher than for single-phase flow due to the presence of the liquid film. They also developed a separate correlation for a laminar condensate film with a linear velocity profile. Hence, the condensation process was divided into three different regions: laminar condensate entrance region, turbulent condensate, and laminar vapor exit region (where a Nusselt analysis was more appropriate).

As discussed in the previous section, Akers *et al.* (1959) defined an all-liquid flow rate that provided the same heat transfer coefficient for condensing annular flow. This all-liquid flow rate was expressed by an “equivalent” mass flux, which was used to define an equivalent Reynolds number. This equivalent Reynolds number was substituted in a single-phase heat transfer equation, which was a function of the liquid Prandtl and Reynolds numbers, to predict the two-phase condensation Nusselt number. Thus, the equivalent liquid mass flux G_{eq} is composed of the actual liquid condensate flux G_l , in addition to a liquid flux G'_l that replaces the vapor core mass flux and produces the same interfacial shear stress as the vapor core; $G_{eq} = G_l + G'_l$. By equating the shear stress due to the new liquid flux G'_l and the original vapor core flux G_v , they obtained:

$$G'_l = G_v \sqrt{\frac{\rho_l}{\rho_v}} \sqrt{\frac{f_v}{f_l}} \quad (6.103)$$

At this point, they assumed that f_l and f_v would be constant due to a presumed fully rough interface, and also that $f_l = f_v$, which resulted in $G_{eq} = G_l + G_v \sqrt{\rho_l / \rho_v}$. This G_{eq} was used to define Re_{eq} , which when substituted into a typical single-phase turbulent heat transfer equation yields:

$$Nu = 0.0265 Re_{eq}^{0.8} Pr^{1/3} \quad (6.104)$$

This equation is typically recommended for $Re_l > 5000$ and $Re_v(\mu_v/\mu_l)(\rho_l/\rho_v)^{0.5} > 20,000$.

Akers and Rosson (1960) developed three different experimentally validated heat transfer correlations for condensation inside horizontal tubes for “semi-stratified” flow (annular condensation and run down superimposed on stratified flow), laminar annular flow, and turbulent annular flow. Local values of the condensation heat transfer coefficient were determined experimentally for methanol and R-12 flowing inside a 15.88-mm horizontal tube. For $Re_l < 5000$, the heat transfer coefficient was a function of the Prandtl number, vapor Reynolds number, and wall temperature difference. For this region, the constant multiplier for the Nusselt number was determined from the experimental data. This constant and the exponent for Re_v were different for Re_v above and below 20,000, the resulting

expressions being:

$$\begin{aligned}
 1000 < \frac{DG_v}{\mu_l} \left(\frac{\rho_l}{\rho_v} \right)^{0.5} < 20,000 & \quad \frac{hD}{k_l} = 13.8 \text{Pr}_l^{1/3} \left(\frac{h_{fg}}{C_p \Delta T} \right)^{1/6} \left[\frac{DG_v}{\mu_l} \left(\frac{\rho_l}{\rho_v} \right)^{0.5} \right]^{0.2} \\
 20,000 < \frac{DG_v}{\mu_l} \left(\frac{\rho_l}{\rho_v} \right)^{0.5} < 100,000 & \quad \frac{hD}{k_l} = 0.1 \text{Pr}_l^{1/3} \left(\frac{h_{fg}}{C_p \Delta T} \right)^{1/6} \left[\frac{DG_v}{\mu_l} \left(\frac{\rho_l}{\rho_v} \right)^{0.5} \right]^{2/3}
 \end{aligned} \tag{6.105}$$

For turbulent liquid films, the correlation developed by Akers *et al.* (1959), which neglected the wall temperature difference, was employed.

Ananiev *et al.* (1961) suggested that the two-phase heat transfer coefficient can be related to the corresponding single-phase heat transfer coefficient with the entire mass flux flowing as a liquid, $h = h_o \sqrt{\rho_l / \rho_m}$, where the mixture density is given by $1/\rho_m = (1/\rho_l)(1-x) + (1/\rho_v)x$. Boyko and Kruzhilin (1967) used this approach to correlate steam condensation data for $10 < D < 17$ mm from Miropolsky (1962), with a Dittus–Boelter-type single-phase heat transfer coefficient proposed by Mikheev (1956) of the form $(h_o D/k) = C \text{Re}^{0.8} \text{Pr}_b^{0.43} (\text{Pr}_b/\text{Pr}_w)^{0.25}$. Different leading constants C were required for the single-phase heat transfer coefficient to fit the data from tubes of different materials.

Soliman *et al.* (1968) developed a model for predicting the condensation heat transfer coefficient for annular flow. In this work, they note that Carpenter and Colburn (1951) did not appropriately account for the momentum contribution to the wall shear stress. They evaluated the wall shear stress as a combination of friction, momentum, and gravity contributions, and used the resulting expression to evaluate the heat transfer coefficient, much like the approach used by Carpenter and Colburn (1951). Soliman *et al.* (1968) performed momentum balances around the vapor core and the liquid film. To obtain the shear stress at the vapor–liquid interface, they used the Lockhart–Martinelli (1949) two-phase multiplier, representing it as $\phi_v = 1 + 2.85 X_{tt}^{0.523}$, yielding

$$\tau_i = \frac{D}{4} \left(-\frac{dP}{dz} \right)_F \left(-\frac{dP}{dz} \right)_F = \phi_g^2 \left(-\frac{dP}{dz} \right)_v \tag{6.106}$$

in the usual manner. The momentum term accounts for the slowing down of the condensing vapor as it converts into the liquid phase. Depending on whether the liquid film is laminar or turbulent, the interface velocity is related to the mean film velocity as $U_{li} = \beta U_l$, where $\beta = 2$ for a laminar film, and $\beta = 1.25$ for a turbulent film. The shear due to momentum change is then represented as follows:

$$\tau_m = \frac{D}{4} \left(\frac{G^2}{\rho_v} \right) \left(\frac{dx}{dz} \right) \sum_{n=1}^5 a_n \left(\frac{\rho_v}{\rho_l} \right)^{n/3} \tag{6.107}$$

The respective coefficients $a_1 \dots a_5$ in terms of the local quality and the velocity ratio β are available in their paper as well as in Carey (1992). For the general case of an inclined

tube, the shear due to gravity is given by:

$$\tau_g = \frac{D}{4}(1 - \alpha)(\rho_l - \rho_g)g \sin \theta \quad (6.108)$$

where the void fraction is calculated using the Zivi (1964) correlation. The three shear stress terms are summed as follows to yield the wall shear stress:

$$\tau_w = \tau_i + \tau_m + \tau_g \quad (6.109)$$

Parametric analyses on the various components of the shear term were also conducted to determine their relative significance along the condensation path. The friction term dominated at high and intermediate x , and progressively decreased toward the end of the condenser due to the decreasing vapor velocities. The gravity term is negligible at high x , and increases with increasing film thickness as condensation proceeds. The momentum term consists of the contribution due to the momentum added to the liquid film by the condensing vapor (positive term), and the reverse shear stress at the wall due to momentum recovery of the vapor (only significant at low void fractions). Momentum effects are significant for high liquid-to-gas density ratios and become important at low x in the absence of a gravity field. These considerations were also used to predict the onset of flooding in countercurrent gas–liquid flow. They commented that while some investigators may have obtained reasonable agreement between their heat transfer data and models even when ignoring or incorrectly accounting for momentum effects, this may simply be due to the relative unimportance of these terms at the tested conditions. Due to the variations of the constituent terms in the overall shear stress, however, these terms must be properly accounted for, so that the model can be valid over a wide range of conditions. With the wall shear evaluated, the following expression for the heat transfer coefficient was developed using the data from several investigators:

$$\frac{h\mu_l}{k_l\rho_l^{1/2}} = 0.036\text{Pr}_l^{0.65}\tau_w^{1/2} \quad (6.110)$$

The above equation is valid for $7.44 < D < 11.66$ mm, the fluids steam, R-113, ethanol, methanol, toluene, trichloroethylene, and R-22, $1 < \text{Pr} < 10$, $6 < U_v < 300$ m/s, $0.03 < x < 0.99$, for horizontal as well as vertical downward condensation when annular flow prevails.

Traviss *et al.* (1973) used the heat–momentum analogy and the von Karman universal velocity distribution in the liquid film to develop a correlation for the Nusselt number in annular flow condensation. The turbulent vapor core prompted the assumption that the vapor core and vapor–liquid interface temperatures were the same. The pressure gradient was considered to be due to friction, gravity, and momentum change. In a manner analogous to that used by Soliman (1968), they computed the frictional term using the Lockhart–Martinelli (1949) two-phase multiplier approach with the expression for ϕ_g developed by Soliman (1968). They also used Zivi's (1964) void fraction model to compute the gravitational term. For the momentum term, assuming that the liquid film was thin compared to

the tube length, flat-plate flow was used. The ratio of the interface velocity to the average liquid film velocity, β (defined above in the discussion of the work of Soliman (1968)), was obtained from the universal velocity profile as a function of the non-dimensional film thickness. The eddy diffusivity ratio (i.e. the turbulent Prandtl number) was assumed to be unity. Using the assumed liquid velocity profile, a relationship for the condensation heat transfer coefficient was determined as a function of the turbulent film thickness. They then derived a relationship for the liquid Reynolds number as a function of this film thickness. By arguing that the interfacial shear to wall shear ratio was approximately unity, the final relationship for the condensation heat transfer coefficient was developed as follows:

$$\frac{hD}{k_l} = \frac{0.15\text{Pr}_l\text{Re}_l^{0.9}}{F_T} \left(\frac{1}{X_{tt}} + \frac{2.85}{X_{tt}^{0.476}} \right) \quad \text{Re}_l = \frac{G(1-x)D}{\mu_l} \quad (6.111)$$

where F_T is given as follows:

$$\begin{aligned} F_T &= 5\text{Pr}_l + 5 \ln(1 + 5\text{Pr}_l) + 2.5 \ln(0.0031\text{Re}_l^{0.812}) \quad \text{Re}_l > 1125 \\ &= 5\text{Pr}_l + 5 \ln[1 + \text{Pr}_l(0.0964\text{Re}_l^{0.585} - 1)] \quad 50 < \text{Re}_l < 1125 \\ &= 0.707\text{Pr}_l\text{Re}_l^{0.5} \quad \text{Re}_l < 50 \end{aligned} \quad (6.112)$$

The results were compared with experiments conducted on R-12 and R-22 condensing in an 8-mm tube for $161 < G < 1533 \text{ kg/m}^2\text{-s}$. Agreement with the experimental data was good for qualities as low as 0.1, and the quality range from 0 to 0.1 (presumed by them to be slug flow) was predicted well by conducting a linear interpolation between this model and a single-phase heat transfer correlation. When the turbulent Martinelli parameter was below 0.155, the correlation produced good results. However, for Martinelli parameters above 0.155, most probably a mist flow (high quality and mass flux) condition, the experimental data were underpredicted by the correlation. A correction factor was proposed to improve predictions in this area.

One of the most widely used general purpose condensation correlations, due to the large database from 21 investigators used for its development, and also its ease of use, is the Shah (1979) correlation. Shah reasoned that in the absence of nucleate boiling, condensation heat transfer should be similar to evaporative heat transfer when the tube is completely wet, and extended the correlation developed previously (Shah, 1976) for evaporation to condensation as follows:

$$\begin{aligned} \frac{h}{h_{lo}} &= (1-x)^{0.8} + \frac{3.8x^{0.76}(1-x)^{0.04}}{(P/P_{\text{crit}})^{0.38}} \\ h_{lo} &= 0.023 \left(\frac{k_l}{D} \right) \left(\frac{GD}{\mu_l} \right) 0.8\text{Pr}_l^{0.4} \end{aligned} \quad (6.113)$$

He validated the correlation using data for water, R-11, R-12, R-22, R-113, methanol, ethanol, benzene, toluene, and trichloroethylene condensing inside horizontal, inclined and vertical tubes, as well as an annulus. The mean deviation between the predictions and the 474 data points used for correlation development was 17%. Some noticeable discrepancies

included the underprediction of the data at high qualities (85–100%), which could be due to entrance or entrainment effects. The operating conditions included $11 < G < 211 \text{ kg/m}^2\text{-s}$, $21^\circ\text{C} < T_{\text{sat}} < 310^\circ\text{C}$, $3 < U_v < 300 \text{ m/s}$, reduced pressure from 0.002 to 0.44, and $1 < \text{Pr}_1 < 13$, for tube diameters between 7 and 40 mm. Shah recommended that the correlation should be used only for $\text{Re}_1 > 350$ due to the lack of lower Re_1 data for the development of the correlation.

Soliman (1986) developed a heat transfer correlation for condensation in annular–mist flow. The annular–mist transition criterion developed by him was discussed in a previous section of this chapter. He stated that previous approaches for modeling mist flow heat transfer had primarily tried to modify annular flow models, with limited success. Therefore, he developed a model specifically for this regime, using data from several investigators, selected because of the existence of mist flow. Thus, the selected data included data for steam, R-113, and R-12, $7.4 < D < 12.7 \text{ mm}$, horizontal and vertical orientations, $21^\circ\text{C} < T_{\text{sat}} < 310^\circ\text{C}$, $80 < G < 1610 \text{ kg/m}^2\text{-s}$, $0.20 < x < 0.95$, $8 < \text{We} < 140$, and $1 < \text{Pr}_1 < 7.7$. Of the five data sets chosen, one was in the annular flow regime, one was in annular and mist flow, and three were predominantly in mist flow, facilitating the development of this correlation. He found that although the Akers *et al.* (1959) correlation was successful in predicting the data for $\text{We} > 20$, the data were seriously underpredicted for $\text{We} > 30$. The Traviss *et al.* (1973) correlation was also found to seriously underpredict the data. Based on these observations, Soliman assumed that the flow would occur as a homogeneous mixture in thermodynamic equilibrium. Vapor shear would entrain the condensate into the bulk flow, leaving alternate dry spots and thin ridges of liquid at the wall. Heat transfer to this alternately dry or thin-film covered wall should therefore result in higher heat transfer coefficients than those predicted by annular flow models. The analogy between heat and momentum transfer for single-phase turbulent flow was used as a starting point. Thereafter, the effect of wall temperature difference was accounted for, which resulted in the following correlation (valid for $\text{We} > \sim 30\text{--}35$):

$$\text{Nu} = 0.00345 \text{Re}_m^{0.9} \left(\frac{\mu_G h_{\text{LG}}}{k_G (T_{\text{sat}} - T_w)} \right)^{1/3} \quad (6.114)$$

where the mixture Reynolds number is given by $\text{Re}_m = GD/\mu_m$, and the mixture viscosity given by $1/\mu_m = x/\mu_G + (1 - x)/\mu_L$.

Chen *et al.* (1987) developed a film condensation heat transfer correlation based on analytical and empirical approaches. They noted that at moderate film Re , waves on the film increase the surface area, which enhances heat transfer above the Nusselt predictions. At higher film Re ($\text{Re} > 1800$), the enhancement was attributed to turbulent transport in the condensate film. At high vapor velocities, as noted by others, they state that vapor shear modifies the condensate film, making it thinner in co-current flow, and thicker in countercurrent flow. Thus, in this work, they included the effects of interfacial shear, interface waviness, and turbulent transport. They considered the limiting cases of film condensation and interpolated between these limits to obtain a more general correlation. For laminar film condensation in a quiescent vapor, they accounted for the effect of waves at the interface by using Chun and Seban's (1971) expression $\text{Nu}_l = 0.823 \text{Re}_x^{-0.22}$. For turbulent films, they used the data of Blangetti and Schlunder (1978) for steam condensation in

a vertical tube, which leads to increasing Nu at increasing Re due to higher turbulent intensities, to express the Nusselt number as $Nu_T = 0.00402 Re_x^{0.4} Pr^{0.65}$. For condensation with high interfacial shear stress, they neglected the gravitational and momentum terms at high qualities to develop a simple relationship assuming that the wall shear stress was equal to the interfacial shear stress. Thus, the equation developed by Soliman *et al.* (1968) was simplified to $Nu_i = 0.036 Pr^{0.65} \tau_i^{*1/2}$, where $\tau_i^* = \tau_i / \rho_L (g v_L)^{2/3}$ for vertical as well as horizontal film condensation. Having developed expressions for individual regimes, they combined these using the technique of Churchill and Usagi (1972). They first developed an expression for gravity-dominated film condensation in a quiescent vapor by combining the wavy-laminar and turbulent expressions discussed above as follows:

$$Nu_0 = [(Nu_L^{n_1}) + (Nu_T^{n_1})]^{1/n_1} \quad (6.115)$$

The resulting Nu_0 for quiescent vapor condensation was combined with Nu_i for high interfacial shear condensation in like manner to yield:

$$Nu_x = [(Nu_0^{n_2}) + (Nu_i^{n_2})]^{1/n_2} \quad (6.116)$$

Using the data of Blangetti and Schlunder for downflow condensation of steam in a 30-mm vertical tube over a wide range of film Re and vapor velocities, they determined that $n_1 = 6$ and $n_2 = 2$, which yields the following correlation for local film condensation heat transfer:

$$Nu_x = \frac{h_x}{k_L} \left(\frac{v_L}{g} \right)^{1/3} = \left[\left(0.31 Re_x^{-1.32} + \frac{Re_x^{2.4} Pr^{3.9}}{2.37 \times 10^{14}} \right)^{1/3} + \frac{Pr^{1.3}}{771.6} \tau_i^* \right]^{1/2} \quad (6.117)$$

Based on the findings of Chen *et al.* (1984), they assumed that the interfacial shear for a turbulent vapor core would be the same for condensing and adiabatic flows, and used the shear stress relationship of Dukler (1960) to compute the Nusselt number above:

$$\tau_i^* = A(Re_T - Re_x)^{1.4} Re_x^{0.4} \quad A = \frac{0.252 \mu_L^{1.177} \mu_g^{0.156}}{D^2 g^{2/3} \rho_L^{0.553} \rho_g^{0.78}} \quad (6.118)$$

where Re_T is the film Re if the entire vapor flow condenses, and the parameter A accounts for gravitational and viscous forces. The resulting Nusselt number is valid for co-current annular film condensation in vertical tubes. For horizontal annular film condensation, the gravity terms are neglected to yield a simplified version of the Nusselt number equation as follows:

$$Nu_x = 0.036 Pr^{0.65} A^{0.5} (Re_T - Re_x)^{0.7} Re_x^{0.2} \quad (6.119)$$

Chen *et al.* cautioned that these equations would not apply at the very entrance of the tube when high vapor velocities could cause significant entrainment and mist flow, and toward the end of the condensation process, where stratified and slug flows would prevail.

They also developed expressions for the average Nusselt numbers for film condensation using the corresponding limiting expressions as the basis (rather than integrating the local Nu_x), which resulted in the following:

$$\overline{Nu} = \left(Re_T^{-0.44} + \frac{Re_T^{0.8} Pr^{1.3}}{1.718 \times 10^5} + \frac{A Pr^{1.3} Re_T^{1.8}}{2075.3} \right)^{1/2} \quad (6.120)$$

for vertical co-current condensation, and

$$\overline{Nu} = 0.036 Pr^{0.65} \bar{\tau}_i^{-*1/2} \\ \bar{\tau}_i^* = A \frac{Re_L^2}{Re_T^{0.2}} \left(\frac{Re_L}{Re_T} \right)^{-1.6} \left(1.25 + 0.39 \frac{Re_L}{Re_T} \right)^{-2} \quad (6.121)$$

for horizontal condensation. Using similar considerations, Chen *et al.* also developed expressions for the Nusselt number in countercurrent annular flow (reflux condensation), details of which are available in their paper.

Tandon *et al.* (1995) conducted condensation experiments for R-12 and R-22 flowing through a 10-mm horizontal tube, primarily in the wavy flow regime. They combined these data with previously reported data in the annular and semi-annular regimes for an overall range of $20^\circ\text{C} < T_{\text{sat}} < 40^\circ\text{C}$ and $175 < G < 560 \text{ kg/m}^2\text{-s}$ to propose modifications to the Akers–Rosson (1960) correlations. They found that at the same vapor mass flux, the heat transfer coefficient for R-22 was higher than that for R-12, primarily due to the higher thermal conductivity and latent heat of R-22. They noted that the heat transfer coefficient trends showed a change in slope at $Re_v \sim 3 \times 10^4$, indicating a transition from wavy to annular or semi-annular flow. This prompted them to propose the following correlations for shear-controlled and gravity-controlled flow regimes:

$$Re_v > 3 \times 10^4 \quad Nu = 0.084 Pr_L^{1/3} \left(\frac{h_{fg}}{C_p \Delta T} \right)^{1/6} Re_v^{0.67} \\ Re_v < 3 \times 10^4 \quad Nu = 23.1 Pr_L^{1/3} \left(\frac{h_{fg}}{C_p \Delta T} \right)^{1/6} Re_v^{1/8} \quad (6.122)$$

Chitti and Anand (1995) developed an analytical model for annular flow condensation in smooth horizontal round tubes. The results were compared with data for R-22 condensing inside an 8-mm tube. Their model used the Prandtl mixing length theory with van Driest's hypothesis (1956) (for the law of the wall) to obtain the momentum diffusivity, and $Pr_t = 0.9$. Thus, the computation of the shear stress distribution, pressure drop, and void fraction was avoided, and the heat flux was evaluated through continuity in the radial direction, with the film thickness being calculated iteratively. For closure, the friction velocity is calculated through the use of the empirical Lockhart–Martinelli (1949) two-phase multiplier ϕ_{vv}^2 from Azer *et al.* (1972). The model showed reasonable agreement with their data, with a mean deviation of 15.3%, about the same as the agreement achieved with the Traviss *et al.* (1973) model and the Shah (1979) correlation. Agreement with the equivalent mass

flux-type models of Akers *et al.* (1959) and Boyko and Kruzhilin (1967), however, was not particularly good, and they attributed this to the lack of a strong physical basis for these latter models. Chitti and Anand (1996) later extended the experiments to R-32/R-125 mixtures (50/50 by weight) with oil concentrations of 0%, 2.6%, and 5.35%, and pure R-22 condensing in the 8-mm horizontal tube, primarily in the annular regime based on the Taitel–Dukler (1976) map. They found a minimal effect ($\sim 10\%$) of condensing temperature on the heat transfer coefficient because the operating conditions ($24\text{--}38^\circ\text{C}$) were well below the critical temperature. Heat transfer coefficients for R-32/R-125 mixtures were about 15% higher than those for R-22, and the effect of polyolester oil was also found to be minimal, within the uncertainty estimates.

Moser *et al.* (1998) noted that the Akers *et al.* (1959) equivalent mass velocity model discussed above had been shown to consistently underpredict the data of several investigators. They stated that this was primarily due to two assumptions in their model that could not be adequately supported: (1) the assumption of constant and equal friction factors for the vapor core and the liquid film, because the latter would most certainly be affected by the Re_l , (2) the driving temperature differences for single-phase ($T_b - T_w$) and condensing flows ($T_\delta - T_w$) are completely different, something that the Akers *et al.* model does not take into account. To correct the first problem, they related the friction in the vapor and liquid phases through the two-phase multiplier concept, rather than assuming the friction factors to be equal. This led to the following definition of the equivalent Reynolds number: $Re_{eq} = \phi_{lo}^{8/7} Re_{lo}$. To evaluate ϕ_{lo}^2 , they recommended the use of the Friedel (1979) correlation. For the driving temperature difference, they related the single-phase and condensing ΔT_s as follows: $F = (T_b - T_w)/(T_\delta - T_w)$. Using a boundary-layer analysis similar to that of Traviss *et al.* (1973), along with the single-phase ΔT being determined by the Petukhov (1970) equation, the correction factor F was expressed as follows:

$$F = 1.31(R^+)^{C_1} Re_l^{C_2} Pr_l^{-0.185} \quad C_1 = 0.126 Pr_L^{-0.448} \quad C_2 = -0.113 Pr_l^{-0.563} \quad (6.123)$$

The dimensionless pipe radius was obtained through the friction velocity and the use of the Blasius friction factor, to yield $R^+ = 0.0994 Re_{eq}^{7/8}$. The final Nusselt number equation was as follows:

$$Nu = \frac{hD}{k_l} = \frac{0.0994 C_1 Re_l^{C_2} Re_{eq}^{1+0.875C_1} Pr_l^{0.815}}{(1.58 \ln Re_{eq} - 3.28)(2.58 \ln Re_{eq} + 13.7 Pr_l^{2/3} - 19.1)} \quad (6.124)$$

This model was shown to predict data from a variety of sources for $3.14 < D < 20$ mm with a mean deviation of 13.6%, about as well as the empirical Shah (1979) correlation, and better than the Traviss *et al.* (1973) correlation. In general, the trend was toward underprediction of data, which they stated could be corrected by the application of better pressure drop models for the evaluation of the two-phase multiplier required for this model. In addition, accounting for entrainment and stratified annular film would yield better predictions.

It was mentioned in the previous section that Hurlburt and Newell (1999) developed scaling equations for condensing flows that would enable the prediction of void fraction, pressure drop, and heat transfer for a refrigerant at a given condition and tube diameter from

the available results for another similar fluid (R-11, R-12, R-22, and R-134a) operating at a different condition in the diameter range 3–10 mm. They developed an equivalent average film thickness model assuming annular flow, which enabled the prediction of shear stress. Like several other researchers, they assumed that the primary resistance to heat transfer occurs in the viscous and buffer layers of the film, regardless of the actual thickness. Film and core flows were modeled after the approach of Rohsenow *et al.* (Rohsenow *et al.*, 1957; Bae *et al.*, 1971; Traviss *et al.*, 1973), assuming turbulent vapor and liquid films, and a law-of-the-wall universal velocity and temperature profiles. They used data from Sacks (1975) for R-11, R-12, and R-22, and the R-22 and R-134a data of Dobson (1994) to validate their model. Using these considerations, they developed the following scaling equation for heat transfer prediction:

$$h_2/h_1 = (\rho_{g2}/\rho_{g1})^{-0.375}(\rho_{L2}/\rho_{L1})^{0.375}(\mu_{g2}/\mu_{g1})^{-0.75}(\mu_{L2}/\mu_{L1})^{0.062} \\ \times (C_{pL2}/C_{pL1})(Pr_{L2}/Pr_{L1})^{-0.25}(G_2/G_1)(x_2/x_1)^{0.82} \left(\frac{1-x_2}{1-x_1} \right)^{0.19} \quad (6.125)$$

Upon comparison with the data of Dobson (1994), they commented that diameter effects may not be fully accounted for with the above approach, and perhaps the above equation should also have included the factor $(D_2/D_1)^{-0.15}$. Also, the fluid property exponents in this equation were different from those found in the literature; specifically, the thermal conductivity exponent varied from 0.35 for Chen *et al.* (1987), 0.38 for Shah (1979), and 0.65 for Cavallini and Zecchin (1974), while the above equation shows an exponent of 0.25 through the Prandtl number. They noted that several properties together determine the thicknesses of the various layers; therefore, differences in the dependence on an individual property may not be too significant.

6.5.1.3. Multi-regime condensation

For films under the simultaneous influence of shear and gravity, Kosky (1971) provided a simple algebraic equation for the convenient evaluation of the non-dimensional film thickness to facilitate closed-form computations. Thus, the work of Dukler (1960) (considered accurate close to the wall and for thick films) and Kutateladze (1963) (considered accurate for thick films, $\delta^+ > \sim 10$) were combined to obtain the following simplified expressions: $\delta^+ = (Re_L/2)^{1/2}$ for $\delta^+ < 25$, and $\delta^+ = 0.0504 Re_L^{7/8}$ for $\delta^+ > 25$. Jaster and Kosky (1976) performed experiments on condensing steam inside a 12.5-mm horizontal tube. Coupled with the experimental results from Kosky and Staub (1971), the mass flux ranged from 12.6 to 145 kg/m²-s. A stress ratio $F = \tau_w/(\rho_L g \delta)$ (axial shear-to-gravity) was used to divide the data into annular ($F > 29$), transition ($29 \geq F \geq 5$), and stratified ($F < 5$) regimes. The heat and momentum transfer analogy was applied to determine the annular flow heat transfer, with the two-phase gas multiplier ϕ_g^2 used to determine the shear stress and the non-dimensional film thickness obtained from Kosky (1971). For stratified flow, they related the half-angle subtended by the liquid pool β to the void fraction α using Zivi's (1964) model approximately as $\cos(\beta) = 2\alpha - 1$, which resulted in a modified version of the Nusselt condensation equation with the leading constant of 0.725 and a

multiplier of $\alpha^{3/4}$. In the transition regime, a linear interpolation between the two was suggested:

$$\text{Nu}_{\text{tr}} = \text{Nu}_{\text{an}} + \frac{F - 29}{24}(\text{Nu}_{\text{an}} - \text{Nu}_{\text{str}}) \quad (6.126)$$

It was stated in a previous section that Breber *et al.* (1979; 1980) developed a four flow zone map based on data for a variety of fluids for diameters as small as 4.8 mm. The corresponding transition criteria were listed with that discussion. For Zone I (annular flow, $j_g^* > 1.5, X < 1.0$), they recommend convective-type correlations:

$$\begin{aligned} \text{Re}_l > 1500 \quad h_l &= 0.024 \left(\frac{k_l}{D} \right) \text{Re}_l^{0.8} \text{Pr}_l^{1/3} (\mu_l/\mu_w)^{0.14} \\ \text{Re}_l < 1500 \quad h_l &= 1.86 \left(\frac{k_l}{D} \right) \left(\frac{\text{Re}_l \text{Pr}_l D}{L} \right)^{1/3} (\mu_l/\mu_w)^{0.14} \\ h_{\text{annular}} &= h_l (\phi^2)^{0.45} \end{aligned} \quad (6.127)$$

For Zone II (wavy or stratified flow, $j_g^* < 0.5, X < 1.0$), they recommend a Nusselt-type correlation:

$$h_{\text{stratified}} = F_g \left[\frac{k_l^3 \rho_l (\rho_l - \rho_v) g h_{lv}}{4 \mu_l (T_{\text{sat}} - T_{\text{wall}}) D} \right]^{1/4} \quad (6.128)$$

where the factor F_g is a function of the liquid volume fraction and the vapor Reynolds number, but may be approximated by $F_g = 0.79$ as suggested by Palen *et al.* (1977). For Zone III (intermittent flow, $j_g^* < 1.5, X > 1.5$), in view of the lack of appropriate models, they suggest the use of the annular flow correlation, because in their view, the convective mechanism governs, and also because it approaches the single-phase convection limit as $x \rightarrow 0$. For Zone IV (bubble flow, $j_g^* > 1.5, X > 1.5$), once again they suggest the convective equation presented above. For transitions between Zones I and II, they recommend interpolation between h_{annular} and $h_{\text{stratified}}$ based on j_g^* , while for transitions between Zones II and III, they recommend interpolation based on X .

Nitheanandan *et al.* (1990) evaluated the available condensation correlations using condensation data from several sources for flow inside horizontal tubes with the intention of developing a more accurate approach spanning multiple flow regimes for the design of condensers. The heat transfer database included R-12, R-113, and steam condensing inside tubes with diameters ranging from 7.4 to 15.9 mm, divided into three regimes: wavy, annular, and mist flow. Following the work of Soliman (1982; 1983; 1986), they recommended the use of the following heat transfer correlations for the respective regimes:

Mist flow ($\text{We} \geq 40, \text{Fr} \geq 7$)	Soliman (1986)
Annular flow ($\text{We} < 40, \text{Fr} \geq 7$)	Shah (1979)
Wavy flow ($\text{Fr} < 7$)	Akers and Rosson (1960)

It should be noted that the $\text{We} = 40$ criterion to determine the mist-annular transition was different from the value of 30 recommended earlier by Soliman (1986). Similar

recommendations were also made for condensation in vertical tubes based on the Hewitt and Roberts (1969) flow regime map.

Dobson *et al.* (1994) investigated condensation of R-12 and R-134a in a 4.57-mm horizontal tube at $75 < G < 500 \text{ kg/m}^2\text{-s}$ at 35°C and 60°C saturation temperature. They found that the $Fr = 7$ criterion proposed by Soliman (1982) was adequate for establishing the wavy to wavy-annular flow transition. In addition, they introduced $Fr = 18$ as the transition criterion for the wavy-annular to annular transition, and also stated that the $We = 30$ criterion of Soliman (1986) was appropriate for the annular-to-mist flow transition. Having thus divided their data into gravity- and shear-driven regions, they interpreted several trends in heat transfer coefficients. In annular flow, the heat transfer coefficient increased with mass flux and quality, due to the increased shear and the thinning of the liquid film. The heat transfer coefficients for R-134a were about 20% higher than those for R-12 at constant mass flux. In wavy flow, the heat transfer coefficient was independent of mass flux, and showed a slight increase with quality. As the primary heat transfer in this region occurs in the upper portion due to Nusselt-type condensation, with very little heat transfer through the liquid pool, the slight increase in heat transfer coefficients with quality was attributed to the thinning of the pool and a smaller pool depth at the higher qualities. In wavy flow, the R-134a heat transfer coefficients were about 10% higher than those for R-12. The heat transfer coefficients for R-134a were about 15% higher at 35°C than at 60°C because of the decrease in the ratio of the densities of the vapor and liquid phases, which leads to lower slip ratios, and also because of a decrease in the thermal conductivity at the higher temperature. To correlate their data in the wavy flow regime, they employed the Chato (1962) type correlation, but changed the leading coefficient from 0.555 to a function of the Lockhart–Martinelli parameter to account for the change in void fraction with quality, yielding:

$$Nu_{\text{gravity}} = \frac{0.375}{X_{\text{tt}}^{0.23}} \left[\frac{g \rho_l (\rho_l - \rho_v) D^3 h'_{\text{lv}}}{\mu_l (T_{\text{sat}} - T_{\text{wall}}) k_l} \right]^{0.25} \quad (6.129)$$

For annular flow, they used the familiar two-phase multiplier approach:

$$Nu_{\text{annular}} = 0.023 Re_L^{0.80} Pr_L^{0.3} \left(\frac{2.61}{X_{\text{tt}}^{0.805}} \right) \quad (6.130)$$

They also found that the annular flow heat transfer coefficients predicted by this equation are quite similar to those for convective evaporation found by Wattelet *et al.* (1994), implying similar heat transfer mechanisms for the two convective phase-change processes. Finally, they stated that several widely used correlations in the literature (Traviss *et al.*, 1973; Cavallini and Zecchin, 1974; Shah, 1979) overpredicted their data. Subsequently, Dobson and Chato (1998) extended this work to 3.14- and 7.04-mm tubes, and also to the fluids R-22 and mixtures of R-32/R-125. Data from these latter two tubes were used for the development of updated heat transfer correlations. The only discernible effect of tube diameter in their work was that transition to annular flow happened at higher mass fluxes and qualities in the larger tubes, although they were able to predict this using the large-diameter correlations. Thus, surface tension effects were not seen within this diameter range. Due to a variety of compensating influences such as thermophysical properties, different reduced

pressures and different void fractions, the effect of the particular fluid used on the heat transfer coefficient was at most 10% in the wavy regime, with a slightly better performance of R-134a in annular flow. In developing the revised correlations, they noted that the boundary-layer analyses used by several investigators, including primarily Traviss *et al.* (1973), could be shown to be similar in basis to the two-phase multiplier approach used by others. Noting also that the primary thermal resistance in annular flow occurs in the laminar and buffer layers (even the presence of waves at the interface or the varying film thickness around the circumference would not significantly affect the near-wall behavior), they did not find it necessary to include a multi-region model of the liquid film resistance. The role of entrainment was also not found to be very significant in affecting heat transfer coefficients, because they found that rarely did true mist flow without a thin annular film coating the wall exist. With these considerations, the following annular flow correlation was proposed:

$$\text{Nu}_{\text{annular}} = 0.023 \text{Re}_L^{0.80} \text{Pr}_L^{0.3} \left(1 + \frac{2.22}{X_{\text{tt}}^{0.89}} \right) \quad (6.131)$$

For the stratified wavy flow region, they accounted for the film condensation at the top of the tube and forced convection in the liquid pool as follows:

$$\text{Nu}_{\text{wavy}} = \frac{0.23 \text{Re}_{\text{vo}}^{0.12}}{1 + 1.11 X_{\text{tt}}^{0.58}} \left[\frac{\text{GaPr}_l}{\text{Ja}_l} \right]^{0.25} + (1 - \theta_l/\pi) \text{Nu}_{\text{forced}} \quad (6.132)$$

where the forced convection term is given by:

$$\text{Nu}_{\text{forced}} = 0.0195 \text{Re}_L^{0.80} \text{Pr}_L^{0.4} \sqrt{1.376 + \frac{c_1}{X_{\text{tt}}^{c_2}}} \quad (6.133)$$

The constants c_1 and c_2 in the above equation are given as follows:

For $0 < \text{Fr}_l \leq 0.7$:

$$c_1 = 4.172 + 5.48 \text{Fr}_l - 1.564 \text{Fr}_l^2 \quad c_2 = 1.773 - 0.169 \text{Fr}_l \quad (6.134)$$

and for $\text{Fr}_l > 0.7$, $c_1 = 7.242$, $c_2 = 1.655$. The angle from the top of the tube to the liquid pool level, θ_l , was approximated as follows:

$$1 - \frac{\theta_l}{\pi} \simeq \frac{\arccos(2\alpha - 1)}{\pi} \quad (6.135)$$

The void fraction required for the above equation was calculated using Zivi's (1964) correlation. They recommended that the above equations should be used as follows:

$$\begin{array}{lll} G \geq 500 \text{ kg/m}^2\text{-s} & \text{Nu} = \text{Nu}_{\text{annular}} & \\ G < 500 \text{ kg/m}^2\text{-s} & \text{Nu} = \text{Nu}_{\text{annular}} & \text{for } \text{Fr}_{\text{so}} > 20 \\ & \text{Nu} = \text{Nu}_{\text{wavy}} & \text{for } \text{Fr}_{\text{so}} < 20 \end{array} \quad (6.136)$$

It should be noted that the single-value demarcation on the basis of G shown above could result in sharp discontinuities between the heat transfer coefficient predictions in the neighborhood of $G = 500 \text{ kg/m}^2\text{-s}$ as the annular or wavy correlations are used. The more gradual

transition between wavy, wavy-annular, annular, and mist flows in their flow visualization work may have warranted correspondingly gradual transitions between heat transfer coefficient models. Also, they cautioned that for the small diameter (3.14 mm) tube, the data had large uncertainties due to difficulties in measuring small heat transfer rates accurately, which led to relatively larger deviations from the above correlations.

Wilson *et al.* (2003) reported heat transfer coefficients for 7.79-, 6.37-, 4.40-, and 1.84-mm tubes made by progressively flattening 8.91-mm round smooth tubes and tubes with axial and helical microfin tubes. Refrigerants R-134a and R-410A were condensed at 35°C in these tubes at $75 < G < 400 \text{ kg/m}^2\text{-s}$. Heat transfer coefficients were seen to increase over corresponding smooth-tube values as the tube was flattened. (It should be noted that their smooth-tube condensation heat transfer coefficients were consistently lower by 20–30% than the Dobson and Chato (1998) predictions, somewhat surprising because these experiments were conducted by researchers from the same group; the Dobson and Chato predictions were therefore artificially increased by the factor required to match the data. Since the enhancements observed were primarily in the 1.5–3.5 range, presumably including the 60% enhancement due to surface area increases in the microfinned tubes, these discrepancies could affect the conclusions considerably.) The enhancement was the highest for the flattened tubes with 18° helix angle microfins. Tentative explanations for these trends were provided including: potential early transition from stratified to annular flow, “modifications to the flow field without altering flow field configuration,” formation of different flow field configurations, and others. No predictive models or correlations were proposed, but it was noted that flattening to 5-mm height would lead to about a 10% reduction in condenser size, 70% increase in pressure drop, and 40% reduction in refrigerant charge for the example case studied. A similar study on condensation of R-404A in 9.52-mm OD tubes at 40°C and $200 < G < 600 \text{ kg/m}^2\text{-s}$ by Infante Ferreira *et al.* (2003) also showed enhancements of 1.8 to 2.4 in microfin and cross-hatched tubes.

In a set of related papers, Cavallini *et al.* (2001; 2002a, b) obtained heat transfer and pressure drop data for a variety of refrigerants and blends (R-22, R-134a, R-125, R-32, R-236ea, R-407C, and R-410A) condensing in smooth 8-mm horizontal tubes, and developed multiple-flow regime models to predict their own data as well as data from other investigators. The experiments covered the temperature range $30 < T_{\text{sat}} < 50^\circ\text{C}$, and $100 < G < 750 \text{ kg/m}^2\text{-s}$. When comparing the available correlations against these data, they noted that the data were often outside the recommended range of applicability for many of these correlations, especially for the newer high-pressure refrigerants such as R-125, R-32, and R-410A. The predictions of some of the empirical correlations were also not satisfactory within the stated range of applicability. They systematically plotted the various correlations in the literature in different graphs for low and high-pressure refrigerants, adhering to the recommended ranges of applicability to demonstrate the inadequacy of most of these correlations as general purpose predictive tools. Therefore, they tried to develop new procedures patterned after the approach of Breber *et al.* (1979; 1980) that would span the primary flow regimes encountered in condensation in horizontal tubes; that is, annular, stratified, wavy, and slug. For annular flow, for which they chose $j_{\text{g}}^* > 2.5$; $X_{\text{tt}} < 1.6$ as the transition criterion, they recommended the use of the Kosky and Staub (1971) model, which relates the heat transfer coefficient to the frictional pressure gradient through the interfacial shear stress τ . However, to compute the necessary frictional pressure gradient

for this model, they modified the Friedel (1979) correlation to apply only to annular flow, whereas it had originally been intended for annular and stratified regimes. This restricted version was intended to match the single-regime data better. Their modified annular flow model is given by the following equations:

$$h_{\text{annular}} = \frac{\rho_L C_{pL} (\tau/\rho_L)^{0.5}}{T^+} \quad (6.137)$$

where the dimensionless temperature is given by the following:

$$\begin{aligned} T^+ &= \delta^+ \text{Pr}_L & \delta^+ &\leq 5 \\ T^+ &= 5 \{ \text{Pr}_L + \ln[1 + \text{Pr}_L(\delta^+/5 - 1)] \} & 5 < \delta^+ < 30 \\ T^+ &= 5 [\text{Pr}_L + \ln(1 + 5\text{Pr}_L) + 0.495 \ln(\delta^+/30)] & \delta^+ \geq 30 \end{aligned} \quad (6.138)$$

with:

$$\delta^+ = (\text{Re}_L/2)^{0.5} \quad \text{for } \text{Re}_L \leq 1145; \quad \delta^+ = 0.0504 \text{Re}_L^{7/8} \quad \text{for } \text{Re}_L > 1145 \quad (6.139)$$

The shear stress is evaluated from the two-phase pressure drop in the usual manner as follows:

$$\tau = \frac{(dP/dz)_f}{4}; \quad \text{where } (dP/dz)_f = \phi_{\text{LO}}^2 (dP/dz)_{\text{LO}} = \phi_{\text{LO}}^2 f_{\text{LO}} \left(\frac{G^2}{D\rho_L} \right) \quad (6.140)$$

The two-phase multiplier contains several modifications from the original Friedel (1979) model; therefore, it is presented completely below:

$$\phi_{\text{LO}}^2 = E + \frac{1.262FH}{\text{We}^{0.1458}} \quad (6.141)$$

The parameters E , F , and H are given by:

$$\begin{aligned} E &= (1-x)^2 + x^2 \frac{\rho_L f_{\text{GO}}}{\rho_G f_{\text{LO}}} \\ F &= x^{0.6978} \\ H &= \left(\frac{\rho_L}{\rho_G} \right)^{0.3278} \left(\frac{\mu_G}{\mu_L} \right)^{-1.181} \left(1 - \frac{\mu_G}{\mu_L} \right)^{3.477} \end{aligned} \quad (6.142)$$

The Weber number is defined based on the total mass flux and the gas phase density instead of the mixture density, $\text{We} = G^2 D / \rho_G \sigma$. For $j_g^* < 2.5$; $X_{tt} < 1.6$, stratification begins, and they compute the heat transfer coefficient in this region using a combination of the annular model evaluated at the $j_g^* = 2.5$ boundary and a stratified heat transfer model. It should be noted that throughout the region $0 < j_g^* < 2.5$; $X_{tt} < 1.6$, a progressively decreasing contribution of the annular term is included; that is, the flow is never treated as exclusively

stratified. Therefore they refer to this region as “annular–stratified transition and stratified region.” The interpolation formula recommended is as follows:

$$h_{\text{transition}} = (h_{\text{annular}, j_G^*=2.5} - h_{\text{stratified}}) (j_G^*/2.5) + h_{\text{stratified}} \quad (6.143)$$

where the stratified flow contribution is evaluated in the usual manner as a combination of film condensation at the top and forced convection in the liquid pool:

$$h_{\text{stratified}} = 0.725 \left\{ 1 + 0.82 \left[\frac{1-x}{x} \right]^{0.268} \right\}^{-1} \left[\frac{k_L^3 \rho_L (\rho_L - \rho_G) g h_{LG}}{\mu_L D (T_{\text{sat}} - T_{\text{wall}})} \right]^{0.25} + h_L \left(1 - \frac{\theta}{\pi} \right) \quad (6.144)$$

where the forced convection heat transfer coefficient in the liquid pool is given by:

$$h_L = 0.023 \frac{k_L}{D} \left(\frac{G(1-x)D}{\mu_L} \right)^{0.8} \text{Pr}_L^{0.4} \quad (6.145)$$

and the liquid pool angle θ is defined using the Zivi (1964) void fraction model as follows:

$$1 - \frac{\theta}{\pi} = \frac{\arccos(2\alpha - 1)}{\pi} \quad (6.146)$$

Cavallini *et al.* commented that the liquid pool heat transfer term is significant at high values of reduced pressure. For conditions where $j_g^* < 2.5$; $X_{\text{tt}} > 1.6$, transition from stratified to intermittent flows starts to occur. This transition, however, occurs at a varying value of X_{tt} , and is defined by a transition mass flux, $G > G_W$, defined by Rabas and Arman (2000) as the mass flux required to fill the tube when being discharged to a gas-filled space. For slug flow, they used data from Dobson and Chato (1998) and Tang (1997) to curve-fit a single-phase heat transfer correlation. Smooth transition between the heat transfer coefficients in stratified and slug flows is provided once again by an interpolation technique. Thus, the stratified–slug transition and slug flow region heat transfer coefficient is given by:

$$h_{\text{stratified-slug}} = h_{\text{LO}} + \left(\frac{x}{x_{X_{\text{tt}}=1.6}} \right) (h_{X_{\text{tt}}=1.6} - h_{\text{LO}}) \quad (6.147)$$

The transition quality can be simply calculated from the definition of X_{tt} as follows:

$$x_{X_{\text{tt}}=1.6} = \frac{(\mu_L/\mu_G)^{1/9} (\rho_G/\rho_L)^{5/9}}{1.686 + (\mu_L/\mu_G)^{1/9} (\rho_G/\rho_L)^{5/9}} \quad (6.148)$$

The liquid-only (h_{LO}) and liquid-phase ($h_{X_{\text{tt}}=1.6}$) heat transfer coefficients required above are calculated using the Dittus–Boelter (1930) equation at Re_{LO} and Re_L (at the x for $X_{\text{tt}} = 1.6$), respectively.

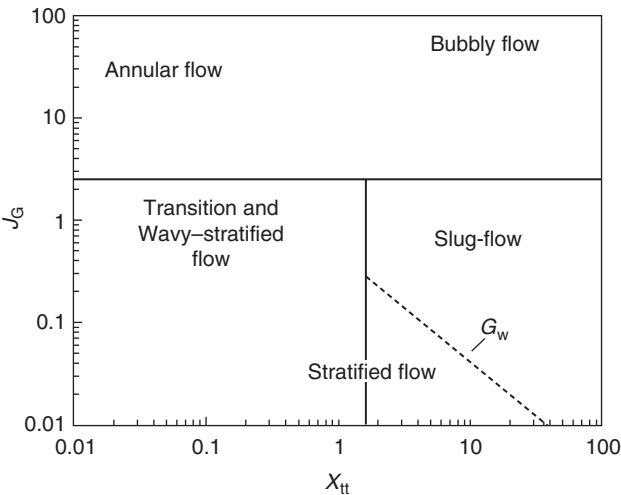


Fig. 6.26. Illustration of Cavallini *et al.* (2002a) model implementation. From Cavallini, A., Censi, G., Del Col, D., Doretti, L., Longo, G. A. and Rossetto, L. Condensation of halogenated refrigerants inside smooth tubes, *HVAC and R Research*, **8**(4), pp. 429–451 (2002) with permission from the American Society of Heating, Refrigerating and Air-Conditioning Engineers.

There is also a possibility for an annular-to-slug transition across $j_g^* = 2.5$ at high values of X_{tt} ; however, in common practice, this rarely occurs because it requires $G > 1000 \text{ kg/m}^2\text{-s}$ and very low qualities for most refrigerants. However, in such instances, they recommend a linear interpolation between h_{annular} and h_{LO} based on the vapor quality. At high values of j_g^* and X_{tt} , especially at high reduced pressures, bubbly flow is encountered, and once again, in the absence of reliable correlations in this region, they recommend the use of the annular flow correlation. This multi-region map is recommended for the refrigerants listed above, and for the following conditions:

$$3 < D < 21 \text{ mm} \quad p_R < 0.75 \quad \rho_L/\rho_G > 4 \tag{6.149}$$

This composite model was shown to predict their own data and data from several investigators with an average absolute deviation of about 10%. A chart for the use of the above heat transfer coefficient correlations is provided in Fig. 6.26. For the prediction of pressure drops, Cavallini *et al.* recommend the use of the modified Friedel two-phase multiplier ϕ_{LO}^2 developed by them for annular flow when $j_g^* > 2.5$; for $j_g^* < 2.5$, the original Friedel (1979) model is recommended.

El Hajal *et al.* (2003) and Thome *et al.* (2003) conducted another detailed exercise (similar to that of Cavallini *et al.* (2001; 2002a, b; 2003) described above) of developing flow regime-based heat transfer correlations over a wide range of conditions by fitting data from several different investigators for many different fluids. They patterned this work after the similar work of Kattan *et al.* (1998a, b, c) on flow boiling. Their basic premise is that void fraction is the most important variable in determining flow regimes, pressure drop, and heat transfer. However, reliable void fraction data were not available, especially at high reduced pressures. Therefore, they first used the Steiner (1993) horizontal tube

version of the Rouhani–Axelsson (1970) drift-flux void fraction map because it includes mass flux and surface tension effects:

$$\alpha = \frac{x}{\rho_V} \left([1 + 0.12(1 - x)] \left[\frac{x}{\rho_V} + \frac{1 - x}{\rho_L} \right] + \frac{1.18 (1 - x) [g\sigma (\rho_L - \rho_V)]^{0.25}}{G \rho_L^{0.5}} \right)^{-1} \quad (6.150)$$

The void fraction predicted by this model does not approach the homogeneous void fraction as the critical pressure is approached. Therefore, they set about trying to improve upon this model by indirect means. They stated that turbulent annular flow condensation heat transfer data could in fact be used to deduce the applicable void fraction. This is because the corresponding liquid film heat transfer coefficient may be represented as $h = c \text{Re}_L^\eta \text{Pr}_L^{0.5} (k_L/\delta)$, where the film thickness δ is simply by definition $\delta = D(1 - \alpha)/4$. Substituting this expression back into the heat transfer coefficient equation, it is clear that $h \propto (1 - x)^n/(1 - \alpha)$. Since void fractions in annular flow are very large, the denominator in this expression, representative of the liquid film thickness, is a small quantity that affects the heat transfer coefficient significantly. It is this sensitivity of the heat transfer coefficient to void fraction that they sought to exploit in deducing the void fraction from available heat transfer data. Thus, they used the annular flow data from Cavallini *et al.* (2001; 2002a, b) to statistically curve-fit the leading constant and exponent for Re_L in the heat transfer expression, and assumed the Pr exponent to be 0.5 instead of 0.4. Although reasonable prediction was achieved, the prediction accuracy seemed to show a strong saturation pressure dependency. Therefore, they decided, somewhat arbitrarily, that the actual void fraction would in fact lie somewhere between the Axelsson–Rouhani prediction and the homogeneous value. They then chose a logarithmic mean of these two values to represent the actual void fraction:

$$\alpha = \frac{\alpha_{\text{homogeneous}} - \alpha_{\text{Axelsson-Rouhani}}}{\ln \left(\frac{\alpha_{\text{homogeneous}}}{\alpha_{\text{Axelsson-Rouhani}}} \right)} \quad (6.151)$$

This formulation was then used to curve-fit the heat transfer data again, which demonstrated an improvement in the prediction of the heat transfer data over a larger range of reduced pressures, which they took to be a validation of the void fraction curve-fit. Once this was established, they plotted the transitions between stratified, wavy, intermittent, annular, mist, and bubbly flow on G – x coordinates, adapting the transition expressions presented by Kattan *et al.* (1998a, b, c) (with updates by Zurcher *et al.* (1999)) for boiling to the condensing situation. For example, allowance is made for the fact that dryout does not occur in condensing flows; thus they remove that portion of the wavy transition line and arbitrarily extend it from the minima of that transition to the $x = 1$ location. Various liquid–vapor cross-sectional areas and perimeters are derived from the void fraction to enable plotting of the transition lines. A representative map constructed in this manner is shown in Fig. 6.27. It should be noted that because the void fraction is dependent on the mass flux, strictly speaking, these maps have to be redrawn for each mass flux under consideration, even though G is in fact one of the coordinates. However, El Hajal *et al.* state that the transition lines are not very sensitive to the mass flux, and a first approximation may be achieved by choosing a representative mass flux to plot the transition lines. They demonstrate qualitative agreement

allows them to use a gravity-driven Nusselt (1916) film condensation expression (with an assumption of zero vapor shear) in the upper part of the tube, coupled with the forced-convective annular flow expression for the lower portion of the circumference for what would otherwise be a liquid pool. The rest of the model is simply a weighted average of these different contributions based on the fraction of the circumference occupied by the “stratified” portion:

$$h = \frac{h_{\text{falling-film}} r \theta + h_{\text{convective}} (2\pi - \theta) r}{2\pi r} \quad (6.152)$$

Like most other models discussed in this section, all of the multiple regimes identified in the first part of the study are handled either as (a) fully annular forced-convective, or as (b) consisting of varying combinations of upper gravity-driven, and lower forced-convective terms. It is stated that intermittent flow is very complex, and is therefore assumed to be predicted by annular flow equations. Similarly, mist flow is handled as annular flow, assuming that the liquid inventory entrained in the vapor phase can be viewed as an unsteady annular film. Bubbly flow is not modeled in this work, partly because it is not commonly encountered. The novel manner of handling the stratified pool does, however, yield smoother transitions between the heat transfer coefficient predictions across transitions. Further, the degree of stratification is itself obtained through quadratic interpolation across the flow regime transition lines, ensuring a smooth introduction of the stratification component into the heat transfer coefficient:

$$\theta = \theta_{\text{strat}} \left(\frac{G_{\text{wavy}} - G}{G_{\text{wavy}} - G_{\text{strat}}} \right)^{0.5} \quad (6.153)$$

Another innovation introduced is the accounting of the effects of interfacial waves, using concepts of the “most dangerous” wavelength from stability considerations, and developing an enhancement factor due to interfacial roughness in terms of the slip ratio and the roughness amplitude:

$$f_i = 1 + \left(\frac{u_V}{u_L} \right)^j \left(\frac{(\rho_L - \rho_V) g \delta^2}{\sigma} \right)^k \left(\frac{G}{G_{\text{strat}}} \right) \quad (6.154)$$

The exponents j and k are picked to be $\frac{1}{2}$ and $\frac{1}{4}$ without discussion or substantiation from physical principles. The presence of the surface tension in the denominator correctly implies a decrease in the intensity (damping) of the interfacial waves at high surface tension values. In addition, the last term in the equation ensures that the waves are progressively damped out upon approach to fully stratified conditions, although why this term should be a linear decrease (evidenced by the exponent of 1 for this term) and not raised to another exponent is not made clear. The authors present numerous graphs to demonstrate that the predictions are not biased toward underprediction or overprediction with respect to the independent variables. Their model predicts the data from the large database over a wide range of fluids, operating conditions, and diameters (with the caution stated above about the applicability to the 3.14-mm diameter) well, with 85% of the refrigerant heat transfer data predicted within 20%. It is interesting to note that this is about the same

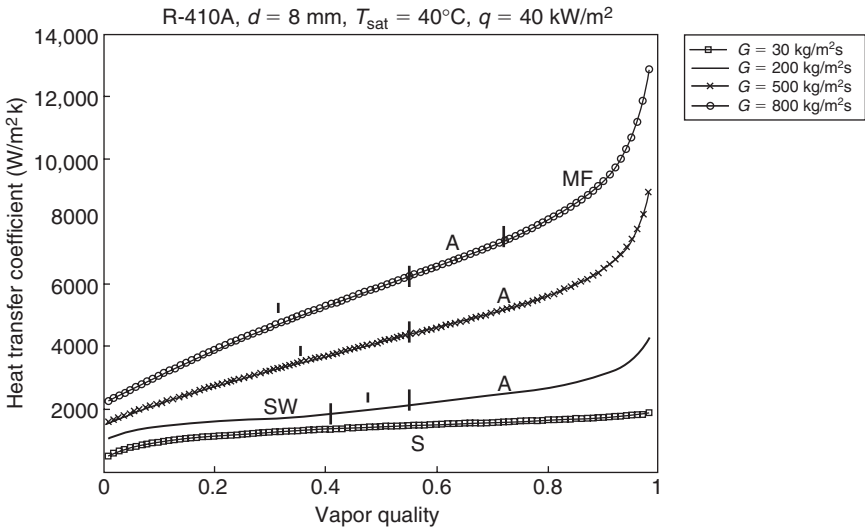


Fig. 6.28. Heat transfer coefficient trends predicted by the Thome *et al.* (2003) model. Reprinted from Thome, J. R., El Hajal, J. and Cavallini, A., Condensation in horizontal tubes, Part 2: New heat transfer model based on flow regimes, *International Journal of Heat and Mass Transfer*, **46**(18), pp. 3365–3387 (2003) with permission from Elsevier.

level of predictive accuracy as the earlier multi-flow regime correlations proposed by Cavallini *et al.* (2002a). This model does offer some new approaches – heat transfer data are used to refine a void fraction model, which is then used to predict flow regime transitions, which are in turn used to predict a “tuned blend” of stratified-convective heat transfer coefficients. It achieves smoothly varying heat transfer coefficients across multiple regimes (Fig. 6.28) with good accuracy, using some first principles concepts and several key assumptions and empirical constants or curve-fitted terms at appropriate locations for closure. Additional substantiation of the use of an average of homogeneous and Steiner (1993)/Rouhani–Axelsson (1970) void fractions, and the physical basis for extensions of transition lines determined from boiling considerations would lend further credence to the model. Measurement, rather than deduction from heat transfer data, of the fundamental underlying quantity (void fraction), to which the authors credit much of the success of this approach, would also enhance its predictive abilities. This would be particularly important if the model were to be extended in the future to microchannels.

Goto *et al.* (2003) measured heat transfer coefficients for the condensation of R-410A and R-22 inside five different helical and herringbone internally grooved tubes of about 8.00-mm OD. Local heat transfer coefficients were measured for $130 < G < 400 \text{ kg/m}^2\text{-s}$ and $T_{\text{sat}} = 30^\circ\text{C}$ and 40°C by dividing a 1-m long test section into 10 small sections. Unlike most other studies discussed in this chapter, the heat transfer tests were conducted in a complete vapor compression system. The reported uncertainties in the heat transfer coefficients were very high, about 40%. Heat transfer coefficients of the herringbone grooved tube were found to be about twice as large as those for the helical grooved tubes. Using Koyama and Yu’s (1996) $Nu = (Nu_{\text{annular}}^2 + Nu_{\text{stratified}}^2)^{0.5}$ correlation for stratified

and annular condensation as a starting point, they developed new expressions for the annular flow portion based on their data. A turbulent liquid film basis, $Nu = Re_L^* Pr_L / T_i^*$, was used, with the liquid Reynolds number $Re_L^* = (\rho_L \sqrt{\tau_w / \rho_L} D) / \mu_L$ computed from the friction velocity with the two-phase multiplier of Goto *et al.* (2001) $\phi_v = 1 + 1.64 X_{tt}^{0.79}$ for the computation of the wall shear stress. This approach resulted in following correlation for helical and cross microfins:

$$Nu_{\text{annular}} = 0.743 \sqrt{f} \left(\frac{\phi_v}{X_{tt}} \right) \left(\frac{\mu_L}{\mu_v} \right)^{0.1} \left(\frac{x}{1-x} \right)^{0.1} Re_L^{0.7} \quad (6.155)$$

while herringbone microfin tubes required a leading constant of 2.34, and a Re exponent of 0.62. These correlations predicted the data within 20%. Individual equations were reported for each tube for the friction factor required in the above equation.

6.5.2. Condensation in small channels

There has been a slow progression toward the measurement and modeling of heat transfer coefficients in small channels, and unlike the studies on flow regimes, void fraction and pressure drop cited in previous sections, there are few studies that address $D_h \leq 1$ mm.

Yang and Webb (1996a) measured heat transfer in single- and two-phase flow of refrigerant R-12 at 65°C in rectangular plain and microfin tubes with $D_h = 2.64$ and 1.56 mm, respectively, using the modified Wilson plot technique. The companion pressure drop study (Yang and Webb, 1996b) was discussed in the previous section. The measurements were conducted at somewhat higher mass fluxes ($400 < G < 1400$ kg/m²-s) than those of interest for refrigeration and air-conditioning applications. They found that the Shah (1979) correlation significantly overpredicted the data, while the Akers *et al.* (1959) correlation showed better agreement, except at high mass fluxes, where it also overpredicted the data. The microfin tube heat transfer coefficients showed steeper slopes than those for the plain tubes when plotted against quality, especially at the lower mass fluxes. The heat transfer coefficients also showed a heat flux dependence ($h \propto q''^{0.2}$); such heat flux dependence is typically seen in stratified flows (which is certainly not the case at such high mass fluxes) and in boiling. They explained this dependence based on the work of Soliman *et al.* (1968), who argued that the momentum contribution will cause an increase in heat transfer coefficient when q'' is increased. Their results also showed that the heat transfer enhancement due to the microfins decreased with increasing mass flux. By plotting the heat transfer data against the equivalent mass velocity Reynolds number proposed by Akers *et al.* (1959), they showed that while data for different mass fluxes and qualities collapsed to a single curve for plain tubes, this only occurred at low qualities for the microfin tube. This led them to explain the different trends on the basis of the drainage of the liquid film by the microfins. They reasoned that at high qualities, the microfins are not fully submerged in liquid; therefore, they act like Gregorig (1962) surfaces, helping to drain the film to the base of the fins, thus increasing heat transfer over the plain tube values. At low qualities, however, the fins are submerged; therefore, the drainage mechanism is not active. According to them, this mechanism is particularly important at low mass fluxes, because at high mass fluxes, vapor shear exerts the dominant influence on heat transfer. It should be noted

that in the companion work, Yang and Webb (1996b) had concluded that surface tension did not play a role in determining the pressure drop in these same tubes.

Yang and Webb (1997) continued this work to develop a heat transfer model for condensation of R-12 and R-134a in extruded microchannels ($D_h = 1.41$ and 1.56 mm) with microfins (0.2- and 0.3-mm deep). The data for these channels were reported in their earlier papers cited above. They used the observations discussed above about the contribution of vapor shear and surface tension to represent the heat transfer coefficient as follows:

$$h = h_u \frac{A_u}{A} + h_f \frac{A_f}{A} \quad (6.156)$$

where the subscripts u and f refer to unflooded and flooded portions of the channel, respectively. They calculated the surface and cross-sectional areas of the liquid in the drainage regions using the geometric features of the microfin, and the Zivi (1964) void fraction model to estimate the liquid volume occupying the drainage region. For flooded conditions (e.g. at low vapor qualities) they used a slightly modified version of the Akers *et al.* (1959) model (which corresponds to their experimentally derived single-phase Nusselt number $Nu_{D_h} = 0.10 Re_{D_h}^{0.73} Pr_1^{1/3}$) to compute the shear-driven heat transfer coefficient. When the microfins were unflooded, they assumed a thin laminar film draining on the walls of the microfin and computed the pressure gradients in the axial and microfin wall directions due to vapor shear and surface tension, respectively. These perpendicular vapor shear (sh) and surface tension (st) stresses were combined to yield the wall shear stress, which was then related to the unflooded heat transfer coefficient, $h_u^2 = h_{sh}^2 + h_{st}^2$. Relating the surface-tension-driving force to the microfin profile and the Weber number $We = (G_{eq}^2 D_h)/(\rho_l \sigma)$, they developed the following expression for the surface tension contribution to the heat transfer coefficient:

$$h_{st} = C \frac{\tau_z - \tau_i}{dp/dz} k_l \frac{d(1/r)}{ds} \frac{Re_{eq} Pr_1^{1/3}}{We} \quad (6.157)$$

where z refers to the axial direction, subscript i refers to the interface, and C was derived through regression of their data to be 0.0703. The relative fractions of the surface tension and vapor shear contributions to the heat transfer coefficient were plotted to show that at low mass flux ($G = 400$ kg/m²-s) and $x > 0.5$, the surface tension contribution could equal and exceed the vapor shear term. At high mass fluxes ($G = 1400$ kg/m²-s), the surface tension contribution was very small. A small fin tip radius enhanced the heat transfer, while a large inter-fin drainage area allowed the surface tension effect to be activated at lower qualities.

Kim *et al.* (2003) conducted a study similar to that of Yang and Webb (1996a, b; 1997) above, on similar tubes ($D_h = 1.41$ smooth, 1.56-mm microfin with 39% greater surface area than the smooth tube), with a similar experimental set up using R-22 and R-410A for $200 < G < 600$ kg/m²-s at 45°C. Representative tube cross-sections and the test section used for the experiments is shown in Fig. 6.29. To test the tubes, they formed a jacket around the channel with a 1-mm gap. Since the Wilson plot technique was used, it was important to minimize the coolant-side resistance (an issue not recognized or stated by investigators often enough.) In their tests, the coolant side constituted approximately 1/3 of total resistance. Further decreases could not be achieved because the required higher coolant flow rates would result in an extremely small coolant temperature rise, which

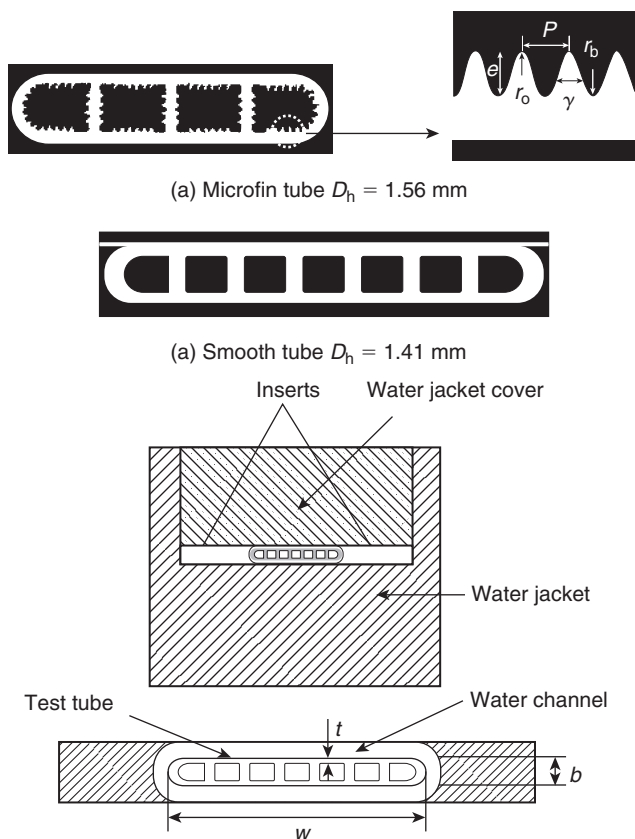


Fig. 6.29. Representative plain and microfin extruded channels and test section used by Yang and Webb (1996a) and Kim *et al.* (2003). Reprinted from Kim, N.-H., Cho, J.-P., Kim, J.-O. and Youn, B., Condensation heat transfer of R-22 and R-410A in flat aluminum multi-channel tubes with or without micro-fins, *International Journal of Refrigeration*, **26**(27), pp. 830–839 (2003) with permission from Elsevier and International Institute of Refrigeration (iifir@iifir.org or www.iifir.org).

would significantly decrease the accuracy of heat duty measurement. At the low mass flux conditions, the heat duties were measured using a 1.3°C coolant temperature rise. For R-22, the microfin tubes yielded higher heat transfer coefficients than the smooth tube, with the enhancement decreasing to 1 at a mass flux of $600\text{ kg/m}^2\text{-s}$. For R-410A, the microfin tube heat transfer coefficients were similarly higher than those of the smooth tubes at low mass fluxes, but in fact decreased to values lower than those for the smooth tube at $G = 600\text{ kg/m}^2\text{-s}$. Using the rationale provided by Carnavos (1979; 1980) for single-phase performance in finned tubes, they explained this decrease in heat transfer by postulating that fins reduce the inter-fin velocity, thus decreasing heat transfer. They further point out that in condensing flows, the surface tension drainage force that is prominent at low mass fluxes compensates for the decrease in velocity, whereas at high mass flux, the velocity reduction effect dominates. No detailed validation of this hypothesis is provided. They found also that in smooth tubes, R-410A heat transfer coefficients were slightly higher

than those of R-22, while the opposite was true for microfin tubes. In smooth tubes, the higher R-410A heat transfer coefficients were attributed to its larger thermal conductivity and smaller viscosity. In microfin tubes, however, they noted that the Weber number of R-22 was 2.7 times lower than that of R-410A at the test conditions, leading to greater surface tension drainage and heat transfer. The two times larger vapor-to-liquid volume ratio of R-22 was also believed to have resulted in a larger fraction of the fin surface being exposed to the vapor, thus enhancing heat transfer. Several other plausible explanations in terms of the fluid properties are provided, although additional validation would be necessary to confirm these explanations of the small differences in heat transfer coefficients, especially in view of the uncertainties in the measurement of heat transfer coefficients at these small heat transfer rates. Based on these trends, they recommended the use of Moser *et al.*'s (1998) model with a modified two-phase multiplier for the smooth tubes, and Yang and Webb's (1997) model with minor modifications for the microfin tubes.

Yan and Lin (1999) measured heat transfer coefficients during condensation of R-134a through a bank of 2-mm tubes arranged in parallel. Their pressure drop results were discussed in the previous section. Copper plates, 5-mm thick, were soldered on to the bank of refrigerant tubes, and coolant tubes were in turn soldered on to the copper plates to provide a crossflow cooling orientation. The authors state that the tubes and the plate had good thermal contact, eliminating the need for avoiding gaps between the tubes and the plates. However, they provide no substantiation that the thermal resistance from the refrigerant to the coolant through the refrigerant and coolant tubes, the gaps between the plates and the tubes, and the two 5-mm thick copper plates was either accounted for properly, or was in fact small in magnitude. The issue of mal-distribution through the 28 parallel channels was also not discussed in detail, except to state that the inlet and outlet headers were appropriately designed. Their single-phase friction factors were significantly higher than the predictions of the Blasius equation, and the single-phase heat transfer coefficients were also higher than the predictions of the Gnielinski (1976) correlations. Entrance length effects and tube roughness may have accounted for some of this, according to the authors. Condensation heat transfer coefficients were higher at the lower saturation temperatures, especially at the higher qualities. They attributed this to the lower thermal conductivity of R-134a at the higher temperatures. The heat transfer coefficients also decreased significantly as the heat flux was increased, particularly at the higher qualities. This is not typical of condensation heat transfer, where any heat flux (or ΔT) dependence is usually seen at the lower qualities in gravity-dominated flow. The graphs they presented to demonstrate the effect of mass flux show inflection points where the heat transfer coefficient first increased sharply as quality is increased from around 10–20%, followed by a flattening with further increases in quality at the lower mass fluxes, finally again increasing with quality. Adequate explanations for these trends are not provided. They proposed the following correlation for their data:

$$\frac{hD}{k_l} \text{Pr}_l^{-0.33} \text{Bo}^{0.3} \text{Re} = 6.48 \text{Re}_{\text{eq}}^{1.04} \quad \text{Bo} = \frac{q''}{h_{\text{fg}} G} \quad (6.158)$$

It is not clear why the Reynolds number as well as the equivalent Reynolds number according to the Akers *et al.* (1959) model were required to correlate the data.

Rectangular channels with $D_h = 1.46$ mm (1.50×1.40 mm) were investigated by Wang *et al.* (2002) for the condensation of R-134a at 61.5–66°C over the mass flux range 75–750 kg/m²-s. The experiments were conducted in 610-mm long tubes with finned 10 multi-port channels cooled by air in crossflow. Flow visualization experiments were also conducted by replacing one aluminum wall of the tube with a glass window to help determine the applicable flow regimes. The authors report inlet qualities to the test section, which were controlled over a wide range; however, the quality change across the test section was substantial, indicating that for many of the tests, the experiments did not yield local heat transfer coefficients over small increments of quality. From the combination of flow visualization and heat transfer experiments, they note that even in a channel this small, stratified (wavy) flows were seen at the low mass fluxes. The heat transfer coefficients were insensitive to quality at the low mass fluxes. At the high mass fluxes, the dependence on quality was strong, signifying annular flow. Of the available heat transfer correlations, the Akers *et al.* (1959) equivalent Re correlation was found to agree most with their data in the annular flow regime, while the Jaster and Kosky (1976) correlation agreed best with their stratified flow data. However, they noted that the Re_{eq} concept of Akers *et al.* (1959) does not explicitly account for the applicable flow regime, because Re_{eq} can be the same for different flow regimes. They attempted to improve the predictions by developing their own stratified and annular flow correlations. They separated the data into stratified and annular regimes using the Breber *et al.* (1980) and Soliman (1982; 1986) transition criteria. Their stratified–annular transition occurred at a lower gas superficial velocity ($j_g^* = 0.24$ m/s) than that predicted by the Breber *et al.* map, because the corners of the rectangular channel aided the formation of annular flow. This earlier transition to annular flows was also observed with respect to the Soliman map, while the annular–mist transition was not observed. For annular flow, they conducted a boundary-layer analysis similar to Traviss *et al.* (1973), and through the analysis of their data, proposed the following curve-fits for the two-phase multiplier, and unlike most other researchers, for the dimensionless temperature as well:

$$\phi_v = \sqrt{1.376 + 8X_{tt}^{1.655}} \quad T_\delta^+ = 5.4269 \left(\frac{Re_l}{x} \right)^{0.2208} \quad (6.159)$$

The resulting annular flow correlation was as follows:

$$Nu_{\text{annular}} = 0.0274 Pr_l Re_l^{0.6792} x^{0.2208} \left(\frac{1.376 + 8X_{tt}^{1.655}}{X_{tt}^2} \right)^{0.5} \quad (6.160)$$

For stratified flows, they used the Chato (1962) correlation for the film condensation portion, and the Dittus–Boelter (1930) correlation for forced convection in the liquid pool, combining the two as follows:

$$Nu_{\text{stratified}} = \alpha Nu_{\text{film}} + (1 - \alpha) Nu_{\text{convection}} \quad (6.161)$$

Therefore, they essentially used the Zivi (1964) void fraction as a measure of the liquid pool height in this rectangular channel. In addition, for design purposes, especially

since their condensation tests were conducted over large quality changes, they proposed a weighted average between these two correlations using the quality at Soliman Froude number $Fr_{so} = 8$ as the transition between the regimes.

Koyama *et al.* (2003b) conducted a study on the condensation of R-134a in two multi-port extruded aluminum tubes with eight 1.11-mm channels, and nineteen 0.80-mm channels, respectively. Local heat transfer coefficients were measured at every 75 mm of the 600-mm long cooling section using heat flux sensors. They acknowledged that it is very difficult to accurately measure local heat transfer coefficients in such small channels using the temperature rise in the coolant or a Wilson plot method due to the inaccuracies associated with the measurement of low heat transfer rates and small temperature differences. The tests were conducted over the range $100 < G < 700 \text{ kg/m}^2\text{-s}$ at 60°C . For correlating their data, they used a combination of convective and film condensation terms to yield $Nu = (Nu_{\text{annular}}^2 + Nu_{\text{stratified}}^2)^{0.5}$. The individual annular and stratified terms were obtained from the work of Haraguchi *et al.* (1994a, b), except that their two phase multiplier was replaced by the multiplier proposed by Mishima and Hibiki (1996). They stated that this was an improvement over several other correlations; however, the graphs of predicted and experimental Nusselt numbers show consistent and large (as high as 80%) overpredictions of all their data at almost all conditions.

In some recent studies, Wang, Rose, and co-workers have developed analytical approaches for addressing condensation heat transfer in triangular (Wang and Rose, 2004) and square (Wang *et al.*, 2004; Wang and Rose, 2005) microchannels. For film condensation of R-134a in horizontal 1-mm triangular channels, Wang and Rose (2004) assumed that the condensate was in laminar flow, and developed one of the first models that accounts for surface tension, shear stress, and gravity. They were able to predict and substantiate the varying condensate flow pattern across the cross-section as well as along the length of the channel. Thus, they were able to model the corresponding variations in heat transfer coefficient. Using a similar approach, Wang *et al.* (2004) developed a model for film condensation of R-134a in square, horizontal, 1-mm microchannels. As these papers account for the three primary governing influences in microchannel condensation, they provide a good start for the modeling of phenomena specific to microchannels. Furthermore, the respective forces can be “switched on or off” to understand their respective significances (Fig. 6.30).

In another recent study, Cavallini *et al.* (2005) conducted measurements of heat transfer coefficients and pressure drops during condensation of R-134a and R-410A inside multiple parallel 1.4-mm D_h channels. The test section was divided into three separate segments to provide quasi-local pressure drops and heat transfer coefficients. They deduced the frictional pressure drop from the measured drop in saturation temperature and found good agreement between the data for R-134a and the correlations of Friedel (1979), Zhang and Webb (2001), Mishima and Hibiki (1996), and Mueller-Steinhagen and Heck (1986). All of these correlations were found to overpredict the R-410A data, however. Their heat transfer coefficients were obtained from wall temperature measurements, and they found that the available models in the literature (Akers *et al.*, 1959; Moser *et al.*, 1998; Zhang and Webb, 2001; Cavallini *et al.*, 2002a; Wang *et al.*, 2002; Koyama *et al.*, 2003a) underestimated their results, particularly at high values of mass flux. They attributed these differences to the much higher gas velocities in their experiments where mist flow might prevail, whereas the available correlations are primarily for annular flow in larger diameter tubes.

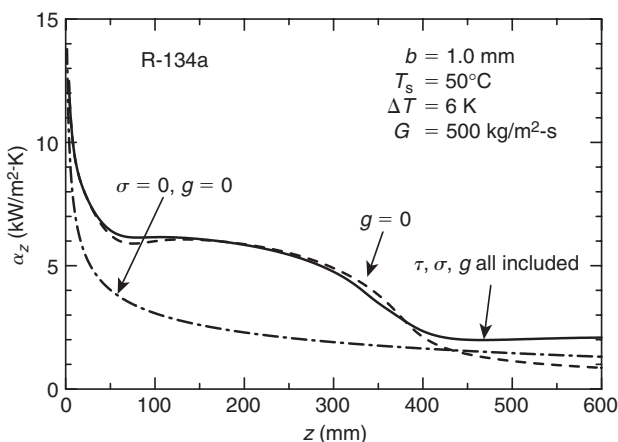


Fig. 6.30. Variation of mean heat transfer coefficient along a square 1-mm channel. Reprinted from Wang, H. S. and Rose, J. W., A theory of condensation in horizontal non-circular microchannels, *ASME Journal of Heat Transfer*, in press (2005).

Shin and Kim (2005) used a technique that matched the outlet temperature of an electrically heated air stream with that of a similar air stream heated by condensing refrigerant R-134a to measure small, local condensation heat transfer rates. Circular and square channels with $0.5 < D_h < 1$ mm were tested for the mass flux range $100 < G < 600$ kg/m²-s at 40°C. For circular and square channels, they also found that most of the available models and correlations discussed above (Akers *et al.*, 1959; Soliman *et al.*, 1968; Traviss *et al.*, 1973; Cavallini and Zecchin, 1974; Shah, 1979; Dobson, 1994; Moser *et al.*, 1998) underpredict their data at the low mass fluxes, which they deemed to be the important range for engineering applications. The agreement with these correlations improved somewhat at the higher mass fluxes. Although they found no significant effect of the heat flux, they noted that at lower mass fluxes, square channels had higher heat transfer coefficients than those for circular channels, whereas the reverse was true for high mass fluxes. No satisfactory explanation was provided for these trends.

Garimella and Bandhauer (2001) conducted heat transfer experiments using the tubes ($0.4 < D_h < 4.9$ mm) that were used for the pressure drop experiments of Garimella *et al.* (2002; 2003a, b; 2005) described above. They specifically addressed the problems in heat transfer coefficient determination due to the high heat transfer coefficients and low mass flow rates in microchannels. For the small Δx required for local measurements, the heat duties at the mass fluxes of interest are relatively small, and to ensure reasonable accuracies in heat duty measurement, the coolant inlet-to-outlet temperature difference must be increased to minimize uncertainties. However, since this requires low coolant flow rates, the coolant-side thermal resistance becomes dominant, making it difficult to deduce the refrigerant-side resistance from the measured UA . These conflicting requirements for the accurate measurement of heat duty and the refrigerant heat transfer coefficients were resolved by developing a thermal amplification technique (Fig. 6.31) that decoupled these two issues. Thus, the test section was cooled using water flowing in a closed (primary) loop at a high flow rate to ensure that the condensation side presented the governing thermal

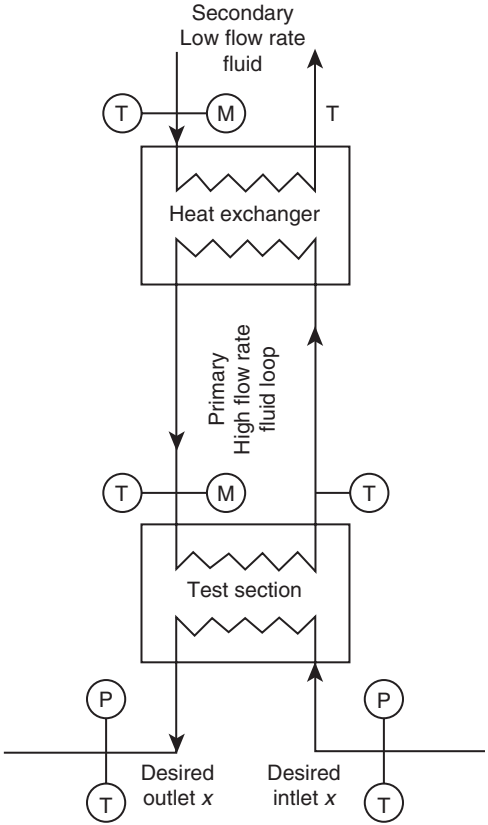


Fig. 6.31. Thermal amplification technique. Reprinted from Bandhauer, T. M., Agarwal, A. and Garimella, S., Measurement and modeling of condensation heat transfer coefficients in circular microchannels, *Journal of Heat Transfer*, in press (2006).

resistance. Heat exchange between this primary loop and a secondary cooling water stream at a much lower flow rate was used to obtain a large temperature difference, which was in turn used to measure the condensation duty. The secondary coolant flow rate was adjusted as the test conditions change to maintain a reasonable ΔT and also small condensation duties in the test section. By ensuring that the pump heat dissipation in the primary loop and the ambient heat loss were small fractions of the condensation load, the sensitivity to these losses and gains was minimized. Local heat transfer coefficients were therefore measured accurately in small increments for the entire saturated vapor–liquid region. Additional details of this thermal amplification technique are provided in Garimella and Bandhauer (2001). The thermal amplification resulted in uncertainties typically as low as $\pm 2\%$ in the measurement of the secondary loop heat duty even at the extremely small heat transfer rates under consideration. Combining the errors in the secondary loop duty, the pump heat addition, and the ambient heat loss, the local condensation duty in these small channels was typically known to within a maximum uncertainty of $\pm 10\%$. The large coolant flow rate and the enhancement in surface area (indirect area of about 4.7 times the direct area) provided by the coolant port walls on both sides of the microchannel tube resulted

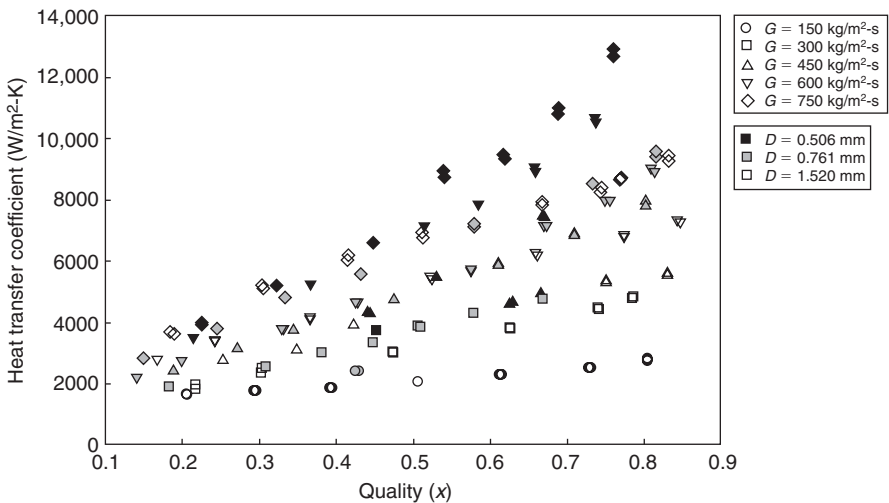


Fig. 6.32. Microchannel condensation heat transfer coefficients. From Bandhauer, T. M., Agarwal, A. and Garimella, S., Measurement and modeling of condensation heat transfer coefficients in circular microchannels, *Journal of Heat Transfer*, in press (2006).

in high refrigerant-to-coolant resistance ratios (between 5 and 30). With this high resistance ratio, even an uncertainty of $\pm 25\%$ in the tube-side heat transfer coefficient did not appreciably affect the refrigerant-side heat transfer coefficient, ensuring low uncertainties. Representative heat transfer coefficients reported by Bandhauer *et al.* (2005) are shown in Fig. 6.32. In general, the heat transfer coefficient increases with decreasing diameter, with the effect of diameter becoming more significant at the higher qualities ($x > 0.45$) and mass fluxes. Thus, h increases between 10% and 40% for $x > 0.45$ as D_h is reduced from 1.524 to 0.506 mm, with the effect of D_h being more significant for a decrease in D_h from 0.761 to 0.506 mm. Gravity-driven correlations were found to be poor predictors of the data, with the Chato (1962) correlation underpredicting the data considerably, the Jaster and Kosky (1976) correlation resulting in significant overprediction, and the Rosson and Myers (1965) and Dobson and Chato (1998) correlations being somewhat better – these latter correlations account for heat transfer through the bottom of the tube. This is not surprising because these models are not appropriate for Garimella and Bandhauer's data, which were demonstrated to be not in the stratified wavy regimes (Coleman and Garimella, 2000a; 2003). Among correlations that use a two-phase multiplier approach, the Moser *et al.* correlation predicted the data reasonably well (14% average deviation), with the Shah (1979) and Cavallini and Zecchin (1974) correlations resulting in some overprediction. Homogeneous flow correlations of Boyko and Kruzhilin (1967) and the mist flow correlation of Soliman (1986) were better at predicting the data, with the Soliman correlation leading to some overprediction. Shear-dominated annular flow correlations using boundary-layer treatments also showed reasonable agreement: Soliman *et al.* (1968) (18% average deviation), Chen and Kocamustafaogullari (1987) (13% average deviation.) However, in spite of the theoretical basis of the Traviss *et al.* (Traviss and Rohsenow, 1973; Traviss *et al.*, 1973) correlation, as reported by several investigators, this model showed the largest average deviation (38%) among shear-driven treatments.

Bandhauer *et al.* (2005) noted that during the condensation process, the flow changes from mist flow (where applicable) to annular film flow to intermittent, with large overlaps in the types of flow resulting in transition flow (intermittent/annular, intermittent/annular/mist, and annular/mist). Based on the work of Coleman and Garimella (2000a; 2003), wavy flow was not expected in any of the channels considered. Due to the large overlap regions between these flows, with the bulk of the data being in transition between annular flow and other regimes, they developed a heat transfer model based on annular flow considerations. They noted that many of the available shear-driven models, though sound in formulation, led to poor predictions because of the inadequate calculation of shear stresses using pressure drop models that were not applicable to microchannels. Thus, their model is based on boundary-layer analyses, but with the requisite shear stress being calculated from the pressure drop models of Garimella *et al.* (2005) developed specifically for microchannels. Since in annular flow, the condensate layer might become turbulent at very low Re_l (~ 240) (Carpenter and Colburn, 1951) due to the turbulent vapor core and the destabilizing effect of condensation (Schlichting and Gersten, 2000), a model based on turbulent parameters with appropriate modifications for the conditions under study was developed. The friction velocity $u^* = \sqrt{\tau_i/\rho_l}$ was expressed in terms of the interfacial shear stress, rather than the commonly used wall shear stress. The turbulent dimensionless temperature was defined as follows:

$$T^+ = \frac{\rho_l \times C_{p_l} \times u^*}{q''} (T_i - T_w) \quad (6.162)$$

The shear stress and heat flux were expressed in the usual manner:

$$\tau = (\mu + \rho \times \varepsilon_m) \frac{du}{dy} \quad (6.163)$$

$$q'' = -(k + \varepsilon_h \times \rho \times C_p) \frac{dT}{dy} \quad (6.164)$$

Assuming that the all of the heat is transferred in the liquid film results in the following expression for the heat transfer coefficient, where the interface is at the saturation temperature:

$$h = \frac{q''}{(T_{\text{sat}} - T_w)} = \frac{\rho_l \times C_{p_l} \times u^*}{T^+} \quad (6.165)$$

The heat flux above yields the dimensionless temperature gradient:

$$\frac{dT^+}{dy^+} = \left(\frac{1}{Pr_l} + \frac{\rho_l \times \varepsilon_h}{\mu_l} \right)^{-1} \quad (6.166)$$

To integrate this, the turbulent film thickness $\delta = (1 - \sqrt{\alpha})D/2$ is determined using the Baroczy (1965) model, which is different from the manner in which Traviss *et al.* (Traviss and Rohsenow, 1973; Traviss *et al.*, 1973) determined film thickness. The dimensionless

turbulent film thickness is then $\delta^+ = (\delta \rho_l u^*) / \mu_l$. Also $\tau = (1 - y/R) \tau_w$ yields the following equation:

$$\frac{\rho_l \varepsilon_m}{\mu_l} = \frac{1 - y^+/R^+}{du^+/dy^+} - 1 \quad (6.167)$$

In a manner analogous to the development by Traviss *et al.* (1973), with the assumptions of small film thickness compared to the tube radius, and $\varepsilon_m \cong \varepsilon_h$, the following simplified *two-region* turbulent dimensionless temperature expressions were proposed: for $Re_l < 2100$:

$$T^+ = 5Pr_l + 5 \ln \left[Pr_l \left(\frac{\delta^+}{5} - 1 \right) + 1 \right] \quad (6.168)$$

for $Re_l > 2100$:

$$T^+ = 5Pr_l + 5 \ln(5Pr_l + 1) + \int_{30}^{\delta^+} \frac{dy^+}{\left(\frac{1}{Pr_l} - 1 \right) + \frac{y^+}{5} \left(1 - \frac{y^+}{R^+} \right)} \quad (6.169)$$

The only unknown quantity, the interfacial shear stress for determining u^* , is obtained from the annular flow portion of the multiple-flow regime pressure drop model by Garimella *et al.* (2005) discussed in the previous section. Thus, the interfacial friction factor (and then the interfacial shear stress) is computed from the corresponding liquid-phase Re and friction factor, the Martinelli parameter, and the surface tension parameter: $f_i/f_l = AX^a Re_l^b \psi^c$. Additional details are available in the previous section. In summary, to obtain the heat transfer coefficient, the interfacial shear stress is first calculated using the pressure drop model. The resulting shear stress is used to compute the friction velocity u^* and the dimensionless film thickness δ^+ . The dimensionless temperature T^+ is then calculated, which yields the heat transfer coefficient. This model predicted 86% of the data within $\pm 20\%$, with an average absolute deviation of 10%. A more explicit accounting of the heat transfer in the liquid slugs, vapor bubbles, and the film-bubble interface in intermittent flow, and of the entrainment of liquid into the vapor core in mist flow would improve the predictions further. The data and the predictions at representative mass fluxes for each tube are shown in Fig. 6.33. The heat transfer coefficient increases with an increase in mass flux and quality, and with a decrease in the tube diameter. As the liquid film becomes thinner with increasing vapor quality, the heat transfer coefficient increases. The steep slope at the higher qualities represents an approach to a vanishingly thin film. However, it must be noted that the actual behavior in this region will be dependent on the inlet conditions of a condenser, including the inlet superheat, the coolant temperature, and the consequent wall subcooling – these phenomena are not accounted for in this model. Although the model was developed based on an annular flow mechanism, it appears to predict the heat transfer coefficients in the mist and mist–annular overlap regions in the high mass flux and high-quality cases adequately. At the extreme end of the graph ($x > 80\%$), the flow may be exclusively in the mist flow region. For a given flow rate, the quality at which the mist flow regime occurs could

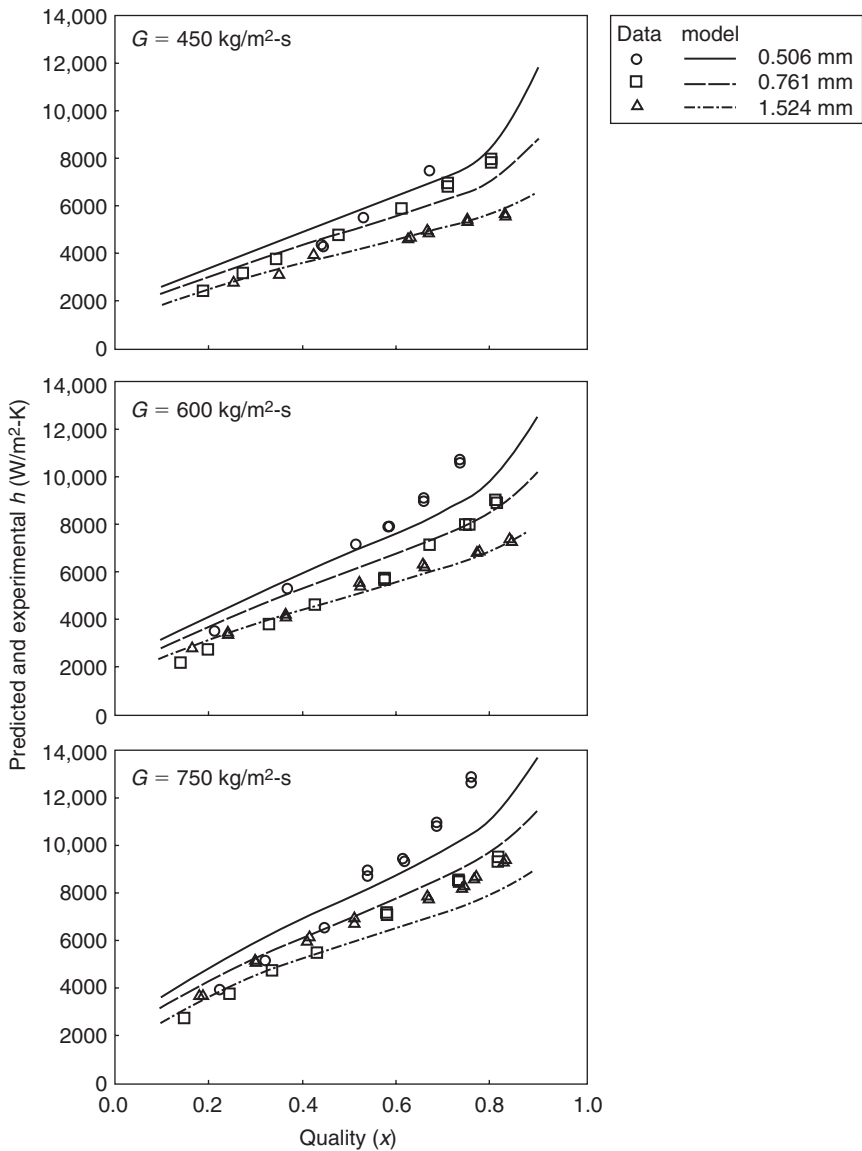


Fig. 6.33. Microchannel condensation heat transfer coefficient predictions. From Bandhauer, T. M., Agarwal, A. and Garimella, S., Measurement and modeling of condensation heat transfer coefficients in circular microchannels, *Journal of Heat Transfer*, in press (2006).

decrease with decreasing diameter due to increased interfacial shedding. As liquid entrainment increases, the heat transfer coefficient will increase due to the thinning of the liquid film (Soliman, 1986). Although liquid entrainment and mist formation are not explicitly accounted for in the heat transfer part of this model, the trends in the data (the steeper slope in the data at the higher qualities, particularly for small D_h) can be interpreted on this basis.

6.5.3. Summary observations and recommendations

The above discussion of the available literature on condensation heat transfer shows that much of the available information is on tubes larger than about 7 mm. In these tubes, heat transfer models have treated the multitude of flow regimes identified by many investigators and discussed in the previous sections as either stratified or annular flow regimes. Thus, almost all the available models in essence still use only gravity- or shear-dominated approaches. What differs from investigator to investigator is the specific analysis that addresses these two modes. In models of gravity-dominated condensation for example, the earliest models were patterned very closely after the Nusselt condensation analysis. They then progressed from neglecting the heat transfer in the liquid pool to accounting for it in some manner, usually through the application of single-phase liquid forced-convective heat transfer correlations. The apportioning of film condensation and forced convection regions within this stratified flow has also differed in the minor details. Most of these models use some void fraction model, usually the one by Zivi (1964), to determine the liquid and vapor fractions of the cross-section (which is usually quantified as the liquid pool angle), which then allows them to predict the surface area over which these two submodels are applied. In many cases, however, the void fraction models were originally based on annular flow data or analyses. A few models have also attempted to account for vapor shear on the falling-film condensation portion of the tube.

In annular flow models, the technique of relating the interfacial shear (through a boundary-layer analysis that usually uses the von Karman velocity profile) to the heat transfer across the liquid film has been used widely, starting with the work of Carpenter and Colburn (1951), with refinements and improvements to the contribution of various forces to the interfacial shear, for example by Soliman (1968), Traviss *et al.* (1973), and others. There have also been some attempts such as the work of Chen *et al.* (1987) to develop general purpose annular flow correlations starting with asymptotic limits, and blending them through some simple combination of the terms at the respective limits. Another approach has been to directly apply a multiplication factor to a single-phase liquid or vapor phase heat transfer correlation, with the multiplier determined using adaptations of the Lockhart–Martinelli (1949) and Friedel (1979) pressure drop multipliers. This approach is in fact analogous to the boundary-layer shear stress analysis used by many investigators. The only essential difference is in where the multiplier is applied: the first type of models use the multiplier first for shear stress determination, and calculate the heat transfer coefficient directly thereafter; the second type calculate the single-phase heat transfer coefficient directly, and apply the multiplier thereafter. An explanation of the similarity of these two approaches is provided in Dobson and Chato (1998). One correlation that continues to be used frequently is the purely empirical Shah (1979) correlation, because of its simplicity, the wide range of data that were utilized in its development, and its comparatively good predictions for annular flows. Another model that has been used widely until recently is the Akers *et al.* (1959) technique of determining an equivalent mass flux that would provide the same shear as the two-phase flow; thus replacing the vapor core with an additional liquid flow rate, and then treating the combined flux as being in single-phase flow. At the time of its development, this approach was perhaps motivated by the desire to facilitate computation of heat transfer coefficients in a manner more familiar

to most designers (i.e. single-phase analysis). However, recent papers have shown that the predictions of these models are not very good, and also that the appropriate friction factors and driving temperature difference are not applied when transforming the two-phase flow to an equivalent single-phase flow. Although corrected versions (Moser *et al.*, 1998) of this model are now available, implementing the corrected versions renders them as involved as the boundary-layer analyses, and does not seem to offer any additional ease of use.

In recent years, large experimental efforts or analyses of data from multiple researchers have been undertaken to develop models that address the entire process of condensation from inlet to outlet, spanning a wide range of mass fluxes, diameters, and fluids. Representative models include Dobson and Chato (1998), Cavallini *et al.* (2002a), and Thome *et al.* (2003). While these studies have yielded smoother, and in general, more accurate predictions over a wide range of conditions, they too still group the multitude of flow regimes into only stratified/wavy and annular flows. This is in stark contrast to the flow visualization studies discussed in previous sections, where the tendency is more toward identifying and categorizing every single nuance of the flow structure. Important flow regimes (and increasingly so with the progression toward smaller diameter channels) such as intermittent and mist flow have, until now, not been successfully modeled, except as unsubstantiated extensions of annular flow. A quasi-homogeneous model of Soliman (1986) is one of the few examples of a model dedicated to one such flow regime (mist).

The availability of reliable local condensation heat transfer measurements and models in microchannels of $D < 3$ mm is especially limited. (The wealth of gravity-dominated condensation models in large tubes are of little relevance to condensation in microchannels.) A group of researchers led by Webb (Yang and Webb, 1996a, b; 1997; Webb and Ermis, 2001; Zhang and Webb, 2001) has made some progress in measuring heat transfer coefficients in extruded aluminum tubes with multiple parallel ports of $D_h < 3$ mm, although the mass fluxes they have focused on are at the high end of the range of interest for common refrigeration and air-conditioning applications. In these papers, they have attempted several different approaches to modeling the heat transfer coefficients including typical shear stress models and equivalent mass flux models. A reliable model that predicts and explains the variety of trends seen in these results has however yet to be developed. While surface tension has been mentioned routinely as an important and governing parameter in microchannel flows, there is almost no model that explicitly tracks surface tension forces on a first principles basis from pressure gradient to heat transfer evaluation. At best, some investigators such as Bandhauer *et al.* (2005) have indirectly accounted for surface tension through a surface tension parameter in the pressure drop model used for the shear stress calculation, which has yielded accurate microchannel heat transfer predictions over a wide range of conditions. Also, Yang and Webb (1997) are one of the few researchers who explicitly account for surface tension forces in microchannels (with microfins) by computing the drainage of the liquid film from the microfin tips and the associated heat transfer enhancement when the fin tips are not flooded. The analytical treatments proposed recently by Wang *et al.* (Wang and Rose, 2004; Wang *et al.*, 2004) for microchannels with $D \sim 1$ mm that account for the combined influence of surface tension, shear, and gravity as condensation proceeds also hold promise.

The use of representative heat transfer correlations and models discussed in this section is illustrated in Example 6.4.

6.6. Conclusions

This chapter has provided an overview of the available literature that is relevant to the modeling of condensation in microchannels. Microchannel definitions and governing influences, flow regimes and transition criteria, void fraction correlations, pressure drop and heat transfer were addressed. Based on the information presented, it can be said that the building blocks for the modeling of condensation in microchannels are slowly becoming available, although the bulk of the available information is on larger channels. These macrochannel studies and models serve as a starting point for corresponding studies on microchannels. By far the most progress on addressing microchannel flows has been in the area of flow regime determination: adiabatic and condensing flows have been documented in detail in mini channels, while in channels with $D_h < \sim 3$ mm, there are few studies of condensing flows, almost all the research being on adiabatic two-phase flow. It is not clear whether these results for adiabatic flows can be reliably extrapolated to refrigerants with lower surface tension, larger vapor densities, and other property differences. Void fractions required for closure of most heat transfer and pressure drop models have primarily been for annular flows, with recent advances yielding some empirical correlations based on video analysis for adiabatic flows in channels of $D_h \approx 1$ mm and lower. Models for pressure drops during condensation are primarily available for channels with $D_h >$ about 3 mm, and they continue to use two-phase multiplier approaches, with some modifications to the multipliers to match the data. A few flow regime-based pressure drop models for condensing flows in microchannels are beginning to emerge.

Heat transfer coefficients for condensation present additional challenges that must be addressed with great care while designing and running experiments. The widely used Wilson plot techniques that were ubiquitously used for large channels are limited in their utility for small channels. Controlled experiments that can measure heat transfer rates of the order of a few watts for local condensation ($\Delta x \approx 0.05$) in microchannels are particularly challenging. Innovative techniques, including non-intrusive measurements, and attention to the many sources of uncertainty are essential to ensure providing an accurate database for which models can be developed. As stated in this chapter, this challenge of small heat duties is coupled with the large condensing heat transfer coefficients, which imply that heat is often being transferred across $\Delta T < \sim 0.5^\circ\text{C}$. Any appreciable uncertainties in temperature measurement would render the resulting heat transfer coefficients unreliable and inaccurate. On the analysis front, models for heat transfer coefficients reflect the cumulative effects of reliable or unreliable establishment of flow regimes, modeling of void fractions, and computation of shear stress through pressure drop, and of course uncertainties in the measurement of heat transfer coefficients. Thus, models that account for the underlying phenomena, including surface tension considerations unique to microchannels, are particularly important.

The research needs also extend to practical issues such as mal-distribution of refrigerant flows through multiple channels – many innovative designs fail or are infeasible because adequate consideration is not given to establishing uniform distribution of two-phase fluid through parallel channels. Similarly, models for “minor” losses through expansions, bends, and contractions should be developed to provide the designer a complete set of tools.

Environmental and other concerns will continue to change the refrigerants that are acceptable and allowable for use in practical air-conditioning and refrigeration systems.

Therefore, the models developed must be robust enough to be used for a variety of fluids, including refrigerant blends. If the chosen refrigerants are zeotropic blends, techniques for handling the additional mass transfer resistance must either be validated using large channel methodologies as a basis, or new modeling techniques should be developed. The acceptable synthetic refrigerant blends and natural refrigerants such as CO₂ are increasingly higher-pressure refrigerants; therefore, the effect of the approach to critical pressure on condensation phenomena requires special attention. Also, fluids such as CO₂ and steam have high thermal conductivities, specific heats, and latent heat of condensation, which make measurement of the resulting higher heat transfer coefficients particularly challenging.

These are but a few of the foreseeable research challenges and needs; given the state of infancy of understanding and modeling condensation in microchannels, a considerable amount of careful effort is required to obtain a comprehensive understanding. The achievement of such a fundamental understanding of condensation at the microscales will yield far reaching benefits not only for the air-conditioning and refrigeration industries, but also for other as-yet untapped applications such as portable personal cooling devices, hazardous duty, and high ambient air-conditioning, sensors, and medical/surgical devices, to name a few.

Example 6.1. Flow regimes determination

Determine the applicable flow regime for the flow of refrigerant R-134a in a 1 mm diameter tube at a pressure of 1500 kPa, at mass fluxes of 150, 400, and 750 kg/m²-s and qualities of 0.2, 0.5, and 0.8. Use the flow regime maps and transition criteria of Sardeesai *et al.* (1981), Tandon *et al.* (1982), Dobson and Chato (1998), Breber *et al.* (1980), Soliman (1982; 1986), Coleman and Garimella (2000a, b; 2003) and Garimella (2004), and Cavallini *et al.* (2002a), and compare and comment on the flow regimes predicted by each model.

Refrigerant properties

Saturation temperature $T_{\text{sat}} = 55.21^{\circ}\text{C}$
Surface tension $\sigma = 0.00427 \text{ N/m}$

Liquid phase	Vapor phase
$\rho_l = 1077 \text{ kg/m}^3$	$\rho_v = 76.5 \text{ kg/m}^3$
$\mu_l = 1.321 \times 10^{-4} \text{ kg/m-s}$	$\mu_v = 1.357 \times 10^{-5} \text{ kg/m-s}$

For $G = 400 \text{ kg/m}^2\text{-s}$ and $x = 0.5$:
Liquid Reynolds number,

$$\text{Re}_l = \frac{GD(1-x)}{\mu_l} = \frac{400 \times 0.001 \times (1-0.5)}{1.321 \times 10^{-4}} = 1514$$

Vapor Reynolds number,

$$\text{Re}_v = \frac{GDx}{\mu_v} = \frac{400 \times 0.001 \times 0.5}{1.357 \times 10^{-5}} = 14743$$

Vapor-only Reynolds number,

$$\text{Re}_{vo} = \frac{GD}{\mu_v} = \frac{400 \times 0.001}{1.357 \times 10^{-5}} = 29486$$

Using the Churchill (1977) correlation for the single-phase friction factors, assuming a smooth tube, $f_l = 0.0423$, and $f_v = 0.0279$. The corresponding single-phase pressure drops are:

$$\left(\frac{dP}{dz} \right)_l = \frac{f_l G^2 (1-x)^2}{2D\rho_l} = \frac{0.0423 \times 400^2 (1-0.5)^2}{2 \times 0.001 \times 1077} = 784.6 \text{ Pa/m}$$

$$\left(\frac{dP}{dz} \right)_v = \frac{f_v G^2 x^2}{2D\rho_v} = \frac{0.0279 \times 400^2 \times 0.5^2}{2 \times 0.001 \times 76.5} = 7304 \text{ Pa/m}$$

The predictions from each model listed above are computed as follows.

Sardesai *et al.* (1981)

Martinelli parameter,

$$X = \left[\frac{(dP/dz)_l}{(dP/dz)_v} \right]^{1/2} = \left[\frac{784.6}{7304} \right]^{1/2} = 0.3278$$

Superficial gas velocity,

$$j_v = \frac{xG}{\rho_v} = \frac{0.5 \times 400}{76.5} = 2.615 \text{ m/s}$$

Modified Froude number:

$$F = \sqrt{\frac{\rho_v}{\rho_l - \rho_v}} \times \frac{j_v}{\sqrt{Dg}} = \sqrt{\frac{76.5}{1077 - 76.5}} \times \frac{2.615}{\sqrt{0.001 \times 9.81}} = 7.298$$

Function $\beta = (0.7X^2 + 2X + 0.85)F = (0.7 \times 0.3278^2 + 2 \times 0.3278 + 0.85) \times 7.298 = 11.54$.

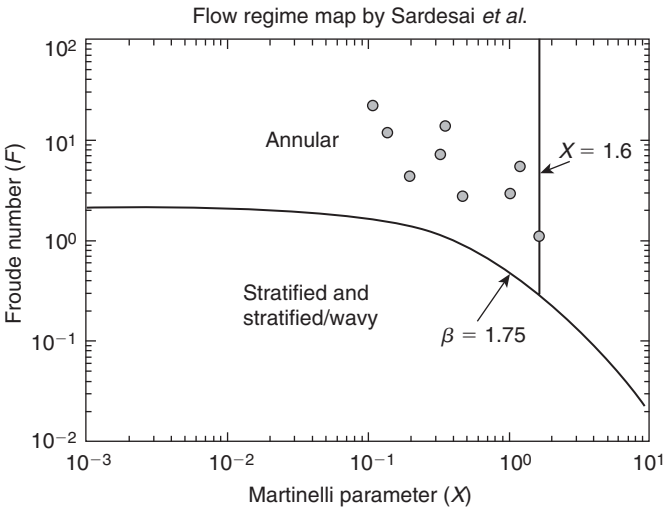
The corresponding values for the other conditions are also calculated in a similar manner, and the regimes are assigned as follows:

$\beta < 1.75$: Stratified and stratified/wavy flow

$\beta \geq 1.75$: Annular flow

The resulting flow regimes are listed and plotted below.

G	x	X	β	Flow regime
150	0.2	1.631	6.538	Annular
150	0.5	0.4666	5.297	Annular
150	0.8	0.01974	5.571	Annular
400	0.2	1.024	10.61	Annular
400	0.5	0.3278	11.54	Annular
400	0.8	0.1375	13.29	Annular
750	0.2	1.212	23.55	Annular
750	0.5	0.3527	22.47	Annular
750	0.8	0.1082	23.53	Annular



Tandon *et al.* (1982)
For the sample condition with $G = 400 \text{ kg/m}^2\text{-s}$ and $x = 0.5$, the required parameters are calculated below.
Dimensionless gas velocity:

$$j_g^* = \frac{Gx}{\sqrt{Dg\rho_v(\rho_l - \rho_v)}} = \frac{400 \times 0.5}{\sqrt{0.001 \times 9.81 \times 76.5(1077 - 76.5)}} = 7.298$$

Void fraction,

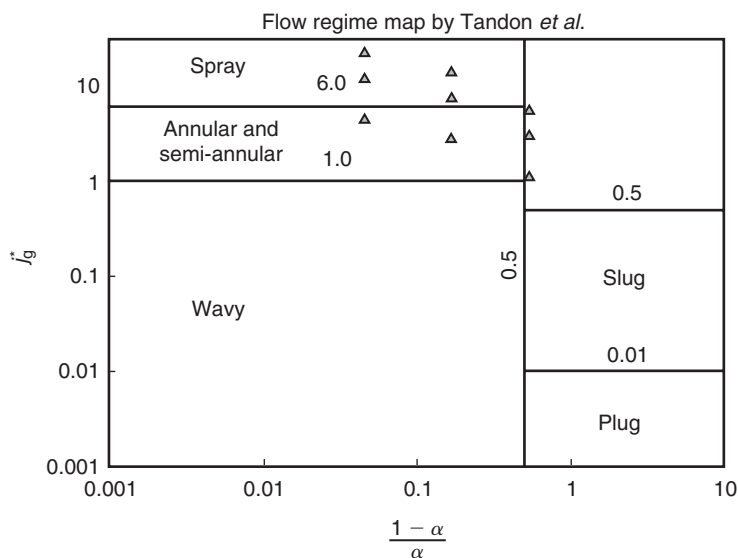
$$\alpha = \left\{ 1 + \frac{\rho_v}{\rho_l} \left(\frac{1-x}{x} \right) \left[0.4 + 0.6 \sqrt{\frac{\frac{\rho_l}{\rho_v} + 0.4 \left(\frac{1-x}{x} \right)}{1 + 0.4 \left(\frac{1-x}{x} \right)}} \right] \right\}^{-1}$$

$$\Rightarrow \alpha = \left\{ 1 + \frac{76.5}{1077} \left(\frac{1-0.5}{0.5} \right) \left[0.4 + 0.6 \sqrt{\frac{\frac{1077}{76.5} + 0.4 \left(\frac{1-0.5}{0.5} \right)}{1 + 0.4 \left(\frac{1-0.5}{0.5} \right)}} \right] \right\}^{-1} = 0.858$$

$$\Rightarrow \frac{1-\alpha}{\alpha} = 0.1654$$

In a similar manner, these parameters are computed for each of the conditions, and the flow regimes assigned according to the transition criteria listed in Section 6.2.2.

G	x	j_g^*	$\frac{1-\alpha}{\alpha}$	Flow regime
150	0.2	1.095	0.5322	Undesignated
150	0.5	2.737	0.1654	Annular and semi-annular
150	0.8	4.379	0.04535	Annular and semi-annular
400	0.2	2.919	0.5322	Undesignated
400	0.5	7.298	0.1654	Spray
400	0.8	11.68	0.04535	Spray
750	0.2	5.473	0.5322	Undesignated
750	0.5	13.68	0.1654	Spray
750	0.8	21.89	0.04535	Spray



Dobson and Chato (1998)

For the sample condition $G = 400 \text{ kg/m}^2\text{-s}$ and $x = 0.5$, the required parameters are as follows.

$$X_{tt} = \left(\frac{1-x}{x} \right)^{0.9} \left(\frac{\rho_v}{\rho_l} \right)^{0.5} \left(\frac{\mu_l}{\mu_g} \right)^{0.1}$$

$$\Rightarrow X_{tt} = \left(\frac{1-0.5}{0.5} \right)^{0.9} \left(\frac{76.5}{1077} \right)^{0.5} \left(\frac{1.321 \times 10^{-4}}{1.357 \times 10^{-5}} \right)^{0.1} = 0.3346$$

Void fraction:

$$\alpha = \left[1 + \frac{1-x}{x} \left(\frac{\rho_v}{\rho_l} \right)^{2/3} \right]^{-1}$$

$$\Rightarrow \alpha = \left[1 + \frac{1-0.5}{0.5} \left(\frac{76.5}{1077} \right)^{2/3} \right]^{-1} = 0.8536$$

Galileo number,

$$Ga = g \rho_l (\rho_l - \rho_v) \frac{(\sqrt{\alpha} D)^3}{\mu_l^2}$$

$$\Rightarrow Ga = 9.81 \times 1077 (1077 - 76.5) \frac{(\sqrt{0.8536} \times 0.001)^3}{(1.321 \times 10^{-4})^2} = 478,182$$

$$Fr_{so} = \begin{cases} 0.025 \times Re_l^{1.59} \left(\frac{1 + 1.09 X_{tt}^{0.039}}{X_{tt}} \right)^{1.5} \frac{1}{Ga^{0.5}} & \text{for } Re_l \leq 1250 \\ 1.26 \times Re_l^{1.04} \left(\frac{1 + 1.09 X_{tt}^{0.039}}{X_{tt}} \right)^{1.5} \frac{1}{Ga^{0.5}} & \text{for } Re_l > 1250 \end{cases}$$

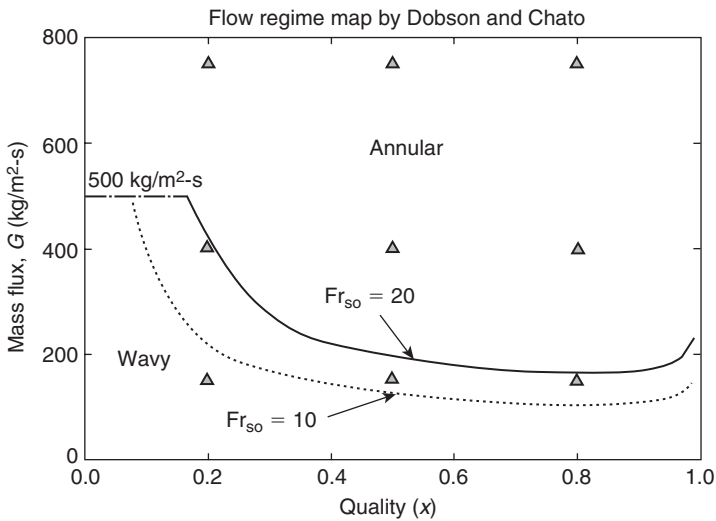
Therefore for $Re_l = 1514$,

$$Fr_{so} = 1.26 \times Re_l^{1.04} \left(\frac{1 + 1.09 X_{tt}^{0.039}}{X_{tt}} \right)^{1.5} \frac{1}{Ga^{0.5}}$$

$$\Rightarrow Fr_{so} = 1.26 \times 1514^{1.04} \left(\frac{1 + 1.09 \times 0.3346^{0.039}}{0.3346} \right)^{1.5} \frac{1}{478,182^{0.5}} = 55.86$$

In a similar manner, these parameters are computed for each of the conditions, and the flow regimes assigned according to the transition criteria based on Fr_{so} and G listed in Section 6.2.2. The respective flow regimes are follows:

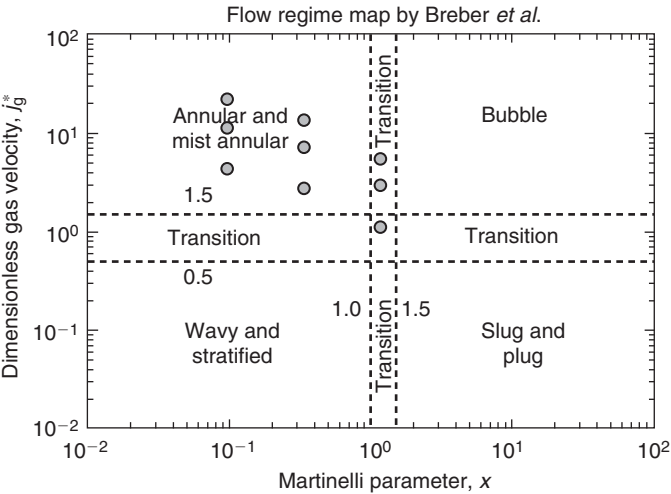
G	x	Fr_{so}	Flow regime
150	0.2	5.797	Wavy
150	0.5	13.08	Wavy
150	0.8	17.49	Wavy
400	0.2	19.12	Wavy
400	0.5	55.86	Annular
400	0.8	83.17	Annular
750	0.2	36.77	Annular
750	0.5	107.4	Annular
750	0.8	226	Annular



Breber *et al.* (1980)

For the sample condition $G = 400$ kg/m²-s and $x = 0.5$, the dimensionless gas velocity, $j_g^* = 7.298$, and the Martinelli parameter $X_{tt} = 0.3346$ from the calculations above. The respective flow regimes are assigned based on the specific values of these parameters as shown below.

G	x	X	j_g^*	Flow regime
150	0.2	1.165	1.095	Transition between all four regimes
150	0.5	0.3346	2.737	Annular and mist annular
150	0.8	0.0961	4.379	Annular and mist annular
400	0.2	1.165	2.919	Transition from annular and mist annular flow regime to bubble flow regime
400	0.5	0.3346	7.298	Annular and mist annular
400	0.8	0.0961	11.68	Annular and mist annular
750	0.2	1.165	5.473	Transition from annular and mist annular flow regime to bubble flow regime
750	0.5	0.3346	13.68	Annular and mist annular
750	0.8	0.0961	21.89	Annular and mist annular



Soliman (1982; 1986)

The annular to wavy and intermittent transition (Soliman, 1982) was established based on the Froude number and the annular to mist transition (Soliman, 1986) was based on the modified Weber number. The Froude number is calculated using the following equations:

$$\begin{aligned} \text{Re}_l &= 10.18 \text{Fr}^{0.625} \text{Ga}^{0.313} (\phi_v/X_{tt})^{-0.938} & \text{for } \text{Re}_l \leq 1250 \\ \text{Re}_l &= 0.79 \text{Fr}^{0.962} \text{Ga}^{0.481} (\phi_v/X_{tt})^{-1.442} & \text{for } \text{Re}_l > 1250 \end{aligned}$$

From the above calculations, for $G = 400 \text{ kg/m}^2\text{-s}$ and $x = 0.5$, liquid Reynolds number $\text{Re}_l = 1514$, and Martinelli parameter $X_{tt} = 0.3346$. The Galileo number for this model is

defined as $Ga = gD^3(\rho_l/\mu_l)^2$. Thus,

$$Ga = 9.81 \times 0.001^3 \left(\frac{1077}{1.321 \times 10^{-4}} \right)^2 = 652,650$$

The curve-fit for the square root of the two-phase multiplier, is given by:

$$\phi_v = 1 + 1.09 X_{tt}^{0.039} = 1 + 1.09 \times 0.3346^{0.039} = 2.044$$

The values are substituted into the Reynolds number equation to yield:

$$1514 = 0.79 Fr^{0.962} \times 652650^{0.481} \left(\frac{2.044}{0.3346} \right)^{-1.442}; \quad Fr = 48.22$$

The modified Weber number is given by:

$$We = \begin{cases} 2.45 Re_v^{0.64} \left(\frac{\mu_v^2}{\rho_v \sigma D} \right)^{0.3} \phi_v^{-0.4} & \text{for } Re_l \leq 1250 \\ 0.85 Re_v^{0.79} \left(\frac{\mu_v^2}{\rho_v \sigma D} \right)^{0.3} \left[\left(\frac{\mu_v}{\mu_l} \right)^2 \left(\frac{\rho_l}{\rho_v} \right) \right]^{0.084} (X_{tt}/\phi_v^{2.55})^{0.157} & \text{for } Re_l > 1250 \end{cases}$$

For the present condition, therefore:

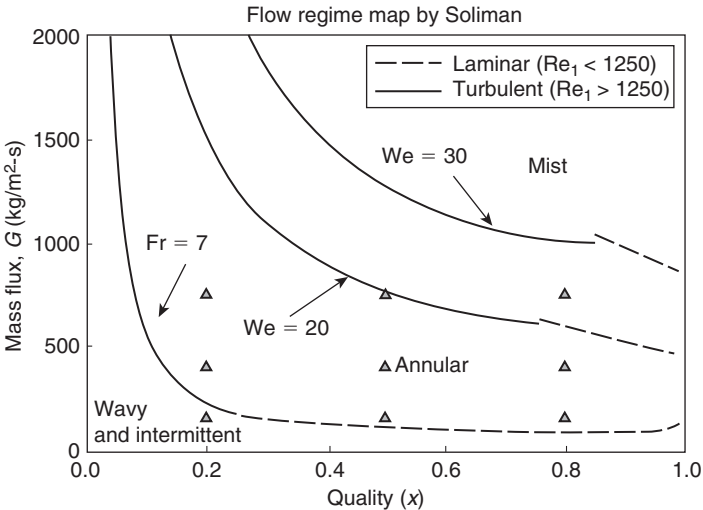
$$\begin{aligned} We &= 0.85 \times 14743^{0.79} \left(\frac{(1.357 \times 10^{-5})^2}{76.5 \times 4.27 \times 10^{-3} \times 0.001} \right)^{0.3} \\ &\quad \times \left[\left(\frac{1.357 \times 10^{-5}}{1.321 \times 10^{-4}} \right)^2 \left(\frac{1077}{76.5} \right) \right]^{0.084} \left(\frac{0.3346}{2.044^{2.55}} \right)^{0.157} \\ &= 12 \end{aligned}$$

Now,

$Fr < 7$	Wavy and intermittent
$Fr > 7$ and $We < 20$	Always annular
$Fr > 7$ and $We > 30$	Always mist

Thus, at $G = 400 \text{ kg/m}^2\text{-s}$ and $x = 0.5$, flow regime is annular. The flow regimes for the other points are shown below.

G	x	Fr	We	Flow regime
150	0.2	3.908	3.36	Wavy and intermittent
150	0.5	11.54	6.10	Annular
150	0.8	16.7	8.324	Annular
400	0.2	12.58	7.008	Annular
400	0.5	48.22	12.00	Annular
400	0.8	80.20	15.59	Annular
750	0.2	24.17	11.52	Annular
750	0.5	92.68	19.72	Annular
750	0.8	219.3	23.32	Annular/mist transition



Coleman and Garimella (2000b; 2000a; 2003) and Garimella (2004)

Simple algebraic curve-fits to their G - x transition lines are given below.

Intermittent flow to intermittent and annular film flow:

$$G = \frac{547.7 - 1227x}{1 + 2.856x}$$

Intermittent and annular film flow to annular film flow:

$$G = -56.13 + 125.4/x$$

Annular film flow to annular film and mist flow:

$$G = 206.1 + 85.8/x$$

Annular film and mist flow to mist flow:

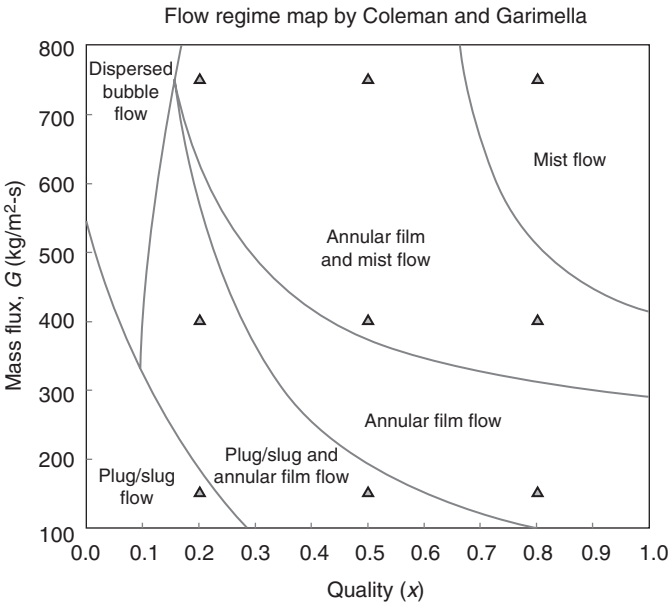
$$G = \frac{207.2 - 527.5x}{1 - 1.774x}$$

Dispersed bubble flow:

$$G = 1376 - 97.1/x$$

The respective lines and the conditions of interest are shown in the graph below.
Thus, the flow regimes are assigned as follows:

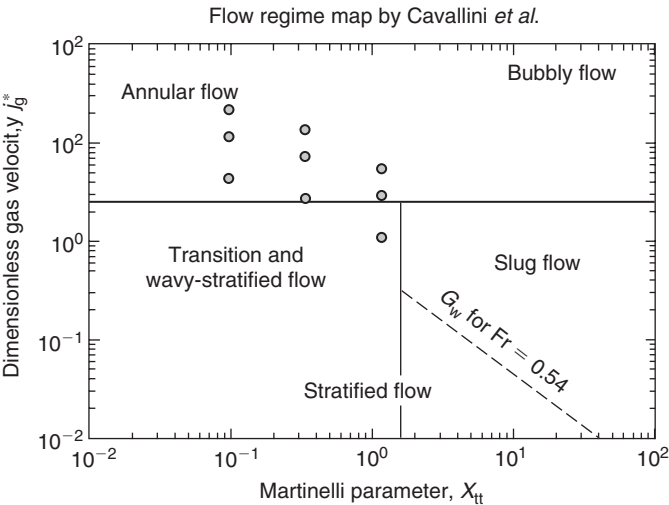
G	x	Flow regime
150	0.2	Intermittent flow
150	0.5	Intermittent and annular film flow
150	0.8	Annular film flow
400	0.2	Intermittent and annular film flow
400	0.5	Annular film and mist flow
400	0.8	Annular film and mist flow
750	0.2	Annular film and mist flow
750	0.5	Annular film and mist flow
750	0.8	Mist flow



Cavallini *et al.* (2002a)

The Cavallini *et al.* map is similar to the Breber *et al.* map, being based on the Martinelli parameter and the dimensionless gas velocity, both of which were calculated above. The flow regime assignment for all the conditions of interest is shown below, and also plotted on their map.

G	x	X_{tt}	j_g^*	Flow regime
150	0.2	1.165	1.095	Annular-stratified flow transition and stratified flow
150	0.5	0.3346	2.737	Annular
150	0.8	0.0961	4.379	Annular
400	0.2	1.165	2.919	Annular
400	0.5	0.3346	7.298	Annular
400	0.8	0.0961	11.68	Annular
750	0.2	1.165	5.473	Annular
750	0.5	0.3346	13.68	Annular
750	0.8	0.0961	21.89	Annular



A comparison of the predictions of each of these maps is shown below. This comparison shows that the different investigators predict a wide range of regimes for the conditions of interest in this example. The bulk of the points are in annular flow according to most models and transition criteria, although the criteria of Dobson and Chato predict wavy flow for all the $G = 150 \text{ kg/m}^2\text{-s}$ conditions, as well as for the low quality, $G = 400 \text{ kg/m}^2\text{-s}$ case. It should be noted that in Dobson and Chato’s paper, a discussion appears about the $10 < Fr < 20$ region being some form of a transition region between wavy and annular flow, although in their recommended criteria, $Fr = 20$ is stated as a unique transition line. Tandon *et al.*, Breber *et al.*, and Coleman and Garimella predict

some form of mist flow, either in combination with annular flow, or by itself, at the higher mass fluxes and qualities. The similarities in the bases between the Breber *et al.* and Cavallini *et al.* maps are also evident in this table. Of these maps, only the Coleman and Garimella criteria are reported to apply for condensation in tubes as small as 1 mm, while the Dobson and Chato criteria apply down to $D = 3.14$ mm, and many of the other criteria were for tubes with $D > 4.8$ mm, with most being primarily based on tubes with $D \geq 8$ mm. Flow regime studies for the channels much smaller than 1 mm were not represented in the above illustration because they are all for adiabatic air–water or nitrogen–water flow, and many of them do not propose explicit transition equations.

Condition	Sardesai <i>et al.</i>	Tandon <i>et al.</i>	Dobson and Chato	Breber <i>et al.</i>	Soliman	Cavallini <i>et al.</i>	Coleman and Garimella
$G = 150 \text{ kg/m}^2\text{-s}$ $x = 0.2$	Annular	–	Wavy	Transition between all four regimes	Wavy and intermittent	Annular- stratified flow transition and stratified flow	Plug/slug flow
$G = 150 \text{ kg/m}^2\text{-s}$ $x = 0.5$	Annular	Annular and semi-annular	Wavy	Annular and mist annular	Annular	Annular	Plug/slug and annular film flow
$G = 150 \text{ kg/m}^2\text{-s}$ $x = 0.8$	Annular	Annular and semi-annular	Wavy	Annular and mist annular	Annular	Annular	Annular film flow
$G = 400 \text{ kg/m}^2\text{-s}$ $x = 0.2$	Annular	–	Wavy	Transition from annular and mist annular flow regime to bubble flow regime	Annular	Annular	Plug/slug and annular film flow
$G = 400 \text{ kg/m}^2\text{-s}$ $x = 0.5$	Annular	Spray	Annular	Annular and mist annular	Annular	Annular	Annular film and mist flow
$G = 400 \text{ kg/m}^2\text{-s}$ $x = 0.8$	Annular	Spray	Annular	Annular and mist annular	Annular	Annular	Annular film and mist flow
$G = 750 \text{ kg/m}^2\text{-s}$ $x = 0.2$	Annular	–	Annular	Transition from annular and mist annular flow regime to bubble flow regime	Annular	Annular	Annular film and mist flow
$G = 750 \text{ kg/m}^2\text{-s}$ $x = 0.5$	Annular	Spray	Annular	Annular and mist annular	Annular	Annular	Annular film and mist flow
$G = 750 \text{ kg/m}^2\text{-s}$ $x = 0.8$	Annular	Spray	Annular	Annular and mist annular	Transition	Annular	Mist flow

Example 6.2. Void fraction calculation

Compute the void fraction for refrigerant R-134a flowing through a 1-mm tube at a pressure of 1500 kPa, at mass fluxes 150, 400, and 750 kg/m²-s and qualities of 0.2, 0.5, and 0.8. Use the homogeneous model and correlations by Kawahara *et al.* (2002), Baroczy (1965), Zivi (1964), Lockhart and Martinelli (1949), Thom (1964), Steiner (1993), Tandon *et al.* (1985b), El Hajal *et al.* (2003), Smith (1969), Premoli *et al.* (1971), and Yashar *et al.* (2001). Compare the values predicted by each model and comment.

Refrigerant properties

Saturation temperature: $T_{\text{sat}} = 55.21^{\circ}\text{C}$

Surface tension: $\sigma = 4.27 \times 10^{-3} \text{ N/m}$

Representative calculations are shown here for the $G = 400 \text{ kg/m}^2\text{-s}$, $x = 0.5$ case.

Liquid phase	Vapor phase
$\rho_l = 1077 \text{ kg/m}^3$	$\rho_v = 76.5 \text{ kg/m}^3$
$\mu_l = 1.321 \times 10^{-4} \text{ kg/m-s}$	$\mu_v = 1.357 \times 10^{-5} \text{ kg/m-s}$

Homogeneous model

The void fraction is given by:

$$\alpha = \left[1 + \frac{1-x}{x} \left(\frac{\rho_v}{\rho_l} \right) \right]^{-1} = \left[1 + \frac{1-0.5}{0.5} \left(\frac{76.5}{1077} \right) \right]^{-1} = 0.9337$$

Some investigators, for example, Triplett *et al.* (1999a) recommend the homogeneous model for calculation of void fraction in channels with $D_h \sim 1 \text{ mm}$.

Kawahara *et al.* (2002)

Kawahara *et al.* (2002) recommend the following correlation for void fraction in tubes of diameters 100 and 50 μm .

$$\alpha = \frac{C_1 \alpha_h^{0.5}}{1 - C_2 \alpha_h^{0.5}}$$

where, α_h is the homogeneous void fraction

$$C_1 = \begin{cases} 0.03 & \text{For } D = 100 \mu\text{m} \\ 0.02 & \text{For } D = 50 \mu\text{m} \end{cases} \quad \text{and} \quad C_2 = \begin{cases} 0.97 & \text{For } D = 100 \mu\text{m} \\ 0.98 & \text{For } D = 50 \mu\text{m} \end{cases}$$

Based on experimental data, they recommend that for $D > 250 \mu\text{m}$, the void fraction be computed using the homogeneous model. Therefore, for this case ($D = 1 \text{ mm}$), the void fraction is 0.9337.

Baroczy (1965)

The Baroczy void fraction is calculated as follows:

$$\alpha = \left[1 + \left(\frac{1-x}{x} \right)^{0.74} \left(\frac{\rho_v}{\rho_l} \right)^{0.65} \left(\frac{\mu_l}{\mu_v} \right)^{0.13} \right]^{-1}$$

$$\Rightarrow \alpha = \left[1 + \left(\frac{1-0.5}{0.5} \right)^{0.74} \left(\frac{76.5}{1077} \right)^{0.65} \left(\frac{1.321 \times 10^{-4}}{1.357 \times 10^{-5}} \right)^{0.13} \right]^{-1} = 0.8059$$

Koyama *et al.* (2004) recommend this correlation for smooth tubes, but mention that it does not predict the void fraction in microfin tubes well.

Zivi (1964)

This widely used correlation is given by:

$$\alpha = \left[1 + \frac{1-x}{x} \left(\frac{\rho_v}{\rho_l} \right)^{2/3} \right]^{-1}$$

$$\Rightarrow \alpha = \left[1 + \frac{1-0.5}{0.5} \left(\frac{76.5}{1077} \right)^{2/3} \right]^{-1} = 0.8536$$

Lockhart and Martinelli (1949)

This correlation is given by:

$$\alpha = \left[1 + 0.28 \left(\frac{1-x}{x} \right)^{0.64} \left(\frac{\rho_v}{\rho_l} \right)^{0.36} \left(\frac{\mu_l}{\mu_v} \right)^{0.07} \right]^{-1}$$

$$\Rightarrow \alpha = \left[1 + 0.28 \left(\frac{1-0.5}{0.5} \right)^{0.64} \left(\frac{76.5}{1077} \right)^{0.36} \left(\frac{1.321 \times 10^{-4}}{1.357 \times 10^{-5}} \right)^{0.07} \right]^{-1} = 0.8875$$

Based on experimental data for air–water flow in 6.6 and 33.2 mm diameter tubes, Ekberg *et al.* (1999) recommend the Lockhart and Martinelli correlation for void fraction calculations.

Thom (1964)

The calculation is as follows:

$$\alpha = \left[1 + \left(\frac{1-x}{x} \right) \left(\frac{\rho_v}{\rho_l} \right)^{0.89} \left(\frac{\mu_l}{\mu_v} \right)^{0.18} \right]^{-1}$$

$$\Rightarrow \alpha = \left[1 + \left(\frac{1-0.5}{0.5} \right) \left(\frac{76.5}{1077} \right)^{0.89} \left(\frac{1.321 \times 10^{-4}}{1.357 \times 10^{-5}} \right)^{0.18} \right]^{-1} = 0.8748$$

Steiner (1993)

$$\alpha = \frac{x}{\rho_v} \left([1 + 0.12(1-x)] \left[\frac{x}{\rho_v} + \frac{1-x}{\rho_l} \right] + \frac{1.18(1-x) [g \times \sigma(\rho_l - \rho_v)]^{0.25}}{G \times \rho_l^{0.5}} \right)^{-1}$$

$$\Rightarrow \alpha = \frac{0.5}{76.5} \left([1 + 0.12(1-0.5)] \left[\frac{0.5}{76.5} + \frac{1-0.5}{1077} \right] + \frac{1.18(1-0.5) [9.81 \times 4.27 \times 10^{-3} \times (1077 - 76.5)]^{0.25}}{400 \times 1077^{0.5}} \right)^{-1}$$

The resulting void fraction is $\alpha = 0.8675$.

Tandon *et al.* (1985b)

The liquid Reynolds number required for this correlation is given by:

$$\text{Re}_l = \frac{GD(1-x)}{\mu_l} = \frac{400 \times 0.001 \times (1-0.5)}{1.321 \times 10^{-4}} = 1514$$

The Martinelli parameter is given by:

$$X_{tt} = \left(\frac{1-x}{x} \right)^{0.9} \left(\frac{\rho_v}{\rho_l} \right)^{0.5} \left(\frac{\mu_l}{\mu_v} \right)^{0.1} = \left(\frac{1-0.5}{0.5} \right)^{0.9} \left(\frac{76.5}{1077} \right)^{0.5} \left(\frac{1.321 \times 10^{-4}}{1.357 \times 10^{-5}} \right)^{0.1}$$

$$= 0.3346$$

The parameter F is given by:

$$F(X_{tt}) = 0.15 [X_{tt}^{-1} + 2.85 X_{tt}^{-0.476}]$$

$$\Rightarrow F(X_{tt}) = 0.15 [0.3346^{-1} + 2.85 \times 0.3346^{-0.476}] = 1.168$$

The void fraction is given by:

$$\alpha = \begin{cases} 1 - 1.928 \text{Re}_l^{-0.315} [F(X_{tt})]^{-1} + 0.9293 \text{Re}_l^{-0.315} [F(X_{tt})]^{-2} & 50 < \text{Re}_l < 1125 \\ 1 - 0.38 \text{Re}_l^{-0.088} [F(X_{tt})]^{-1} + 0.0361 \text{Re}_l^{-0.176} [F(X_{tt})]^{-2} & \text{Re}_l > 1125 \end{cases}$$

In the present case:

$$\alpha = 1 - 0.38 \times 1514^{-0.088} [1.168]^{-1} + 0.0361 \times 1514^{-0.176} [1.168]^{-2} = 0.8365$$

El Hajal *et al.* (2003)

El Hajal *et al.* (2003) proposed the following correlation that uses the void fraction calculated by the homogeneous model and the correlation by Steiner (1993).

$$\alpha = \frac{\alpha_h - \alpha_{\text{Steiner}}}{\ln \left(\frac{\alpha_h}{\alpha_{\text{Steiner}}} \right)}$$

where α_h and α_{Steiner} are the void fractions calculated by the homogeneous model and the correlation by Steiner (1993). In the present case, $\alpha_h = 0.9337$, and $\alpha_{\text{Steiner}} = 0.8675$. Therefore,

$$\alpha = \frac{0.9337 - 0.8675}{\ln \left(\frac{0.9337}{0.8675} \right)} = 0.9002$$

Smith (1969)

This correlation is given by:

$$\alpha = \left\{ 1 + \left(\frac{\rho_v}{\rho_l} \right) \left(\frac{1-x}{x} \right) \times \left[K + (1-K) \sqrt{\frac{\left(\frac{\rho_l}{\rho_v} \right) + K \left(\frac{1-x}{x} \right)}{1 + K \left(\frac{1-x}{x} \right)}} \right] \right\}^{-1}$$

Smith found good agreement with experimental data (air–water and steam–water, 6–38-mm diameter tubes) for $K = 0.4$. In the present case:

$$\alpha = \left\{ 1 + \left(\frac{76.5}{1077} \right) \left(\frac{1-0.5}{0.5} \right) \times \left[0.4 + (1-0.4) \sqrt{\frac{\left(\frac{1077}{76.5} \right) + 0.4 \left(\frac{1-0.5}{0.5} \right)}{1 + 0.4 \left(\frac{1-0.5}{0.5} \right)}} \right] \right\}^{-1} = 0.858$$

Tabatabai and Faghri (2001) found the best agreement with their data for 4.8–15.88-mm tubes (refrigerants) and 1–12.3-mm tubes (air–water) with the Smith and Lockhart–Martinelli correlations. They preferred the Smith correlation for its wide range of applicability.

Premoli *et al.* (1971)

The liquid-only Reynolds number is given by:

$$\text{Re}_{lo} = \frac{GD}{\mu_l} = \frac{400 \times 1 \times 10^{-3}}{1.321 \times 10^{-4}} = 3028$$

The liquid-only Weber number is given by:

$$\text{We}_{lo} = \frac{G^2 D}{\sigma \rho_l} = \frac{400^2 \times 1 \times 10^{-3}}{0.00427 \times 1077} = 34.78$$

The parameters E_1 and E_2 are calculated as follows:

$$E_1 = 1.578 \text{Re}_{lo}^{-0.19} \left(\frac{\rho_l}{\rho_v} \right)^{0.22} = 1.578 \times 3028^{-0.19} \times \left(\frac{1077}{76.5} \right)^{0.22} = 0.6157$$

$$E_2 = 0.0273 \text{We}_{lo} \text{Re}_{lo}^{-0.51} \left(\frac{\rho_l}{\rho_v} \right)^{-0.08} = 0.0273 \times 34.78 \times 3028^{-0.51} \times \left(\frac{1077}{76.5} \right)^{-0.08} = 0.01289$$

The parameter y is a function of the homogeneous void fraction:

$$y = \frac{\beta}{1 - \beta} = \frac{\alpha_h}{1 - \alpha_h} = \frac{0.9337}{1 - 0.9337} = 14.08$$

The slip ratio is calculated as follows:

$$S = 1 + E_1 \left[\left(\frac{y}{1 + yE_2} \right) - yE_2 \right]^{1/2}$$
$$\Rightarrow S = 1 + 0.6157 \times \left[\left(\frac{14.08}{1 + 14.08 \times 0.01289} \right) - 14.08 \times 0.01289 \right]^{1/2} = 3.11$$

Finally, the void fraction is given by:

$$\alpha = \frac{x}{x + S(1 - x) \rho_v / \rho_l} = \frac{0.5}{0.5 + 3.11 \times (1 - 0.5) \times 76.5 / 1077} = 0.8191$$

Yashar *et al.* (2001)

The Froude rate defined them is evaluated as follows:

$$Ft = \left[\frac{G^2 x^3}{(1 - x) \rho_v^2 g D} \right]^{0.5} = \left[\frac{400^2 \times 0.5^3}{(1 - 0.5) \times 76.5^2 \times 9.81 \times 1 \times 10^{-3}} \right]^{0.5} = 26.4$$

The Martinelli parameter was calculated above, $X_{tt}=0.3346$. The void fraction is calculated in terms of these two parameters as follows:

$$\alpha = \left[1 + \frac{1}{Ft} + X_{tt} \right]^{-0.321} = \left[1 + \frac{1}{26.4} + 0.3346 \right]^{-0.321} = 0.9034$$

The void fractions predicted by the different models and correlations for all the conditions of interest are shown below.

G kg/m ² -s	x	Homo- geneous	Baroczy (1965)	Zivi (1964)	Lockhart and Martinelli (1949)	Thom (1964)	Steiner (1993)	Tandon <i>et al.</i> (1985b)	El Hajal <i>et al.</i> (2003)	Smith (1969)	Premoli <i>et al.</i> (1971)	Yashar <i>et al.</i> (2001)
150	0.2	0.7788	0.5981	0.5932	0.7647	0.636	0.6274	0.9639*	0.7004	0.6527	0.5964	0.7296
150	0.5	0.9337	0.8059	0.8536	0.8875	0.8748	0.8461	0.8685	0.8892	0.858	0.7909	0.8904
150	0.8	0.9826	0.9205	0.9589	0.9504	0.9655	0.9489	0.8987	0.9656	0.9566	0.9017	0.9622
400	0.2	0.7788	0.5981	0.5932	0.7647	0.636	0.6769	0.6694	0.7267	0.6527	0.6239	0.7597
400	0.5	0.9337	0.8059	0.8536	0.8875	0.8748	0.8675	0.8365	0.9002	0.858	0.8191	0.9034
400	0.8	0.9826	0.9205	0.9589	0.9504	0.9655	0.9555	0.9256	0.969	0.9566	0.9264	0.9676
750	0.2	0.7788	0.5981	0.5932	0.7647	0.636	0.6922	0.6855	0.7347	0.6527	0.6433	0.7691
750	0.5	0.9337	0.8059	0.8536	0.8875	0.8748	0.8737	0.845	0.9034	0.858	0.8414	0.9071
750	0.8	0.9826	0.9205	0.9589	0.9504	0.9655	0.9574	0.9299	0.9699	0.9566	0.9445	0.9692

* Note: $Re_l = 908.5$ and thus the equation for $50 < Re_l < 1125$ was used. However, if the equation for $Re_l > 1125$ is used, then $\alpha = 0.6428$, which is much closer to the results from the other models.

The results shown above indicate that the void fractions predicted by several of the models are quite close to each other. A graph depicting these values is shown in Section 6.3. Caution must be exercised, however, because, as stated by El Hajal *et al.* (2003) and Thome *et al.* (2003), $(1 - \alpha)$ is an indicator of the film thickness in annular flow, and small changes in void fraction imply large changes in liquid film thickness, which therefore alters the heat transfer coefficient. It should also be noted that many of the correlations assume annular flow, and although some of the authors recommend that they can be used irrespective of the flow regime, in the flow regimes specific to microchannels, this should be validated further.

Example 6.3. Pressure drop calculation

Compute the frictional pressure gradient during condensation of refrigerant R-134a flowing through a 1 mm diameter tube, at a mass flux of $300 \text{ kg/m}^2\text{-s}$, at a mean quality of 0.5 and a pressure of 1500 kPa. Use the correlations by Lockhart and Martinelli (1949), Friedel (1979; 1980), Chisholm (1973), Mishima and Hibiki (1996), Lee and Lee (2001), Tran *et al.* (2000), Wang *et al.* (1997b), Chen *et al.* (2001), Wilson *et al.* (2003), Souza *et al.* (1993), Cavallini *et al.* (2001; 2002a; 2002b), and Garimella *et al.* (2005) and compare the values predicted by each model.

Refrigerant properties

Saturation temperature	$T_{\text{sat}} = 55.21^\circ\text{C}$
Surface tension	$\sigma = 0.00427 \text{ N/m}$

Liquid phase	Vapor phase
$\rho_l = 1077 \text{ kg/m}^3$	$\rho_v = 76.5 \text{ kg/m}^3$
$\mu_l = 1.321 \times 10^{-4} \text{ kg/m-s}$	$\mu_v = 1.357 \times 10^{-5} \text{ kg/m-s}$

Some common parameters that are used by several correlations are calculated below first.

Liquid Reynolds number,

$$\text{Re}_l = \frac{GD(1-x)}{\mu_l} = \frac{300 \times 0.001 \times (1-0.5)}{1.321 \times 10^{-4}} = 1136$$

Vapor Reynolds number,

$$\text{Re}_v = \frac{GDx}{\mu_v} = \frac{300 \times 0.001 \times 0.5}{1.357 \times 10^{-5}} = 11054$$

Liquid-only Reynolds number,

$$\text{Re}_{l0} = \frac{GD}{\mu_l} = \frac{300 \times 0.001}{1.321 \times 10^{-4}} = 2271$$

Vapor-only Reynolds number,

$$\text{Re}_{\text{vo}} = \frac{GD}{\mu_v} = \frac{300 \times 0.001}{1.357 \times 10^{-5}} = 22108$$

For this illustration, the single-phase friction factors are calculated using the Churchill (1977) correlation:

$$f = 8 \left[\left(\frac{8}{\text{Re}} \right)^{12} + \left\{ \left[2.457 \times \ln \left(\frac{1}{\left(\frac{7}{\text{Re}} \right)^{0.9} + 0.27\varepsilon/D} \right) \right]^{16} + \left(\frac{37530}{\text{Re}} \right)^{16} \right\}^{-1.5} \right]^{1/12}$$

Assuming a smooth tube, that is, $\varepsilon = 0$, $f_l = 0.05635$, $f_v = 0.03016$, $f_{lo} = 0.03047$, and $f_{vo} = 0.0252$. The corresponding single-phase pressure gradients are given by:

$$\left(\frac{dP}{dz} \right)_l = \frac{f_l G^2 (1-x)^2}{2 D \rho_l} = \frac{0.05635 \times 300^2 (1-0.5)^2}{2 \times 0.001 \times 1077} = 588.5 \text{ Pa/m}$$

$$\left(\frac{dP}{dz} \right)_v = \frac{f_v G^2 x^2}{2 D \rho_v} = \frac{0.03016 \times 300^2 \times 0.5^2}{2 \times 0.001 \times 76.5} = 4436 \text{ Pa/m}$$

$$\left(\frac{dP}{dz} \right)_{lo} = \frac{f_{lo} G^2}{2 D \rho_l} = \frac{0.03047 \times 300^2}{2 \times 0.001 \times 1077} = 1273 \text{ Pa/m}$$

$$\left(\frac{dP}{dz} \right)_{vo} = \frac{f_{vo} G^2}{2 D \rho_v} = \frac{0.0252 \times 300^2}{2 \times 0.001 \times 76.5} = 14823 \text{ Pa/m}$$

Lockhart and Martinelli (1949)

The Martinelli parameter is given by:

$$X = \left[\frac{(dP/dz)_l}{(dP/dz)_v} \right]^{1/2} = \left[\frac{588.5}{4436} \right]^{1/2} = 0.3642$$

Two-phase multiplier is given by:

$$\phi_1^2 = 1 + \frac{C}{X} + \frac{1}{X^2}; \quad C = \begin{cases} 20 & \text{Liquid Turbulent} & \text{Vapor Turbulent} \\ 12 & \text{Liquid Laminar} & \text{Vapor Turbulent} \\ 10 & \text{Liquid Turbulent} & \text{Vapor Laminar} \\ 5 & \text{Liquid Laminar} & \text{Vapor Laminar} \end{cases}$$

In this case:

$$\phi_1^2 = 1 + \frac{12}{X} + \frac{1}{X^2} = 1 + \frac{12}{0.3642} + \frac{1}{0.3642^2} = 41.4865$$

The two-phase pressure gradient is:

$$\frac{\Delta P}{L} = \phi_1^2 \left(\frac{dP}{dz} \right)_l = 41.4865 \times 588.5 = 24,414 \text{ Pa/m}$$

Friedel (1979; 1980)

The parameters E , F , and H are evaluated as follows:

$$E = (1 - x)^2 + x^2 \frac{\rho_l f_{vo}}{\rho_v f_{lo}}$$

$$\Rightarrow E = (1 - 0.5)^2 + 0.5^2 \times \frac{1077 \times 0.0252}{76.5 \times 0.03047} = 3.161$$

$$F = x^{0.78} \times (1 - x)^{0.24} = 0.5^{0.78} \times (1 - 0.5)^{0.24} = 0.4931$$

$$H = \left(\frac{\rho_l}{\rho_v} \right)^{0.91} \left(\frac{\mu_v}{\mu_l} \right)^{0.19} \left(1 - \frac{\mu_v}{\mu_l} \right)^{0.7}$$

$$\Rightarrow H = \left(\frac{1077}{76.5} \right)^{0.91} \left(\frac{1.357 \times 10^{-5}}{1.321 \times 10^{-4}} \right)^{0.19} \left(1 - \frac{1.357 \times 10^{-5}}{1.321 \times 10^{-4}} \right)^{0.7} = 6.677$$

The two-phase mixture density is calculated as follows:

$$\rho_{TP} = \left(\frac{x}{\rho_v} + \frac{1 - x}{\rho_l} \right)^{-1} = \left(\frac{0.5}{76.5} + \frac{1 - 0.5}{1077} \right)^{-1} = 142.8 \text{ kg/m}^3$$

The Froude and Weber numbers are given by:

$$\text{Fr} = \frac{G^2}{gD\rho_{TP}^2} = \frac{300^2}{9.81 \times 0.001 \times 142.8^2} = 449.6$$

$$\text{We} = \frac{G^2 D}{\rho_{TP} \sigma} = \frac{300^2 \times 0.001}{142.8 \times 4.27 \times 10^{-3}} = 147.5$$

The resulting two-phase multiplier is now calculated as follows:

$$\phi_{lo}^2 = E + \frac{3.24 \times FH}{\text{Fr}^{0.045} \text{We}^{0.035}} = 3.161 + \frac{3.24 \times 0.4931 \times 6.677}{449.6^{0.045} \times 147.5^{0.035}} = 9.967$$

Finally, the two-phase pressure gradient is given by:

$$\frac{\Delta P}{L} = \phi_{lo}^2 \left(\frac{\Delta P}{L} \right)_{lo} = 9.967 \times 1273 = 12,688 \text{ Pa/m}$$

Chisholm (1973)

The ratio of the vapor- to liquid-only pressure gradients is given by:

$$Y = \sqrt{\frac{(dP/dz)_{vo}}{(dP/dz)_{lo}}} = \sqrt{\frac{14,823}{1273}} = 3.412$$

The two-phase multiplier is given by:

$$\phi_{10}^2 = 1 + (Y^2 - 1) [Bx^{(2-n)/2}(1-x)^{(2-n)/2} + x^{2-n}]$$

where the parameter B is given by:

$$B = \begin{cases} \frac{55}{\sqrt{G}} & \text{for } 0 < Y < 9.5 \\ \frac{520}{Y\sqrt{G}} & \text{for } 9.5 < Y < 28 \\ \frac{15000}{Y^2\sqrt{G}} & \text{for } 28 < Y \end{cases}$$

and n is the power to which Reynolds number is raised in the friction factor

$$n = \begin{cases} 1 & \text{Re}_{10} \leq 2100 \\ 0.25 & \text{Re}_{10} > 2100 \end{cases}$$

Thus for the current example,

$$B = \frac{55}{\sqrt{G}} = \frac{55}{\sqrt{300}} = 3.175 \quad \text{and} \quad n = 0.25.$$

The two-phase multiplier can now be calculated as follows:

$$\begin{aligned} \phi_{10}^2 &= 1 + (Y^2 - 1) \times [3.175x^{(2-0.25)/2}(1-x)^{(2-0.25)/2} + x^{2-0.25}] \\ &= 1 + (3.412^2 - 1) \times [3.175 \times 0.5^{(2-0.25)/2}(1-0.5)^{(2-0.25)/2} + 0.5^{2-0.25}] \\ &= 14.213 \end{aligned}$$

The pressure gradient is evaluated as follows:

$$\frac{\Delta P}{L} = \phi_{10}^2 \left(\frac{\Delta P}{L} \right)_{10} = 14.213 \times 1273 = 18,093 \text{ Pa/m}$$

Mishima and Hibiki (1996)

Martinelli parameter (calculated above) is $X = 0.3642$. The two-phase multiplier is given by:

$$\phi_1^2 = 1 + \frac{C}{X} + \frac{1}{X^2}$$

For small diameter tubes, Mishima and Hibiki recommend the following expression for C :

$$C = 21(1 - e^{-0.319D})$$

$$\Rightarrow C = 21(1 - e^{-0.319 \times 1}) = 5.736$$

With this value of C , the two-phase multiplier is given by:

$$\Rightarrow \phi_1^2 = 1 + \frac{5.736}{X} + \frac{1}{X^2} = 1 + \frac{5.736}{0.3642} + \frac{1}{0.3642^2} = 24.285$$

The two-phase pressure gradient is then calculated as follows:

$$\frac{\Delta P}{L} = \phi_1^2 \left(\frac{dP}{dz} \right)_1 = 24.285 \times 588.5 = 14,292 \text{ Pa/m}$$

Lee and Lee (2001)

The Martinelli parameter, calculated above is $X = 0.3642$. For the C parameter in the two-phase multiplier, Lee and Lee suggested $C = A \lambda^q \psi^r \text{Re}_{10}^s$, where, $\lambda = \frac{\mu_l^2}{\rho_l \sigma D}$, $\psi = \frac{\mu_l j}{\sigma}$, and j = liquid slug velocity, also given by $j = j_V + j_L$. The value of constants A , q , r , and s are determined based on the following Table:

Flow regime							
Liquid	Vapor	A	q	r	s	X -Range	Re_{10} Range
Laminar	Laminar	6.833×10^{-8}	-1.317	0.719	0.557	0.776–14.176	175–1480
Laminar	Turbulent	6.185×10^{-2}	0	0	0.726	0.303–1.426	293–1506
Turbulent	Laminar	3.627	0	0	0.174	3.276–79.415	2606–17642
Turbulent	Turbulent	0.408	0	0	0.451	1.309–14.781	2675–17757

It should be noted that surface tension effects are important only in the laminar–laminar flow regimes. For all other flow regimes, the exponents of ψ and λ are almost zero. Thus, for these flow regimes, C is merely a function of Re_{10} . The above table also provides the range of X and Re_{10} for the data from which these constants were determined. The liquid Reynolds number for this case, calculated above, is $\text{Re}_{10} = 2271$. For the current example (laminar liquid film and turbulent vapor core), the coefficient C is evaluated as follows:

$$C = 6.185 \times 10^{-2} \times \text{Re}_{10}^{0.726} = 6.185 \times 10^{-2} \times 2271^{0.726} = 16.9$$

The two-phase multiplier is therefore:

$$\phi_1^2 = 1 + \frac{16.9}{X} + \frac{1}{X^2} = 1 + \frac{16.9}{0.3642} + \frac{1}{0.3642^2} = 54.953$$

Finally, the two-phase pressure gradient is calculated as follows:

$$\frac{\Delta P}{L} = \phi_1^2 \left(\frac{dP}{dz} \right)_1 = 54.953 \times 588.5 = 32,340 \text{ Pa/m}$$

Tran *et al.* (2000)

Tran *et al.* modified the two-phase multiplier correlation of Chisholm (1973) to the following expression that includes the confinement number:

$$\phi_{lo}^2 = 1 + (4.3Y^2 - 1) \times N_{conf} x^{0.875} (1 - x)^{0.875} + x^{1.75}$$

where, confinement number is given by:

$$N_{conf} = \frac{\left[\frac{\sigma}{g(\rho_l - \rho_v)} \right]^{1/2}}{D} = \frac{\left[\frac{4.27 \times 10^{-3}}{9.81(1077 - 76.5)} \right]^{1/2}}{0.001} = 0.6595$$

for the current example. With $Y = 3.412$ calculated above,

$$\phi_{lo}^2 = 1 + (4.3 \times 3.412^2 - 1) \times 0.6595 \times 0.5^{0.875} \times (1 - 0.5)^{0.875} + 0.5^{1.75} = 10.916$$

The two-phase pressure gradient is evaluated in the usual manner:

$$\frac{\Delta P}{L} = \phi_{lo}^2 \left(\frac{\Delta P}{L} \right)_{lo} = 10.916 \times 1273 = 13,897 \text{ Pa/m}$$

Wang *et al.* (1997b)

According to their correlation, for $G < 200 \text{ kg/m}^2\text{-s}$ $\phi_v^2 = 1 + 9.4X^{0.62} + 0.564X^{2.45}$. For $G > 200 \text{ kg/m}^2\text{-s}$, they modified the parameter C in the Lockhart–Martinelli (1949) correlation as follows:

$$C = 4.566 \times 10^{-6} X^{0.128} \times \text{Re}_{lo}^{0.938} \left(\frac{\rho_l}{\rho_v} \right)^{-2.15} \left(\frac{\mu_l}{\mu_v} \right)^{5.1}$$

In this example, $G = 300 \text{ kg/m}^2\text{-s}$; therefore:

$$C = 4.566 \times 10^{-6} \times 0.3642^{0.128} \times 2271^{0.938} \left(\frac{1077}{76.5} \right)^{-2.15} \left(\frac{1.321 \times 10^{-4}}{1.357 \times 10^{-5}} \right)^{5.1} = 2.099$$

The two-phase multiplier is then given by:

$$\phi_1^2 = 1 + \frac{2.099}{X} + \frac{1}{X^2} = 1 + \frac{2.099}{0.3642} + \frac{1}{0.3642^2} = 14.304$$

And the two-phase pressure gradient is:

$$\frac{\Delta P}{L} = \phi_1^2 \left(\frac{dP}{dz} \right)_1 = 14.304 \times 588.5 = 8416 \text{ Pa/m}$$

Chen *et al.* (2001)

Chen *et al.* modified the homogenous model and the Friedel (1979; 1980) correlation to determine the pressure drop in microchannels. The modification to the Friedel correlation is illustrated here. Thus,

$$\frac{dP}{dz} = \frac{dP}{dz} \Big|_{\text{Friedel}} \Omega; \quad \Omega = \begin{cases} \frac{0.0333 \times \text{Re}_{\text{lo}}^{0.45}}{\text{Re}_v^{0.09} (1 + 0.4 \exp(-\text{Bo}))} & \text{Bo} < 2.5 \\ \frac{\text{We}^{0.2}}{(2.5 + 0.06\text{Bo})} & \text{Bo} \geq 2.5 \end{cases}$$

where Weber number, $\text{We} = \frac{G^2 D}{\sigma \rho_m}$ and Bond number, $\text{Bo} = g(\rho_l - \rho_v) \left(\frac{(D/2)^2}{\sigma} \right)$. For this case:

$$\text{Bo} = g(\rho_l - \rho_v) \left(\frac{(D/2)^2}{\sigma} \right) = 9.81(1077 - 76.5) \left(\frac{(0.001/2)^2}{4.27 \times 10^{-3}} \right) = 0.5748$$

Because $\text{Bo} < 2.5$, the modifier to the Friedel correlation is given by:

$$\Rightarrow \Omega = \frac{0.0333 \times \text{Re}_{\text{lo}}^{0.45}}{\text{Re}_v^{0.09} (1 + 0.4 \exp(-\text{Bo}))} = \frac{0.0333 \times 2271^{0.45}}{11054^{0.09} (1 + 0.4 \exp(-0.5748))} = 0.3808$$

Therefore, the two-phase pressure gradient is:

$$\frac{dP}{dz} = \frac{dP}{dz} \Big|_{\text{Friedel}} \Omega = 12688 \times 0.3808 = 4831 \text{ Pa/m}$$

Wilson *et al.* (2003)

Wilson *et al.* recommended the liquid-only two-phase multiplier of Jung and Radermacher (1989):

$$\phi_{\text{lo}}^2 = 12.82 X_{\text{tt}}^{-1.47} (1 - x)^{1.8}$$

With the Martinelli parameter (calculated above), $X_{\text{tt}} = 0.3346$, the two-phase multiplier is:

$$\phi_{\text{lo}}^2 = 12.82 \times 0.3346^{-1.47} (1 - 0.5)^{1.8} = 18.413$$

which yields a two-phase pressure gradient of

$$\frac{\Delta P}{L} = \phi_{\text{lo}}^2 \left(\frac{dP}{dz} \right)_{\text{lo}} = 18.413 \times 1273 = 23,434 \text{ Pa/m}$$

Souza *et al.* (1993)

The two-phase liquid multiplier given by them is as follows:

$$\phi_1^2 = 1.376 + C_1 X_{tt}^{-C_2}$$

where, for $Fr_1 < 0.7$

$$C_1 = 4.172 + 5.48 Fr_1 - 1.564 Fr_1^2$$

$$C_2 = 1.773 - 0.169 Fr_1$$

and for $Fr_1 > 0.7$, $C_1 = 7.242$; $C_2 = 1.655$.

In the present case, the Froude number is:

$$Fr_1 = \frac{G}{\rho_l \sqrt{gD}} = \frac{300}{1077 \sqrt{9.81 \times 0.001}} = 2.812$$

Therefore, $C_1 = 7.242$; $C_2 = 1.655$, which yields a two-phase multiplier of:

$$\phi_1^2 = 1.376 + 7.242 \times 0.3346^{-1.655} = 45.725$$

For the corresponding single-phase friction factor, they recommend the Colebrook (1939) friction factor:

$$\frac{1}{\sqrt{f_1}} = -2 \log \left(\frac{\varepsilon/D}{3.7} + \frac{2.51}{Re_1 \sqrt{f_1}} \right)$$

Thus for smooth tubes:

$$\frac{1}{\sqrt{f_1}} = -2 \log \left(0 + \frac{2.51}{1136 \sqrt{f_1}} \right) \Rightarrow f_1 = 0.05983$$

The single-phase liquid pressure drop is calculated as follows:

$$\left(\frac{dP}{dz} \right)_1 = \frac{f_1 G^2 (1-x)^2}{2D \rho_1} = \frac{0.05983 \times 300^2 (1-0.5)^2}{2 \times 0.001 \times 1077} = 624.8 \text{ Pa/m}$$

Finally, the two-phase pressure drop, using the two-phase multiplier is given by:

$$\frac{\Delta P}{L} = \phi_1^2 \left(\frac{dP}{dz} \right)_1 = 45.725 \times 624.8 = 28,568 \text{ Pa/m}$$

Cavallini *et al.* (2001; 2002a, b)

Cavallini *et al.* recommended modifications to the Friedel (1979; 1980) correlation. The parameter E is the same as in his correlation, $E = 3.161$. The parameter F is modified

to $F = x^{0.6978}$, which in this case is $F = 0.5^{0.6978} = 0.6165$. The modified parameter H is given by:

$$H = \left(\frac{\rho_l}{\rho_v} \right)^{0.3278} \left(\frac{\mu_v}{\mu_l} \right)^{-1.181} \left(1 - \frac{\mu_v}{\mu_l} \right)^{3.477}$$

For the present condition,

$$H = \left(\frac{1077}{76.5} \right)^{0.3278} \left(\frac{1.357 \times 10^{-5}}{1.321 \times 10^{-4}} \right)^{-1.181} \left(1 - \frac{1.357 \times 10^{-5}}{1.321 \times 10^{-4}} \right)^{3.477} = 23.99$$

The Weber number is defined in terms of the gas-phase density:

$$We = \frac{G^2 D}{\rho_v \sigma} = \frac{300^2 \times 0.001}{76.5 \times 4.27 \times 10^{-3}} = 275.5$$

The two-phase multiplier is then calculated as follows:

$$\phi_{lo}^2 = E + \frac{1.262 \times FH}{We^{0.1458}} = 3.161 + \frac{1.262 \times 0.6165 \times 23.99}{275.5^{0.1458}} = 11.391$$

The two-phase pressure drop is calculated based on this multiplier as follows:

$$\frac{\Delta P}{L} = \phi_{lo}^2 \left(\frac{\Delta P}{L} \right)_{lo} = 11.391 \times 1273 = 14,501 \text{ Pa/m}$$

Garimella *et al.* (2005)

The case of $G = 300 \text{ kg/m}^2\text{-s}$ and $x = 0.5$ represents annular flow, according to the transition criteria of Coleman and Garimella (2000a, b; 2003) and Garimella (2004). While Garimella *et al.* developed a multi-regime (including intermittent/discrete wave and annular/mist/disperse wave) model to span the entire quality range as described in Section 6.4.4, for this condition, the annular flow model applies. For the annular flow model, the individual phase Reynolds numbers are computed in terms of the cross-sectional areas occupied by the phases. Therefore, the void fraction is first calculated using the Baroczy (1965) correlation:

$$\alpha = \left[1 + \left(\frac{1-x}{x} \right)^{0.74} \left(\frac{\rho_v}{\rho_l} \right)^{0.65} \left(\frac{\mu_l}{\mu_v} \right)^{0.13} \right]^{-1}$$

For the present case,

$$\alpha = \left[1 + \left(\frac{1-0.5}{0.5} \right)^{0.74} \left(\frac{76.5}{1077} \right)^{0.65} \left(\frac{1.321 \times 10^{-4}}{1.357 \times 10^{-5}} \right)^{0.13} \right]^{-1} = 0.8059$$

Therefore, the liquid and vapor Re values are given by:

$$\text{Re}_l = \frac{GD(1-x)}{(1+\sqrt{\alpha})\mu_l} = \frac{300 \times 0.001 \times (1-0.5)}{(1+\sqrt{0.8059})1.321 \times 10^{-4}} = 598.5$$

$$\text{Re}_v = \frac{GDx}{\mu_v\sqrt{\alpha}} = \frac{300 \times 0.001 \times 0.5}{1.357 \times 10^{-5} \times \sqrt{0.8059}} = 12316$$

The friction factor for the laminar film is $f_l = 64/\text{Re}_l = 64/598.5 = 0.1069$. The turbulent vapor friction factor is calculated using the $f_v = 0.316 \times \text{Re}_v^{-0.25} = 0.316 \times 12316^{-0.25} = 0.03$. With these friction factors, the corresponding single-phase pressure gradients are given by:

$$\left(\frac{dP}{dz}\right)_l = \frac{f_l G^2 (1-x)^2}{2D\rho_l} = \frac{0.1069 \times 300^2 (1-0.5)^2}{2 \times 0.001 \times 1077} = 1117 \text{ Pa/m}$$

$$\left(\frac{dP}{dz}\right)_v = \frac{f_v G^2 x^2}{2D\rho_v} = \frac{0.03 \times 300^2 \times 0.5^2}{2 \times 0.001 \times 76.5} = 4412 \text{ Pa/m}$$

The Martinelli parameter is calculated from the definition as follows:

$$X = \left[\frac{(dP/dz)_l}{(dP/dz)_v} \right]^{1/2} = \left[\frac{1117}{4412} \right]^{1/2} = 0.5031$$

The superficial velocity is given by:

$$j_l = \frac{G(1-x)}{\rho_l(1-\alpha)} = \frac{300 \times (1-0.5)}{1077 \times (1-0.8059)} = 0.7172 \text{ m/s}$$

This velocity is used to evaluate the surface tension parameter:

$$\psi = \frac{j_l \mu_l}{\sigma} = \frac{0.7172 \times 1.321 \times 10^{-4}}{4.27 \times 10^{-3}} = 0.02218$$

The interface friction factor is then calculated as follows:

$$\frac{f_i}{f_l} = AX^a \text{Re}_l^b \psi^c$$

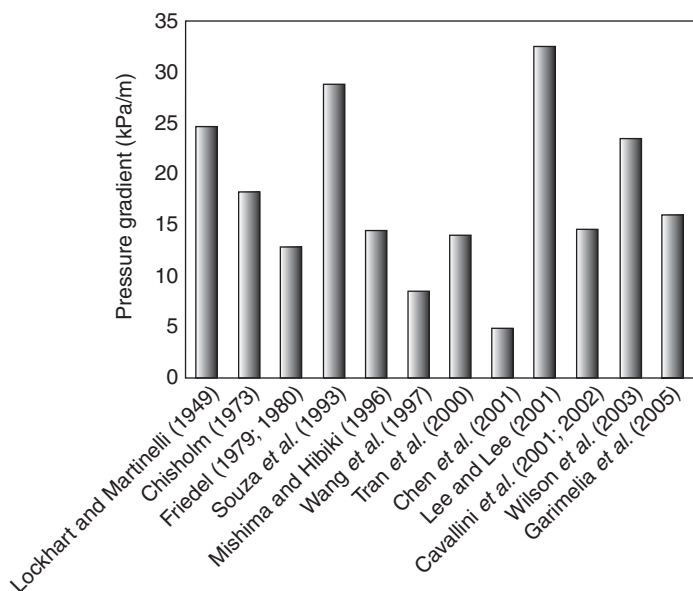
Since $\text{Re}_l < 2100$, $A = 1.308 \times 10^{-3}$; $a = 0.4273$; $b = 0.9295$; $c = -0.1211$, which yields:

$$\begin{aligned} \frac{f_i}{f_l} &= 1.308 \times 10^{-3} \times X^{0.4273} \times \text{Re}_l^{0.9295} \times \psi^{-0.1211} \\ &= 1.308 \times 10^{-3} \times 0.5031^{0.4273} \times 598.5^{0.9295} \times 0.02218^{-0.1211} \\ &= 0.5897 \end{aligned}$$

The resulting interface friction factor is $f_i = 0.5897 \times f_l = 0.5897 \times 0.1069 = 0.06306$. The interfacial friction factor is used to determine the pressure gradient as follows:

$$\begin{aligned} \frac{\Delta P}{L} &= \frac{1}{2} f_i \frac{G^2 x^2}{\rho_v \alpha^{2.5}} \frac{1}{D} \\ &= \frac{1}{2} \times 0.06306 \times \frac{300^2 \times 0.5^2}{69.82 \times 0.8509^{2.5}} \times \frac{1}{0.001} \\ &= 15,907 \text{ Pa/m} \end{aligned}$$

A comparison of the pressure drops predicted by each of these correlations is shown below. It can be seen that the predicted pressure drops vary considerably, from 4.8 to 32.3 kPa. This large variation is attributed to the considerably different two-phase multipliers developed by the various investigators. The only recommendation that can be made is to choose a model that is based on the geometry, fluid and operating conditions similar to those of interest for a given application. This information is available in Section 6.4 as well as in Table 6.3.



Example 6.4. Calculation of heat transfer coefficients

Compute the heat transfer coefficient for condensation of refrigerant R-134a flowing through a 1-mm tube, at a mass flux of $300 \text{ kg/m}^2\text{-s}$, at a mean quality of 0.5 and at a pressure of 1500 kPa. The wall temperature of the tube is 52°C . Use the correlations by Shah (1979), Soliman *et al.* (1968), Soliman (1986), Traviss *et al.* (1973), Dobson and

Chato (1998), Moser *et al.* (1998), Chato (1962), Boyko and Kruzhilin (1967), Cavallini *et al.* (2002a), and Bandhauer *et al.* (2005) and compare the values predicted by each model.

Refrigerant properties

Saturation temperature	$T_{\text{sat}} = 55.21^{\circ}\text{C}$
Critical pressure	$P_{\text{crit}} = 4059\text{ kPa}$
Reduced pressure	$P_{\text{red}} = 0.37$
Surface tension	$\sigma = 0.00427\text{ N/m}$
Heat of vaporization	$h_{\text{lv}} = 145,394\text{ J/kg}$

Liquid phase	Vapor phase
$\rho_l = 1077\text{ kg/m}^3$	$\rho_v = 76.5\text{ kg/m}^3$
$\mu_l = 1.321 \times 10^{-4}\text{ kg/m-s}$	$\mu_v = 1.357 \times 10^{-5}\text{ kg/m-s}$
$Cp_l = 1611\text{ J/kg-K}$	$Cp_v = 1312\text{ J/kg-K}$
$h_l = 131,657\text{ J/kg}$	$h_v = 277,051\text{ J/kg}$
$k_l = 0.06749\text{ W/m-K}$	$k_v = 0.0178\text{ W/m-K}$
$Pr_l = 3.152$	$Pr_v = 1$

Shah (1979)

- Applicability range:
- $0.002 < P_{\text{red}} < 0.44$
 - $21^{\circ}\text{C} < T_{\text{sat}} < 310^{\circ}\text{C}$
 - $3 < V_v < 300\text{ m/s}$
 - $10.83 < G < 210.56\text{ kg/m}^2\text{-s}$

The velocity of the vapor phase is given by:

$$V_v = \frac{xG}{\rho_v} = \frac{0.5 \times 300}{76.5} = 1.961\text{ m/s}$$

In the present case, the vapor velocity and mass flux are beyond the range of applicability of the correlation.

The liquid-only Reynolds number Re_{l0} was calculated in Example 6.3 to be $Re_{l0} = 2271$. The liquid-only heat transfer coefficient is calculated as follows:

$$\begin{aligned} h_{l0} &= 0.023\text{ } Re_{l0}^{0.8}\text{ } Pr_l^{0.4} \times \frac{k_l}{D} \\ &= 0.023 \times 2271^{0.8} \times 3.152^{0.4} \times \frac{0.06749}{0.001} \\ &= 1190\text{ W/m}^2\text{-K} \end{aligned}$$

From this single-phase heat transfer coefficient, the condensation heat transfer coefficient is obtained by applying the multiplier as follows:

$$\begin{aligned}
 h &= h_{lo} \left[(1-x)^{0.8} + \frac{3.8x^{0.76}(1-x)^{0.04}}{P_{\text{red}}^{0.38}} \right] \\
 &= 1190 \left[(1-0.5)^{0.8} + \frac{3.8 \times 0.5^{0.76}(1-0.5)^{0.04}}{\left(\frac{1500}{4059}\right)^{0.38}} \right] \\
 &= 4474 \text{ W/m}^2\text{-K}
 \end{aligned}$$

Soliman *et al.* (1968)

For this correlation, a quality change per unit length is also required, and for illustrative purposes, it is assumed that $\Delta x = 0.10$ over a length of 0.3048 m. This correlation was based on data for the following range of conditions:

$$\begin{aligned}
 6.096 &< V_v < 304.8 \text{ m/s} \\
 0.03 &< x < 0.99 \\
 1 &< \text{Pr} < 10
 \end{aligned}$$

The vapor velocity here is 1.961 m/s, which is outside the range of applicability of the correlation.

The vapor-only Reynolds number Re_{v0} was calculated in Example 6.3 to be 22114, and the liquid Reynolds number $\text{Re}_l = 1136$. F_f represents the effect of two-phase friction:

$$\begin{aligned}
 F_f &= 0.0225 \times \frac{G^2}{\rho_v} \text{Re}_{v0}^{-0.2} \left[x^{1.8} + 5.7 \left(\frac{\mu_l}{\mu_v} \right)^{0.0523} (1-x)^{0.47} x^{1.33} \left(\frac{\rho_v}{\rho_l} \right)^{0.261} \right. \\
 &\quad \left. + 8.11 \left(\frac{\mu_l}{\mu_v} \right)^{0.105} (1-x)^{0.94} x^{0.86} \left(\frac{\rho_v}{\rho_l} \right)^{0.522} \right]
 \end{aligned}$$

For the present case,

$$\begin{aligned}
 F_f &= 0.0225 \times \frac{300^2}{76.5} \times 22114^{-0.2} \\
 &\times \left[0.5^{1.8} + 5.7 \left(\frac{1.321 \times 10^{-4}}{1.357 \times 10^{-5}} \right)^{0.0523} (1-0.5)^{0.47} \times 0.5^{1.33} \left(\frac{76.5}{1077} \right)^{0.261} \right. \\
 &\quad \left. + 8.11 \left(\frac{1.321 \times 10^{-4}}{1.357 \times 10^{-5}} \right)^{0.105} (1-0.5)^{0.94} \times 0.5^{0.86} \left(\frac{76.5}{1077} \right)^{0.522} \right] \\
 &= 6.999
 \end{aligned}$$

F_m represents the effect of momentum change:

$$F_m = \frac{DG^2}{4\rho_v} \left(-\frac{dx}{L} \right) \left[2(1-x) \left(\frac{\rho_v}{\rho_l} \right)^{2/3} + \left(\frac{1}{x} - 3 + 2x \right) \left(\frac{\rho_v}{\rho_l} \right)^{4/3} + (2x - 1 - \beta x) \right. \\ \left. \times \left(\frac{\rho_v}{\rho_l} \right)^{1/3} + \left(2\beta - \frac{\beta}{x} - \beta x \right) \left(\frac{\rho_v}{\rho_l} \right)^{5/3} + 2(1-x-\beta+\beta x) \left(\frac{\rho_v}{\rho_l} \right) \right]$$

where,

$$\beta = \begin{cases} 2 & \text{for } Re_l \leq 2000 \\ 1.25 & \text{for } Re_l > 2000 \end{cases}$$

For the present case,

$$F_m = \frac{0.001 \times 300^2}{4 \times 76.5} \left(-\frac{0.1}{0.3048} \right) \\ \times \left[2(1-0.5) \left(\frac{76.5}{1077} \right)^{2/3} + \left(\frac{1}{0.5} - 3 + 2 \times 0.5 \right) \left(\frac{76.5}{1077} \right)^{4/3} \right. \\ \left. + (2 \times 0.5 - 1 - 2 \times 0.5) \left(\frac{76.5}{1077} \right)^{1/3} + \left(2 \times 2 - \frac{2}{0.5} - 2 \times 0.5 \right) \left(\frac{76.5}{1077} \right)^{5/3} \right. \\ \left. + 2(1-0.5-2+2 \times 0.5) \left(\frac{76.5}{1077} \right) \right] \\ = 0.03144$$

F_a represents the effect of the axial gravitational field on the wall shear stress. In case of horizontal condensation in microchannels, this term can be neglected. The net shear stress is therefore:

$$F_0 = F_f + F_m \pm F_a \\ = 6.999 + 0.03144 \\ = 7.031$$

The heat transfer coefficient is given by:

$$h = 0.036 \times \frac{k_l \times \rho_l^{0.5}}{\mu_l} \times Pr_l^{0.65} \times F_0^{1/2}$$

For the present case:

$$h = 0.036 \times \frac{0.06749 \times 1077^{0.5}}{1.321 \times 10^{-4}} \times 3.152^{0.65} \times 7.031^{1/2} \\ = 3377 \text{ W/m}^2\text{-K}$$

Soliman (1986)

This correlation should only be used for mist flow ($We > 30$), which is not the case here, but the calculations are shown below to illustrate the procedure and investigate the value of the resulting heat transfer coefficient. With $Re_l = 1136$, $Re_v = 11,057$, $X_{tt} = 0.3346$, $\phi_v = 1 + 1.09 \times X_{tt}^{0.039} = 2.044$, all illustrated above or in the previous example, the Weber number can be calculated as follows:

$$We = \begin{cases} 2.45 \times Re_v^{0.64} \frac{\left(\frac{\mu_v^2}{\rho_v \sigma D}\right)^{0.3}}{\phi_v^{0.4}} & \text{for } Re_l \leq 1250 \\ 0.85 \times Re_v^{0.79} \left(\frac{\mu_v^2}{\rho_v \sigma D}\right)^{0.3} \left[\left(\frac{\mu_v}{\mu_l}\right)^2 \left(\frac{\rho_l}{\rho_v}\right)\right]^{0.084} \left(\frac{X_{tt}}{\phi_v^{2.55}}\right)^{0.157} & \text{for } Re_l \leq 1250 \end{cases}$$

For $Re_l = 1136$:

$$We = 2.45 \times Re_v^{0.64} \frac{\left(\frac{\mu_v^2}{\rho_v \sigma D}\right)^{0.3}}{\phi_v^{0.4}} = 2.45 \times 11,057^{0.64} \frac{\left(\frac{(1.357 \times 10^{-5})^2}{76.5 \times 0.00427 \times 0.001}\right)^{0.3}}{2.044^{0.4}} = 9.509$$

Clearly, the flow is not in the mist flow regime. The mixture viscosity required for the heat transfer coefficient is given by:

$$\mu_m = \left(\frac{x}{\mu_v} + \frac{1-x}{\mu_l}\right)^{-1} = \left(\frac{0.5}{1.357 \times 10^{-5}} + \frac{1-0.5}{1.321 \times 10^{-4}}\right)^{-1} = 2.46 \times 10^{-5} \text{ kg/m-s}$$

With this mixture viscosity, the corresponding Reynolds number is:

$$Re_m = \frac{GD}{\mu_m} = \frac{300 \times 0.001}{2.46 \times 10^{-5}} = 12,193$$

With the Reynolds number calculated, the Nusselt number is given by:

$$Nu = 0.00345 \times Re_m^{0.9} \left(\frac{\mu_v h_{lv}}{k_v (T_{sat} - T_{wall})}\right)^{1/3}$$

which, for the present case yields:

$$\begin{aligned} Nu &= 0.00345 \times 12193^{0.9} \left(\frac{1.357 \times 10^{-5} \times 145394}{0.0178(55.21 - 52)}\right)^{1/3} \\ &= 53.46 \end{aligned}$$

The two-phase heat transfer coefficient is therefore:

$$h = Nu \frac{k_l}{D} = 53.46 \times \frac{0.06749}{0.001} = 3608 \text{ W/m}^2\text{-K}$$

Traviss *et al.* (1973)

This correlation was developed from data for the condensation of R-22 in an 8-mm tube over the following range of conditions:

$$\begin{aligned} 25^{\circ}\text{C} < T_{\text{sat}} < 58.3^{\circ}\text{C} \\ 161.4 < G < 1532 \text{ kg/m}^2\text{-s} \end{aligned}$$

The required liquid Reynolds number and Martinelli parameter are $\text{Re}_l = 1136$ and $X_{\text{tt}} = 0.3346$, respectively. With these quantities, the correlation for the shear-related term F in the liquid film is calculated as follows:

$$F = \begin{cases} 0.707 \times \text{Pr}_l \text{Re}_l^{0.5} & \text{for } \text{Re}_l < 50 \\ 5 \text{Pr}_l + 5 \ln(1 + \text{Pr}_l(0.09636 \text{Re}_l^{0.585} - 1)) & \text{for } 50 \leq \text{Re}_l \leq 1125 \\ 5 \text{Pr}_l + 5 \ln(1 + 5 \text{Pr}_l) + 2.5 \ln(0.00313 \text{Re}_l^{0.812}) & \text{for } \text{Re}_l > 1125 \end{cases}$$

For the present case:

$$\begin{aligned} F &= 5\text{Pr}_l + 5 \ln(1 + 5\text{Pr}_l) + 2.5 \ln(0.00313 \text{Re}_l^{0.812}) \\ &= 5 \times 3.152 + 5 \ln(1 + 5 \times 3.152) + 2.5 \ln(0.00313 \times 1136^{0.812}) \\ &= 29.72 \end{aligned}$$

Finally, the heat transfer coefficient is calculated as follows:

$$\begin{aligned} h &= \frac{k_l}{D} \left(\frac{1}{X_{\text{tt}}} + \frac{2.85}{X_{\text{tt}}^{0.476}} \right) \left(\frac{0.15 \times \text{Pr}_l \times \text{Re}_l^{0.9}}{F} \right) \\ &= \frac{0.06749}{0.001} \left(\frac{1}{0.3346} + \frac{2.85}{0.3346^{0.476}} \right) \left(\frac{0.15 \times 3.152 \times 1136^{0.9}}{29.72} \right) \\ &= 4700 \text{ W/m}^2\text{-K} \end{aligned}$$

Dobson and Chato (1998)

The relevant basic parameters (calculated above) are as follows: $\text{Re}_l = 1136$, $\text{Re}_{\text{vo}} = 22114$, and $X_{\text{tt}} = 0.3346$. The void fraction is calculated using Zivi's (1964) model:

$$\alpha = \left[1 + \frac{1-x}{x} \left(\frac{\rho_v}{\rho_l} \right)^{2/3} \right]^{-1} = \left[1 + \frac{1-0.5}{0.5} \left(\frac{76.5}{1077} \right)^{2/3} \right]^{-1} = 0.8536$$

The Galileo number was calculated in Example 6.1 for the present case, resulting in $Ga = 478,182$. The modified Soliman Froude number is then calculated using the following equation:

$$Fr_{so} = \begin{cases} 0.025 Re_l^{1.59} \left(\frac{1 + 1.09 \times X_{tt}^{0.039}}{X_{tt}} \right)^{1.5} \frac{1}{Ga^{0.5}} & \text{for } Re_l \leq 1250 \\ 1.26 Re_l^{1.04} \left(\frac{1 + 1.09 \times X_{tt}^{0.039}}{X_{tt}} \right)^{1.5} \frac{1}{Ga^{0.5}} & \text{for } Re_l > 1250 \end{cases}$$

For the present case with $Re_l = 1136$,

$$\begin{aligned} Fr_{so} &= 0.025 Re_l^{1.59} \left(\frac{1 + 1.09 \times X_{tt}^{0.039}}{X_{tt}} \right)^{1.5} \frac{1}{Ga^{0.5}} \\ &= 0.025 \times 1136^{1.59} \left(\frac{1 + 1.09 \times 0.3346^{0.039}}{0.3346} \right)^{1.5} \frac{1}{478,182^{0.5}} \\ &= 39.37 \end{aligned}$$

Since $Fr_{so} > 20$, the annular flow correlation proposed by them is used:

$$Nu_{\text{annular}} = 0.023 \times Re_l^{0.8} \times Pr_l^{0.4} \left(1 + \frac{2.22}{X_{tt}^{0.89}} \right)$$

Substituting the relevant parameters, the Nusselt number for the present case is:

$$\begin{aligned} Nu &= 0.023 \times 1136^{0.8} \times 3.152^{0.4} \left(1 + \frac{2.22}{0.3346^{0.89}} \right) \\ &= 69.68 \end{aligned}$$

The resulting heat transfer coefficient is:

$$h = Nu \times \frac{k_l}{D} = 69.68 \times \frac{0.06749}{0.001} = 4703 \text{ W/m}^2\text{-K}$$

Moser *et al.* (1998)

This correlation was based on data from tubes with $3.14 < D < 20$ mm. The various phase Reynolds numbers are, $Re_l = 1136$, $Re_{lo} = 2271$, and $Re_{vo} = \frac{GD}{\mu_v} = \frac{300 \times 0.001}{1.357 \times 10^{-5}} = 22,114$. The two-phase homogeneous density is given by:

$$\rho_{tp} = \left(\frac{x}{\rho_v} + \frac{1-x}{\rho_l} \right)^{-1} = \left(\frac{0.5}{76.5} + \frac{1-0.5}{1077} \right)^{-1} = 142.8 \text{ kg/m}^3$$

The corresponding Froude and Weber numbers are:

$$\text{Fr}_{\text{tp}} = \frac{G^2}{gD\rho_{\text{tp}}^2} = \frac{300^2}{9.81 \times 0.001 \times 142.8^2} = 449.6$$

$$\text{We}_{\text{tp}} = \frac{G^2 D}{\sigma \rho_{\text{tp}}} = \frac{300^2 \times 0.001}{0.00427 \times 142.8} = 147.5$$

For the calculation of the equivalent Reynolds number, the required friction factors are obtained as follows:

$$f_{\text{lo}} = 0.079 \times \text{Re}_{\text{lo}}^{-0.25} = 0.079 \times 2271^{-0.25} = 0.01144$$

$$f_{\text{vo}} = 0.079 \times \text{Re}_{\text{vo}}^{-0.25} = 0.079 \times 22114^{-0.25} = 0.006478$$

Constants required for the two-phase multiplier evaluation are calculated as follows:

$$A_1 = (1-x)^2 + x^2 \left(\frac{\rho_l}{\rho_v} \right) \left(\frac{f_{\text{vo}}}{f_{\text{lo}}} \right) = (1-0.5)^2 + 0.5^2 \left(\frac{1077}{76.5} \right) \left(\frac{0.006478}{0.01144} \right) = 2.243$$

$$\begin{aligned} A_2 &= x^{0.78} (1-x)^{0.24} \left(\frac{\rho_l}{\rho_v} \right)^{0.91} \left(\frac{\mu_v}{\mu_l} \right)^{0.19} \left(1 - \frac{\mu_v}{\mu_l} \right)^{0.70} \\ &= 0.5^{0.78} (1-0.5)^{0.24} \left(\frac{1077}{76.5} \right)^{0.91} \left(\frac{1.357 \times 10^{-5}}{1.321 \times 10^{-4}} \right)^{0.19} \left(1 - \frac{1.357 \times 10^{-5}}{1.321 \times 10^{-4}} \right)^{0.70} \\ &= 3.293 \end{aligned}$$

Two-phase multiplier is obtained from the parameters calculated above:

$$\phi_{\text{lo}}^2 = A_1 + \frac{3.24 \times A_2}{\text{Fr}_{\text{tp}}^{0.045} \times \text{We}_{\text{tp}}^{0.035}} = 2.243 + \frac{3.24 \times 3.293}{449.6^{0.045} \times 147.5^{0.035}} = 3.008$$

The equivalent Reynolds Number is calculated in terms of this multiplier as follows:

$$\text{Re}_{\text{eq}} = \phi_{\text{lo}}^{8/7} \times \text{Re}_{\text{lo}} = 3.008^{8/7} \times 2271 = 7996$$

The Nusselt number is calculated in terms of this equivalent Reynolds number as follows:

$$\text{Nu} = \frac{0.0994^{0.126 \times \text{Pr}_l^{-0.448}} \times \text{Re}_l^{-0.113 \times \text{Pr}_l^{-0.563}} \times \text{Re}_{\text{eq}}^{1+0.11025 \times \text{Pr}_l^{-0.448}} \times \text{Pr}_l^{0.815}}{(1.58 \times \ln \text{Re}_{\text{eq}} - 3.28) (2.58 \times \ln \text{Re}_{\text{eq}} + 13.7 \times \text{Pr}_l^{2/3} - 19.1)}$$

For the present case,

$$\begin{aligned} \text{Nu} &= \frac{0.0994^{0.126 \times 3.152^{-0.448}} \times 1136^{-0.113 \times 3.152^{-0.563}} \times 7996^{1+0.11025 \times 3.152^{-0.448}} \times 3.152^{0.815}}{(1.58 \times \ln 7996 - 3.28) (2.58 \times \ln 7996 + 13.7 \times 3.152^{2/3} - 19.1)} \\ &= 55.77 \end{aligned}$$

Finally, the heat transfer coefficient is given by:

$$h = \text{Nu} \times \frac{k_l}{D} = 55.77 \times \frac{0.06749}{0.001} = 3764 \text{ W/m}^2\text{-K}$$

Chato (1962)

This model was proposed for stratified annular flow conditions when $\text{Re}_v < 35,000$. The modified latent heat of vaporization, which accounts for wall subcooling is given by:

$$\begin{aligned} h'_{lv} &= h_{lv} \times \left[1 + 0.68 \times \frac{Cp_l \times (T_{\text{sat}} - T_{\text{wall}})}{h_{lv}} \right] \\ &= 145,394 \times \left[1 + 0.68 \times \frac{1611 \times (55.21 - 52)}{145,394} \right] \\ &= 148,910 \text{ J/kg} \end{aligned}$$

The heat transfer coefficient is obtained as follows:

$$h = 0.728 \times K_c \times \left[\frac{g \times \rho_l \times (\rho_l - \rho_v) \times k_l^3 \times h'_{lv}}{\mu_l \times (T_{\text{sat}} - T_{\text{wall}}) \times D} \right]^{1/4}$$

With $K_c = 0.76$,

$$\begin{aligned} \Rightarrow h &= 0.728 \times 0.76 \times \left[\frac{9.81 \times 1077 \times (1077 - 76.5) \times 0.06749^3 \times 148910}{1.321 \times 10^{-4} \times (55.21 - 52) \times 0.001} \right]^{1/4} \\ &= 3216 \text{ W/m}^2\text{-K} \end{aligned}$$

Boyko and Kruzhilin (1967)

This correlation relates the heat transfer coefficient in single-phase flow with the entire fluid flowing as a liquid to the two-phase heat transfer coefficient based on the mixture density, $\rho_m = 142.8 \text{ kg/m}^3$, calculated above. The bulk and wall Prandtl numbers are also required. Here the Prandtl number at the refrigerant pressure and wall temperature, $\text{Pr}_w = 3.144$. The single-phase heat transfer coefficient is calculated as follows:

$$h_0 = 0.024 \times \frac{k_l}{D} \times \left(G \times \frac{D}{\mu_l} \right)^{0.8} \times \text{Pr}_l^{0.43} \times \left(\frac{\text{Pr}_l}{\text{Pr}_w} \right)^{0.25}$$

For the present case,

$$\begin{aligned} h_0 &= 0.024 \times \frac{0.06749}{0.001} \times \left(300 \times \frac{0.001}{1.321 \times 10^{-4}} \right)^{0.8} \times 3.152^{0.43} \times \left(\frac{3.152}{3.144} \right)^{0.25} \\ &= 1286 \text{ W/m}^2\text{-K} \end{aligned}$$

The two-phase heat transfer coefficient is obtained as follows:

$$h = h_0 \sqrt{\frac{\rho_l}{\rho_m}} = 1286 \sqrt{\frac{1077}{142.8}} = 3531 \text{ W/m}^2\text{-K}$$

Cavallini *et al.* (2002a)

The applicable flow regime is first found from the Martinelli parameter $X_{tt} = 0.3346$, and the dimensionless gas velocity:

$$j_g^* = \frac{Gx}{\sqrt{Dg\rho_v(\rho_l - \rho_v)}} = \frac{300 \times 0.5}{\sqrt{0.001 \times 9.81 \times 76.5(1077 - 76.5)}} = 5.473$$

Based on the transition criteria presented in example 6.1, the flow is in the annular regime. The two-phase multiplier and the pressure gradient required for the calculation of the shear stress were presented in Example 6.3. Thus, $\Delta P/L = 14,500 \text{ Pa/m}$. The shear stress, is given by:

$$\tau = \left(\frac{dp}{dz} \right)_f \frac{D}{4} = 14500 \times \frac{0.001}{4} = 3.625 \text{ Pa}$$

The dimensionless film thickness is based on the liquid-phase Reynolds number:

$$\delta^+ = \begin{cases} \left(\frac{\text{Re}_l}{2} \right)^{0.5} & \text{for } \text{Re}_l \leq 1145 \\ 0.0504 \times \text{Re}_l^{7/8} & \text{for } \text{Re}_l > 1145 \end{cases}$$

In the present case $\text{Re}_l = 1136$, which yields:

$$\delta^+ = \left(\frac{\text{Re}_l}{2} \right)^{0.5} = \left(\frac{1136}{2} \right)^{0.5} = 23.83$$

The dimensionless temperature is given by:

$$T^+ = \begin{cases} \delta^+ \text{Pr}_l & \delta^+ \leq 5 \\ 5 \left\{ \text{Pr}_l + \ln \left[1 + \text{Pr}_l \left(\frac{\delta^+}{5} - 1 \right) \right] \right\} & 5 < \delta^+ < 30 \\ 5 \left[\text{Pr}_l + \ln(1 + 5 \text{Pr}_l) + 0.495 \ln \left(\frac{\delta^+}{30} \right) \right] & \delta^+ \geq 30 \end{cases}$$

For the present case,

$$\begin{aligned} T^+ &= 5 \left\{ \text{Pr}_l + \ln \left[1 + \text{Pr}_l \left(\frac{\delta^+}{5} - 1 \right) \right] \right\} \\ &= 5 \left\{ 3.152 + \ln \left[1 + 3.152 \left(\frac{23.83}{5} - 1 \right) \right] \right\} = 28.54 \end{aligned}$$

Finally, the heat transfer coefficient is calculated as follows:

$$h = \frac{\rho_l C_{pl} \left(\frac{\tau}{\rho_l} \right)^{0.5}}{T^+} = \frac{1077 \times 1611 \times \left(\frac{3.625}{1077} \right)^{0.5}}{28.54} = 3527 \text{ W/m}^2\text{-K}$$

Bandhauer *et al.* (2005)

This model was based on heat transfer data for $0.5 < D < 1.5$ mm and $150 < G < 750$ kg/m²-s, and the underlying pressure drop model was based on data for a much wider range of hydraulic diameters ($0.4 < D < 4.9$ mm). The pressure gradient calculation was discussed in Example 6.3, and resulted in a value of $\Delta P/L = 15,907$ Pa/m. The corresponding interfacial shear stress is:

$$\begin{aligned} \tau_i &= \left(\frac{\Delta P}{L} \right) \frac{D_i}{4} = \left(\frac{\Delta P}{L} \right) \frac{\sqrt{\alpha} \times D}{4} \\ &= 15.907 \times 10^3 \times \frac{\sqrt{0.8059} \times 0.001}{4} = 3.57 \text{ Pa} \end{aligned}$$

The friction velocity is calculated from the interfacial shear stress as follows:

$$u^* = \sqrt{\frac{\tau_i}{\rho_l}} = \sqrt{\frac{3.57}{1077}} = 0.05756 \text{ m/s}$$

The film thickness is directly calculated from the definition of the void fraction as follows:

$$\delta = (1 - \sqrt{\alpha}) \frac{D}{2} = (1 - \sqrt{0.8059}) \frac{0.001}{2} = 5.115 \times 10^{-5} \text{ m}$$

This thickness is used to obtain the dimensionless film thickness as follows:

$$\delta^+ = \frac{\delta \times \rho_l \times u^*}{\mu_l} = \frac{5.115 \times 10^{-5} \times 1077 \times 0.05756}{1.321 \times 10^{-4}} = 24.02$$

The turbulent dimensionless temperature is given by:

$$T^+ = \begin{cases} 5 \text{Pr}_l + 5 \ln \left[\text{Pr}_l \left(\frac{\delta^+}{5} - 1 \right) + 1 \right] & \text{if } \text{Re}_l < 2100 \\ 5 \text{Pr}_l + 5 \ln(5 \text{Pr}_l + 1) + \int_{30}^{\delta^+} \frac{dy^+}{\left(\frac{1}{\text{Pr}_l} - 1 \right) + \frac{y^+}{5} \left(1 - \frac{y^+}{R^+} \right)} & \text{if } \text{Re}_l \geq 2100 \end{cases}$$

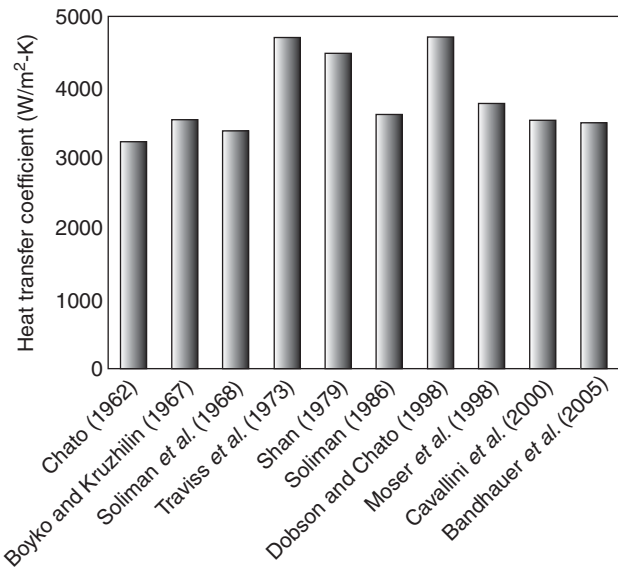
Thus, for the current example, with $\text{Re}_l = 598.5$:

$$\begin{aligned} T^+ &= 5 \text{Pr}_l + 5 \ln \left[\text{Pr}_l \left(\frac{\delta^+}{5} - 1 \right) + 1 \right] \\ &= 5 \times 3.152 + 5 \ln \left[3.152 \left(\frac{24.02}{5} - 1 \right) + 1 \right] = 28.58 \end{aligned}$$

Therefore, the heat transfer coefficient is:

$$h = \frac{\rho_1 \times C_{p1} \times u^*}{T^+} = \frac{1077 \times 1611 \times 0.05756}{28.58} = 3495 \text{ W/m}^2\text{-K}$$

The heat transfer coefficients predicted by the above models are depicted in the following graph.



It can be seen from this graph that there are considerable variations between the heat transfer coefficients predicted by these different models and correlations. One of the main reasons for these variations is that most of these correlations have been applied in this case outside their ranges of applicability, either in the mass flux, the phase velocities, or parameters such as the Weber and Froude numbers as applicable. But the most important reason for the differences is that all except the Bandhauer *et al.* (2005) model were based primarily on tube diameters in the ~8 mm range, with a few correlations being proposed based on limited data on ~3 mm tubes. The channel under consideration in this example is a 1-mm channel.

6.7. Exercises

- (1) Plot simulated air–water data points at different equally spaced combinations of gas and liquid superficial velocities in the range 0.1–100 m/s, and 0.01–10.0 m/s, respectively, as is typically done in air–water studies. Now plot on the same graph, refrigerant R-134a (at 40°C) points for the mass flux range 100–800 kg/m²-s in 100 kg/m²-s increments and quality increments of 0.10; that is compute the vapor and liquid superficial velocities for these G, x combinations and plot on the air–water

superficial velocity graph. Assume a 3 mm ID channel. Use this graph to comment on extending air–water flow regime maps to refrigerant condensation. Propose appropriate means to transform air–water results to refrigerant predictions based on comparisons of the relevant properties.

- (2) Flow regime maps are often plotted on the basis of superficial velocities, in which the phases are assumed to occupy the entire channel cross section. While this is a commonly used practice out of convenience, what are the disadvantages of choosing superficial velocities instead of actual phase velocities? Quantify for a range of flow patterns.
- (3) Conduct a dimensional analysis to identify the dimensionless parameters that would quantify transitions between the four principal regimes: intermittent, wavy, annular, and mist flow, by considering viscous, surface tension, inertia, and gravity forces. Conduct parametric analyses to choose the most significant parameters across the scales.
- (4) Estimate liquid film thickness as a function of three different void fraction models in annular flow, and its effect on the heat transfer coefficient. Refer to El Hajal (2003) and Thome (2003) for guidance. How would your conclusions change for intermittent or stratified flows?
- (5) One of the uncertainties often overlooked in reporting pressure drop results in microchannels is the effect tolerances in tube diameter. Conduct a parametric analysis of the change in pressure drop in a 1-mm channel during annular flow condensation of refrigerant R-22 across the quality range $0.3 < x < 0.8$. Use a reasonable range of tolerances in the tube diameter to illustrate these effects. Use a mass flux of $400 \text{ kg/m}^2\text{-s}$, at a saturation temperature of 45°C . Comment on how this variation would change at evaporating conditions (e.g. 5°C).
- (6) Develop a quantitative indicator of momentum coupling of liquid and vapor phases in condensing flows based on the papers of Lee and Lee (2001), the origin of the C coefficient expression developed by Chisholm (1967) for the Lockhart–Martinelli (1949) two-phase multiplier approach, and the discussions in the papers by Kawahara *et al.* (2002) and Chung and Kawaji (2004). Estimate numerical values of this measure for $10 \mu\text{m} < D_h < 10 \text{ mm}$.
- (7) Estimate the difference in saturation temperature decrease due to the flow of refrigerant R-22 in a 0.5-mm channel at a mass flux of $200 \text{ kg/m}^2\text{-s}$ by computing the condensation in 10% quality increments and accounting for frictional and deceleration contributions. Assume an appropriate bulk-wall temperature difference. Plot the pressure drop in each increment, and the corresponding decrease in saturation temperature. Use two different pressure drop models, one based on air–water studies, another based on refrigerant condensation.
- (8) Microchannels are especially attractive due to the high heat transfer coefficients they offer. In measuring these heat transfer coefficients, one has to measure the heat transfer rate using, typically, a rise in coolant temperature, and a temperature difference between the refrigerant and the wall. Assume channel $D_h = 0.5 \text{ mm}$. Assume further that the heat transfer coefficient needs to be measured in increments of $\Delta x = 0.10$. First estimate the heat transfer rate to achieve this condensation at this mass flux. How accurately can this heat transfer rate be measured in a single microchannel?

What changes in coolant temperature would be required to effect this heat transfer across the test section? Is this realistic – estimate the uncertainties in heat transfer rate measurement using reasonable thermocouple and mass flow rate measurement uncertainties. In an attempt to improve the uncertainties, multiple channels in parallel are proposed. How many channels would be required to achieve accurately measurable heat transfer rates? What are the drawbacks to using multiple channels. Next, estimate the heat transfer coefficient in condensing R-134a at $450 \text{ kg/m}^2\text{-s}$ and 50°C using one of the available models. What refrigerant-wall temperature difference would this cause in a channel that accomplishes the 10% quality change? (you will have to choose a reasonable test section length). How accurately can this temperature difference be measured? What would be the resulting heat transfer coefficient uncertainty? How would the uncertainty vary with mass flux – quantify? How would the uncertainty change if R-134a is substituted with steam?

- (9) It has been stated in this chapter that boundary-layer analyses in the liquid film and two-phase multiplier approaches are essentially equivalent methods of analyzing annular flow heat transfer. Refer to Dobson and Chato (1998) for background on this matter. Conduct parallel derivations of these two approaches to point out the essential similarities. Also comment on any significant differences.
- (10) Most heat transfer models recommend simply extending annular flow models to the intermittent flow. Develop a methodology for conducting this extension on a rational basis by accounting for the slug/bubble frequency.
- (11) Will intermittent flow heat transfer coefficients be higher or lower than those in annular flow? Why? Will they be higher or lower than those in single-phase gas or single-phase liquid flow? Why? Demonstrate through approximate models, using R-134a condensing at a 35°C through a $200 \mu\text{m}$ channel at $100 \text{ kg/m}^2\text{-s}$.
- (12) Assuming that condensing flows would go through a progression of annular–mist-homogeneous flow as the reduced pressure is increased, identify the most important fluid properties and the corresponding dimensionless parameters, and investigate changes in these quantities as the pressure is increased from $0.2 \times p_r$ to $0.9 \times p_r$. How would the pressure drop and heat transfer be affected in this progression?
- (13) Design an R-22 condenser that transfers 3 kW at a saturation temperature of 55°C , with the refrigerant entering as a saturated vapor and leaving as a saturated liquid. Dry air flowing in crossflow at $4.8\text{E-}01 \text{ m}^3/\text{s}$, with an inlet temperature of 35°C and a heat transfer coefficient of $50 \text{ W/m}^2\text{-K}$ is the cooling medium. Use copper tubing with copper fins on the air side that yield a factor of 10 surface area enhancement. The efficiency of the fins can be assumed to be 90%. Choose the tubing size and wall thickness from standard tables such that the drop in refrigerant saturation temperature (due to the pressure drop) is less than 1.5°C . Account for the flow regime variation over the length of the heat exchanger. Choose quality and/or tube length increments of reasonable size that demonstrate the flow phenomena and the heat transfer coefficient and pressure drop variations. Assume a horizontal orientation.
- (14) Repeat problem 13 by changing the design to an optimal parallel-serpentine arrangement of extruded Aluminum tubes with twenty 0.7 mm microchannel tubes with the same amount of air-side Aluminum fin surface area enhancement as in problem 13. Thus, decrease the number or tubes per pass as condensation proceeds so that a

larger flow area is provided in the initial passes to account for the higher flow velocities, and decrease the number of parallel tubes in subsequent passes. Compare the sizes (total material volume of each heat exchanger including tube and fin volume) resulting from these two approaches (Problems 13 and 14) and comment.

References

- Akers, W. W., Deans, H. A., and Crosser, O. K., Condensation heat transfer within horizontal tubes, *Chem. Eng. Prog. Symp. Series*, **55(29)**, 171–176, 1959.
- Akers, W. W. and Rosson, H. F., Condensation inside a horizontal tube, *Chem. Eng. Prog. Symp. Series*, **59**, 145–149, 1960.
- Ali, M. I., Sadatomi, M., and Kawaji, M., Adiabatic two-phase flow in narrow channels between two flat plates, *Can. J. Chem. Eng.*, **71(5)**, 657–666, 1993.
- Alves, G. E., Cocurrent liquid–gas flow in a pipe-line contactor, *Chem. Eng. Prog.*, **50(9)**: 449–456, 1954.
- Ananiev, E. P., Boyko, L. D., and Kruzhilin, G. N., Heat transfer in the presence of steam condensation in a horizontal tube, *Proc. First Int. Heat Trans. Conf. Part II*: 290, 1961.
- Annunziato, M. and Girardi, G., Horizontal two phase flow: a statistical method for flow pattern recognition, Paper F1, *3rd Int. Conf. Multi-Phase Flow, The Hague, Netherlands*, The Hague, Netherlands, 169–185, 1987.
- Armand, A. A., The resistance during the movement of a two-phase system in horizontal pipes, *Izv. Vses. Teploekh. Inst.*, **1**, 16–23 (AERE-Lib/Trans 828), 1946.
- Azer, N. Z., Abis, L. V., and Soliman, H. M., Local heat transfer coefficients during annular flow condensation, *ASHRAE Transactions*, **78 (Part 2)**, 135–143, 1972.
- Bae, S., Maulbetsch, J. S., and Rohsenow, W. M., Refrigerant forced-convection condensation inside horizontal tubes, **77 (Part 2)**, 104–113, 1971.
- Baker, O., Simultaneous flow of oil and gas, *Oil Gas J.*, **53**, 185–195, 1954.
- Bandhauer, T. M., Agarwal, A., and Garimella, S., Measurement and modeling of condensation heat transfer coefficients in circular microchannels, *Proceedings of ICMM2005, The 3rd International Conference on Microchannels and Minichannels*, June 13–15, 2005, ICMM2005- 75248, Toronto, Ontario, Canada, 2005.
- Barajas, A. M. and Panton, R. L., The effects of contact angle on two-phase flow in capillary tubes, *Int. J. Multiphase Flow*, **19(2)**, 337–346, 1993.
- Barnea, D., Luninski, Y., and Taitel, Y., Flow pattern in horizontal and vertical two phase flow in small diameter tubes, *Can. J. Chem. Eng.*, **61(5)**, 617–620, 1983.
- Baroczy, C. J., Correlation of liquid fraction in two-phase flow with applications to liquid metals, *Chem. Eng. Prog. Symp. Series*, **61(57)**, 179–191, 1965.
- Baroczy, C. J., Systematic correlation for two-phase pressure drop, *Chem. Eng. Prog. Symp. Series*, **62(64)**, 232–249, 1966.
- Baroczy, C. J. and Sanders, V. D., Pressure drop for flowing vapors condensing in straight horizontal tube, *ASME Meeting WA-257*, November 26–December 1 1961, American Society of Mechanical Engineers (ASME), New York, NY, USA, 16, 1961.
- Beattie, D. R. H. and Whalley, P. B., A simple two-phase frictional pressure drop calculation method, *Int. J. Multiphase Flow*, **8(1)**, 83–87, 1982.
- Blangetti, F. L. and Schlunder, E. U., Local heat transfer coefficients of condensation in a vertical tube, *Proceedings of the Sixth International Heat Transfer Conference*, 437–442, 1978.

- Boyko, L. D. and Kruzhilin, G. N., Heat transfer and hydraulic resistance during condensation of steam in a horizontal tube and in a bundle of tubes, *Int. J. Heat Mass Trans.*, **10**(3), 361–373, 1967.
- Brauner, N. and Maron, D. M., Identification of the range of small diameters conduits, regarding two-phase flow pattern transitions, *Int. Commun. Heat Mass Trans.*, **19**(1), 29–39, 1992.
- Breber, G., Palen, J. W., and Taborek, J., Prediction of horizontal tubeside condensation of pure components using flow regime criteria, *Condens Heat Transfer, Presented at National Heat Transfer Conference*, 18th, August 6–8 1979, 1–8, 1979.
- Breber, G., Palen, J. W., and Taborek, J., Prediction of horizontal tubeside condensation of pure components using flow regime criteria, *J. Heat Trans., Transac. ASME*, **102**(3), 471–476, 1980.
- Butterworth, D., A comparison of some void-fraction relationships for co-current gas–liquid flow, *Int. J. Multiphase Flow*, **1**(6), 845–850, 1975.
- Cai, Y., Wambsganss, M. W., and Jendrzeczyk, J. A., Application of chaos theory in identification of two-phase flow patterns and transitions in a small, horizontal, rectangular channel, *J. Fluid. Eng., Trans. ASME*, **118**(2), 383–390, 1996.
- Carey, V. P., *Liquid–vapor Phase-change Phenomena: An Introduction to the Thermophysics of Vaporization and Condensation Processes in Heat Transfer Equipment*. Washington, DC, Taylor & Francis Series, Hemisphere Pub. Corp, 1992.
- Carnavos, T. C., Cooling air in turbulent flow with internally finned tubes, **1**(2), 41–46, 1979.
- Carnavos, T. C., Heat transfer performance of internally finned tubes in turbulent flow, **1**(4), 32–37, 1980.
- Carpenter, F. G. and Colburn, A. P., The effect of vapor velocity on condensation inside tubes, *General Discussion of Heat Transfer, The Institute of Mechanical Engineers and ASME*, 20–26, 1951.
- Cavallini, A. and Zecchin, R., Dimensionless correlation for heat transfer in forced convection condensation, *International Heat Transfer Conference, 5th, Proceeding*, 309–313, 1974.
- Cavallini, A., Del Col, D., Doretti, L., Longo, G. A., and Rossetto, L., Heat transfer and pressure drop during condensation of refrigerants inside horizontal enhanced tubes: Transfert de chaleur et chute de pression lors de la condensation de frigorigènes a l’intérieur de tubes horizontaux a surface augmentee, *Int. J. Refrig.*, **23**(1), 4–25, 2000.
- Cavallini, A., Censi, G., Del Col, D., Doretti, L., Longo, G. A., and Rossetto, L., Experimental investigation on condensation heat transfer and pressure drop of new HFC refrigerants (R134a, R125, R32, R410A, R236ea) in a horizontal smooth tube: [Etude experimentale sur le transfert de chaleur lors de la condensation et sur la chute de pression des nouveaux frigorigènes HFC (R134a, R125, R32, R410A, et R236ea) dans un tube lisse horizontal], *Int. J. Refrig.*, **24**(1), 73–87, 2001.
- Cavallini, A., Censi, G., Del Col, D., Doretti, L., Longo, G. A., and Rossetto, L., Condensation of halogenated refrigerants inside smooth tubes, *HVAC and R Research*, **8**(4), 429–451, 2002a.
- Cavallini, A., Censi, G., Del Col, D., Doretti, L., Longo, G. A., Rossetto, L., and Mathur, G. D., In-tube condensation of halogenated refrigerants, *2002 ASHRAE Winter Meeting*, January 13–16 2002, Atlantic City, NJ, Amer. Soc. Heating, Ref. Air-Conditioning Eng. Inc., 146–161, 2002b.
- Cavallini, A., Censi, G., Del Col, D., Doretti, L., Longo, G. A., Rossetto, L., and Zilio, C., Condensation inside and outside smooth and enhanced tubes – a review of recent research, *Int. J. Refrig.*, **26**(4), 373–392, 2003.
- Cavallini, A., Del Col, D., Doretti, L., Matkovic, M., Rossetto, L., and Zilio, C., Condensation heat transfer and pressure gradient inside multiport minichannels, *Heat Trans. Eng.*, **26**(3), 45–55, 2005.
- Chaddock, J. B., Film condensation of vapor in horizontal tube, *Refrig. Eng.*, **65**(4), 36–41, 1957.

- Chato, J. C., Laminar condensation inside horizontal and inclined tubes, *ASHRAE J.*, **4(2)**, 52–60, 1962.
- Chen, I. Y. and Kocamustafaogullari, G., Condensation heat transfer studies for stratified, cocurrent two-phase flow in horizontal tubes, *Int. J. Heat Mass Trans.*, **30(6)**, 1133–1148, 1987.
- Chen, I. Y., Yang, K.-S., Chang, Y.-J., and Wang, C.-C., Two-phase pressure drop of air–water and R-410A in small horizontal tubes, *Int. J. Multiphase Flow*, **27(7)**, 1293–1299, 2001.
- Chen, S. J., Reed, J. G., and Tien, C. L., Reflux condensation in a two-phase closed thermosyphon, *Int. J. Heat Mass Trans.*, **27(9)**, 1587–1594, 1984.
- Chen, S. L., Gerner, F. M., and Tien, C. L., General film condensation correlations, *Exp. Heat Trans.*, **1(2)**, 93–107, 1987.
- Chexal, B. and Lellouche, G. S., *A full range drift-flux correlation for vertical flow*, Electric Power Research Institute report EPRI-NP-3989-SR (revision 1), Palo Alto, CA, 1986.
- Chexal, B., Lellouche, G. S., Horowitz, J., and Healzer, J., A void fraction correlation for generalized applications, *Prog. Nucl. Energy*, **27**, 255–295, 1992.
- Chexal, B., Merilo, M., Maulbetsch, J., Horowitz, J., Harrison, J., Westacott, J. C., Peterson, C., Kastner, W., and Schmidt, H., Void fraction technology for design and analysis, Electric Power Research Institute, Palo Alto, CA, 1997.
- Chisholm, D., A theoretical basis for the Lockhart–Martinelli correlation for two-phase flow, *Int. J. Heat Mass Trans.*, **10(12)**, 1767–1778, 1967.
- Chisholm, D., Pressure gradients due to friction during the flow of evaporating two-phase mixtures in smooth tubes and channels, *Int. J. Heat Mass Trans.*, **16(2)**, 347–358, 1973.
- Chisholm, D., *Two-phase flow in pipelines and heat exchangers*. London, New York: G. Godwin in association with the Institution of Chemical Engineers, 1983.
- Chisholm, D. and Sutherland, L. A., Prediction of pressure gradients in pipeline systems during two-phase flow, *Proc. Instit. Mech. Eng.*, 24–32, 1969–70.
- Chitti, M. S. and Anand, N. K., An analytical model for local heat transfer coefficients for forced convective condensation inside smooth horizontal tubes, *Int. J. Heat Mass Trans.*, **38(4)**, 615–627, 1995.
- Chitti, M. S. and Anand, N. K., Condensation heat transfer inside smooth horizontal tubes for R-22 and R-32/125 mixture, *HVAC&R Res.*, **2(1)**, 79–101, 1996.
- Chun, K. R. and Seban, R. A. Heat transfer to evaporating liquid films, *J. Heat Trans.*, **93 Ser C(4)**, 391–396, 1971.
- Chung, P. M.-Y. and Kawaji, M., The effect of channel diameter on adiabatic two-phase flow characteristics in microchannels, *Int. J. Multiphase Flow*, **30(7–8)**, 735–761, 2004.
- Chung, P. M.-Y., Kawaji, M., Kawahara, A., and Shibata, Y., Two-phase flow through square and circular microchannels – effects of channel geometry, *J. Fluid. Eng.*, **126(4)**, 546–552, 2004.
- Churchill, S. W., Friction-factor equation spans all fluid-flow regimes, *Chem. Eng. Prog.*, **84(24)**, 91–92, 1977.
- Churchill, S. W. and Usagi, R., A general expression for the correlation of rates of transfer and other phenomena, *AIChE J.*, **18(6)**, 1121–1128, 1972.
- Cicchitti, A., Lombardi, C., Silvestri, M., Soldaini, G., and Zavattarelli, R., Two-phase cooling experiments: pressure drop, heat transfer and burnout measurements, *Energ. Nucl.*, **7(6)**, 407–425, 1960.
- Clarke, N. N. and Rezkallah, K. S., A study of drift velocity in bubbly two-phase flow under microgravity conditions, *Int. J. Multiphase Flow*, **27(9)**, 1533–1554, 2001.
- Colebrook, C. F., Turbulent flow in pipes, with particular reference to the transition between the smooth and rough pipe laws, *J. Instit. Civil Eng.*, **11**, 133–156, 1939.

- Coleman, J. W. and Garimella, S., Characterization of two-phase flow patterns in small diameter round and rectangular tubes, *Int. J. Heat Mass Trans.*, **42(15)**, 2869–2881., 1999.
- Coleman, J. W. and Garimella, S., Two-phase flow regime transitions in microchannel tubes: the effect of hydraulic diameter, Orlando, FL: *American Society of Mechanical Engineers, Heat Transfer Division*, 71–83, 2000a.
- Coleman, J. W. and Garimella, S., Visualization of two-phase refrigerant flow during phase change, *Proceedings of the 34th National Heat Transfer Conference*, Pittsburgh, PA, ASME, 2000b.
- Coleman, J. W. and Garimella, S., Two-phase flow regimes in round, square and rectangular tubes during condensation of refrigerant R134a, *Int. J. Refrig.*, **26(1)**, 117–128, 2003.
- Collier, J. G. and Thome, J. R., *Convective boiling and condensation*, Oxford, New York: Clarendon Press, Oxford University Press, 1994.
- Cornwell, K. and Kew, P. A., Boiling in small parallel channels, *Energy Efficiency in Process Technology*, P. A. Pilavachi, New York: Elsevier, 624–638, 1993.
- Damianides, C. A. and Westwater, J. W., Two-phase flow patterns in a compact heat exchanger and in small tubes, *Second UK National Conference on Heat Transfer (2 Vols)*, Scotland: Glasgow, 1257–1268, 1988.
- Das, R. K. and Pattanayak, S., Electrical impedance method for flow regime identification in vertical upward gas–liquid two-phase flow, *Measurem. Sci. Technol.*, **4(12)**, 1457–1463, 1993.
- Das, R. and Pattanayak, S., Measurement of void fraction in different flow regimes of a vertical gas–liquid flow through narrow tubes, *Measurem. Sci. Technol.*, **5(12)**, 1538–1545, 1994a.
- Das, R. K. and Pattanayak, S., Bubble to slug flow transition in vertical upward two-phase flow through narrow tubes, *Chem. Eng. Sci.*, **49(13)**, 2163–2172, 1994b.
- Das, R. and Pattanayak, S., Bubble to slug flow transition in vertical upward two-phase flow of cryogenic fluids, *Cryogenics*, **35(7)**, 421–426, 1995a.
- Das, R. and Pattanayak, S., Flow regime identification in cryogenic gas–liquid flow through vertical tubes, *Cryogenics*, **35(6)**, 393–398, 1995b.
- Das, R. and Pattanayak, S., Detection and analysis of transition from annular to intermittent flow in vertical tubes, *Can. J. Chem. Eng.*, **74(1)**, 49–57, 1996.
- Dittus, W. and Boelter, L. M. K., Heat transfer in automobile radiators of the tubular type, *University of California – Publications in Engineering*, **2(13)**, 443–461, 1930.
- Dobson, M. K., Heat transfer and flow regimes during condensation in horizontal tubes, PhD Thesis, Mechanical and Industrial Engineering, University of Illinois at Urbana-Champaign, Urbana-Champaign, IL, 1994.
- Dobson, M. K. and Chato, J. C., Condensation in smooth horizontal tubes, *J. Heat Trans., Transac. ASME*, **120(1)**, 193–213, 1998.
- Dobson, M. K., Chato, J. C., Hinde, D. K., and Wang, S. P., Experimental evaluation of internal condensation of refrigerants R-12 and R-134a, *Proceedings of the ASHRAE Winter Meeting*, January 23–26 1994, New Orleans, LA, USA, ASHRAE, Atlanta, GA, USA, 744–754, 1994.
- Dukler, A. E., Fluid mechanics and heat transfer in vertical falling film systems, *Chem. Eng. Prog. Symp. Series*, **56(30)**, 1–10, 1960.
- Dukler, A. E. and Hubbard, M. G., A model for gas–liquid slug flow in horizontal and near horizontal tubes, *Ind. Eng. Chem. Fund.*, **14(4)**, 337–347, 1975.
- Dukler, A. E., Wicks III, M., and Cleveland, R. G., Frictional pressure drop in two-phase flow, *AIChE J.*, **10(1)**, 38–51, 1964.
- Eckels, S. J., Doerr, T. M., and Pate, M. B., In-tube heat transfer and pressure drop of R-134a and ester lubricant mixtures in a smooth tube and a micro-fin tube: part I – evaporation, *Proceedings of the ASHRAE Annual Meeting*, June 25–29 1994, Orlando, FL, USA, ASHRAE, Atlanta, GA, USA, 265–282, 1994.

- Ekberg, N. P., Ghiaasiaan, S. M., Abdel-Khalik, S. I., Yoda, M., and Jeter, S. M., Gas-liquid two-phase flow in narrow horizontal annuli, *Nucl. Eng. Des.*, **192(1)**, 59–80, 1999.
- El Hajal, J., Thome, J. R., and Cavallini, A., Condensation in horizontal tubes, part 1: two-phase flow pattern map, *Int. J. Heat Mass Trans.*, **46(18)**, 3349–3363, 2003.
- Elkow, K. J. and Rezkallah, K. S., Statistical analysis of void fluctuations in gas-liquid flows under 1 – g and μ – g conditions using a capacitance sensor, *Int. J. Multiphase Flow*, **23(5)**, 831–844, 1997a.
- Elkow, K. J. and Rezkallah, K. S., Void fraction measurements in gas-liquid flows under 1 – g and μ – g conditions using capacitance sensors, *Int. J. Multiphase Flow*, **23(5)**, 815–829, 1997.
- Feng, Z. and Serizawa, A., Visualization of two-phase flow patterns in an ultra-small tube, *Proceedings of the 18th Multiphase Flow Symposium of Japan*, Suita, Osaka, Japan, 33–36, 1999.
- Feng, Z. and Serizawa, A., Measurement of steam-water bubbly flow in ultra-small capillary tube, *Proceedings of the 37th National Heat Transfer Symposium of Japan*, 351–352, 2000.
- Friedel, L., Improved friction pressure drop correlations for horizontal and vertical two phase pipe flow, *European Two Phase Flow Group Meeting*, Ispra, Italy, paper E2, 1979.
- Friedel, L., Pressure drop during gas/vapor-liquid flow in pipes, *Int. Chem. Eng.*, **20(3)**, 352–367, 1980.
- Fukano, T. and Kariyasaki, A., Characteristics of gas-liquid two-phase flow in a capillary tube, *Nucl. Eng. Des.*, **141(1–2)**, 59–68, 1993.
- Fukano, T., Kariyasaki, A., and Kagawa, M., Flow patterns and pressure drop in isothermal gas-liquid concurrent flow in a horizontal capillary tube, *Proceedings of the 1989 ANS National Heat Transfer Conference*, Philadelphia, 153–161, 1989.
- Galbiati, L. and Andreini, P., Flow pattern transition for vertical downward two-phase flow in capillary tubes. Inlet mixing effects, *Int. Commun. Heat Mass Trans.*, **19(6)**, 791–799, 1992a.
- Galbiati, L. and Andreini, P., The transition between stratified and annular regimes for horizontal two-phase flow in small diameter tubes, *Int. Commun. Heat Mass Trans.*, **19(2)**, 185–190, 1992b.
- Galbiati, L. and Andreini, P., Flow pattern transition for horizontal air-water flow in capillary tubes. A microgravity equivalent system simulation, *Int. Commun. Heat Mass Trans.*, **21(4)**, 461–468, 1994.
- Garimella, S., Condensation flow mechanisms in microchannels: basis for pressure drop and heat transfer models, *Heat Trans. Eng.*, **25(3)**, 104–116, 2004.
- Garimella, S., Condensation flow mechanisms, pressure drop and heat transfer in microchannels. *Microscale Heat Transfer- Fundamental and Applications*, S. Kakac, L. L. Vasiliev, Y. Bayazitoglu, Y. Yener eds., The Netherlands: Kluwer Academic Publishers, 2005.
- Garimella, S., Agarwal, A., and Killion, J. D., Condensation pressure drop in circular microchannels, *Heat Trans. Eng.*, **26(3)**, 1–8, 2005.
- Garimella, S. V. and Singhal, V., Single-phase flow and heat transport and pumping considerations in microchannel heat sinks, *Heat Trans. Eng.*, **25(1)**, 15–25, 2004.
- Garimella, S. V. and Sobhan, C. B., Transport in microchannels – a critical review. *Ann. Rev. Heat Trans.*, **13**, 2003.
- Garimella, S. and Wicht, A., Air-cooled condensation of ammonia in flat-tube, multi-louver fin heat exchangers, *Proceedings of the 1995 ASME International Mechanical Engineering Congress and Exposition*, November 12–17 1995, San Francisco, CA, ASME, New York, NY, 47–58, 1995.
- Garimella, S. and Bandhauer, T. M., Measurement of condensation heat transfer coefficients in microchannel tubes, *2001 ASME International Mechanical Engineering Congress and Exposition*, New York, NY, American Society of Mechanical Engineers, 243–249, 2001.

- Garimella, S., Killion, J. D., and Coleman, J. W., An experimentally validated model for two-phase pressure drop in the intermittent flow regime for circular microchannels, *J. Fluid. Eng.*, **124**(1), 205–214, 2002.
- Garimella, S., Agarwal, A., and Coleman, J. W., Two-phase pressure drops in the annular flow regime in circular microchannels, *21st IIR International Congress of Refrigeration*, Washington, DC, International Institute of Refrigeration, 2003a.
- Garimella, S., Killion, J. D., and Coleman, J. W., An experimentally validated model for two-phase pressure drop in the intermittent flow regime for noncircular microchannels, *J. Fluid. Eng.*, **125**(5), 887–894, 2003b.
- Geraets, J. J. M. and Borst, J. C., A capacitance sensor for two-phase void fraction measurement and flow pattern identification, *Int. J. Multiphase Flow*, **14**(3), 305–320, 1988.
- Gibson, A. H., On the motion of long air-bubbles in a vertical tube, *Phil. Mag.*, **26**, 952–965, 1913.
- Gnielinski, V., New equations for heat and mass transfer in turbulent pipe and channel flow, *Int. Chem. Eng.*, **16**(2), 359–368, 1976.
- Goto, M., Inoue, N., and Ishiwatari, N., Condensation and evaporation heat transfer of R410A inside internally grooved horizontal tubes, *Int. J. Refrig.*, **24**(7), 628–638, 2001.
- Goto, M., Inoue, N., and Yonemoto, R., Condensation heat transfer of R410A inside internally grooved horizontal tubes, *Int. J. Refrig.*, **26**(4), 410–416, 2003.
- Govier, G. W. and Omer, M. M., The horizontal pipeline flow of air–water mixtures, *Can. J. Chem. Eng.*, 93–104, 1962.
- Govier, G. W. and Short, W. L., The upward vertical flow of air–water mixtures, *Can. J. Chem. Eng.*, 195–202, 1958.
- Govier, G. W., Radford, B. A., and Dunn, J. S. C., The upward vertical flow of air water mixtures. Part 1: effect of air and water rates on flow pattern, hold-up and pressure drop, *Can. J. Chem. Eng.*, **35**, 58–70, 1957.
- Graham, D., Chato, J. C., and Newell, T. A., Heat transfer and pressure drop during condensation of refrigerant 134a in an axially grooved tube, *Int. J. Heat Mass Trans.*, **42**(11), 1935–1944, 1999.
- Gregorig, R., Verfahrenstechnisch günstigere führung der mittel der Wärmeübertragung beim verdampfen und kondensieren, *Int. J. Heat Mass Trans.*, **5**(3–4), 175–188, 1962.
- Griffith, P. and Lee, K. S., Stability of annulus of liquid in tube, *Transac. ASME, J. Basic Eng.*, **86**(4), 666–668, 1964.
- Guo, Z., Condensation of R-410a in horizontal rectangular channel, PhD thesis, Mechanical Engineering, Texas A&M University, College Station, TX, 1998.
- Guo, Z. and Anand, N. K., Analytical model to predict condensation of R-410A in a horizontal rectangular channel, *J. Heat Trans. Transac. ASME*, **122**(3), 613–620, 2000.
- Haraguchi, H., Koyama, S., and Fujii, T., Condensation of refrigerants HCFC22, HFC134a and HCFC123 in a horizontal smooth tube (1st report, proposal of empirical expressions for the local frictional pressure drop), *Transac. JSME (B)*, **60**(574), 239–244, 1994a.
- Haraguchi, H., Koyama, S., and Fujii, T., Condensation of refrigerants HCFC22, HFC134a and HCFC123 in a horizontal smooth tube (2nd report, proposal of empirical expressions for the local heat transfer coefficient), *Transac. JSME (B)*, **60**(574), 245–252, 1994b.
- Hashizume, K., Flow pattern, void fraction and pressure drop of refrigerant two-phase flow in a horizontal pipe—I. Experimental data, *Int. J. Multiphase Flow*, **9**(4), 399–410, 1983.
- Hashizume, K. and Ogawa, N., Flow pattern, void fraction and pressure drop of refrigerant two-phase flow in a horizontal pipe—III: comparison of the analysis with existing pressure drop data on air/water and steam/water systems, *Int. J. Multiphase Flow*, **13**(2), 261–267, 1987.
- Hashizume, K., Ogiwara, H., and Taniguchi, H., Flow pattern, void fraction and pressure drop of refrigerant two-phase flow in a horizontal pipe—II: analysis of frictional pressure drop, *Int. J. Multiphase Flow*, **11**(5), 643–658, 1985.

- Hetsroni, G., *Handbook of Multiphase Systems*, New York: Hemisphere, 1982.
- Hewitt, G. F. and Roberts, D. N., *Studies of Two-Phase Flow Patterns by Simultaneous X-Ray and Flash Photography*, AERE-M 2159, London, UK: Her Majesty's Stationery Office, 1969.
- Hewitt, G. F., Shires, G. L., and Bott, T. R., *Process Heat Transfer*. Boca Raton: CRC Press; Begell House, 1994.
- Hibiki, T. and Mishima, K., Approximate method for measurement of phase-distribution in multiphase materials with small neutron-dashattenuation using a neutron beam as a probe, *Nucl. Instrum. Meth. in Phys. Res. Sec. A: Acceler., Spectr., Detect. Assoc. Equip.*, **374(3)**, 345–351, 1996.
- Hibiki, T. and Mishima, K., Flow regime transition criteria for upward two-phase flow in vertical narrow rectangular channels, *Nucl. Eng. Des.*, **203(2–3)**, 117–131, 2001.
- Hibiki, T., Mishima, K., and Nishihara, H., Measurement of radial void fraction distribution of two-phase flow in a metallic round tube using neutrons as microscopic probes, *Nucl. Instrum. Meth. Phys. Res. Sec. A: Acceler., Spectr., Detec. Assoc. Equip.*, **399(2–3)**, 432–438, 1997.
- Hosler, E. R., Flow patterns in high pressure two-phase (steam–water) flow with heat addition, *AIChE Symposium Series*, 54–66, 1968.
- Hughmark, G. A., Holdup in gas–liquid flow, *Chem. Eng. Prog.*, **58(4)**, 62–65, 1962.
- Hurlburt, E. T. and Newell, T. A., Characteristics of refrigerant film thickness, pressure drop, and condensation heat transfer in annular flow, *HVAC&R Res.*, **5(3)**, 229–248, 1999.
- Ide, H., Matsumura, H., and Fukano, T., Velocity characteristics of liquid lumps and its relation to flow patterns in gas–liquid two-phase flow in vertical capillary tubes, *Proceedings of the 1995 ASME/JSME Fluids Engineering and Laser Anemometry Conference and Exhibition*, August 13–18 1995, Hilton Head, SC, USA, ASME, New York, NY, USA, 1–8, 1995.
- Ide, H., Matsumura, H., Tanaka, Y., and Fukano, T., Flow patterns and frictional pressure drop in gas–liquid two-phase flow in vertical capillary channels with rectangular cross section, *Nippon Kikai Gakkai Ronbunshu, B Hen/Trans. JSME, Part B*, **63(606)**, 452–460, 1997.
- Infante Ferreira, C. A., Newell, T. A., Chato, J. C., and Nan, X., R404A condensing under forced flow conditions inside smooth, microfin and cross-hatched horizontal tubes, *Int. J. Refrig.*, **26(4)**, 433–441, 2003.
- Isbin, H. S., Sher, N. C., and Eddy, K. C., Void fractions in two-phase steam–water flow, *AIChE J.*, **3(1)**, 136–142, 1957.
- Ishii, M., One-dimensional drift-flux model and constitutive equations for between phases in various two-phase flow regimes, ANL Report ANL-77-47, 1977.
- Jaster, H. and Kosky, P. G., Condensation heat transfer in a mixed flow regime, *Int. J. Heat Mass Trans.*, **19(1)**, 95–99, 1976.
- Jenkins, R., Two-phase two-component flow of water and air, MS, University of Delaware, 1947.
- Jiang, Y. and Garimella, S., Compact air-coupled and hydronically coupled microchannel heat pumps, *2001 ASME International Mechanical Engineering Congress and Exposition*, November 11–16 2001, New York, NY, USA, American Society of Mechanical Engineers, 227–239, 2001.
- Jones Jr., O. C. and Zuber, N., The interrelation between void fraction fluctuations and flow patterns in two-phase flow, *Int. J. Multiphase Flow*, **2(3)**, 273–306, 1975.
- Jung, D. S. and Radermacher, R., Prediction of pressure drop during horizontal annular flow boiling of pure and mixed refrigerants, *Int. J. Heat Mass Trans.*, **32(12)**, 2435–2446, 1989.
- Kariyasaki, A., Fukano, T., Ousaka, A., and Kagawa, M., Characteristics of time-varying void fraction in isothermal air–water cocurrent flow in horizontal capillary tube, *Transac. JSME*, **57(B)(544)**, 4036–4043, 1991.
- Kariyasaki, A., Fukano, T., Ousaka, A., and Kagawa, M., Isothermal air–water two-phase up and downward flows in a vertical capillary tube (1st report, flow pattern and void fraction). *Trans. JSME (Ser. B)*, **58**, 2684–2690, 1992.

- Kattan, N., Thome, J. R., and Favrat, D., Flow boiling in horizontal tubes: part 1 – development of a diabatic two-phase flow pattern map, *J. Heat Trans. Transac. ASME*, **120(1)**, 140–147, 1998a.
- Kattan, N., Thome, J. R., and Favrat, D., Flow boiling in horizontal tubes: part 2 – new heat transfer data for five refrigerants, *J. Heat Trans. Transac. ASME*, **120(1)**, 148–155, 1998b.
- Kattan, N., Thome, J. R., and Favrat, D., Flow boiling in horizontal tubes: part 3 – development of a new heat transfer model based on flow pattern, *J. Heat Trans., Transac. ASME*, **120(1)**, 156–165, 1998c.
- Kawahara, A., Chung, P. M.-Y, and Kawaji, M., Investigation of two-phase flow pattern, void fraction and pressure drop in a microchannel, *Int. J. Multiphase Flow*, **28(9)**, 1411–1435, 2002.
- Kawahara, A., Sadatomi, M., Okayama, K., Kawaji, M., and Chung, P. M.-Y., Effects of channel diameter and liquid properties on void fraction in adiabatic two-phase flow through microchannels, *Heat Trans. Eng.*, **26(3)**, 13–19, 2005.
- Keska, J. K., Fernando, R. D., and Hamer, M. T., Experimental investigation of average parameters for air–water two-phase flow in a horizontal channel based on in-situ measurements, *28th National Heat Transfer Conference and Exhibition*, August 9–12 1992, San Diego, CA, USA, Publ by ASME, New York, NY, USA, 7–18, 1992.
- Kew, P. A. and Cornwell, K., Correlations for the prediction of boiling heat transfer in small-diameter channels, *Appl. Therm. Eng.*, **17(8–10)**, 705–715, 1997.
- Kim, N.-H., Cho, J.-P., Kim, J.-O., and Youn, B., Condensation heat transfer of R-22 and R-410A in flat aluminum multi-channel tubes with or without micro-fins, *Int. J. Refrig.*, **26(7)**, 830–839, 2003.
- Kolb, W. B. and Cerro, R. L., Coating the inside of a capillary of square cross section, *Chem. Eng. Sci.*, **46(9)**, 2181–2195, 1991.
- Kolb, W. B. and Cerro, R. L., Film flow in the space between a circular bubble and a square tube, *J. Colloid Interf. Sci.*, **159(2)**, 302–311, 1993.
- Kosky, P. G., Thin liquid films under simultaneous shear and gravity forces, *Int. J. Heat Mass Trans.*, **14(8)**, 1220–1224, 1971.
- Kosky, P. G. and Staub, F. W., Local condensing heat transfer coefficients in the annular flow regime, *AIChE J.*, **17(5)**, 1037–1043, 1971.
- Koyama, S. and Yu, J., Condensation heat transfer of pure refrigerant inside an internally grooved horizontal tube, *Proceedings of the JAR Annual Conference*, 173–176, 1996.
- Koyama, S., Kuwahara, K., and Nakashita, K., Condensation of refrigerant in a multi-port channel, *First International Conference on Microchannels and Minichannels*, April 24–25 2003, Rochester, NY, USA, American Society of Mechanical Engineers, 193–205, 2003a.
- Koyama, S., Kuwahara, K., Nakashita, K., and Yamamoto, K., An experimental study on condensation of refrigerant R134a in multi-port extruded tube, *Int. J. Refrig.*, **26(4)**, 425–432, 2003b.
- Koyama, S., Lee, J., and Yonemoto, R., An investigation on void fraction of vapor–liquid two-phase flow for smooth and microfin tubes with R134a at adiabatic condition, *Int. J. Multiphase Flow*, **30(3)**, 291–310, 2004.
- Kureta, M., Kobayashi, T., Mishima, K., and Nishihara, H., Pressure drop and heat transfer for flow-boiling of water in small-diameter tubes, *JSME Int. J., Series B*, **41(4)**, 871–879, 1998.
- Kureta, M., Akimoto, H., Hibiki, T., and Mishima, K., Void fraction measurement in subcooled-boiling flow using high-frame-rate neutron radiography, *Nucl. Technol.*, **136(2)**, 241–254, 2001.
- Kureta, M., Hibiki, T., Mishima, K., and Akimoto, H., Study on point of net vapor generation by neutron radiography in subcooled boiling flow along narrow rectangular channels with short heated length, *Int. J. Heat Mass Trans.*, **46(7)**, 1171–1181, 2003.
- Kutateladze, S. S., *Fundamentals of Heat Transfer*, New York: Academic Press, 1963.
- Lee, H. J. and Lee, S. Y., Pressure drop correlations for two-phase flow within horizontal rectangular channels with small heights, *Int. J. Multiphase Flow*, **27(5)**, 783–796, 2001.

- Lin, S., Kwok, C. C. K., Li, R.-Y., Chen, Z.-H., and Chen, Z.-Y., Local frictional pressure drop during vaporization of R-12 through capillary tubes, *Int. J. Multiphase Flow*, **17**(1), 95–102, 1991.
- Liu, D. and Garimella, S. V., Investigation of liquid flow in microchannels, *J. Thermophys. Heat Trans.*, **18**(1), 65–72, 2004.
- Lockhart, R. W. and Martinelli, R. C., Proposed correlation of data for isothermal two-phase, two-component flow in pipes, *Chem. Eng. Prog.*, **45**(1), 39–45, 1949.
- Lowe, D. C. and Rezkallah, K. S., Flow regime identification in microgravity two-phase flows using void fraction signals *Int. J. Multiphase Flow*, **25**(3), 433–457, 1999.
- Lowry, B. and Kawaji, M., Adiabatic vertical two-phase flow in narrow flow channels, *Heat Transfer – Houston 1988, Papers Presented at the 25th National Heat Transfer Conference*, Houston, TX, AIChE, New York, NY, 133–139, 1988.
- Mandhane, J. M., Gregory, G. A., and Aziz, K., A flow pattern map for gas–liquid flow in horizontal pipes, *Int. J. Multiphase Flow*, **1**(4), 537–553, 1974.
- Matuszkiewicz, A., Flamand, J. C., and Boure, J. A., The bubble–slug flow pattern transition and instabilities of void fraction waves, *Int. J. Multiphase Flow*, **13**(2), 199–217, 1987.
- McAdams, W. H., *Heat Transmission*, New York: McGraw-Hill, 1954.
- Mikheev, M. A., *Heat Transfer Fundamentals*, Moscow: Gosenergoizdat, 1956.
- Miropolsky, Z. L., Heat transfer during condensation of high pressure steam inside a tube, *Teploenergetika*, **3**, 79–83, 1962.
- Mishima, K. and Hibiki, T., Some characteristics of air–water two-phase flow in small diameter vertical tubes, *Int. J. Multiphase Flow*, **22**(4), 703–712, 1996.
- Mishima, K. and Ishii, M., Flow regime transition criteria for upward two-phase flow in vertical tubes, *Int. J. Heat Mass Trans.*, **27**(5), 723–737, 1984.
- Mishima, K. and Hibiki, T., Development of high-frame-rate neutron radiography and quantitative measurement method for multiphase flow research, *Nucl. Eng. Des.*, **184**(2–3), 183–201, 1998.
- Mishima, K., Hibiki, T., and Nishihara, H., Some characteristics of gas–liquid flow in narrow rectangular ducts, *International Journal of Multiphase Flow International Conference on Multiphase Flows 91 – Tsukuba (ICM'91)*, September 23–27 1991, **19**(1), 115–124, 1993.
- Mishima, K., Hibiki, T., and Nishihara, H., Visualization and measurement of two-phase flow by using neutron radiography, *Nucl. Eng. Des.*, **175**(1–2), 25–35, 1997.
- Moore, A. E. and Turley, D. N., Two phase flow information from simple, rapid response time instruments, *Papers Presented at the International Conference on the Physical Modelling of Multi-Phase Flow*, April 19–21 1983, Coventry, UK, BHRA, 353–376, 1983.
- Moriyama, K., Inoue, A., and Ohira, H., Thermohydraulic characteristics of two-phase flow in extremely narrow channels (the frictional pressure drop and heat transfer of boiling two-phase flow, analytical model), *Heat Trans. – Jap. Res.*, **21**(8), 838–856, 1992a.
- Moriyama, K., Inoue, A., and Ohira, H., Thermohydraulic characteristics of two-phase flow in extremely narrow channels (the frictional pressure drop and void fraction of adiabatic two-component two-phase flow), *Heat Trans. – Jap. Res.*, **21**(8), 823–837, 1992b.
- Moser, K. W., Webb, R. L., and Na, B., A new equivalent Reynolds number model for condensation in smooth tubes, *Transac. ASME, J. Heat Trans.*, **120**(2), 410–417, 1998.
- Muller-Steinhagen, H. and Heck, K., A simple friction pressure drop correlation for two-phase flow in pipes, *Chem. Eng. Proces.*, **20**(6), 297–308, 1986.
- Nicholson, M. K., Aziz, K., and Gregory, G. A., Intermittent two phase flow in horizontal pipes: predictive models., **56**(6), 653–663, 1978.
- Nitheanandan, T., Soliman, H. M., and Chant, R. E., A proposed approach for correlating heat transfer during condensation inside tubes, *ASHRAE Trans. (1990 Winter Meeting, Atlanta, GA)*, **96**(1), 230–241, 1990.

- Nusselt, W., Die Oberflächen Kondensation des Wasserdampfes, *Zeit. Ver. Deut. Ing.*, **60(27, 28)**, 541–546, 569–575, 1916.
- Owens, W. L., Two-phase pressure gradient, *International Development in Heat Transfer, Part II*. New York: ASME, 1961.
- Palen, J. W., Breber, G., and Taborek, J., Prediction of flow regimes in horizontal tubeside condensation, *Proceedings of the 17th National Heat Transfer Conference, Salt Lake City, UT*, Salt Lake City, AIChE Paper No. 5, 1977.
- Palm, B., Heat transfer in microchannels, *Microscale Thermophys. Eng.*, **5(3)**, 155–175, 2001.
- Petukhov, B. S., Heat transfer and friction in turbulent pipe flow with variable physical properties, *Adv. Heat Trans.*, **6**, 503–564, 1970.
- Premoli, A., Francesco, D., and Prina, A., A dimensionless correlation for determining the density of two-phase mixtures, *La Termotecnica*, **25**, 17–26, 1971.
- Rabas, T. J. and Arman, B., Effect of the exit condition on the performance of in-tube condensers, *Heat Trans. Eng.*, **21(1)**, 4–14, 2000.
- Rezkallah, K. S., Recent progress in the studies of two-phase flow at microgravity conditions, *Adv. Space Res.*, **16(7)**, 123–132, 1995.
- Rezkallah, K. S., Weber number based flow-pattern maps for liquid–gas flows at microgravity, *Int. J. Multiphase Flow*, **22(6)**, 1265–1270, 1996.
- Rezkallah, K. S. and Zhao, L., A flow pattern map for two-phase liquid–gas flows under reduced gravity conditions, *Adv. Space Res.*, **16(7)**, 133–136, 1995.
- Rice, C. K., Effect of void fraction correlation and heat flux assumption on refrigerant charge inventory predictions, *ASHRAE Transactions: Technical and Symposium Papers Presented at the 1987 Winter Meeting*, New York, NY, ASHRAE, Atlanta, GA, 341–367, 1987.
- Richardson, B. L., Some problems in horizontal two-phase two-component flow, PhD Thesis, Mechanical Engineering, Purdue University, West Lafayette.
- Rohsenow, W. M., Heat transfer and temperature distribution in laminar–film condensation, *Am. Soc. Mech. Eng. – Transac.*, **78(8)**, 1645–1648, 1956.
- Rohsenow, W. M., Webber, J. H., and Ling, A. T., Effect of vapor velocity on laminar and turbulent–film condensation, *Am. Soc. Mech. Eng. – Transac.*, **78(8)**, 1637–1642, 1956.
- Rohsenow, W. M., Webber, J. H., and Ling, A. T., Effect of vapor velocity on laminar and turbulent–film condensation, *Am. Soc. Mech. Eng. – Transac.*, **78(8)**, 1637–1642, 1957.
- Rosson, H. F. and Myers, J. A., Point values of condensing film coefficients inside horizontal pipe, *Chem. Eng. Prog. Symp. Series*, **61(59)**, 190–199, 1965.
- Rouhani, S. Z. and Axelsson, E., Calculation of void volume fraction in the subcooled and quality boiling regions, *Int. J. Heat Mass Trans.*, **13(2)**, 383–393, 1970.
- Rouhani, S. Z. and Becker, K. M., Measurements of void fraction for flow boiling of heavy water in vertical round duct, *Aktebolaget Atomenergies Rep.* **AE-106**, 1963.
- Rufer, C. E. and Kezios, S. P., Analysis of two-phase, one-component stratified flow with condensation, *Am. Soc. Mech. Eng. – Transac. – J. Heat Trans.*, **88(3)**, 265–275, 1966.
- Sacks, P. S., Measured characteristics of adiabatic and condensing single-component two-phase flow of refrigerant in a 0.377-in. diameter horizontal tube, *Proceedings of the American Society of Mechanical Engineers Winter Annual Meeting*, 75-WA/HT-24, ASME, 12, 1975.
- Sadatomi, M., Sato, Y., and Saruwatari, S., Two-phase flow in vertical noncircular channels, *Int. J. Multiphase Flow*, **8(6)**, 641–655, 1982.
- Sardesai, R. G., Owen, R. G., and Pulling, D. J., Flow regimes for condensation of a vapour inside a horizontal tube, *Chem. Eng. Sci.*, **36(7)**, 1173–1180, 1981.
- Schlichting, H. and Gersten, K., Laminar–turbulent transition, *Boundary Layer Theory*, Springer: 415–490, 2000.

- Serizawa, A. and Feng, Z., Two-phase flow in micro-channels, *Proceedings of the 4th International Conference on Multiphase Flow*, New Orleans, LA, 2001.
- Serizawa, A. and Feng, Z., Two-phase fluid flow, *Heat Transfer and Fluid Flow in Microchannels*, G. P. Celata ed., New York, NY: Begell House, **1**, 91–117, 2004.
- Serizawa, A. and Kawara, Z., Two-phase flow in micro-channels, *Proceedings of the 39th European Two-Phase Flow Group Meeting*, Averio, Portugal, 2001.
- Serizawa, A., Feng, Z., and Kawara, Z., Two-phase flow in microchannels, *Exp. Therm. Fluid Sci.*, **26(6–7)**, 703–714, 2002.
- Shah, M. M., New correlation for heat transfer during boiling flow through pipes, *Proc. Annu. Meet.*, June 27–July 1 1976, **82(part)2**, 66–86, 1976.
- Shah, M. M., A general correlation for heat transfer during film condensation inside pipes, *Int. J. Heat Mass Trans.*, **22(4)**, 547–556, 1979.
- Shin, J. S. and Kim, M. H., An experimental study of flow condensation heat transfer inside circular and rectangular mini-channels, *Heat Trans. Eng.*, **26(3)**, 36–44, 2005.
- Singh, A., Ohadi, M. M., and Dessiatoun, S. V., Empirical modeling of stratified-wavy flow condensation heat transfer in smooth horizontal tubes, *ASHRAE Transac.*, **102(2)**, 596–603, 1996.
- Smith, S. L., Void fractions in two-phase flow: a correlation based upon an equal velocity head model, *Proceedings of the Institution of Mechanical Engineers, Thermodynamics and Fluid Mechanics Group*, 647–657, 1969.
- Sobhan, C. B. and Garimella, S. V., A comparative analysis of studies on heat transfer and fluid flow in microchannels, *Micros. Thermophys. Eng.*, **5(4)**, 293–311, 2001.
- Soliman, H. M., On the annular-to-wavy flow pattern transition during condensation inside horizontal tubes, *Can. J. Chem. Eng.*, **60(4)**, 475–481, 1982.
- Soliman, H. M., Correlation of mist-to-annular transition during condensation, *Can. J. Chem. Eng.*, **61(2)**, 178–182, 1983.
- Soliman, H. M., Mist–annular transition during condensation and its influence on the heat transfer mechanism, *Int. J. Multiphase Flow*, **12(2)**, 277–288, 1986.
- Soliman, H. M., Schuster, J. R., and Berenson, P. J., A general heat transfer correlation for annular flow condensation, *J. Heat Trans.*, **90**, 267–276, 1968.
- Souza, A. L., Chato, J. C., Wattleit, J. P., and Christoffersen, B. R., Pressure drop during two-phase flow of pure refrigerants and refrigerant-oil mixtures in horizontal smooth tubes, *29th National Heat Transfer Conference*, August 8–11 1993, Atlanta, GA, ASME, New York, NY, 35–41, 1993.
- Souza, D. A. L. and Pimenta, M. D. M., Prediction of pressure drop during horizontal two-phase flow of pure and mixed refrigerants, *Proceedings of the 1995 ASME/JSME Fluids Engineering and Laser Anemometry Conference and Exhibition*, August 13–18 1995, Hilton Head, SC, ASME, New York, NY, 161–171, 1995.
- Steiner, D., Heat transfer to boiling saturated liquids. *VDI-Wär meatlas (VDI Heat Atlas)*. Düsseldorf, VDI-Gesellschaft Verfahrenstechnik und Chemieingenieurwesen (GCV), (Translator: J.W. Fullarton), 1993.
- Sugawara, S., Katsuta, K., Ishihara, I., and Muto, T., Consideration on the pressure loss of two-phase flow in small-diameter tubes, *Proceeding 4th National Heat Transfer Symposium of Japan (in Japanese)*, 169–172, 1967.
- Suo, M. and Griffith, P., Two-phase flow in capillary tubes, *J. Basic Eng.*, **86**, 576–582, 1964.
- Tabatabai, A. and Faghri, A., A new two-phase flow map and transition boundary accounting for surface tension effects in horizontal miniature and micro tubes, *J. Heat Trans.*, **123(5)**, 958–968, 2001.
- Taitel, Y. and Dukler, A. E., A model for predicting flow regime transitions in horizontal and near horizontal gas–liquid flow, *AIChE J.*, **22(1)**, 47–55, 1976.
- Taitel, Y., Bornea, D., and Dukler, A. E., Modelling flow pattern transitions for steady upward gas–liquid flow in vertical tubes, **26(3)**, 345–354, 1980.

- Tandon, T. N., Varma, H. K., and Gupta, C. P., New flow regimes map for condensation inside horizontal tubes, *J. Heat Trans.*, **104**(4), 763–768, 1982.
- Tandon, T. N., Varma, H. K., and Gupta, C. P., Prediction of flow patterns during condensation of binary mixtures in a horizontal tube, *J. Heat Trans., Transac. ASME*, **107**(2), 424–430, 1985a.
- Tandon, T. N., Varma, H. K., and Gupta, C. P., A void fraction model for annular two-phase flow, *Int. J. Heat Mass Trans.*, **28**(1), 191–198, 1985b.
- Tandon, T. N., Varma, H. K., and Gupta, C. P., Heat transfer during forced convection condensation inside horizontal tube, *Int. J. Refrig.*, **18**(3), 210–214, 1995.
- Tang, L., Empirical study of new refrigerant flow condensation inside horizontal smooth and micro-fin tubes, PhD Dissertation, University of Maryland at College Park, 1997.
- Thom, J. R. S., Prediction of pressure drop during forced circulation boiling of water, *Int. J. Heat Mass Trans.*, **7**(7), 709–724, 1964.
- Thome, J. R., El Hajal, J., and Cavallini, A., Condensation in horizontal tubes, part 2: new heat transfer model based on flow regimes, *Int. J. Heat Mass Trans.*, **46**(18), 3365–3387, 2003.
- Tran, T. N., Chyu, M.-C., Wambsganss, M. W., and France, D. M., Two-phase pressure drop of refrigerants during flow boiling in small channels: an experimental investigation and correlation development, *Int. J. Multiphase Flow*, **26**(11), 1739–1754, 2000.
- Traviss, D. P. and Rohsenow, W. M., Flow regimes in horizontal two-phase flow with condensation, *ASHRAE Transac.*, **79**(Part 2), 31–39, 1973.
- Traviss, D. P., Rohsenow, W. M., and Baron, A. B., Forced-convection condensation inside tubes: a heat transfer equation for condenser design, *ASHRAE Transac.*, **79**(1), 157–165, 1973.
- Triplett, K. A., Ghiaasiaan, S. M., Abdel-Khalik, S. I., LeMouel, A., and McCord, B. N., Gas–liquid two-phase flow in microchannels: part II: void fraction and pressure drop, *Int. J. Multiphase Flow*, **25**(3), 395–410, 1999a.
- Triplett, K. A., Ghiaasiaan, S. M., Abdel-Khalik, S. I., and Sadowski, D. L., Gas–liquid two-phase flow in microchannels: part I: two-phase flow patterns, *Int. J. Multiphase Flow*, **25**(3), 377–394, 1999b.
- Troniewski, L. and Ulbrich, R., Two-phase gas–liquid flow in rectangular channels, *Chem. Eng. Sci.*, **39**(4), 751–765, 1984.
- Tung, K. W. and Parlange, J. Y., Note on the motion of long bubbles in closed tubes – influence of surface tension, *Acta Mech.*, **24**(3–4), 313–317, 1976.
- Unesaki, H., Hibiki, T., and Mishima, K., Verification of neutron radioscopic measurement of void fraction by Monte Carlo simulation, *Nucl. Instrum. Meth. Phys. Res. Sec. A: Acceler., Spectr., Detect. Assoc. Equip.*, **405**(1), 98–104, 1998.
- Ungar, E. K. and Cornwell, J. D., Two-phase pressure drop of ammonia in small diameter horizontal tubes, *AIAA paper 92-3891*, 1992.
- van Driest, E. R., On turbulent flow near a wall, *J. Aeronaut. Sci.*, **23**, 1007–1011, 1956.
- Wadekar, V. V., Flow boiling. A simple correlation for convective heat transfer component, *Heat Transfer, Proceedings of the International Heat Transfer Conference*, 87, 1990.
- Wallis, G. B., *One-Dimensional Two-Phase Flow*. New York, NY: McGraw-Hill, 1969.
- Wambsganss, M. W., Jendrzeczyk, J. A., and France, D. M., Two-phase flow patterns and transitions in a small, horizontal, rectangular channel, *Int. J. Multiphase Flow*, **17**(3), 327–342, 1991.
- Wambsganss, M. W., Jendrzeczyk, J. A., France, D. M., and Obot, N. T., Frictional pressure gradients in two-phase flow in a small horizontal rectangular channel, *Exp. Therm. Fluid. Sci.*, **5**(1), 40–56, 1992.
- Wambsganss, M. W., Jendrzeczyk, J. A., and France, D. M., Determination and characteristics of the transition to two-phase slug flow in small horizontal channels, *J. Fluid. Eng., Transac. ASME*, **116**(1), 140–146, 1994.

- Wang, C. C., Chiang, C. S., Lin, S. P., and Lu, D. C., Two-phase flow pattern for R-134a inside a 6.5-mm (0.25-in.) smooth tube, *Proceedings of the 1997 ASHRAE Winter Meeting*, January 26–29 1997, Philadelphia, PA, ASHRAE, Atlanta, GA, 803–812, 1997a.
- Wang, C.-C., Chiang, C.-S. and Lu, D.-C., Visual observation of two-phase flow pattern of R-22, R-134a, and R-407C in a 6.5-mm smooth tube, *Exp. Therm. Fluid Sci.*, **15**(4), 395–405, 1997b.
- Wang, H. S. and Rose, J. W., Film condensation in horizontal triangular section microchannels: A theoretical model, *Proceedings of the Second International Conference on Microchannels and Minichannels (ICMM2004)*, June 17–19 2004, Rochester, NY, USA, American Society of Mechanical Engineers, New York, NY 10016-5990, USA, 661–666, 2004.
- Wang, H. S. and Rose, J. W., A theory of condensation in horizontal non-circular microchannels, *ASME J. Heat Trans.*, **in press**, 2005.
- Wang, H. S., Rose, J. W., and Honda, H., A theoretical model of film condensation in square section horizontal microchannels, *Chem. Eng. Res. Des.*, **82**(4), 430–434.
- Wang, W. W.-W., Radcliff, T. D., and Christensen, R. N., A condensation heat transfer correlation for millimeter-scale tubing with flow regime transition, *Exp. Therm. Fluid Sci.*, **26**(5), 473–485, 2002.
- Wattelet, J. P., Chato, J. C., Souza, A. L., and Christoffersen, B. R., Evaporative characteristics of R-12, R-134a, and a mixture at low mass fluxes, *Proceedings of the ASHRAE Winter Meeting*, January 23–26 1994, New Orleans, LA, ASHRAE, Atlanta, GA, 603–615, 1994.
- Webb, R. L. and Ermis, K., Effect of hydraulic diameter on condensation of R-134A in flat, extruded aluminum tubes, *J. Enhanc. Heat Trans.*, **8**(2), 77–90, 2001.
- Webb, R. L. and Lee, H., Brazed aluminum condensers for residential air conditioning, *J. Enhanc. Heat Trans.*, **8**(1), 1–13, 2001.
- Weisman, J., Duncan, D., Gibson, J., and Crawford, T., Effects of fluid properties and pipe diameter on two-phase flow patterns in horizontal lines, *Int. J. Multiphase Flow*, **5**(6), 437–462, 1979.
- Wilmarth, T. and Ishii, M., Two-phase flow regimes in narrow rectangular vertical and horizontal channels, *Int. J. Heat Mass Trans.*, **37**(12), 1749–1758, 1994.
- Wilson, M. J., Newell, T. A., Chato, J. C., and Infante Ferreira, C. A., Refrigerant charge, pressure drop, and condensation heat transfer in flattened tubes, *Int. J. Refrig.*, **26**(4), 442–451, 2003.
- Xu, J., Experimental study on gas–liquid two-phase flow regimes in rectangular channels with mini gaps, *Int. J. Heat Fluid Flow*, **20**(4), 422–428, 1999.
- Xu, J. L., Cheng, P., and Zhao, T. S., Gas–liquid two-phase flow regimes in rectangular channels with mini/micro gaps, *Int. J. Multiphase Flow*, **25**(3), 411–432, 1999.
- Yan, Y.-Y. and Lin, T.-F., Condensation heat transfer and pressure drop of refrigerant R-134a in a small pipe, *Int. J. Heat Mass Trans.*, **42**(4), 697–708, 1999.
- Yang, C.-Y. and Shieh, C.-C., Flow pattern of air–water and two-phase R-134a in small circular tubes, *Int. J. Multiphase Flow*, **27**(7), 1163–1177, 2001.
- Yang, C.-Y. and Webb, R. L., Condensation of R-12 in small hydraulic diameter extruded aluminum tubes with and without micro-fins, *Int. J. Heat Mass Trans.*, **39**(4), 791–800, 1996a.
- Yang, C.-Y. and Webb, R. L., Friction pressure drop of R-12 in small hydraulic diameter extruded aluminum tubes with and without micro-fins, *Int. J. Heat Mass Trans.*, **39**(4), 801–809, 1996b.
- Yang, C.-Y. and Webb, R. L., Predictive model for condensation in small hydraulic diameter tubes having axial micro-fins, *J. Heat Trans., Transac. ASME*, **119**(4), 776–782, 1997.
- Yashar, D. A., Graham, D. M., Wilson, M. J., Chato, J. C., Kopke, H. R., and Newell, T. A., Investigation of refrigerant void fraction in horizontal, microfin tubes, *HVAC&R Res.*, **7**(1), 67–82, 2001.
- Zhang, M. and Webb, R. L., Correlation of two-phase friction for refrigerants in small-diameter tubes, *Exp. Therm. Fluid Sci.*, **25**(3–4), 131–139, 2001.
- Zhao, L. and Rezkallah, K. S., Pressure drop in gas–liquid flow at microgravity conditions, *Int. J. Multiphase Flow*, **21**(5), 837–849, 1995.

- Zhao, T. S. and Bi, Q. C., Co-current air–water two-phase flow patterns in vertical triangular microchannels, *Int. J. Multiphase Flow*, **27(5)**, 765–782, 2001a.
- Zhao, T. S. and Bi, Q. C., Pressure drop characteristics of gas–liquid two-phase flow in vertical miniature triangular channels, *Int. J. Heat Mass Trans.*, **44(13)** 2523–2534, 2001b.
- Zivi, S. M., Estimation of steady-state steam void-fraction by means of the principle of minimum entropy production, *J. Heat Trans.*, **86**, 247–252, 1964.
- Zuber, N. and Findlay, J. A., Average volumetric concentration in two-phase flow systems, *J. Heat Trans.*, **87**, 453, 1965.
- Zukoski, E. E., Influence of viscosity, surface tension, and inclination angle on motion of long bubbles in closed tubes, *J. Fluid Mech.*, **25(Part 4)**, 821–837, 1966.
- Zurcher, O., Thome, J. R., and Favrat, D., Evaporation of ammonia in a smooth horizontal tube: heat transfer measurements and predictions, *J. Heat Trans., Trans. ASME*, **121(1)**, 89–101, 1999.

Chapter 7

BIOMEDICAL APPLICATIONS OF MICROCHANNEL FLOWS

Michael R. King

*Departments of Biomedical Engineering and Chemical Engineering, University of Rochester,
Rochester, NY, USA*

7.1. Introduction

As more is learned about the molecular and cellular biology of human and model organism cells in the contexts of normal physiological function and disease pathology, it is the role of bioengineers to apply this knowledge towards the improvement of public health and alleviation of human suffering. The control and manipulation of living cells outside of the body presents technical challenges which physical conditions such as temperature and pH must be maintained close to their physiological values of 37°C and 7.4, respectively; if these quantities deviate by as much as 10% then cells cannot survive for long periods of time. With greater deviations from physiological baseline, proteins and other macromolecules themselves begin to degrade. The complete sequencing of the human genome at the start of the 21st century has placed an increased interest in the development of high-throughput microfluidic technologies to assay thousands of genes simultaneously. The interest in transporting, manipulating, and synthesizing biomolecules in smaller and smaller conduits is motivated by a desire to automate biochemical protocols and eliminate some of the most mundane technical tasks, as well as a need to operate on extremely small sample sizes: for instance to identify individuals based on minute samples in forensic applications crime scenes or to detect biochemical factors that may be produced in the body's tissues at nanomolar concentrations.

Microfluidics and microchannel transport processes have also led to the development of new research tools. We now have the ability to peer inside of microscopic cells and measure the interior rheology of their cytoplasm, and visualize the co-localization of specific proteins within various organelles. Micron-sized pipettes are able to enter a cell, remove its nuclear material, and inject this DNA “soup” into a different cell to achieve cloning of animals and humans (in the case of humans, therapeutic rather than reproductive). Another

E-mail: mike_king@urmc.rochester.edu

area of great research interest is in the precise measurement of the specific adhesion of cells with other contacting surfaces. Many of the surface receptor proteins presented by cells are themselves exquisitely sensitive detectors of soluble chemical concentration, and force transducers that can initiate rapid chain reactions within the cell compartments. In this chapter we discuss some of the different technological applications of microchannels and minichannels to measure the strength and frequency of individual cell adhesion, grow cells to replace vital organs, peel cells from protein-coated surfaces using well-defined forces, and characterize the deformability of different cell types. In each case, we apply fundamentals from transport phenomena to understand and model these biological applications.

7.2. Microchannels to probe transient cell adhesion under flow

Microchannels with functionalized biochemical surfaces have been quite useful in elucidating the molecular mechanisms governing the transient adhesion between circulating white blood cells (leukocytes) and the blood vessel wall during inflammation. The selectins are a family of adhesion molecules that recognize a tetrasaccharide moiety called sialyl Lewis^x presented by many glycoprotein ligands expressed on cell surfaces, and are involved in the trafficking of leukocytes throughout the systemic and lymphatic circulations (Lasky, 1995; Ebnet and Vestweber, 1999). The selectin-carbohydrate bond is of high specificity, high affinity, and exhibits fast rates of formation and dissociation. The rate of dissociation is a dominant physical parameter, distinct for each of the three identified selectins P-, E-, and L-selectin, and has been demonstrated to exhibit an exponential dependence on the force loading on the bond (Smith *et al.*, 1999). The same molecular mechanisms that mediate acute inflammatory responses under physiological conditions are also responsible for chronic inflammation, vessel occlusion, and other disease states featuring abnormal accumulations of adherent leukocytes or platelets (Ramos *et al.*, 1999). Many of the biological complexities of this myriad of surface interactions between leukocytes, platelets, and endothelial cells have been revealed using idealized microchannel assays and semi-quantified using knockout mice. There is currently a tremendous opportunity to advance our understanding of selectin biology in the context of inflammatory and cardiovascular disease by applying engineering tools to integrate this knowledge into descriptive and predictive models of blood cell interactions in more realistic settings.

In addition to creating a well-defined flow field to study the balance between fluid forces and chemical adhesion of blood cells, microchannels, minichannels, and corresponding numerical simulations have been successfully developed to more closely mimic flow irregularities found in the diseased human circulatory system. The deposition of platelets on surfaces in complex flow geometries such as stenosis, aneurysm, or flow over a protrusion, has been characterized *in vitro* by several groups (Karino and Goldsmith, 1979; Tippe *et al.*, 1992; Schoephoerster *et al.*, 1993; Slack and Turitto, 1994). These studies support the idea that flow non-idealities are important in modulating thrombotic phenomena, yet lack the spatial and temporal resolution necessary to support detailed cellular-scale modeling. In hypercholesterolemic rabbits and mice, monocytes preferentially deposit around aortic and celiac orifices, due to local flow characteristics in these regions (Back *et al.*, 1995; Walpolá *et al.*, 1995; Nakashima *et al.*, 1998; Iiyama *et al.*, 1999;

Truskey *et al.*, 1999). Endothelial cell layers respond to disturbed shear fields (e.g. flow over a rectangular obstacle) by upregulating expression of adhesion molecules, resulting in a general increase in the number of cells recruited downstream of such an obstacle (DePaola *et al.*, 1992; Pritchard *et al.*, 1995; Barber *et al.*, 1998). Multiple groups have attempted to model the particulate flow of blood through complex vessel geometries with and without particle deposition at the walls, while neglecting hydrodynamic cell–cell interactions (Perktold, 1987; Lei *et al.*, 1997). Despite theoretical limitations, such studies have been applied towards providing recommendations for surgical reconstruction procedures, and the design of commercial grafts that minimize particle deposition based on stresses exerted by the fluid on the wall surfaces. Others have computationally studied shear-activation and surface deposition of platelets by treating the cells as infinitesimal points (Bluestein *et al.*, 1999; Kuharski and Fogelson, 2001). The MAD simulation (King and Hammer, 2001a, b) joins a rigorous calculation of multiparticle fluid flow with a realistic model for specific cell–cell adhesion. Work with MAD has revealed biophysical mechanisms that control dynamic cell adhesion under flow, that have been verified experimentally both in microchannel experiments (King and Hammer, 2003) and *in vivo* (King *et al.*, 2003). Further understanding of the rate of atherogenesis and risk of acute thrombotic events will occur through careful computer and *in vitro* models that are developed to consider the near-wall cell–cell hydrodynamic interactions that occur during cell deposition in diseased vessel geometries.

7.2.1. Different types of microscale flow chambers

The most common types of microchannels used in cell adhesion and flow studies are the radial flow chamber (Kuo and Lauffenberger, 1993; Goldstein and DiMilla, 1998), and the parallel-plate flow chamber (Sung *et al.*, 1985; Palecek *et al.*, 1997). Such systems have found widespread use for the following applications:

- (a) measurement of transient adhesion of circulating (i.e. blood) cells to reactive surfaces under flow,
- (b) use of well-defined shear stresses to measure the detachment force of strongly adherent cells,
- (c) measurement of the biological response of a cell layer to long-term exposure to physiological levels of steady or pulsatile shear stress,
- (d) monitoring the real-time formation of biofilms on flow-exposed surfaces.

Figure 7.1 shows a diagrammatic representation of the radial and parallel-plate flow chamber geometries. The main advantage of the radial flow chamber comes from the fact that as the fluid introduced at the center of the chamber flows radially outward, it passes through a larger and larger cross-section around the perimeter and thus the linear velocity of the fluid decreases smoothly as it flows from the inner to outer regions. As a result, the fluid samples a wide range of wall shear stresses, from a high value near the center to a minimum value at the outer edge of the chamber. If the entire surface of interest is imaged from below at low magnification, then one can obtain interaction data such as the number of adherent cells or the cell translational velocities for a range of shear stress values at once rather than having to perform repeated experiments at many different flow rates. It

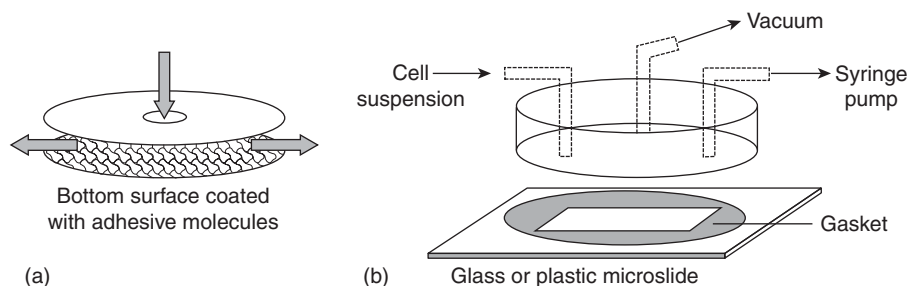


Fig. 7.1. Diagram of (a) radial and (b) parallel-plate cell perfusion chambers.

is straightforward to show (see Problem 7.1) that the wall shear stress in the radial flow assay will exhibit the following dependence on radial position r :

$$\tau = \frac{3Q\mu}{\pi r H^2} \quad (7.1)$$

where Q is the volumetric flowrate, μ is the fluid viscosity, and H is the spacing between the upper and lower surfaces.

A more detailed diagram of the parallel-plate flow chamber assay is depicted in Fig. 7.1(b). This shows a common design, where a reusable upper surface is brought into contact with a rubber gasket laid over a disposable glass or plastic microslide. The microslide can be incubated with relevant adhesion or extracellular matrix proteins of interest, or else cultured with cells until a confluent monolayer is achieved. The upper surface of the flow chamber is fitted with luer fittings that attach to inlet and outlet streams to allow for the perfusion of cell media, or suspensions of cells or microsphere particles coated with their own appropriate molecules. A third fitting is commonly attached to a vacuum line, which for typical chamber sizes and physiological fluid flowrates is sufficient to hold together the top and bottom of the chamber without the use of bolts or mechanical clamps. The flow domain is defined by a rectangular, cut-out region in the rubber gasket, which necessarily overlaps with the inlet and outlet ports (but not with the vacuum port). Most cell perfusion chambers are specially designed so that the outer dimensions are compatible with standard sizes of polystyrene tissue culture plates or round glass coverslips, which facilitate the exchange of materials and protocols between different laboratories. Many such parallel-plate cell perfusion assays are now commercially available, in smaller and smaller volumes to minimize the amount of rare and valuable materials needed to conduct each experiment. Table 7.1 shows a sampling of the parallel-plate chambers currently available commercially, along with the reported ranges of channel dimension.

7.2.2. Inverted systems: well-defined flow and cell visualization

The flat lower wall of the parallel-plate microchannel provides an excellent surface to study cellular adhesive interactions. As discussed below, the slightly greater density of cells relative to saline buffer or cell media (\approx water) causes sedimentation of cells to the lower

Table 7.1

Some commercially available microchannels and minichannels for cell perfusion.

Model	Manufacturer	Channel height H (μm)
ECIS flow system	Applied BioPhysics	1000
Stovall flow cell	Stovall Life Science, Inc.	1000
DH-40i micro-incubator	Warner Instruments, Inc.	800–980
Flow chamber system	Oligene	300–500
Cell adhesion flow chamber	Immunogenics, Inc.	250
Vacu-cell	C & L Instruments, Inc.	250
Circular flow chamber	Glycotech Corporation	125–250
Focht chamber system 2	Intracel Ltd.	100–1000

surface. Thus, relatively dilute systems of 10^6 cells/ml (volume fraction $\sim 5 \times 10^{-4}$ for 10- μm -diameter cells) can be used while still obtaining a large number of individual interactions for study. Although the geometry of the microcirculation more closely resembles circular glass capillaries, and capillaries can be commercially purchased with very accurate inner diameters ranging from 3–1000 μm , round capillaries have some disadvantages compared to planar channels. The circular outer geometry of capillaries creates lensing effects which interfere with accurate imaging of the inner surface. Submersion of the entire capillary within index of refraction-matched objective oil improves this to some degree. However, due to sedimentation effects, the surface area available for cellular interactions is less in the capillary geometry. For these reasons as well as to simplify theoretical modeling, the parallel-plate geometry is the most popular method for studying cell–surface interactions under flow. High-quality images of cells adhesively attaching to molecular surfaces can be obtained as shown in Fig. 7.2, and cells grown under a variety of conditions can be exposed to fluid flow or brought into contact with suspended particles of interest.

A crucial element of bioengineering experiments in parallel-plate flow chambers is that near the lower wall of the microchannel, the parabolic fluid velocity profile can be approximated as linear shear flow. In most cases this assumption is valid, and simplifies the analysis. Figure 7.3 shows a comparison of parabolic versus linear flow in a 200 μm channel, within 10 μm of the lower wall. This distance is relevant to most cell adhesion studies, where cells above this distance are readily identified and ignored since they are too far from the molecular lower surface to interact adhesively. In Fig. 7.3 the parabolic velocity lies within 5% of the linear approximation for $x \leq 10 \mu\text{m}$.

Different optical techniques are useful for tracking the motion of individual cells near the surface when physiological concentrations of blood cells are used. For instance, it is often difficult to obtain clear images through whole blood in either bright field or phase contrast imaging modes, since visualization of the lower surface on an inverted microscope using a trans-illumination modality requires light transmission from the condenser through the entire sample of the dense suspension of red cells. Epifluorescence mode, on the other hand, is illuminated from below and thus there is minimal light loss due to the red cells flowing above the surface. Additionally, for large-scale cell deposition studies it is not necessary to resolve individual cells, but rather, an intensity average over the entire view can be taken and related to the average concentration of fluorescently labeled cells within the image.

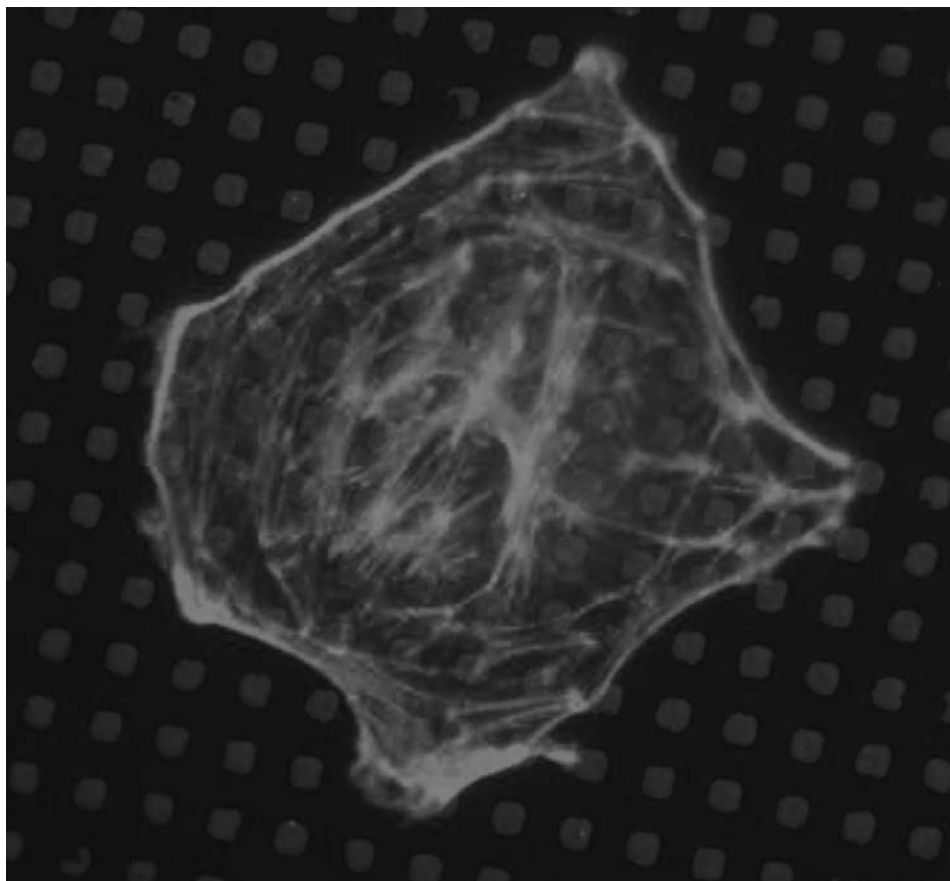


Fig. 7.2. Bovine aortic endothelial cell fluorescently labeled with phalloidin, which shows the interior cytoskeleton of the cell. The cell is adhering to a $3 \times 3 \mu\text{m}$ micropattern of fibronectin protein, also fluorescently labeled. Such cell growth experiments can be performed on the lower surface of a parallel-plate microchannel, to later expose cells to fluid shear stress or to easily exchange the fluid environment. Image courtesy of M. Mancini, K. Fujiwara, G. Csucs, and M. King.

Many fluorescent dyes are available for different blood cells that do not affect their surface adhesiveness, such as fluorochrome carboxyfluorescein diacetate succinimidyl ester for blood platelets, or calcein-AM for leukocytes.

Despite the obvious advantages to the inverted microchannel geometry, one must be aware of anomalous behavior that may be less important within the body. Most previous studies of leukocyte adhesion under flow have been performed with dilute leukocyte suspensions in a parallel-plate flow chamber, with observation of the lower surface on an inverted microscope. There it is recognized that gravitational sedimentation promotes initial contact between the cells and the reactive surface. Indeed, in similar dilute experiments Lawrence *et al.* (1997) showed that inverting the flow chamber completely abolishes new interactions, but previously rolling cells will continue to roll under flow. *In vivo*, at

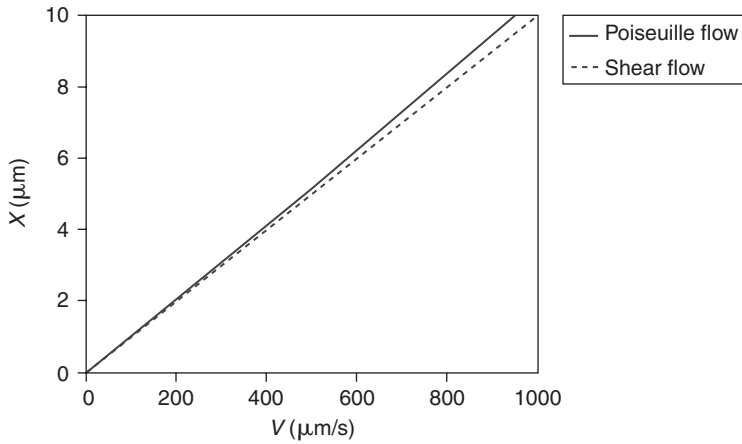


Fig. 7.3. Comparison of parabolic Poiseuille flow and linear shear flow in the vicinity of the lower wall in a $200\text{ }\mu\text{m}$ microchannel. The wall shear rate has been set at 100 s^{-1} .

physiological concentrations of red blood cells, the situation is quite different, with red cells migrating toward the center of the vessel and displacing the less deformable leukocytes to the near-wall region (a process called “margination”; see for instance Goldsmith and Spain, 1984). An erythrocyte-depleted plasma layer, containing leukocytes and platelets, is formed adjacent to the vessel wall. Cell collisions can promote initial contact between leukocytes and the vessel wall; this may help to explain how roughly equal numbers of rolling leukocytes are visible on the upper and lower walls of intact mouse and hamster microvessels. There is a subtle effect of gravity in real vessels however, as evidenced by a study by Bishop *et al.* (2001) who observed flow of whole blood in horizontally and vertically oriented microvessels in rat spinotrapezius muscle. They observed a symmetrical plasma layer in vertically oriented venules, whereas in horizontally oriented venules the plasma layer formed near the upper wall. Similarly, gravitational effects of whole blood flow in rectangular channels can be minimized by orienting the channel vertically (Abbitt and Nash, 2001), yet when optically imaging leukocytes through regions $>40\text{ }\mu\text{m}$ the same complications of fluorescence labeling occur as described above. A theoretical comparison of gravitational effects and normal forces at the tips of leukocyte microvilli suggest that surface interactions can dominate over gravity under the proper conditions (Zhao *et al.*, 2001). To summarize, gravity plays a more important role in microchannel flow chamber experiments compared to *in vivo*. However, control experiments can be performed by density-matching the solution to the suspended cells, via addition of high-molecular weight dextran (shown to not interfere with selectin adhesion; Chen and Springer, 2001) to separate out any artifactual effects of gravitational sedimentation.

7.2.3. Lubrication approximation for a gradually converging (or diverging) channel

One potential application of microchannels in the study and manipulation of circulating cells is the use of very small-gap channels ($H \leq 10\text{ }\mu\text{m}$) to continuously exert

high mechanical stresses on 8–10 μm blood cells or blood cell precursors as they pass through such a device. Indeed, such mechanical stresses, that approximate the close-packing of cells within the bone marrow, may in fact be necessary for proper maturation of red blood cells and explain why production of healthy red cells has proven to be so challenging *in vitro* (Waugh *et al.*, 2001). In such small microchannels created by the orientation of two parallel plates in close proximity to each other, whether the gap is maintained by rubber gaskets or particulate spacers, one must be concerned about the exact alignment of the bounding walls. Specifically, a slight tilt to either surface with respect to the primary flow direction will create either a converging or diverging flow, which could significantly influence bulk flow characteristics and design issues such as the total pressure drop across the microchannel. If polystyrene slides are used as the bounding surfaces, flexing of the wall at high pressures could also result in a deviation from parallel alignment.

Figure 7.4 shows a diagram of the gradually converging channel geometry, symmetric about the centerline $x = 0$. The corresponding plane Poiseuille flow solution for the velocity profile is:

$$v_z = \frac{H^2}{8\mu} \left(-\frac{dp}{dz} \right) \left[1 - \left(\frac{2x}{H} \right)^2 \right] \quad (7.2)$$

where the differential version of the pressure drop is used, to allow generalization to a slowly varying channel cross-section. Similarly, for plane Poiseuille flow the flow rate per unit width, q is:

$$q = \frac{H^3}{12\mu} \left(-\frac{dp}{dz} \right) \quad (7.3)$$

For small variation in the channel spacing, $(H_1 - H_2)/H_1 \ll 1$, it can be assumed that the flow will deviate from the plane Poiseuille solution only slightly. Thus, we are justified in assuming that Eqs. (7.2) and (7.3) will remain valid for the case depicted in Fig. 7.4, only with H as a slowly varying function of z . Since the flowrate through any cross-section must be a constant, we conclude that the local pressure gradient must have the following spatial dependence:

$$\frac{dp}{dz} \sim \frac{1}{H^3(z)} \quad (7.4)$$

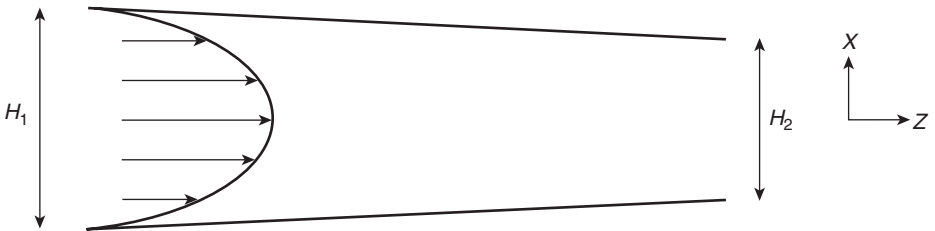


Fig. 7.4. Pressure-driven flow through a gradually converging channel. In the general case of a curved upper surface, the position of the upper wall is defined by $x = H(z)$.

Thus, rearranging Eq. (7.3) for the local pressure drop in the gradually converging channel yields the expression:

$$\frac{dp}{dz} = -\frac{12\mu q}{H^3(z)} \quad (7.5)$$

Equation (7.5) can be integrated over the length of the channel $L = z_2 - z_1$, to give the overall pressure drop across the converging channel,

$$\Delta p = -12\mu q \int_{z_1}^{z_2} H^{-3}(z) dz \quad (7.6)$$

For a simple linear variation in channel height of the form

$$H(z) = H_1 + \left(\frac{H_1 - H_2}{z_1 - z_2} \right) (z - z_1) \quad (7.7)$$

the solution to Eq. (7.6) becomes

$$\Delta p = -6\mu q \left(\frac{L}{H_1 - H_2} \right) \left[\frac{1}{H_2^2} - \frac{1}{H_1^2} \right] \quad (7.8)$$

This can be compared to the pressure drop across a uniform planar channel,

$$\Delta p = -12\mu q \left(\frac{L}{H} \right) \frac{1}{H^2} \quad (7.9)$$

Figure 7.5 shows the ratio of the total pressure drop across the converging channel to the total pressure drop in a truly parallel channel evaluated at either the initial height (upper, solid line),

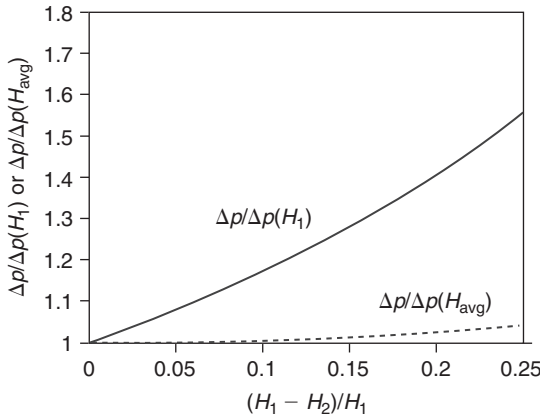


Fig. 7.5. Plot of the ratio of the pressure drop over a gradually converging channel to the pressure drop in a parallel channel evaluated at either the initial height (upper, solid line) or the average height (lower, dashed), as a function of the dimensionless height difference. Note from the upper curve that a dimensionless height difference of $(H_1 - H_2)/H_1 = 0.25$ results in an increase in total pressure drop of 55% relative to a parallel channel with a spacing of H_1 (upper curve), however, evaluating the pressure drop at the mean channel height (lower curve) captures all but 5% of this increase.

solid curve) or evaluated at the average height (lower, dashed curve). Note that using the average height in Eq. (7.9) yields an estimate for the pressure drop in a converging channel that is accurate to within 90%.

7.3. Microchannels and minichannels as bioreactors for long-term cell culture

Bioreactors are liquid vessels in which live populations of suspended or surface-attached cells can be maintained for extended periods of time, either for expansion and differentiation of a desired cell type, or for the mass production of a biomolecule produced by the cells. Bioreactors usually feature gas and/or liquid exchange, to replenish nutrients to the cells as they are consumed and to remove waste and other products made by the cells. While commercial cell-based production of small molecules (e.g., ethanol) or proteins involves the scale up of bioreactors to > 1000 gallon tanks, there is much interest in miniaturizing bioreactors for use as bioartificial organ replacement of the pancreas (Sullivan *et al.*, 1991), liver (Juaregui *et al.*, 1997), and kidney (Cieslinski and Humes, 1994). These bioartificial organs, in which one or more live cell populations are combined with artificial engineered materials, must replace the following functions of the native organs (Fournier, 1999):

- (i) *Pancreas*: The main purpose of the pancreas is to regulate glucose levels in the body by hosting insulin-producing cells in small clusters of cells called the “islets of Langerhans”. There is a great need for the restoration of pancreatic function among those afflicted with insulin dependent diabetes mellitus (IDDM).
- (ii) *Liver*: The human liver is a large (~1500 g), highly vascularized organ that receives 25% of the cardiac output, and performs a variety of crucial life functions. The liver stores and releases excess glucose, is the primary organ for fat metabolism, and produces virtually all of the plasma proteins other than antibodies. The main engineering challenge in developing a bioartificial liver replacement is that the organ is home to nearly 250 billion hepatocyte cells, each around 25 μm in diameter!
- (iii) *Kidney*: Among the vital responsibilities of the kidneys are filtration of, and waste removal from, the blood, regulation of red cell production within the bone marrow, and rapid control of blood pressure through the production of vasoactive molecules.

Microchannels and minichannels provide an excellent opportunity to maximize surface area available for monolayer cell attachment, while enabling good temperature regulation and rapid exchange of liquid media. Successful miniaturization of bioreactors for organ replacement could result in a device that may be comfortably worn outside the body, or even potentially implanted within the abdominal cavity. Another potential advantage of microchannels as bioreactors and the local flow environments that they are able to produce is that many cell types such as osteoblasts (bone cells) and endothelial cells (blood vessel lining) have evolved to prefer constant exposure to shear stresses >1 dyne/cm and exhibit normal phenotype only in such an environment.

7.3.1. Radial membrane minichannels for hematopoietic blood cell culture

Hematopoietic stem and precursor cells (HSPC) in the bone marrow are able to differentiate and produce all of the different types of blood cells in the body. Bone marrow cells grown

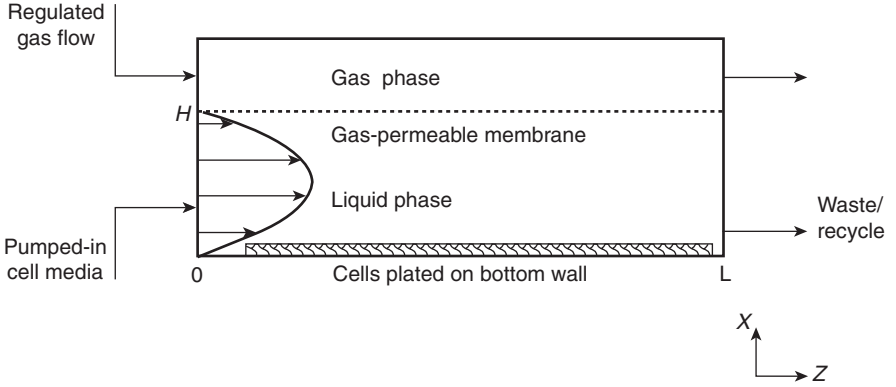


Fig. 7.6. Minichannel membrane bioreactor.

ex vivo maintain this pluripotent nature, and there is great interest in expanding blood cell populations in bioreactors for later transplantation to treat various blood disorders. The difficulty in growing large quantities of mammalian cells in culture is that oxygen is rapidly consumed and must be continuously replenished somehow. Peng and Palsson (1996) examined the potential of a radial membrane bioreactor to culture primary human mononuclear cells subjected to several growth factors (interleukin-3, granulocyte-macrophage colony-stimulating factor, erythropoietin) known to induce production of white and red blood cells. Figure 7.6 shows a diagram of a radial membrane bioreactor. Cell media saturated with oxygen enters the chamber from the left-hand-side, at a well-developed laminar velocity $u(x)$. Oxygen in the media is consumed by the cells near the lower surface. The fluid near the upper, gas-permeable membrane is assumed to be in equilibrium with the gas, and at the saturation oxygen concentration C_S . In such a system, the fluid velocity is chosen to be very low – typical transit times equal about 1.33 days. For comparison, the diffusivity of oxygen in protein solutions at 37°C has been measured to be $D = 2.69 \times 10^{-5} \text{ cm}^2/\text{s}$ (Goldstick, 1966). For a channel height of 3 mm, the characteristic time for diffusion from the upper membrane to the cell layer at the bottom of the channel is 1 h. Thus, in this case convective transport can be neglected and the oxygen transport is modeled as a one-dimensional diffusion equation of the form,

$$D \frac{\partial^2 C}{\partial x^2} = 0 \quad (7.10)$$

The boundary condition at the upper membrane is that the fluid is saturated with oxygen:

$$C = C_S \quad @x = H \quad (7.11)$$

and at the lower wall the flux is equal to the cellular uptake rate N_0 :

$$N_0 = D \frac{\partial C}{\partial x} \quad @x = 0 \quad (7.12)$$

Subject to these two conditions the solution to Eq. (7.10) is simply a linear concentration profile,

$$C(x) = C_S + \frac{N_0}{D}(x - H) \quad (7.13)$$

The uptake rate N_0 obeys Michaelis–Menten kinetics given by:

$$N_0 = \frac{qXC_0}{K_m + C_0} \quad (7.14)$$

where C_0 is the oxygen concentration at the lower wall, that is, the oxygen concentration experienced by the cells, q is the oxygen uptake rate on a per-cell basis, and X is the cell density. The Michaelis constant K_m , which can be interpreted as the concentration at which the uptake rate is half-maximum, has been measured to be about 1–5% of C_S (Ozturk, 1990). This implies that the oxygen consumption operates at near zeroth-order kinetics. Substituting Eq. (7.14) into Eq. (7.13) and evaluating the solution at $x = 0$ yields a quadratic expression for C_0 :

$$C_0^2 + (K_m - C_S + qXH/D)C_0 - C_SK_m = 0 \quad (7.15)$$

In terms of the fractional saturation $\sigma = C/C_S$, Eq. (7.15) becomes,

$$\sigma_0^2 + (\kappa + \phi - 1)\sigma_0 - \kappa = 0 \quad (7.16)$$

where we have introduced two dimensionless parameters, a dimensionless Michaelis constant $\kappa = K_m/C_S$, and

$$\phi = qXH/DC_S = \frac{H^2/D}{HC_S/qX} \quad (7.17)$$

which is the ratio of the characteristic time for diffusion to the characteristic time for cellular oxygen uptake. The parameter ϕ depends on the cell density, which changes with time as the cells on the surface divide and double in number every 24–48 h. There is only one physically reasonable root to Eq. (7.16), since the other will always be negative. This fractional saturation design equation can be used to determine the range of parameter values for which the cells receive sufficient oxygen to support proliferation.

7.3.2. The Bioartificial liver: membranes enhance mass transfer in planar microchannels

Many types of cells can be grown *in vitro* more successfully when co-cultured in the presence of a second cell type such as 3T3-J2 fibroblasts, which are robust and can produce vital nutrients that support the growth of the cells of interest. Tilles *et al.* (2001) studied the co-culture of rat hepatocytes (liver cells) with 3T3-J2 fibroblasts in microchannel

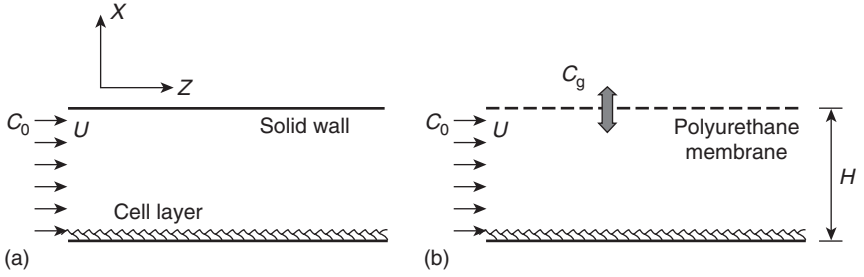


Fig. 7.7. Microchannel bioreactors (a) without and (b) with an internal membrane oxygenator.

bioreactors ($H = 85\text{--}500\ \mu\text{m}$). Their analysis of the effects that an oxygenating membrane has on hepatocyte growth and protein production (see Fig. 7.7) provides a useful set of design equations for the development of microchannel membrane-based bioreactors.

For simplicity, we assume uniform, or “plug”, flow within the microchannel (see Problem 7.4 for a modification of this approximation). The flow direction is defined with the z -coordinate, and oxygen diffusion occurs in the x -direction normal to the wall and is consumed by hepatocytes at $x = 0$. Once the oxygen concentration $C(x, z)$ is non-dimensionalized with the inlet concentration C_{in} , and the x and z variables non-dimensionalized with the height (H) and length (L) of the bioreactor, respectively, then the dimensionless steady-state convection-diffusion equation becomes

$$\frac{\partial C^*}{\partial z} = \frac{\gamma}{\text{Pe}} \frac{\partial^2 C^*}{\partial x^2} \quad (7.18)$$

Where we have introduced the dimensionless length ratio $\gamma = L/H$, and the Peclet number $\text{Pe} = UH/D$. Here U is the average velocity and D is the oxygen diffusivity. The boundary conditions for Eq. (7.18) are

$$\begin{aligned} C^* &= 1 & @z = 0, \quad 0 \leq x \leq 1 \\ \frac{\partial C^*}{\partial x} &= \text{Da} & @x = 0, \quad 0 \leq z \leq 1 \\ \frac{\partial C^*}{\partial x} &= \begin{cases} 0 & @x = 1, \quad 0 \leq z \leq 1 \\ \text{Sh}[C_g^* - C^*] & @x = 1, \quad 0 \leq z \leq 1 \end{cases} \end{aligned} \quad (7.19)$$

where there exist two different flux conditions at the upper surface depending on whether there is no membrane oxygenation, or with membrane oxygenation. We have introduced two additional dimensionless groups, the Damkohler number

$$\text{Da} = \frac{V_m H X}{D C_{\text{in}}} \quad (7.20)$$

and the Sherwood number

$$\text{Sh} = \frac{\sigma H}{D} \quad (7.21)$$

where the zeroeth-order uptake of oxygen by the hepatocytes is defined as V_m , the surface density of cells as X , and σ is the membrane permeability to oxygen. We have non-dimensionalized the gas phase oxygen concentration with C_{in} as $C_g^* = C_g/C_{in}$. A similar differential system has been solved analytically by Carslaw and Jaeger (1959), which can be applied to yield the cell surface oxygen concentration along the length of the bioreactor either without internal membrane oxygenation:

$$C^*(0, z) = 1 - z \frac{\gamma}{Pe} Da - \frac{Da}{3} + \frac{2Da}{\pi^2} \sum_{n=1}^{\infty} \frac{(-1)^n}{n^2} \cos(n\pi) \exp \left[-\frac{\gamma n^2 \pi^2 z}{Pe} \right] \quad (7.22)$$

or with internal membrane oxygenation:

$$C^*(0, z) = C_g^* - Da - \frac{Da}{Sh} + \sum_{n=1}^{\infty} B_n \exp \left[-\frac{\gamma \lambda_n^2 z}{Pe} \right] \quad (7.23)$$

In Eq. (7.23), the coefficients B_n are defined by:

$$B_n = \frac{4Da(1 - \cos \lambda_n) + 4\lambda_n \sin \lambda_n (1 - C_g^* + Da/Sh)}{[\lambda_n \sin 2\lambda_n + 2\lambda_n^2]} \quad (7.24)$$

and λ_n are the roots of the transcendental equation:

$$\tan \lambda_n = \frac{Sh}{\lambda_n} \quad (7.25)$$

Example 7.1 (see page 434) illustrates the use of these design equations (7.22–7.25).

7.3.3. Oxygen and lactate transport in micro-grooved minichannels for cell culture

As stated in Section 7.3.1, there is considerable interest in culturing and expanding hematopoietic stem cell populations *ex vivo*, for later autologous (donor = recipient) or allogeneic (donor ≠ recipient) transplantation for the treatment of hematological or immunological disorders and to treat complications of cancer therapies. In their native environment in the bone marrow, hematopoietic cells are not strongly adherent to their surroundings but are retained in the marrow in part due to adhesion to a second type of cells called stromal cells. It has been recognized that *ex vivo* cell perfusion systems for long-term culture that are able to retain weakly adherent cells would hold many advantages over co-culture systems (Sandstrom *et al.*, 1996). Horner *et al.* (1998) analyzed the solute transport in a micro-grooved minichannel designed to retain non-adherent cells within microscale cavities oriented perpendicular to the main flow, as depicted in Fig. 7.8. Flow through the main minichannel generates a form of lid-driven flow within each cavity known as nested Moffatt eddies (Moffatt, 1964). These eddies provide convection-enhanced mass transfer between the cells resting at the bottom of each cavity and the main chamber, while sheltering the cells from the high wall shear stresses that would be experienced in a comparable flat-bottomed channel.

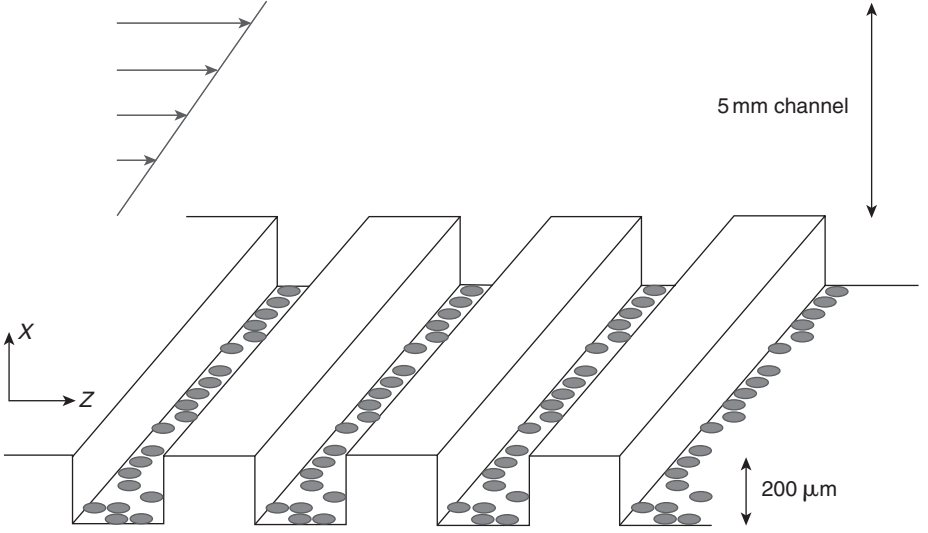


Fig. 7.8. Micro-grooved, minichannel bioreactor for the culture of weakly adherent cells. Note that the cells are sheltered within the grooves and do not become entrained in the flow. The exterior flow induces Moffett eddies that exchange solutes between the groove cavities and the minichannel region.

For a relatively wide channel of several centimeters, the aspect ratio is such that the third dimension (vorticity direction) can be neglected and the problem treated as two-dimensional. As in our previous bioreactor examples, we take the flow direction as z and the velocity gradient direction as x . At steady-state, the Navier–Stokes equation in two-dimensions simplifies to:

$$\begin{aligned}\rho \left(v_x \frac{\partial v_x}{\partial x} + v_z \frac{\partial v_x}{\partial z} \right) &= -\frac{\partial p}{\partial x} + \mu \left(\frac{\partial^2 v_x}{\partial x^2} + \frac{\partial^2 v_x}{\partial z^2} \right) \\ \rho \left(v_x \frac{\partial v_z}{\partial x} + v_z \frac{\partial v_z}{\partial z} \right) &= -\frac{\partial p}{\partial z} + \mu \left(\frac{\partial^2 v_z}{\partial x^2} + \frac{\partial^2 v_z}{\partial z^2} \right)\end{aligned}\quad (7.26)$$

Note that unlike previous examples where the flow was assumed unidirectional in the z -direction and diffusion in the z -direction neglected relative to convection, leading to simplifications to the governing equations, the lid-driven cavity flow is expected to be fully two-dimensional and these full equations must be integrated. The solute balance for species i , at steady-state, takes the form:

$$v_x \frac{\partial C_i}{\partial x} + v_z \frac{\partial C_i}{\partial z} = -D_i \left(\frac{\partial^2 C_i}{\partial x^2} + \frac{\partial^2 C_i}{\partial z^2} \right) \quad (7.27)$$

The solutes of main biological interest (oxygen and lactate) are dilute small molecules that do not appreciably affect the fluid density and viscosity. Thus, the fluid velocity field may

be solved independently of the solute balance equation. It is reasonable to impose a well-developed parabolic velocity profile at the channel inlet, provided that the cell-containing region occurs after the entrance length given by:

$$\frac{L_{\text{ent}}}{H} = a \text{Re} \quad (7.28)$$

where the Reynolds number is defined for channel flow as:

$$\text{Re} = \frac{\rho \langle v \rangle H}{\mu} \quad (7.29)$$

In Eq. (7.28), the coefficient a is equal to 0.034 to ensure that the centerline velocity is within 98% of the theoretical Poiseuille flow limit (Bodoia and Osterle, 1961), and the angled brackets denote an averaged quantity. For typical bioreactor conditions, the entrance length is reached within a fraction of one channel height ($< 0.05H$). No-slip conditions are enforced at the upper, lower, and micro-groove walls. The general flux condition at the lower wall of the micro-groove cavities, plated with hematopoietic cells, is obtained by setting the surface solute flux equal to a Michaelis–Menten kinetic rate of solute consumption or production (e.g., oxygen or lactate, respectively). This boundary condition at the cell surface takes the form:

$$N_0 = -D \frac{\partial C}{\partial x} = \frac{qXC_0}{K_m + C_0} \quad (7.30)$$

where a sign change from Eq. (7.12) is introduced for a local coordinate system within the cavity corresponding to an upper cavity opening at $x = 0$ and the positive x -coordinate directed downward. The system of Eqs. (7.26), (7.27), and (7.30), subject to no-slip at the wall and given inlet velocity and solute concentration conditions, can be readily solved for the spatial concentration profiles using a commercial computational fluid dynamics (CFD) code such as *FIDAP* (Fluent, Inc., Lebanon, NH). Horner *et al.* (1998) have used full numerical analysis of the micro-grooved minichannel system to derive constitutive equations that describe the solute concentration within the groove cavities as a function of various physical parameters such as flowrate, channel dimensions, and zeroth-order solute consumption (production) rate.

7.4. Generation of normal forces in cell detachment assays

Hydrodynamic flow in parallel-plate microchannels is often used to detach firmly adhered cells from substrates, as a measure of the strength of integrin:matrix protein bonds (Fig. 7.9). However, the high flowrates necessary to detach spread cells, when flowing over a flat cell with a raised nuclear region, may produce a negative pressure over the nucleus (the so-called “Bernoulli effect”) that can potentially equal or exceed the shear forces that one is trying to generate (Fig. 7.10). Thus, here we model this problem as inviscid, irrotational flow over a wavy wall as developed by Michelson (1970), keeping

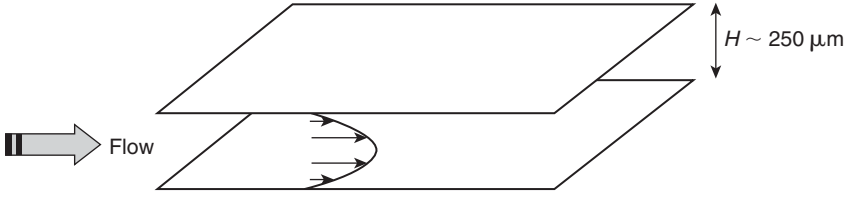


Fig. 7.9. Microchannel geometry for cell detachment.

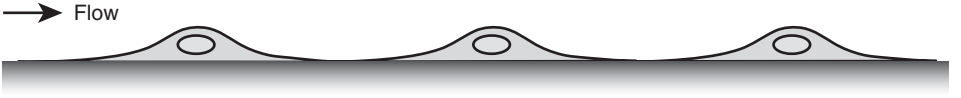


Fig. 7.10. The nuclei of adherent cells project into the flow field.

in mind that this will only be valid for Reynolds numbers much greater than unity (often achieved in previous experimental studies as discussed below).

Figure 7.9 depicts the dimensions of a typical cell detachment flow chamber. From the literature, the force required for cell detachment from an adhesive substrate can be estimated as between 10^{-9} and 10^{-7} N. In saline buffer ($\mu = 1$ cP), this requires flow rates of $U_{\text{avg}} = 1\text{--}100$ cm/s. In such an experiment, the highest Reynolds number studied would be

$$\text{Re} = \frac{Qw}{\nu} = 256 \quad (7.31)$$

Thus, not only is inertia important in this microscale system, but may be expected to dominate over viscous effects.

7.4.1. Potential flow near an infinite wall

Our starting point for modeling the flow over a cell monolayer is the set of non-linear Euler's equations:

$$\begin{aligned} u \frac{\partial u}{\partial x} + v \frac{\partial u}{\partial y} + \frac{1}{\rho} \frac{\partial p}{\partial x} &= -\frac{\partial U}{\partial x} \\ u \frac{\partial v}{\partial x} + v \frac{\partial v}{\partial y} + \frac{1}{\rho} \frac{\partial p}{\partial y} &= -\frac{\partial U}{\partial y} \end{aligned} \quad (7.32)$$

which describes steady, two-dimensional *frictionless* flows subject to conservative forces (i.e. derived from a potential U) such as gravity.

When a rigid body rotates at angular speed ω , the velocity components of a point located at (x, y) are

$$u = -\omega y, \quad v = \omega x \quad (7.33)$$

Eliminating x and y from Eq. (7.33) yields a definition for the vorticity ω ,

$$2\omega = \left\{ \frac{\partial v}{\partial x} - \frac{\partial u}{\partial y} \right\} \quad (7.34)$$

a measure of the local fluid rotation. Kelvin's theorem states that the vorticity is a constant in incompressible, frictionless flows, when the only forces are derived from potentials such as gravity. Therefore, Kelvin's theorem gives us an additional relation:

$$\frac{\partial v}{\partial x} - \frac{\partial u}{\partial y} = 0 \quad (7.35)$$

along with the continuity equation for incompressible flow,

$$\frac{\partial u}{\partial x} + \frac{\partial v}{\partial y} = 0 \quad (7.36)$$

We define the velocity potential $\phi(x, y)$ as

$$u = -\frac{\partial \phi}{\partial x}, \quad v = -\frac{\partial \phi}{\partial y} \quad (7.37)$$

which identically satisfies the irrotational condition. Substituting this definition into the continuity equation yields

$$\frac{\partial^2 \phi}{\partial x^2} + \frac{\partial^2 \phi}{\partial y^2} = 0 \quad (7.38)$$

Thus, the velocity potential for plane irrotational flow of an incompressible fluid is a solution to Laplace's equation. This equation is solved for the uniform flow past a flat wall in Example 7.2 (see page 436).

7.4.2. Linearized analysis of uniform flow past a wavy wall

To model the disturbance flow generated by a uniform flow over a periodic layer of cells, one of the streamlines of uniform flow is modified to be everywhere only nearly parallel to the x -axis. We expect that the velocities elsewhere will differ slightly from U , and the associated pressure variations will be small. Fig. 7.11 shows a slightly curved boundary wall of sinusoidal form,

$$y = h \sin \lambda x \quad (7.39)$$

The length of the whole cycle of the sine wave is $L = 2\pi/\lambda$ and here h is the wave height. We require that h be small as: $h \ll L$ which corresponds to an assumption of "slight waviness". The flow velocity components are assumed to differ only slightly from $(U, 0)$ and can be written as:

$$u = U + u', \quad v = v' \quad (7.40)$$

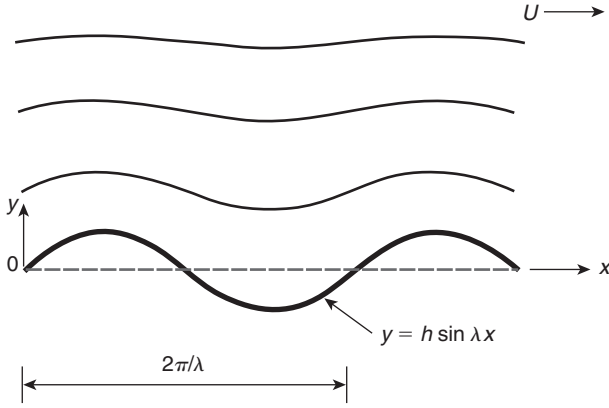


Fig. 7.11. Geometry of the linearized analysis near a wavy wall.

where the primes indicate velocity perturbations that vanish with h , and

$$u' \ll U, \quad v' \ll U \quad (7.41)$$

Because of the irrotationality condition,

$$\frac{\partial v'}{\partial x} - \frac{\partial u'}{\partial y} = 0 \quad (7.42)$$

the velocity potential $\phi(x, y)$ may be taken to refer only to the perturbations

$$u' = -\frac{\partial \phi}{\partial x}, \quad v' = -\frac{\partial \phi}{\partial y} \quad (7.43)$$

This yields the following expression for the total flow:

$$u = U - \frac{\partial \phi}{\partial x}, \quad v = -\frac{\partial \phi}{\partial y} \quad (7.44)$$

Bernoulli's theorem can now be applied:

$$\frac{u^2}{2} + \frac{p}{\rho} + \text{potential} = \text{constant} \quad (7.45)$$

which is valid at different points along a single streamline. Thus, the linearized version of the governing equation becomes

$$p(x, y) - p_0 = \rho U \frac{\partial \phi}{\partial x} \quad (7.46)$$

where we have subtracted off the quantity $p_0 + \rho U^2 = cst.$ evaluated far from the wall. In Eq. (7.46), p_0 denotes the pressure in those parts of the flow where the velocity reaches its uniform value U .

The velocity potential is a harmonic function given by the equation

$$\frac{\partial^2 \phi}{\partial x^2} + \frac{\partial^2 \phi}{\partial y^2} = 0 \quad (7.47)$$

We must now find the particular solution to Eq. (7.47) out of the many general solutions to Laplace's equation. First, we note the farfield condition $\phi(x, \infty) = 0$. At the boundary, we enforce that the slope of the velocity vector equals the boundary slope:

$$\frac{v}{u} = h\lambda \cos \lambda x \quad (7.48)$$

From our earlier development, the left-hand-side of Eq. (7.48) is given by

$$LHS = -\frac{\partial \phi / \partial y}{U - \partial \phi / \partial x} = -\frac{1}{U} \frac{\partial \phi}{\partial y} \quad (7.49)$$

where we have neglected higher order terms. We may write an approximate boundary condition evaluated at $y = 0$:

$$-\frac{\partial \phi}{\partial y}(x, 0) = Uh\lambda \cos \lambda x \quad (7.50)$$

Note that the differential equation, boundary conditions, and pressure relationship are all linear in ϕ -derivatives. This problem admits a separable solution of the form:

$$\begin{aligned} X(x) &= A \cos kx + B \sin kx \\ Y(y) &= C \exp(-ky) + D \exp(ky) \end{aligned} \quad (7.51)$$

which combine to give the following potential function:

$$\phi(x, y) = \{A \cos kx + B \sin kx\} \{C \exp(-ky) + D \exp(ky)\} \quad (7.52)$$

where the term $D \exp(ky)$ vanishes in order to satisfy the farfield condition. We are thus left with two remaining constants AC and BC , and can set $C = 1$ without loss of generality. The boundary condition at $y = 0$ takes the form

$$Uh\lambda \cos \lambda x = k\{A \cos kx + B \sin kx\} \quad (7.53)$$

which, upon manipulation, yields the result

$$Uh\lambda = kA, \quad B = 0, \quad k = \lambda \quad (7.54)$$

These constants can be inserted into our general solution to give

$$\phi(x, y) = Uh \exp(-\lambda y) \cos \lambda x \quad (7.55)$$

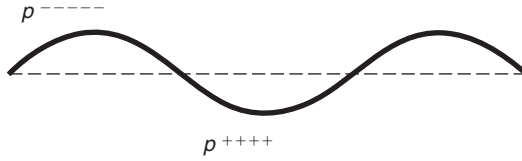


Fig. 7.12. Pressure distribution at the surface of the wall.

for the velocity potential, and the following expression for the pressure at any point in the flow:

$$p(x, y) = p_0 - \rho U^2 h \lambda \sin \lambda x \exp(-\lambda y) \quad (7.56)$$

Thus, the linear approximation to the pressure on the boundary wall $y = 0$ is

$$p(x, 0) = p_0 - \rho U^2 h \lambda \sin \lambda x \quad (7.57)$$

Equation (7.57) implies that the pressure is a minimum at the peaks of the wavy wall ($\lambda x = \pi/2$) and reaches a maximum at the wave troughs, as depicted in Fig. 7.12.

Typical parameter values for cell detachment experiments yield the following estimate for the peak (negative) pressure above the cell nucleus:

$$\rho U^2 h \lambda = (1000 \text{ kg/m}^3)(1 \text{ m/s})^2(2 \times 10^{-6} \text{ m})(2\pi/20 \times 10^{-6} \text{ m}) \quad (7.58)$$

Thus, the pressure above the cell nucleus is predicted to have magnitude $p = 628 \text{ N/m}^2$, or assuming a characteristic cell area of $100 \mu\text{m}^2$, a negative pressure of magnitude $F = |63 \text{ nN}|$. This value for the normal force induced by the Bernoulli effect is of the same order as the shear forces generated by the imposed flow! Reanalysis of many previous experiments using cell detachment assays show the generation of large normal forces in both the microchannel geometry (VanKooten *et al.*, 1992; Schnittler *et al.*, 1993; Sank *et al.*, 1994; Thompson *et al.*, 1994; Wechazak *et al.*, 1994; Kapur and Randolph, 1998; Sirois *et al.*, 1998; Chan *et al.*, 1999; Malek *et al.*, 1999; Grandas *et al.*, 2001) as well as the spinning disk assay (Garcia *et al.*, 1997; Boettiger *et al.*, 2001; Deligianni *et al.*, 2001; Miller and Boettiger, 2003). To reduce the Reynolds number, and thus reduce the normal forces relative to shear forces, one should simply increase the fluid viscosity with a high-molecular weight molecule such as dextran. For instance, a 7.5 weight percent dextran solution, of molecular weight $M_W = 2 \times 10^6 \text{ g/mol}$, would result in a relative viscosity of

$$\frac{\mu}{\mu_0} = 20.5$$

7.5. Small-bore microcapillaries to measure cell mechanics and adhesion

The human circulatory system represents a challenging system for engineering modeling, due to the wide variation in vessel geometry, linear flow velocity, and Reynolds

Table 7.2
Typical flow parameters in the human systemic circulation.

Structure	Diameter (cm)	Blood velocity (cm/s)	Tube Reynolds number
Ascending aorta	2.0–3.2	63	3600–5800
Descending aorta	1.6–2.0	27	1200–1500
Large arteries	0.2–0.6	20–50	110–850
Arterioles	0.001–0.015	0.5–1.0	0.014–0.43
Capillaries	0.0005–0.001	0.05–0.1	0.0007–0.003
Venules	0.001–0.02	0.1–0.2	0.0029–0.11
Large veins	0.5–1.0	15–20	210–570
Vena cavae	2.0	11–16	630–900

Data from Cooney, 1976; Whitmore, 1968; Schneck, 2000.

numbers, starting at the major aortic vessels down to the smallest microscopic capillaries. Table 7.2 shows the range of these values in a typical human, assuming a constant blood viscosity of 0.035 P and mean peak velocities reported for the pulsatile flow of arterial flow.

It is evident that the human circulation covers the entire range of flow behavior from creeping (non-inertial) flow up to fully developed turbulence. We see in the arterioles, capillaries, and venules that the length scales span the range of fluid physics encountered in microchannel and minichannel flow. In the largest vessels of the body, blood behaves as a non-Newtonian fluid and constitutive equations are usually successful in describing behavior (e.g. blunted velocity profiles) at the continuum level. At the scale of the smallest vessels however, the particulate nature of blood and its constituent cells must be taken into account (King *et al.*, 2004). In the capillaries of the lungs, for instance, the mechanical properties of individual white blood cells significantly influence the transit time through these vessels (Bathe *et al.*, 2002).

Suspensions of erythrocytes (red blood cells, or RBCs) flowing through microcapillaries ($d \sim 40 \mu\text{m}$) are well known to concentrate at the tube center, resulting in velocity profiles blunted from parabolic. Trajectories of individual RBCs have been visualized both *in vitro* (Goldsmith and Marlow, 1979) and *in vivo* (Lominadze and Mchedlishvili, 1999), showing radial drift velocities and random walks that attenuate as the cell approaches the centerline. The single-file motion of RBCs through small capillaries ($d \sim 4\text{--}20 \mu\text{m}$) has been modeled theoretically subject to various simplifying assumptions: $x\text{--}y$ two-dimensionality (Sugihara-Seki *et al.*, 1990), symmetry about the center axis (Secomb and Hsu, 1996), or approximation via multipole expansion (Olla, 1999). The radial drift of RBCs is known to produce a cell-free plasma layer in microvessels (Yamaguchi *et al.*, 1992), suggesting that RBCs have only a secondary influence on the dynamics of leukocytes once they are displaced to the vessel wall (Goldsmith and Spain, 1984). Furthermore, leukocytes have a dramatic influence on total blood viscosity in the microcirculation despite their relatively low numbers in blood as compared to RBCs (Helmke *et al.*, 1998), highlighting the need to better understand the motion of leukocytes through microcapillaries.

Example 7.3 (see page 437) provides an estimate of the blood transit time through a capillary, where the majority of oxygen exchange takes place.

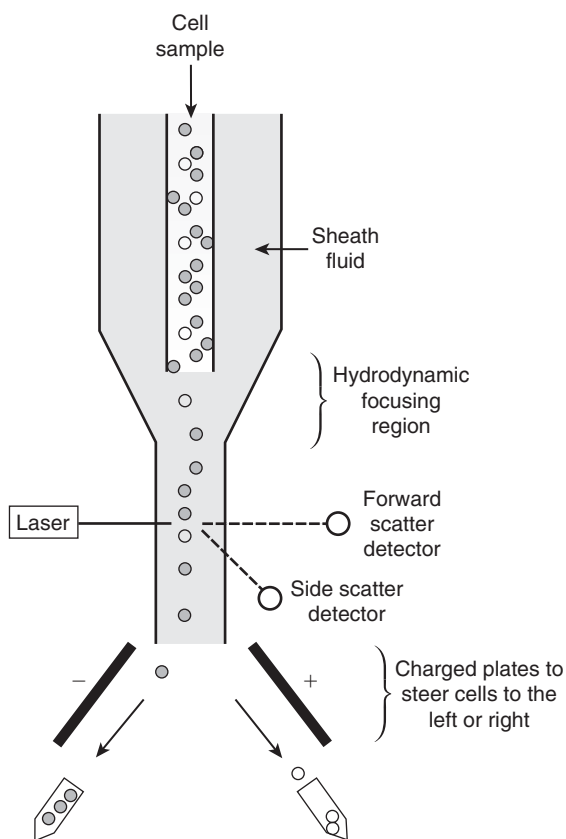


Fig. 7.13. Schematic of a flow cytometer, and fluorescence activated cell sorting (FACS).

7.5.1. Flow cytometry

Flow cytometry is a powerful analysis tool in biomedical research, that utilizes microscale flow for automated single cell characterization and sorting. The concentration of any fluorescently labeled molecule on the surface of the cell can be measured relative to some standard, and these cells can furthermore be sorted according to the concentration of this marker or according to size. Antibodies against many of the known receptors on the surface of human or animal cells can be obtained commercially. Figure 7.13 shows a schematic of a typical system. The cell suspension (possibly containing a mixture of different cell types) is introduced through a circular conduit. This conduit opens into a larger flow domain containing a flowing annulus of “sheath fluid” which acts to focus the stream of cells into a single-file configuration within a narrow jet of fluid ($<100\text{ }\mu\text{m}$ diameter). This stream of cells then passes through a quartz chamber where they are characterized for their scattering and fluorescent properties. Most commonly, a beam of light from an argon laser is used to excite the fluorophore of interest. The emitted light from this

fluorophore is then collected at one of two photomultiplier tubes. Downstream of these optics, the outlet stream is ruptured into a series of droplets, each containing a single cell, via piezoelectric vibration. An electrical field is then used to steer positively or negatively charged individual droplets (a charge imposed depending on the previous fluorescence intensity of the corresponding cell) into multiple collection vessels. The whole process is automated so that commercially available flow cytometers can sort cells at a rate of over 10^4 cells/s. In addition to characterizing individual cells for clinical applications, flow cytometry has been used to measure the size of small blood cell aggregates, where up to pentuplets of neutrophils can be successfully identified (Simon *et al.*, 1990; Neelamegham *et al.*, 2000).

7.5.2. Micropipette aspiration

Small-bore glass microcapillaries are often used to either characterize the mechanics and deformability of individual cells, or to test the surface adhesion of cells contacting other cells or artificial bead surfaces (Lomakina *et al.*, 2004; Spillmann *et al.*, 2004). Capillaries with inner diameter less than the major diameter of cells such as blood cells are used to partially aspirate the cell, with the projection length of the cell within the capillary interior being a measure of the cortical tension of the cell exterior (Herant *et al.*, 2003). Once the cell is ejected from the micropipette, its shape recovery can also yield information on the viscoelastic parameters of the cell (Dong *et al.*, 1988). Capillaries with inner diameter larger than the cell diameter can be used to translate the cell back and forth within the pipette to bring a cell into repeated contact with another nearby surface. In this manner, the probability for cell adhesion can be determined in the presence of various biological stimuli. Shao and Hochmuth (1996) calculated the pressure drop caused by the gap flow in the annular region between a spherical cell and a larger cylindrical micropipette. The geometry considered is depicted in Fig. 7.14.

Assuming axisymmetric flow, and neglecting inertia, yields the following form of the Navier–Stokes equations in cylindrical coordinates:

$$\begin{aligned}\frac{1}{r} \frac{\partial}{\partial r}(ru) + \frac{\partial w}{\partial z} &= 0 \\ \frac{\partial p}{\partial r} &= \mu \left(\frac{\partial^2 u}{\partial r^2} + \frac{1}{r} \frac{\partial u}{\partial r} - \frac{u}{r^2} + \frac{\partial^2 u}{\partial z^2} \right) \\ \frac{\partial p}{\partial z} &= \mu \left(\frac{\partial^2 w}{\partial r^2} + \frac{1}{r} \frac{\partial w}{\partial r} + \frac{\partial^2 w}{\partial z^2} \right)\end{aligned}\tag{7.59}$$

where p is the pressure, u and w are the local fluid velocities in the r - and z -directions, respectively, and μ is the fluid viscosity. No-slip conditions are enforced at all boundaries, and the total volumetric flowrate through any circular cross-section of the pipette is a constant Q . After considerable manipulations, useful analytical expressions can be obtained relating the total pressure drop Δp , sphere velocity U , and external force acting on the sphere F , for two simplified cases: (i) stationary sphere, and (ii) force-free sphere.

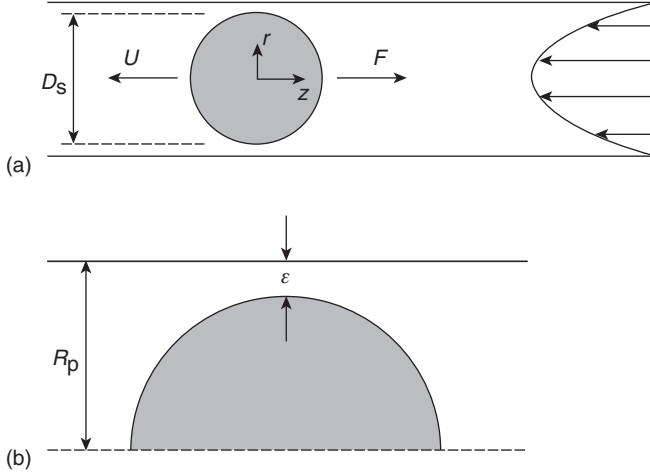


Fig. 7.14. (a) Spherical cell positioned at the centerline within a larger micropipette. (b) Close-up of the upper half of the cylindrical region.

First, the force necessary to hold a sphere stationary within a pressure-driven flow in a micropipette is:

$$F = \frac{\pi R_p^2 \Delta p}{\left(1 + \frac{4}{3} \bar{\varepsilon}\right) + \frac{8(L_{eq} - D_s)}{R_p} \left(\frac{2\sqrt{2}}{9\pi} \bar{\varepsilon}^{5/2} - \frac{8}{9\pi^2} \bar{\varepsilon}^3\right)} \quad (7.60)$$

where L_{eq} is the total pipette length, and the gap spacing has been non-dimensionalized with the pipette radius. For a neutrally buoyant or force-free sphere, on the other hand, the relationship between the total pressure drop and the sphere velocity is given by:

$$\Delta p = \frac{\mu U}{R_p} \left[\left(\frac{4\sqrt{2}\pi}{\bar{\varepsilon}^{1/2}} - \frac{71}{5} \right) + \frac{8(L_{eq} - D_s)}{R_p} \left(1 - \frac{4}{3} \bar{\varepsilon} \right) \right] \quad (7.61)$$

7.5.3. Particle transport in rectangular microchannels

The transport of suspended cells in rectangular microchannels is of interest in the analysis of red cell dimensions (Gifford *et al.*, 2003), the study of blood coagulation and thrombotic vessel occlusion (Kamada *et al.*, 2004), measurement of intracellular signaling in Jurkat cells (Li *et al.*, 2004), and viral-based transfection (Walker *et al.*, 2004). When the channel height approaches the same order of magnitude as the diameter of the transported cells, the particles are influenced by the presence of the walls and assuming that the particles travel with the local fluid velocity no longer remains valid. Staben *et al.* (2003) numerically calculated using a boundary-integral algorithm the motion of spherical and spheroidal particles within a rectangular channel. Both the translational and rotational velocities of individual particles are affected by the presence of the walls of the channel. As can be seen

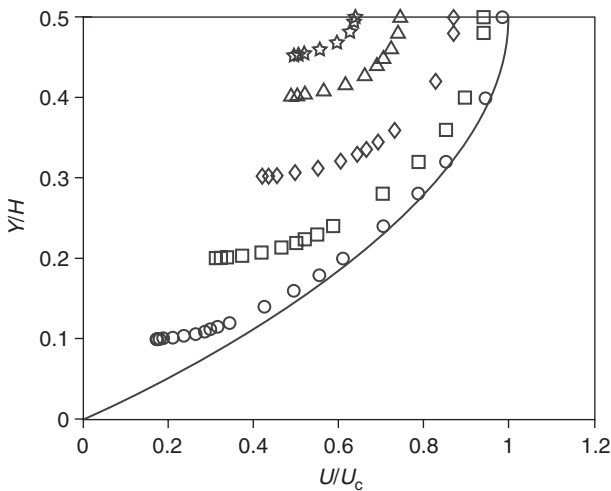


Fig. 7.15. The dimensionless translational velocity of a sphere in a two-dimensional Poiseuille flow in a rectangular channel. Solid curve represents the fluid velocity, and the symbols represent particles, which when non-dimensionalized with the height of the channel, have the following diameters: 0.2 (circles), 0.4 (squares), 0.6 (diamonds), 0.8 (triangles), and 0.9 (stars). All velocity curves are symmetric about $Y/H = 0.5$. Data from Staben *et al.* (2003).

in Fig. 7.15 this retardation effect can be quite pronounced when the cell diameter is 20–90% of the entire gap width. Interestingly, because the particle centers are excluded from a region one radius thick at the upper and lower walls (where the fluid velocity is smallest), the average particle velocity for a collection of spheres can actually be greater than the average velocity of the suspending fluid itself. Specifically, Staben *et al.* showed that randomly-distributed particles with diameter $\leq 82\%$ of the gap height will have an average velocity greater than the average fluid velocity, and that this effect is most pronounced for particles with diameter $d = 0.42 H$, which will travel at a velocity 18% greater than the average fluid velocity.

7.6. Solved examples

Example 7.1

Compare graphically the two solutions describing the spatial dependence of the cell surface oxygen concentrations without and with an internal membrane oxygenator, for parameter values of $\gamma = 100$, $Da = 0.25$, $Pe = 25$, $Sh = C_g = 1$.

We will use the Matlab programming language to calculate and display our two solutions.

First, we plot the left- and right-hand-sides of our transcendental Eq. (7.25) to approximately locate the value of the first few roots λ_n , using the commands:

```
lambda = linspace(1e-4,12,1000);
semilogy(lambda,tan(lambda),lambda,1./lambda,'-')
```

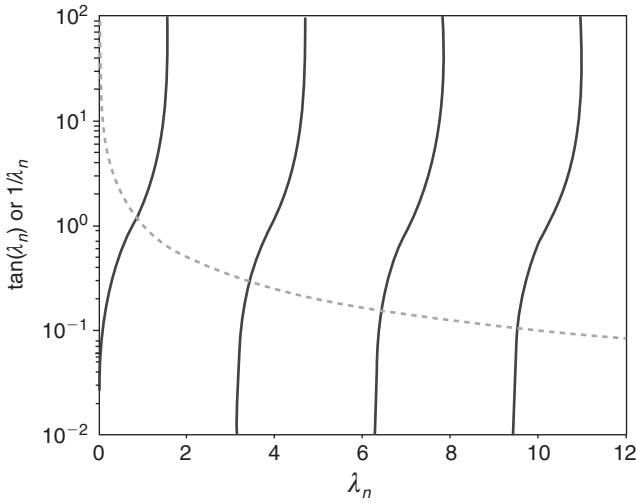


Fig. 7.16. Matlab plot to determine the approximate location of the first few roots to the transcendental equation for λ_n .

where minor figure formatting commands have been omitted. Note that the lambda vector was started at 10^{-4} to avoid the singularity at $\lambda = 0$. Figure 7.16 shows this plot, where it is evident that the two sides of the transcendental equation cross each other at around 1, 3, 6, 9, and it is clear that the higher order roots will be separated by a distance of about 3.14. Now that we know the approximate location of the first few roots, we can use a built-in non-linear root-finding routine to find these more accurately. The following commands accomplish this:

```
guess = [1 3 6 9 12];
for i=1:length(guess)
    lambda_n(i) = fzero('tan(x)-1/x',guess(i));
end
```

Executing the above commands produces the following roots for the first five λ_n 's: 0.8603, 3.4256, 6.4373, 9.5293, 12.6453. Now we are ready to calculate the two surface concentration distributions and compare them. We will store the first five eigenfunctions in the second through sixth rows of two matrices, called `C_no_mem` and `C_mem`, and sum them up before plotting:

```
z=linspace(0,1,100);    Pe=25; Da=0.25;
C_no_mem(1,:)=1-z*100/Pe*Da-Da/3;
C_mem(1,:)=(1-Da-Da)*ones(size(x));
for n=1:5
    C_no_mem(n+1,:)=2*Da/pi^2*(-1)^n/n^2*cos(n*pi)*...
        exp(-100*n^2*pi^2*z/Pe);
```

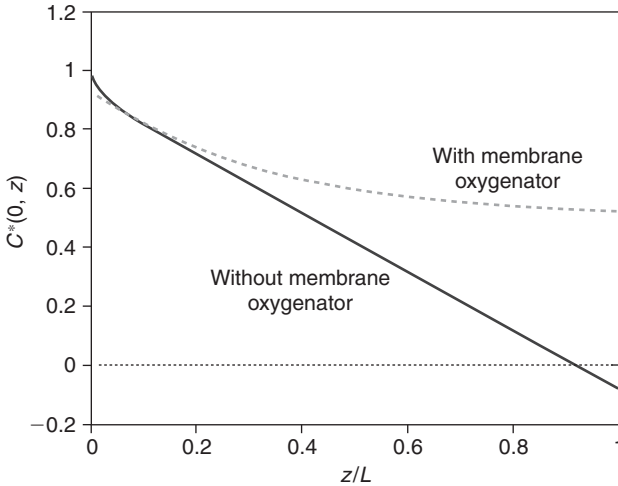


Fig. 7.17. Results from the analytical model of oxygen transport in a microchannel bioreactor. Note that without a membrane oxygenator, the cell surface will be completely devoid of oxygen before the end of the channel is reached.

```

Bn = (4*Da*(1-cos(lambda_n(n)))) + ...
      4*lambda_n(n)*sin(lambda_n(n))*(1-1+Da))/...
      (lambda_n(n)*sin(2*lambda_n(n))+2*lambda_n(n)^2);
C_mem(n+1,:) = Bn*exp(-100*lambda_n(n)^2*z/Pe);
end
plot(z, sum(C_no_mem), z, sum(C_mem))

```

Figure 7.17 shows these results, where it is evident that the microchannel without membrane oxygenation will be fully depleted of oxygen at the surface at a dimensionless position of about $z = 0.9$.

Example 7.2

As an example we consider the case of uniform potential flow. This serves as the base state for our analysis of the flow over a wavy cell surface in Section 7.4.2. In uniform flow, the potential is given by:

$$\phi_1 = -Ux \quad (7.62)$$

where U is a constant. The corresponding velocity components are then given by:

$$u_1 = -\frac{\partial \phi_1}{\partial x} = U = \text{constant} \quad (7.63)$$

$$v_1 = -\frac{\partial \phi_1}{\partial y} = 0$$

as expected.

Example 7.3

Consider the demand for effective mass transport in the microcirculation. Cooney (1976) showed through simple scaling arguments that the rate of mass transport rates across blood capillaries must be quite effective owing to the relatively short residence time of blood in these vessels. The typical capillary diameter is about $8\text{ }\mu\text{m}$, which allows deformable red and white blood cells ($d \sim 8\text{--}10\text{ }\mu\text{m}$) to squeeze through these smallest vessels. The number of systemic capillaries in the body can be estimated to be about $n = 10^9$, and the cardiac output about $Q = 5\text{ l/min}$. Thus, the linear velocity of blood flow in the capillaries can be readily calculated as:

$$v = \frac{Q}{n\pi r^2} = \frac{5000\text{ cm}^3/\text{min}}{10^9(3.142)(4 \times 10^{-4}\text{ cm})^2} = 9.95\text{ cm/min} = 0.166\text{ cm/s} \quad (7.64)$$

If we assume that each capillary is 1 mm long, the characteristic blood residence time in the capillary is thus:

$$t = \frac{1\text{ mm}}{1.66\text{ mm/s}} = 0.6\text{ s} \quad (7.65)$$

Thus, mass transfer of metabolites and waste products through the capillary wall cannot encounter much barrier to mass transport since so little time for exchange is provided before the blood begins flowing back through the arterial tree back to the heart.

7.7. Practice problems

1. Calculate the velocity profile for a radial flow assay as a function of r and z , in terms of the volumetric flowrate and the channel dimensions. Neglect the central region and assume that the inlet radius is small. Then, use your solution for the velocity field to derive the wall shear stress expression given by Eq. (7.1).
2. Consider a slowly converging channel. Assuming a desired gap height of $H = 8\text{ }\mu\text{m}$, a channel width and length of $W = 25\text{ mm}$ and $L = 75\text{ mm}$, respectively, but an actual gap height achieved of $H_1 = 8$ and $H_2 = 7\text{ }\mu\text{m}$, calculate the required pressure head by neglecting the additional pressure drop across fittings and tubing. Based on your value, will gravity-driven flow or a commercially available syringe pump be more appropriate for this application? Noting that the wall shear stress varies as the inverse of H squared, will the average wall shear stress within the channel simply be that for a straight channel using the average channel height? Calculate the average wall shear stress in such a channel, for arbitrary height change, by computing the area-averaged integral of the wall shear stress down the length of the flow domain.
3. Calculate the total pressure drop in a microchannel that experiences a symmetric buckling of the upper and lower walls in a parabolic shape, in terms of the fluid properties, flow rate, the initial/final height, and the height at the center of the channel. How much

Table 7.3
Parameter values for hepatocyte/3T3 fibroblast
co-culture in a microchannel bioreactor.

Parameter	Value
H	100 μm
α	10^5 hepatocytes/ cm^2
Q	0.1 mL/min
U	7×10^{-2} cm/s
V_m	0.4 nmol/s per 10^6 cells
σ	5 $\mu\text{m/s}$
D	2×10^{-5} cm^2/s
Pe	30
Da	0.1
Sh	0.25

- error is introduced by only measuring the gap height in the center of the channel and assuming that the gap is constant?
- Reformulate the model of Section 7.3.2 for a parabolic velocity profile, instead of assuming a uniform velocity. For the parameter values of Table 7.3, obtain a numerical solution to this modified system of equations, and calculate how much error is introduced by the simplified velocity profile. Show that without a membrane oxygenator, a fraction of the hepatocyte culture will not receive sufficient oxygen, and report this fraction.
 - Calculate the force exerted on a stationary spherical cell with diameter 9 μm , within a cylindrical micropipette of inner diameter 10 μm , in terms of the total pressure drop. Compare this to the solution if curvature is neglected and the flow within the gap is approximated as planar channel flow.
 - If particles enter a microchannel at the centerline height, and slowly sediment towards slower moving streamlines close to the lower wall as they flow through the chamber, will this result in a net accumulation of particles within the flow chamber? Use the results of Section 7.5.3 to estimate the extent of this effect for 12 μm diameter particles with density 1.05 g/ cm^3 , suspended in water. Assume that the channel has height 30 μm and length 1.0 cm, and neglect the effect of the side walls (i.e., two-dimensional channel). How does this differ from the case when the transported particles are infinitesimal points?

References

Abbitt, K. B. and Nash, G. B., Characteristics of leukocyte adhesion directly observed in flowing whole blood *in vitro*, *Brit. J. Haematol.*, **112**, 55–63, 2001.

Back, M. R., Carew, T. E., and Schmid-Schoenbein, G. E., Deposition pattern of monocytes and fatty streak development in hypercholesterolemic rabbits, *Atherosclerosis*, **116**, 103–115, 1995.

Barber, K. M., Pinero, A., and Truskey, G. A., Effects of recirculating flow on U-937 cell adhesion to human umbilical vein endothelial cells, *Am. J. Physiol.*, **275**, H591–H599, 1998.

- Bathe, M., Shirai, A., Doerschek, C. M., and Kamm, R. D., Neutrophil transit times through pulmonary capillaries: the effects of capillary geometry and fMLP-stimulation, *Biophys. J.*, **83**, 1917–1933, 2002.
- Bishop, J. J., Nance, P. R., Popel, A. S., Intaglietta, M., and Johnson, P. C., Erythrocyte margination and sedimentation in skeletal muscle venules, *Am. J. Physiol. Heart Circ. Physiol.*, **281**, H951–H958, 2001.
- Bluestein, D., Gutierrez, C., Londono, M., and Schoepfoerster, R. T., Vortex shedding in steady flow through a model of an arterial stenosis and its relevance to mural platelet deposition, *Annals Biomed. Eng.*, **27**, 763–773, 1999.
- Bodoia, J. R. and Osterle, J. F., Finite difference analysis of plane poiseuille and couette flow developments, *Appl. Sci. Res.*, **A10**, 265–276, 1961.
- Boettiger, D., Lynch, L., Blystone, S., *et al.*, Distinct ligand-binding modes for integrin $\alpha(v)\beta(3)$ -mediated adhesion to fibronectin versus vitronectin, *J. Biol. Chem.*, **276**, 31684–31690, 2001.
- Carslaw, H. S. and Jaeger, J. C., *Conduction of Heat in Solids*, London: Oxford University Press, 1959.
- Cieslinski, D. A. and Humes, H. D., Tissue engineering of a bioartificial kidney, *Biotechnol. Bioeng.*, **43**, 678–681, 1994.
- Chan, B. P., Bhat, V. D., Yegnasubramanian, S., *et al.*, An equilibrium model of endothelial cell adhesion via integrin-dependent and integrin-independent ligands, *Biomaterials*, **20**, 2395–2403, 1999.
- Chen, S. and Springer, T. A., Selectin receptor-ligand bonds: formation limited by shear rate and dissociation governed by the Bell model, *Proc. Natl. Acad. Sci. U.S.A.*, **98**, 950–955, 2001.
- Cooney, D. O., *Biomedical Engineering Principles: An Introduction to Fluid, Heat, and Mass Transport Processes*, New York: Marcel Dekker, Inc., 1976.
- Deligianni, D. D., Katsala, N. D., Koutsoukos, P. G., *et al.*, Effect of surface roughness of hydroxyapatite on human bone marrow cell adhesion, proliferation, differentiation and detachment strength, *Biomaterials*, **22**, 87–96, 2001.
- DePaola, N., Gimbrone, M. A., Jr., Davies, P. F., and Dewey, C. F., Jr., Vascular endothelium responds to fluid shear stress gradients, *Arterio. & Thromb.*, **12**, 1254–1257, 1992.
- Dong, C., Skalak, R., Sung, K. L., Schmid-Schonbein, G. W., and Chien, S., Passive deformation analysis of human leukocytes, *J. Biomech. Eng.*, **110**, 27–36, 1998.
- Ebnet, K. and Vestweber, D., Molecular mechanisms that control leukocyte extravasation: the selectins and the chemokines, *Histochem. Cell Biol.*, **112**, 1–23, 1999.
- Fournier, R. L., *Basic Transport Phenomena in Biomedical Engineering*, Philadelphia: Taylor & Francis, 1999.
- Garcia, A. J., Ducheyne, P., and Boettiger, D., Quantification of cell adhesion using a spinning disk device and application to surface-reactive materials, *Biomaterials*, **18**, 1091–1098, 1997.
- Gifford, S. C., Frank, M. G., Derganc, J., Gabel, C., Austin, R. H., Yoshida, T., and Bitensky, M. W., Parallel microchannel-based measurements of individual erythrocyte areas and volumes, *Biophys. J.*, **84**, 623–633, 2003.
- Goldsmith, H. L. and Marlow, J. C., Flow behavior of erythrocytes. II. Particle motions in concentrated suspension of ghost cells, *J. Colloid Interface Sci.*, **71**, 383–407, 1979.
- Goldsmith, H. L. and Spain, S., Margination of leukocytes in blood flow through small tubes, *Microvasc. Res.*, **27**, 204–222, 1984.
- Goldstein, A. S. and DiMilla, P. A., Comparison of converging and diverging radial flow for measuring cell adhesion, *AIChE J.*, **44**, 465–473, 1998.
- Goldstick, T. K., *Diffusion of Oxygen in Protein Solution*, Ph.D. Thesis, University of California-Berkeley, 1966.

- Grandas, O. H., Costanza, M. J., Donnell, R. L., *et al.*, Effect of retroviral transduction of canine microvascular endothelial cells on beta(1) integrin subunit expression and cell retention to PTFE grafts, *Cardiovasc. Surg.*, **9**, 595–599, 2001.
- Herant, M., Marganski, W. A., and Dembo, M., The mechanics of neutrophils: synthetic modeling of three experiments, *Biophys. J.*, **84**, 3389–3413, 2003.
- Helmke, B. P., Sugihara-Seki, M., Skalak, R., and Schmid-Schönbein, G. W., A mechanism for erythrocyte-mediated elevation of apparent viscosity by leukocytes *in vivo* without adhesion to the endothelium, *Biorheology*, **35**, 437–448, 1998.
- Horner, M., Miller, W. M., Ottino, J. M., and Paoutsakis, E. T., Transport in a grooved perfusion flat-bed bioreactor for cell therapy applications, *Biotechnol. Prog.*, **14**, 689–698, 1998.
- Iiyama, K., Hajra, L., Iiyama, M., Li, H., DiChiara, M., Medoff, B. D., and Cybulsky, M. I., Patterns of Vascular Cell Adhesion Molecule-1 and Intercellular Adhesion Molecule-1 expression in rabbit and mouse atherosclerotic lesions and at sites predisposed to lesion formation, *Circ. Res.*, **85**, 199–207, 1999.
- Juaregui, H. O., Mullon, C. J. P., and Solomon, B. A., Extracorporeal artificial liver support, in *Principles of Tissue Engineering*, eds., R. P. Lanza, R. Langer, and W. L. Chick, Boulder, CO, R.G. Landes, pp.463–479: 1997.
- Kamada, H., Hattori, K., Hayashi, T., and Suzuki, K., *In vitro* evaluation of blood coagulation and microthrombus formation by a microchannel array flow analyzer, *Thrombosis Res.*, **114**, 195–203, 2004.
- Kapur, R. and Rudolph, A. S., Cellular and cytoskeleton morphology and strength of adhesion of cells on self-assembled monolayers of organosilanes, *Exp. Cell Res.*, **244**, 275–285, 1998.
- Karino, T. and Goldsmith, H. L., Aggregation of human platelets in an annular vortex distal to a tubular expansion, *Microvasc. Res.*, **17**, 217–237, 1979.
- King, M. R., Bansal, D., Kim, M. B., Sarelius, I. H., and Hammer, D. A., The effect of hematocrit and leukocyte adherence on flow direction in the microcirculation, *Annals Biomed. Eng.*, **32**, 803–814, 2004.
- King, M. R. and Hammer, D. A., Multiparticle adhesive dynamics: interactions between stably rolling cells, *Biophys. J.*, **81**, 799–813, 2001a.
- King, M. R. and Hammer, D. A., Multiparticle adhesive dynamics: hydrodynamic recruitment of rolling cells, *Proc. Natl. Acad. Sci. USA*, **98**, 14919–14924, 2001b.
- King, M. R. and Hammer, D. A., Hydrodynamic recruitment of rolling cells *in vitro*, *Biophys. J.*, **84**, 4182, 2003.
- King, M. R., Kim, M. B., Sarelius, I. H. and Hammer, D. A., Hydrodynamic interactions between rolling leukocytes *in vivo*, *Microcirculation*, **10**, 401–409, 2003.
- Kuharski, A. L. and Fogelson, A. L., Surface-mediated control of blood coagulation: the role of binding site densities and platelet deposition, *Biophys. J.*, **80**, 1050–1074, 2001.
- Kuo, S. C. and Lauffenburger, D. A., Relationship between receptor/ligand binding affinity and adhesion strength, *Biophys. J.*, **65**, 2191–2200, 1993.
- Lasky, L. A., Selectin-carbohydrate interactions and the initiation of the inflammatory response, *Annu. Rev. Biochem.*, **64**, 113–139, 1995.
- Lawrence, M. B., Kansas, G. S., Kunkel, E. J., and Ley, K., Threshold levels of fluid shear promote leukocyte adhesion through selectins (CD62L,P,E), *J. Cell Biol.*, **136**, 717–727, 1997.
- Lei, M., Kleinstreuer, C., and Archie, J. P., Hemodynamic simulations and computer-aided designs of graft-artery junctions, *J. Biomech. Eng.*, **119**, 343–348, 1997.
- Li, P. C. H., de Camprieux, L., Cai, J., and Sangar, M., Transport, retention and fluorescent measurement of single biological cells studied in microfluidic chips, *Lab Chip*, **4**, 174–180, 2004.
- Lomakina, E. B., Spillmann, C. M., King, M. R., and Waugh, R. E., Rheological analysis and measurement of neutrophil indentation, *Biophys. J.*, **87**, 4246–4258, 2004.

- Lominadze, D. and Mchedlishvili, G., Red blood cell behavior at low flow rate in microvessels, *Microvasc. Res.*, **58**, 187–189, 1999.
- Malek, A. M., Zhang, J., Jiang, J. W., *et al.*, Endothelin-1 gene suppression by shear stress: pharmacological evaluation of the role of tyrosine kinase, intracellular calcium, cytoskeleton, and mechanosensitive channels, *J. Mol. Cell Cardiol.*, **31**, 387–399, 1999.
- Michelson, I., *The Science of Fluids*, New York: Van Nostrand Reinhold Co., 1970.
- Miller, T. and Boettiger, D., Control of intracellular signaling by modulation of fibronectin conformation at the cell–materials interface, *Langmuir*, **19**, 1723–1729, 2003.
- Moffatt, H. K., Viscous and resistive eddies near a sharp corner, *J. Fluid Mech.*, **18**, 1–18, 1964.
- Nakashima, Y., Raines, E. W., Plump, A. S., Breslow, J. L., and Ross, R., Upregulation of VCAM-1 and ICAM-1 at atherosclerosis-prone sites on the endothelium in the ApoE-deficient mouse, *Arterio. Thromb. Vasc. Biol.*, **18**, 842–851, 1998.
- Neelamegham, S., Taylor, A. D., Shankaran, H., Smith, C. W., and Simon, S. I., Shear and time-dependent changes in Mac-1, LFA-1, and ICAM-3 binding regulate neutrophil homotypic adhesion, *J. Immunol.*, **164**, 3798–3805, 2000.
- Olla, P., Simplified model for red cell dynamics in small blood vessels, *Phys. Rev. Lett.*, **82**, 453–456, 1999.
- Ozturk, S., *Characterization of Hybridoma Growth, Metabolism, and Monoclonal Antibody Production*, Ph.D. Thesis, University of Michigan, Ann Arbor, 1990.
- Palacek, S. P., Loftus, J. C., Ginsberg, M. H., Lauffenburger, D. A., and Horwitz, A. F., Integrin-ligand binding properties govern cell migration speed through cell-substratum adhesiveness, *Nature*, **385**, 537–540, 1997.
- Peng, C.-A. and Palsson, B. O., Determination of specific oxygen uptake rates in human hematopoietic cultures and implications for bioreactor design, *Ann. Biomed. Eng.*, **24**, 373–381, 1996.
- Perktold, K., On the paths of fluid particles in an axisymmetrical aneurysm, *J. Biomech.*, **20**, 311–317, 1987.
- Pritchard, W. F., Davies, P. F., Derafshi, Z., Polacek, D. C., Tsao, R., Dull, R. O., Jones, S. A., and Giddens, D. P., Effects of wall shear stress and fluid recirculation on the localization of circulating monocytes in a three-dimensional flow model, *J. Biomech.*, **28**, 1459–1469, 1995.
- Ramos, C. L., Huo, Y. Q., Jung, U. S., Ghosh, S., Manka, D. R., Sarembock, I. R., and Ley, K., Direct demonstration of P-selectin- and VCAM-1-dependent mononuclear cell rolling in early atherosclerotic lesions of apolipoprotein E-deficient mice, *Circ. Res.*, **84**, 1237–1244, 1999.
- Sandstrom, C. E., Bender, J. G., Miller, W. M., and Papoutsakis, E. T., Development of novel perfusion chamber to retain nonadherent cells and its use for comparison of human “mobilized” peripheral blood mononuclear cell cultures with and without irradiated stroma, *Biotechnol. Bioeng.*, **50**, 493–504, 1996.
- Sank, A., Wei, D., Reid, J., *et al.*, Human endothelial-cells are defective in diabetic vascular-disease, *J. Surg. Res.*, **57**, 647–653, 1994.
- Schneck, D. J., An outline of cardiovascular structure and function, in *Biomedical Engineering Handbook, Vol. 1*, J. D. Bronzino, eds. CRC Press, 2000.
- Schnittler, H. J., Franke, R. P., Akbay, U., *et al.*, Improved *in vitro* rheological system for studying the effect of fluid shear-stress on cultured-cells, *Am. J. Physiol.*, **265**, C289–C298, 1993.
- Schoephoerster, R. T., Oynes, F., Nunez, G., Kapadvanjwala, M., and Dewanjee, M. K., Effects of local geometry and fluid dynamics on regional platelet deposition on artificial surfaces, *Arterioscler. Thromb.*, **13**, 1806–1813, 1993.
- Secomb, T. W. and Hsu, R., Motion of red blood cells in capillaries with variable cross-sections, *J. Biomech. Eng.*, **118**, 538–544, 1996.
- Shao, J.-Y. and Hochmuth, R. M., Micropipette suction for measuring piconewton forces of adhesion and tether formation from neutrophil membranes, *Biophys. J.*, **71**, 2892–2901, 1996.

- Simon, S. I., Chambers, J. D., and Sklar, L. A., Flow cytometric analysis and modeling of cell-cell adhesive interactions: the neutrophil as a model, *J. Cell Biol.*, **111**, 2747–2756, 1990.
- Sirois, E., Charara, J., Ruel, J., *et al.*, Endothelial cells exposed to erythrocytes under shear stress: An *in vitro* study, *Biomaterials*, **19**, 1925–1934, 1998.
- Slack, S. M. and Turitto, V. T., Flow chambers and their standardization for use in studies of thrombosis, *Thromb. Haemostasis*, **72**, 777–781, 1994.
- Smith, M. J., Berg, E. L., and Lawrence, M. B., A direct comparison of selectin-mediated transient, adhesive events using high temporal resolution, *Biophys. J.*, **77**, 3371–3383, 1999.
- Spillmann, C. M., Lomakina, E., and Waugh, R. E., Neutrophil adhesive contact dependence on impingement force, *Biophys. J.*, **87**, 4237–4245, 2004.
- Staben, M. E., Zinchenko, A. Z., and Davis, R. H., Motion of a particle between two parallel plane walls in low-Reynolds-number Poiseuille flow, *Phys. Fluids*, **15**, 1711–1733, 2003.
- Sugihara-Seki, M., Secomb, T. W., and Skalak, R., Two-dimensional analysis of two-file flow of red cells along capillaries, *Microvasc. Res.*, **40**, 379–393, 1990.
- Sullivan, S. J., Maki, T., Borland, K. M., Mahoney, M. D., Solomon, B. A., Muller, T. E., Monaco, A. P., and Chick, W. L., Biohybrid artificial pancreas: longterm implantation studies in diabetic, pancreatectomized dogs, *Science*, **252**, 718–721, 1991.
- Sung, L. A., Kabat, E. A., and Chien, S., Interaction energies in lectin-mediated erythrocyte aggregation, *J. Cell Biol.*, **101**, 652–659, 1985.
- Thompson, M. M., Budd, J. S., Eady S. L., *et al.*, Effect of pulsatile shear-stress on endothelial attachment to native vascular surfaces, *Brit. J. Surg.*, **81**, 1121–1127, 1994.
- Tilles, A. W., Baskaran, H., Roy, P., Yarmush, M. L., and Toner, M., Effects of oxygenation and flow on the viability and function of rat hepatocytes cocultured in a microchannel flat-plate bioreactor, *Biotechnol. Bioeng.*, **73**, 379–389, 2001.
- Tippe, A., Reininger, A., Reininger, C., and Rieß R., A method for quantitative determination of flow induced human platelet adhesion and aggregation, *Thromb. Res.*, **67**, 407–418, 1992.
- Truskey, G. A., Herrmann, R. A., Kait, J., and Barber, K. M., Focal increases in vascular cell adhesion molecule-1 and intimal macrophages at atherosclerosis-susceptible sites in the rabbit aorta after short-term cholesterol feeding, *Arterioscler. Thromb. Vasc. Biol.*, **19**, 393–401, 1999.
- Van Kooten, T. G., Schakenraad, J. M., Vandermei, H. C., *et al.*, Influence of substratum wettability on the strength of adhesion of human fibroblasts, *Biomaterials*, **13**, 897–904, 1992.
- Walker, G. M., Ozers M. S., and Beebe, D. J., Cell infection within a microfluidic device using virus gradients, *Sensors Actuators B – Chemical*, **98**, 347–355, 2004.
- Walpol, P. L., Gotlieb, A. I., Cybulsky, M. I., and Langille, B. L., Expression of ICAM-1 and VCAM-1 and monocyte adherence in arteries exposed to altered shear stress, *Arterioscler. Thromb. Vasc. Biol.*, **15**, 2–10, 1995.
- Waugh, R. E., Mantalaris, A., Bauserman, R. G., Hwang, W. C., and Wu, J. H. D., Membrane instability in late-stage erythropoiesis *Blood*, **97**, 1869–1875, 2001.
- Wechezak, A. R., Viggers, R. F., Coan, D. E., *et al.*, Mitosis and cytokinesis in subconfluent endothelial-cells exposed to increasing levels of shear-stress, *J. Cell Physiol.*, **159**, 83–91, 1994.
- Whitmore, R. L., *Rheology of the Circulation*, Oxford: Pergamon, 1968.
- Yamaguchi, S., Yamakawa, Y., and Niimi, H., Cell-free plasma layer in cerebral microvessels, *Biorheology*, **29**, 251–260, 1992.
- Zhao Y. H., Chien, S., and Weinbaum, S., Dynamic contact forces on leukocyte microvilli and their penetration of the endothelial glycocalyx, *Biophys. J.*, **80**, 1124–1140, 2001.

SUBJECT INDEX

- AC electric field, 157
AC electroosmotic flow, 157–163
acceleration pressure drop, 205, 218, 219
accommodation coefficients, 29–30, 57, 62, 71, 72, 74
accommodation pumping, 69–70
accumulation techniques, 54
adhesion molecules expression, 410–411
adiabatic air–water flow, 239, 244, 245, 248, 258, 263, 280
adiabatic flow, 232, 264, 272, 280, 281, 286, 288, 292, 294, 304, 353
adiabatic liquid–vapor studies, 288–290
adiabatic two-phase flow, 206, 306
air-side pressure drops, 228
air–water criteria, 239
air–water flow, 243, 244, 245, 251, 252, 273, 278, 292
air–water pair, 239
air–water studies, 291–294, 302–305
air–water tests, 289
annular film condensation, 324
annular flow, 192, 193, 197, 239, 240, 241, 244, 247, 248, 249, 250, 254, 258, 260, 262, 270, 271, 272, 274, 277, 280, 291, 321, 329, 332, 343
annular–wavy transition criterion, 255
annulus, 259, 299
apparent friction factor, 93, 94, 120, 127
applied electrical field, 163, 168, 170
area ratio, 297
Armand correlation, 272, 278, 279, 293
artificial cavity, 197
aspect ratio, 39, 52, 53, 73–74, 110, 145, 247–248, 263
augmented Burnett (AB) equation, 33
average electroosmotic flow velocity, 148, 150
average film velocity, 300
average gas bubble velocity, 305
average gas phase velocity, 305
average heat transfer coefficient, 318
average liquid film velocity, 322
average liquid velocity, 305
average wall shear, 41
axial coordinate, 39
Baroczy void fraction model, 302
BGK–Burnett (BGKB) equation, 33
binary intermolecular collision, 11–14, 36
bioartificial liver, 420–422
biomedical applications, 409
biomolecules, 409
bioreactors, 418–424
Blasius equation, 295, 302, 342
blood viscosity, 430
boiling number, 182
Bond number, 182, 184, 251, 289
boundary conditions, 18, 23, 25–28, 28–29, 49, 113, 159, 421, 424, 428
Bovine aortic endothelial cell, 414
Boyle–Mariotte’s law, 21
bridges, 246, 247
bubble, 177, 229, 230, 232, 239, 241, 246, 248, 249
bubble-free electroosmotic flow, 157
bubble growth, 176, 177, 180, 190, 191–192, 193, 194–195, 195–197
bubble length, 305
bubble nucleation, 176
bubble spacing, 249
bubble velocity, 299
bubbles coalescence, 244, 248, 293
bubbles collision, 248
buoyancy effects, 239
Burnett equations, 30–36

C coefficient, 304
C parameter, 288, 292, 293
caged fluorescent dye, 146
candidate applications, 227
capacitance sensors, 280
capillary bubble, 246
capillary forces, 240
capillary geometry, 413
capillary number, 182, 251–252
cell adhesion, 410, 411, 432
cell collisions, 415
cell density, 420
cell detachment, 424–429
cell mechanics and adhesion, 429–434
cell perfusion, 413
cellular uptake rate, 419, 420

- channel cross-section, 1, 40, 91, 98, 191, 193, 416
- channel diameter, 2, 175, 192, 244, 250, 251, 279, 304
- channel objectives, 1
- channel spacing variation, 416
- channel wall, 1, 91, 101, 139, 184, 193, 197
- channels, 116, 139, 250–253, 263, 264, 287, 292
- Chapman–Enskog method, 12, 36
- Chato correlation, 343, 347
- Chisholm correlation, 283, 286, 293
- Chisholm parameter, 287, 288, 292
- churn flow, 244, 249, 274, 275
- circular channel, 252
- circular microchannels, 244
- circular microtube heat transfer, 73
- circular microtubes, 39, 44–46, 73
- circular tube, 252
- classic boundary conditions, 22, 23
- classical correlations, 286–287
- Clausius–Clapeyron equation, 178
- collars, 246, 247
- collision models, 11–14, 14, 27
- collision rate, 11, 13, 14
- compact devices, 227
- compact geometries, 227
- compact layer, 138
- complex flow geometries, 410
- complimentary analysis technique, 146
- compressibility effect, 20, 42
- compressible flow, 73
- concentration field, 166, 167, 168, 170
- condensation, 227, 230–231, 232, 259, 260, 261, 288, 294–302, 339
- condensing flow, 254–263, 288, 306, 326
- confined bubble, 184, 189
- confinement number, 230, 293, 376
- conservation equations, 23, 24, 196
- constant of proportionality, 291
- constant-pressure technique, 54
- constant-volume technique, 54
- contact angle, 179, 253–254
- continuity equation, 24, 49, 153, 169, 426
- continuum assumption, 2, 14–17, 90
- continuum flow regime, 18, 22–23
- continuum NS–QGD–QHD equations, 24–25
- continuum theory, 3
- contraction coefficient, 203, 297
- control volume analysis, 299
- convection-diffusion equation, 421
- convection number, 182, 210
- conventional channel models and correlations, 314
- conventional tubes, 232, 265
- converging channel, 415–418
- Couette–Poiseuille flow, 299
- critical heat flux (CHF), 183, 194–195
- cylindrical region, 433
- Damkohler number, 421
- Darcy form, 301
- Darcy friction factor, 99, 103, 105, 302
- Debye–Huckel parameter, 141
- deep reactive ion etching (DRIE), 39
- Deissler boundary condition, 49, 53
- dense gas, 11, 25
- density ratio, 239, 321
- developing laminar flow, 92–95
- developing turbulent flow, 95–96
- diffuse layer of EDL, 138, 139
- diffuse reflection, 26, 28, 51, 70
- diffusion coefficient, 24, 153, 163, 165
- dilute gases, 11, 14, 25
- dimensionless film thickness, 349, 390, 391
- dimensionless length ratio, 421
- dimensionless Michaelis constant, 420
- dimensionless temperature, 72, 332, 343, 348, 349, 390, 391
- dimensionless translational velocity, 434
- direct simulation Monte Carlo (DSMC)
 - method, 12, 28, 36–37, 70
- dispensing process, 168, 170–171
- distribution coefficient, 276
- distribution parameter, 273
- Dittus–Boelter correlation, 317, 343
- diverging channel, 415–418
- drift-flux model, 267, 268, 273, 274
- drift velocity, 273, 276
- DSMC flow chart, 38
- dye-based microflow, 146, 171
- dye injection technique, 146
- dynamic diode effect, 66
- dynamic viscosity, 11, 14, 22, 75, 78
- eddy diffusive ratio, 322
- electrode double layer (EDL) field, 137, 138–139, 140, 142, 153, 158, 171
- electrokinetic mean, 151, 164
- electrokinetic micromixer, 166, 167

- electrokinetic mixing, 163–167
- electrokinetic process, 137, 139
- electrokinetic sample dispensing, 168–171
- electroosmosis, 137, 139, 147, 157
- electroosmotic flow, 139–145, 145–151, 151–156, 157–163
- electroosmotic pumping, 140
- electroosmotic velocity profile, 160, 161
- electrophoresis, 137, 151, 164
- energy accommodation coefficient, 27
- energy equation, 24, 70, 71, 73, 316, 318
- enhanced microchannels, 118–121
- enhanced microfluidic mixing, 163
- entrance effects, 41, 45, 63–64
- entrance loss, 203–206
- entrance region effects, 112, 116, 203
- Eotvos number, 241
- epifluorescence mode, 413
- equilateral triangular channels, 244, 293
- equivalent friction factor, 294
- equivalent liquid mass flux, 319
- equivalent mass flux, 319, 351, 352
- equivalent mass velocity, 294, 326, 339
- evaporation investigations, 185–188
- evaporation literature, 188–189
- evaporation process, 183, 185–188
- exit loss, 97, 98, 100, 101, 203–206
- extended hydrodynamic equation (EHE), 30–32
- extrapolation, 231, 232, 264
- falling-film condensation, 314, 315, 351
- Fanning friction factor, 90–91, 92, 95, 99, 103, 104
- film-bubble interface, 299, 349
- film condensation, 317, 323, 324, 325, 330, 333, 336, 337, 343, 344, 351
- film heat transfer coefficient, 316
- fin spacing ratio, 116, 117
- first-order slip boundary conditions, 25–28, 79
- first-order solution, 40–42, 44–46, 48–49
- floor distance to mean line, 104
- flow boiling, 175–176, 189, 195–199, 200–203, 206–207
- flow channel classification, 2–3
- flow cytometry, 431–432
- flow direction, 144, 177, 190, 421, 423
- flow field, 140, 151, 157, 163, 168, 169, 170, 331
- flow level angle, 316
- flow mechanisms, 231, 250, 251, 252, 253, 259, 306
- flow passage dimension, 88, 89
- flow patterns, 155, 184, 197, 231, 232, 240, 241, 243, 244, 250, 252, 254
- flow rate measurements, 54–56, 56–62, 57, 100, 394
- flow regimes, 231, 232, 233–238, 239, 240, 241, 244, 245, 246, 247, 248, 249, 251, 252, 253, 257, 259, 261, 262, 276, 298, 338, 354, 364, 365
- flow-related parameters, 231
- flow stabilization, 197–199
- flow visualization, 62, 146, 229, 239, 258, 259, 273, 331, 343
- fluid flow, 3, 5, 6, 9, 20, 37, 39, 53, 54, 57, 66, 87
- fluid properties effects, 239, 252, 258, 279
- fluid property exponents, 327
- fluid viscosity, 412, 429, 432
- fluorescence activated cell sorting (FACS), 431
- forced convection, 330, 333, 343, 351
- Fourier law, 22
- Fourier transform analysis, 191
- free molecular flow, 18, 30–37
- friction factor, 4, 41, 88, 90, 91, 93, 96–101, 104–108, 287, 294–295
- friction multiplier, 304
- friction velocity, 325, 326, 339, 348, 349
- frictional component, 293, 297
- frictional pressure drop, 4, 91, 94, 205, 220, 254, 270, 292, 294, 300, 305, 344
- frictional pressure gradient, 239, 331–332
- Friedel correlation, 292, 295, 377
- Friedel correlation modification, 290, 295, 377
- Froude number, 254, 271, 360, 378
- Froude rate parameter, 271, 280
- fully developed laminar flow, 4, 91–92, 105, 109–110, 127, 216
- fully developed turbulent flow, 95
- future research needs, 74
- Galileo number, 254, 315, 317, 358, 360–361
- gas at molecular level, 10–14
- gas flow, 20, 39, 44–53, 57, 65, 232
- gas superficial velocity, 244, 274, 317, 343
- gas velocity, 254, 256, 273, 355, 356
- geometry-dependent constants, 297–298
- geometry optimization, 116–118
- gravitational drag, 271, 280
- gravitational pressure drop, 206

- gravity-dominated film condensation, 324, 351, 352
- gravity-driven condensation, 255, 314–318
- Green's function approach, 159
- greenhouse gas emissions reduction, 227
- Hagenbach's factor, 93, 94, 98, 125, 130
- Hagen–Poiseuille velocity profile, 45, 91, 92
- hard sphere (HS) model, 12
- heat dissipation, 87, 89, 116, 346
- heat exchanger advantages, 115
- heat removal system, 87
- heat transfer, 3–5, 70–74, 88–89, 109–116, 184, 199–203, 219, 307–313, 327, 352
- heat transfer coefficient, 4, 175, 227, 228, 265, 306, 314, 316, 322, 330, 331, 339, 340, 342, 349, 381
- heat transfer mechanisms, 184, 192, 193
- hematopoietic blood cell culture, 418–420
- hematopoietic stem and precursor cells (HSPC), 418
- hepatocytes, 422
- heterogeneous microchannels, 151–156, 167
- high aspect ratio, 247–249
- high heat fluxes, 175, 206–207, 227
- high heat transfer rates, 227
- high quality annular flow, 184, 192
- higher-order slip boundary conditions, 28–29
- homogeneous boundary condition, 159
- homogeneous flow model modification, 289
- homogeneous mixture, 323
- homogeneous void fraction empirical fit, 278
- human systemic circulation, 430
- hydraulic diameter, 2, 3, 4, 93, 142, 144, 177, 261–262
- hydraulic coupling, 228–229
- ideal gas, 21–22
- ideal refrigerant characteristics, 207
- incident neutron beam, 241
- incompressible flow, 38, 43, 71–73
- incremental pressure defect, 93
- inertia-controlled region, 196
- inertia forces, 182, 192, 276, 291
- infinitely long waves, 240
- inlet mixing effects, 250
- instability, 184, 190, 192, 195
- instantaneous 2-D void fraction profiles, 275
- instantaneous void fractions, 274
- insulin dependent diabetes mellitus (IDDM), 418
- interface velocity, 299, 305, 320, 322, 348
- interfacial friction factor, 285, 301, 302, 349, 381
- interfacial shear stress, 289, 301, 319, 324, 331, 348, 349, 391
- interfacial velocity, 320
- intermittent flow, 241, 261, 263, 272, 298, 336
- internal flows, 90
- internal membrane oxygenator, 421
- inverse power law (IPL) model, 11–14, 16, 22, 44
- inverted systems, 412–415
- isolated bubble, 184, 189
- Jakob number, 183
- Kelvin's theorem, 426
- Kelvin–Helmholtz instability, 240
- kidney, 1, 6, 418
- Knudsen analogy, 17–18, 23
- Kundsen number, 16, 20–21, 22, 27–33, 36, 42, 49, 72, 75–81
- Kutateladze number, 317, 327
- lab-on-a-chip device, 137–139, 151, 163, 168
- lactate transport, 422–424
- Lame coefficient, 22
- laminar condensate film, 314–316, 319
- laminar film condensation, 323–324
- laminar flow, 20, 88, 91–92, 92–95, 98, 103, 105, 108, 109–110, 112–114, 127, 133, 175, 200, 208, 304, 344, 375
- laminar region, 4, 99, 105, 108, 302
- laminar-to-turbulent transition, 101–102, 108–109
- laminar-transition-turbulent correlation, 293
- laplace constant, 229
- lattice Boltzmann method (LBM), 30, 37
- law of resistance, 103
- leukocytes, 410, 430
- linear concentration profile, 420
- linear double layer analysis, 157
- linear interpolation, 94, 101, 109, 123, 124, 200, 255, 302, 310, 315, 322, 328, 334
- linear velocity profile, 319
- linearized analysis geometry, 426–429
- linearized analysis of uniform flow, 426–429
- linked shutoff valves, 272, 280

- liquid bridge, 237, 250, 253
- liquid entry channel, 176, 203
- liquid flow at microscale, 87
- liquid flux, 319
- liquid lumps, 241, 253
- liquid phase, 241, 250, 256, 271, 286, 294, 302, 320
- liquid pool heat transfer coefficient, 316
- liquid pool level angle, 316
- liquid ring flow, 250, 253
- liquid ring motion, 253
- liquid slug, 176, 249, 253, 277, 278, 291, 293, 298, 299, 300, 304
- liquid volume fraction, 247, 328
- little rarefied regime, 57
- liver, 418
- loading process, 168, 170
- local friction pressure gradient, 204
- local heat transfer coefficients, 124–125, 184, 338, 344–346
- local rarefaction number, 18
- Lockhart–Martinelli correlation, 232, 270, 286, 288, 291, 292, 293
- Lockhart–Martinelli parameter, 232, 271, 280, 329
- Lockhart–Martinelli two-phase multiplier, 286, 294, 304, 318, 320, 321, 325
- long-term cell culture, 418
- lubrication approximation, 415–418
- lyse, 6

- Mach number, 16, 20, 27, 38
- MAD simulation, 411
- Martinelli parameter, 182, 204, 254, 255, 265, 271, 286, 302, 322, 349
- mass flow rate, 41, 42, 43, 51–53, 54, 56, 57
- mass flux, 24, 31, 195, 199, 231, 232, 244, 254, 257–258, 259, 260, 261, 271, 272, 289, 317, 320, 335, 345
- mass transfer, 1, 6, 70, 88, 354, 420–422, 437
- maturation of red blood cells, 416
- maximum profile peak height, 103
- Maxwell molecules (MM) model, 13
- mean film velocity, 320
- mean free path, 10, 11, 13, 14, 16, 62
- mean heat transfer coefficient, 345
- mean liquid velocity, 272
- mean space of profile irregularities, 104
- mean volumetric flow rate, 56
- method of moments, 36
- Michaelis constant, 420
- Michaelis–Menten kinetics, 420, 424
- micro electro mechanical systems (MEMS), 9, 139
- micro particle image velocimetry (micro PIV), 145–146, 203
- microcapillaries, 429–434
- microchannels, 89, 96–102, 116–118, 146, 227–230, 277–279, 347, 350, 415, 421
- microcirculation, 430
- microfabrication technology, 117, 119
- microfin tubes, 88, 272, 290, 294, 339–342
- microfluidics, 5, 9, 10, 94, 95, 168
- microgravity, 249–250, 276–277
- micro-grooved minichannel, 422–424
- micromachining technologies, 139–140
- micron-sized pipettes, 409, 432–433
- microscale, 2, 5–6, 68, 87–88, 97, 411–412, 425, 431
- microscopic length scales, 10–11
- minichannel geometry optimization, 116–118
- minichannel membrane bioreactor, 419
- mist–annular transition, 256, 328
- mixture density, 287, 320
- mixture viscosity, 323
- mixture volumetric flux, 273
- modeling fluid flow, 2
- modified enthalpy of vaporization, 314
- modified Friedel correlation, 332
- modified Froude number, 255, 317, 355
- modified Miller equation, 105–106
- molecular mechanisms, 410
- molecular tagging velocimetry (MTV), 62
- momentum coupling decrease, 304, 393
- momentum diffusivity, 325
- momentum equation, 24, 39, 43–44, 47, 48, 49, 50, 70, 71, 78
- multi-regime condensation, 327
- multilouver fins, 228
- multiple-flow-regime model, 303, 331
- multiple streams short paths, 115

- nanomolar concentrations, 409
- narrow rectangular channels, 275
- Navier–Stokes equation, 18, 22–23, 63, 423, 432
- near-azeotropic blend, 257
- negative subcooling, 180, 181
- Nernst–Planck conservation equation, 152, 153, 155
- nested Moffatt eddies, 422
- net enthalpy fluid change, 314

- neutron radiography, 241, 273, 274, 280
Newtonian fluid, 22, 49, 90
nitrogen–water flow, 250, 251, 278, 304
non-dimensional numbers, 181–184
non-wetting system transitions, 253
normal forces generation, 424–429
novel technique, 157
nucleate boiling absence, 322
nucleation, 176–181, 194, 197–199
Nusselt film condensation, 316
Nusselt number, 4, 72, 73, 91, 92, 109–110, 111, 112–113, 115, 118, 120, 123, 124, 129, 133, 208, 314, 315, 318, 319, 321, 324–326, 340, 344, 385, 387–388
- offset strip-fins, 117, 118
Ohnesorge number, 182
one-dimensional diffusion equation, 419
onset of nucleate boiling (ONB), 180
optical distortion effects, 250
original vapor core flux, 319
orthogonal Hermite polynomial, 36
outlet Knudsen number, 42, 43–44, 53, 58–62
overlap zones, 251, 255
oxygen, 419, 420, 421, 422–424
ozone depletion, 227
- pancreas, 418
parabolic velocity profile, 300, 413
parallel channel instabilities, 190
parallel-plate cell perfusion chambers, 412
parallel-plate flow chamber, 411
parameters combination, 293
particle deposition, 411
particle transport in rectangular microchannels, 433–434
peak flow velocity, 157
Peclet number, 153, 165, 167, 421
photo-injection process, 146
physical property corrections, 239
pipe diameters, 232, 239
planar microchannels, 420–422
plane flow between parallel plates, 39–44
plane microchannel, 71–73
plug, 139, 232, 240, 244, 246, 248, 291, 293
Poiseuille flow, 41, 299, 415, 416, 424, 434
Poiseuille number, 41, 43, 47, 92, 105
Poisson–Boltzmann equation, 138, 139, 140, 158
polydimethylsiloxane (PDMS) plate, 166
polymerase chain reaction (PCR), 5
- potential flow near infinite wall, 425–426
power law profile, 299
practical condensation process, 258
practical cooling systems, 206–207
Prandtl mixing length, 257, 288, 325
Prandtl number, 28, 72, 315, 319, 322
pressure change, 296, 297
pressure data, 62
pressure distribution, 42, 46, 53, 429
pressure-driven flow, 416
pressure-driven steady slip flows, 37
pressure drop, 3–5, 90–96, 195–196, 198, 203–206, 231, 239, 254, 281, 282–285, 286, 288, 289, 290, 291, 292, 293, 298, 299, 300, 301, 302, 334, 371, 377, 417, 418
pressure fluctuation, 65–66, 184, 190, 191, 239
pressure gradient, 249, 294, 299, 316, 321, 340
pressure loss, 203, 300
primary resistance heat transfer, 289, 327
probability density functions (PDFs), 276, 277
property ratio method, 115–116
pulsed gas flows, 65–67
- quadratic interpolation, 337
quasi-gas dynamic (QGD) equation, 23, 24–25
quasi-hydrodynamic (QHD) equation, 23, 24–25
quasi-steady state time periodic solution, 160
quiescent vapor, 323, 324
- radial cell perfusion chambers, 412
radial flow chamber, 411
radial membrane minichannels, 418–420
radial position, 412
rarefaction in microflows, 10, 17–18, 20
rarefied flows, 37, 67
reactive ion etching (RIE), 39
rectangular channel, 91, 184, 189, 247–249
rectangular microchannel, 47–53, 73–74
red blood cells (RBCs), 415, 430
refractive index matching, 250
refrigerant charge prediction, 271
refrigerant condensation, 239, 296, 303
regimes flow classification, 18
relative roughness, 88, 102, 103, 113
replacing process, 148–151
representative distribution, 274
reversed diode effect, 67
reversed flow, 195

- Reynolds number, 4, 20, 27, 96, 250, 251, 254, 256, 287, 288, 293, 294, 299, 302, 314, 315, 318, 319, 322, 323, 326, 328, 339, 342, 355, 371, 388, 424
- ring-slug flow pattern, 252
- rough tubes, 109
- roughness, 102–109, 113–114
- sampling volume, 14, 15–16
- scaling equation, 289
- Schmidt number, 24
- second-order solution, 42–44, 46, 49–53
- selectin–carbohydrate bond, 410
- semi-triangular microchannels, 244
- separated flow multiplier, 204, 297
- Shah correlation, 322–323
- shear balance, 299
- shear-driven condensation, 318–327
- shear plane, 138
- Sherwood number, 421
- simple gas, 10
- single phase electrokinetic flow, 137
- single-phase friction factor, 287, 290, 291, 293, 294, 300, 342
- single-phase gas flow, 9
- single-phase liquid flow, 87, 90–96, 102–109, 177, 209, 279
- single-phase velocity profiles, 248
- single stability criteria, 240
- slip, 18, 23–30, 53, 54, 58, 61, 65, 72, 265, 270, 275, 276, 279
- slug, 176, 232, 239, 242, 244, 246, 247, 249, 250, 253, 291, 293, 299, 300
- slug–annular flow, 244, 277
- slugging, 240
- Soliman-modified Froude number, 258
- species transport, 151, 164
- specular reflection, 26
- stabilizing effects of surface tension, 240–241
- Stanton number, 118, 121
- statistical fluctuation level, 15
- steady-state time period, 160, 161
- steam–water flow, 252
- stratified flow, 239, 240, 241, 247, 254, 257, 271, 280, 288, 301, 314, 318, 327, 333, 336, 339, 343
- stress tensor, 22
- subcooled entry, 176
- subsonic flow, 20
- superficial gas phase velocity, 255, 274, 317
- superficial liquid phase friction factor, 318
- superficial liquid velocities, 244, 274, 302, 317
- superficial velocities, 246, 249, 250
- supersonic flow, 20
- surface area-to-volume ratios, 227, 228
- surface effects in small channels, 253
- surface heterogeneity, 151
- surface phenomena, 230
- surface properties, 253–254
- surface tension, 184, 240, 246, 247, 250, 253, 279, 293, 302, 335, 340
- surface wettability effects, 254
- system energy efficiencies, 227
- Taitel–Dukler model, 240, 242, 248, 250, 254, 255
- tangential momentum accommodation coefficient, 26
- Taylor bubble, 249–250, 276
- temperature jump distance, 27, 72
- thermal amplification technique, 345, 346
- thermal boundary condition, 113
- thermal conductivity exponent, 327
- thermal entry length, 110
- thermal neutrons, 241
- thermal resistance, 315, 318–319
- thermal transpiration, 68
- thermally developing flow, 110–111
- thermally driven gas microflows, 67–70
- thermodynamic equilibrium, 14–17, 323
- three flow pattern, 184, 189
- time-averaged 2-D void fraction, 275
- time periodic electroosmotic flow, 157
- total pipette length, 433
- total slug volume, 247
- trafficking, 410
- transient cell adhesion, 410–418
- transient stage velocity, 162
- transition criterion, 230, 250, 255
- transition flow, 18, 30–37
- transition mass flux, 333
- transition regime, 255, 328
- translational kinetic temperature, 21
- transpiration pumping, 68–69
- transport process, 1
- triangular channel, 246
- T-shaped microfluidic mixing system, 163
- tube diameter, 195, 199, 204, 232, 241–242, 273, 288, 292, 300, 323, 329, 349, 392, 393
- tube inclination, 316
- tube shape effects, 240–241, 262, 338
- tumbling regime, 151

- turbulent dimensionless temperature, 348, 349, 391
turbulent film, 322, 323–324, 348–349
turbulent flow, 20, 95–96, 103, 115–116, 199, 205, 265, 266, 375
turbulent region, 104, 106, 204, 302
turbulent vapor core, 289, 321, 324, 348, 375
two-phase entry, 176, 203
two-phase flow, 3, 181, 183, 190, 194, 212–214, 230, 231, 232, 239, 240, 241, 246, 247, 249, 250, 263, 274, 293, 294, 305, 351
two-phase horizontal flow patterns, 239
two-phase mixture density, 287, 373
two-phase multiplier, 204, 214, 232, 286, 288, 290, 291, 293, 294, 304, 317, 318, 321, 326, 329, 330, 332, 343, 361, 372, 373–379, 388
two-phase pressure drop, 182, 206, 214, 216, 232, 286, 294, 295, 297, 332, 378, 379
two-phase pressure gradient, 294, 372, 373, 375, 376, 377
typical flow parameters, 430
- uncaged dye images, 147
unit cell for intermittent flow, 298
unstable wavelength, 247
- vacuum generation, 9, 18, 67–70
vapor bubble growth, 194, 195
vapor-cutback phenomenon, 194
vapor friction force, 319
vapor kinetic energy, 271, 280
vapor–liquid quality, 232
vapor mass flux, 325
vapor phase inertia, 256
vapor shear, 314, 315, 316, 318, 323, 337, 339, 340, 351
variable hard sphere (VHS) model, 12
variable property effects, 115–116
variable soft sphere (VSS) model, 12
velocity distribution, 40, 43, 45, 47, 72, 73, 77, 78, 79, 93, 270
velocity gradient direction, 423
velocity ratio, 320
vertical equilateral triangular channels, 244
viscosity ratio, 239, 295
viscous dissipation, 24, 101
viscous effect, 20, 101
viscous stress tensor, 22, 30
visualization methods, 146, 171
void fraction, 231, 244, 246, 247, 249, 265, 266–269, 272, 273, 274, 275, 276, 277, 280, 281, 291, 321, 334–335, 351, 353, 366–371
void fractions for air–water flow, 273, 278, 280
volume ratio, 1, 193, 270, 342
volumetric flow rate, 56, 140, 144, 145
volumetric flux, 273, 276
volumetric quality, 248
volumetric void fraction, 273, 274, 276, 279, 280
von Karman analogy, 315, 316, 318
von Karman universal velocity profile, 254, 270, 319
- wall effects in microflows, 10, 18–20
wall shear, 90, 239, 250, 254, 279, 315, 318, 320, 321, 322, 324, 339, 411, 412, 415, 422, 437
wall temperature difference, 208, 319, 320, 323
Wallis dimensionless gas velocity, 254
wavy–slug transition, 255, 311
Weber number, 183, 249, 250, 251, 256, 289, 295, 332, 340, 342, 360, 361, 369, 377, 379
wetting liquid, 240
wide range qualities, 258
Wilson plot technique, 339, 340, 344, 353
- Yan and Lin correlation, 201, 342
- zeroeth order oxygen uptake, 422
zeta potential, 138, 140, 142, 144, 165, 172
Zivi correlation, 266, 317, 321, 330, 367
Zivi void fraction, 266, 280, 321, 327, 333, 340, 343, 351, 370, 386